

國立臺灣大學工學院應用力學研究所

博士論文

Institute of Applied Mechanics

College of Engineering

National Taiwan University

Doctoral Dissertation

CMOS-MEMS 振撞共振器

CMOS-MEMS Vibro-Impact Resonators

蔡淳樸

Chun-Pu Tsai

指導教授： 李尉彰 博士

Advisor: Wei-Chang Li, Ph.D.

中華民國 115 年 1 月

January 2026

doi:10.6342/NTU202600018

國立臺灣大學博士學位論文
口試委員會審定書

DOCTORAL DISSERTATION ACCEPTANCE CERTIFICATE
NATIONAL TAIWAN UNIVERSITY

CMOS-MEMS 振撞共振器

CMOS-MEMS Vibro-Impact Resonators

本論文係蔡淳樸（D08543001）國立臺灣大學應用力學研究所完成之博士學位論文，於民國 114 年 12 月 17 日承下列考試委員審查通過及口試及格，特此證明。

The undersigned, appointed by the Institute of Applied Mechanics on 17th December, 2025 have examined a Doctoral Dissertation entitled above presented by CHUN-PU TSAI (D08543001) candidate and hereby certify that it is worthy of acceptance.

口試委員 Oral examination committee:

李尉彰 李尉彰 （指導教授 Advisor）

張培仁 張培仁

方維倫 方維倫

李昇憲 李昇憲

李銘晃 李銘晃

曾聖翔 曾聖翔

李世偉 李世偉

葉勝凱 葉勝凱

所長 Director: 陳瑞琳 陳瑞琳

doi:10.6342/NTU202600018

致謝

碩加博總共十年光陰。我花費莫大的心力，某些能力卻仍沒得到想要的成長。我似乎還是難以從容面對人與人之間的溝通。或許對於同儕間的合作我是感到愉快的，但一遇到長輩、主管、或甚至在給各個教授寫信，都覺得躊躇難展。常覺得自己是個生活白癡，需要感受數天到數周才可以想好決定。記憶力差到幾乎不能吵架、開會也是經常迷思方向，講完一句話就忘記剛剛討論的點是甚麼，凡事都必須有黑板與紙筆才能進行。另一方面，我還是對自己的英文有一定程度的自卑，還有很大的進步空間。就在此立下一個戳記，看看未來將有甚麼變化吧。

—幸運地是，我至少對事物的批判與思維有了徹底的改變。

傅校長有一句讓我記憶很深的句子:「一天只有二十一小時，剩下三小時是用來沉思的」。寫博士論文是一個很有趣的過程，它得以讓我好好的思考並回味、整理我腦中的思緒。已經連續兩年未實際投稿國際會議與下線，讓我花了更多的時間思考人生，也花了更多時間學習新知，為下一個階段任務作準備。對短期未來的想像在博士論文撰寫的過程中，慢慢的清晰了起來。或許還有許多懵懂無知，但總是可以多唸唸書，多看看，思考思考。

有鑑於常看到米蘭理工大學微機電領域相關博士論文多半是不公開的(可能是因為與意法半導體的商業合作)，老實說原本博士論文是想寫中文的。希望自己學了很久的內容得以在台灣以母語這種比較輕鬆地方式好好散播。另一方面，寫成中文就不會有相似性抄襲的問題(?)。但同時也希望自己的觀念可以幫助到相關領域的一些人。最終，這篇論文可能只有致謝可以用中文來分享。因此，我希望在致謝給讀者一些我的想像，分享些經歷。感謝你/妳對我的論文有興趣、感謝過去幫助過我的人並給讀者些點鼓勵。

我想大部分的博士，日子都過得不好，我們並不是每天都樂在其中。或者

doi:10.6342/NTU202600018

說，縱使博士生涯大部分是有趣的，有時還是無可避免地—乏味、令人困惑甚至沮喪。整個博士生涯沒有幾篇期刊論文，但都長的不行，最驕傲與最喜歡的兩篇，莫過於 *JMM* 的回顧與 *JMEMS* 的碰撞特性分析這兩篇。有紀錄的日子，一篇從 2021/12/8 寫到 2023/04/09 遞出並於 2023/05/31 經過一次修改後於 2023/08/08 發表；一篇則從 2023/12/29 寫到 2025/05/30 遞出並在 2025/7/28 經過一次修改後於 2025/09/02 被接受發表。實在是，很冗長，快樂不起來。若把這個過程: 學習、思考、融合、產出、寫論文比喻成作畫或書寫，那結果肯定是只有某些人可以欣賞地—亂七八糟又—精彩萬分。想像，下筆或沉著細膩或刻意塗抹地，上上下下將幾份白紙塗黑、揉煉、交雜一起，心境還真是難描述(你心裡有畫面嗎?)，這筆這麼深那麼醜，有些又淺的不可思議，到底怎麼塗的? 在幹嘛?

—在學甚麼? 在試甚麼? 方向對嗎? 好是掙扎。

—偶爾逃避、偶爾堅持，完成那些我難以達成的事情。

—摁...即使可能只有我面對這問題如此掙扎，痛苦又快樂的堅持著，哈。

細部地論述，我認為研究不是一個線性的過程，我常常發散到其他領域，包含光學、電磁學、自動控制、半導體元件物理、量子力學、波動力學、流體力學、有限元素等領域，這邊撇一下那邊描兩圈，饒是有趣。我有時覺得這樣縮短/浪費了好好鑽研的時間，也可能是這樣所以我唸了好久，但我實在沒辦法一直在想不到的答案上思考，他們這麼有趣又有這麼多共通的地方! 儘管常常感到慌張，我還是認為這樣的行為幫助我創造力很多。此外，對於那些比較深邃的內容，學習過程常是痛苦的，讀了又讀，很可能還是看不懂。因此我傾向「好讀書，不求甚解」的心態。多讀、多看、多查，看不懂就繼續看，放下心來看，別馬上把同一篇重複看，看一篇不夠看三篇，看三篇還不夠就再看五篇，過一陣子再回去查查，再回來看看，腦袋會在一個奇怪的情況下，就學會了!

doi:10.6342/NTU202600018

另一方面，我認為，那些有意義的事情/題目大部分就等於困難的事情，又有時候這些創意是突然就出現的，我們能做的就是抓到時間就思考思考，花大量的時間投入，總是會有東西出現的。這份挑戰，可能因為每個人能力的不同而有不同的意義，很可能我的龐大努力對某些人來說不過是三天工夫。我只希望能在自己的能力階級盡所可能的突破—那就是最完美的了。對這些工作的熱情彷彿說著:「盡情的折磨自己吧! 那將是做好的選擇!」

回往今生，不得不承認有時候我們很難做出所謂的「好的選擇」，畢竟做選擇的時候，我們沒辦法每個都經歷過，再回頭做選擇。當然，也沒有甚麼後悔的餘地。因此我的觀念是，不如讓所做的每個決定變成正確的決定—每個選擇都是最好的! 有時候，做選擇是下「決心」，有時候，卻只是下「興趣」。人非聖賢，我也非強者，所以至少我，大部分都只能下「興趣」，而「興趣」與「決心」的差別在於: 下「決心」時可以做出較多的犧牲，你可以不運動、不睡覺、不娛樂、不休閒，提分手(?) ，但你就是要完成某些事情。而不是找藉口表示只是「興趣」，可以放棄。因此，我首先想謝謝自己，縱使做了很多次「興趣」，但也成功做了幾次「決心」。在我的程度好好地提出了一些有趣也有用的東西。我想，我們不需要每次都下「決心」，放寬心反而走的久，但只要十次選擇中得以做出幾次，就很好了。有時候做「興趣」，也是很重要的，就玩玩兒吧! 若把這個思維延伸，我也鼓勵常常給自己下挑戰，這周我要寫完甚麼甚麼、我要弄懂甚麼甚麼或要量測完甚麼甚麼，即使沒有次次成功，若能成功一兩次，玩一玩，也很是完美了。

最後，你一定很常聽到大家四年畢業，甚至聰明過人者三年畢業。儘管我也被許多學長姐叮嚀過，我還是唸了好久。說起來沒甚麼說服力，但我會鼓勵讀者從入學前，找老師時，就開始想著如何即早畢業。我覺得我已經十分努力了，但沒做到，或許方向不對，值得檢討，或許這就是這個當下該發生的樣貌。但身為過來人，我知道，第五年、第六年與接近最後一年時，是十

doi:10.6342/NTU202600018

分令人恐慌與不安的，你不知道該幹嘛來挽救人生，頻繁失眠、日夜顛倒且非常疲倦，逃避現實後開始大量運動/爬山/健身嘗試恢復一切，最快樂的時候是為自己的租屋處大掃除(喔!我終於有用了!)，我覺得對身心都不健康，共勉之。(BTW, 好像大部分博士都懂打掃租屋處的感覺，笑)

在學研塗塗抹抹的過程中，指導教授—李尉彰教授扮演著特別地角色。遙想 RESOLAB 當年，為了實驗室成長與學生的教育，我們有很多深度的交流。我花了十年經歷天秤[1]擺盪的混沌(chaotic)行為，並了解這是所謂的命定混沌(deterministic chaos)[2]。想要好好地感謝您將那些注重細節、深入淺出、學術就該做秀—請把大便寫成黃金的思維刻入我的思維，影響我的餘生。也想讓您知道，自由的學風一直是我在這快樂的泉源。除了在研究經費上的資助之外，這些發表有很大部分是基於您的文采與數次指導而成功地。那些有趣的研究題目也多半是基於您與我不同—跳脫性的思考。若您可以不要那麼忙，多幫助我一點論文寫作，下輩子再謝謝您一次，哈哈。阿，如果不要每次都已讀我一個禮拜，我也會覺得很不錯，笑死。最後，想請您感到驕傲，您的第一個博士班學生終於要畢業了。我們一起創造了許多實驗室的回憶，奠定了許多基礎資源，陪伴了許多人經歷挫折、成長最後離開實驗室(不是離開人世真是太好了?)。RESOLAB 將是我們永遠的家，這裡的回憶通常很累，但有人一起成長、一起熬夜、一起被幹成白癡、一起快點回「收到，謝謝老師!」，真的是很棒的回憶。引用「How will you measure your life? by Clayton Christensen, James Allworth and Karen Dillon」的一句話:「I think that's the way

[1] 比喻(1)指導教授本人，與(2)人生總是在做選擇，評量好壞，但其實長期結果不可預測。
[2] 於非線性動力學中，命定混沌常被縮寫為混沌，用以描述某種系統其穩態響應對初始條件極度敏感，使得任何於初始條件上的微小變化終使系統達到不同的穩態。然而，這樣的系統不代表其為隨機(random)系統，事實上系統仍是有序(order)的，且其短期預測(short-term predilection)是可執行的。此處借翻譯字「命定」與非線性名詞「混沌」轉喻(1)老天爺決定的有趣的緣分、(2)實驗室早期成立模糊不清的狀態、(3)指導教授的決策行為與(4)與非線性動力學的緣分。

doi:10.6342/NTU202600018

it will work for us all. Don't worry about the level of individual prominence you have achieved; *worry about the individuals you have helped become better people*.」。這裡有許多傳承，也因此有很多人受惠且變厲害，變堅韌，培養出自信，發現自己可以做到某些事情，並進入好的公司，為世界的推進發揮一點功用。這將是您對世界最大且無可取代的貢獻，它明確表示了您的成功。

令人感到興奮與緊張的另一部分，除了感謝替我擋招並協助我在緊張中梳理問題的指導教授，我想感謝口試委員: 張培仁老師、方維倫老師、李昇憲老師、李銘晃老師、李世偉博士、曾聖翔博士與葉勝凱博士撥冗前來擔任口試委員。我的老天，我幾乎是看著各位的碩博士論文乃至期刊發表長大的，前輩們的觸及領域囊括了好大一部份的微機電，能有幸邀請到各位擔任口試委員真的是我的榮幸。這場長達數小時的討論與問答，不僅完善了這本論文的架構，更對學生思辨與生涯方向有所幫助。

感謝方維倫老師對於微機電元件於物理極限的深刻提點。您關於「天險」與微機電馬達在磨耗以及應力對建模影響的討論，讓我重新審視了共振開關的工程價值；或許我現在並沒有很好的答案，也對元件壽命的到底應該要多長才夠用沒有明確的定義。但我會將元件應用在其物理限制的思索放在心上，持續思考。感謝李昇憲老師對於我在建模研究投入肯定，特別是您提到附錄內容對於實驗室學弟妹具有參考價值，是對我莫大的鼓勵，也是我當初花心思寫下來所想達成的 。感謝您對於 RF MEMS switch 發展歷史與應用限制的宏觀探討，以及針對平台選擇、材料優化與驅動機制的專業建議。想特別讓您知道，您的評語:「我認為以一個博士論文來說，你可以是工程落地，也可以是非常科學或甚至是模擬取向的，*所以不用改變你自己喜歡的東西*。」對我有碩大的影響。有一種在自己肯定自己前，被敬仰的人肯定的感覺，很是幸福。感謝張培仁老師以創業家的角度提出「致命的問題」。我會記得您在口試最後的諄諄教誨: 「很好，你如果自己去創業的話，我問你在困難回答

doi:10.6342/NTU202600018

的問題，你都不可以退縮喔!」。感謝李銘晃老師在理論驗證上的嚴格把關。您問了許多很細緻的問題，從鋁材料楊氏係數的數值逆算，到 IF Bandwidth 對量測結果的影響，這些細節的探討讓我深刻體會到資深 MEMS 人對這些細節的要求與注意。也想誠懇地感謝您在信件中的鼓勵與支持。感謝曾聖翔博士針對模型「預測力 vs. 解釋力」的靈魂拷問，讓我更進一步思考了量產時製程變異與量測手法對理論模型的影響與挑戰。最後，不僅僅於下方所列內容，但想特別感謝葉勝凱博士與李世偉博士在論文架構與寫作細節上的悉心指導。兩位的建議與邏輯梳理，讓整本論文的敘事更加系統化；對於模型準確度的釐清以及應用面的反思，以及對文中錯字與引用格式的細心確認，都讓這份論文更臻完美 。

於另一個長期的層面上，我想感謝張培仁教授與胡毓忠教授於每周會議對我的研究提出寶貴的建議與思維。胡老師總是很愛方程式，我們常常停留在方程式那頁很久，讓我記憶很深。雖然我們的交流說不上非常地多，但您總是很穩定與開朗，笑笑地面對許多事情。我會記得您勇敢的背影與您的指導。我很崇拜張培仁教授，經過好幾年團隊會議，有時候我會變得焦躁，想要趕緊結束攏長又多到不行的每周會議。但張老師每每都會將會議帶到一個很有教育意義的高度。例如，在一些會議的預口試環節，張老師會鼓勵大家做得很好(他們真的做的很好，回想我小時候(i.e., 碩士時)，實在好得太多，但有時候聽多了總會讓我有過分的要求)，也會尋求在場有經驗的人進行心得分享，或傳授一些進步的方法與思維。除了那些存在骨子裡的學術觀念，張老師絕對是研究、教育與生活的風範。我十分感激自己有機會獲得張老師的教育，也將永遠記得，即使只是實驗室聖誕晚會遊戲，張老師也很有求勝精神的樣貌。

同時，於過往研究生活上，我想感謝於實驗室所有共患難的朋友: 嘉仁、文睿、佳翰、彥瑜、偉宸、(許)承恩、易昀、士元、鈺紓、宣緯、洪森、典

doi:10.6342/NTU202600018

諺、庭毅、品淳、藝軒、庭瑞、宜潔、哲諭、一飛、承名、楷崴、信喆、楷媞、Basu、奕文、薇如、芝維、奕翔、喬甄、聖凱、(鄭)承恩、珖煜、昀蒨，感謝你/妳們啟發性的對話、偶爾的耍寶以及生活排解。謝謝來實驗室做專題的北一女小學妹們: 廷瑄、佳萱與紫瑜，妳們真的太厲害了，社團、創業到出國深造，看著妳們進入大學然後發光發熱真的是拓展我人生視野的一部分，我只能說，妳們的人生發展比連續劇還好看，很謝謝妳們進入我的人生的一部份。感謝助理美芳，在行政上以及方方面面的幫助與指點，我對於一些應退進退實在很爛，很感謝妳的各種細心提醒與叮嚀，也想感謝您每次尾牙、聖誕節與迎新送舊時的鼓勵與支持。感謝張培仁老師研究團隊，景翰、銘哲、贊宇、承序、昱傑、柏翰、上裕、家卉、秉和、暐瀚、宇竹、禹傑、仲璿、子森、邦祥、文澤、宸曜、家偉、賀筌、旻政、璿昱、建均、政全、榮峻、嘉信、昱顧、芝安，於過往的砥礪與支持 (怎麼有那麼多人? 這是甚麼祖譜寫法，笑)。總地來說，你/妳們不乏善解人意與幽默的特性，並且認真又努力。碩/博士在這邊被我折磨，一定很辛苦吧? 謝謝你/妳們當初的體諒、忍耐與幫助。其中，要特別感謝宣緯在 TRANS'21 的幫忙，單邊與雙邊振撞共振器頻譜響應探討有很大部分是基於你的實驗結果而推論驗證出來的。感謝易昀讓我有機會得以學習許多台灣半導體研究中心的製程機台與製程方法，來回新竹奔波真的很累，也是做過一次就可以了。還想特別感謝承恩、庭毅、典諺、品淳、宜潔、家卉、秉和、一飛與喬甄，總感覺很常吵你/妳們，常常拜託你們做有得沒的，生活上許多雜事或遊玩行程也是由你/妳們幫忙完成的，還交派給你們過多的瑣事，但你/妳們就很貼心好用阿，謝謝啦!當然，還要感謝我在碩論提及過的大學長們!自 R/D05 級以來 Reso/PZ/433 實驗室以及沒寫到的凱瑞大哥/姊們 (真的數不完阿)。

於課業與研究思想上，我想特別提及應力所林哲宇老師(543 M5180)、郭茂坤老師(543 M5160)、潘思文老師(543 M6480)、機械系陳振山老師(522

doi:10.6342/NTU202600018

M4200)、材料科學與工程學研究所謝宗霖老師(527 M4400)與各位老師所開設的課程，這些老師的心態與課程對我研究上思維與物理現象理解有舉足輕重的幫助。我很崇拜哲宇老師的精神，總是很正面又很令人啟發，常看到哲宇老師與老婆從河堤跑步出來，真浪漫；也時時想起茂坤老師細膩的教學，偶爾在早上於停車場遇到茂坤老師踩著緩慢但扎實的步伐，總有種看到大神的感覺。想想還是令人很振奮阿!

感謝臺大奈米機電系統研究中心(北微)林順區博士在製程與結構特性上的鼎力相助，能夠進入北微做廠務工程師是很難得的經驗，工讀的薪水支持了我博士班早期的生活開支，也讓我在無塵室中學習到很多，對我在製程設計與理解上有非常大的幫助。區哥，雖然您離開北微後未有聯繫，但沒想到在昇佳卻跟您搭上線了，希望您離開北微後一切順遂，也恭喜你獲得一個好的職位!

我還想感謝所辦公室許文珍小姐以及應用力學實驗課程導師—陳國慶老師、朱錦洲老師、胡文聰老師、沈弘俊老師、陳建甫老師、江宏仁老師與陳志鴻老師讓我得以擔任六個學期的應力實驗課程助教。實際地說，這是一份輕鬆愉快的工作，鮮少有學生會跑來與助教討論實驗內容(咦?)，大家總是可以自己尋找到答案並享受過程。我很快樂於在每次口試考試時或多或少的提問某些關鍵的基礎問題並嘗試在考試後提出我的解釋。我很感謝老師們的信任並把某些工作交給我，並讓我得以傳遞一些我對物理與力學的想像。並特別感謝許文珍小姐提攜，使我得以擔任博士班學生代表與課程委員會學生代表參加所務會議與課程委員會議聽取報告與發表意見。

於此，還想特別感謝微奈米系統工程學會於研討會最佳論文提供的獎學金、南亞科技股份有限公司未來之星獎學金與財團法人台灣晶技教育基金會應用力學研究所獎學金，他們鼓勵學子投入研究並提供實際的支持。在我唸博士的初期，雖然有許多獎學金存在，但有些必須有工作綁定地要求，有些必須

doi:10.6342/NTU202600018

要是特殊身分，並不是一般的博士生得以申請，也不像現在教育部、校方、財團，四方積極補助博士從事研究。這些實際的幫助確實得以讓當時一般的博士生得以自給自足並安心地從事研究。還想感謝科技部與傑出人才發展基金會於每次出國開會的補助，並特別感謝李尉彰老師、張培仁老師、胡毓忠老師、郭茂坤老師、陳國慶老師與林哲宇老師協助學生於不同年度申請科技部國內研究生出席國際學術會議補助或傑出人才發展基金會的優秀學生出國開會補助，讓學生得以出國報告，並在過程中拓展國際視野。

在研究的最後一段時光，我很感謝經由導師的幫助進入昇佳電子股份有限公司進行暑期實習。這是一段令人難以忘記的過程，想在此特別感謝世偉學長與世雄學長。暑期實習的過程，基本上是巴著世雄學長學習的，許多商業元件特性要求與量測方法、結果都仰賴於學長的教導。能在暑期實習期間得以弄出結果需要特別感謝您的鼎力相助!；世偉學長在實習過程中曾與我有多次對談，學長總是散發出一種靈性德國的氣息。我們曾談及「我們是做正確的事還是在取巧」也曾提到「如何做人處事，如何待人」，在後期甚至討論過「人生規劃」。細部地說，我很難想像一個人可以如此友善並用一個溫和的姿態讓團隊成員發表各式各樣的意見與想像，在每一個發表中透過提問讓團員思考與進步，並在一個適合的角度要求員工做事。世偉學長非常關心每個人，我甚至在實習後仍收到許多封近況分享或學術討論的信件，那是很舒服的一種交流模式，很期待未來可以與您共事並從您身上學到更多，一起做外星科技!

嗨，親愛的朋友們，有些人已經於碩論提及，有些人因各種原因與考量未能提及於此。博士論文要謝的人很多很多，若沒看到妳/你的名字，絕不代表妳/你不重要，我真摯地想感謝大家的參與，這份成果，離不開妳/你們，謝謝妳/你們!

doi:10.6342/NTU202600018



最後，我要感謝我的親人、女友與我親愛的母親，無私地成為我的依靠並陪伴著我成長。願大家快快樂樂、穩定、簡單、享受尋找人生意義的過程、不被越來越紊亂的社會影響、熱情地活著，我愛你們!謝謝!

蔡淳樸

中華民國一一五年一月 謹誌於國立台灣大學

doi:10.6342/NTU202600018

摘要

做為微機電振撞共振器的分支，原子力顯微鏡透過共振操作懸臂樑量測樣品奈米尺度元件之表面拓譜與材料性質，從而推動了軟物質、物理學、材料科學和奈米磨擦學巨大的發展；射頻開關透過低損失和高隔離的導通/開路狀態切換操作，成為無線通訊系統與元件快速測試平台中的關鍵元件；能量擷取器、致動器與慣性開關透過設計此一強非線性碰撞操作提高元件輸出、精密度或頻寬。雖然已經有許多文獻探討振撞共振器的系統行為，隨著元件尺度的縮小，靜電非線性、幾何非線性與材料非線性將影響系統行為並使得元件響應複雜而難以設計與優化。

本研究針對微機電振撞共振器進行了深度的探索並拓展對其系統響應於週期驅動下之了解。開發、設計與探討兩種新型元件—微機電共振開關與吸引子交換器—之性能、應用與理論基礎。基於互補式金屬氧化物半導體-微機電系統製程平台，本研究理論與實驗性地揭示了摺疊樑梳狀電極制動微機電振撞共振器於非線性操作下的系統響應。基於平均法與 SIMULINK 系統級別模型，元件輕敲操作下之頻譜響應、暫態行為、穩態行為與其於穩態峰值排斥力的模型已被分析並與實驗結果比較。

基於操作豐富的非線性行為，本研究設計與應用微機電共振開關—內嵌電性操作地微機電振撞共振器於喚醒接收器與脈波密度調變器，機械式地簡化複雜電子電路元件。此外，透過對系統進一步的了解，本研究提出間隙連續式與振撞擾動式吸引子交換器。此二吸引子交換器透過不同操作原理對元件施加擾動，於開迴路狀況下控制一非線性元件於多穩態條件下之運動狀態。這些結果促進了微機電振撞共振器與共振開關之理解和進步，為開發高性能共振開關與擾動式非線性元件控制奠定了基礎。

doi:10.6342/NTU202600018

關鍵字: CMOS-MEMS、振撞共振器、共振開關、吸引子交換器。



doi:10.6342/NTU202600018

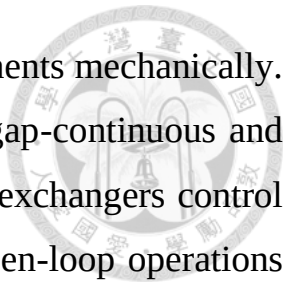
Abstract

In previous few decades, various micromechanical structures and systems that utilize parts with mechanical vibro-impact have been proposed and developed, including vibro-impact energy harvesters, impact actuators, inertial switch, just to name a few. In particular, the tapping-mode atomic force microscopy (AFM) and radio frequency (RF) switch are two of great importance invention in which the AFM spurred on the development of nanoscience and nanotribology while RF switch become the key component on the wireless communications/production test supporting the integration of multiple radios/device that use a single antenna/instrument. Although, some of the underlying mechanism already developed in previous works, there is a gap to develop micro-electro-mechanical systems (MEMS) resoswitch, a particular case of MEMS vibro-impact resonators that incorporate with electrical hot-switching operation, as the device's dimension shrinks day by day.

This work delves into the MEMS vibro-impact resonator under periodic excitation to enhance the understanding of its system response further, motivated by the need for optimizing of the device performance and nonlinear behavior of MEMS resoswitches. Utilizing the CMOS-MEMS process platform, this work theoretically, numerically and experimentally examines the nonlinearity of a folded-beam comb-driven vibro-impact resonator. Based on a 1-DOF lumped governing equation, the work predicts, through the method of averaging and SIMULINK system-level simulation platform, the tapping mode frequency response, transient motion and steady-state peak repulsive force. These predictions are compared to experimental results and show a good agreement.

Nevertheless, this work designs, evaluates and develops two novel components—all-mechanical pulse density modulator and attractor exchangers. By leveraging the complex nonlinear behavior, the designed resoswitch is implemented as a pulse

doi:10.6342/NTU202600018



density modulator to simplify intricate electronic circuit components mechanically. Additionally, this work proposes innovative devices, namely, gap-continuous and vibro-impact perturbation attractor exchangers. These attractor exchangers control the state of nonlinear devices in a multi-stable region under open-loop operations through distinct operating principles. These findings advance the understanding of MEMS vibro-impact resonators and resoswitch, laying the groundwork for the development of high-performance resoswitch and perturbation-based control of nonlinear devices.

Keywords: CMOS-MEMS, vibro-impact resonator, resoswitch, attractor exchanger.

doi:10.6342/NTU202600018

Contents

口試委員審定書 i
致謝 ii
摘要 xii
Abstract xiv
Contents xvi
List of Figures xxii
List of Tables xlvi
List of Abbreviations xlviii
List of Notations and Symbols li
VITA lxv
1 General Introduction 1
1.1 Motivation and Objectives 5
1.2 Dissertation Organization 7
2 Foundations and Background 10
2.1 Introduction 10
2.2 Characteristics and Analysis Tools 13
2.2.1 Model and Behavior Representation 13
2.2.2 Analysis Tools for Specific Parameters 16
2.2.2.1 Time Series and Phase Portraits 16
2.2.2.2 Poincaré Map 18
2.2.3 Analysis Tools for Varying Parameters 19
2.2.3.1 Frequency Response and Bifurcation Diagram 20
2.2.3.2 Basins of Attraction 23
2.2.4 The Effect of Intrinsic Nonlinearity in MEMS Vibro-impact Resonators 26
2.3 Interaction Force Formulation 27
2.3.1 Classical Contact Models 29
2.3.1.1 Rigid Contact (The Coefficient of Restitution) 32
2.3.1.2 Elastic and Inelastic Contact (w/o or w/ Dampers) 33

doi:10.6342/NTU202600018

2.3.1.3 Hertz Model 35
2.3.2 Modified Hertz Contact Models 37
2.3.2.1 JKR Model 37
2.3.2.2 DMT Model 38
2.3.2.3 Intermolecular Pair Potentials for Adhesive Contact 39
2.3.2.4 Amendments and Remarks 41
2.4 Analytical and Numerical Method 45
2.4.1 Analytical Approximation Methods 47
2.4.2 Finite Difference and Finite Element Methods 49
2.4.3 Parameter Continuation Method 52
2.5 Micromechanical Vibro-Impact Applications 53
2.5.1 Tapping-mode Atomic Force Microscope (AFM) 53
2.5.2 Impact Microactuators 57
2.5.3 Impacting Energy Harvesters 59
2.5.4 Vibro-impact Resonators and Resoswitches (Resonant Switches) 62
2.5.5 RF Switches and Inertial Force Switches 65
2.6 Discussion and Conclusion 67
3 Developments on Dynamical Modeling 70
3.1 Introduction 70
3.2 Device Design, Implementation, and Operation 74
3.2.1 Comb-driven Folded-beam Resonator 74
3.2.2 Device Implementation 76
3.2.3 Linear Operation 83
3.3 Modeling of Resoswitches 89
3.3.1 Contact Surface Interaction Force and Contact Area 89
3.3.2 Stiffness and Damping Nonlinearities 94
3.3.3 Electrical Contact Resistance and Material Selection 97
3.3.4 The Effect of the Back-end RC Circuit 99
3.4 Theoretical Analysis of Resoswitches 104
3.4.1 Numerical simulation Set-up 104

doi:10.6342/NTU202600018

3.4.2 Force-Distance Plot 108
3.4.3 Hot Switching Responses 109
3.4.4 Frequency Responses 112
3.4.5 Steady-State Peak Repulsive Force 115
3.5 Device Characterization 119
3.5.1 Measurement Set-up 119
3.5.2 Ring-Down Responses 122
3.5.3 Frequency Domain Response and Electrical Model 123
3.5.4 Forced Time-Transient Responses 130
3.5.5 Hot Switching Output 133
3.6 Discussion 137
3.6.1 Influence of Effective *Q* on Contact Force and Switching Behavior 137
3.6.2 Impact of Period-Doubling on Contact Force and Switching Voltage 139
3.6.3 Resoswitch Modulation Techniques for Communication Applications 140
3.6.4 The Role of Viscoelastic Damping in Phase Response 143
3.6.5 Contact Material Considerations 143
3.7 Conclusion 144
4 Developments on MEMS All-mechanical Circuits 146
4.1 Resoswitch-embedded Wake-up Receiver 146
4.1.1 Introduction 146
4.1.2 Resonant Switch as a Filtering Amplifier 148
4.1.3 Structure and Operation 149
4.1.4 Experimental Results 150
4.1.5 Conclusions 153
4.2 Pulse Density Modulator 155
4.2.1 Introduction 156
4.2.2 Period-Doubling Bifurcation 157
4.2.3 Structure and Operation 159
4.2.4 Experimental Results 159

doi:10.6342/NTU202600018

4.2.5 Conclusions 161
5 Developments on MEMS Attractor Exchangers 163
5.1 Gap-Continuation Based Attractor Exchanger 163
5.1.1 Introduction 163
5.1.2 Gap-spacing Sweeping Technique 165
5.1.3 Structure and Operation 167
5.1.4 Experimental Results 167
5.1.5 Conclusions 170
5.2 Vibro-Impact Perturbation-Based Attractor Exchanger 171
5.2.1 Introduction 171
5.2.2 Vibro-impact Perturbation Technique 173
5.2.3 Structure and Operation 175
5.2.4 Experimental Results 176
5.2.5 Conclusions 178
6 Conclusions and Remarks 180
6.1 Results Summary 180
6.2 Future Research Directions 180
6.2.1 Model and Simulation Capability Improvement 181
6.2.1.1 Material Properties Investigation 181
6.2.1.2 Modal Analysis and Optimization for the Resoswitch 181
6.2.1.3 Surface Roughness and Time-Dependent Contact Physics 182
6.2.1.4 Prediction of the Maximum Peak Repulsive Force in the Transient State 182
6.2.2 Reliability and Sensitivity Improvements 183
6.2.2.1 Contact Material Engineering 183
6.2.2.2 Optimized Bleeding Circuit and Time Constant 184
6.2.2.3 Mechanical Engineering on the Output Electrode 184
6.2.3 Packaging and Integration 186
6.2.4 On-Chip Vibro-impact Perturbation-based Stiction Solver 186
Appendix A: Time and Frequency Domain Responses of Single-DOF m-b-k

doi:10.6342/NTU202600018

Systems 188
A.1 Linear Frequency Response 189
A.2 Linear Time Response and Switching Time 196
A.3 Ring-down Response 202
A.4 Beating Phenomenon and Transient Response 206
A.5 Stability of 1-DOF Linear and Nonlinear Systems 208
Appendix B: Equivalent Circuit, Two-Port Networks, Transmission, and Parameter Extraction 211
B.1 Wave Analogy for Few Types of Energy 213
B.2 Introduction to the Network Analyzer 240
B.3 Matrix Representation of the Electrical Power Wave 244
B.4 Practice, Error Source and Correction 259
B.5 Equivalent Circuit of Linear Electrostatic MEMS Resonators 271
B.6 Parameter Extraction and Initial Guess 284
B.7 Multiple Ports, Multiple DOF and Coupled Systems 288
B.8 Lorentzian Response and Application of FFT 293
Appendix C: Introduction to the Surface Interaction Forces 296
Appendix D: Characteristic of Vibro-impact Resonators 305
D.1 Parametrically Numerical Investigations 305
D.2 Periodic-Doubling Bifurcation and Comb Generation 322
D.3 Double-sided Vibro-Impact Resonator 334
Appendix E: Introduction to Perturbation Theory 344
E.1 Illustrative Example based on Asymptotic Analysis 345
E.2 Nondimensionalization Technique 350
E.3 Method of Multiple Scale 353
E.4 Method of Averaging (MOA) 360
E.5 Stability Analysis based on Slowly Varying Equation 372
E.6 Nonlinear Ring-down Envelop Equation 375
E.7 Jump-up Frequency of Duffing Oscillators 377
Appendix F: Derivation of Peak Repulsive Force Formulas and Scaling Laws .. 380

doi:10.6342/NTU202600018

F.1 Governing Equation, Assumptions and Remarks 380
F.2 Main Derivation on Peak Repulsive Force Formulars 385
F.3 Arranging, Extension and Discussion 391
Appendix G: The Temperature Coefficient of Frequency and Abnormal Frequency Responses 392
G.1 TCF and TCQ of the Comb-driven Resonator 392
G.2 Influence of Parasitic Current on the Tapping-mode Frequency Response 392
Reference 396

doi:10.6342/NTU202600018

List of Figures

Figure 1-1: Overview to the dissertation organization. 9
Figure 2-1: (a) A lumped-parameter model showing a 1-DOF vibro-impact oscillator with an elastic stopper. (b) The associated plot of the total restoring force against displacement, demonstrating the non-smooth, piecewise-linear stiffness that results from impact at the gap $d0$. Reproduced with permission of [107], Copyright of © IOP Publishing. 15
Figure 2-2: A comparison of computed responses for a linear (non-impact) motion and a near-grazing impact motion, based on simulations of (2-1). The system's dynamics are visualized using several tools: (a) the integral curve in extended phase space, (b) time-domain histories for displacement, velocity, and acceleration, (c) the steady-state phase portrait, and (d) the corresponding Poincaré map. The two cases were generated in MATLAB & Simulink using forcing amplitudes (A) of 0.2 and 0.4, respectively, with other parameters being $k = 1$, $m = 2.533 \times 10 - 4$, $b = 1.6 \times 10 - 3$, $d0 = 1$, $kc = 250$, and $\omega = 8.5$. For the Poincaré map in (d), the section for the period-2 motion is defined at the impact boundary, while the section for the period-1 motion is taken at the maximum displacement. Reproduced with permission of [107], Copyright of © IOP Publishing. 17
Figure 2-3: Bifurcation analysis of the vibro-impact oscillator. (a) The system's frequency response is presented as a one-parameter bifurcation diagram, with the dotted horizontal line indicating the nondimensionalized gap spacing. (b) A two-parameter bifurcation set illustrates how the bifurcation points evolve in the forcing ratio versus driving frequency space. The specific points labeled in (a) (GR_1, PD_1, PD_2, SN_1, GR_2, and SN_2) are determined by the intersections of the dashed horizontal line with the various bifurcation curves. (c) Another two-parameter bifurcation set is shown for the stiffness ratio versus frequency ratio space. Reproduced with permission of [107], Copyright of © IOP Publishing..... 23
Figure 2-4: Evolution of the basins of attraction for a vibro-impact oscillator at different frequency ratios (ω) of (a) 1.10, (b) 1.18, (c) 1.25, (d) 1.35, (e) 1.45, (f) 1.52, corresponding to the response shown in Figure 2-3 (a). The frequencies for plots (a) and (f) lie outside the bistable (SN_1-SN_2) region, each showing a single attractor. In contrast, plots (b) through (e) are for frequencies within the bistable region, where two attractors coexist. The

doi:10.6342/NTU202600018

red dot indicates the high-energy attractor (upper branch), while the green dot denotes the low-energy one (lower branch). Each colored area represents the basin of attraction for its corresponding attractor. Reproduced with permission of [107], Copyright of © IOP Publishing. 24
Figure 2-5: An example of complex dynamics involving multiple coexisting attractors in a vibro-impact oscillator. (a) A bifurcation diagram reveals a frequency region where several stable solutions are present simultaneously. (b) The basin of attraction map is shown for the specific frequency indicated by the dashed line in (a), with colored regions corresponding to different orbits. (c) The individual phase portraits for each of these coexisting attractors are detailed. In these portraits, the dashed vertical line marks the nondimensionalized gap spacing, while the red dots represent the points of the Poincaré map. The Poincaré map shown here is constructed by taking 4000 points once per period of the external force. Reproduced with permission of [107], Copyright of © IOP Publishing..... 26
Figure 2-6: A collection of experimentally measured frequency responses for MEMS vibro-impact resonators, illustrating how different intrinsic nonlinearities affect the system's behavior. The plots show (a) a response dominated by a hardening effect, (b) a response primarily characterized by softening, and (c) a response exhibiting a mixed softening-hardening behavior. Reproduced with permission of [107], Copyright of © IOP Publishing. 27
Figure 2-7: Comparison of force-indentation curves for various contact models. (a) Plots for several non-dissipative models (Linear, Hertz, DMT, JKR, and Bradley) are shown, illustrating their distinct attractive and repulsive force profiles. The inset defines the coordinates for displacement (x), indentation (δ), interatomic spacing ($a0$), and gap ($d0$). (b) and (c) Simulated curves for the dissipative Kelvin and Hunt-Crossley models are presented, with insets showing their respective mechanical representations. The hysteresis in these plots indicates energy loss during contact. For the purpose of this illustration, the interatomic spacing for the Hertz and linear spring models is set to zero, but it can be incorporated if necessary. The insets in (b) and (c) show the mechanical model of the colliding body with the fixed soft base. The result in (a) for the JKR model is based on a fixed-load approach; the fixed-grips condition is another possible approach. The simulation conditions were as follows: (a) JKR Model: $a0 = 0.165 \times 10 - 9$, $H = 40 \times 10 - 20$, $R1 = R* = 150 \times 10 - 9$, $E1 = E2 = 42.4 \times 109$, $\nu = 0.42$, $klinear = 335$; (b) Linear Spring Model: $k = 335, mk = 1 \times 10 - 10,$

doi:10.6342/NTU202600018

$vbefore = 0.003$; (c) Hertz Model: $k = 335$, $mHC = 1 \times 10 - 10$, $vbefore = 0.15$. Reproduced with permission of [107], Copyright of © IOP Publishing. 30
Figure 2-8: Graphical representation of the 12-6 Lennard-Jones potential, plotting interaction energy against the distance between two particles. The curve illustrates the attractive forces at longer distances and the strong repulsive forces at short distances, with the insets depicting the particles in these different regimes. The minimum of the potential well corresponds to the equilibrium position—the interatomic spacing—where the net force between the particles is zero. The simulation conditions used are $\epsilon = 5.29$ and $\sigma = 2.9511 \times 10 - 10$. Reproduced with permission of [107], Copyright of © IOP Publishing..... 40
Figure 2-9: The adhesion map for elastic spheres, developed from the Maugis-Dugdale model, which helps in selecting the most suitable contact theory. Different regions on the map correspond to conditions where the Bradley (rigid), DMT, JKR, or Hertz models are most accurate The map categorizes regimes based on two key dimensionless parameters: the elasticity parameter (λ)— a measure of the ratio of the elastic indentation of the surface at the point of separation to the effective range of surface forces characterized by interatomic spacing, and the nondimensional load (P)— a measure of the ratio of the applied load to the adhesive pull-off force. The boundary curves are labeled with the chosen values defined in [223]. Reproduced with permission of [107], Copyright of © IOP Publishing. 42
Figure 2-10: (a) A schematic showing the experimental AFM setup from [58]. (b) The potential energy curve for a single-well system, which is considered monostable, is shown with (c) its corresponding phase portrait. (d) An asymmetric double-well potential energy curve is also presented; this is generated by a stronger adhesion force and results in a bistable system, shown along with (e) its phase portrait. The double-well potential is generated due to stronger adhesion force compared to the single-well case. The two local minima on the double-well curve represent the two static equilibrium points of the system. One equilibrium point is located away from the sample (~2 nm), while the other is in contact with the sample surface (near zero). Reproduced with permission of [107], Copyright of © IOP Publishing. 54
Figure 2-11: Comparison of the frequency responses and basins of attraction for an AFM system operating in monostable and bistable regions. (a) and (b) show the response for the monostable region, where the frequency

doi:10.6342/NTU202600018

curve exhibits a mixed softening-hardening behavior due to the combination of attractive and repulsive tip-sample forces. (c) and (d) depict the response for the bistable region, which is characterized by two distinct solution branches: an *attractive* motion (lower curve) and an *in-contact* motion (upper curve). In the frequency response plots, solid and dashed lines are used to denote the stable and unstable branches of the attractors, respectively. Reproduced with permission of [107], Copyright of © IOP Publishing. 56
Figure 2-12: (a) A schematic diagram of an impact microactuator along with an illustration of its operational mechanism. Reproduced with permission of [62], , Copyright of © 2023 IEEE. (b) Displacements and voltage time history of a microactuator. (c) Simulated frequency response of a microactuator, showing non-impacting, period-one impacting and period-N impacting motion with saddle-node (also known as cyclic fold, CF) and grazing bifurcation. The device features a movable mass that is accelerated by an electrostatic force until it collides with a stopper. This collision generates a forward inertial impulse, which overcomes static friction and advances the entire actuator frame in a stepwise manner. Reproduced with permission of [63] for (b) and (c), Copyright of © IOP Publishing. 57
Figure 2-13: Two examples of vibro-impact energy harvesters, each shown with its schematic, frequency response, and a sample time-domain trace. (a) A single-resonator energy harvester whose frequency response was measured using a forward sweep [70]. (b) A dual-resonator energy harvester that utilizes a frequency up-conversion mechanism [76]. Its frequency response includes both forward and backward sweeps, revealing a distinct hysteresis loop caused by the impacts. The time-domain plots for both devices clearly show the typical tapping behavior and an impact-induced low-frequency ringing. Reproduced with permission of [107], Copyright of © IOP Publishing. 60
Figure 2-14: (a) An overview of a comb-driven resoswitch, detailing its structure and operation. The figure includes a device schematic with a close-up of the contact mechanism, a simplified equivalent circuit representing the hot-switching process, and the expected output voltage waveform consisting of a train of pulses. (b) An illustration showing how period-adding effects and impact force fluctuation leads to the squegging phenomenon and a corresponding missing signal. Reproduced with permission of [107], Copyright of © IOP Publishing. 63

doi:10.6342/NTU202600018

Figure 2-15: Structure and simulated transient behavior of a cantilever-type electrostatically actuated RF switch. (a) An SEM image and (b) a side-view schematic illustrate the typical device structure. (c) Simulation plots demonstrate the contact bouncing phenomenon, where the switch beam repeatedly impacts the contact before settling, showing how bouncing is influenced by different actuation voltage ratios and quality factors. Reproduced with permission of [107], Copyright of © IOP Publishing. 67
Figure 3-1: (a) Schematic of a comb-driven folded-beam resoswitch with the operation configuration and illustrative displacement and hot switching output waveforms. (b) Label specifications for device geometries. (c) 1-DoF lumped mechanical model for a resoswitch or vibro-impact resonator in general. Reproduced with permission of [316] Copyright of © 2025 IEEE..... 73
Figure 3-2: Cross-sectional view of a CMOS-MEMS structure (a) before and (b) after release, illustrating METAL layers are etched due to finite etching selectivity. Reproduced with permission of [316] Copyright of © 2025 IEEE. 75
Figure 3-3: SEM photos of the fabricated device: (a) overview of the device with close-in top view to the contact gap, (b) and (c) zoom-in to the contact sidewall. (d) and (e) show the SEM photos of a testing structure, where the etched METAL and the TiN/Ti covered VIA layer are observed on the sidewall [326]. Reproduced with permission of [316] Copyright of © 2025 IEEE. 77
Figure 3-4: (a) The 3D profiles of a fabricated device measured by laser scanning confocal microscope. (b) The closed view to the front side near the contact position. (c)-(e) The measured 2D line profile along the labeled lines in (a). Reproduced with permission of [316] Copyright of © 2025 IEEE. 78
Figure 3-5: (a) The postulated etched and equivalent profile for the MET-AL layers. (b) The beam dimensions and assumptions used for TiN property extraction [331]. Reproduced with permission of [316] Copyright of © 2025 IEEE..... 78
Figure 3-6: (a) Equivalent electrical circuit of an electrostatic MEMS resonator and (b) its simplified version. Reproduced with permission of [316] Copyright of © 2025 IEEE. 84
Figure 3-7: (a) Simulated displacement frequency responses with and without considering finite-selectivity etching during release. (b) The operation bandwidth of the resoswitch with varying driving voltage based on

doi:10.6342/NTU202600018

grazing frequencies predicted by (16). Reproduced with permission of [316] Copyright of © 2025 IEEE. 86
Figure 3-8: The single-asperity contact model. Reproduced with permission of [316] Copyright of © 2025 IEEE. 86
Figure 3-9: (a) Equivalent circuit model for resoswitches with the RC envelop detector and its simplified circuits at (b) OFF state and (c) ON state. Reproduced with permission of [316] Copyright of © 2025 IEEE..... 100
Figure 3-10: (a) Simulated hot-switching voltage at the back-end RC circuit for a contact duration of 1.6 μs. The black pulse waveform represents the contact resistance profile. The blue, green, and red curves depict the output voltage for bleeding resistances of 10, 100, and 1000 kΩ, respectively. (b) Output signals after processing through the comparator. (c) Simulated hot-switching voltage for a short contact duration of 0.4 μs. The contact resistance values, extracted using (61), are indicated in both (a) and (c), showing that poor estimation of contact resistance occurs in cases of short contact duration where the RC time constant significantly exceeds the contact duration. Reproduced with permission of [316] Copyright of © 2025 IEEE. 102
Figure 3-11: (a) Systematic block diagram of the resoswitch and its sub-model for (b) surface interaction force modeling and (c) electrical contact resistance modeling. The “MATLAB function” blocks in (b) and (c) are (3-40) and (3-55), respectively. Reproduced with permission of [316] Copyright of © 2025 IEEE..... 107
Figure 3-12: (a) Simulated displacement and interaction force time history with continuous driving at linear resonance frequency. (b) Zoom-in view of the boxed region in (a). Reproduced with permission of [316] Copyright of © 2025 IEEE..... 108
Figure 3-13: (a) Force-indentation plot for the boxed region in Figure 3-12 (a) along with the DMT prediction based on (3-36) and (b) Contact resistance versus surface interaction force plot for the boxed region. The insert figures in (a) and (b) shows the simulated time domain surface interaction force profiles and simulated time-domain contact resistance for one cycle from A to B and back to C, respectively. Reproduced with permission of [316] Copyright of © 2025 IEEE..... 109
Figure 3-14: Time-domain hot switching responses with zoom-in to the one-cycle steady-state contact resistance history using the Simulink model. The parametric studies on aspects of (a) viscoelastic contact damping, (b) Hamaker contact, (c) Young’s modulus of contact material, (d) tip radius,

doi:10.6342/NTU202600018

(e) driving frequency, and (f) driving voltage. Reproduced with permission of [316] Copyright of © 2025 IEEE..... 110
Figure 3-15: (a) Simulated frequency responses and (b) the zoomed-in to the indentation region. (c) the corresponding phase difference responses and (d) the zoomed-in to the left bifurcation region. Several cases with varying viscoelastic contact damping, Hamaker constant, nonlinear stiffness and damping are conducted. The dashed lines show the results by the method of averaging. The solid line with rectangle and circle represents the response simulated by the RKDP method with forward and backward sweeping, respectively. Reproduced with permission of [316] Copyright of © 2025 IEEE. 112
Figure 3-16: Simulated frequency responses with nonlinear stiffness i.e., the Duffing term, of (a) zoom-in to the indentation region and (b) the whole span. (a) also compares varying nonlinear damping, i.e., the van der Pol term. Reproduced with permission of [316] Copyright of © 2025 IEEE..... 113
Figure 3-17: Simulated peak repulsive force map as a function of (a) driving voltage, (b) zoom-in to the small driving voltage region from (a), and (c) gap clearance. Reproduced with permission of [316] Copyright of © 2020 IEEE. 117
Figure 3-18: Measurement set-up for (a) time-domain motional current, (b) electrical frequency response, and (c) hot switching operation, respectively. Reproduced with permission of [316] Copyright of © 2025 IEEE. 119
Figure 3-19: Measured motional current output responses of (a) a resonator (without stoppers) and (b) a resoswitch for the ring-down test. Reproduced with permission of [316] Copyright of © 2025 IEEE..... 121
Figure 3-20: (a) Equivalent circuit for the experimental set-up of frequency response measurement using the network analyzer. (b) The equivalent circuit when using a transimpedance amplifier. (c) The simplified equivalent circuit for (b). Reproduced with permission of [316] Copyright of © 2025 IEEE. 122
Figure 3-21: (a) Measured transmissions of the resonator with and without the transimpedance amplifier and calibration. (b) Measured transmissions of the resonator with varying driving power level. In (b), the transmission peak is banded to the left due to negative Duffing term and the transmission level decreases as the driving power increases due to the present of the van der Pol term. Reproduced with permission of [316] Copyright of © 2025 IEEE. 124

doi:10.6342/NTU202600018

Figure 3-22: Measured responses of the resoswitch from the linear to tapping mode. (a) and (b) are the responses before de-embedding, and (c) and (d) are the responses after de-embedding. In (b), the feedthrough screens the actual phase features of the device while in (d), the phase difference at the linear resonant frequency approaches 90° as the driving power increases. Reproduced with permission of [316] Copyright of © 2025 IEEE. 125
Figure 3-23: Measured and simulated frequency responses with the input power cycling between 0 dBm and 20 dBm. (a) and (b) show the transmission and phase measurement results at 0 dBm for each run, respectively, while (c) and (d) show the transmission and phase measurement results at 20 dBm for each run. (e), (f), (g), and (h) represent simulations based on curve fitting of the effective tip radius. Reproduced with permission of [316] Copyright of © 2025 IEEE. 128
Figure 3-24: Measured motional current output responses of (a) a resonator (without stoppers) and (b) a resoswitch for forced vibration test with varying driving voltage. The results illustrate the effect of nonlinearities under different driving levels. Reproduced with permission of [316] Copyright of © 2025 IEEE. 131
Figure 3-25: Measured current output responses and associated phase responses for signal peak envelope when driving the resoswitch at (a) $f0-1$ kHz, (b) $f0$, and (c) $f0+1$ kHz. Significant overshooting and beating phenomenon can be observed when the device is driven at off-resonance condition in the non-tapping region. The overshooting can also be seen in the tapping region especially for large driving voltage. The overshooting in the tapping region is referred to transient squegging in this work. Reproduced with permission of [316] Copyright of © 2025 IEEE. 132
Figure 3-26: Measured hot switching output with a bleeding resistance of (a) 0.1 MΩ and (b) 1 MΩ at varying driving voltage. As illustrated in (b), a larger bleeding resistance results in a longer discharging time and higher hot switching output. Reproduced with permission of [316] Copyright of © 2025 IEEE. 134
Figure 3-27: Measured hot switching output with the input duty cycle of (a) 25%, (b) 50%, and (c) 75%. For the largest duty cycle of (c), the output exhibits unstable response due to reduced contact force similar to that observed in Figure 3-26. Reproduced with permission of [316] Copyright of © 2025 IEEE. 135

doi:10.6342/NTU202600018

Figure 3-28: Measured hot switching outputs showing (a) changed re-sponse during operation and (b) the response measured again after (a). The measurement is performed using a single-sided configuration with a bias voltage of 60 V and input voltage of 8 VPP at its linear resonant frequency. The structure bias is 2 V and the bleeding resistance is 1 kΩ. Reproduced with permission of [316] Copyright of © 2025 IEEE. 136
Figure 3-29: (a) Measured and simulated switching time. The theoretical formula from the linear model (i.e., (3-35)), nonlinear simulation (i.e., (3-43) with numerical integration) and the approximated solution shown in (3-83) are compared against the measurement results at $fd = f0$. (b) the absolute error between models and measurement results along varying driving voltages. The averaged errors are about 23.8, 8.9 and 19.8% for (3-35), (3-43) and (3-83), respectively. Reproduced with permission of [316] Copyright of © 2025 IEEE. 137
Figure 3-30: Simulated (a) peak repulsive force and (b) switching time with varying effective Q. The comparison of Material A and B il-lustrates how the material property, specifically minimum con-tact force required for electrical conduction, determines sensitivity and corresponding switching time. Reproduced with permission of [316] Copyright of © 2025 IEEE..... 138
Figure 3-31: Simulated hot switching output (a, c) and zoom-in to the steady state (b, d) with driving level of 7.8 VPP and 7.9 VPP. The phase and contact force are also plotted as the second y-axis, where (d) exhibits the period-doubled response. The driving voltage is near the bifurcation boundary so a small change on the driving voltage changes the response on contact force therefore significantly altering the hot switching output. Reproduced with permission of [316] Copyright of © 2025 IEEE..... 139
Figure 3-32: Simulated (a) peak repulsive force and (b) switching time with varying effective Q. The comparison of Material A and B il-lustrates how the material property, specifically minimum con-tact force required for electrical conduction, determines sensitivity and corresponding switching time. Reproduced with permission of [316] Copyright of © 2025 IEEE..... 140
Figure 3-33: Simulated responses for two different bit rates with varying driving voltage. (a) and (b) represent a 1.3-kbps bit rate (50 cycle per message packet), while (c) and (d) correspond to a 6.7-kbps bit rate (10 cycle per message packet). The pre-amble signal is around 3.76 ms long (500 cycle) for all simulation while the modulation factor and duty cycle are 0.33 and

doi:10.6342/NTU202600018

0.5, respectively, for ASK modulated signal. The bit rates are chosen to illustrate the effect of pre-amble, pre-energization and driving level. Reproduced with permission of [316] Copyright of © 2025 IEEE..... 141
Figure 4-1: A comparison of FSK receiver architectures, showing (a) a conventional RF front-end utilizing a filter and LNA, and (b) an alternative design based on a CMOS-MEMS resoswitch. Reproduced with permission of [89], Copyright of © 2020 IEEE. 147
Figure 4-2: (a) The circuit diagram for a zero-quiescent power OOK/FSK receiver, which is based on a CMOS-MEMS folded-beam comb-driven resoswitch and a digital decoder. (b) An SEM image of the fabricated resoswitch after release. Reproduced with permission of [89], Copyright of © 2020 IEEE. 148
Figure 4-3: The measurement setup for the OOK/FSK receiver. The inset on the right shows an optical photograph of the PCB, which holds the two bonded dies for the digital decoder circuit and the resoswitch. Reproduced with permission of [89], Copyright of © 2020 IEEE..... 149
Figure 4-4: (a) Measured frequency responses for the receiver, showing both forward and backward sweeps at different input power levels. (b) A plot of the extracted forward and overlapped bandwidths, highlighting the actual operating bandwidth available for single-frequency driving. ... 150
Figure 4-5: Oscilloscope waveforms captured during receiver operation, showing the demodulation of (a) an OOK input signal and (b) an FSK input signal. The resoswitch's filtering capability enables it to distinguish the in-channel signal from the out-of-channel signal. Reproduced with permission of [89], Copyright of © 2020 IEEE. 152
Figure 4-6: Measured power consumption during switching for (a) the resoswitch and (b) the inverter decoder. The static power drawn by the decoder is primarily due to the oscilloscope's load resistance. Reproduced with permission of [89], Copyright of © 2020 IEEE..... 153
Figure 4-7: (a) A 1-DOF mechanical model of a vibro-impact resonator. (b) An illustrative frequency response for a nonlinear tapping-mode vibro-impact resonator. The plot highlights key dynamic features: grazing bifurcations (GR_1-PD_1 and SN_1-GR_2), the period-doubling and reverse period-doubling region (PD_1 to PD_2), and saddle-node bifurcations (SN_1 and SN_2). The labels GR_1-PD_1 and SN_1-GR_2 are used because, in typical cases with significant stopper stiffness and contact force, the grazing points (GR) are nearly coincident with the first period-doubling (PD_1) and second saddle-node (SN_2) bifurcations. Reproduced with permission of

doi:10.6342/NTU202600018

[237], Copyright of © 2022 IEEE. 155
Figure 4-8: (a) A depiction of the system's dynamics across various regions of the frequency response, including time-domain waveforms, phase portraits, and Poincaré maps (indicated by green dots). The phase portraits display the system's trajectories, including the discontinuity boundary, while the Poincaré maps reveal the motion's state at specific phase conditions, showing a complex fractal pattern when chaos is present. (b) An illustration comparing the FFT spectra for continuous motion versus motion induced by period-doubling. Reproduced with permission of [237], Copyright of © 2022 IEEE. 157
Figure 4-9: (a) A schematic diagram of the CMOS-MEMS comb-driven resoswitch, including its testing setup. (b) SEM images of the fabricated and released resoswitch. Reproduced with permission of [237], Copyright of © 2022 IEEE. 158
Figure 4-10: The experimental setup for measuring frequency transmission, the output frequency spectrum, and the modulated signal output. The inset displays the measured frequency transmission curves for several different driving voltages. Reproduced with permission of [237], Copyright of © 2022 IEEE. 160
Figure 4-11: A collection of measured data for the resoswitch. (a) The frequency transmission response under specified conditions. (b) Time-domain waveforms of the hot-switching signals (V_{RC}). (c) The corresponding PDM output signal waveforms (V_O). (d) The frequency spectra of the hot-switching signals at five points within the period-doubling region. (e) A plot of the frequency combs across a range of driving frequencies in the reverse period-doubling region, demonstrating an increase in the squegging frequency as the driving frequency is increased. Reproduced with permission of [237], Copyright of © 2022 IEEE. 161
Figure 5-1: A conceptual illustration of the gap-spacing continuation technique, shown with its corresponding mechanical model for an attractor exchanger integrated with a nonlinear device. Reproduced with permission of [273], Copyright of © 2023 IEEE. 164
Figure 5-2: (a) A diagram illustrating the gap-spacing continuation technique, which displays the frequency response curves of a Duffing resonator under varying gap spacing and reveals a new, smooth gap-spacing continuation branch. (b) A simulated time-domain plot showing the evolution of a Duffing oscillator's displacement amplitude during the gap-spacing continuation process. (Note: SN_i and GR_i denote the saddle-node and

doi:10.6342/NTU202600018

grazing bifurcations, respectively, while SN_1-GR_2 indicates a point where these two bifurcations are very close). Reproduced with permission of [273], Copyright of © 2023 IEEE. 165
Figure 5-3: (a) A schematic of the attractor exchanger, which consists of an arc-beam thermal actuator driven by a Joule-heating current (IJH), shown with the comb-driven resonator and its experimental setup. (b) An SEM image of the released arc-beam thermal actuator integrated with the comb-driven vibro-impact resonator. Reproduced with permission of [273], Copyright of © 2023 IEEE. 166
Figure 5-4: The measurement setup used for characterizing the frequency transmission and validating the functionality of the gap-spacing continuation. The inset provides photographs of the probe station, its associated feedthrough, and a detailed view of the DC probe. Reproduced with permission of [273], Copyright of © 2023 IEEE..... 167
Figure 5-5: A plot demonstrating the functionality of the gap-spacing continuation technique, measured using the sweeper function of a lock-in amplifier. The frequency transmission of the vibro-impact resonator is shown for applied currents of 0, 15, 30, 48, and 65 mA (gradual red lines), with solid and dashed lines indicating forward and backward sweeps, respectively. The system's operating state is shown to switch from the lowest attractor to higher ones in response to pulsed Joule-heating currents. Reproduced with permission of [273], Copyright of © 2023 IEEE..... 168
Figure 5-6: The measured bifurcation set for the vibro-impact resonator, plotting driving voltage against the frequency locations of the bifurcation points (BP), both with and without an applied current of 60 mA. This plot provides a detailed view of the functional region for attractor exchange. Reproduced with permission of [273], Copyright of © 2023 IEEE..... 169
Figure 5-7: A conceptual illustration of the vibro-impact perturbation technique, shown with its corresponding mechanical model for an attractor exchanger integrated with a general nonlinear device. Reproduced with permission of [306], Copyright of © 2023 IEEE..... 172
Figure 5-8: (a) A 2-DOF model of the vibro-impact resonator with the proposed attractor exchanger. (b) The general frequency response of a vibro-impact resonator, illustrating the hysteresis and multi-valued region. (c) Time-domain histories and phase portraits for the higher and lower energy orbits indicated in (b). (d) The time-domain response of the resonator and exchanger during the orbit exchange. (e) The phase portrait showing the two orbits and the transient trajectory connecting

doi:10.6342/NTU202600018

them. Reproduced with permission of [306], Copyright of © 2023 IEEE. Parameters used for the numerical simulations are: $mi = 1{,}2 = 1$ (kg), $bi = 1{,}2 = 0.01$ (N•s/m), $ki = 1{,}2 = 1$ (N/m), $kc, 1 = 2500$ (N/m), $kc, 2 = 1$ (N/m), $A1 = 3$ (N), $A2 = 4$ (N), $d1 = 1$ (m) and $d2 = 2$ (m). 174
Figure 5-9: An SEM image of the released comb-driven vibro-impact resonator with an integrated attractor exchanger. The device structure is composed of the entire metal layer stack from METAL1 to METAL4 of the 0.35-μm CMOS process. Reproduced with permission of [306], Copyright of © 2023 IEEE..... 175
Figure 5-10: The measurement setup for characterizing the frequency transmission and validating the vibro-impact perturbation technique. The inset on the right provides an optical image of the DUT under test. The insets on the left display the measured frequency responses for the two resonators in both linear and tapping-mode operation. Reproduced with permission of [306], Copyright of © 2023 IEEE. 176
Figure 5-11: (a) A plot validating the vibro-impact perturbation technique, measured using a standard frequency sweep. The resonator's orbit is shown to successfully switch between the upper and lower branches when the exchanger is driven by a 3000-cycle, 1-Hz burst signal at 131.3 kHz. (b) Measured backward-sweeping transmission responses of the vibro-impact resonator with the exchanger driven at different frequencies, demonstrating that the attractor exchange is only effective when the exchanger operates at its resonance frequency. Reproduced with permission of [306], Copyright of © 2023 IEEE..... 177
Figure 5-12: A map detailing the success of attractor exchange as a function of the number of burst cycles and the initial phase difference between the driving signals of the target resonator and the exchanger. The results are compared for two different target resonator frequencies: (a) 131.5 kHz and (b) 132.0 kHz. Reproduced with permission of [306], Copyright of © 2023 IEEE..... 178
Figure A-1: Transfer function of compliance, mobility, accelerance, dynamic stiffness, mechanical impedance and dynamic mass, representing a system with different input and output variable. 193
Figure A-2 Time history simulation results of (A-73) and (A-76) for a resonator starting from rest, showing comparisons for (a) varying driving voltage levels, (b) varying quality factors, and (c) three combinations with the same voltage-quality factor product..... 202

doi:10.6342/NTU202600018

Figure A-3: (a) A graphic representation of the transformation used in (A-84). (b) simulation results of (A-84) and (A-85), representing the ring-down response and its corresponding envelope for a resonator with an initial displacement of 1 μm. 205
Figure A-4: (a) An illustration of *Q* factor extraction methods, showing (a) extraction based on a fixed amplitude ratio and (b) extraction based on a fixed number of ring-down cycles. 206
Figure A-5: A displacement-time history plot for a resonator, illustrating (a) the beating phenomenon when driven near resonance and (b) the fast-growing response when driven exactly at resonance. 207
Figure A-6: Additional examples of the beating phenomenon for a resonator driven at frequencies significantly (a) lower and (b) higher than its resonance frequency. The inset provides a detailed view of the initial interaction between the homogenous and particular solutions. 207
Figure B-1: The relationship between distributed-parameter modeling and the lumped-parameter modeling approach, illustrating the connection between the electromagnetic wave and the equivalent circuit model. Also, the goal of this appendix is marked. 211
Figure B-2: A conceptual illustration of material particle movement for a longitudinal, transverse, and Rayleigh wave, respectively. 213
Figure B-3: A summary of useful properties for an electromagnetic wave..... 215
Figure B-4: A diagram of the energy transduction path, showing the energy transfer from an electrical signal to an electromagnetic (EM) wave through electrical-mechanical, piezoelectric, and electromagnetic transduction mechanisms. 216
Figure B-5: Free body diagram of (a) a rod and (b) a wire. 218
Figure B-6: An illustration of wave propagation, showing the spatial evolution from (a) an initial state to (b) a later time, and the temporal evolution at a fixed observation point from (c) an initial state to (d) a later time. 220
Figure B-7: (a) The initial disturbance at $t = 0$. (b) The time evolution of the disturbance up to time t, determined using the method of images to model the fixed end by introducing an extended, inverted initial condition. 221
Figure B-8: An illustration of the effect of impedance on wave reflection and transmission. (a) A general case of a wave propagating between two media. (b) Wave behavior on a string with varying densities: (i) from low to high density, (ii) from high to low density, and (iii) a control case with uniform density 222

doi:10.6342/NTU202600018

Figure B-9: An illustration of wave propagation with (a) fixed-free and (b) free-free boundary conditions, showing the infinite set of extended initial conditions created by the method of images at $t = 0$..... 224
Figure B-10: (a) A comparison between a static dipole's electric field and the principle of radiation generation from an oscillating dipole. (b) An illustration of a continuous electromagnetic wave generated by a dipole antenna, where an applied RF signal forces charges to accelerate and decelerate periodically, in turn generating the wave. Noted, the EM wave and electric field on the left-hand side have been omitted for clarity of representation. 228
Figure B-11: A schematic of a basic 1-port network, with the coaxial cable situated between a source and a load..... 230
Figure B-12: An illustration of the effects on phase delay and voltage change at the load end, considering (a) the signal's wavelength and (b) the cable's length. 231
Figure B-13: (a) A schematic diagram of a coaxial cable. (b) A cross-sectional view illustrating the electric (E) and magnetic (H) fields in the transverse electromagnetic (TEM) mode. 233
Figure B-14: Diagrams showing the integration paths used to calculate the electrical properties of a coaxial cable, for (a) the electric field and (b) the magnetic field. 234
Figure B-15: A schematic illustrating the lumped-parameter modeling approach for a transmission line, where the continuous line is represented by a series of discrete equivalent circuits..... 236
Figure B-16: Simulation results from LTspice for a 1-meter coaxial cable modeled by five cascaded lumped elements, showing the propagation of a unit step function and the resulting signal delay along the cable. 239
Figure B-17: An overview of a vector network analyzer (VNA), including (a) a simplified block diagram, (b) a representation of the frequency-down conversion function of a mixer, (c) a photograph of a Keysight E5080A VNA, and (d) a sample S-parameter measurement of a MEMS resonator. 242
Figure B-18: (a) A general schematic of a two-port network. (b) The ideal setup for device characterization. (c) A more realistic representation of a measurement setup, including the effects of cables and connections. 243
Figure B-19: (a) A schematic diagram of a simple one-port network. (b) Its simplified equivalent circuit representation. 244

doi:10.6342/NTU202600018

Figure B-20: (a) A schematic diagram of a simple two-port network. (b) Its simplified equivalent circuit representation. 246
Figure B-21: (a) A schematic of a two-port network where the DUT's output signal is amplified by a gain stage (G). (b) The equivalent circuit representation from the amplifier's output to Port 2. 249
Figure B-22: A representation of a real-world measurement scenario, illustrating the error boxes that account for non-ideal effects in the test fixture and cables. 250
Figure B-23: (a) A schematic illustrating the input and output variables for a generic two-port network. (b) An example circuit diagram showing a series impedance (Z) configured as a two-port network..... 251
Figure B-24: (a) A diagram showing the placement of error boxes relative to a device under test (DUT) in a two-port network. (b) The block diagram for the 8-term error model, which highlights the calibration error terms for each port. 259
Figure B-25: (a) The three-term error model for a one-port network is depicted as a block diagram. (b) A schematic view of the error box that is associated with a one-port network measurement. 261
Figure B-26: (a) A block diagram of the 12-term error model for a two-port network, illustrating the forward and backward error adapters that account for measurement system imperfections when characterizing a device under test (DUT). (b) A schematic representation of the error boxes associated with the two-port network measurement. 262
Figure B-27: This schematic shows a measurement setup with a DUT placed in a test fixture. It highlights the fixture's inherent parasitic elements, which are not removed by calibration and must be corrected through de-embedding for accurate results. 264
Figure B-28: (a) A photograph of a Keysight Technology 85033E calibration kit used for network analyzer measurements. (b) A screenshot of the software interface on the network analyzer during a Short-Open-Load-Thru (SOLT) calibration. 267
Figure B-29: Measurement results demonstrating the effectiveness of calibration and de-embedding techniques on a two-port network. The techniques are evaluated using several device under test (DUT) configurations, including (a) a through connection, (b) a 1-kΩ DUT, and (c) a 1-kΩ DUT with a parallel 1-kΩ feedthrough resistor. Part (d) illustrates the results after the de-embedding process has been applied, confirming the successful removal of measurement errors. 268

doi:10.6342/NTU202600018

Figure B-30: Photographs showing the Mini-Circuit ZFBT-282-1.5A+ bias-tee used in the experiments. View (a) displays the device's exterior from the front, while views (b) and (c) show the internal printed circuit board (PCB) from the front and back, respectively. 269
Figure B-31: Characterization of the bias tee insertion loss, measured as the forward transmission coefficient (S_{21}) using a network analyzer, under two distinct DC port termination conditions: (a) connection to ground (GND) and (b) termination with a high-impedance (High-Z) load. 270
Figure B-32: Validation of the bias tee insertion loss using a function generator and oscilloscope, showing the measured voltage loss and extracted shunt impedance for two configurations: (a) a single bias tee connected to the high-impedance oscilloscope input, and (b) two bias tees connected in parallel at the driving input. 270
Figure B-33: (a) An equivalent circuit diagram of a one-port electrostatic MEMS resonator, representing the electromechanical transduction mechanism as a transformer. (b) The simplified Butterworth-Van Dyke (BVD) equivalent circuit model for the resonator. 273
Figure B-34: (a) A diagram of an ideal transformer, illustrating the relationship between its primary and secondary circuits. (b) The equivalent circuit demonstrates how a load impedance (ZL) on the secondary side is reflected to the primary side, appearing as an equivalent impedance ($ZL*$)..... 274
Figure B-35: (a) A schematic representation of the comb-driven resonator frequently featured in this dissertation. (b) A detailed view of the interdigitated comb fingers. (c) The lumped-parameter model representing the resonator's mechanical components. 274
Figure B-36: A two-port MEMS resonator configuration is illustrated, which features distinct transduction mechanisms for actuation at Port 1 ($\eta 1$) and sensing at Port 2 ($\eta 2$). 276
Figure B-37: Equivalent circuit models for a one-port electrostatic MEMS resonator, illustrating two common representations. The first one (a) is a comprehensive model that includes the resonator's motional (i.e., Rx, Lx, Cx) and static ($C0$, $L0$) components, along with external parasitic resistance (Rp), inductance (Lp,), and capacitance (Cp). The second one (b) is the simplified and widely used model, which represents the core resonator elements in parallel with a single lumped parasitic capacitance ($Cp*$). 278
Figure B-38: Simulated frequency response of a MEMS resonator illustrating the

doi:10.6342/NTU202600018

impact of various parasitic elements. The plots compare the (a) transmission ($S21$) and (b) phase responses of an ideal resonator against those incorporating parasitic resistance (Rp), inductance (Lp), or capacitance (Cp). These results demonstrate that parasitic capacitance exerts the most significant influence on the overall device characteristics. 279
Figure B-39: Equivalent circuit models representing an electrostatic MEMS resonator configured as (a) a one-port device and (b) a two-port device. 281
Figure B-40: Comparison of the motional, feedthrough, and total currents in a MEMS resonator at three distinct operating frequencies: (a) below resonance, (b) at resonance, and (c) at anti-resonance. 281
Figure B-41: An illustration of the effects of parasitic capacitance on the frequency response of a MEMS resonator, detailing the (a) transmission ($S21$) and (b) phase response. As parasitic capacitance increases, the anti-resonance frequency shifts closer to the resonance frequency, causing significant distortion of the peak shape. The inset in (a) demonstrates how this effect can impede the extraction of the quality factor (Q-factor) using the -3 dB method. Concurrently, the phase response is altered, with the phase angle at resonance shifting toward 90° as the parasitic capacitance increases. 282
Figure B-42: Demonstration of an inaccurate quality factor extraction resulting from a frequency response distorted by parasitic capacitance. Although the -3 dB points are identifiable in this scenario, the non-ideal shape of the resonance peak invalidates the assumptions of the extraction method, leading to an erroneous calculation. 283
Figure B-43: The influence of amplifier gain on the measured frequency response. (a) The transmission ($S21$) plot demonstrates that higher gain improves the signal-to-noise ratio (SNR) and reveals signals previously obscured by the noise floor. (b) The noisy output could make the phase response unreliable and therefore correlated to the SNR of the transmission. See Figure 3-22 for real measurement results. 284
Figure B-44: Measured frequency response and corresponding successful curve fit for a resonator characterized by low parasitic capacitance. The data is presented for two distinct measurement configurations: (a) without a transimpedance amplifier (TIA) and (b) with a TIA. 285
Figure B-45: (a) An illustration of a measured frequency response of a resonator with high parasitic capacitance, a condition that necessitates an improved

doi:10.6342/NTU202600018

initial guess for a successful curve fit. (b) An example illustration demonstrates that a more accurate parameter extraction can be achieved by limiting the fit to a narrow bandwidth around the resonance peak, as the algorithm is able to detect the distorted peak shape even when the anti-resonance is not apparent. 285
Figure B-46: (a) A example schematic of a multi-port MEMS resonator and (b) its equivalent lumped-element circuit model. The terms $vi1$ and $vi2$ represent the input ac signal, $v0$ is the output voltage at port 3 and $C0i$ represent the rest capacitance of port *i*. 288
Figure B-47: (a) A mechanical coupling beam and (b) its equivalent circuit representation. The diagram illustrates the analogy between the mechanical domain (force, velocity) and the electrical domain (voltage, current). 289
Figure B-48: (a) A lumped-element model of a second-order coupled resonator. (b) Its frequency response, showing the split resonance peaks corresponding to the in-phase 290
Figure B-49: (a) A example schematic of a CC-beam MEMS resonator considering several modes. (b) Equivalent circuit representations of (a)..... 291
Figure B-50: (a) Time-domain simulation of a two-mode ring-down response. (b) The corresponding frequency spectrum obtained via FFT (black dots), showing the fitted resonance peaks for the first (red) and second (green) modes according to (B-189). 295
Figure C-1: Illustrations of a water molecule, showing (a) its structural formula, (b) a schematic of the molecule and its atoms, (c) its resulting dipole moment, and (d) its ionization process. 296
Figure C-2: A depiction of various intermolecular and ionic interactions, including (a) Coulombic, (b) Keesom, (c) Debye, and (d) London dispersion forces. 298
Figure C-3: Schematic diagrams illustrating the interaction forces between (a) a single molecule and an infinite planar surface, and (b) two parallel infinite planar surfaces. 299
Figure D-1: (a) The 1-DOF lumped mechanical model for the vibro-impact resonators being analyzed. (b) An illustration of the contact model, which incorporates attractive, repulsive, and contact viscoelastic forces. 306
Figure D-2: The simulation workflow is depicted alongside its implementation as a Simulink block diagram. The KV-DMT model is computed within a dedicated block that is based on a *MATLAB* function. 307
Figure D-3: Simulated time-domain responses for a vibro-impact resonator that is driven at its resonance frequency, starting from rest. The complete time

doi:10.6342/NTU202600018

histories for (a) displacement and (b) the corresponding contact force are presented. A comparison between the transient and steady-state phases is provided through detailed views: (c) and (d) highlight the initial transient behavior, which features a significant overshoot, while (e) and (f) show the stable, lower-amplitude response in the steady state. ... 309
Figure D-4: Computed frequency responses for the resonator, demonstrating the effects of intrinsic nonlinearities. (a) The response is shown for different levels of nonlinear damping while excluding nonlinear stiffness. (b) The amplitude-dependent characteristic of the damping is illustrated by maintaining a constant product of the quality factor and driving voltage. (c) The influence of varying both positive and negative nonlinear (Duffing) stiffness is displayed. (d) A similar analysis with a constant product of quality factor and driving voltage is performed, this time including the nonlinear stiffness effects. 311
Figure D-5: Numerically generated frequency responses for the vibro-impact resonator, illustrating a parametric study of the system's behavior. The individual plots show the effects of varying (a) driving voltage, (b) quality factor, (c) contact viscoelastic damping, (d) Young's modulus of the contact material, (e) gap spacing, and (f) Hamaker constant..... 312
Figure D-6: Magnified views of the tapping responses from Figure D-5. These plots offer a closer look at the complex dynamics near the onset of impact, including the period-doubling bifurcations that are difficult to see in the full-scale plots. 313
Figure D-7: A comparison of simulated frequency responses for the vibro-impact resonator under different conditions. (a) The effect of varying the product of driving voltage and quality factor is shown for a system without contact viscoelastic damping. (b) The same analysis is repeated for a system that includes contact viscoelastic damping. (c) The impact of varying nonlinear damping is illustrated. (d) The influence of varying nonlinear stiffness on the frequency response is presented. 314
Figure D-8: Magnified views of the tapping responses from Figure D-7. These plots offer a more detailed look at the complex dynamics occurring near the contact region. 315
Figure D-9: (a) The simulated frequency response of the linear system is shown for a range of driving voltages and quality factors. (b) The corresponding grazing frequencies, extracted from the response curves in (a), are plotted to illustrate their dependence on driving voltage. 316
Figure D-10: A plot of the extracted nonlinear resonance frequency versus the

doi:10.6342/NTU202600018

driving voltage for a vibro-impact resonator, illustrating the effect of varying contact viscoelastic damping. The curves show that the resonance frequency undergoes an initial development, followed by rapid growth, and eventual saturation as the driving voltage is increased. 317
Figure D-11: An analysis of the system's bistable behavior, demonstrating how initial conditions determine the final steady-state motion. (a) The frequency response from Figure D-5 (a) is reproduced to identify the bistable region where high- and low-energy attractors coexist. (b) Time-domain simulations starting from two different initial conditions, $x, \acute{x} = (-1\ \mu m, 0)$ and $x, \acute{x} = (-2\ \mu m, 0)$ show that the system evolving to two distinct steady-state responses. (c) The complete trajectories are visualized in a phase portrait, which displays the initial conditions (I.C.s), the transient phase, and the final steady-state solutions. (d) A basin of attraction map, calculated for a driving frequency of 170 kHz, illustrates the sets of initial conditions that converge to each of the two stable attractors..... 319
Figure D-12: A validation of the simulation platform is presented by comparing its output to the results from [58]. The excellent agreement between the simulation and the previously published data confirms the accuracy and reliability of the developed model. Reproduced with permission of [58], Copyright © 2002 by American Physical Society. 320
Figure D-13: A diagrammatic representation of the period-doubling route to chaos in a nonlinear system. As control parameters such as force and frequency are adjusted, the system's motion evolves from a stable fixed point to a limit cycle, followed by a grazing impact, and then progresses through a cascade of period-doubling motions, ultimately leading to chaos. 324
Figure D-14: A comparison of the system's frequency response at driving voltages of (a) 30 V, (b) 60 V, and (c) 120 V. To further analyze the dynamics, bifurcation diagrams corresponding to the 60 V and 120 V cases are presented in (d) and (e), respectively. These diagrams were derived using a stroboscopic Poincaré section taken at the maximum displacement. 324
Figure D-15: The time-domain steady-state motion of the system at five distinct driving frequencies, along with their associated FFT spectra. The waveforms are shown for (a) 60 kHz, (b) 110 kHz, (c) 119 kHz, (d) 128 kHz, and (e) 129 kHz. The corresponding frequency spectra for each case are displayed in (f-j)..... 325

doi:10.6342/NTU202600018

Figure D-16: The bifurcation plot from Figure D-14 (e) is displayed again, this time representing the system's motion by plotting both (a) the maximum and (b) the minimum displacement of the periodic orbits. 326
Figure D-17: (a) An SEM photograph of the 80-kHz comb-driven folded-beam resonator is displayed, along with the experimental setup. (b) The device's linear frequency response is presented, which was measured using a network analyzer and indicates a quality factor of approximately 2700. 327
Figure D-18: (a) The measured tapping responses of the resonator are presented for several driving voltages, using both forward and backward frequency sweeps. (b) The bifurcation frequencies derived from the data in (a) are plotted as a function of the driving voltage. 327
Figure D-19: Experimentally observed frequency comb spectra are presented for the resonator under various operating parameters. (a) The spectral evolution is detailed for an increasing driving voltage, which induces a progression through several dynamic regimes, including asymmetric, chaotic, and symmetric patterns. (b) A distinct frequency comb that was generated under a lower driving voltage is also shown. (c) The sensitivity of the comb structure to the driving frequency is demonstrated, highlighting the resulting shifts between chaotic and asymmetric responses..... 328
Figure D-20: (a) An SEM image of the 2.2-MHz clamped-clamped (CC) beam resonator is shown, including its experimental setup. (b) The device's linear frequency response, measured with a network analyzer. 330
Figure D-21: (a) The measured tapping responses of the CC-beam resonator are shown for various driving voltages, using both forward and backward frequency sweeps. (b) The bifurcation frequencies, extracted from the data in (a), are plotted as a function of driving voltage, revealing the evolution of the grazing (GR) and saddle-node (SN) points. 331
Figure D-22: An experimentally derived map illustrating the occurrence of frequency combs. The shaded green areas indicate the specific driving voltage and frequency ranges where frequency comb generation was observed.. 332
Figure D-23: A collection of measured frequency comb spectra for the CC-beam resonator under different operating conditions. The plots show the symmetric comb patterns generated at driving voltages of (a) 4.2 V, (b) 5.2 V, and (c) 6.2 V, corresponding to the different operational regions identified in Figure D-22. 333
Figure D-24: A comparison of resonator models using 1-DOF lumped diagrams for (a) a single-sided stopper and (b) a double-sided stopper. (c) A force-

doi:10.6342/NTU202600018

displacement plot showing the resulting piecewise-linear system stiffness. (d) A comparison of frequency responses for resonators with soft contact, hard contact, and double-sided hard contacts. Reproduced with permission of [192], Copyright of © 2021 IEEE. 335
Figure D-25: (a) A schematic diagram and (b) an SEM image of the fabricated comb-driven folded-beam micromechanical vibro-impact resonator, featuring symmetrical double-sided stoppers. Reproduced with permission of [192], Copyright of © 2021 IEEE. 337
Figure D-26: Measured frequency responses for vibro-impact resonators with a polarization voltage of 36 V and driving signal levels from 0 dBm to 20 dBm, comparing (a) a single-sided stopper configuration with (b) a double-sided stopper configuration. Reproduced with permission of [192], Copyright of © 2021 IEEE. 339
Figure D-27: Simulated nonlinear tapping-mode frequency responses for (a) a single-sided and (b) a double-sided stopper structure, with driving power levels from -10 dBm to 20 dBm. Reproduced with permission of [192], Copyright of © 2021 IEEE. 339
Figure D-28: (a) A plot comparing the measured tapping bandwidth versus driving voltage for single-sided and double-sided vibro-impact resonators. (b) An analysis of measured tapping bandwidth versus driving voltage for double-sided resonators with different gap spacing configurations. Reproduced with permission of [192], Copyright of © 2021 IEEE. 341
Figure D-29: A comparison of numerically simulated responses for linear, single-sided, and double-sided impact configurations, showing (a) the frequency responses and (b) the phase portraits. Detailed views of the phase portraits at the stopper locations are provided in (c) and (d). Reproduced with permission of [192], Copyright of © 2021 IEEE. 342
Figure E-1: (a) A diagram of the projectile motion problem, showing the trajectory over time. (b) The corresponding simulation results are presented in both nondimensional and dimensional forms. 346
Figure E-2: Three diagrams illustrating one cycle of oscillation for a vibro-impact resonator with a single-sided contact. The representations show different integration paths over the phase angle: (a) from 0 to 2π, (b) from the contact angle θc to $2\pi + \theta c$ and (c) from 0 to 2π with the contact occurring near π instead of 0 or 2π. 367
Figure F-1: Simulated frequency responses based on (E-123), comparing systems (a) without the nonlinear damping term $b3 = 0$ and (b) with the nonlinear damping term $b3 = b30$. 382

doi:10.6342/NTU202600018

Figure F-2: Integral paths for the nonlinear surface interaction forces over the phase angle θ, shown for the (a) KV-DMT, (b) DMT and (c) simplified model, respectively. 386
Figure G-1: Experimental characterization of the resonator's thermal properties, showing (a) the frequency response, (b) the Temperature Coefficient of Frequency (TCF), and (c) the Temperature Coefficient of Quality Factor (TCQ). 392
Figure G-2: The measured forward-sweeping frequency response of the resonator, shown (a) before and (b) after the application of a de-embedding procedure to correct for parasitic effects. 394
Figure G-3: The measured backward-sweeping frequency response of the resonator, comparing the data (a) without de-embedding and (b) with de-embedding applied. 395

doi:10.6342/NTU202600018

List of Tables

TABLE 2-1: SUMMARY OF LITERATURES ON THE VIBRO-IMPACT APPLICATION AND MODEL ASSOCIATED. REPRODUCED WITH PERMISSION OF [107], COPYRIGHT OF © IOP PUBLISHING. 31
TABLE 2-2: EXAMPLES OF THE INTERACTION FORCE MODEL SELECTION FROM [204]. REPRODUCED WITH PERMISSION OF [107], COPYRIGHT OF © IOP PUBLISHING. 44
TABLE 2-3: SUMMARY OF SOLVING TECHNIQUES WITH APPLICATION FROM LITERATURES. REPRODUCED WITH PERMISSION OF [107], COPYRIGHT OF © IOP PUBLISHING. 46
TABLE 3-1: ETCHING RATES OF SILOX VAPOX III. REPRODUCED WITH PERMISSION OF [316] COPYRIGHT OF © 2025 IEEE. 79
TABLE 3-2: PREDICTED ETCHED DEPTH FOR METAL LAYERS AND RELEASE TIME. REPRODUCED WITH PERMISSION OF [316] COPYRIGHT OF © 2025 IEEE. 80
TABLE 3-3: YOUNG'S MODULUS AND DENSITY FOR AYERS/MATERIALS USED. REPRODUCED WITH PERMISSION OF [316] COPYRIGHT OF © 2025 IEEE. 82
TABLE 3-4: PARAMETERS AND PERFORMANCES OF THE DESIGNED RESOSWITCH. REPRODUCED WITH PERMISSION OF [316] COPYRIGHT OF © 2025 IEEE. 92
TABLE 3-5: CONTACT FORCE REQUIRED FOR STABLE CONTACT IN COMMON METALS AND THE ASSOCIATED RESISTIVITY AND CONTACT RESISTANCE. REPRODUCED WITH PERMISSION OF [316] COPYRIGHT OF © 2025 IEEE. 98
TABLE 4-1 COMPARISON OF RECEIVER SPECIFICATIONS. REPRODUCED WITH PERMISSION OF [89], COPYRIGHT OF © 2020 IEEE. 154
TABLE A-1: THE CLASSIFICATION OF THE STABILITY AND PHASE PORTRAIT OF 1-DOF SYSTEMS. 210
TABLE B-1 THE SUMMARY OF COMMON CIRCUITS' ABCD MATRIX. 253
TABLE B-2 SUMMARY FOR THE CONVERSION EQUATION, ASSUMING PORT IMPEDANCES ARE MATCHED TO CHARACTERISTIC IMPEDANCE $Z01 = Z02 = Z0$ 255
TABLE B-3: A SUMMARY OF S-PARAMETER VALUES FOR DIFFERENT DEVICE UNDER

doi:10.6342/NTU202600018

TEST (DUT) IMPEDANCES, RANGING FROM A SHORT (0 Ω) TO AN OPEN (∞ Ω) CIRCUIT. 258
TABLE B-4: THE ANALOGY BETWEEN KEY QUANTITIES IN MECHANICAL TRANSLATIONAL SYSTEMS AND ELECTRICAL CIRCUIT SYSTEMS. 272
TABLE D-1 SUMMARY OF THE USED PARAMETERS FOR THE SIMULATIONS. 308
TABLE D-2: SUMMARY OF THE USED PARAMETERS FOR THE SIMULATIONS 340

doi:10.6342/NTU202600018

List of Abbreviations

Abbreviations	Definition
AC	Alternating current
AFM	Atomic force microscopy
AI	Artificial intelligence
AM	Amplitude modulation
ARW	Angle random walk
ASK	Amplitude shift keying
BAW	Bulk acoustic wave
BI	Bias stability
BVD	Butterworth-Van Dyke
CBC	Control-based continuation
CMOS-MEMS	Complementary metal-oxide-semiconductor micro-electro-Mechanical systems
CWA	Current waveform analyzer
D	Dimension
DC	Direct current
DE	Differential evolution
DLVO	Derjaguin-Landau-Verwey-Overbeek
DMT	Derjaguin-Muller-Toporov
DOF	Degree-of-freedom
DUT	Device under test
EA	Evolutionary algorithm
ECR	Electrical contact resistance
EM	Electromagnetic
ENEPIG	Electroless nickel electroless palladium immersion gold
ENIG	Electroless nickel immersion gold

doi:10.6342/NTU202600018



ENImAg	Electroless nickel immersion silver
FDM	Finite-difference method
FDTD	Finite-difference time-domain
FEA	Finite element analysis
FETD	Finite-element time-domain
FFT	Fast Fourier transform
FSK	Frequency-shift keying
FUC	Frequency up-conversion
GA	Genetic algorithms
HAM	Homotopy analysis method
I.C.	Initial condition
IC	Integrated circuits
ICE	Implicit condensation and expansion
IMD	Intermediate oxide
IoT	Internet of things
IRS	Improved reduced system
JKR	Johnson-Kendall-Roberts
KV-DMT	Kelvin-Voigt Derjaguin-Muller-Toporov
LF	Low-frequency
LJ	Lennard-Jones
LNA	Low noise amplifier
LRM	Line-reflect-match
mBVD	Modified BVD
MEMS	Micro-electro-mechanical systems
MOA	Method of averaging
MOR	Model order reduction
NA or ENA	Network analyzer or electrical network analyzer
ODE	Ordinary differential equations

doi:10.6342/NTU202600018

OOK	On-off keying
PCB	Printed circuit board
PDE	Partial differential equations
PDM	Pulse density modulation
PGD	Proper generalized decomposition
PKE	Passive keyless entry
POD	Proper orthogonal decomposition
PSO	Particle swarm optimization
QSMA	Quasi-static modal analysis
Resoswitch	Resonant switch
RF	Radio frequency
RFID	Radio frequency identification
RKDP	Runge-Kutta Dormand–Prince
ROM	Reduced order modeling
RPD	Reverse period doubling
SAO	Simulated annealing optimization
SEM	Scanning electron microscope
SNA	Scalar network analyzer
SOLT	Short-open-load-through
SWR	Standing wave ratio
TE	Transverse electric
TED	Thermal elastic damping
TEM	Transverse electromagnetic mode
TM	Transverse magnetic
TRL	Thru-reflect-line
VNA	Vector network analyzer
MMS	Method of multiple scale

doi:10.6342/NTU202600018

List of Notations and Symbols

Latin symbols	Description
a_0	Interatomic spacing or equilibrium spacing between the two objects
a_c	Effective contact radius
a_i	Normalized energy wave propagating in positive direction
$a_{p.l}$	Displacement amplitude of the linear m-b-k system
$a_{l.p.0} = A_{0.max}$	Maximum amplitude considering the effect of linear damping (i.e., amplitude at resonance frequency)
$a_{l.p.n} = A_0$	Approximated maximum amplitude for high Q devices
$a_{0.lb}$	Lower bound of interatomic spacing obtained by the work of adhesion calculated by JKR model
$a_{0.ub}$	Upper bound of interatomic spacing obtained by the work of adhesion calculated by JKR model
$\widehat{a_0}$	Dimensionless intermolecular spacing
$\widehat{a_{p.vdP}}$	Dimensionless displacement amplitude considering van der Pol term for ring-down response
$\widehat{a_{p.T}}$	Dimensionless displacement amplitude considering all the nonlinearity (i.e., van der Pol term, Duffing term and KV-DMT model)
$\widehat{a_{p.vD.D}}$	Dimensionless displacement amplitude considering all the nonlinearity except contact damping (i.e., van der Pol term, Duffing term and DMT model)
A	Voltage ratio
A	Cross-sectional area
A_0	Maximum displacement at practical resonance

doi:10.6342/NTU202600018



$A_{i=1,2,3,4,}$	Elements in Jacobian matrix
A_d	Driving force amplitude
A_{di}	Driving force amplitude of resonator *i*
$A_{d.p}$	Driving force amplitude at port *p*
A_{trans}	Overlapped area of comb fingers in transverse direction
A_{ratio}	Amplitude ratio
A_{VIA}	Area of the VIA layers
$\bar{\bar{A}}$	Lumped coefficient for resonance frequency term in $x_{DMT.f}$
$\bar{A}$	Lumped coefficient for resonance frequency term in $x_{l.f}$
$\hat{A}$	Lumped coefficient for resonance frequency term in x_{KV-DMT}
$\boldsymbol{A}$	Jacobian matrix
$\widehat{A_d} = \xi = \frac{1}{Q}$	Dimensionless forcing amplitude
b_3	Cubic nonlinear damping or van der Pol term
b_c	Viscous (damping) coefficient during contact or contact damping
b_i	Effective damping of object *i*
b_i	Normalized energy wave propagating in negative direction
b_r	Equivalent damping of the resonator
$b_{m.j}$	Width of the *j* METAL layer
b_K	Contact-damping parameter of the Kelvin model
b_{IMD}	Width of the IMD layers
b_{VIA}	Width of the VIA layers
B	Open circuited conductance
B_3	Dimensionless van der Pol coefficient
B_d	Bit rate of an ASK wave signal
$\hat{B}$	Lumped coefficient for damping term in x_{KV-DMT}

doi:10.6342/NTU202600018

$\bar{B}$	Lumped coefficient for damping term in $x_{l.f}$
$\bar{\bar{B}}$	Lumped coefficient for damping term in $x_{DMT.f}$
$\vec{B}$	Magnetic field
c	Wave speed of any problem in general
c_1	Interaction coefficient of the attractive potential
c_2	Interaction coefficient of the repulsive potential
c_s	Wave speed of an electrical signal/electron in a standard cable/ transmission line
$c_{l.r}$	Longitudinal mechanical wave speed in the rod
$c_{l.m}$	Longitudinal wave speed of media
$c_{t.s}$	Transverse mechanical wave speed in a string
C	Short circuited resistance
C_r	Coefficient of restitution
C_p	Parasitic capacitance of the capacitive MEMS resonator
C_x	Equivalent motional capacitance of the capacitive MEMS resonator
C_{ts}	Coefficient of the general tip-sample interaction force's attractive force term
C_{vdP}	Additional damping contributed by van der Pol term in the averaged system
C_{vis}	Effective contact damping due to nonconservative term of the DMT model
C_{vdW}	Material constant for W_{vdW}
C_{long}	Capacitance of the comb finger electrode in longitudinal direction
C_{trans}	Capacitance of comb fingers in transverse direction
C_B	Bleeding capacitance

doi:10.6342/NTU202600018

$\bar{C}$	Effective capacitance per unit length
d	Distance between object such as planar wall of molecule
d_0	Clearance between vibrating structure and the stopper
d_{ff}	Distance between the comb fingers
d_{sf}	Initial spacing between the tip of fixed comb fingers and the shuttle
$d_{0.op}$	Optimal gap spacing of the averaged system
$d_{etch.t.i}$	Etching depth of the top METAL of the *i* METAL layer.
$d_{etch.b.i}$	Etching depth of the bottom METAL of the *i* METAL layer
d_{VIA}	The distance between parallel axis and centroidal axis
d^*_{etch}	Effective etch depth
$\widehat{d_0}$	Dimensionless gap spacing
D	Current Ratio
D	Nondimensionalized gap spacing
D_d	Duty cycle of an ASK wave signal
D_i	Derivative operator to T_i
D_{ts}	Coefficient of the general tip-sample interaction force's repulsive force term
e	Elementary charge
E_i	Young's modulus of the object *i*
E_{eq}	Effective Young's modulus of the folded beams
E^+	Total kinetic energy of the two objects before impact
E^-	Total kinetic energy of the two objects after impact
E^*	Effective Young's modulus
$\vec{E}$	Electric field
f_0	Resonance frequency
f_d	Driving frequency

doi:10.6342/NTU202600018

f_{op}	Required frequency for the operation
$f_{GR,1}$	1st grazing frequency considering linear counterpart only
$f_{GR,2}$	2nd grazing frequency considering linear counterpart only
$F = P$	Applied load for contact
F_c	Contact force function
F_d	Driving force function
F_l	Contact force function of the linear elastic contact model
F_B	Contact force function of the Bradley model
F_K	Contact force function of the Kelvin model
$F_{ad} = P_a$	Pull-off force or adhesive force
F_{kb}	Contact force function of the general elastic contact model
F_{nl}	Lumped nonlinear force function representing some possible nonlinearity
$F_{ad.B}$	Pull-off force of the Bradley model
F_{vdw}	van der Waals force function
F_{JKR}	Contact force function of the JKR model
F_{DMT}	Contact force function of the DMT model
F_{Hertz}	Contact force function of the Hertz model
$F_{ad,DMT}$	Pull-off force of the DMT model
$F_{ad,JKR}$	Pull-off force of the JKR model
$F_{DMT.op}$	Optimal/Maximum peak repulsive force of the averaged system for a given driving force in steady state
F_{KV-DMT}	Force function of KV-DMT model
$F_{DMT.peak}$	Peak repulsive force in the steady state
$\boldsymbol{F}$	Vector field of the system
g_0	Standard gravitational acceleration
g_x	Gravitational acceleration function

doi:10.6342/NTU202600018

G_A	Gain of the amplifier/transimpedance amplifier
GR_i	*i* th grazing bifurcation point
$\bar{G}$	Effective conductance per unit length
h	Height of the device layer
$h_{m.j}$	Height of the *j* METAL layer
h_{IMD}	Heigh of the IMD layers
$h_{VIA,l}$	Heigh of the *l* VIA layer
$H = H_{12}$	Hamaker constant for material 1 and 2 within air
H_a	Hamaker constant of the attractive potential
H_r	Hamaker constant of the repulsive potential
$H(x - d_0)$	Heaviside step function
i_x	Motional current of the capacitive MEMS resonator
$I_{i=1,2,3,4,5,6}$	Integration function of the nonlinearities
I_c	Contact current (i.e., the current flow through the contact region)
I_{m_j}	Moment of inertia of *j* METAL layer of the folded beams
I_{total}	Moment of inertia of the folded beams
I_0^*	Measured motional current at the beginning of ring-down
$I_{IMD,k}$	Moment of inertia of *k* IMD layer of the folded beams
$I_{VIA,l}$	Moment of inertia of *l* VIA layer of the folded beams
$\bar{I}$	Current in phasor form
$\vec{J}$	Current density
k	Material constant representing the effect of the surrounding medium
k_3	Cubic nonlinear stiffness or Duffing term
$k_{3.m}$	Cubic nonlinear stiffness form geometric nonlinearity
$k_{3.e}$	Cubic nonlinear stiffness form electrostatic nonlinearity

doi:10.6342/NTU202600018

k_c	Contact stiffness of the stopper
k_{c1}	Contact stiffness between the stopper and resonator 1
k_{c2}	Contact stiffness between the resonator 1 and 2
k_i	Effective stiffness of object *i*
k_l	Contact stiffness of the linear elastic contact model
k_r	Equivalent stiffness of the resonator
k_B	Boltzmann constant
k_K	Contact-stiffness parameter of the Kelvin model
K	Contact-stiffness parameter in general
K_3	Dimensionless Duffing coefficient
K_{vdw}	Effective contact stiffness due to Van der Waals term of the DMT model
K_D	Additional stiffness contributed by Duffing term in the averaged system
K_H	Effective contact stiffness due to Hertz term of the DMT model
K^*	Contact modulus
l_{ff}	Overlapped comb finger length
L_b	Length of the folded beams
L_e	Lorentz number of ideal conductors
L_p	Additional inductance implemented in numerical simulation for convergence
L_x	Equivalent motional inductance of the capacitive MEMS resonator
$\bar{L}$	Effective inductance per unit length
m_i	Effective mass of resonator *i*
m_r	Equivalent mass of the resonator
M_b	Total mass of the folded beams
M_c	Cycle number form initial to N_c times lower value in ring-

doi:10.6342/NTU202600018

	down
M_d	Modulation factor of an ASK wave signal
M_s	Total mass of the shuttle
M_t	Total mass of the truss
n	Geometry dependent coefficient for contact model
N	Number of the comb fingers
N_c	Amplitude drop ratio
N_P	Number of turns in a winding of primary circuit
N_S	Number of turns in a winding of slave circuit
P_L	Averaged power delivered to the load
PD_i	*i* th period-doubling bifurcation point
$\bar{P}$	Contact pressure ratio
q	Charge
q_i	Charge of the ion *i*
Q	Quality factor
$Q_{m.time}$	Extracted quality factor from ring-down response
$Q_{m.freq}$	Extracted quality factor from frequency response with 3-dB formular
r	Separation of the interacting ions 1 and 2
r	Distance between the two particles
r_{min}	Characteristic distance for which potential energy between the particles is at its minimum
R_c	Electrical contact resistance
R_x	Equivalent motional resistance of the capacitive MEMS resonator
R_p	Additional resistance implemented in numerical simulation for convergence
R_B	Bleeding resistance

doi:10.6342/NTU202600018

R_E	Radius of the Earth
R_M	Constriction film resistance
R_S	Contamination resistance
R^*	Effective radius of curvature
$\bar{R}$	Effective resistance per unit length
$S = P_{in.min}$	Grazing sensitivity of the resoswitch as a receiver in power if the impedance is matched
S_{11}	Input reflection/return loss
S_{12}	Gain from reverse transmission
S_{21}	Gain from forward transmission
S_{22}	Output reflection/return loss
$S_{21.A}$	Gain from forward transmission with an amplifier
SN_i	*i* th saddle-node bifurcation point
t_c	Contact time
t_r	Reference values for the time
t_s	Scaling factor for the time
t_{op}	Required time constant for the operation
t_{sw}	Switching time
t_{off}	Required time constant for the OFF state
$\hat{t}$	Dimensionless time
T_0	Room temperature
T_s	Supertemperature
T_{on}	Duration of ON state of an ASK wave signal
T_{off}	Duration of OFF state of an ASK wave signal
u_i^+	Velocity of object *i* before contact
u_i^-	Velocity of object *i* after contact
v_0	Initial condition of the velocity

doi:10.6342/NTU202600018

v_i	Poisson's ratio of the object *i*
v_i	Driving voltage signal
v^+	Relative velocity between the two objects before contact
v^-	Relative velocity between the two objects after contact
$V_{o.on}$	Time response of the output voltage in ON state
$v_{i.max}$	Maximum voltage in an ASK wave signal (i.e., bit 1)
$v_{i.min}$	Minimum voltage in an ASK wave signal (i.e., bit 0)
$V_{o.max}$	The maximum output voltage
$V_{o.off}$	Time response of the output voltage in OFF state
$V_{on.end}$	Initial condition of OFF state (i.e., the end state of the ON state)
$V_{o.off.end}$	Initial condition of ON state (i.e., the end state of the OFF state)
$v_{i.min@f_0}$	Grazing sensitivity of the resoswitch as a receiver
$v_{LJ,n-m}$	Lennard-Jones (LJ) potential model with exponents in *n* and *m*
V_C	Contact voltage (i.e., the voltage between contacting two objects)
V_d	Driving voltage amplitude
V_G	Voltage source from the instrument's transmitting end
V_P	Bias voltage or polarization voltage
V_S	Structure bias or voltage supply for hot switching operation
V_T	Required threshold voltage for next stage
V^+	Voltage propagation in positive direction
V^-	Voltage propagation in negative direction
$\bar{V}$	Voltage in phasor form
$W = W_{12}$	Work of adhesion for object 1 and 2 within air
W_b	Width of the folded beams

doi:10.6342/NTU202600018

W_{ikj}	Work of adhesion for object *i* and *j* within the liquid medium *k*
W_{ion}	Interaction energy between ions in a medium
W_{vdW}	Van der Waals interaction between two molecules in vacuum
W_{JKR}	Work of adhesion calculated by JKR model
W_{DMT}	Work of adhesion calculated by DMT model
x_0	Initial condition of the displacement in ramp-up phase
x_n	Homogenous solution of the displacement
x_p	Particular solution of the displacement
x_r	Reference values for the displacement
x_s	Scaling factor for the displacement
x_{en}	Upper envelope curve of the forced linear m-b-k system
$x_{l.f}$	Frequency response function of the forced linear m-b-k system
$x_{l.t}$	Time response function of the forced linear m-b-k system
$x_{en.RD}$	Upper envelope curve of x_{RD}
$x_{en.RD.vdP}$	Slow varying response in ring-down (i.e., upper envelope curve in ring-down considering the effect of van der Pol term)
x_{RD}	Ring-down response function of linear m-b-k system
x_{DMT}	Frequency response function of the m-b-k system cooperated with DMT model
x_T	Frequency response function of the m-b-k system cooperated with KV-DMT model, Duffing term and van der Pol term
$x_0^* = d_{0.SEM}$	(1) Reference scale for averaged system considering the effect of van der Pol damping and (2) initial condition for ring-down response function
$\hat{x}$	Dimensionless displacement
$\dot{\boldsymbol{x}}$	State variables
$\hat{x}_1 = \hat{x}$	State variable representing displacement

doi:10.6342/NTU202600018

$\hat{x}_2 = \hat{x}'$	State variable representing velocity
z	Characteristic parameter for subharmonic impact motion
z_1	Valences of the interacting ion 1
z_2	Valences of the interacting ion 2
Z_r	Equivalent motional impedance of the capacitive MEMS resonator
Z_T	Impedance of the instrument's transmitting end
Z_R	Impedance of the instrument's receiving end
$Z_{G.out}$	Output impedance of the transimpedance amplifier
$Z_{Amp.in}$	Input impedance of the amplifier
$Z_{Amp.out}$	Output impedance of the amplifier

Greek symbols	Description
ω_n	Natural angular frequency or pure resonance angular frequency
α	Material dependent coefficient for coefficient of restitution
α	Dimensionless Hamaker constant
β	Stiffness ratio or nondimentional contact-stiffness parameter
γ	Nondimentional contact damping coefficient
γ_i	Surface energy of object *i*
γ_{ij}	Interfacial free surface energy of object *i* and *j*
Γ	Interpolation function used to describe transition from diffusive to ballistic regime
Γ_{11}	Reflection coefficient for the propagating wave
Γ_{21}	Transmission coefficient for the propagating wave
δ	Indentation
δ_p	Unit impulse function or Dirac delta function
Δf_{3dB}	3dB frequency bandwidth

doi:10.6342/NTU202600018

ε_0	Permittivity of free space
ε_r	Relative permittivity of the medium
ϵ	Well depth of two particles
η	Overall electro-mechanical coupling coefficient
θ_0	Impact phase at beginning and end of contact
λ	Elasticity parameter or Maugis parameter
λ_e	Electron mean free path
$\lambda_{q=1,2}$	*q-th* eigenvalue
λ_r	Real part of the eigenvalue
λ_i	Imaginary part of the eigenvalue
λ_s	Wavelength of an electrical signal/electron in a standard cable/ transmission line for a given frequency
μ	Tabor parameter
μ_0	Magnetic permittivity of free space
μ_j	Control parameters of the system
ξ	Damping ratio
ρ_e	Electrical resistivity
ρ_c	Charge density
$\rho_{m.i}$	Density of molecules per volume unit for the wall *i*
σ	Characteristic distance for which potential energy between the two particles is zero
τ_n	Nondimentional time scale
τ_{on}	Time constant in ON state
τ_{off}	Time constant in OFF state
ϕ	Phase difference between forcing function and displacement
ϕ	Magnetic flux
χ	Hysteresis-damping factor in general

doi:10.6342/NTU202600018

χ	Frequency response function in $F_{DMT.peak}$
χ_D	Frequency response function in $F_{DMT.peak}$ considering the effect of Duffing term
χ_{HC}	Hysteresis-damping factor of the Hunt-Crossley model
$\omega_{n.D.d_0}$	Center frequency of Duffing oscillator when vibration amplitude equaled to d_0
$\omega_0 = \omega_{d.max}$	Practical resonance frequency or resonance frequency
ω_0	Resonance angular frequency
$\omega_{3dB.1}$	Lower 3dB angular frequency
$\omega_{3dB.2}$	Upper 3dB angular frequency
ω_d	Driving angular frequency
$\omega_{n.D}$	Nonlinear resonance frequency considering the contribution of the Duffing term
$\omega_{n.KV-DMT}$	Nonlinear resonance frequency considering the contribution of the KV-DMT model, Duffing term and van der Pol term
$\omega_{JU.D}$	Jump-up frequency of the Duffing oscillator
Ω_d	Frequency ratio or nondimentional driving frequency

Letter like	Description
$\mathcal{L}[\cdot]$	Laplace transform operator
°C	Degree Celsius

doi:10.6342/NTU202600018

VITA

1994/06	New Taipei City, Taiwan
2014/09-2016/06	B.S. in Mechanical Engineering, Southern Taiwan University of Science and Technology, Tainan City, Taiwan
2016/09-2019/08	M.S. in Institute of Applied Mechanics, National Taiwan University, Taiwan
2018/04-2023/04	Facility Assistant Engineer in Nano-Electro-Mechanical-System Research Center, National Taiwan University, Taiwan
2019/09-2020/01 & 2020/09-2022/09	Graduate Teaching Assistant of Experiments on Applied Mechanics I (AM7012), National Taiwan University, Taiwan
2019/09-2023/10	Ph.D. Student Representative in Institute of Applied Mechanics, National Taiwan University, Taiwan
2023/05-2023/08	Summer Internship in Department of MEMS Device Engineering, Sensortek Technology Corporation, Hsinchu City, Taiwan
2019/09-2025/12	Ph.D. in Institute of Applied Mechanics, National Taiwan University, Taiwan

Field of Study

Major field: mechanical engineering

Focus area: micro-electro-mechanical systems (MEMS), nonlinear vibration, vibro-impact oscillator, resoswitch

doi:10.6342/NTU202600018

Publications

Journal Paper (Total: 10, First Author: 3)

- [Master's degree] S.-C. Lu, **C.-P. Tsai**, Y.-C. Huang, W.-R. Du, and W.-C. Li, "Surface Condition Influence on the Nonlinear Response of MEMS CC-Beam Resoswitches," *IEEE Electron Device Letters (EDL)*, vol. 39, no. 10, pp. 1600-1603, Oct. 2018.
- [Master's degree] J.-R. Liu, S.-C. Lu, **C.-P. Tsai**, and W.-C. Li, "A CMOS-MEMS clamped – clamped beam displacement amplifier for resonant switch applications," *J. Micromech. Microeng. (JMM)*, vol. 28, no. 6, pp. 065001, Mar. 2018.
- [Master's degree] J.-R. Liu, **C.-P. Tsai**, W.-R. Du, T.-Y. Chen, J.-S. Chen, and W.-C. Li, "Vibration Mode Suppression in Micromechanical Resonators Using Embedded Anti-Resonating Structures," *IEEE J. Microelectromech. Syst. (JMEMS)*, vol. 30, no. 1, pp. 53-63, Feb. 2021.
- **C.-P. Tsai** and W.-C. Li, "CMOS-MEMS Vibro-Impact Devices and Applications," *Front. Mech. Eng.*, vol. 8, 898328, Jun. 2022.
- Y. Yi, **C.-P. Tsai**, and W.-C. Li, "Sensitivity enhancement for micromechanical vibro-impact resonators using snap-through curved beams," *Micro. Nano. Lett.*, vol. 18, no. 1, pp. 1-6, Jan. 2023.
- **C.-P. Tsai** and W.-C. Li, "Micromechanical Vibro-Impact Systems: A Review," *J. Micromech. Microeng. (JMM)*, vol. 33, no. 9, pp. 093001, Aug., 2023.
- T.-Y. Chen, **C.-P. Tsai**, and W.-C. Li, "Temperature Event Triggered Sensors Using Internal Resonance Frequency Combs," *J. Micromech. Microeng. (JMM)*, vol. 35, no. 8, p. 085004, Aug., 2025.
- T.-Y. Chen, **C.-P. Tsai**, and W.-C. Li, "Ultrasensitive Sensing via Internal Resonance Induced Frequency Combs in Micromechanical Resonators," *IEEE J. Microelectromech. Syst. (JMEMS)*, vol. 34, no. 5, pp. 557-570, Oct., 2025.
- X. Cheng, T.-Y. Chen, **C.-P. Tsa**i, D. Li, H. Zhou, W.-C. Li, and C. Lee, "Unraveling the Far-Field Coupling of Multi-Layered Chiral Metamaterials for CMOS-enabled Mid-Infrared Imaging," ACS Nano, vol. 19, no. 33, pp. 30292–30302, 2025.
- **C.-P. Tsai** and W.-C. Li, "CMOS-MEMS Resoswitches—Design, Modeling, and Characterization," *IEEE J. Microelectromech. Syst. (JMEMS)*, vol. 34, no. 6, pp. 730-743, Dec., 2025. (JMEMS Right Now Paper)(Front Cover)
- I-C. Hsieh, T.-Y. Chen, **C.-P. Tsai**, H.-S. Zheng, and W.-C. Li, "Temperature-Stable CMOS-MEMS Resonators via Arc-Beam-Induced Electrical Stiffness Tuning," *IEEE J. Microelectromech. Syst. (JMEMS)*, vol. 34, no. 6, pp. 795-801, Dec., 2025.

doi:10.6342/NTU202600018

International Conference Paper (Total: 25, First Author: 6)

- [Master's degree] S.-C. Lu, **C.-P. Tsai**, and W.-C. Li, "A CMOS-MEMS CC-beam metal resoswitch for zero quiescent power receiver applications," in the 31st IEEE Int. Conf. on Micro Electro Mechanical Systems (MEMS' 18), Belfast, North Ireland, UK, Jan. 21-25, 2018, pp. 801-804.
- [Master's degree] S.-C. Lu, W.-R. Du, Y.-C. Huang, **C.-P. Tsai**, and W.-C. Li, "MEMS surface coating condition monitoring via nonlinear tapping of resoswitches," in 2018 IEEE Frequency Control Symposium (IFCS' 18), Olympic Valley, CA, May 21-24, 2018. (Student Best Paper Finalist)
- **C.-P. Tsai**, Y.-Y. Liao, and W.-C. Li, "A 125-kHz CMOS-MEMS Resoswitch Embedded Zero Quiescent Power OOK/FSK Receiver," Proc., 33rd IEEE Int. Conf. on Micro Electro Mechanical Systems (MEMS' 20), Vancouver, Canada, Jan. 18-22, 2020. (Oral Presentation)
- **C.-P. Tsai**, J.-R. Liu, and W.-C. Li, "Experimental Study on Frequency Stability of Micromechanical Resonators Operating in the Nonlinear Tapping Mode," Proc., 2020 IEEE Int. Frequency Control Symposium (IFCS' 20), Virtual Conference, July 19-23, 2020.
- **C.-P. Tsai**, H.-W. Wang, and W.-C. Li, "Tapping Bandwidth Widening of CMOS-MEMS Vibro-Impacting Resonators Based on Double-Sided Stopper Structure," in the 21st Int. Conf. on Solid-State Sensors & Actuators (TRANSDUCERS' 21), Virtual Conference, Jun. 20-25, 2021.
- **C.-P. Tsai**, and W.-C. Li, "A Micromechanical Frequency Controlled Pulse Density Modulator," in the 35th IEEE Int. Conf. on Micro Electro Mechanical Systems (MEMS' 22), Tokyo, Japan, Jan. 9-13, 2022. (Hybrid Event)(Oral Presentation)
- P.-C. Huang, T.-Y. Chen, **C.-P. Tsai**, and W.-C. Li, "An Ultrasensitive CMOS-MEMS Tuned-Mass-Damper (TMD) Based Voltmeter," in the 35th IEEE Int. Conf. on Micro Electro Mechanical Systems (MEMS' 22), Tokyo, Japan, Jan. 9-13, 2022. (Hybrid Event)
- H.-S. Zheng, **C.-P. Tsai**, T.-Y. Chen, and W.-C. Li, "CMOS-MEMS Resonators with sub-100-nm Transducer Gap Using Stress Engineering," in the 35th IEEE Int. Conf. on Micro Electro Mechanical Systems (MEMS' 22), Tokyo, Japan, Jan. 9-13, 2022. (Hybrid Event)(Oral Presentation)
- T.-Y. Chen, **C.-P. Tsai**, and W.-C. Li, "1:6 Internal Resonance in CMOS-MEMS Multiple-Stepped CC-Beam," in the 35th IEEE Int. Conf. on Micro Electro Mechanical Systems (MEMS' 22), Tokyo, Japan, Jan. 9-13, 2022. (Hybrid Event)(Oral Presentation)
- **C.-P. Tsai**, and W.-C. Li, "Attractor Exchanger for Open-Loop Operation of

doi:10.6342/NTU202600018

Micromechanical Nonlinear Resonators using Gap-Spacing Continuation,” in the 36th IEEE Int. Conf. on Micro Electro Mechanical Systems (MEMS’23), Munich, Germany, Jan. 15-19, 2023. (Oral Presentation)

- I.-C. Hsieh, H.-S. Zheng, **C.-P. Tsai**, T.-Y. Chen, and W.-C, Li, "Generic Temperature Compensation Scheme for CMOS-MEMS Resonators Based on Arc-Beam Derived Electrical Stiffness Frequency Pulling," in the 36th IEEE Int. Conf. on Micro Electro Mechanical System (MEMS'23), Munich, Germany, Jan. 15-19, 2023.
- Y.-H. Huang, H.-S. Zheng, **C.-P. Tsai**, and W.-C, Li, " Micromechanical RSSI Based on Force Interaction Derived Tapping Bandwidth Variation in Vibro-Impact Resonators," in the 36th IEEE Int. Conf. on Micro Electro Mechanical System (MEMS'23), Munich, Germany, Jan. 15-19, 2023.
- T.-J. Liou, **C.-P. Tsai**, T.-Y. Chen, and W.-C, Li, "Towards a Better CMOS-MEMS Resoswitch using Electroless Plating for Contact Energineering," in the 36th IEEE Int. Conf. on Micro Electro Mechanical System (MEMS'23), Munich, Germany, Jan. 15-19, 2023.
- **C.-P. Tsai**, and W.-C. Li, “Vibro-Impact Perturbation Based Attractor Exchanger For Open-Loop Nonlinear Resonators,” in the 22nd Int. Conf. on Solid-State Sensors, Actuators, & Microsystems (TRANSDUCERS), Kyoto, Japan, Jun. 25-29, 2023. (Oral Presentation)
- T.-Y. Chen, **C.-P. Tsai**, and W.-C. Li, “Constructing Micromechanical Frequency Combs In Bifurcating Attractor Branches For Event Triggered Sensors,” in the 22nd Int. Conf. on Solid-State Sensors, Actuators, & Microsystems (TRANSDUCERS), Kyoto, Japan, Jun. 25-29, 2023. (Oral Presentation)
- C.-M. Lee, T.-J. Liou, **C.-P. Tsai**, T.-Y. Chen, and W.-C. Li, "Toward High-Bit-Rate CMOS-MEMS Resoswitches," in the 37th IEEE Int. Conf. on Micro Electro Mechanical Systems (MEMS’24), Austin, Texas, USA, Jan. 21-25, 2024. (Oral Presentation, Outstanding Student Oral Paper Award Finalist)
- N. Basu, **C.-P. Tsai**, T.-Y. Chen, and W.-C. Li, “A Quick-Settling Enhancement-Mode Resoswitch,” in the 38th IEEE Int. Conf. on Micro Electro Mechanical Systems (MEMS’25), Kaohsiung, Taiwan, Jan. 19-23, 2025. (Oral Presentation)
- H. Zhou, T.-Y. Chen, Z. Ren, D. Li, C. Xu, **C.-P. Tsai**, W.-C. Li, and C. Lee, “MEMS-Driven Electrically Reconfigurable Platform for Photonic Quasi-bound States in the Continuum,” in the 23rd Int. Conf. on Solid-State Sensors & Actuators (TRANSDUCERS’25), Orlando, Florida, USA, Jun. 29-Jul. 3, 2025. (Oral Presentation)
- D. Li, T.-Y. Chen, **C.-P. Tsai**, C. Xu, Z. Hong, Z. Ren, W.-C. Li, and C. Lee, “Metasurfaces for Bulk Suppression and Wavelength-Dependent Midinfrared Imaging,” in the 23rd Int. Conf. on Solid-State Sensors & Actuators

doi:10.6342/NTU202600018

(TRANSDUCERS'25), Orlando, Florida, USA, Jun. 29-Jul. 3, 2025. (Oral Presentation)

- C. Xu, T.-Y. Chen, **C.-P. Tsai**, D. Li, Z. Hong, W.-C. Li, and C. Lee, "Multi-layered Chiral Metamaterials Using Standard CMOS for Polarization-Dependent Mid-Infrared Imaging," in the 23rd Int. Conf. on Solid-State Sensors & Actuators (TRANSDUCERS'25), Orlando, Florida, USA, Jun. 29-Jul. 3, 2025.
- N. Basu, T.-Y. Chen, **C.-P. Tsai**, and W.-C. Li, "Harnessing Vibro-Impact Dynamics for High-Performance MEMS-Based Reservoir Computing," in the 39th IEEE Int. Conf. on Micro Electro Mechanical Systems (MEMS'26), Salzburg, Austria, Jan. 25-29, 2026.
- Y.-X. Chen, T.-Y. Chen, **C.-P. Tsai**, and W.-C. Li, "A CMOS-MEMS Tunable Clock Generator Based on Vibro-Impact Beating Dynamics," in the 39th IEEE Int. Conf. on Micro Electro Mechanical Systems (MEMS'26), Salzburg, Austria, Jan. 25-29, 2026.
- C.-J. Hsueh, **C.-P. Tsai**, I.-F. Chung, T.-Y. Chen, and W.-C. Li, "CMOS-MEMS PUF Exploiting Mode Localization in a Multi-DOF Tuned-Mass-Damper Resonator," in the 39th IEEE Int. Conf. on Micro Electro Mechanical Systems (MEMS'26), Salzburg, Austria, Jan. 25-29, 2026.
- J.-W. Lin, **C.-P. Tsai**, N. Basu, and W.-C. Li, "A Fast-Settling CMOS-MEMS Resoswitch Using a Structurally Damped Output Electrode," in the 39th IEEE Int. Conf. on Micro Electro Mechanical Systems (MEMS'26), Salzburg, Austria, Jan. 25-29, 2026.

Domestic Conference Paper (Total: 10, First Author: 5):

- [Master's degree] J.-R. Liu, S.-C. Lu, **C.-P. Tsai**, and W.-C. Li, "CMOS-MEMS-based arrayed-CC-Beam displacement amplifiers," in the 3rd Association of Computational Mechanics Taiwan (ACMT) Conference (第 3 屆台灣計算力學會議), Tainan, Oct. 19-20, 2017.
- [Master's degree] **C.-P. Tsai**, W.-R. Du, and W.-C. Li, "Nonlinear contact dynamics modeling for comb-driven folded-beam micromechanical resoswitches," in the 21st Nano Engineering and Microsystem Technology Conference (第 21 屆奈米工程暨微系統技術研討會), Taipei, Jun. 1-2, 2018. (Oral Presentation) (最佳論文獎)
- **C.-P. Tsai**, and W.-C. Li, "A CMOS-MEMS Comb-Driven Resoswitch for Zero-Quiescent Communication Receiver," in the 4th International Society of Mechatronic Engineering (ISME) National Conference (第 4 屆台灣機電工程國際學會全國學術研討會), Kaohsiung, Feb. 15-16, 2019. (Oral Presentation) (Best Oral Paper Award)
- **C.-P. Tsai**, and W.-C. Li, "Experimental Study on Frequency Stability of

doi:10.6342/NTU202600018

Micromechanical Resonators Operating in the Nonlinear Tapping Mode," in the ICSS 2020 International Conference on Smart Sensors (暨第 25 屆台灣化學感測器科技研討會/第 23 屆微奈米系統工程研討會), NSYSU, Kaohsiung, Oct. 19-20, 2020. (Oral Presentation) (Best Oral Paper Award)

- **C.-P. Tsai** and W.-C. Li, "Numerical Investigations of Bifurcation Phenomenon and Motion Behavior for Single-Sided Vibro-Impacting Resonators," in the ICSS 2021 International Conference on Smart Sensors (暨第 26 屆台灣化學感測器科技研討會/第 24 屆微奈米系統工程研討會), NTU, Taipei, Oct. 14-15, 2021.
- T.-Y. Chen, **C.-P. Tsai**, and W.-C. Li, "Study on High-Order Internal Resonance of a Non-Uniform CMOS-MEMS CC-Beam Resonator," 第 18 屆自動化科技國際研討會暨 109 年自動化學門成果發表會 (Automation 2021), Kinmen, Nov. 11-14, 2021. (學生論文競賽金牌獎)
- T.-Y. Chen, **C.-P. Tsai**, and W.-C. Li, "An Achievement of CMOS-MEMS Temperature Sensor with Ultra High Sensitivity Based on Internal Resonance," in Symposium on Nano-Device Circuits and Technology (SNDCT 2022), Hsinchu, Taiwan, May. 19-20, 2021. (Oral Presentation) (入圍獎)
- **C.-P. Tsai** and W.-C. Li, "Parametric Study on the Contact Force of MEMS Resoswitches," in the ICSS 2022 International Conference on Smart Sensors (暨第 27 屆台灣化學感測器科技研討會/第 25 屆微奈米系統工程研討會), NTU, Taipei, Oct. 14-15, 2021. (Oral Presentation) (Best Oral Paper Award)
- Y.-H. Huang, **C.-P. Tsai**, and W.-C. Li, "Constructive Utilization Nonlinearity for Increasing Operating Bandwidth of Micromechanical Resoswitches," in the ICSS 2022 International Conference on Smart Sensors (暨第 27 屆台灣化學感測器科技研討會/第 25 屆微奈米系統工程研討會), NCHU, Taichung, Oct. 22-23, 2022. (Oral Presentation)
- D.-Y. Wu, **C.-P. Tsai**, and W.-C. Li, "CMOS-MEMS Resoswitch Embedded Zero Standby Power Wake-up Receivers," 第 19 屆自動化科技國際研討會暨 110 年自動化學門成果發表會 (Automation 2022), Kaohsiung, Nov. 11-13, 2022.

Patents (Total: 1):

- W.-C. Li, **C.-P. Tsai**, H.-W. Wang, "Device and method for monitoring surface condition of contact surface of detected object," US 2022/0002148 A1, Dec. 7th, 2020.

doi:10.6342/NTU202600018

1 General Introduction

Historical Background

Historically, micro-electro-mechanical systems (MEMS) technology originated in the 1960s, alongside the development of integrated circuits (ICs) [1-4]. At that time, semiconductor manufacturing processes were employed to create micro-mechanical actuators and miniaturized sensors, such as strain gauges, resonators (the device was even given the Esperanto-based name *resonistor* at the beginning of the original IBM paper [5], how an interesting thing!) and pressure sensors. In 1970s, the active research field moves to development of various MEMS devices and processes, including accelerometers, surface micromachining, and bulk etching techniques [1-4, 6]. By the 1980s and 1990s, silicon-based MEMS sensors began to replace traditional, larger size sensing devices for everyday applications [6]. The well-known development of micromachined ink-jet nozzle appeared in this period [7]. From 1990 to 2000, MEMS technology experienced significant growth due to its advantages of low power consumption, small size, and suitability for mass production. Numerous innovative development such as AFM, wafter bonding and integration technology, Bosch process, micro motor, micro mirror, high-volume accelerometer, appeared during this time [1-4, 8].

In 1990s and 2000s, traditional MEMS components are often designed to operate within a lower resonance frequency and under linear operation region to avoid frequency drift caused by nonlinearities, as well as stability degradation [9]. Researcher during this period focused on understanding the causes and effects of nonlinearity and finding ways to mitigate them.

Along the line on resonant MEMS, the attention shifted towards leveraging nonlinear effects and operational methods, such as bifurcation-based sensor, parametric resonance- and internal resonance-based sensing around 2010.

doi:10.6342/NTU202600018

Marketing and Requirement

Today, with the rise of the internet of things (IoT), big data technologies, artificial intelligence (AI) assistant and the application of sensor-controlled robot, various MEMS sensors are integrated into manufacturing and daily life. MEMS pressure sensors, microphones, bulk acoustic wave (BAW) filters, inertial measurement unit (known as IMU, i.e., accelerometers and gyroscopes), oscillators, micromirror, and RF switch have dominated the MEMS market while the potential functional component includes micromachined ultrasonic transducer (MUT), physical reservoir computer, cooling device, etc. [10-12]. Noted, the resonant components, such as BAW filters and oscillators, rely on the resonant properties such as high-quality factors (Q) of mechanical structures to surpass the limitations of purely electrical components, achieving superior frequency selection and stability characteristics. Accelerometer/gyroscopes that utilize inertial/Coriolis force generated through a moveable/resonating structure offer unique features, approaching tactical grade application recently, even at a compact size of ~10 mm^3 level and even small [13, 14].

As reported in [15], the performance of commercial inertia sensors in last decade are actually remine almost no change since the device optimization for minimizing MEMS device is such important to lower the cost and footprint size in industry. The minimized sensors with low power and small size are motivated by the need to integrate to automotive and consumer application with mass volume. The major energy loss sources for resonant MEMS are air damping (i.e., squeeze-film and sliding film damping), thermal elastic damping (TED), anchor loss, phonon-to-phonon interaction dissipation (i.e., material properties dependent). The scaling law on different loss source and the performance indicators such as angle random walk (ARW), bias stability (BI), sensitivity and robustness to environment impact are most important guide for optimization.

On the other hand, as mass production of MEMS devices increased, reliability analysis became a popular research topic during the 2000–2010 period. Significant

doi:10.6342/NTU202600018

advancements were made in understanding the multi-scale nature of failure mechanisms—from shock testers to PCBs, packages, and down to the MEMS device level—as well as in multi-physics interactions, including mechanical, thermal, electrical, and fluidic domains [16, 17]. These two development directions were pursued to improve device stability, bandwidth, and sensitivity.

Looking to the details on MEMS product, micromechanical structures are highly susceptible to environmental conditions. Design spaces such as operating pressure, operating environment gas, operating frequency, material properties, sensing method, packaging, fabrication method and mismatch, and motion magnitude can all affect the stability, performance and reliability of MEMS devices. Therefore, not only the encapsulation (i.e., zero-level packaging that totally different than standard IC, the protection of sensitive MEMS structures with bounded cap layer on the MEMS substrate) but also packaging (i.e., not only zero level packaging but also first and second-level packaging similar to standard IC packaging in which the interconnections from chip level to printed circuit board (PCB) level) is part of the device function.

Design and Modeling

The MEMS devices such as gyroscope are typically complex structure with serval types of beam structure, decoupling frame and complex mode shape that cannot deal without the help of finite element analysis (FEA). However, such large scale (i.e., lager degree of freedom in nodal space after meshing) device is hard to achieve parametric analysis and transient response investigation. As reason, the linear reduced order modeling (ROM) is getting interesting and applied to MEMS in 2000s [18-21], with few leading modes approximation, it provides deeper understanding for MEMS devices on transient state response during shock environment [22] and parametric model for optimization [23-25], reducing the computational cost 10 to 1000 times than using a full FEA model. Based on ROM implementation procedures, [26] classify these reduced-order models into two broad categories: node and domain methods. [26] also concluded that node methods, such as Guyan method and improved reduced system

doi:10.6342/NTU202600018

(IRS) method, perform poorly in predicting transients, large motions, and nonlinear behavior compared to domain methods. Thus, the studies usually implement linear ROMs using domain methods such as Galerkin procedure to convert a continuous operator problem in weak form (i.e., continuous/distributed parameter model) into a discrete problem (i.e., lumped-parameter model) by applying linear constraints determined by finite sets of basis functions (i.e., mode shape function). Thus, what the linear reduced order modeling stated here are mostly refereed to mode superposition technique.

The linear ROMs cannot handle the nonlinear analysis without extension. Therefore, the nonlinear reduced order modeling has been an active research field for resonant MEMS recently [27, 28]. For the best of author's knowledge, the popular and effective domain-based model order reduction (MOR) method nowadays includes proper orthogonal decomposition (POD), proper generalized decomposition (PGD), quasi-static modal analysis (QSMA), implicit condensation and expansion (ICE) method [29, 30], and direct normal form [31], to name a few. In particular, the ICE method boosts the development of nonlinear MEMS devices hugely and it is recommended to enter the field of nonlinear ROM though this method [32-34]. On the other hand, because of the low dissipation (i.e., high *Q* and long transient time) in MEMS devices, the deep learning techniques is believed as a useful tool to achieve real-time simulation for new generation of MEMS as highlight in [35].

Structure Optimization

Recent methods for optimizing MEMS can be classified into two main categories: (1) local optimization, which is guided by design expertise, and (2) evolutionary algorithms (EAs), which are designed to achieve global optimization [36]. The EAs are worth notable sine local optimization have limited search ability that might make the design goal unachievable. Several EAs have been successfully implemented for MEMS design, including genetic algorithms (GA), simulated annealing optimization (SAO), etc. In particular, the differential evolution (DE) and particle swarm

doi:10.6342/NTU202600018

optimization (PSO) are arguably the most widely used EAs for MEMS shape optimization [37]. Besides, recent publications of [38, 39] present a critical result via node-based optimization algorithm in which the morphing technique on nodes and gradient of constraints such as frequency and critical dimension of fabrication limit are implemented to optimization. The methodology present large design space and results a strange spring shape which are beyond human intuition and lead to favorable nonlinear properties.

This general introduction presents the brief history and related activating research topics for MEMS, creating the high-level view and keyword cloud for readers. Noted, the history and background of bio-MEMS devices, power MEMS device, environment sensor, chemical sensor, micro robot, etc., are another story that are beyond the scope of this dissertation.

As said by Nikola Tesla, "*if you want to find the secrets of the universe, think in terms of energy, frequency and vibration*". It is believed that the MEMS are of great important to the world and the resonant properties of MEMS are of great important to the MEMS. A narrow scope is true that "*If you want to find the secrets of the MEMS, think in terms of energy, frequency and vibration".*

1.1 Motivation and Objectives

Recently, MEMS researchers are increasingly attracted to event trigger sensors, bifurcation-based sensors, zero-power sensor, mechanical computing, and in-sensor computing due to one to few of the advantage of low (training) cost, low power consumption, high performance, and light weight, aligning with market demands for AI era. These technologies typically rely on nonlinear MEMS devices.

In fact, there is a device called MEMS vibro-impact systems exhibiting a wealth of intriguing nonlinear dynamics with much more complex behaviors than linear systems and regular nonlinear systems. The well-known device of MEMS vibro-impact resonator is atomic force microscopy (AFM), in which the sensitivity enhancement though nonlinear modal interaction and model-based control design through ROM are

doi:10.6342/NTU202600018

the essential part for identification of material properties and surface topology [40].

Particularly, vibro-impact resonators exhibit complex dynamics and potentially great to achieve high sensitivity application and deep understanding for nonlinear properties, paving the way for future research and applications. The deep understanding of the inherent highly nonlinear features of vibro-impact resonator could enable countless opportunities for fundamental and ground-break applied research, as author believed.

Some of the underlying mechanism already developed in previous works for vibro-impact resonator, however, there is a gap to develop MEMS resoswitch, a particular case of MEMS vibro-impact resonators that incorporate with electrical hot-switching operation, as the device's dimension shrinks day by day. This work aims to bridge the gap between theoretical modeling and practical implementation of vibro-impact resonators, providing a framework for understanding and utilizing MEMS vibro-impact resonators in two innovative applications—resoswitches and attractor exchangers.

This dissertation focuses on the design, analysis, and application of vibro-impact resonators on complementary metal-oxide-semiconductor micro-electro-mechanical systems (CMOS-MEMS) platform, specifically targeting the challenges posed by their inherent nonlinear dynamics such as electrostatic nonlinearity, geometric nonlinearity and, of course, the nonlinear interactions at contact surfaces. The study begins with an extensive investigation of the contact phenomenon in MEMS vibro-impact devices, conducting the possible modeling and analysis approaches for such devices. It explores the current issues in modeling, emphasizing the difficulties in analyzing and predicting the behavior of these nonlinear systems. The side effect on electrostatic and geometric nonlinearity and recent applications are summarized, providing a good foundation and background in this field.

It then characterizes and analyze a CMOS-MEMS vibro-impact resonator. Based on the experimental characterization, the results reveal the existence of nonlinear

doi:10.6342/NTU202600018

stiffness, the non-conservative nonlinearity (called nonlinear damping or van der Pol term in this dissertation), in particular, the unexpected surface interaction force in which the dissipation during contact (called contact damping in this dissertation) is found. Some material properties and nonlinearities are extracted and analyzed herein through model-based curve fitting. The numerical model based on MATLAB & SIMULINK and analytical solution based on the method of averaging (MOA) are followed, providing a basis for further development. With this, the development moves to the applications. The work first presents the wake-up receiver and pulse density modulator based on resoswitch and then presents the detail of two novel devices, the so-called gap-continuation based and vibro-impact perturbation-based attractor exchanger, respectively.

As mentioned, to lower the gap to enter this interesting field, the basis for source of nonlinearities, derivation, and full description of modeling, mathematical treatment and characterization method are shown in Appendixes.

1.2 Dissertation Organization

Figure 1-1 provides an overview of the dissertation organization. This dissertation begins with Chapter 2, which discusses the fundamental principles and observation of MEMS vibro-impact systems from the previous literatures, covering their design, modeling, and experimental verification. The analysis tools for nonlinear dynamics and the selection of contact force formulation are introduced. Next, Chapter 3 delves into the dynamical modeling of CMOS-MEMS resoswitches, including the electrical contact resistance modeling. The analytical formula of steady-state peak repulsive force is presented in Chapter 3, revealing the parameter dependency and providing the design guild for resoswitch-based receivers. The analysis tools introduced in Chapter 2 are used to present the nonlinear responses in detail. Chapter 4 showcases practical applications of MEMS all-mechanical circuit based on the resoswitches, highlighting the possibility of all-mechanical circuit on the applications of low power consumption receiver and pulse-density modulator. Chapter 5 focuses on MEMS attractor

doi:10.6342/NTU202600018

exchangers, detailing their structure, operation, and experimental findings along with the qualitative theoretical analysis. Finally, Chapter 6 concludes with a summary of research findings and future research directions.

The appendices serve to support the main text with detailed derivations and background. Appendices A and B lay the groundwork for MEMS device characterization and equivalent circuit analysis. Appendix C provides a conceptual overview of surface interaction forces, followed by Appendix D, which details numerical parametric studies and experimental observation of the vibro-impact resonators. Appendices E and F provide the rigorous mathematical proofs for the perturbation analysis and contact force laws used in this study. Finally, Appendix G presents additional characterization results regarding the tapping response and temperature coefficients.

doi:10.6342/NTU202600018

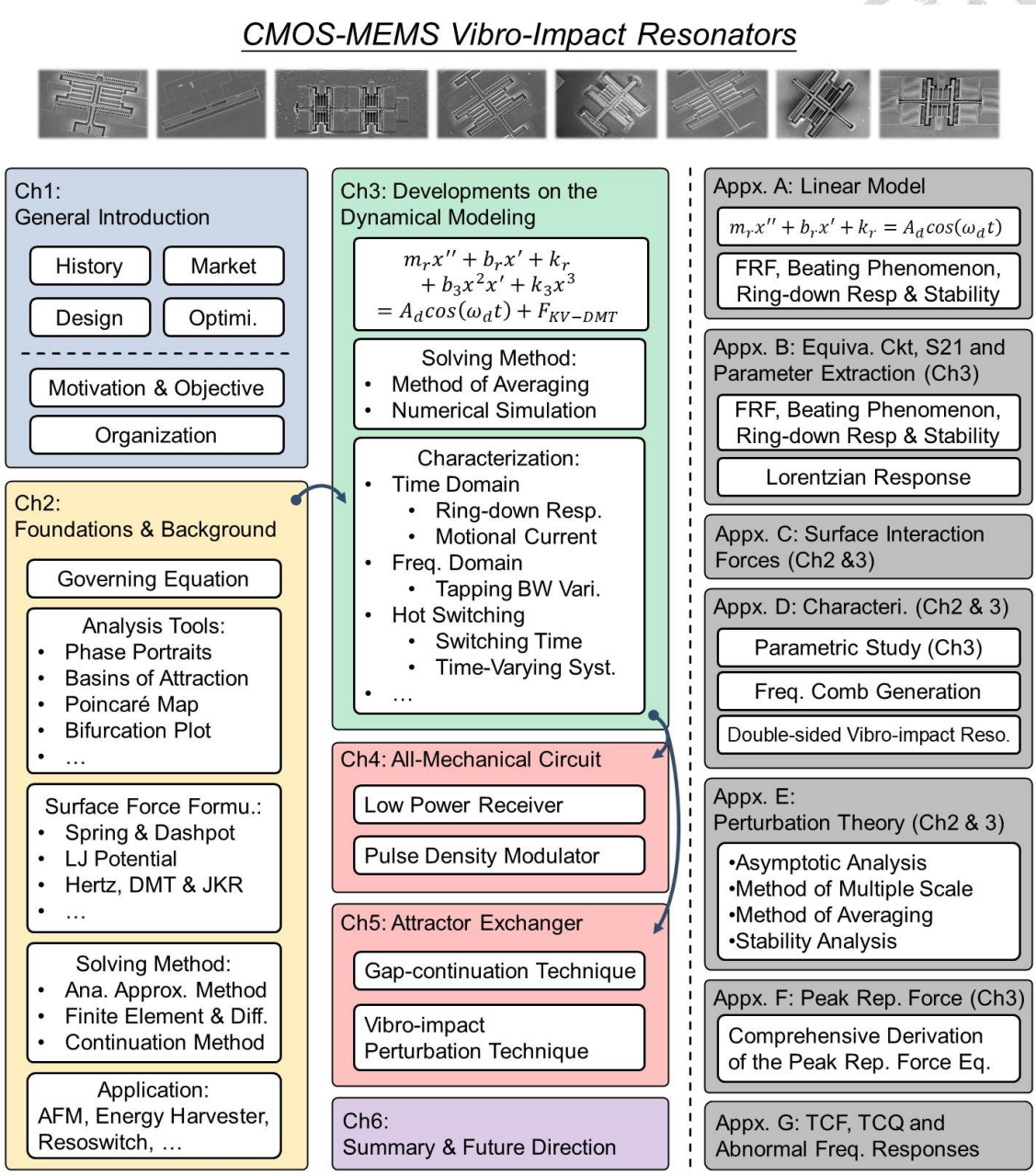


Figure 1-1: Overview to the dissertation organization.

doi:10.6342/NTU202600018



2 Foundations and Background

Catalyzed by the inception of tapping-mode atomic force microscopy three decades prior, a diverse array of micromechanical structures and systems employing components subject to mechanical impact has been conceptualized and advanced. Although these systems exhibit dynamical characteristics largely analogous to those of macroscopic vibro-impact systems and draw upon established theoretical frameworks, their microscale equivalents are distinguished by a greater dominance of surface force, elevated resonance frequency and Q, and more pronounced material and structural nonlinearities. These distinct attributes engender unique phenomena and facilitate practical applications unattainable within macroscopic vibro-impact systems.

The subsequent sections of this chapter will first elucidate the fundamental principles of vibro-impact systems and the methodologies employed for scrutinizing their nonlinear behaviors, followed by a survey of contact force modeling and numerical analysis tools. Ultimately, a critical examination of diverse applications utilizing microscale vibro-impact systems is presented. This overview endeavors to offer a holistic perspective on MEMS vibro-impact systems, with the objective of stimulating novel applications that fully leverage the elegant complexity inherent in nonlinear vibro-impact dynamics at the microscale.

2.1 Introduction

Vibro-impact systems are ubiquitous across the spectrum of mechanical and civil engineering disciplines. These mechanisms are integral to a diverse array of apparatuses, ranging from siege engines and pile drilling machinery to industrial machining operations and even handheld percussion massage gun. Such systems demonstrate substantial complexity, manifesting dynamic behaviors that are subject to drastic variation. To illustrate, within the context of a percussion massager, the vibration intensity may escalate markedly when the device transitions from muscular

doi:10.6342/NTU202600018

tissue to bone. Unlike their linear counterparts, nonlinear vibro-impact systems display distinctive characteristics governed by determinants such as the magnitude and frequency of the driving force, contact stiffness, stiction force, and separation. Fluctuations in these governing parameters possess the capacity to fundamentally modify the system's operational behavior.

The theoretical evolution of modeling vibro-impact systems and their associated behaviors spans a significant duration [41-49]. A plethora of mathematical techniques and methodologies has been proposed to circumvent the limitations of conventional mathematical frameworks—originally designed for linear systems—when addressing nonlinear vibro-impact systems defined by their discontinuous nature. Since exact closed-form solutions are infrequent, the reliance on numerical approaches and approximations remains essential for the accurate modeling of these nonlinear systems [50-53]. Furthermore, contemporary strides in MEMS technology have engendered the proliferation of vibro-impact systems at the microscale. A prominent instance is atomic force microscopy (AFM) [54-61], which employs probe tips with dimensions as minute as a few nanometers—fabricated via MEMS processes—to quantify interaction forces between the tip and the contact surface at the atomic level. Additional examples of microscale vibro-impact systems encompass impact actuators [62-66], energy harvesters [67-70] incorporating a frequency up-conversion mechanism [71-76], RF switches [77-79], and resoswitches [80-89]. These devices exploit distinct facets of impact-induced phenomena: impact actuators achieve precision positioning via impact-induced inertial motion; energy harvesters attain a broadened operating bandwidth through impact events; and resoswitches amalgamate impact switches with resonance operation to ameliorate deficiencies inherent in conventional MEMS switches.

The modeling of vibro-impact dynamics within microscale systems presents considerable impediments. In contrast to macroscale systems, the nonlinear behavior in microscale systems—characterized by more potent nonlinear surface forces and

doi:10.6342/NTU202600018

elevated displacement motions—is inadequately represented by linear models [49]. Moreover, microscale vibro-impact systems are distinct from nano- and macroscale counterparts regarding the quantity of asperities engaged in contact. Whereas nanoscale systems typically involve single asperities and macroscale systems engage a multitude, microscale systems occupy an intermediate regime characterized by an indeterminate quantity of asperities. The geometric profile of the contact tip at the microscale is frequently undefined, further obfuscating the analysis. Given the substantial diminution of contact size at the microscale, roughness assumes a critical role. Consequently, the formulation of the dynamical process for microscale systems is predicated on several cardinal factors: (1) the equations of motion in the absence of impact; (2) the interaction force model during contact; and (3) the equivalent contact area. Minor deviations in these variables can precipitate significant disparities in the system's response. Accordingly, a holistic review and synthesis of the modeling, behaviors, and applications of MEMS-based vibro-impact systems, alongside an evaluation of the challenges and opportunities presented by microscale nonlinear dynamics, are imperative.

Pertinent research has, indeed, been conducted within this field. For example, [90] offers a comprehensive survey of the nonlinear dynamics of MEMS resonators, encompassing vibro-impact systems. Additionally, [63] investigates modeling and simulation methodologies for impact actuators to facilitate robust and consistent designs. Nevertheless, the intricate mathematical models and complex characteristics of vibro-impact systems may present formidable barriers for engineers attempting to integrate this mechanism into their devices. Drawing inspiration from [91], this chapter endeavors to elucidate the nonlinear dynamics derived from vibro-impact in micromechanical resonators from an engineering vantage point. It will encompass an overview of microscale vibro-impact systems and a discussion of the anticipated behaviors of nonlinear impact systems in Section 2.2, the modeling and formulation of the force in Section 2.3, the mathematical and analytical tools available for resolving

doi:10.6342/NTU202600018

these models in Section 2.4, and the applications of vibro-impact structures in Section 2.5. Finally, Section 2.6 will conclude by delineating the challenges and prospective opportunities associated with micromechanical vibro-impact systems.

2.2 Characteristics and Analysis Tools

By virtue of their intrinsic intricacy, vibro-impact systems manifest additional nonlinearity stemming from the force impulses induced by impacts, a characteristic analogous to that observed in generic nonlinear systems. Consequently, scholars have devised specialized methodologies to scrutinize the dynamics of vibro-impact systems [41, 45, 47-49, 92-95]. For a comprehensive understanding of nonlinear dynamics, one may consult a diverse spectrum of resources, encompassing foundational treatises dedicated to this discipline [43, 52, 53, 96-99].

2.2.1 Model and Behavior Representation

While macroscale vibro-impact applications encompass a spectrum ranging from elementary two-body collisions to complex interactions involving hundreds of bodies—exemplified by ball pools—the majority of microscale applications are restricted to two- or three-body impacts, a constraint imposed by the limited degrees of freedom inherent in these devices. Figure 2-1 (a) depicts a fundamental mechanical model of a single degree-of-freedom (DOF) two-body vibro-impact oscillator equipped with a stopper possessing a stiffness of k_c. The mass is actuated by a periodic external force F_d operating at, or in close proximity to, its linear resonance frequency. Figure 2-1 (b) delineates the total restoring force relative to displacement, highlighting the sharp discontinuities in force magnitude that arise upon impact, thereby exposing the system's non-smooth nature. The governing equation defining this system is expressed as

$$m_r x'' + b_r x' + k_r x = F_d - F_c \tag{2-1}$$

wherein x signifies the displacement. The parameters m_r, b_r, k_r, F_d and F_c designate the mass, damping coefficient, system stiffness, driving force, and contact force,

doi:10.6342/NTU202600018

correspondingly. To incorporate material and structural nonlinearities, the damping coefficient and stiffness are formulated as functions dependent upon displacement and velocity, expressed as $b = b(x, x')$ and $k = k(x, x')$.

As aforementioned, the aggregate dynamic behavior characterizing vibro-impact systems is governed by the nonlinear damping and stiffness, acting in conjunction with impact-induced nonlinearity. Section 2.4 will examine the consequences of these amalgamated intrinsic and impact-induced nonlinearities, whereas comprehensive modeling methodologies are detailed in [100-106].

The driving force and contact force presented in (2-1) are expressed via the subsequent formulations

$$F_d = A_d \cos(\omega_d t) \tag{2-2}$$

and

$$F_c = k_c(x - d_0)H(x - d_0) \tag{2-3}$$

In this formulation, ω signifies the driving angular frequency, k_c represents the contact stiffness of the stopper, and d_0 denotes the gap spacing. The Heaviside step function is characterized as

$$H(x - d_0) = \begin{cases} 0, x < d_0 \\ 1, x \geq d_0 \end{cases} \tag{2-4}$$

and A_d is the forcing amplitude.

The motion equation permits conversion into the state-space matrix configuration, expressed as

$$m_r \begin{bmatrix} \dot{x_1} \\ \dot{x_2} \end{bmatrix} = \begin{Bmatrix} x_2 \\ [F_d - F_c - (b_r x_2 + k_r x_1)]/m_r \end{Bmatrix} \tag{2-5}$$

Through the definition of $x_1 = x(t)$ and $x_2 = x'(t)$, the high-order differential equation presented in (2-1) is condensed into a system of coupled first-order differential equations. Equation (2-5) delineates the temporal progression of the states x_1 and x_2. Such a state-space representation is frequently employed within the realms

doi:10.6342/NTU202600018

of control theory and nonlinear dynamic analysis. Furthermore, this configuration is indispensable for computer-aided numerical analysis, which mandates the first-order differential equation structure to facilitate time integration.

Physical device structures often exist as continuous bodies exhibiting multiple eigenmodes. Under such circumstances, (2-5) encompasses multiple DOF, assuming the *n*-state general formulation [13]

$$\dot{\boldsymbol{x}} = \boldsymbol{F}\big(x_i(t); \mu_j\big), i = 1,2, \ldots p; j = 1,2, \ldots q \tag{2-6}$$

wherein x_i represent real-number state variables possessing a finite dimension of p, formulated as $\boldsymbol{x} = [x_1 \quad \cdots \quad x_p] \in \mathbb{R}^p$, analogous to the displacement and velocity detailed in (2-5). The set μ_j, comprising k, b, m, F_d and F_c derived from (2-5), constitutes the control parameters with a finite dimension of q, defined as $\mu_j = [\mu_1 \quad \cdots \quad \mu_q] \in \mathbb{R}^q$. Finally, $\boldsymbol{F}$ signifies the vector field of the system.

Figure 2-1 (a) delineates a mechanical model that functions within two distinct operational states: one involving impact and the other devoid of it. Whenever the mass collides with the elastic stopper, it induces a specific degree of indentation, resulting in a diminished vibration magnitude relative to the non-impact scenario. This collision event injects nonlinearity into the system, thereby augmenting the overall stiffness and elevating the resonance frequency to a level surpassing the fundamental resonance

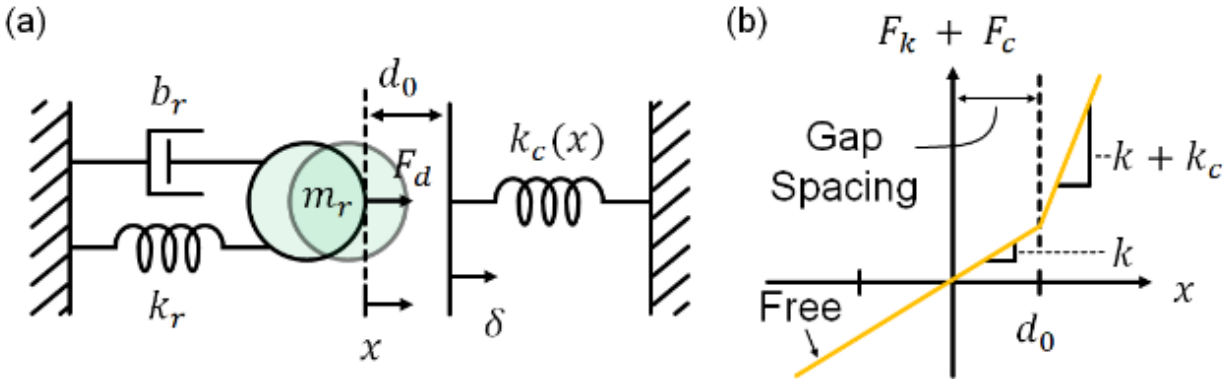


Figure 2-1: (a) A lumped-parameter model showing a 1-DOF vibro-impact oscillator with an elastic stopper. (b) The associated plot of the total restoring force against displacement, demonstrating the non-smooth, piecewise-linear stiffness that results from impact at the gap d_0. Reproduced with permission of [107], Copyright of © IOP Publishing.

doi:10.6342/NTU202600018

angular frequency, $\omega_0 \approx \sqrt{k_r/m_r}$. Both the resonance angular frequency and the comprehensive dynamic behavior of the system are governed by parameters such as the stiffness ratio, k_c/k_r, the damping ratio, $b_r/(\sqrt{m_r k_r})$, forcing ratio, $A_d/d_0 k_r$ and frequency ratio, ω_d/ω_0. It is pertinent to acknowledge that the resonance angular frequency is only marginally affected by damping as defined by $\omega_0 = \omega_n\sqrt{1-1/(2Q^2)}$; nevertheless, in the context of MEMS high Q devices, this influence renders itself negligible, $\omega_0 \approx \omega_n$.

2.2.2 Analysis Tools for Specific Parameters

The utilization of analytical instruments—specifically time series, phase portraits, and Poincaré maps—enables the rigorous investigation of the dynamical behaviors exhibited by the vibro-impact system under a defined set of parameters. The ensuing discussion aims to delineate a concise synopsis of each methodology, elucidating the specific insights derived from their application.

2.2.2.1 Time Series and Phase Portraits

Prior to delineating the specific analytical instruments, it is requisite to establish that $\mathbb{R}^n$ signifies an *n*-dimensional real-number domain, wherein $\boldsymbol{x} = [x_1 \quad \cdots \quad x_n]$ is identified as a *state space*. An extended state space constitutes an $\mathbb{R}^n \times \mathbb{R}$ dimensional manifold, formed by the augmentation of the state space through the inclusion of a temporal dimension. A state space of $\mathbb{R}^2$ dimensions, explicitly comprised of displacement and velocity, is formally termed a *phase space* [52]. *Trajectories* or *orbits* traversing state spaces, inclusive of phase spaces, are categorized as *solution curves*, whereas an aggregation of such trajectories within the phase space is denominated as *phase portraits*. Within the context of extended state spaces, solution curves are recognized as *integral curves* [52].

doi:10.6342/NTU202600018

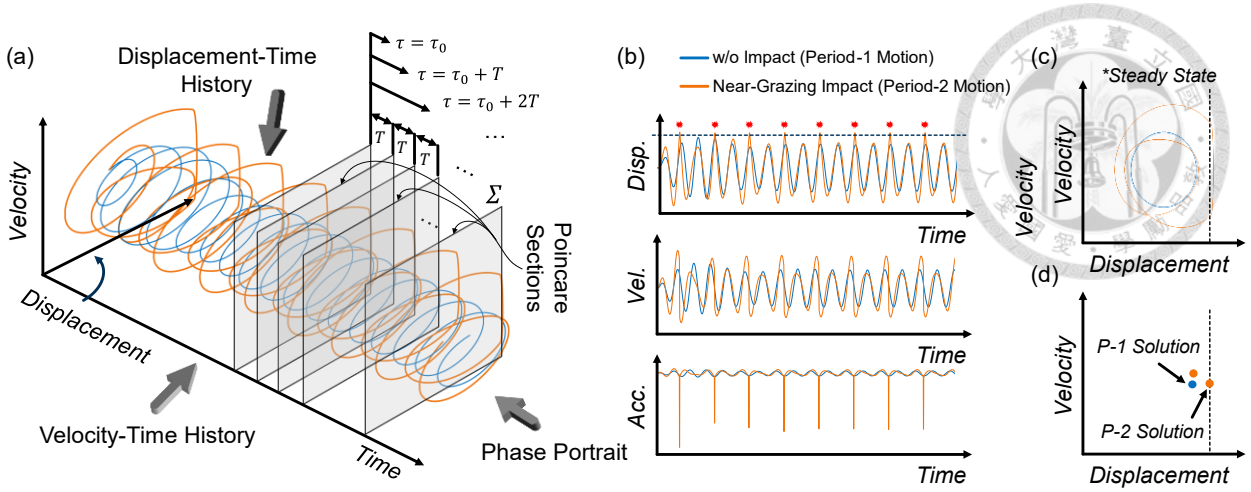


Figure 2-2: A comparison of computed responses for a linear (non-impact) motion and a near-grazing impact motion, based on simulations of (2-1). The system's dynamics are visualized using several tools: (a) the integral curve in extended phase space, (b) time-domain histories for displacement, velocity, and acceleration, (c) the steady-state phase portrait, and (d) the corresponding Poincaré map. The two cases were generated in MATLAB & Simulink using forcing amplitudes (A) of 0.2 and 0.4, respectively, with other parameters being $k = 1$, $m = 2.533 \times 10^{-4}$, $b = 1.6 \times 10^{-3}$, $d_0 = 1$, $k_c = 250$, and $\omega = 8.5$. For the Poincaré map in (d), the section for the period-2 motion is defined at the impact boundary, while the section for the period-1 motion is taken at the maximum displacement. Reproduced with permission of [107], Copyright of © IOP Publishing.

Figure 2-2 (a) delineates the integral curves residing within the extended state space, representing scenarios of both linear motion without impact and near-grazing impact. A grazing impact is characterized by an impact event transpiring at zero velocity. Figure 2-2 (b) displays the associated time histories encompassing displacement, velocity, and acceleration. Typically, such time series plots offer inadequate granularity for a complete comprehension of the dynamical behaviors inherent in a nonlinear system. Utilizing the established trajectories, Figure 2-2 (c) formulates the phase portraits for both instances by projecting displacement and velocity coordinates from the time-extended state space into the phase space. This methodology elucidates both the operational behavior and the periodicity characterizing the dynamical system. To fully disclose the attractors and evolutionary trends toward which the dynamical behaviors ultimately converge, it is necessary to generate a comprehensive phase

doi:10.6342/NTU202600018

portrait incorporating a diversity of initial conditions [52]. For an entity to be classified as an attractor, it is obligated to satisfy specific criteria [53]. Elementary non-chaotic attractors encompass fixed points, wherein the system relaxes into a stationary state following a distinct transient time, as well as periodic solutions, in which the system assumes a regular periodic motion [99].

2.2.2.2 Poincaré Map

Figure 2-2 (d) depicts the *Poincaré map*—alternatively termed the *first return map*—corresponding to two distinct magnitudes of driving force. In contrast to phase portraits, which encompass the entirety of continuous temporal data, Poincaré maps function by sampling and plotting the phase portraits at discrete temporal intervals determined by the definition of *Poincaré sections*. This methodology generates a discrete dynamical system possessing a dimensionality reduced by one relative to the original continuous-time system. As noted in [108], the procedure for establishing the Poincaré section is complex and arduous, lacking a standardized protocol for ascertaining the sampling timestamps; furthermore, the map itself defies explicit definition [52, 96]. Notwithstanding these difficulties, it is standard practice within vibro-impact systems to employ one-sided Poincaré sections that align with the forcing period $T_d = 2\pi/\omega_d$ maintained at a constant phase difference with respect to the excitation phase [94, 109-115]. This configuration yields a *stroboscopic Poincaré map*, a tool extensively utilized in both the experimental and numerical examination of vibro-impact systems [99, 116-119].

By mitigating dimensionality through the exclusion of the time variable, Poincaré maps facilitate the analysis of intricate system behaviors and prove particularly advantageous for stability analysis. As illustrated, a Poincaré map manifesting single or multiple points signifies motion characterized by a period commensurate with, or exceeding, that of the driving force, respectively. Specifically, in the latter instance, the motion oscillates periodically among these plural solution points in reaction to the driving force, thereby yielding a period of greater duration than the driving force itself.

doi:10.6342/NTU202600018

Typically, within MEMS vibro-impact systems—which frequently employ one-sided Poincaré sections synchronized with the forcing period—a period-*n* motion is correlated with a Poincaré map displaying *n* distinct points.

Regarding the near-grazing impact demonstrated in Figure 2-2 (d), the Poincaré map discloses two points, wherein one specific point denotes an impact occurring beyond the gap spacing. The motion period inherent to this scenario extends to two times the duration of the excitation period. Such periodic motion is designated as subharmonic motion, given that its frequency is subordinate to the excitation frequency. Should an impact transpire, the phenomenon is classified as *subharmonic impact motion* and is defined by the parameter z, which equals 1/2 in this specific case [49, 120-123]

$$z = \frac{number\ of\ impact}{number\ of\ excitation\ cycle} \tag{2-7}$$

2.2.3 Analysis Tools for Varying Parameters

In the scenario of near-grazing impact, the structure engages with the stopper at minimal velocities; under these conditions, even minor disturbances, such as variations in driving frequency or impact-induced stiffness changes, can drastically modify the system's behavior [124-126]. Conventional visualization methods, including the aforementioned time series or Poincaré map, may prove insufficient for completely characterizing these phenomena, given that such plots are typically generated for fixed parameter configurations. Consequently, to achieve a more comprehensive understanding of the dynamical behaviors, it is essential to utilize diverse analysis tools capable of addressing the effects of parameter fluctuations, including gap spacing, forcing amplitude, and driving frequency.

The nondimensionalization technique is frequently adopted to streamline the assessment of how parameter variations affect dynamical behavior. By implementing this method on (2-1) or (2-5), one obtains a concise mathematical representation characterized by a diminished quantity of parameters, such as

doi:10.6342/NTU202600018

$$\hat{x}'' + \xi\hat{x}' + \hat{x} = \widehat{A_d}cos(\Omega_d\hat{t}) - \beta_l(\hat{x} - \widehat{d_0})H(\hat{x} - \widehat{d_0}) \quad (2\text{-}8)$$

or

$$\begin{bmatrix}\hat{x}_1' \\ \hat{x}_2'\end{bmatrix} = \begin{Bmatrix}\hat{x}_2 \\ \widehat{A_d}sin(\Omega_d\tau) - 2\xi\hat{x}_2 - \hat{x}_1 - \beta_l(\hat{x}_1 - \widehat{d_0})H(\hat{x}_1 - \widehat{d_0})\end{Bmatrix} \quad (2\text{-}9)$$

predicated on the definitions of $\hat{x} = \hat{x}_1 = x_1/x_s$, $\hat{x}_2 = \hat{x}'$, $\tau = t_s = \sqrt{m_r/k_r} = 1/\omega_n$, $\widehat{d_0} = d_0/x_s$, $\xi = b_r/(\sqrt{m_r k_r}) = 1/Q$, $\beta_l = k_c/k_r$, $\Omega_d = \omega_d/\omega_n$, $\widehat{A_d} = \xi$, where x_s signifies an arbitrary scaling distance [94, 95, 115]. Within this dimensionless formulation, (2-9) isolates four distinct dimensionless parameters: Ω_d (frequency ratio), ξ (damping ratio), β_l (stiffness ratio), and D (nondimensionalized gap spacing). By judiciously selecting the scaling factors, t_s and x_s, the amplitude of forcing is normalized to unity. This normalization significantly facilitates the comparative analysis of parameter variation effects across systems operating at disparate scales.

2.2.3.1 Frequency Response and Bifurcation Diagram

While customarily utilized in the analysis of linear and nonlinear Duffing systems, frequency responses are also extensively employed within the context of vibro-impact systems. Figure 2-3 (a) depicts the distinct *bird's beak* profile characteristic of the frequency response in a vibro-impact system, delineating the nondimensionalized displacement (specifically, $\hat{x}_1$ in (2-9)) as a function of the nondimensionalized frequency (denoted as Ω_d in (2-9)) [127]. Once the gap spacing exceeds the threshold defined by $max(\hat{x}) > \widehat{d_0}$ (with $\widehat{d_0} = 1$ predicated on $x_s = d_0$ as in [127]), impact is initiated. Consequently, the supplemental stiffness generated by this impact compels the frequency response to curve toward the higher frequency range. Several specific bifurcations are designated, including grazing (GR), period-doubling (PD), and saddle-node (SN), where the subscript *i* signifies the *i*-th manifestation of a given bifurcation. As characterized in [127], a bifurcation denotes an abrupt transition in dynamic behavior triggered by minute adjustments in parameter values. Fundamentally, Figure 2-3 (a) functions as a bifurcation diagram wherein frequency acts as the control

doi:10.6342/NTU202600018

parameter—a representation designated as a *one-parameter bifurcation diagram*. Of the numerous bifurcations documented, these three represent the most predominant types encountered within vibro-impact systems. The critical threshold at which impact initially manifests is termed *grazing bifurcation*, precipitating a transition in the system's motion from regular oscillation to a regime containing mixed intervals with and without impact. The coordinates of the grazing points (GR_1 and GR_2), with respect to Ω_d and ξ allow for analytical determination by substituting $\hat{x} = \widehat{d_0}$ into (2-8) [127]

$$\xi^2 {\Omega_d}^2 + \left[1 - {\Omega_d}^2\right]^2 = \frac{{\widehat{A_d}}^2}{{\widehat{d_0}}^2} \tag{2-10}$$

At the locus of grazing bifurcation (GR), characterized by negligible contact velocity and force, even minor perturbations can exert a profound influence on the system's dynamics. Impact events precipitate an abrupt alteration in stiffness and establish a phase shift between the excitation signal and the structural response; this phenomenon induces dissipation and suppresses vibration amplitude through destructive interference. Such dissipation causes the structural displacement to remain insufficient for engaging the stoppers until adequate energy is accrued for the subsequent impact. Consequently, a cascade of *period-doubling bifurcations* is customarily observed in the proximity of GR, potentially yielding period-doubling motion (defined as period-n motion where $n > 1$) and conceivably chaotic motions [125].

A period-doubling bifurcation manifests when the periodicity of the emergent orbit becomes twice or half (in the case of reverse period-doubling) that of the precursor orbit. The manifestation of period- n period-doubling motions across distinct n values is contingent upon the initial conditions, excitation magnitude, driving frequency, and additional governing factors. As delineated in (2-7) and illustrated in Figure 2-2 (b), a single impact event transpires exclusively within a specific integer number of excitation cycles, a behavior broadly recognized as the period-adding phenomenon.

Saddle-node bifurcation is characterized by a coordinate exhibiting an infinite

doi:10.6342/NTU202600018

gradient, which precipitates *jumps* during the frequency sweep process. The approximate location of the upper saddle-node bifurcation point (SN_2) is amenable to analytical derivation via the method of averaging (MOA), as elaborated in [67, 73, 75, 128], and is formulated as

$$\frac{\widehat{A_d}^2}{\widehat{a_{p.k}}^2} = (\xi\Omega_d)^2 + [1 + K_c - \Omega_d^2]^2 \tag{2-11}$$

where $K_c = \frac{\beta_l}{\widehat{a_{p.k}}^2\pi}\left[\widehat{a_{p.k}}\theta_{c.k} + \frac{1}{2}\widehat{a_{p.k}}\sin^2(\theta_{c.k}) - 2\widehat{d_0}\sin(\theta_{c.k})\right]$, $\widehat{a_{p.k}}$ represents the amplitude of nondimensional displacement (specifically, $\hat{x} = \widehat{a_{p.k}}cos(\Omega_d\hat{t})$) and $\theta_{c.k} = \cos^{-1}\left(\widehat{d_0}/\widehat{a_{p.k}}\right)$ signifies the contact angle. Refer to Appendix E, particularly section E.4.2, for comprehensive elaborations.

The inset provided in Figure 2-3 (a) proximate to GR_1 displays a period-two solution. In this instance, the displacements associated with both motions exceed the gap spacing; however, they demonstrate distinct indentation amounts. Multiple trajectories exist within the interval spanning SN_1 and SN_2. In contrast to the interval between PD_1 and PD_2, which yields a solitary period-two motion solution, the zone bounded by SN_1 and SN_2 encompasses two distinct stable period-one motions. These paired solution curves correspond to separate attractors, wherein the system's motion gravitates toward one specific attractor contingent upon the initial conditions. The interplay between these competing attractors is examined in the subsequent subsection.

As evidenced by (2-10) and (2-11), the locations of bifurcation points are governed by dimensionless parameters. Within Figure 2-3 (a), a one-parameter bifurcation diagram is generated by modulating a single parameter while maintaining the remaining variables at fixed values. Figure 2-3 (b) characterizes the bifurcations with respect to the force ratio η and driving frequency Ω_d, where the dashed line denotes the specific condition η = 0.3 utilized in Figure 2-3 (a). The specific frequency ratios at which this trajectory intersects the dashed line correlate directly with the bifurcation coordinates identified in Figure 2-3 (a).

doi:10.6342/NTU202600018

As demonstrated in Figure 2-3 (c), maintaining a constant force ratio results in an expansion of the period-doubling region (bounded by PD_1 and PD_2) and an elevation in the effective resonance frequency (specifically, the frequency of SN_2) as a function of the stiffness ratio β. Conversely, the frequency associated with GR_1 remains invariant, as its determination is exclusively contingent upon the driving force. With the escalation of β the points corresponding to, PD_2, SN_1 and SN_2 exhibit a tendency to converge toward distinct frequency values.

As depicted in Figure 2-3 (b) and (c), *two-parameter bifurcation diagrams* (alternatively termed *bifurcation sets*) are presented, mapping the force ratio η and stiffness ratio β [117] relative to the frequency of the bifurcation points. These plots elucidate the modifications in bifurcation behavior occurring in response to variations in these two parameters. The trajectory representing the development of an individual bifurcation point within the two-parameter plane is designated as a bifurcation curve.

2.2.3.2 Basins of Attraction

As noted earlier, Figure 2-3 (a) depicts a hysteresis loop spanning the interval between SN_1 and SN_2 signifying the simultaneous existence of two potential period-

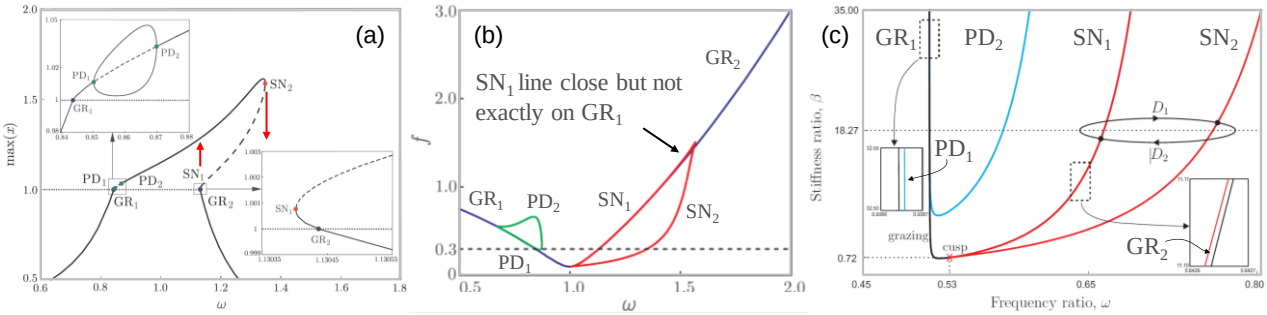


Figure 2-3: Bifurcation analysis of the vibro-impact oscillator. (a) The system's frequency response is presented as a one-parameter bifurcation diagram, with the dotted horizontal line indicating the nondimensionalized gap spacing. (b) A two-parameter bifurcation set illustrates how the bifurcation points evolve in the forcing ratio versus driving frequency space. The specific points labeled in (a) (GR_1, PD_1, PD_2, SN_1, GR_2, and SN_2) are determined by the intersections of the dashed horizontal line with the various bifurcation curves. (c) Another two-parameter bifurcation set is shown for the stiffness ratio versus frequency ratio space. Reproduced with permission of [107], Copyright of © IOP Publishing.

doi:10.6342/NTU202600018

one solutions. Conventionally, the characterization of MEMS vibro-impact devices employs bidirectional frequency sweeps (forward and backward), yielding fractional solution curves punctuated by jump phenomena at SN_2 and SN_1, respectively. Nevertheless, although aggregating data from both sweep directions allows for the reconstruction of the frequency response, this approach fails to elucidate the mechanism by which the system stabilizes onto a specific solution. Furthermore, sweep parameters—specifically step size and sweep rate—function effectively as initial conditions at each discrete frequency, thereby influencing the measurement outcomes [129]. To mitigate such ambiguity, the utilization of a *basin of attraction map* (alternatively termed a *domain of attraction*) is recommended.

A basin of attraction encompasses the specific set of initial conditions that converge

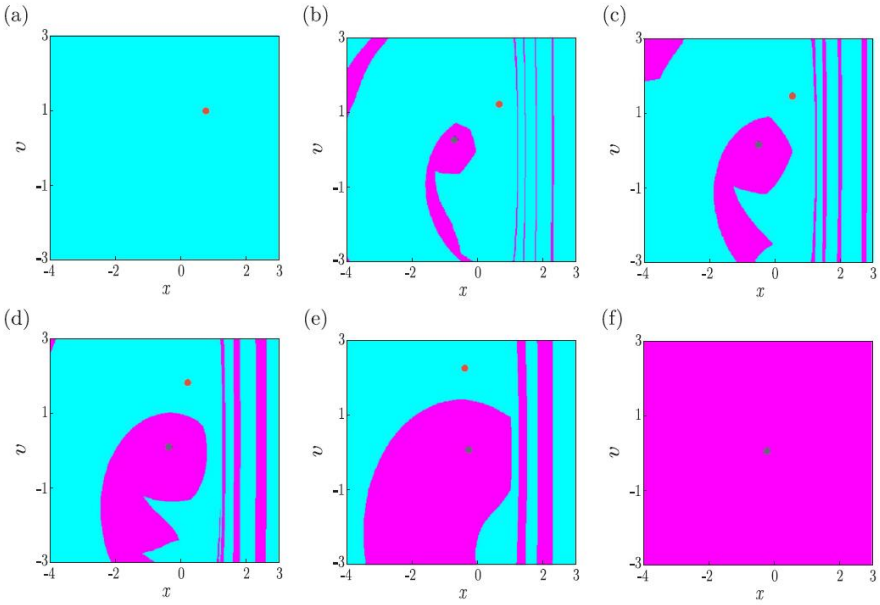


Figure 2-4: Evolution of the basins of attraction for a vibro-impact oscillator at different frequency ratios (ω) of (a) 1.10, (b) 1.18, (c) 1.25, (d) 1.35, (e) 1.45, (f) 1.52, corresponding to the response shown in Figure 2-3 (a). The frequencies for plots (a) and (f) lie outside the bistable (SN_1-SN_2) region, each showing a single attractor. In contrast, plots (b) through (e) are for frequencies within the bistable region, where two attractors coexist. The red dot indicates the high-energy attractor (upper branch), while the green dot denotes the low-energy one (lower branch). Each colored area represents the basin of attraction for its corresponding attractor. Reproduced with permission of [107], Copyright of © IOP Publishing.

doi:10.6342/NTU202600018

toward an identical asymptotic trajectory behavior [99]. This visualization delineates attractors via points and their associated basins of attraction through chromatic regions. Figure 2-4 demonstrates the progression of these basins starting from a frequency below SN_1 and extending past SN_2, highlighting variations in the surface area of the basin associated with the upper branch (represented by the red dot in Figure 2-4 (a)) and the lower branch (the green dot in Figure 2-4 (f)). Within the driving frequency interval bounded by SN_1 and SN_2 (Figure 2-4 (b)-(e)), the resulting motion converges to either the upper or lower state, contingent upon whether the initial condition resides within the light blue or magenta zone, respectively.

In reality, the dynamics of a vibro-impact system exhibit greater complexity than the simplified scenario featuring merely two attractors depicted in Figure 2-4. Figure 2-5 (a) displays a near-grazing bifurcation diagram sourced from [119], which encompasses five distinct attractors denoted by differing colors. Figure 2-5 (b) portrays the basins of attraction corresponding to four separate motions at a frequency ratio of 0.8044—marked by the dashed line in Figure 2-5 (a)—unveiling a highly convoluted pattern that demonstrates the determinative role of initial conditions on the ultimate system motion. Regarding each attractor plotted in Figure 2-5 (a), the abrupt emergence or vanishing of line segments signifies discontinuous bifurcations, predominantly of the saddle-node type. To illustrate, the blue trajectories in Figure 2-5 (a) denote a saddle-node bifurcation occurring just above 0.806. The orange region within the basin of this attractor, depicted in orange in Figure 2-5 (b), corresponds to conditions at a frequency ratio of 0.8044, wherein the five black dots signify periodically recurring states. Figure 2-5 (c) exhibits the phase portraits associated with the four unique motions. Within this set, the Poincaré map derived from the blue curves aligns with the black dots in Figure 2-5 (b), evidencing a $z = 3/5$ motion (specifically, period-five three-impact).

doi:10.6342/NTU202600018

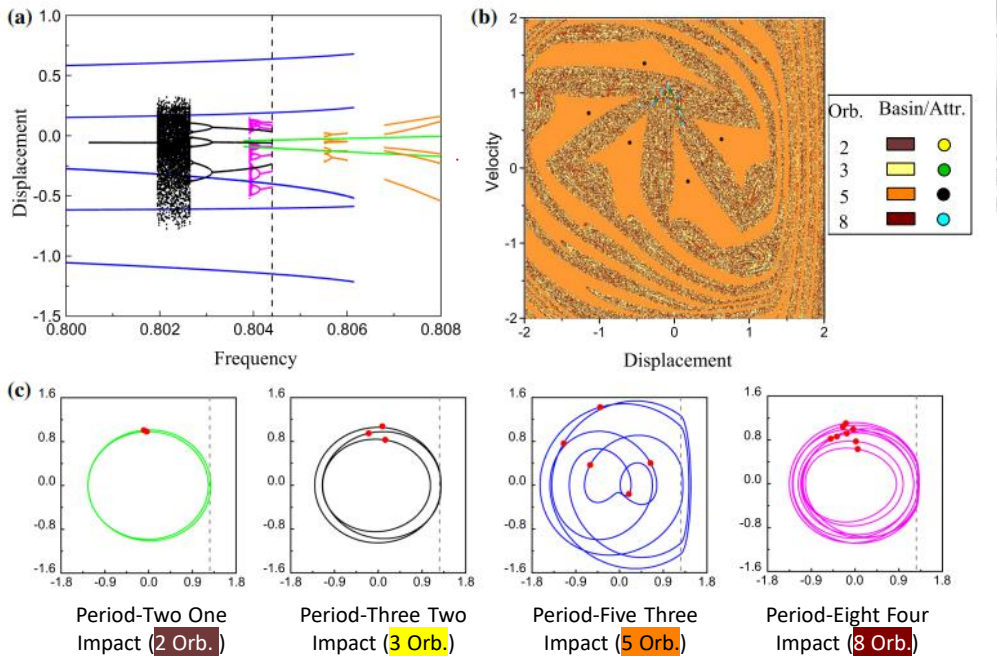


Figure 2-5: An example of complex dynamics involving multiple coexisting attractors in a vibro-impact oscillator. (a) A bifurcation diagram reveals a frequency region where several stable solutions are present simultaneously. (b) The basin of attraction map is shown for the specific frequency indicated by the dashed line in (a), with colored regions corresponding to different orbits. (c) The individual phase portraits for each of these coexisting attractors are detailed. In these portraits, the dashed vertical line marks the nondimensionalized gap spacing, while the red dots represent the points of the Poincaré map. The Poincaré map shown here is constructed by taking 4000 points once per period of the external force. Reproduced with permission of [107], Copyright of © IOP Publishing.

2.2.4 The Effect of Intrinsic Nonlinearity in MEMS Vibro-impact Resonators

In standard operational scenarios, vibro-impact devices function within regimes characterized by the pronounced manifestation of intrinsic nonlinearities inherent to MEMS resonators. Figure 2-6 elucidates the influence of nonlinear stiffness upon the frequency response of MEMS vibro-impact architectures, delineating (a) a hardening characteristic with impact, (b) a softening characteristic with impact, and (c) a hybrid manifestation exhibiting both hardening and softening phenomena. As illustrated, these inherent nonlinear attributes precipitate hysteresis within the frequency response

doi:10.6342/NTU202600018

profiles and generate additional bifurcations. The behavior exemplified in Figure 2-6 (c) is especially prominent in contexts such as atomic force microscopy (AFM), attributable to substantial attractive surface forces. Comprehensive elaboration is reserved for Section 2.5.

MEMS vibro-impact systems display intrinsic nonlinearities analogous to those identified in standard MEMS resonators [100, 105, 130], encompassing: (1) squeeze-film damping; (2) viscoelastic material response under dynamic conditions; (3) geometric stiffness nonlinearity resulting from extensive deflection; (4) driving force nonlinearity, notably within electrostatic actuation; and (5) residual axial stress stemming from fabrication procedures. Furthermore, complex dynamical phenomena such as parametric resonance [131], internal or auto-parametric resonance [132], and chaotic motion accompanied by period-doubling bifurcation cascades [133]—conventionally observed in MEMS resonators—can coalesce with impact-induced nonlinearity within MEMS vibro-impact systems.

2.3 Interaction Force Formulation

The domain of contact mechanics has seen extensive investigation into contact force modeling [134-141]. A significant portion of research regarding microscale vibro-impact systems employs contact theories rooted in the traditional Hertz model and its derivatives. These extensions, which account for adhesion force or dissipation, serve

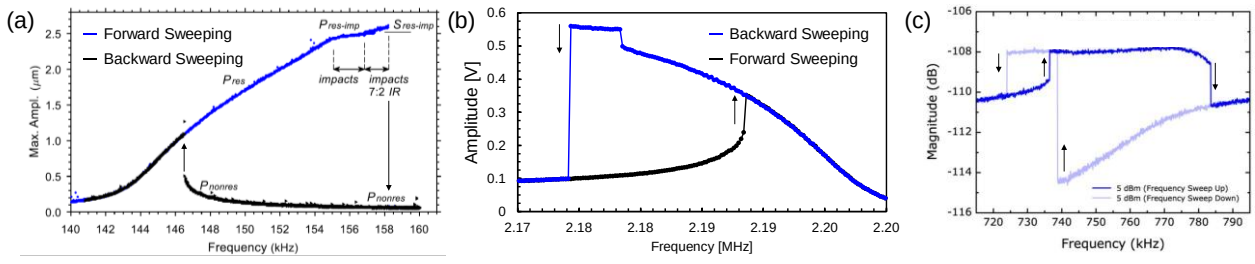


Figure 2-6: A collection of experimentally measured frequency responses for MEMS vibro-impact resonators, illustrating how different intrinsic nonlinearities affect the system's behavior. The plots show (a) a response dominated by a hardening effect, (b) a response primarily characterized by softening, and (c) a response exhibiting a mixed softening-hardening behavior. Reproduced with permission of [107], Copyright of © IOP Publishing.

doi:10.6342/NTU202600018

as the cornerstone of contact mechanics. Alternative methodologies incorporate intermolecular potential models alongside classical principles such as Newton's Experimental Law and Hooke's Law (specifically, the framework illustrated in Figure 2-1). Within the spectrum of available contact models, frameworks integrating surface forces prove more appropriate for microscale contact, largely attributed to the elevated surface-to-volume ratio. In particular, surface characteristics inherent to microscale contact—including adhesion forces, long-range non-contact forces, contact area, and roughness—exert a substantially greater influence on the aggregate contact force than is observed at the macroscale [142-144]. Nonetheless, frameworks that neglect adhesion forces, such as the standard Hertz contact theory, or those that circumvent direct force calculations, like Newton's experimental law of impacts, remain valuable for characterizing the dynamic behaviors of micromechanical vibro-impact systems [63, 64, 70, 83, 145, 146]. As notably remarked by British statistician *George E. P. Box*, "*All models are wrong, but some are useful*" [147]. This observation highlights the intrinsic limitations and imperfections present in all models, regardless of their complexity. However, their utility stems from their capacity to offer meaningful insights and predictions despite such deficiencies. The selection of an adequate model is contingent upon the distinct necessities of the application and the trade-off between computational simplicity and precision.

TABLE 2-1 tabulates a range of micromechanical vibro-impact systems alongside their respective contact models. Frequently utilized frameworks for contact modeling encompass the Hertz model, JKR model, DMT model, Lennard-Jones potential, coefficient of restitution, and inelastic contact represented by a spring and damper combination. Figure 2-7 displays the tip-sample force-distance curve corresponding to each contact model, with the exception of the coefficient of restitution, which is derived from velocity alterations rather than force interactions.

Within the context of vibro-impact systems, the dynamics characterizing contact events may be categorized into rigid, elastic, plastic, adhesive, anelastic, and

doi:10.6342/NTU202600018

viscoelastic types. These states are best represented by the previously mentioned force models, utilizing either continuous or discrete methodologies to manage the transition between contact and non-contact phases [148-150]. Discrete methodologies, such as the impulse-momentum method [149], rigid method, and non-smooth method [113], minimize computational duration by obviating the requirement for minute time steps, though this often occurs at the expense of accuracy. In contrast, continuous strategies—including the force-based method [149], compliant method, regularized method [151], and smooth method [152] within multibody system dynamics—demand greater computational resources and meticulous time step selection, yet they typically yield superior precision relative to discrete approaches.

The subject of contact force modeling has been the focus of substantial research and review. For example, [149] offers an exhaustive survey of general contact force modeling methodologies; [136, 140, 204-206] address adhesive contact force modeling in AFM; while [134] contrasts diverse adhesion contact theories. Furthermore, [152, 207-209] investigate the physics of viscoelasticity, corroborated by findings from both simulations and experiments. The following subsections will examine the prevalent force models utilized in micromechanical vibro-impact systems. It is important to acknowledge that the optimal model may vary between cases, often necessitating iterative calibration to align with experimental results.

2.3.1 Classical Contact Models

This research categorizes established contact force models into Hertzian and non-Hertzian frameworks. The Hertzian classification is predicated on the fundamental Hertz contact theory. Conversely, non-Hertzian models encompass techniques such as the coefficient of restitution, alternatively referred to as Newton's experimental law, as well as the implementation of springs coupled with dampers to represent elastic or inelastic impact constraints.

doi:10.6342/NTU202600018

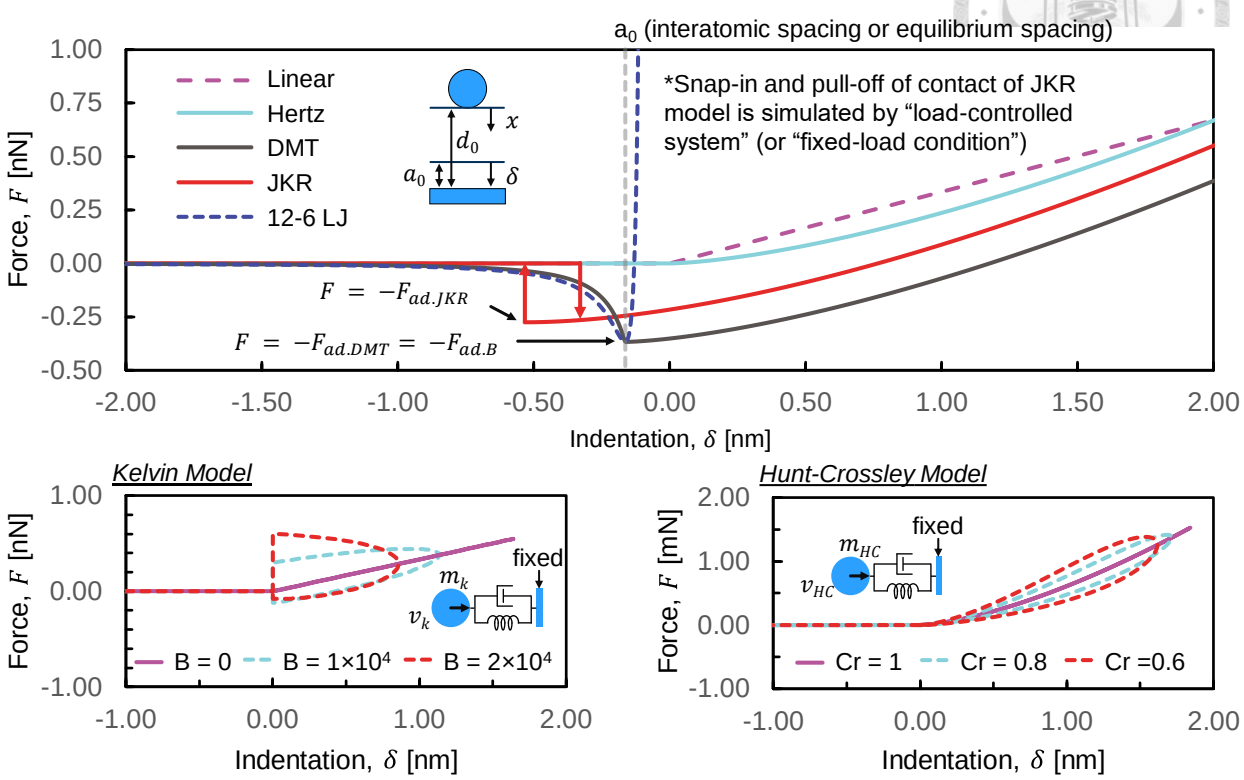


Figure 2-7: Comparison of force-indentation curves for various contact models. (a) Plots for several non-dissipative models (Linear, Hertz, DMT, JKR, and Bradley) are shown, illustrating their distinct attractive and repulsive force profiles. The inset defines the coordinates for displacement (x), indentation (δ), interatomic spacing (a_0), and gap (d_0). (b) and (c) Simulated curves for the dissipative Kelvin and Hunt-Crossley models are presented, with insets showing their respective mechanical representations. The hysteresis in these plots indicates energy loss during contact. For the purpose of this illustration, the interatomic spacing for the Hertz and linear spring models is set to zero, but it can be incorporated if necessary. The insets in (b) and (c) show the mechanical model of the colliding body with the fixed soft base. The result in (a) for the JKR model is based on a fixed-load approach; the fixed-grips condition is another possible approach. The simulation conditions were as follows: (a) JKR Model: $a_0 = 0.165 \times 10^{-9}$, $H = 40 \times 10^{-20}$, $R_1 = R^* = 150 \times 10^{-9}$, $E_1 = E_2 = 42.4 \times 10^9$, $\nu = 0.42$, $k_{linear} = 335$; (b) Linear Spring Model: $k = 335$, $m_k = 1 \times 10^{-10}$, $v_{before} = 0.003$; (c) Hertz Model: $k = 335$, $m_{HC} = 1 \times 10^{-10}$, $v_{before} = 0.15$. Reproduced with permission of [107], Copyright of © IOP Publishing.

doi:10.6342/NTU202600018

TABLE 2-1: SUMMARY OF LITERATURES ON THE VIBRO-IMPACT APPLICATION AND MODEL ASSOCIATED.

REPRODUCED WITH PERMISSION OF [107], COPYRIGHT OF © IOP PUBLISHING.

	Application					
	AFM	RF Switch	Resoswitch	Energy Harvester	Impact Actuator	Other Devices
Combination of Spring and Dashpot	[153, 154]	[77, 155, 156]	[86]	[67-69, 73, 75, 157-164]	[165-168]	[169]
Coefficient of Restitution	-	-	[84, 146]	[70]	[63-66, 170-174]	-
Lennard-Jones Force/Bradley Model	[175-180]	[78]	-	-	-	-
DMT	[57-59, 142, 181-190]	-	-	-	-	[191, 192]
JKR	[142]	[79, 193]	-	-	-	-
[a]Others	[54, 55, 143, 194-196]	[197-202]	-	[203]	-	-

[a] Note:
[54, 196]: non-classical DMT model including the viscoelastic effect
[55]: constant adhesion force only
[143] : classical inelastic contact model + constant adhesion force
[194] : Hertz model + constant adhesion force
[195] : non-classical inelastic contact model
[197]: combined two type linear spring to considering adhesion force
[198]: elastic-plastic Hertz model
[199]: w/ consideration of asperity height distribution by Gaussian probability
[200-202]: linear spring + van der Waals force
[203]: modeling as 2-DOF lumped system

doi:10.6342/NTU202600018

2.3.1.1 Rigid Contact (The Coefficient of Restitution)

As indicated earlier, the coefficient of restitution quantifies the energy dissipation occurring during the collision of two bodies; this parameter is derived from the ratio of relative velocities subsequent to and preceding the impact, as opposed to relying on the contact force [209]

$$C_r = \frac{u_1^+ - u_2^+}{u_1^- - u_2^-} \equiv \frac{v^+}{v^-} \tag{2-12}$$

wherein the relative velocities of the interacting bodies preceding and following the impact are designated as $v^-$and v^+, respectively.

This conservation of momentum yields

$$m_1 u_1^- - m_2 u_2^- = m_1 u_1^+ + m_2 u_2^+ \tag{2-13}$$

Substituting (2-13) into (2-12) gives

$$\begin{cases} u_1^+ = [m_1 u_1^- + m_2 u_2^- - m_2 C_r v^-]/(m_1 + m_2) \\ u_2^+ = [m_1 u_1^- + m_2 u_2^- + m_2 C_r v^-]/(m_1 + m_2) \end{cases} \tag{2-14}$$

Consequently, the energy ratio preceding and following the contact event, formulated as a function of the coefficient of restitution, is defined as

$$\frac{E^+}{E^-} = \frac{(v^+)^2}{(v^-)^2} = C_r^2 \tag{2-15}$$

In this context, the variables $E^-$and E^+ characterize the kinetic energy prior to and following the impact, respectively. In the instance where $C_r = 1$, the system experiences a perfectly elastic collision, thereby maintaining the conservation of kinetic energy. Within the majority of actual micromechanical systems, one interacting body often functions as a stopper featuring a rigid anchor and zero velocity ($u_2^- = u_2^+ = 0$), which leads to the conditions $v^+ = u_1^+$ and $v^- = u_1^-$, and consequently $u_1^+ = C_r u_1^-$. It is recognized that the coefficient of restitution fluctuates according to the impact velocity. As a result, the suggested contact map is capable of precisely characterizing the local dynamics only within a constrained interval of impact

doi:10.6342/NTU202600018

velocities. This simplified representation differs from the continuous modeling approach, facilitating a more straightforward characterization of the contact phase. Nevertheless, implementing this contact map can diminish computation time substantially, often by several orders of magnitude [64]. This specific model, which omits considerations of contact force and surface deformation, is ideally suited for investigating hard materials characterized by transient contact durations and relatively invariant contact surfaces.

2.3.1.2 Elastic and Inelastic Contact (w/o or w/ Dampers)

In contrast to the coefficient of restitution, which adopts a discontinuous methodology to represent the impact event, a linear spring generating a contact force offers an alternative, straightforward characterization of the contact [77]

$$F_l(x) = k_l(x - d_0);\ x \geq d_0 \tag{2-16}$$

In scenarios involving a rigid stopper characterized by high contact stiffness—where contact duration and indentation remain negligible—the spring-based continuous contact model can yield outcomes comparable to the coefficient of restitution with $C_r \sim 1$ during a rigid contact involving minimal energy dissipation [148, 150]. Nevertheless, the implementation of a pure linear spring model is infrequent in microscale devices for reasons analogous to those affecting the coefficient of restitution, specifically its failure to account for energy dissipation during contact. Nonetheless, this spring-based contact model finds application in certain energy harvester systems functioning at elevated resonance frequencies, wherein the solid body undergoes minor and uniform deformation [67-69, 158].

To achieve a more precise representation of energy dissipation and actual conditions, dampers have been incorporated into the spring-based contact model for more extensive utility. The Kelvin approach pioneered the integration of a linear damper alongside a linear spring within the contact model [210]

$$F_K(x) = k_K(x - d_0) + b_K x';\ x \geq d_0 \tag{2-17}$$

doi:10.6342/NTU202600018

While the Kelvin model possesses theoretical drawbacks—notably the presence of discontinuous force jumps at the initiation and termination of contact resulting from the derivative of x— it continues to be utilized for dissipative contact modeling due to its mathematical simplicity. Diverse spring-based frameworks have been developed to capture contact nonlinearity. For example, [152] investigated contact force models utilizing nonlinear power functions, which have been synthesized in various configurations for specialized fields such as granular materials and biomechanics. Additionally, at micro and nano scales, numerous materials exhibit viscoelastic or anelastic behavior, rendering these hybrid models appropriate [207]. Broadly, contact force models merging nonlinear springs and dampers are typically formulated using expressions such as [152, 207, 211]

$$F_{kb}(x) = K(x - d_0)^n + \chi(x - d_0)^m x'; x \geq d_0 \tag{2-18}$$

In this formulation, the variable K characterizes the contact-stiffness parameter, while χ signifies the hysteresis-damping factor. The Hunt-Crossley contact force model, which is predicated on (2-18), is extensively utilized within multibody dynamic modeling [212] owing to its precision in estimating contact force. This specific framework has been implemented in the study of MEMS energy harvesters [76]. According to the foundational research by Hunt and Crossley, the relationship between the coefficient of restitution and the impact velocity is established by

$$C_r = 1 - \alpha v^- \tag{2-19}$$

In this expression, α represents a coefficient contingent upon the material properties, geometric configuration, and kinematics of the colliding entities. The hysteresis-damping factor featured in (2-18) is defined as

$$\chi = \frac{3}{2}\alpha K \tag{2-20}$$

By integrating (2-19) and (2-20) the following expression is derived

doi:10.6342/NTU202600018

$$\chi_{HC} = \frac{3(1-C_r)}{2}\frac{K}{v^-} \tag{2-21}$$

The contact-stiffness parameter K is determined by the specific local geometry and inherent material properties. For the interaction between two spheres possessing a radius R, the contact-stiffness parameter is computed as

$$K = \frac{4}{3}E^*\sqrt{R^*} \tag{2-22}$$

The contact-stiffness parameter K , which originates from Hertz theory, will be examined in greater detail in the subsequent subsection. Alternative mathematical representations for the hysteresis-damping factor χ can be found in the literature [152, 212].

2.3.1.3 Hertz Model

The Hertz model serves as a cornerstone of traditional contact mechanics and is derived from analytical solutions within the theory of elasticity for non-adhesive contacts [213-216]. This framework characterizes the interplay between the applied force, contact areas, and indentation depth across diverse contact geometries, including sphere-on-flat half-space, sphere-on-sphere, and conical indenter-on-flat half-space configurations. The validity of the Hertz model is predicated on several core assumptions: (1) the materials exhibit linear elastic, homogeneous, and isotropic behavior, possessing perfectly smooth surfaces devoid of friction (specifically, monolithic materials lacking coatings where the thickness substantially exceeds the indentation depth); and (2) the dimensions of the contact area remain significantly smaller than the primary structural dimensions [204].

Consider a scenario where a sphere of radius R_1 interacts with a flat half-space ($R_2 \to \infty$). Under these conditions, the effective contact radius is determined by [213-216]

doi:10.6342/NTU202600018

$$a_c^3 = \frac{FR^*}{K^*} \tag{2-23}$$

In this particular instance, F represents the applied load, while the effective radius of curvature R^* is defined by the relation $R^{*-1} = (1/R_1 + 1/R_2)^{-1}$, which simplifies to R_1. The contact modulus K^*, alternatively termed the reduced elastic modulus, is contingent upon the contact geometry and is formulated as [152, 213-216]

$$K^* = \frac{4}{3}E^* = K/\sqrt{R^*} \tag{2-24}$$

Within this equation, $E^* = [(1 - v_1^2)/E_1 + (1 - v_2^2)/E_2]^{-1}$ signifies the effective Young's modulus, whereas v_i and E_i (with subscripts 1 and 2) designate the Poisson's ratio and Young's modulus of the respective materials. Because terms like E, E^*, K^* and K are frequently utilized synonymously across various contact mechanics literature, (2-24) serves to explicitly define their mathematical connections.

The magnitude of indentation, which quantifies the depth to which the sphere infiltrates the flat half-space, is expressed as [213-216]

$$\delta = x - d_0 = \frac{a_c^2}{R^*} \tag{2-25}$$

By synthesizing (2-23) and (2-25), the Hertz contact force is established as [215]

$$F_{Hertz}(x) = K(x - d_0)^{n=1.5};\ x \geq d_0 \tag{2-26}$$

The contact-stiffness parameter K, being geometry-dependent, fluctuates according to the specific configuration; consequently, the exponent n in (2-26) may vary. For example, $n = 2$ in the case of a cone-to-flat half-space contact interaction [215]. Although certain underlying assumptions are rarely perfectly satisfied in actual settings, the Hertz model remains highly advantageous, particularly for the characterization of stiff materials in AFM [204], or for components operating within fluid environments where interfacial forces are attenuated [204].

doi:10.6342/NTU202600018

2.3.2 Modified Hertz Contact Models

In the microscale regime, adapted Hertzian frameworks such as the Johnson-Kendall-Roberts (JKR) [217] and Derjaguin-Muller-Toporov (DMT) [218] models are commonly employed. These paradigms incorporate adhesion forces, which exert a substantial influence at the microscale due to the increased surface-to-volume ratio.

2.3.2.1 JKR Model

Within the context of AFM applications, the JKR model is frequently implemented to characterize adhesive contact forces, specifically in instances where the tip-sample interaction entails a compliant surface, an expanded contact area, or intensified short-range adhesion. Evolving from the Hertz model, the JKR model integrates adhesive effects directly into the contact area, contact radius, and indentation depth. For a rigid sphere interacting with a compliant flat plane, JKR theory defines the effective contact radius and indentation as [79, 134, 204, 217]

$$a_c^3 = \frac{R^*}{K^*}\left[F + 3\pi W R^* + \sqrt{6\pi W R^* F + (3\pi W R^*)^2}\right] \tag{2-27}$$

or

$$a_c^3 = \frac{R^*}{K^*}\left(\sqrt{F_{ad.JKR}} + \sqrt{F + F_{ad.JKR}}\right)^2 \tag{2-28}$$

and

$$\delta = x - d_0 + a_0 = \frac{a_c^2}{R^*} - \sqrt{\frac{8\pi a W}{3K^*}} \tag{2-29}$$

In these expressions, H, R^* and K^* designate the work of adhesion, the effective radius of curvature, and the contact modulus, respectively. The work of adhesion $W = \gamma_1 + \gamma_2 - \gamma_{12}$ signifies the energy required to decouple two surfaces, where γ_1 and γ_2 represent the surface energies of the two spheres, and γ_{12} denotes the interfacial free surface energy [135, 204]. This parameter serves to quantify the magnitude of the attractive force between the surfaces. For two solid materials, 1 and 2, immersed in a

doi:10.6342/NTU202600018

liquid medium 3, the work of adhesion is formulated as

$$W_{132} = \gamma_{13} + \gamma_{23} - \gamma_{12} \tag{2-30}$$

where γ_{13} and γ_{23} correspond to the surface energies of bodies 1 and 2 within the liquid environment 3. If the materials 1 and 2 are of the same substance (i.e., $\gamma_{13} = \gamma_{23}$), the interfacial free surface energy vanishes, causing the work of adhesion to align with the work of cohesion, which equates to double the surface energy (i.e., $W_{131} = 2\gamma_{13}$). Comprehensive discussions regarding the work of adhesion are provided in [139, 140]. For the sake of simplicity, W_{132}, γ_{13} and γ_{23} are designated as W, γ_1 and γ_2 respectively. The indentation and contact force are established as implicit functions requiring numerical solution. The pull-off force specific to the JKR model is identified by determining a real solution for (2-28), which yields $F = -F_{ad,JKR} = -\frac{3}{2}\pi W R^*$[204, 217].

2.3.2.2 DMT Model

The DMT model incorporates both long-range and short-range attractive interactions and, in contrast to the JKR model, is generally applied to situations involving rigid structures with restricted contact areas. DMT theory modifies the Hertz model by integrating the adhesion force characterized by Bradley to represent deformable entities [219]. For a spherical body interacting with a planar surface, the effective contact radius and indentation are defined as follows [134]

$$a_c^3 = \frac{R^*}{K^*}[F + 2\pi W R^*] \tag{2-31}$$

and

$$\delta = x - d_0 + a_0 = \frac{a_c^2}{R^*} = \left(\frac{F + 2\pi W R^*}{R^* K^*}\right)^{\frac{1}{3}} \tag{2-32}$$

When considering exclusively the van der Waals force between two bodies, the DMT model is formulated as [206, 215]

doi:10.6342/NTU202600018

$$F_{DMT}(x) = \begin{cases} -\dfrac{HR^*}{6(d_0 - x)^2}; x < d_0 - a_0 \\ -\dfrac{HR^*}{6a_0^2} + K(x - d_0 + a_0)^{3/2}; x \geq d_0 - a_0 \end{cases} \quad (2\text{-}33)$$

where a_0 signifies the interatomic spacing (or equilibrium spacing) separating the tip and the sample, with typical values spanning 0.1 to 0.5 nm [204]. y assigning a value of zero to (2-31) the pull-off force is identified as $F = -F_{ad,DMT} = -2\pi WR^*$ [215]. The correlation between the Hamaker constant and the work of adhesion, under the assumption of pure van der Waals forces, is expressed as

$$H = 12\pi W a_0^2 \quad (2\text{-}34)$$

2.3.2.3 Intermolecular Pair Potentials for Adhesive Contact

In the domain of adhesive contact, mathematical frameworks characterizing intermolecular forces have been implemented to elucidate the interactions between two bodies in proximity. For example, the Lennard-Jones (LJ) potential serves to model the adhesion force acting between two rigid particles. Figure 2-8 illustrates a typical intermolecular potential profile between a pair of particles based on the LJ potential, formulated as [204, 220]

$$v_{LJ,12-6} = 4\epsilon\left[\left(\frac{\sigma}{r}\right)^{12} - \left(\frac{\sigma}{r}\right)^{6}\right] \quad (2\text{-}35)$$

or

$$v_{LJ,12-6} = \epsilon\left[\left(\frac{r_{min}}{r}\right)^{12} - \left(\frac{r_{min}}{r}\right)^{6}\right] \quad (2\text{-}36)$$

or

$$v_{LJ,12-6} = \frac{H_a}{r^{12}} - \frac{H_r}{r^6} \quad (2\text{-}37)$$

In these expressions, ϵ designates the well depth, which quantifies the magnitude of

doi:10.6342/NTU202600018

the attractive force between the particles; σ represents the separation distance at which the intermolecular potential energy vanishes; and r_{min} denotes the distance corresponding to the minimum potential energy. The exponents 12 and 6, which represent the repulsive and attractive components respectively, may be generalized to *n* and *m* [221].

Numerous investigations [175, 176, 179, 222] employ an alternative 7-1 pair potential to characterize the interactions between a rigid sphere and a rigid flat surface. This potential is obtained by integrating the molecular attractions across every molecular pair—initially represented by the 12-6 LJ potential—and is formulated as

$$v_{LJ,7-1} = \frac{H_a R^*}{1260(x - d_0 + a_0)^7} - \frac{H_r R^*}{6(x - d_0 + a_0)} \tag{2-38}$$

where H_a and H_r signify the Hamaker constants for the attractive and repulsive potentials, defined as $H_a = \pi^2 \rho_1 \rho_2 c_1$ and $H_r = \pi^2 \rho_1 \rho_2 c_2$. In these definitions, ρ_1 and ρ_2 represent the molecular number densities of the interacting media, while $c_1 =$

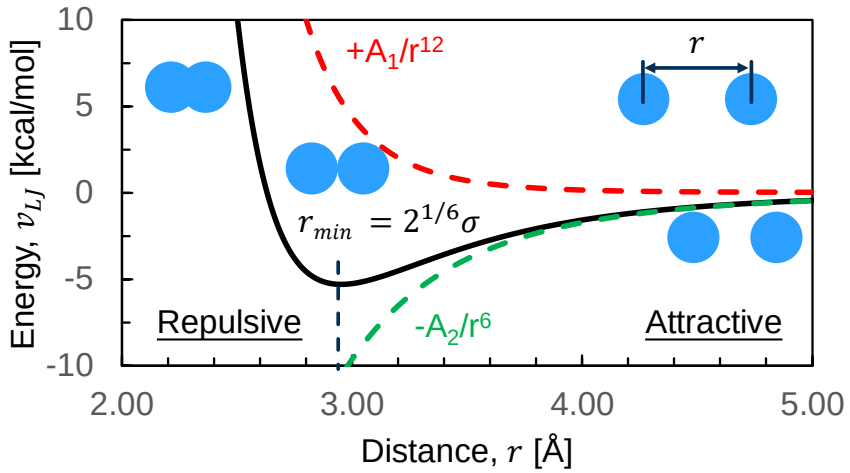


Figure 2-8: Graphical representation of the 12-6 Lennard-Jones potential, plotting interaction energy against the distance between two particles. The curve illustrates the attractive forces at longer distances and the strong repulsive forces at short distances, with the insets depicting the particles in these different regimes. The minimum of the potential well corresponds to the equilibrium position—the interatomic spacing—where the net force between the particles is zero. The simulation conditions used are $\epsilon = 5.29$ and $\sigma = 2.9511 \times 10^{-10}$. Reproduced with permission of [107], Copyright of © IOP Publishing.

doi:10.6342/NTU202600018

$4\epsilon\sigma^{12}$ and $c_2 = 4\epsilon\sigma^6$ denote the interaction coefficients of the intermolecular pair potential. The resulting interaction force is subsequently derived as

$$F_{LJ,7-1} = -\frac{\partial v_{LJ,7-1}}{\partial x} = \frac{H_a R^*}{180(x - d_0 + a_0)^8} - \frac{H_r R^*}{6(x - d_0 + a_0)^2} \quad (2\text{-}39)$$

In this context, R^* denotes the effective radius of curvature. The application of the Lennard-Jones (LJ) potential necessitates a comprehensive understanding of material and geometric characteristics, such as H_a and H_r and R^*, which can be difficult to determine at the microscale. Because the LJ potential is designed to represent atomic-level interactions by capturing both attractive and repulsive forces at minute scales, atomic force microscopy (AFM) represents the vibro-impact application most fundamentally linked to the LJ potential model, as AFM facilitates the quantification of these microscale properties.

Based on the 12-6 Lennard-Jones potential, Bradley [219] established the pull-off force between a rigid sphere and a rigid surface, denoted as $F = -F_{ad.B} = -2\pi W R^*$, which takes the following form [219, 223, 224]

$$F_B = \frac{8\pi W R^*}{3}\left[\frac{1}{4}\left(\frac{a_0}{x - d_0 + a_0}\right)^{-8} - \left(\frac{a_0}{x - d_0 + a_0}\right)^{-2}\right] \quad (2\text{-}40)$$

2.3.2.4 Amendments and Remarks

Illustrated in Figure 2-9, the adhesion map for elastic spheres presented in [223] is delineated as a function of the elasticity parameter (also referred to as the Maugis parameter) λ and the pressure ratio $\bar{P}$. The variable λ ($= 1.157\mu$ [136, 223, 225, 226]) is dependent on the Tabor parameter μ, which is defined as:

$$\mu = \left(\frac{R^* W^2}{E^{*2} a_0^3}\right)^{1/3} \quad (2\text{-}41)$$

The contact pressure ratio $\bar{P}$ is characterized by

doi:10.6342/NTU202600018

$$\bar{P} = \frac{P}{\pi W R^*} \tag{2-42}$$

In this context, P signifies the applied load (equivalent to F in this study). The parameter μ characterizes the scale of elastic deformation, whereas $\bar{P}$ denotes the proportion between the aggregate load and its adhesive component. According to the findings in [223], the JKR model is recommended for $\mu \gg 1$ while the DMT model is deemed appropriate for $\mu \ll 1$. Furthermore, as shown in Figure 2-9, if the applied force substantially exceeds the pull-off force (specifically, $\frac{P_a}{P} = \frac{F_{ad}}{F} < 0.05$, where P_a represents the pull-off force designated in[223], corresponding to F_{ad} here), the standard Hertz model is considered applicable.

Certain studies suggest specific thresholds for μ to dictate model selection: the JKR

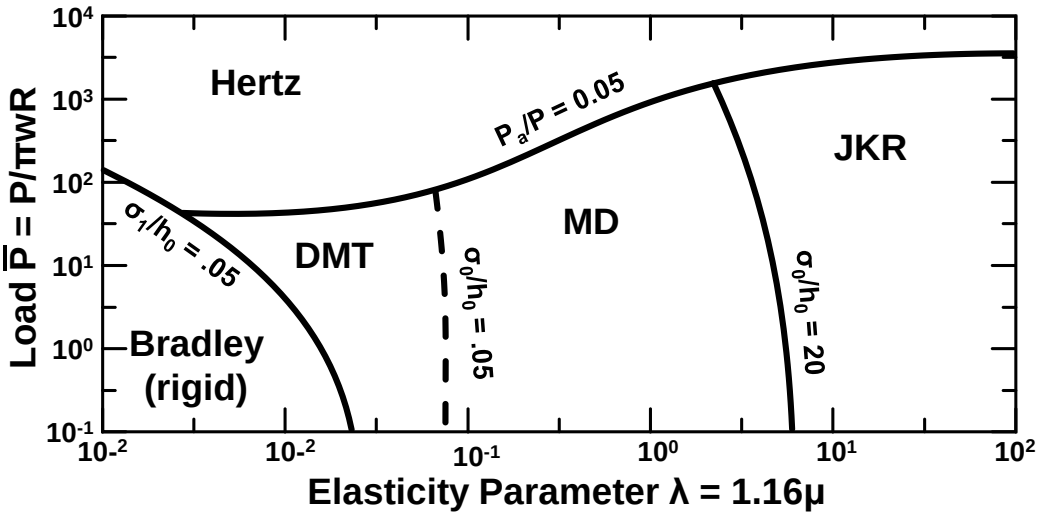


Figure 2-9: The adhesion map for elastic spheres, developed from the Maugis-Dugdale model, which helps in selecting the most suitable contact theory. Different regions on the map correspond to conditions where the Bradley (rigid), DMT, JKR, or Hertz models are most accurate The map categorizes regimes based on two key dimensionless parameters: the elasticity parameter (λ)— a measure of the ratio of the elastic indentation of the surface at the point of separation to the effective range of surface forces characterized by interatomic spacing, and the nondimensional load (P)— a measure of the ratio of the applied load to the adhesive pull-off force. The boundary curves are labeled with the chosen values defined in [223]. Reproduced with permission of [107], Copyright of © IOP Publishing.

doi:10.6342/NTU202600018

model for $\mu > 2$ [141] or $\mu > 5$ [136, 204, 205] and the DMT model for $\mu < 0.1$ [136, 204, 205]. To address the intermediate regime, several researchers have advocated for the Maugis-Dugdale (MD) model [226], depicted in Figure 2-9, as an effective transitionary solution bridging the DMT and JKR models [141, 205]. However, the MD model is less frequently implemented in microscale contact dynamic modeling. Additionally, the Hertz model remains generally valid for scenarios involving high loading forces.

The variables in (2-41) and (2-42), including the work of adhesion, contact tip radius, and interatomic spacing, are difficult to ascertain due to inconsistencies in fabrication processes and measurement constraints. In particular, quantifying these properties for contact sidewalls in in-plane vibro-impact devices presents significant challenges. Consequently, these values are frequently extracted by curve fitting experimental results to reflect the behavior of physical systems. To demonstrate the selection of a force model, TABLE 2-2 tabulates two tip-to-surface contact scenarios from [204]: (1) diamond-to-diamond-like carbon and (2) diamond-to-polyethylene. The equilibrium spacing (interatomic spacing) fluctuates between 0.15 nm to 1 nm, representing the lower bound ($a_{0.lb}$) and upper bound ($a_{0.ub}$), respectively. By utilizing the recorded pull-off force and the associated work of adhesion for both instances, the Tabor parameter can be derived. The Tabor parameter may vary by an order of magnitude due to ambiguities in interatomic spacing and the selected force model, with the boundaries established by W_{JKR} with $a_{0,lb}$ and W_{DMT} with $a_{0,ub}$, respectively. It is widely accepted that the Tabor parameter defining the model boundaries is $\mu > 5$ for the JKR region and $\mu < 0.1$ for the DMT region. As illustrated in Figure 2-9, the Hertz model is applicable to these two cases when the applied force surpasses 60 nN and 3000 nN, respectively.

doi:10.6342/NTU202600018

TABLE 2-2: EXAMPLES OF THE INTERACTION FORCE MODEL SELECTION FROM [204]. REPRODUCED WITH PERMISSION OF [107], COPYRIGHT OF © IOP PUBLISHING.

Case	Material: Tip / Surface	Young's Modulus, E [GPa]	Poisson's Ratio, v	Effective Young's Modulus, E^* [GPa]	Measured Pull-off Force, F_{ad} [nN]	Work of Adhesion, W_{JKR}/W_{DMT} [J/m2]	Tabor Parameter, μ_{ub}/μ_{lb}	Chosen Force Model	[a]Force Boundary for Hertz Model [nN]
1	Diamond / Diamond-like Carbon	1000 / 150	0.1 / 0.2	135.32	-3	0.0127/ 0.0095	0.051/0.006	DMT	60
2	Diamond / Polyethylene	1000 / 0.2	0.1 / 0.45	0.25	-150	0.6366/ 0.4775	45.71/5.66	JKR	3000

Note: The radius of tip (R_1) is 50 nm and radius of surface (R_2) is infinite.

[a]: When the applied force is extremely larger than the pull-off force (i.e., by 20× according to [223] that used $\frac{P_a}{P} < 0.05$ to define the boundary), the attractive force can be negligible, and therefore, the Hertz model could be applied.

doi:10.6342/NTU202600018

In summary, factors such as contact surface plastic deformation, elastic-plastic loading processes, roughness, and friction are generally omitted from the dynamic modeling of micromechanical systems. This exclusion is largely due to the difficulties associated with numerical modeling and mathematical derivation [149]. Nevertheless, these factors are vital for predicting long-term behavior, particularly at the microscale. Furthermore, various other interaction forces, such as capillary forces, squeeze film damping, and specific forces in liquids governed by the DLVO theory, remain outside the scope of this discussion.

2.4 Analytical and Numerical Method

The investigation of MEMS vibro-impact architectures presents greater challenges than the study of conventional nonlinear MEMS designs, primarily owing to pronounced nonlinearities and the instantaneous, non-smooth nature of contact phenomena. To address these complexities, a variety of mathematical frameworks and computational strategies have emerged to derive approximate solutions. A compendium of techniques applied to MEMS vibro-impact analysis is presented in TABLE 2-3 offers a comprehensive overview of the strategies utilized to solve MEMS vibro-impact systems. The distributed-parameter framework is often adopted to evaluate MEMS vibro-impact systems, as it maintains the structural continuity and represents the behavior through continuous variables. Within this methodology, MEMS vibro-impact systems are generally characterized as time-dependent, spatially distributed partial differential equations (PDEs) integrated with nonlinear components, typically grounded in Euler-Bernoulli theory [58, 77, 153, 155, 179, 186, 187, 198, 201]. A standard procedure for managing these PDEs involves transforming them into tractable ordinary differential equations (ODEs) via modal analysis [58, 153, 155, 179, 201], which yields a lumped reduced-order model.

doi:10.6342/NTU202600018

TABLE 2-3: SUMMARY OF SOLVING TECHNIQUES WITH APPLICATION FROM LITERATURES. REPRODUCED WITH PERMISSION OF [107], COPYRIGHT OF © IOP PUBLISHING.

Method	Publications					
	AFM	RF switch	Resoswitch	Energy Harvester	Impact Actuator	Other Devices
Analytical Approximation Method	[104, 139, 145, 146, 150, 151, 156-158]	-	-	[27, 29, 33, 35, 125]	[24]	-
FDTD Method	[148, 149]	[37, 155, 159-162]	-	-	-	-
FETD Method	-	[39, 164]	-	-	-	-
Time Integration	[15, 17-19, 104, 105, 115, 137, 139, 140, 143, 144, 147]	[38, 108, 117, 119, 154, 163]	[46, 108]	[28, 30, 120-124, 126, 165]	[23, 24, 127, 132, 133]	[153] [128-130, 136]
Continuation Method	[18, 116, 138, 141, 145, 146, 158]	-	[118]	-	[23, 25, 26, 134]	-

doi:10.6342/NTU202600018

Modal analysis addresses the issue within modal space by mapping a continuous system dictated by a PDE with infinite degrees of freedom onto a constrained, finite collection of modal equations. Every modal equation is linked to a specific eigenmode of the underlying continuous structure. Estimating the behavior of MEMS vibro-impact systems frequently entails applying the Galerkin method using a restricted number of eigenmodes (commonly ranging from one to four). This technique is viable because of the uncomplicated geometries and clearly established free-vibration mode shapes inherent in MEMS devices [58, 153, 155, 179, 201]. For more intricate geometries, the finite-element method (FEM) may be exploited to perform this estimation.

Conversely, the lumped-parameter approach—alternatively termed the lumped-mass approach—is frequently applied to streamline systems into a finite quantity of degrees of freedom (DOFs). This methodology encompasses: (1) Manually discerning the various segments of the system through space discretization; (2) Conceptualizing specific flexible structural components as rigid bodies; (3) Constructing the equations of motion for every individual part; and (4) Integrating these expressions to depict the global system dynamics. This workflow may incorporate matrix algebra or alternative mathematical tools to condense the governing equations. As a result, a structure can be represented as a sequence of lumped masses joined by massless elastic elements. Reduced-order ODEs derived from modal analysis and space discretization involving minimal DOFs can be solved with markedly lower computational overhead [26]. For sophisticated architectures, space discretization is typically executed via FEM or the finite-difference method (FDM).

The differential equations governing dynamic systems are solvable through four widely adopted techniques: analytical approximation, finite-difference, finite-element, and parameter continuation methods. The following segments will provide a detailed exposition of these methodologies.

2.4.1 Analytical Approximation Methods

To analytically solve weakly nonlinear differential equations, researchers

doi:10.6342/NTU202600018

frequently apply perturbation theory, particularly when the system involves a minor nonlinear parameter designated as the perturbation term. This framework is predicated on the hypothesis that the solution can be formulated as a series expansion based on the perturbation parameter. Generally, perturbation theory is appropriate for weakly nonlinear differential equations where the nonlinear response deviates only marginally from the linear baseline solution. The effectiveness of this perturbation method is strictly contingent upon the magnitude of the perturbation terms; excessive magnitudes can lead to convergence difficulties. For strongly nonlinear systems characterized by substantial perturbation terms, higher-order perturbation series are required, which are often computationally demanding and mathematically arduous to evaluate. One specific iteration of perturbation theory, the method of multiple scales, is frequently utilized for the modeling of AFM [188, 196].

On the other hand, alternative strategies have been formulated to address various categories of nonlinear problems. Regarding MEMS vibro-impact systems, a significant body of research has implemented the method of averaging (MOA) to forecast the frequency response of such architectures [69, 73, 75, 163, 184, 189]. This technique operates under the assumption that the impact-induced fluctuations in vibration amplitude remain invariant throughout a single period. Comprehensive information regarding this MOA is documented in Appendix. E.4.

A large portion of the analytical techniques devised for the nonlinear dynamics of microscale vibro-impact systems was initially derived from the study of tapping-mode AFM. These methodologies encompass the method of multiple scales [188, 196], the differential transformation method [177], the Melnikov method [183, 184], and the KBM asymptotic method [142, 194, 195]. It is important to highlight that these strategies, among others, have been successfully implemented to examine macroscale vibro-impact systems, yielding vital understanding of system behavior. The principal benefit of analytical approximation methods lies in their capacity to rapidly uncover qualitative behaviors—often within seconds—whereas numerical approaches may

doi:10.6342/NTU202600018

require minutes or even hours to reach a solution. Consequently, they are perfectly suited for investigations focusing on parameter dependency. Furthermore, the resulting theoretical solution provides a superior initial guess to facilitate accelerated convergence in numerical simulations [64].

In recent years, the homotopy analysis method (HAM) has been introduced as an analytical approach for nonlinear problems designed to bypass the constraints inherent in perturbation methods [227]. In contrast to perturbation methods, HAM is not dependent on the presence of small parameters within the nonlinear equations, thereby achieving parameter independence. Nevertheless, HAM has not yet been applied to the study of microscale vibro-impact systems [228].

2.4.2 Finite Difference and Finite Element Methods

Although perturbation theory is effective for characterizing the physical phenomena of nonlinear systems, its applicability to strongly nonlinear problems or long-term behavior studies is limited by the magnitude of approximation errors associated with the selected expansion order. Consequently, the finite-element method and finite-difference method have been established to numerically solve steady-state boundary-value differential equations. Both paradigms approximate continuous domain problems by partitioning them into a finite set of subdomains within the spatial dimension. The fundamental distinction between FDM and FEM lies in their discretization strategy: FDM defines the domain through a grid of nodes, whereas FEM defines nodes and implements shape functions to interpolate the field between them.

Discretization can also be extended to the temporal domain using FDM, a technique referred to as the *time integration*, *time marching* or *time stepping method*. This approach is advantageous for investigating the time trajectories of lumped systems. By substituting time derivatives with finite differences, the solution at each discrete increment is derived using data from the current step (explicit scheme) or a combination of current and subsequent steps (implicit scheme). Steady-state solutions extracted via the time integration method enable the generation of frequency responses

doi:10.6342/NTU202600018

by iteratively performing time-domain simulations across a spectrum of frequencies [192, 229].

Moreover, spatial FEM and FDM can be coupled with temporal integration to manage time-dependent problems, yielding the finite-element time-domain (FETD) method and the finite-difference time-domain (FDTD) method, respectively. Within this framework, the finite-element or finite-difference method handles the spatial domain, while the time-domain component refers to the time integration/stepping method applied to the temporal evolution.

In the MEMS field, the FETD method is extensively implemented using commercial platforms such as ANSYS for RF switches [79, 80, 230] and COMSOL Multiphysics [202]. Simultaneously, the FDTD method has been utilized to investigate the time-dependent behavior of switches [77, 193, 197-200] and tapping-mode AFM [186, 187]. However, both strategies demand exhaustive time integration of second-order ODEs, rendering them computationally expensive and often impractical for comprehensive systematic investigation or device optimization. For instance, capturing contact phenomena in vibro-impact problems requires the selection of a precise time step, particularly for low damping MEMS devices. Various approaches, such as adaptive time stepping—which modulates the step size according to the system's dynamics—and implicit time integration methods, which are more robust for stiff contact problems, assist in optimizing the temporal resolution.

Conversely, the duration of the simulation and the initial conditions significantly influence the fidelity of the results, especially in systems characterized by highly nonlinear behavior, multiple co-existing attractors, and intricate motions. In such cases, the transient state induced by the impact can persist for extended intervals, making the acquisition of precise results for behavior analysis quite laborious. In numerical frequency sweeping methods for vibro-impact oscillators functioning near resonance, such as in [192], the steady-state solution from a specific frequency point is frequently utilized as the initial condition for the subsequent point. This strategy facilitates

doi:10.6342/NTU202600018

convergence and is particularly valuable for characterizing the hysteresis response of vibro-impact oscillators. Generally, the motion of a vibro-impact device tracks the current attractor during the transition to the next frequency increment. Consequently, identifying the two co-existing stable solutions within a hysteresis frequency response necessitates both forward and backward sweepings. Furthermore, simulations often commence with the system at rest; thus, to circumvent initial condition and convergence difficulties, the initial frequency point should be situated outside the hysteresis region.

Regarding computational overhead, the total duration for the model and parameters described in [192] or 100 frequency points is approximately 1 hour on a standard PC equipped with an i7-8700 processor and 32 GB of RAM. Additionally, [64] forecasts the bifurcation of an impact actuator using a simplified contact map theoretically in minutes, whereas numerical methods require several days, and numerical methods seeded with theoretical initial conditions take a few hours. Although the specific hardware for these benchmarks is not specified, the data underscores the vast discrepancies in simulation time across different methods, with the analytical approach being significantly more rapid despite providing less detailed responses.

The time integration method remains a robust instrument for modeling the evolution of complex systems. Careful selection of the time step size, initial conditions, and approximation methods is vital for ensuring both efficient and accurate outcomes. While an increased time step may accelerate the computation, it risks inducing convergence problems, particularly in stiff problems where the solution exhibits rapid transitions. For stiff problems featuring a mix of slow and fast dynamic variations—such as those occurring immediately before, during, and after a vibro-impact event—time integration methods can become notably inefficient and time-consuming. Commercial environments such as MATLAB & Simulink, SPICE, Mathematica, and Python are commonly utilized as solvers for nonlinear problems. Furthermore, specialized in-house simulation tools such as VEDA [206], dForce [231], and

doi:10.6342/NTU202600018

pyDAMPF [232] originally designed for tapping mode AFM applications, may be modified for broader use cases.

2.4.3 Parameter Continuation Method

Generating bifurcation diagrams across expansive parameter domains via time integration techniques is frequently characterized by high levels of inefficiency. In contrast, the *parameter continuation method*—alternatively referred to as the *path following method* or simply continuation—provides a streamlined approach for capturing steady-state solutions and analyzing the effects of parameter fluctuations. This methodology is particularly beneficial as it facilitates the tracking of system equilibria over a broad spectrum of parameter settings, even when dealing with highly nonlinear systems that exhibit multiple co-existing solutions. Numerous specialized software suites and toolboxes, including COCO [233], MATCONT [234], AUTO [235], and NLvib [236], have been developed to execute numerical continuation utilizing either time-domain or frequency-domain formulations. The fundamental workflow for continuation entails: (1) deriving a precise initial guess through numerical simulation in instances where no previous system data exists; (2) adopting this initial solution as the foundational starting point; and (3) implementing the continuation method to navigate solution branches using a robust algorithm, such as the pseudo-arclength predictor-corrector scheme [235]. The distinct objectives and operational criteria for each software package are elaborated within their respective user manuals, and the specific test functions employed may differ. When selecting a toolbox, it is vital to evaluate its capacity to identify the specific bifurcation points pertinent to the research problem. Significant advancements in continuation-based modeling for microscale components have been achieved within the domain of tapping-mode AFM utilizing AUTO [58, 176, 179, 183, 184, 196]. While the accuracy and computational speed of the parameter continuation method can be influenced by the choice of increment or step size, it generally maintains a higher efficiency relative to alternative numerical strategies. By bypassing extended transients during the

doi:10.6342/NTU202600018

simulation process, the parameter continuation method can frequently automate the adjustment of simulation parameters, thereby preserving precision while simultaneously reducing computational time.

In conclusion, both analytical and numerical approximation strategies are predicated on various types of approximation formulas, which renders them inherently susceptible to approximation errors. This section serves to offer a comprehensive synthesis of the fundamental frameworks employed to solve nonlinear MEMS vibro-impact challenges and to guide the selection of suitable modeling strategies.

2.5 Micromechanical Vibro-Impact Applications

In this section, representative instances of micromechanical instruments founded upon vibro-impact system are explored. The evolution of these mechanisms mirrors the shifting paradigms within MEMS technology. During the 1990s, an era characterized by an emphasis on instrumentation capabilities, the field witnessed the emergence of tapping-mode AFM, RF switches, and impact microactuators. Subsequently, from the middle to the late of the 2000s, the burgeoning demand for autonomous and low-power sensing solutions drove the advancement of impacting energy harvesters and resoswitches. Since the late 2010s, the trajectory has shifted toward CMOS-MEMS based vibro-impact resonant devices and resoswitches [87, 89, 191, 192, 237] primarily to address contemporary requirements for heterogeneous integration.

2.5.1 Tapping-mode Atomic Force Microscope (AFM)

According to the methodology outlined in [238], tapping-mode AFM (*cf.* Figure 2-10 (a)) determines the tip-sample interaction force via strain gauges or optical sensors, thereby diminishing lateral forces and mitigating the deterioration of the tip and sample. This capability renders it a robust instrument for engineering soft media and biomaterials [239], in addition to evaluating the properties of hard geological materials [240, 241].

doi:10.6342/NTU202600018

Within the expansive body of literature, the current analysis emphasizes research that characterizes AFM as traditional vibro-impact dynamics, prioritizing the behavior of the AFM during tapping mode. Given that the soft specimens analyzed via tapping mode AFMs are fundamentally viscoelastic [143, 238, 239], their mechanical attributes are time-dependent and heavily influenced by variables such as indentation history, environmental temperatures, and excitation frequency. Consequently, the identification of appropriate contact models remains a pivotal and perhaps the most arduous aspect of simulating AFM dynamics.

In contrast, the attractive force within tapping mode AFM architectures is significant and more readily detectable and measurable than in alternative microscale apparatuses. This is attributed to the AFM tip maintaining a close proximity to the specimen surface—typically between 25-150 nm—while contact force is kept minimal.

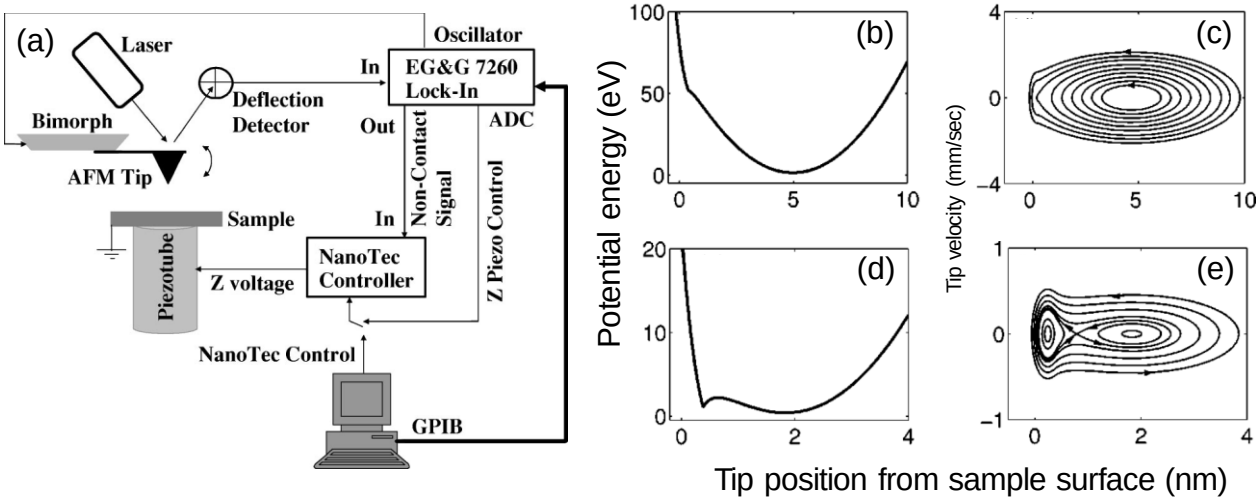


Figure 2-10: (a) A schematic showing the experimental AFM setup from [58]. (b) The potential energy curve for a single-well system, which is considered monostable, is shown with (c) its corresponding phase portrait. (d) An asymmetric double-well potential energy curve is also presented; this is generated by a stronger adhesion force and results in a bistable system, shown along with (e) its phase portrait. The double-well potential is generated due to stronger adhesion force compared to the single-well case. The two local minima on the double-well curve represent the two static equilibrium points of the system. One equilibrium point is located away from the sample (~2 nm), while the other is in contact with the sample surface (near zero). Reproduced with permission of [107], Copyright of © IOP Publishing.

doi:10.6342/NTU202600018

Various investigations have demonstrated that this attractive force exerts a substantial influence on the dynamical behavior of tapping mode AFM in both the time domain [154, 185] and the frequency domain [55, 57, 58, 61, 176, 194, 242]. Figure 2-10 (b) and (c) depict the potential energy curve and the associated phase portrait for highly oriented pyrolytic graphite (HOPG) as captured by a tapping mode AFM silicon tip at a 5-nm gap, exhibiting a single-well potential [58]. Conversely, at a 2-nm gap, Figure 2-10 (d) and (e) display a double-well potential energy curve and phase portrait, highlighting two equilibrium points situated at the local minima. This double-well potential arises from a more intense adhesion force relative to the single-well configuration. Systems characterized by a single-well potential are classified as *monostable*, whereas those possessing a double-well potential are termed *bistable*. The two local minima within the double-well potential energy curve denote the static equilibrium points: one positioned roughly 2 nm from the sample surface, and the other residing in contact with it.

Figure 2-11 (a) and (b) present the frequency response and the basin of attraction for a single-well scenario [179], indicating AFM operation within the monostable regime. As shown in Figure 2-11 (a), the softening effect induced by long-range attractive forces causes the response curve to incline toward lower frequencies. Consequently, the attractive force integrates supplemental saddle-node bifurcations into the frequency response, which otherwise would only manifest impact-induced repulsive forces (as illustrated in Figure 2-3). This behavior, identified as the mixed softening-hardening effect, has been researched extensively in the context of AFM [55, 57-59, 61, 142, 176, 194, 195].

At the specific frequency shown in Figure 2-11 (a), three stable periodic solutions exist, representing the three uniquely colored zones in the basin of attraction in Figure 2-11 (b). In contrast, Figure 2-11 (c) displays the frequency response for a double-well potential scenario, accompanied by a more complex basin of attraction in Figure 2-11 (d). Figure 2-11 (c) demonstrates that once a double-well potential is established, the

doi:10.6342/NTU202600018

cantilever may become trapped by the attractor situated in immediate proximity to the sample.

Furthermore, supplemental research has sought to clarify transient state dynamic behaviors and boost AFM scanning velocity [189, 196]. Separately, [145] empirically examined the development of chaotic and subharmonic motions using excitation frequencies that far exceed the AFM tip's fundamental resonance frequency. [54] parametrically analyzed the tapping mode AFM as a 1-DOF system via the DMT model, accounting for viscoelasticity and noting the impact of surface topography on phase delay. [175] performed numerical and analytical inquiries into complex dynamics, such as chaotic behavior featuring cascaded period-doubling bifurcations, utilizing the LJ potential for cantilever-sample interactions near the linear resonance frequency. Finally, [243] provided a comprehensive experimental account across a variety of operational parameters.

Over the last decade, the one-mode approximation approach has gained significant traction [61, 154, 178, 185, 186, 188, 206]. Although this technique is effective for most vacuum or air conditions, it is insufficient for liquid media. In contexts involving

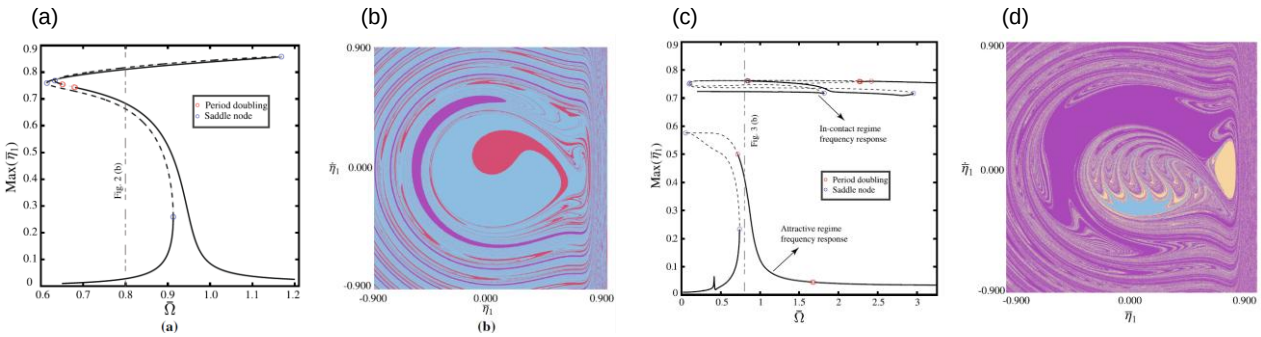


Figure 2-11: Comparison of the frequency responses and basins of attraction for an AFM system operating in monostable and bistable regions. (a) and (b) show the response for the monostable region, where the frequency curve exhibits a mixed softening-hardening behavior due to the combination of attractive and repulsive tip-sample forces. (c) and (d) depict the response for the bistable region, which is characterized by two distinct solution branches: an *attractive* motion (lower curve) and an *in-contact* motion (upper curve). In the frequency response plots, solid and dashed lines are used to denote the stable and unstable branches of the attractors, respectively. Reproduced with permission of [107], Copyright of © IOP Publishing.

doi:10.6342/NTU202600018

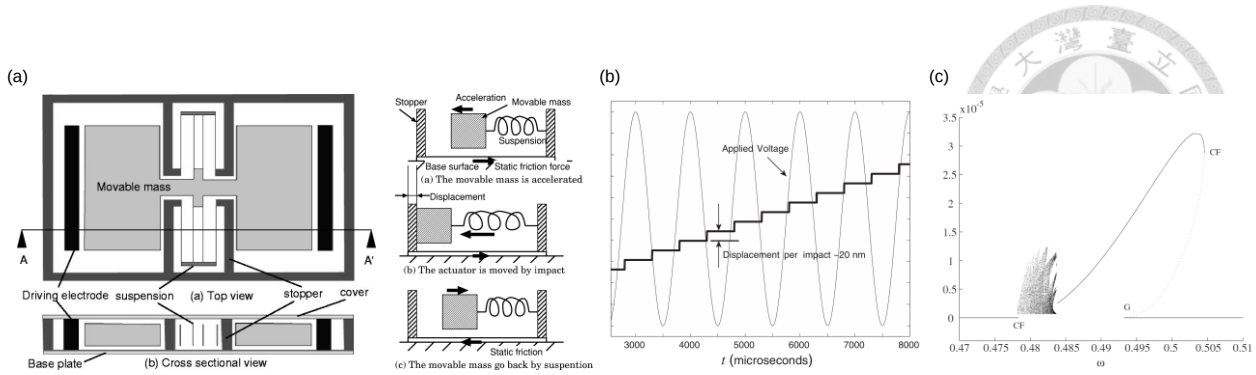


Figure 2-12: (a) A schematic diagram of an impact microactuator along with an illustration of its operational mechanism. Reproduced with permission of [62], , Copyright of © 2023 IEEE. (b) Displacements and voltage time history of a microactuator. (c) Simulated frequency response of a microactuator, showing non-impacting, period-one impacting and period-N impacting motion with saddle-node (also known as cyclic fold, CF) and grazing bifurcation. The device features a movable mass that is accelerated by an electrostatic force until it collides with a stopper. This collision generates a forward inertial impulse, which overcomes static friction and advances the entire actuator frame in a stepwise manner. Reproduced with permission of [63] for (b) and (c), Copyright of © IOP Publishing.

liquids, multi-frequency excitation, or large displacements—where system nonlinearity is pronounced—the higher-order modes of the AFM cantilever become essential to the resulting motion. Integrating these higher-order modes enhances the fidelity of the model, permitting a more rigorous examination of phenomena like modal interaction/internal resonance [180, 190, 243, 244] and intermittent contact [153]. Intermittent contact is defined as the manifestation of several impacts within a single excitation period.

2.5.2 Impact Microactuators

Research has demonstrated that impact microactuators facilitate high-precision positioning for microscale assembly, optical instruments, and scanning probe microscope systems [62]. As depicted in Figure 2-12 the configuration of an impacting actuator typically includes a movable structure, a frame, stoppers, and a set of electrodes. Electrostatic force is employed to drive the movable structure into collisions with the stopper. When the inertial force generated by the impact exceeds the static friction existing between the ground and the frame, the actuator undergoes translation

doi:10.6342/NTU202600018

before coming to a rest due to dynamic friction resistance. This specific impact actuation architecture avoids the requirement for high actuation voltage to generate significant displacement. The inaugural presentation of the impact microactuator was documented in [62], which recorded a step size between 10 and 20 nm and a velocity of roughly 2.7 μm/s. A bidirectional impact microactuator was subsequently presented in [245], reaching an average velocity of 8-9 μm/s and a stepwise displacement of approximately 40 nm. Furthermore, [165] successfully embedded the apparatus onto a printed circuit board, attaining a travel speed of nearly 100 μm/s with a step size of 320 nm per individual impact.

In contrast, direct numerical analysis and nonlinear modeling for these devices, characterized by non-smooth characteristics, were established in [170]. That study investigated occurrences such as period-doubling bifurcation, grazing bifurcation, sticking, and chatter, as well as periodic motion windows situated within chaotic regions. Chatter is defined as a succession of low-velocity impacts occurring within a single excitation period, where complete chatter leads to sticking between the stopper and the mass. Subsequently, a sequence of investigations [63, 65, 171] offered comprehensive perspectives on the dynamics of impact microactuators. These authors distinguished co-existing impacting and non-impacting branches of periodic solutions by utilizing numerical continuation methods and rigid considerations rather than relying on direct numerical simulation, owing to the previously mentioned benefits.

Impact microactuators manifest complex dynamics resulting from the interplay of friction, impact force, and nonlinear electrostatic force. Studies [64-66, 172] have identified co-dimension-two grazing bifurcation, illustrating diverse outcomes within the frequency and driving force domains. To improve the response control of an impact microactuator, [173] implemented a feedback control algorithm, which aids in the achievement of higher moving speeds or the precise regulation of displacement. Instead of a complete device redesign, the grazing bifurcation can be seamlessly modified by shifting the position of the stopper. These collective works provide an exhaustive

doi:10.6342/NTU202600018

evaluation and systematic investigation of impact actuators. For a brief summary of impact actuator systems, see [90].

2.5.3 Impacting Energy Harvesters

Resonant-type energy harvesters are engineered to transmute mechanical energy derived from ambient vibrations into electrical power. The fundamental criteria for assessing these apparatuses are their operating bandwidth and energy generation efficiency. Given that a majority of environmental vibration sources persist below 100 Hz, power generation efficiency at these lower frequencies is significantly attenuated because of the diminished power flow from the source to the harvester [76]. Furthermore, the stochastic fluctuations in ambient vibration frequencies render linear structures suboptimal for energy capture. To mitigate structural damage and prevent stiction, energy harvesters typically employ stopper structures featuring dimple-like contact areas to constrain motion. These stoppers serve a dual purpose: they regulate the displacement of the proof mass while simultaneously broadening the operating bandwidth and bolstering energy conversion efficiency [162]. For a succinct synthesis of vibro-impact energy harvesters, consult [246].

The configuration of vibro-impact energy harvesters is directed toward two primary goals: generating substantial nonlinearity to realize an expanded operational bandwidth and implementing a frequency up-conversion (FUC) mechanism to intensify energy conversion efficiency. Figure 2-13 (a) illustrates an electret-based vibro-impact energy harvester, whereas Figure 2-13 (b) depicts a vibro-impact FUC energy harvester, with both panels providing the corresponding time history and frequency response plots.

doi:10.6342/NTU202600018

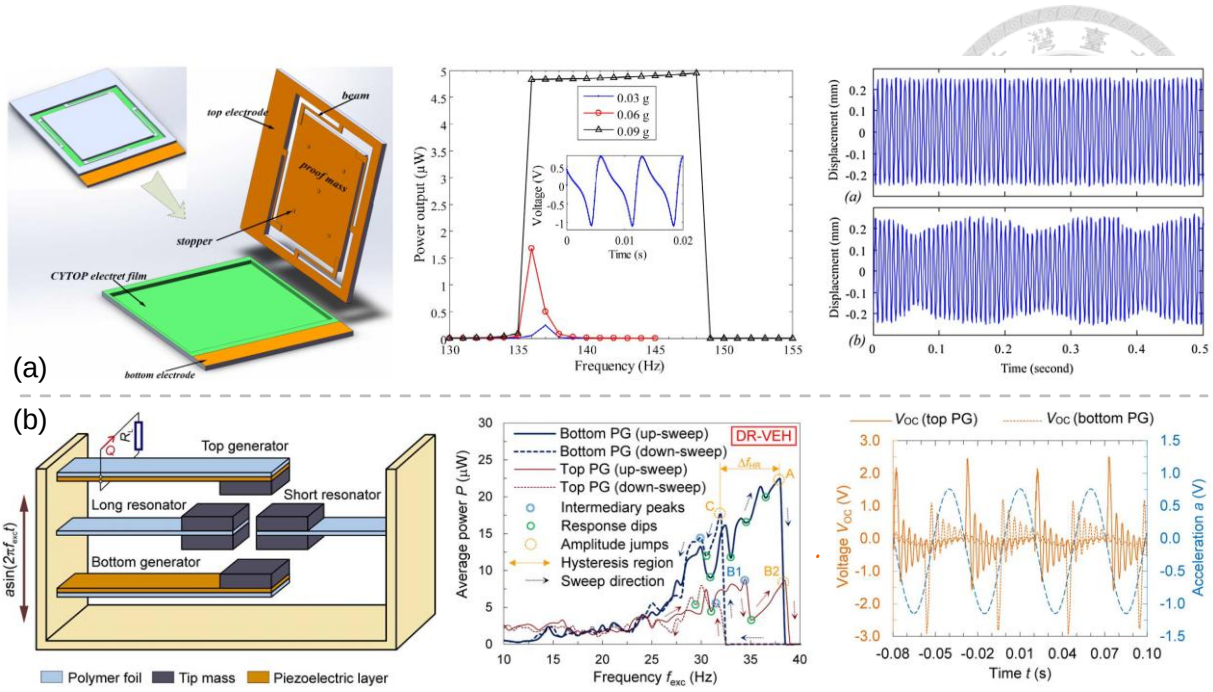


Figure 2-13: Two examples of vibro-impact energy harvesters, each shown with its schematic, frequency response, and a sample time-domain trace. (a) A single-resonator energy harvester whose frequency response was measured using a forward sweep [70]. (b) A dual-resonator energy harvester that utilizes a frequency up-conversion mechanism [76]. Its frequency response includes both forward and backward sweeps, revealing a distinct hysteresis loop caused by the impacts. The time-domain plots for both devices clearly show the typical tapping behavior and an impact-induced low-frequency ringing. Reproduced with permission of [107], Copyright of © IOP Publishing.

Comprehensive mechanical modeling integrated with SPICE-based backend circuit simulations for vibro-impact energy harvesters has been performed by [157, 158, 160-162]. Research by [159] emphasized that the tapping bandwidth is heavily contingent upon both the damping coefficient and the stiffness of the stopper. [67] offered theoretical, numerical, and experimental investigations into the frequency responses of these systems, observing that the harvested energy in a one-sided energy harvester exceeds that of harvesters lacking stoppers by 30%. Comparable inquiries involving both experimentation and simulation were executed by [68] and [163]. It is vital to recognize that an expansion in tapping bandwidth does not inherently signify an increase in the device's overall operating bandwidth. Under single-frequency excitation, the system attains tapping mode only if the frequency resides within the overlapped

doi:10.6342/NTU202600018

region of the backward and forward tapping regions. However, real-world ambient vibration is characterized by random vibration sources containing multiple frequency components rather than a single frequency. Based on the basin of attraction, the initial conditions and the driving waveform dictate whether the mechanism can function within the tapping region.

The initial demonstration of MEMS-based energy harvesters employing the FUC mechanism via mechanical impact was documented by [71], validating the feasibility of the impact-type FUC mechanism under controlled harmonic excitation. This milestone catalyzed significant academic interest in impact-induced FUC-based energy harvesters [72, 203, 247]. Notably, [203] expanded the framework established in [71] by connecting energy harvesters in series to address low power limitations. Nevertheless, the asynchronization condition and resonance frequencies mismatch among the devices resulted in performance metrics that fell short of theoretical projections.

Experimental analyses on the bandwidth and efficiency of cantilever-type energy harvesters operating below 30 Hz were conducted by [73] and [74]. Their data revealed that the average peak power of a high-frequency cantilever can surpass that of a lower-frequency counterpart by a factor of 100. Their work further proposed that for the high-frequency cantilever, the frequency should ideally be 5 to 10 times greater than the low-frequency cantilever, particularly when the resonance frequency of the low-frequency excitation cantilever is below 50 Hz. The researchers also suggested that the optimal frequency ratio should be an integer in the absence of period-doubling motion (alternatively, it may be a fraction with a determinant of n during period-n motion). This iteration of an impact energy harvester operates as a modal-interacted internal resonance nonlinear system, where the coupling strength is governed by the modal frequency ratio, peaking at integer ratios. [247] advanced the principle of synchronized impacting to refine power generation efficiency and contributed an exhaustive study on the coupling between two high-frequency piezoelectric generators and two low-

doi:10.6342/NTU202600018

frequency resonator pairs. This investigation indicated that incorporating additional resonators with resonance frequencies approximating integer ratios can further broaden the usable bandwidth. The vibro-impact coupling between resonators demonstrates non-smooth modal interaction. [75] described a vibro-impact energy harvester featuring double-sided stoppers set with varying clearance distances and analyzed frequency responses across diverse parameters, including acceleration level, damping coefficient, and gap clearance. While most findings align with single-sided stopper results, the tapping bandwidth of energy harvesters with two-sided stoppers is superior due to the additional stiffness. Utilizing a vibro-impact architecture permits the stacking of several devices to achieve elevated power output [70].

Finally, it should be noted that many investigations into macro-scale vibro-impact energy harvesters, such as [248-256], omitted random excitation sources characteristic of actual environments, which might otherwise trigger stochastic resonance and other intricate dynamics.

2.5.4 Vibro-impact Resonators and Resoswitches (Resonant Switches)

In contrast to conventional MEMS switches, which typically function in the DC or near-DC regime far removed from resonance, resonant switches—or resoswitches—are designed to operate in the vicinity of their resonance frequency. This operational mode significantly reduces the actuation threshold compared to standard MEMS counterparts [80]. Contemporary progress in resoswitch technology has been surveyed in [257, 258], with the latter study explicitly highlighting the evolution of CMOS-MEMS resoswitches and vibro-impact resonators.

To the best of the author's current knowledge, the inaugural MEMS vibro-impact resonators were documented in [156], while the initial concept of resoswitches—defined as vibro-impact resonators incorporating hot switching—was detailed in [80, 259]. A schematic representation of a typical comb-driven resoswitch alongside its operational configuration is presented in Figure 2-14. The operation of resoswitches is fundamentally predicated on nonlinear dynamics. Phenomena such as transient

doi:10.6342/NTU202600018

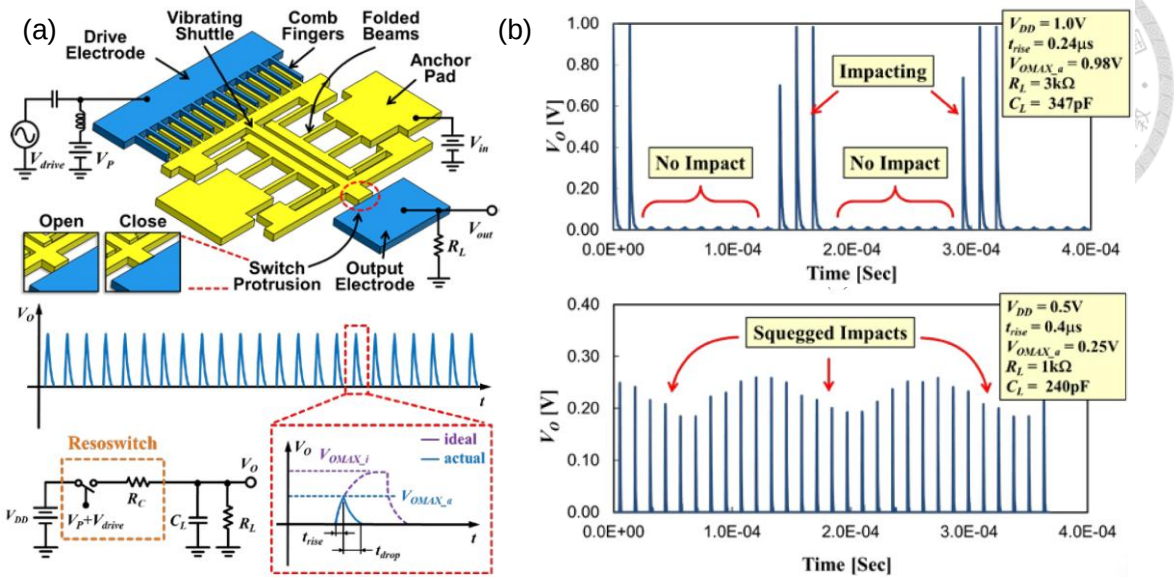


Figure 2-14: (a) An overview of a comb-driven resoswitch, detailing its structure and operation. The figure includes a device schematic with a close-up of the contact mechanism, a simplified equivalent circuit representing the hot-switching process, and the expected output voltage waveform consisting of a train of pulses. (b) An illustration showing how period-adding effects and impact force fluctuation leads to the squegging phenomenon and a corresponding missing signal. Reproduced with permission of [107], Copyright of © IOP Publishing.

behaviors or nonlinear period-adding effects can precipitate squegging or discontinuous output signals [87, 146, 260].

In an effort to mitigate squegging, [146] employed Pt-silicide at the contact interface, noting that squegging is attenuated when the actuation voltage targets the comb fingers aligned with the output electrode. In a parallel approach, [83] deployed a compliant output electrode to facilitate soft-impacting, thereby curbing squegging occurrences and prolonging the contact duration. Furthermore, [261] improved the sensitivity and reliability of CMOS-MEMS resoswitches by integrating an electroless plated hard nickel contact surface. However, there appears to be a trade-off between suppressing squegging and maintaining sensitivity, indicating that additional research is requisite in this domain. Additionally, [262] analyzed the mixed softening-hardening frequency response manifested in an electrostatically softened relay functioning in tapping mode. Distinct from AFM dynamics, this response stems from the synergistic

doi:10.6342/NTU202600018

effects of contact and electrostatic forces. The investigation also identified a frequency shift in the bifurcation point attributed to variations in adhesion force following prolonged cold switching cycles—an effect that is seldom detected at the macro scale.

Beyond standalone components, numerous investigations have examined the deployment of resoswitches across diverse applications, including micromechanical charge pumps [263], RF receivers [83, 88, 89, 191, 264-266], power amplifiers amplifier [265, 267], and clock generators [84, 268]. Notably, [84] leveraged squegging oscillation within resoswitches to facilitate clock generation. Furthermore, [237] showcased a frequency-controlled pulse density modulation circuit utilizing a vibro-impact resonator, exhibiting complex nonlinear dynamical hot switching signals within the tapping region. To improve the bit rate of resoswitch-based receivers, [269] explored the influence of amplitude shift keying (ASK) driving signals. This study introduced a pre-energization technique to diminish the discrepancy between the resoswitch's "ON" and "OFF" states, achieved by either abbreviating the "OFF" duration or augmenting the driving level during the "OFF" phase. Within the context of OOK or ASK operations, the "ON" and "OFF" states correspond to digital bits 1 and 0, respectively. Building upon [269], [270] examined how antennas influence the waveform of on-off keying (OOK) driving signals, observing that the antenna's finite bandwidth could attenuate or omit certain high-frequency components of the OOK signal, consequently limiting the resoswitch's bit rate. Extending beyond radio frequency (RF) signal reception, the resoswitch principle has been adapted for other ultra-low power wake-up sensors, including acceleration wake-up switches [86] and acoustic wake-up switches [85].

Aside from resoswitches, various inquiries have uncovered distinct attributes and applications for general vibro-impact resonators. For example, [169] engineered a strain gauge based on a vibro-impact resonator that exploits pull-in instability to enable an autonomous oscillation scheme, thereby eliminating the requirement for external control circuitry. [271] introduced a self-sustained vibro-impact resonator capable of

doi:10.6342/NTU202600018

generating a frequency comb spectrum, demonstrating that the comb spacing could be modulated via a DC bias. [123] investigated the generation of frequency combs in a soft-impacting vibro-impact resonator, verifying experimental findings of diverse N-cycle M-impact period-doubling motions (i.e., $z = N/M$) through numerical simulations utilizing a piecewise linear contact model.

Furthermore, [191] designed a sensor for monitoring surface conditions by tracking fluctuations in tapping bandwidth as a proxy for variations in surface attractive force. [192] recorded the widening of tapping bandwidth in CMOS-MEMS vibro-impact resonators, observing that the bandwidth expands in correlation with the driving force until it reaches saturation following a specific transition, signaling a change from attractive to repulsive dominant contact forces. More recently, [272] showcased a received signal strength indicator based on a vibro-impact resonator, which utilizes the linear growth sector of the tapping bandwidth response to construct an indoor positioning system featuring a two-staged tapping bandwidth response. [273] unveiled a novel apparatus termed the attractor exchanger, which governs the resonator's state within the hysteresis region via vibro-impact operations. By employing a thermal actuator, this device defined a new parameter space for gap-spacing, permitting the exchange of attractors under a single-frequency drive. Lastly, [274] demonstrated a unique 7:2 internal resonance activation induced by impact with period-doubling, emphasizing that such activation is improbable in the absence of impact.

2.5.5 RF Switches and Inertial Force Switches

The conventional architecture of a cantilever-type electrostatically actuated RF ohmic series switch is depicted in Figure 2-15. Although RF MEMS switches operate primarily in the DC regime rather than at resonance, their transient response remains governed by their inherent dynamic properties. Throughout the switching transition, these devices manifest behaviors comparable to vibro-impact systems; specifically, the switch does not establish immediate, permanent contact with the output electrode but instead undergoes intermittent bouncing following the primary impact. Such bouncing

doi:10.6342/NTU202600018

phenomena can precipitate complications including contact degradation, electrical arcing, and device malfunction resulting from stiction. Furthermore, this behavior has the potential to extend the switching duration and compromise the aggregate performance of the component.

A profound comprehension of RF switch dynamics is requisite for the analysis of transient bouncing behavior. [77] explored the correlation between actuation voltage and distinct temporal markers—specifically the moments of initial closure, the commencement of the first bounce, and the cessation of bouncing—revealing an inverse relationship between these intervals and the applied voltage. Furthermore, [78] and [200] performed extensive parametric investigations regarding the dynamical responses of these switches. Their results indicated that surface adhesion force can impede switching velocity during the contact breaking state and that swift contact opening times are achieved once a critical contact force threshold is reached. Comparable observations were documented in [193, 197, 199, 201, 230] and [275]. To mitigate bouncing issues, [79, 155, 202] employed soft-landing waveform optimization techniques. These methods aim to attenuate impact velocity by leveraging pull-in phenomena, thereby minimizing switch bounces.

In contrast to bulk materials, metamaterials derive their properties from the spatial configuration of artificial unit cells. This allows for the tailoring of mechanical and optical functionalities, facilitating new pathways for applications such as vibro-impact switches [276-279]. Recently, a capacitive shunt RF switch integrated with metamaterials was exhibited, demonstrating enhanced isolation capabilities [280, 281]. Moreover, researchers have altered material structures to augment the permittivity-dependent repulsive Casimir force, thereby resolving the stiction issue in both capacitive RF switches [281, 282] and resistive RF switches [281, 283].

doi:10.6342/NTU202600018

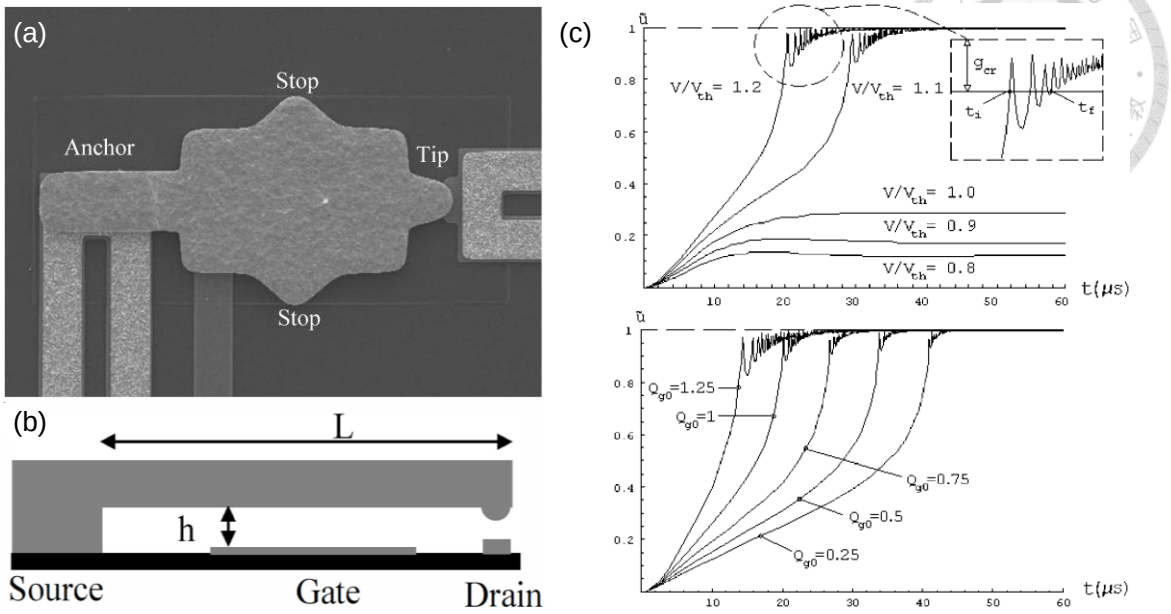


Figure 2-15: Structure and simulated transient behavior of a cantilever-type electrostatically actuated RF switch. (a) An SEM image and (b) a side-view schematic illustrate the typical device structure. (c) Simulation plots demonstrate the contact bouncing phenomenon, where the switch beam repeatedly impacts the contact before settling, showing how bouncing is influenced by different actuation voltage ratios and quality factors. Reproduced with permission of [107], Copyright of © IOP Publishing.

Inertial force switches are extensively utilized within the aerospace and automotive sectors for the detection of sudden acceleration shifts. As noted in [166-168, 174]. the bouncing phenomenon is similarly manifested in these inertial devices. Distinct from RF switches, inertial switches employ a multi-body softening impact structure to dampen the bouncing effect. These studies demonstrate that a thorough grasp of the vibro-impact behavior in both inertial and RF switches provide critical insights into their transient characteristics, ultimately guiding the design of switches with superior reliability.

2.6 Discussion and Conclusion

Although the nonlinear dynamics associated with vibro-impact systems have undergone thorough investigation at the macroscale, several constraints and obstacles persist when attempting to implement these frameworks within microscale

doi:10.6342/NTU202600018

architectures. These difficulties arise from stochastic variations in the manufacturing phase, constraints in experimental metrology, and the sophisticated physical phenomena characterizing contact events. Regulating the geometric parameters, contact surface topology, and material properties of micro-level components represents a substantially more arduous task than that encountered in macro-level systems [284]. Furthermore, it is frequently demanding to measure microscale dynamic characteristics, including contact duration and contact force, while simultaneously integrating physical phenomena such as multi-physics interactions (for instance, the thermal-mechanical-electrical coupling inherent in RF switch failure modes) and plastic deformation. The presence of thin film coatings along with specific surface and material treatments on microscale vibro-impact instruments further complicates the modeling procedure by introducing additional uncertainty.

The manufacturing protocols for MEMS vibro-impact devices align with standard MEMS fabrication paradigms, encompassing (1) CMOS-MEMS platforms, (2) SOI (Silicon on Insulator), (3) surface micromachining, (4) bulk micromachining, and (5) electroplating. AFM tips, frequently fabricated using SOI wafers, possess precisely characterized dimensions, tip radius, and material properties. As an illustration, the AFM tips designated as OMCL-AC240TS by Olympus Corporation feature regulated roughness that is minimized via an oxide-sharpening process [285]. A comprehensive evaluation of RF switches, including their respective production methodologies, is presented in [286]. Additionally, [257] offers a concise summary of resoswitches and vibro-impact resonators, detailing their manufacturing techniques. Generally, the application of dry and wet etching alongside material deposition results in flawed washboard/scalloping patterns [287] and irregular surfaces on the contact sidewalls. Such manufacturing defects exert a marked influence on real roughness [230] and the velocity-dependent sliding friction force [288], factors which remain largely unintegrated into current MEMS vibro-impact system models.

Moreover, the operational reliability of microscale vibro-impact devices,

doi:10.6342/NTU202600018

particularly regarding RF switches and resoswitches, constitutes a major area of concern. These components frequently undergo material removal, transfer, plastic deformation, and joule heating, all of which augment adhesion forces and compromise long-term performance. Standard strategies to mitigate these failure modes involve the integration of nanomaterials, the application of thin films, and the execution of topographical and chemical modifications [289, 290]. Crucially, period-doubling motion may induce a severe escalation in contact force within the tapping region, significantly impacting the structural integrity and reliability of vibro-impact switches [54, 117, 291].

This study intends to stimulate novel developments in MEMS vibro-impact systems by offering a synthesis that highlights particular phenomena, analytical tools, modeling strategies, and practical deployments. MEMS vibro-impact systems demonstrate intriguing nonlinear dynamics, manifesting behaviors of far greater complexity than those of linear systems; consequently, they provide a wealth of prospects for both basic and applied investigations. Prospective inquiries might concentrate on broadening the scope of metamaterials, which encompass passive vibration mitigation/shock protection mechanisms featuring intermodal interactions [292, 293], accelerated steady-state transient times [294], sensing applications [295], sensing elements integrated with mechanical computing [296, 297], while leveraging sophisticated MEMS fabrication technologies to realize these objectives [298, 299].

doi:10.6342/NTU202600018

3 Developments on Dynamical Modeling

Contemporary breakthroughs within the field of MEMS have positioned micro-mechanical resoswitches as pivotal elements for the realization of energy-efficient wireless communication architectures, particularly regarding zero-standby power receivers. However, development within this domain has been hampered by the absence of a comprehensive mathematical framework that can faithfully represent the intricate nonlinear dynamics characteristic of these devices. The efficacy of resoswitch-based mechanical systems stands to be significantly augmented and refined provided that a robust dynamical model is established.

To surmount this deficiency, the present investigation formulates an exhaustive model for MEMS resoswitches, combining elements of the Duffing and van der Pol terms with surface interaction forces formulated from the generalized Derjaguin-Muller-Toporov (DMT) model. Both analytical techniques and numerical simulations are leveraged to interrogate the nonlinear properties of resoswitches, thereby providing more profound physical perspectives into their operational response. Additionally, the framework accommodates electrical contact resistance during hot-switching events by integrating a refined Wexler-based approach, which includes the adjustments proposed by Mikrajuddin.

A 125-kHz comb-driven folded-beam resoswitch was realized through a 0.35-μm CMOS-MEMS process, functioning as an experimental testbed to assess contact nonlinearities, material properties, and various defects inherent to the manufacturing sequence. It is anticipated that the constructed model will function as a fundamental tool for the optimization of resoswitch performance, with its utility transcending the specific CMOS-MEMS process to encompass more diverse designs of vibro-impact mechanisms.

3.1 Introduction

Micromechanical resonant switches, or “resoswitches,” have been identified as

doi:10.6342/NTU202600018

playing a pivotal role in the development of energy-efficient wireless communication systems [300, 301]. Specifically, these components facilitate a reduction in the standby power consumption typically necessitated by maintaining the operation of front-end circuits in communication receivers, as MEMS-based resoswitches function via polarization voltage without requiring active power. Beyond standard hot switching operations, resoswitches may be configured as vibro-impact resonators. This expansion unlocks a diverse array of applications, such as surface condition monitoring [191, 302, 303], clock generators [307, 308], attractor exchangers [305, 306] and frequency controlled pulse width modulators [304]. Within these various implementations, CMOS-MEMS fabrication technology has exhibited significant promise by enabling the monolithic integration of electronic circuitry with micromechanical resoswitches. Concurrently, systematic efforts have been undertaken to surmount inherent process constraints, involving the implementation of design rule derived transducer gap spacing [309] and the exploration of diverse contact material options [310, 311]. These methodologies have effectively mitigated concerns regarding the viability of CMOS-MEMS technology for resonant devices, which historically stemmed from fabrication limitations and the absence of stress control within such standardized platforms.

Notwithstanding these technical achievements, the fundamental nonlinear dynamics arising from the mechanical structures and contact interfaces remain insufficiently characterized. Furthermore, the dynamic interaction forces and the electrical path resulting from discontinuous contact events require more rigorous analysis. While [107] provides a comprehensive summary of modeling techniques and analytical tools for micro-scale vibro-impact devices—offering a theoretical basis that can be adapted for the resoswitch under investigation—limitations remain. For instance [312] introduces a simplified model utilizing Verilog-A to rapidly approximate the influence of contact stiffness on the resultant dynamic motion. This particular model, however, neglects the impact of electrical conduction and fails to account for nonlinear damping, both of which significantly govern the overall dynamics of the system.

doi:10.6342/NTU202600018

To fulfill the requirement, this study examines the influence of contact material properties and establishes a theoretical framework to evaluate the nonlinear dynamics of CMOS-MEMS comb-driven folded beam resoswitches as a representative case study. Within this theoretical framework, the generalized DMT model is employed to characterize the contact interaction [313, 314] , while the method of averaging is implemented to derive the nonlinear frequency responses. To encapsulate the nonlinear time transient response and substantiate the analytical findings, a numerical time integration method is utilized. Furthermore, this research leverages the Mikrajuddin-modified Wexler-based model to account for electrical contact resistance, integrating this framework with the back-end RC circuit to study the electrical performance under hot switching conditions [315]. Additionally, the current study probes the influence of contact material properties alongside various nonlinearities—including geometric and electrical nonlinear stiffness, as well as nonlinear damping—via comprehensive numerical investigation.

doi:10.6342/NTU202600018

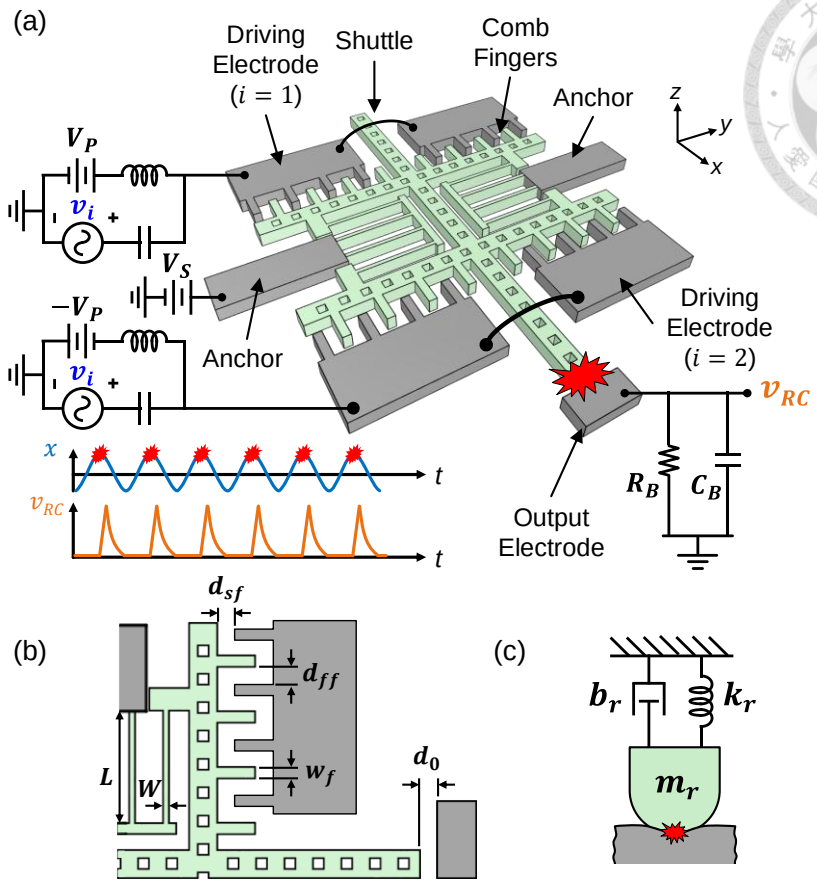


Figure 3-1: (a) Schematic of a comb-driven folded-beam resoswitch with the operation configuration and illustrative displacement and hot switching output waveforms. (b) Label specifications for device geometries. (c) 1-DoF lumped mechanical model for a resoswitch or vibro-impact resonator in general. Reproduced with permission of [316] Copyright of © 2025 IEEE.

The organizational structure of this chapter is delineated as follows: Section 3.2 presents the device structure design and the CMOS-MEMS process platform, while evaluating the operational performance of the component within the linear region. Section 3.3 is dedicated to resoswitch modeling, encompassing contact surface interactions, mechanical and electrical nonlinearities, and the formulation of electrical contact resistance. In Section 3.4, the dynamic behavior of resoswitches is scrutinized via analytical investigations and numerical simulations. Section 3.5 details the device characterization across both frequency and time domains, which enables the identification of electrical and mechanical parameters essential for high-fidelity modeling. Following this, Section 3.6 explores the influence of device Q on switching

doi:10.6342/NTU202600018

time and surface interaction forces, alongside a numerical interrogation of period-doubling nonlinear dynamics and pre-energization technology. Ultimately, the synthesis of findings and the primary conclusions derived from these evaluations are consolidated in Section 3.7.

3.2 Device Design, Implementation, and Operation

A schematic representation of the comb-driven folded-beam resoswitches is depicted in Figure 3-1 (a). The polarization bias V_P and the alternating current (AC) actuation signal v_i—which represents the incoming radio frequency (RF) input in practical implementations—are merged through an LC bias-tee and directed to the input electrode. For the hot switching supply, a structure bias V_S is maintained on the resonator body. Throughout the hot switching operation, the structure periodically establishes and severs the electrical conduction path between the resonator and the output electrode. Distinguished from cold switching, hot switching operation is defined as a scenario wherein the electrical supply remains consistently applied during the operation [317].

As demonstrated in Figure 3-1 (a), back-end RC circuit coupled to the output electrode is leveraged to attenuate the hot switching induced spike signals and to facilitate the process of envelope detection. Beyond the shaping of the output waveform, the magnitudes of the back-end RC components dictate the magnitude of the electrical current traversing the contact interface, thereby influencing long-term device reliability. A detailed examination regarding the selection of contact materials and the optimization of back-end RC parameters is provided in Section 3.3.

3.2.1 Comb-driven Folded-beam Resonator

The engineering of electrostatic comb-driven folded-beam resonators has reached a high level of maturity across a multitude of applications [318, 319]. In these designs, the implementation of electrostatic actuation facilitates the utilization of conventional fabrication materials, distinguishing this approach from the specialized materials necessitated by piezoelectric and magnetic actuation techniques. The folded beam

doi:10.6342/NTU202600018

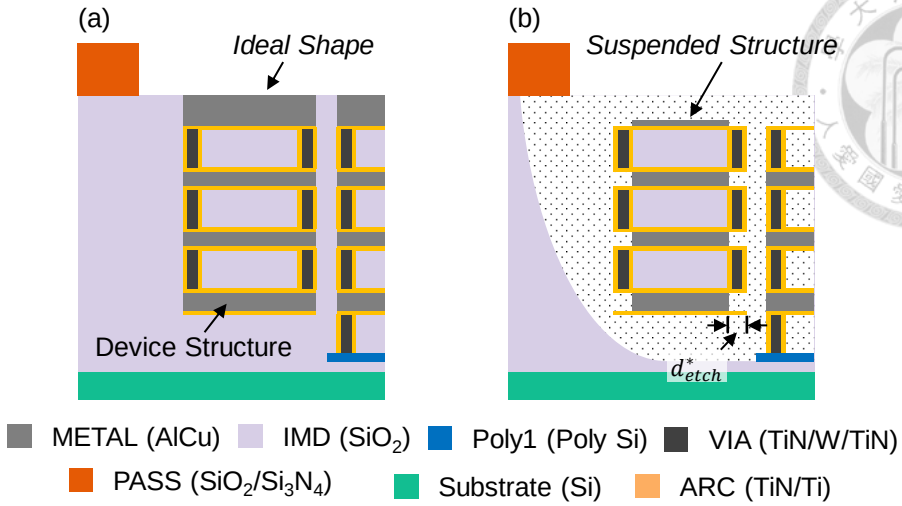


Figure 3-2: Cross-sectional view of a CMOS-MEMS structure (a) before and (b) after release, illustrating METAL layers are etched due to finite etching selectivity. Reproduced with permission of [316] Copyright of © 2025 IEEE.

structure has been validated as a linear spring configuration characterized by low axial stress [320], while the interdigitated comb finger architecture is proven to generate substantial displacement with superior linearity relative to parallel plates [320]. To suppress torsional modes and prevent failures resulting from side instability, the adoption of a balanced structure is typically advocated [321]. Furthermore, the levitation effect—which may manifest prominently under specific conditions—can be attenuated through the strategic design of electrode configurations [322-325].

For the mathematical representation of the device, a 1-Degree-of-Freedom (DoF) lumped mechanical model is frequently employed, as illustrated in Figure 3-1 (c). The governing equation of motion is predicated on the following expression [318]

$$m_r x'' + b_r x' + k_r x + F_{nl} = A_d \cos(\omega_d t) + F_c \qquad (3\text{-}1)$$

In this formulation, m_r, b_r, k_r and A_d denote the equivalent mass, damping coefficient, stiffness, and the magnitude of the driving force relative to the shuttle position, respectively, whereas ω_d represents the driving angular frequency. Regarding the fundamental in-plane flexural vibration mode, the lumped mass m_r and stiffness k_r determined as follows [318]

doi:10.6342/NTU202600018

$$m_r = M_s + \frac{1}{4}M_t + \frac{12}{35}M_b \tag{3-2}$$

$$k_r = 24E_{eq}h_b\left(\frac{W_b}{L_b}\right)^3 \tag{3-3}$$

Within these expressions, M_s, M_t, and M_b correspond to the mass of the shuttle, the truss, and the folded beams, respectively. The parameter E_{eq} signifies the effective Young's modulus, L denotes the length of the folded beam, and W and h specify the cross-sectional width and height of the folded beam structure. The term F_c characterizes the contact surface interaction, while F_{nl} accounts for the lumped nonlinear restoring and damping forces. The current section is predicated on the assumption that $F_{nl} = F_c = 0$ in (3-1), thereby representing the linear operation of a standard resonator.

3.2.2 Device Implementation

As depicted in the cross-sectional illustration in Figure 3-2, the device is manufactured utilizing a 0.35-μm CMOS process. To cover and shield the intermediate oxide (IMD) layers against etching during the structural release process, continuous VIA walls are implemented. The structural release is executed employing Silox Vapox III—a specific HF solution engineered for aluminum compatibility—for a duration of approximately 55 minutes at a temperature of 22°C.

An SEM micrograph of the realized 125-kHz comb-driven resoswitch is presented in Figure 3-3. The experimentally determined contact clearance measures approximately 0.72 μm (*cf.* Figure 3-3 (b)). Detailed SEM views of the contact surface sidewall are provided in Figure 3-3 (c) and (d), which disclose the presence of extruded VIA layers. This extrusion arises from METAL etching defects and fabrication misalignment, despite the edges of the VIA and METAL layers being positioned coincidently in the layout. As demonstrated in Figure 3-3 (c), the METAL4 layer underwent complete etching immediately following the release, suggesting an etch rate

doi:10.6342/NTU202600018

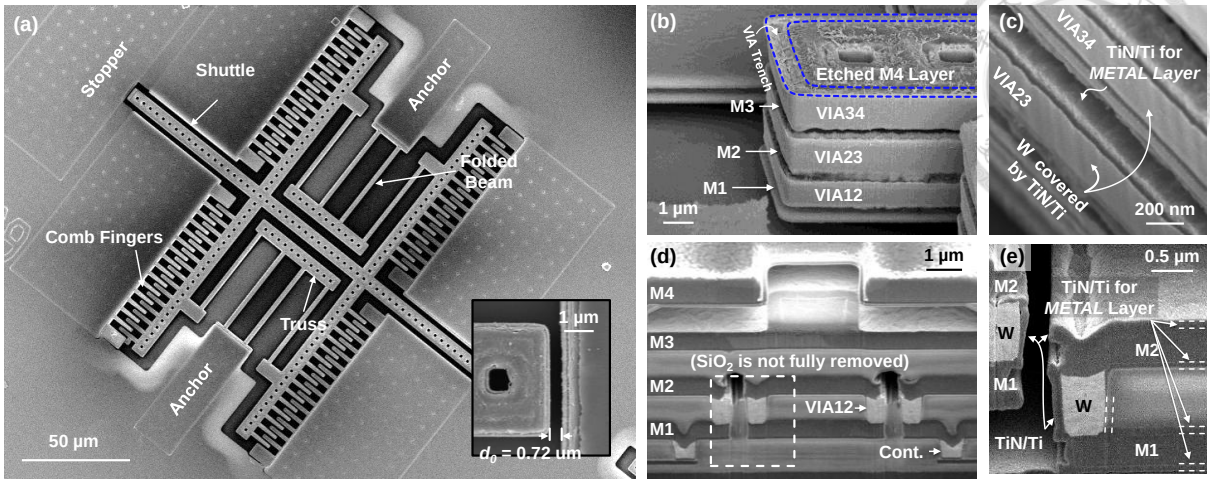


Figure 3-3: SEM photos of the fabricated device: (a) overview of the device with close-in top view to the contact gap, (b) and (c) zoom-in to the contact sidewall. (d) and (e) show the SEM photos of a testing structure, where the etched METAL and the TiN/Ti covered VIA layer are observed on the sidewall [326]. Reproduced with permission of [316] Copyright of © 2025 IEEE.

of at least 14.55 nm/min. This value significantly exceeds the 2.9 nm/min rate documented in [327]. Such a discrepancy potentially originates from thermal and loading effects [326] and necessitates careful consideration during the device design phase. To verify the contact material, a test structure (*cf.* Figure 3-3 (e) and (f)) derived from [326] is implemented. Following a ~18-minute release in Silox Vapox III at 40°C, the test structure reveals that the ARC layer (i.e., TiN/Ti) persists on the VIA sidewalls as well as the upper and lower surfaces of the METAL layers.

The comprehensive and magnified 3D topography of the device, captured via a laser scanning confocal microscope (VK-X200K/VK-X210, Keyence), is displayed in Figure 3-4 (a) and (b). The 2-D line profiles extracted from the cross-section marked in Figure 3-4 (a) are exhibited in Figure 3-4 (c)-(e), depicting the structural deformation that occurred post-release. To quantify the magnitude of this deformation, the radius of curvature (ROC) is calculated. The resulting layer mismatch between the moving structure and the stationary anchor is found to be negligible, as the comb structures remain at virtually identical heights. This indicates that any variation in finger capacitance attributable to structural mismatch can be disregarded [328-330] , and

doi:10.6342/NTU202600018

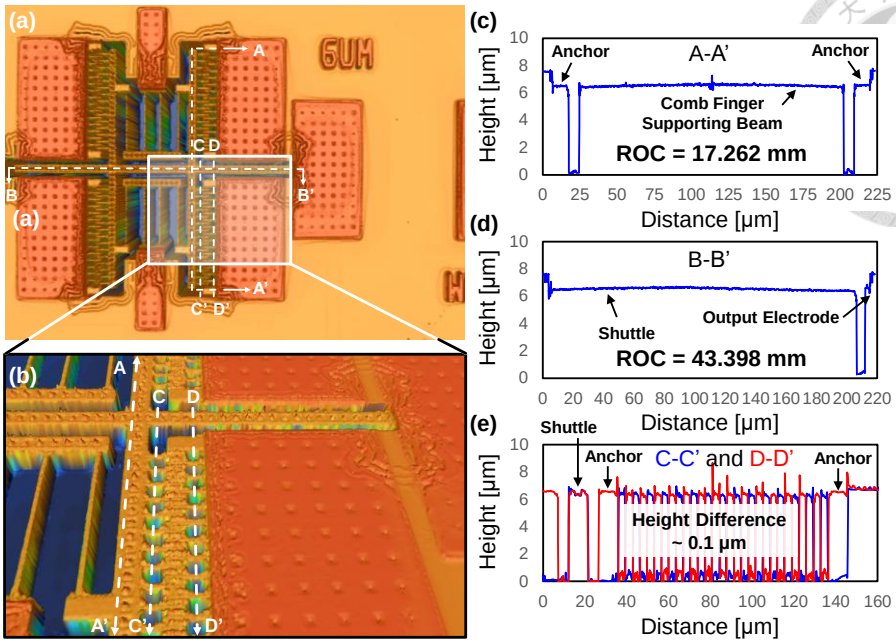


Figure 3-4: (a) The 3D profiles of a fabricated device measured by laser scanning confocal microscope. (b) The closed view to the front side near the contact position. (c)-(e) The measured 2D line profile along the labeled lines in (a). Reproduced with permission of [316] Copyright of © 2025 IEEE.

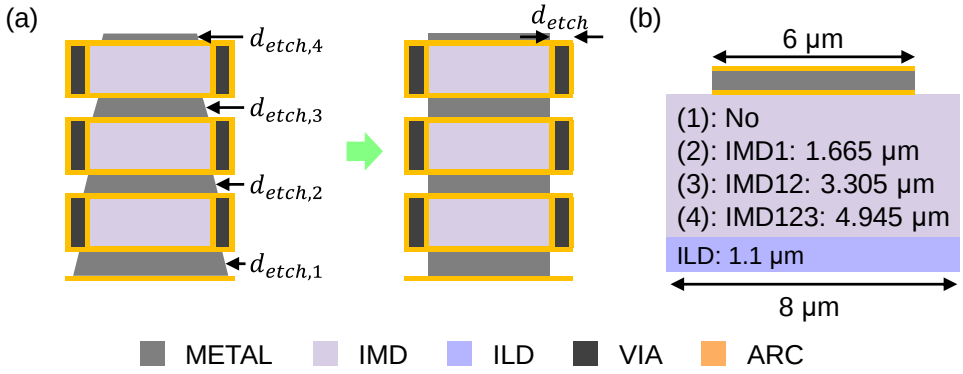


Figure 3-5: (a) The postulated etched and equivalent profile for the MET-AL layers. (b) The beam dimensions and assumptions used for TiN property extraction [331]. Reproduced with permission of [316] Copyright of © 2025 IEEE.

further confirms that the extruded TiN/Ti constitutes the primary contact material.

The dimensional adjustments of the METAL layers resulting from finite etching selectivity during the release phase are depicted in Figure 3-5 (a), where the METAL layers are hypothesized to possess a slanted sidewall characterized by disparate top and bottom dimensions. The lateral and vertical wet etching rates of Silox Vapox III for the

doi:10.6342/NTU202600018

TABLE 3-1: ETCHING RATES OF SILOX VAPOX III. REPRODUCED WITH PERMISSION OF [316] COPYRIGHT OF © 2025 IEEE.

	Lateral Etching Rate (nm/min)	Vertical Etching Rate (nm/min)
IMD	80-96 [327, 335]	~2351 [332]
METAL	2.35-2.9 [327, 335]	2.35-2.9 [327, 335] /14.552
VIA	~0	~0

1: Estimated based on the information provided in [332].
2: Estimated from the experiment conducted in this study for METAL4.

constituent materials of the CMOS process, as documented in [327, 332-335] , are tabulated in TABLE 3-1. This analysis is predicated on the assumption that the etching rate remains constant throughout the duration of the release process. Furthermore, based on established literature and the SEM micrographs acquired during this study, it is inferred that the VIA remains unetched when exposed to Silox Vapox III.

Figure 3-5 (a) exhibits the cross-section of the beam following the release, demonstrating the undercutting of the METAL layers attributable to finite etch selectivity. The mechanical properties across all METAL layers are presumed to be uniform. Utilizing the data from TABLE 3-1, TABLE 3-2 enumerates the calculated etched profiles in conjunction with both predicted and actual release durations. Given the characteristics of in-plane bending, the individual etched depths of the METAL layers can be aggregated into an effective etched depth (*cf.* Figure 3-5 (b))

$$d_{etch}^{*} = \frac{1}{8}\sum_{N=1}^{4}(d_{etch.t.i} + d_{etch.b.i}) \tag{3-4}$$

where $d_{etch.t.i}$ and $d_{etch.b.i}$ represent the etched depths for the upper and lower surfaces of the *i*-th METAL layer, respectively.

Consequently, the effective Young's modulus of the folded beam is derived [336-338] as follows

$$E_{eq} = \frac{\sum(E_i I_i)}{I_{total}} \tag{3-5}$$

doi:10.6342/NTU202600018

TABLE 3-2: PREDICTED ETCHED DEPTH FOR METAL LAYERS AND RELEASE TIME. REPRODUCED WITH PERMISSION OF [316] COPYRIGHT OF © 2025 IEEE.

	Etched Depth (μm) (Top / Bottom)
METAL4, $d_{etch,4}$	0.77 / 0.72
METAL3, $d_{etch,3}$	0.66 / 0.64
METAL2, $d_{etch,2}$	0.57 / 0.55
METAL1, $d_{etch,1}$	0.49 / 0.46
Averaged, d_{etch}	0.608
	Release Time (min)
Estimated/Measured	56.2 / 55

Note: Top / Bottom refers to the top and bottom sides of METAL layer.

Within this framework, the moment of inertia for every rectangular constituent of the METAL/IMD/VIA layers can be computed as

$$I_{m_j} = \frac{h_{m.j} b_{m.j}^3}{12}, j = 1,2,3,4 \tag{3-6}$$

$$I_{IMD,k} = \frac{h_{IMD} b_{IMD}^3}{12} \tag{3-7}$$

$$I_{VIA,l} = \frac{h_{VIA} b_{VIA}^3}{12} + A_{VIA} d_{VIA}^2 \tag{3-8}$$

In these expressions h and b signify the height and width of the respective elements, while the subscripts j, k and l denote the specific layer indices. By way of illustration, $I_{METAL,j=1}$ pertains to the moment of inertia of the METAL1 layer, whereas $I_{VIA,l=23}$ corresponds to the value for VIA23. Furthermore, I_{total} represents the nominal total moment of inertia assuming an unaltered geometric configuration.

TABLE 3-3 Table 4-3 consolidates the Young's modulus and density values for the materials under consideration. The mechanical properties associated with the metal and oxide layers are derived from prior investigations [337, 338] , whereas the equivalent

doi:10.6342/NTU202600018

Young's modulus of METAL1 through METAL3 reported in [331] is utilized to approximate the Young's modulus of ARC layer, accounting for the specific thickness of each constituent layer [339]. Figure 3-5 (b) illustrates the beam cross-sections employed to replicate the findings in [331], , where the experimental cantilever is estimated to possess an oxide width of 8 μm and a primary METAL width of 6 μm. Furthermore, the Young's modulus of tungsten is calibrated to correspond with actual measurements, factoring in the layout geometry and the profile alterations induced by the etching sequence. The density and Young's modulus for the VIA and ARC composite—comprising TiN/Ti, W, and TiN/Ti—are calculated based on discrete widths of 0.12 μm, 0.26 μm, and 0.12 μm, respectively. Although the geometric corrections may not mirror actual conditions with absolute precision, this research proffers a refined estimation by integrating the mechanical properties and fabrication-related phenomena observed in preceding literature.

As stipulated in [340, 341] , the optimal contact material for RF switches must demonstrate several critical attributes: superior electrical conductivity for optimized signal transmission, high thermal conductivity to facilitate heat dissipation, an elevated melting temperature for high-temperature resilience, minimal vulnerability to chemical oxidation to ensure sustained reliability, and adequate hardness to mitigate wear and structural deformation. These performance benchmarks are considered equally vital for the functional integrity of resoswitches.

doi:10.6342/NTU202600018

TABLE 3-3: YOUNG'S MODULUS AND DENSITY FOR AYERS/MATERIALS USED. REPRODUCED WITH PERMISSION OF [316] COPYRIGHT OF © 2025 IEEE.

Layer/Materia[1]	Thickness (μm) [339]	Young's Modulus (GPa)	Density (kg/m3)
IMD	1	73 [331]	2200 [337, 338]
METAL	M1: 0.4 M2: 0.4 M3: 0.4 M4: 0.8	70 [337, 338]	2700 [337, 338]
VIA (W)	1	230[1]	19350 [337, 338]
ARC[2] (TiN/Ti)	(Top / Bottom)[3] M1: 0.14/0.125 M2-3: 0.14/0.1 M4: 0.025/0.1	224.5[5] [331]	5220 [337, 338]
VIA+ARC[4]	1	227.3	12550

1: Adjusted from the common 411 GPa [337, 338] to match the measurement results.
2: Antireflection coating in short.
3: Top / Bottom refers to the top and bottom sides of METAL layer.
4: Averaged value extracted from [331] with the assumptions shown in Figure 3-5. The extracted values for E_{TiN1}, E_{TiN2}, and E_{TiN3} are 208.64, 223.48 and 241.50 GPa, respectively.
5: Calculated values based on adjusted E_W, extracted E_{TiN} and densities from [337, 338], where the thickness/width of TiN and W is assumed as 0.12 and 0.26 μm, respectively. The thickness of TiN is estimated through the reported values of [339, 342-345] and Figure 3-3 (f).

Notwithstanding the restricted material selection available within standard CMOS processes, the current research utilizes VIA layers as the contact material, which consist of a composite of TiN, W, and Ti [339, 346] , as depicted in Figure 3-3 (d) and (f). TiN, W, and Ti are categorized as refractory metals distinguished by their superior resilience against wear, material transfer, arcing, and welding [340, 341, 347, 348]. Previous investigations have demonstrated that employing VIA as the contact interface yields enhanced reliability when contrasted with the aluminum–copper alloy METAL layers native to the CMOS process [310].

Nevertheless, the drawbacks of adopting VIA materials for contact purposes include a propensity for oxide formation, restricted corrosion resistance, and a comparatively elevated electrical resistivity [340, 341, 347]. Consequently, the dominant failure mechanism for the resoswitches featured in this study is identified as high contact

doi:10.6342/NTU202600018

resistance precipitated by contamination or oxidation, rather than the fusion or microwelding typically encountered with softer materials like the Au-Cu found in METAL layers [349].

3.2.3 Linear Operation

In scenarios where the magnitude of the bias voltage significantly exceeds that of the AC driving signal [318], the out-of-resonance force component can be disregarded. Furthermore, by omitting the fringing effect [229] and the static term [318, 350] , the electrostatic force A_d at the resonance frequency can be reduced to the following simplified form

$$A_{d.p=1,2} = \frac{N}{2}\frac{\partial C_p}{\partial x}(V_P + v_i)^2 \approx N\left(\frac{\partial C_{long}}{\partial x}\right)_p V_P v_i \tag{3-9}$$

In this expression, N signifies the total count of fingers, while $\partial C/\partial x$ represents the capacitance gradient per unit displacement along the *x*-direction as delineated in Figure 3-1 (a). i indicates the left-hand side ($i = 1$) and the right-hand side ($i = 2$) electrodes.

In the case of a double-sided excitation configuration, the capacitance change per unit displacement is approximated by the following relation

$$\left(\frac{\partial C_{long}}{\partial x}\right)_p = \begin{cases} -\dfrac{\varepsilon_0 h}{d_{ff}}, i = 1 \\ \dfrac{\varepsilon_0 h}{d_{ff}}, i = 2 \end{cases} \tag{3-10}$$

In this formulation, h represents the device thickness, while d_{ff} denotes the gap spacing between the electrode fingers. Consequently, the expression in (3-9) is transformed as follows [229]

$$A_d = A_{d.1} - A_{d.2} = 2N\frac{\varepsilon_0 h}{d_{ff}} V_P v_i = \eta v_i \tag{3-11}$$

where η is the overall electro-mechanical coupling coefficient.

doi:10.6342/NTU202600018

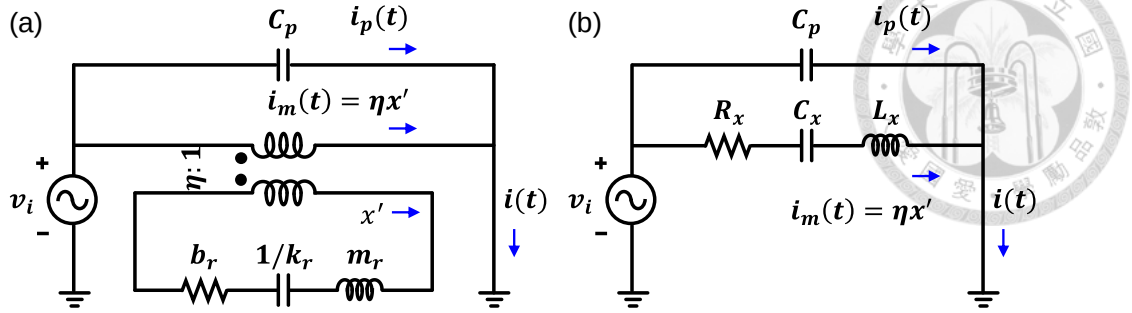


Figure 3-6: (a) Equivalent electrical circuit of an electrostatic MEMS resonator and (b) its simplified version. Reproduced with permission of [316] Copyright of © 2025 IEEE.

Regarding the capacitive transducers utilized in resoswitches, mechanical velocity is transduced into an electrical motional current. Figure 3-6 (a) depicts the equivalent electrical circuit for the input transducer, in which C_p accounts for the parasitic capacitance residing between the input terminal and the device structure. As illustrated in Figure 3-6 (b), the motional elements R_x, L_x, and C_x characterize the resonant response by leveraging the electromechanical analogy between the electrical and mechanical domains, as formulated by [351, 352]

$$R_x = b_r/\eta^2 \tag{3-12}$$

$$L_x = m_r/\eta^2 \tag{3-13}$$

$$C_x = \eta^2/k_r \tag{3-14}$$

The total current flowing from the input port takes the form [353]

$$i(t) \approx i_m + i_p = \eta x' + C_p \frac{dv_i}{dt} \tag{3-15}$$

It should be observed that network analyzers are conventionally employed to characterize such capacitively transduced instruments. An exhaustive model that incorporates the measurement instrumentation is detailed in Section 3.5.

For resoswitches, and vibro-impact resonators more broadly, it is advantageous to determine the specific frequencies at which grazing bifurcation manifests. These are

doi:10.6342/NTU202600018

identified as the frequency coordinates where contact occurs with zero velocity for a specified excitation magnitude. By neglecting the contributions of the impact force F_c and lumped nonlinear force F_{nl}, the steady-state amplitude and phase relative to the driving force F_d—of the displacement in (3-1) would be the following expressions [354]

$$x_{l.f} = \frac{A_d \cos(\omega_d t - \phi)}{m_r \sqrt{\bar{A}^2 + \bar{B}^2}} \tag{3-16}$$

$$\phi = \tan^{-1}(\bar{B}/\bar{A}) \tag{3-17}$$

where the coefficient $\bar{A}$ and $\bar{B}$ are given as

$$\bar{A} = \omega_n^2 - \omega_d^2 \tag{3-18}$$

$$\bar{B} = \omega_n \xi \omega_d \tag{3-19}$$

In this context, $\omega_n = \sqrt{k_r/m_r}$ signifies the natural angular frequency—representing the frequency at which the vibration amplitude is maximized in the absence of damping. When damping is accounted for (often termed the practical resonance), the displacement magnitude and the corresponding resonance frequency can be determined by identifying the maximum value of (3-16) under the condition $\partial x_{l.f}/\partial \omega_d = 0$, which yields

$$A_0 = Q\frac{A_d}{k_r};\ \frac{\omega_0}{\omega_n} = \sqrt{1 - \frac{\xi^2}{2}} \tag{3-20}$$

where $Q = \sqrt{m_r k_r}/b_r$ and $\xi = 1/Q$ represent the quality factor and the damping ratio, respectively. The term ω_0 denotes the angular resonance frequency of the device. For CMOS-MEMS resonators and resoswitches, the quality factor may reach values as high as 10^3 to 10^4 [355], which ensures that $\omega_n \approx \omega_0$.

doi:10.6342/NTU202600018

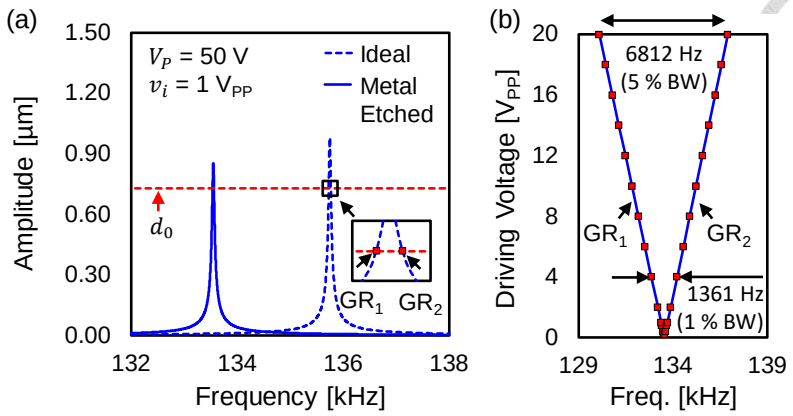


Figure 3-7: (a) Simulated displacement frequency responses with and without considering finite-selectivity etching during release. (b) The operation bandwidth of the resoswitch with varying driving voltage based on grazing frequencies predicted by (16). Reproduced with permission of [316] Copyright of © 2025 IEEE.

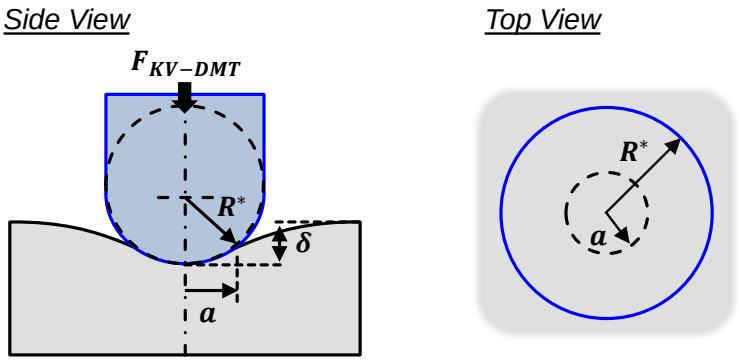


Figure 3-8: The single-asperity contact model. Reproduced with permission of [316] Copyright of © 2025 IEEE.

Consequently, the frequencies associated with the grazing bifurcation can be approximated by setting $x_{l.f} = d_0$ and calculating the corresponding values of ω_d [127]. Figure 3-7 (a) displays the simulated frequency responses for the displacement amplitude, highlighting the grazing bifurcation points where the response curves intersect the gap spacing d_0. Figure 3-7 (b) illustrates the evolution of these dual grazing points as a function of the driving voltage amplitude. As demonstrated, the interval between the two grazing points—which establishes the operational bandwidth of the resoswitch—expands in correlation with increasing driving amplitudes. Furthermore, the specific driving amplitude required for the structure to marginally contact the stopper at the linear resonance frequency, thereby generating a unique,

doi:10.6342/NTU202600018

solitary grazing point, is formulated as:

$$v_{i.min@\omega_0} = \frac{d_0 k_r}{\eta Q} \tag{3-21}$$

The expression in (3-21) has traditionally been regarded as the threshold driving amplitude necessitated for the initiation of hot switching [307, 356, 357]. Nevertheless, as elaborated in Section 3.3.3, the execution of hot switching is contingent upon the contact force surpassing a specific magnitude. The requisite minimum driving amplitude for hot switching must exceed the estimation provided by (3-21). Specifically, the establishment of stable electrical conduction demands a contact force ranging from tens to hundreds of μN, varying according to material properties and contact geometry. Within the scope of this investigation, the minimum driving voltage essential for reliable hot switching is determined to be approximately 5 to 10 times greater than the value predicted by (3-21).

Furthermore, the switching time (or switching speed), which denotes the duration required for a resoswitch to transition from the OFF state to the ON state, represents another critical metric. By examining the equation of motion defined in (3-1), the general solution could be expressed as [354]

$$x_{l.t} = C_1 e^{\lambda_1 t} + C_2 e^{\lambda_2 t} + A\sin(\omega_d t) + B\cos(\omega_d t) \tag{3-22}$$

where the first two terms describe the transient/homogenous solutions while the last two terms describe the steady-state/particular solutions. The eigenvalue λ_1 and λ_2 determined as follows

$$\lambda_1 = \frac{-b_r + \sqrt{b_r^2 - 4m_r k_r}}{2m_r} = \lambda_r + i\lambda_i \tag{3-23}$$

$$\lambda_2 = \frac{-b_r - \sqrt{b_r^2 - 4m_r k_r}}{2m_r} = \lambda_r - i\lambda_i \tag{3-24}$$

and the parameters A, B, C_1 and C_2 are given as

doi:10.6342/NTU202600018

$$A = \frac{A_d}{b_r \omega_d}\left[1 + \left(\frac{k_r - m_r \omega_d^2}{b_r \omega_d}\right)\right]^{-1} \tag{3-25}$$

$$B = A\left[\frac{k_r - m_r \omega_d^2}{b_r \omega_d}\right] \tag{3-26}$$

$$C_1 = x_0 - B - C_2 \tag{3-27}$$

$$C_2 = \frac{v_0 - x_0 \lambda_1 - A\omega_d + B\lambda_1}{\lambda_2 - \lambda_1} \tag{3-28}$$

In this context, x_0 and v_0 designate the initial position and initial velocity, respectively. Here, m_r, b_r and k_r are positive values. Therefore, the eigenvalues are complex conjugate and satisified $\lambda_{r1} = \lambda_{r2} = \lambda_r$ and $\lambda_{i1} = \lambda_{i2} = \lambda_i$. Provided the driving frequency approximates the natural angular frequency—specifically where $\omega_d \approx \omega_n$ ($k_r - m_r \omega_d^2 \approx 0$)—the expressions in (3-25) through (3-28) can be simplified as

$$A = \frac{A_d}{b_r \omega_d} \tag{3-29}$$

$$B = 0 \tag{3-30}$$

$$C_1 = x_0 - C_2 \tag{3-31}$$

$$C_2 = \frac{v_0 - x_0 \lambda_1 - F_d / b_r}{\lambda_2 - \lambda_1} \tag{3-32}$$

By omitting the high-frequency oscillation components, the trajectory of the upper envelope curve can be modeled as

$$x_{l.en} = e^{\xi_r t}[Im(C_2 - C_1)] + A \tag{3-33}$$

In this context, $Im(\cdot)$ denotes the imaginary operator. On the assumption that the device commences from a state of rest, characterized by zero initial displacement and zero initial velocity, the expression in (3-33) reduces to

doi:10.6342/NTU202600018

$$x_{l.en} = e^{\xi_r t}(-A) + A \tag{3-34}$$

Consequently, the switching time can be approximated by equating x_{en} equal to d_0, which results in the following formulation

$$t_{sw} = \ln\left[1 - \frac{d_0 b_r \omega_d}{A_d}\right] / \lambda_r \tag{3-35}$$

The expression in (3-35) demonstrates that an increase in the driving force, a reduction in the gap clearance, diminished damping, or a decrease in the linear resonant frequency results in an accelerated switching time. Furthermore, as evidenced by (3-33), the duration required for switching can be curtailed through the strategic adjustment of the initial displacement or velocity.

3.3 Modeling of Resoswitches

This section articulates the consequences of contact interaction, nonlinearities, and electrical contact resistance, alongside the repercussions of back-end circuits essential for the comprehensive modeling of resoswitches, extending beyond the fundamental linear model detailed in Section 3.2. TABLE 3-4 categorizes the device parameters either implemented during the design phase or extracted from measurements; these values serve as a consistent reference throughout Section 3.3 through 3.5.

3.3.1 Contact Surface Interaction Force and Contact Area

The magnitude of the interaction force and electrical contact resistance at the resoswitch interface is profoundly governed by the contact area. This parameter proves difficult to quantify precisely, as it evolves over time due to phenomena such as dynamic plastic deformation and stress relaxation [358, 359]. Physically, the interface comprises numerous localized asperity peaks, commonly termed *a-spots*; the effective contact area is established by factors including the density, spatial geometry, and height distribution of these a-spots. As reported in [358-360], the actual contact area within micro-structures fabricated from typical silicon or gold materials constitutes only 0.1% to 10% of the nominal geometric surface. Consequently, the effective contact area for

doi:10.6342/NTU202600018

micro-switches is frequently modeled either as a multi-point a-spot distribution or as a single equivalent a-spot [361]. Analytical models for contact surface interaction involving a single a-spot with diverse asperity geometries have been formulated and extensively implemented in contact mechanics [107, 360, 362]. Conversely, models for multiple a-spots incorporate the systemic influences of surface roughness. Techniques for approximating surface roughness distributions are classified into statistical, deterministic, or fractal methodologies [361]. Among these, the Greenwood-Williamson (GW) model, which is predicated on a statistical framework, remains the most prevalent [361, 363, 364].

Alternatively, the coefficient of restitution method has been employed to simulate the contact dynamics in resoswitches [107]. However, because this method characterizes the velocity change of colliding bodies while presuming an instantaneous contact duration, it neglects the contact force and complex mechanics occurring during the contact phase. Consequently, it cannot effectively capture transient dynamic responses quantitatively. To rectify this limitation, [303] and [365] apply the DMT model to integrate the contributions of both repulsive and adhesive forces.

For the sake of analytical simplicity, this research utilizes a single a-spot model for the contact interface, as illustrated in Figure 3-8 , where a spherical geometry with an equivalent tip radius R^* engages a flat surface. According to Hertz theory [138, 204, 366] the distance from the contact boundary to the center, identified as the contact radius a, can be derived from the indentation depth δ and the effective radius of curvature R^* of the tip as follows [138]

$$a_c^2 = R^*\delta \tag{3-36}$$

The contact area then takes the form assuming $\delta \ll R^*$

$$A_c = \pi a_c^2 = \pi R^*\delta \tag{3-37}$$

While a realistic contact interface comprises numerous a-spots, and factors such as material properties and contact surface topology exert significant influence on the

doi:10.6342/NTU202600018

interaction force, a single a-spot model is implemented in this study to facilitate computational simplicity. To account for the cumulative effects of real-world contact characteristics, the radius of curvature R^* is calibrated, thereby ensuring the simulation results align more precisely with actual data.

Given that the van der Waals force constitutes the primary attractive component, its mathematical representation for the single a-spot geometry shown in Figure 3-8, as predicated on the DMT model [107, 204], is expressed as:

$$F_{DMT}(x) = -\begin{cases} -\dfrac{HR^*}{6(d_0 - x)^2}; x < d_0 - a_0 \\ -\dfrac{HR^*}{6a_0^2} + K(\delta)^{3/2}; x \geq d_0 - a_0 \end{cases} \quad (3\text{-}38)$$

In this formulation, $H = 12\pi W a_0^2$ denotes the Hamaker constant, d_0 represents the contact clearance, and a_0 (= 0.165 nm) signifies the selected interatomic spacing. The indentation is determined by the relation $\delta = x - d_0 + a_0$. Furthermore, the effective radius of curvature, R^*, is characterized as $(1/R_1 + 1/R_2)^{-1}$, which simplifies to R_1 in instances where R_2 is assumed to be infinite. The term W indicates the work of adhesion. The adhesion force acting upon the contact surface is quantified as $F_{ad} = HR^*/(6a_0^2)$. Finally, the contact-stiffness parameter K is calculated as

$$K = \frac{4}{3}E^*\sqrt{R^*} \quad (3\text{-}39)$$

In this expression, $E^* = [(1 - v_1^2)/E_1 + (1 - v_2^2)/E_2]^{-1}$ designates the effective Young's modulus, where $v_{i=1,2}$ and $E_{i=1,2}$ denote the Poisson's ratio and Young's modulus of the respective contact materials.

Furthermore, as demonstrated in Section 3.5, contact-induced damping is manifest within the experimental data. To incorporate the effects of contact damping, the Kelvin-Voigt model is integrated with the DMT model, thereby constituting the KV-DMT model. This augmented version of (3-38), termed the generalized DMT model, is expressed as [313, 314]

doi:10.6342/NTU202600018

TABLE 3-4: PARAMETERS AND PERFORMANCES OF THE DESIGNED RESOSWITCH. REPRODUCED WITH PERMISSION OF [316] COPYRIGHT OF © 2025 IEEE.

Parameter	Layout		Measured or extracted	Unit
Folded-Beam Length, L	43.7		43.4	μm
Folded-Beam Width, W	1.5		1.9	μm
Shuttle Width	6		6.5	μm
Finger-to-Finger Gap, d_{ff}	1		0.8	μm
Finger-to-Anchor Gap, d_{sf}	5		4.6	μm
Finger Width, w_f	1.5		1.7	μm
Contact Clearance, d_0	0.6		0.72	μm
Quality Factor, Q	3000		2930	-
Metal Etched	No	Yes	-	-
Lumped Mass, m_r	1.118×10^{-10}	0.9945×10^{-10}	0.9606×10^{-10}	kg
Lumped Stiffness, k_r	81.33	70.05	66.91	N/m
Lumped Damper, b_r	3.178×10^{-8}	2.782×10^{-8}	2.740×10^{-8}	N•s/m
Linear Resonant Frequency, f_0	135.77	133.57	132.80	kHz
Mechanical Nonlinear Stiffness, $k_{3,m}$	0.219×10^{11}	0.189×10^{11}	-1.20×10^{11}	N/m^3
Electrical Nonlinear Stiffness, $k_{3,e}$	-1.198×10^{11}	-0.925×10^{11}		
Nonlinear Damping, b_3	-	-	1.093×10^{5}	$N•s/m^3$
Electromechanical Coupling Coefficient, η	3.4303×10^{-7}	2.5705×10^{-7}	2.5711×10^{-7}	N/V
Equivalent Resistance, R_x	270.07	421.05	414.47	kΩ
Equivalent Inductance, L_x	949.78	1505.06	1453.22	H
Equivalent Capacitance, C_x	1.447	0.9433	0.9879	fF
Parasitic Capacitance, C_p	-	-	155.87	fF
Specific Voltage Loss	-	-	0.6889	-
Hamaker Constant in Vacuum, H	15.73×10^{-20} [367]	J		
Interatomic Spacing, a_0	0.165 [368]	nm		
Electron Mean Free Path, λ	45 [369]	nm		
Electrical Resistivity, ρ	3000[1]	μΩ•cm		
Poisson's Ratio, $v_{i=1,2}$	0.25 [370]	-		

doi:10.6342/NTU202600018

TABLE 4-4: CONTINUED

Parameter	Layout		Measured or extracted	Unit
Young's Modulus, $E_{i=1,2}$	224.54			GPa
Effective Youngs's Modulus, E^*	119.75			GPa
Effective Tip Radius, R^*	400	400	400/400-8000[2]	Nm
Adhesion Force, F_{ad}	0.39	0.39	0.39/0.39-7.8[2]	μN
Viscoelastic Contact Damping, b_c	-	-	2000/50000[2]	N•s/m^2
Ultimate/Grazing Sensitivity, $v_{i.min@\omega_0}$	126.56	109.0	< 137.78	mV_{PP}
Sensitivity in Steady State	-	-	~1380[3]	mV_{PP}
Sensitivity in Transient State			~897[3]	mV_{PP}
Required Minimum Contact Force	-	-	~30[4]	μN
Switching Time at v_i = 1 V_{PP}, $t_{sw,1V}$	0.976	1.157	~1.283	ms
Bleeding Resistance[5], R_B	90.9/1000	90.9/1000	90.9/1000	kΩ
Bleeding Capacitance, C_B	300	300	370	pF

[1]: The resistivity of TiN, depending on the fabrication process used, can vary from as low as 25 μΩ·cm up to 10000 μΩ·cm [371-373]. Here, a resistivity value of 3000 μΩ·cm is chosen based on the measured output signal magnitude, which is a function of the TiN contact resistance and the loading resistance at the output.

[2]: Parameters for hot-switching/non-hot-switching operation.

[3]: The values were derived from successful hot switching results, achieved at the lowest applied driving voltages of 1.3 V_{PP} (not shown) and 2 V_{PP} (*cf.* Figure 3-26), respectively. The voltage difference arises from a 0.69× reduction in the bias tee. Since the sensitivity varies significantly depending on the contact surface conditions, the actual value across the entire device lifespan may be higher or lower than the values here. Systematic evaluations will be required to determine the minimum, average, or maximum sensitivity values.

[4]: Calculated based on the used model for the steady-state hot switching condition at a 2-V_{PP} driving input.

[5]: Values are derived from a 100-kΩ in parallel with the 1-MΩ input resistance of the oscilloscope, or from the oscilloscope itself.

doi:10.6342/NTU202600018

$$F_{KV-DMT}(x) = -\begin{cases} -\dfrac{HR^*}{6(d_0 - x)^2}; x < d_0 - a_0 \\ -\dfrac{HR^*}{6a_0^2} + K(\delta)^{\frac{3}{2}} + b_c\sqrt{R^*}(\delta)^{\frac{1}{2}}x'; x \geq d_0 - a_0 \end{cases} \quad (3\text{-}40)$$

where the b_c represents the viscous (damping) coefficient manifested during the contact phase.

3.3.2 Stiffness and Damping Nonlinearities

The mechanical motion of the device is modulated by forces arising from nonlinear stiffness and damping. Although the characterization of nonlinearities can be laborious when accounting for intricate higher-order components, the present study employs third-order terms for displacement and velocity. This approach proves sufficient for simulating the comprehensive response under the influence of nonlinear phenomena. The nonlinear force is expressed as

$$F_{nl}(x, x') = k_3 x^3 + b_3 x^2 x' \quad (3\text{-}41)$$

In this equation, k_3 and b_3 signify the third-order nonlinear stiffness and damping coefficients, identified as the Duffing term and the van der Pol term (with x^2), respectively.

Generally, the third-order nonlinear stiffness k_3 in capacitively-driven MEMS resonators incorporates both geometric and electrical nonlinearities. For the folded-beam comb-driven structures investigated here, k_3 assumes the following form [229, 374]

$$k_3 = k_{3.m} + k_{3.e} = \frac{432}{70} E_{eq} I h \left(\frac{W}{L}\right)^3 - \frac{4NC_{trans}V_P^2}{d_{sf}^4} \quad (3\text{-}42)$$

where d_{sf} denotes the initial clearance between the comb finger tips and the shuttle or anchor, and $C_{trans} = \varepsilon_0 A_{trans}/d_{sf} = \varepsilon_0 w_f h/d_{sf}$ represents the capacitance governed by d_{sf}.

The reduction in transmission induced by nonlinear damping as the driving power increases has been documented within the CMOS-MEMS platform [332]. Nevertheless,

doi:10.6342/NTU202600018

the underlying physics of nonlinear damping in MEMS resonators remains complex, potentially originating from external environmental factors—such as sliding film and squeeze film air damping—or intrinsic losses inherent to the material [105, 375]. Consequently, this study depends on empirical data to determine the nonlinear damping coefficient b_3 (e.g., via the ring-down characterization detailed in Section 3.5).

By integrating the KV-DMT model from (3-40) with the nonlinear forces in (3-41) and nonlinear damping b_3, the governing equation of motion in (3-1) is transformed into

$$\begin{aligned} m_r x'' + b_r x' + k_r x + b_3 x^2 x' + k_3 x^3 \\ = A_d cos(\omega_d t) + F_{KV-DMT} \end{aligned} \tag{3-43}$$

The steady-state frequency response of (3-43) can be solved through the method of averaging [314, 376, 377], yielding

$$x_{T.f} = \frac{A_d \cos(\omega_d t - \phi)}{m_r \sqrt{\hat{A}^2 + \hat{B}^2}} \tag{3-44}$$

where $\hat{A}$ and $\hat{B}$ are formulated as

$$\hat{A} = (1 + K_H - K_{vdw} + K_D)\omega_n^2 - \omega_d^2 \tag{3-45}$$

$$\hat{B} = \omega_n(\xi + C_{vis} + C_{vdP})\omega_d \tag{3-46}$$

where the stiffness components are defined as

$$\begin{aligned} K_H = \frac{\beta}{\pi}\left(\frac{x}{A_0}\right)^{\frac{1}{2}} \left\{ \int_0^{\theta_0} [cos(\theta) - \zeta_1 + \zeta_2]^{\frac{3}{2}} cos(\theta)\, d\theta \right. \\ \left. + \int_{2\pi-\theta_0}^{2\pi} [\cos(\theta) - \zeta_1 + \zeta_2]^{\frac{3}{2}} \cos(\theta)\, d\theta \right\} \\ \left. + \int_{2\pi-\theta_0}^{2\pi} [\cos(\theta) - \zeta_1 + \zeta_2]^{\frac{3}{2}} \cos(\theta)\, d\theta \right\} \end{aligned} \tag{3-47}$$

$$\begin{aligned} K_{vdw} = \frac{\alpha}{\pi}\left(\frac{x}{A_0}\right)^{-3} \left[\int_0^{\theta_0} \frac{cos(\theta)\, d\theta}{\zeta_2^2} \right. \\ \left. + \int_{\theta_0}^{2\pi-\theta_0} \frac{\cos(\theta)\, d\theta}{(\zeta_1 - \cos(\theta))^2} + \int_{2\pi-\theta_0}^{2\pi} \frac{\cos(\theta)\, d\theta}{\zeta_2^2} \right] \end{aligned} \tag{3-48}$$

doi:10.6342/NTU202600018

$$K_D = 2K_3\left(\frac{x}{A_0}\right)^2\int_0^{2\pi}\cos^4(\theta)\,d\theta = \frac{3}{4}\frac{k_3x^2}{k_r} \tag{3-49}$$

Furthermore, the damping components are formulated as:

$$C_{vdP} = 2B_3\left(\frac{x}{A_0}\right)^2\int_0^{2\pi}\cos^2(\theta)\sin^2(\theta)\,d\theta = \frac{1}{4}\frac{b_3x^2}{m_r\omega_n} \tag{3-50}$$

$$C_{vis} = \frac{\gamma}{\pi}\left(\frac{x}{A_0}\right)^{\frac{1}{2}}\left\{\int_0^{\theta_0}[cos(\theta)-\zeta_1+\zeta_2]^{\frac{1}{2}}\,sin^2(\theta)\,d\theta + \int_{2\pi-\theta_0}^{2\pi}[cos(\theta)-\zeta_1+\zeta_2]^{\frac{1}{2}}\,sin^2(\theta)\,d\theta\right\} \tag{3-51}$$

Within equations (3-47), (3-48), and (3-51), the variables $\alpha = HR^*/(6k_rA_0^3)$, $\beta = 4E\sqrt{R^*A_0}/(3k_r)$, and $\gamma = b_c\sqrt{R^*A_0}/\sqrt{m_rk_r}$ denote nondimensional coefficients that characterize the van der Waals, Hertz, and viscoelastic forces, respectively. The terms $\zeta_1 = d_0/x$ and $\zeta_2 = a_0/x$ represent variables dependent on displacement amplitude, signifying the ratio of the gap distance and the interatomic spacing to the displacement amplitude, respectively. The free vibration amplitude A_0 determined according to (3-20). The variable $\theta_0 = \cos^{-1}(\zeta_1-\zeta_2)$ specifies the impacting angle; consequently, the contact time is calculated as $t_c = 2\theta_0/\omega_d$ [376]. The parameters B_3 and K_3 constitute nondimensional values, defined by $B_3 = b_3A_0^2/(m_r\omega_n)$ and $K_3 = k_3A_0^2/k_r$, respectively.

It should be noted that (3-44) fundamentally maintains the same structure as (3-16) but with $\hat{A}$ and $\hat{B}$, though it substitutes to integrate the nonlinear stiffness and damping arising from surface interaction forces and both electrical and mechanical nonlinearities.

The peak displacement amplitude derived from (3-44) establishes the nonlinear resonance angular frequency. By accounting for the contact interaction forces and nonlinearities detailed above, this can be rendered as a ratio relative to the natural angular frequency

doi:10.6342/NTU202600018

$$\frac{\omega_{nl.KV-DMT}}{\omega_n} = \frac{}{\sqrt{(1 + K_H - K_{vdw} + K_D) - \frac{1}{2}(\xi + C_{vis} + C_{vdP})^2}} \tag{3-52}$$



It is beneficial to observe that if only the Duffing term is retained, the frequency shift at the peak corresponding to the maximum amplitude reduces to $\omega_D^2 = (1 + K_D)\omega_n^2$. By applying a Taylor expansion approximation for small displacement, this expression evolves into

$$\frac{\omega_D}{\omega_n} = \sqrt{1 + K_D} \approx \left(1 - \frac{3}{8} k_3 x^2 / k_r\right) \tag{3-53}$$

This result aligns with the recognized backbone curve equation characteristic of the Duffing oscillator.

3.3.3 Electrical Contact Resistance and Material Selection

Beyond mechanical contact, the integration of electrical conduction is essential for a comprehensive understanding of resoswitch operation. Generally, the mechanisms of current transport are categorized as ballistic, diffusive, or a hybrid of these two modes [361]. Based on Holm's theory [340, 347], in scenarios where the contact radius a is diminished relative to the electron mean free path, the resistance at the contact interface is governed mainly by boundary scattering within the ballistic regime—a phenomenon frequently termed contamination film resistance. In contrast, when the contact radius significantly surpasses the electron mean free path, the electrical contact resistance is dictated by constriction resistance resulting from diffuse scattering.

By incorporating the analytical findings from [378, 379], the electrical contact resistance R_c is formulated as

$$R_c = \Gamma\left(\frac{\lambda_e}{a_c}\right) R_S + R_M = \Gamma\left(\frac{\lambda_e}{a_c}\right) \frac{\rho_e}{2a_c} + \frac{4\rho_e \lambda_e}{3\pi a_c^2} \tag{3-54}$$

doi:10.6342/NTU202600018

TABLE 3-5: CONTACT FORCE REQUIRED FOR STABLE CONTACT IN COMMON METALS AND THE ASSOCIATED RESISTIVITY AND CONTACT RESISTANCE. REPRODUCED WITH PERMISSION OF [316] COPYRIGHT OF © 2025 IEEE.

Material (From Soft to Hard)	Contact Force (μN)	Resistivity (μΩ-cm)	Contact Resistance (Ω)
Gold	50-200 [380, 381]	2.2 [340, 382]	0.03-0.2 [380, 381]
Fine Gold (AuCuCd)	200 [381]	N/A	0.05-0.08 [381]
Hard Gold (AuNi, 5%)	300-450 [381]	12 [382]	<0.1 [381]
Hard Gold (AuNi, 20%)	150 [380]	N/A	1-1.8 [380]
Gold-Palladium (Au-Pd)	200-2000 [381]	N/A	0.5-3 [381]
Silver (Ag)	600 [381]	1.6 [340]	2 [381]
Platinum (Pt)	10-600 [380, 383]	10.6 [340]	3-90 [380, 383]
Palladium (Pd)	600 [381]	10.8 [340]	3 [381]
Rhodium (Rh)	50-900 [380, 381]	4.3 [382]	0.8-3.5 [380, 381]
Ruthenium (Ru)	50-100 [380]	7.1 [382]	7-8 [380]
Ruthenium Oxide (RuO2)	140 [380]	N/A	7-10 [380]
Carbon Nanotube (CNT)	10 [380]	N/A	285 [380]
Nickel (Ni)	N/A	6.8 [340]	>4000 [384]
Titanium Nitride (TiN)	1-260 [385]	30-230 [385]	10-4700 [385]
Tungsten (W)	150 [380]	~5.5 [382]	<1000 [380]

In this formulation, R_S and R_M signify the contamination and constriction film resistances, modeled via Sharvin's and Maxwell's equations, respectively [347]. The parameter ρ corresponds to electrical resistivity, whereas λ designates the electron mean free path, which is approximated at 45 nm for TiN [369]. The interpolation term $\Gamma(\lambda/a)$, initially developed in [386], characterizes the transition regime bridging the ballistic and diffusive regions. This function was subsequently refined by [315] as $\Gamma(\lambda/a) = \frac{2}{\pi}\int_0^\infty sinc\,(z) \times (e^{-(\lambda/a)z}/z)dz$. However, to facilitate numerical

doi:10.6342/NTU202600018

integration, a second-order Padé approximant is employed

$$\Gamma\left(\frac{\lambda_e}{a_c}\right) = \frac{A_{P1} + A_{P2}\left(\frac{\lambda_e}{a_c}\right) + A_{P3}\left(\frac{\lambda_e}{a_c}\right)^2}{B_{P1} + B_{P2}\left(\frac{\lambda_e}{a_c}\right) + B_{P3}\left(\frac{\lambda_e}{a_c}\right)^2} \tag{3-55}$$

where the coefficients are defined as $A_{P1} = 0.9966$, $A_{P2} = 0.7879$, $\mathrm{A_{P3}} = 9.8756 \times 10^{-5}$, $B_{P1} = 1$, $B_{P2} = 1.3264$, and $B_{P3} = 1.2598$. The deviation associated with the approximation in (3-55) remains below 0.8% across a λ/a range of 0.01 to 100, a span that comprehensively encompasses the contact conditions relevant to this investigation.

Equation (3-54) demonstrates that contact resistance is dependent upon the contact radius, which itself is a function of the contact force. As previously noted, achieving stable electrical contact necessitates that the contact force exceed a specific threshold [387]. TABLE 3-5 tabulates the requisite minimum forces for stable electrical contact across disparate materials. These values function as a benchmark for calculating the minimum driving signal necessary for the hot switching of resoswitches utilizing specific contact materials. For practical implementation, a magnitude of 1.5 to 3 times the values presented in TABLE 3-5 is typically recommended as a standard operating guideline [388].

3.3.4 The Effect of the Back-end RC Circuit

Figure 3-9 (a) depicts the schematic representation of the equivalent circuit for the resoswitch integrated with the back-end RC circuit. This back-end RC circuit is employed to attenuate high-frequency components emerging at the output due to the impulsive characteristics of resonant switching, thereby yielding a smoothed output waveform. The impedance magnitude of the RC circuit governs both the timing associated with bit 1/0 switching and the reliability of the resoswitch, as it influences the intensity of the Joule heating current generated during the contact phase.

As demonstrated in Figure 3-9 (b) and (c), the temporal evolution of the output voltage V_o during the OFF and ON states within a single switching cycle is expressed as [389]

doi:10.6342/NTU202600018

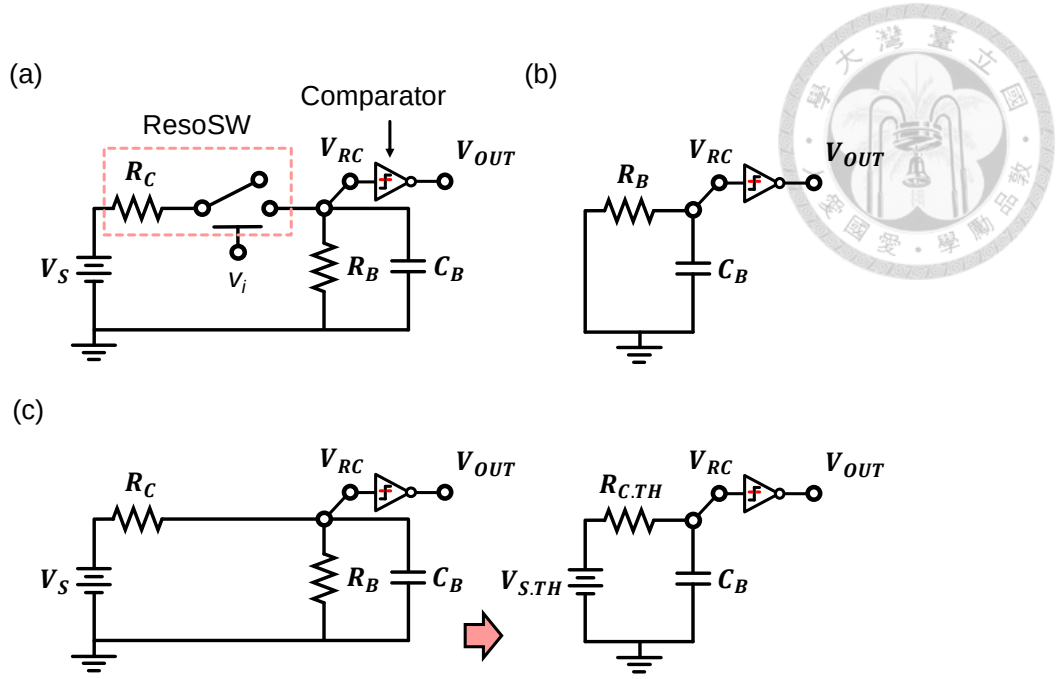


Figure 3-9: (a) Equivalent circuit model for resoswitches with the RC envelop detector and its simplified circuits at (b) OFF state and (c) ON state. Reproduced with permission of [316] Copyright of © 2025 IEEE.

$$V_{o.off}(t) = V_{o.on.end}\mathrm{e}^{-\frac{\mathrm{t}}{\tau_{off}}} \tag{3-56}$$

$$V_{o.on}(t) = \frac{R_B}{R_B + R_C}V_S\left[1 - e^{-\frac{t}{\tau_{on}}}\right] - V_{o.off.end}e^{-\frac{t}{\tau_{on}}} \tag{3-57}$$

where $v_{RC.off.ini}$ and $v_{RC.on.ini}$ designate the initial conditions for the OFF and ON states, respectively; these values correspond to the terminal voltages inherited from the preceding state (specifically, $v_{RC.off.ini} = v_{RC.on.final}$ and $v_{RC.on.ini} = v_{RC.on.final}$). The time constants associated with the OFF and ON states are denoted by $\tau_{off} = C_B R_B$ and $\tau_{on} = R_{C.TH}C_B = C_B R_B R_c/(R_B + R_C)$, respectively. Generally, the contact resistance falls within the range of 100 Ω to fewer than 10 kΩ, a value significantly lower to the bleeding resistance utilized in this study (ranging from 100 kΩ to 1 MΩ). Consequently, the duration required for charging is shorter relative to the discharging interval. Equations (3-56) and (3-57) reveal that the peak voltage manifested during hot switching is dictated not solely by the contact resistance, but also by the contact duration, the operating frequency, and the specific parameters characterizing the RC

doi:10.6342/NTU202600018

circuit. Furthermore, the time constants for the ON- and OFF-states may be modulated by adjusting the bleeding resistance and capacitance to attain the targeted output waveforms and bit duration. For instance, to prevent signal attenuation while receiving bit 1, the RC tank must produce minimal ripples, ensuring that the voltage output does not descend beneath the bit 1/0 threshold of the subsequent comparator circuit. Predicated on the assumption of a negligible contact resistance, where the hot switching output approximates the bias voltage of the structure (i.e., $V_{RC.on.final} \approx V_S$, and given a requisite threshold voltage for the next stage is V_T, the RC time constant must exceed the operating period $T_{op} = 1/f_{op}$ This condition, formulated in (3-58), is necessary to preclude erroneous bit transitions from 1 to 0:

$$C_B R_B > \frac{-t_{op}}{ln\left(\frac{V_T}{V_{o.on.end}}\right)} \tag{3-58}$$

Conversely, to obviate the retention of bit 1 when a transition to 0 is required, the RC time constant must be inferior to the mandatory OFF time constraint T_{off} within a single duty cycle, as expressed in

$$C_B R_B < \frac{-t_{off}}{ln\left(\frac{V_T}{V_{o.on.end}}\right)} \tag{3-59}$$

In practical operation scenarios, this OFF time may be substituted by the clocking duration of the output digitize circuit or other specific timing requisites.

As previously noted, the impedance of the RC circuit establishes the contact voltage V_C across the contact a-spot, which subsequently impacts both contact temperature and system reliability. The terminal asperity temperature for a switch in the ON-state, designated as the *supertemperature*, is defined as [390]:

$$T_s = \sqrt{\frac{\Gamma\left(\frac{\lambda_e}{a_c}\right) R_M}{4 L_e R_S} V_c^2 + T_0^2} \tag{3-60}$$

doi:10.6342/NTU202600018

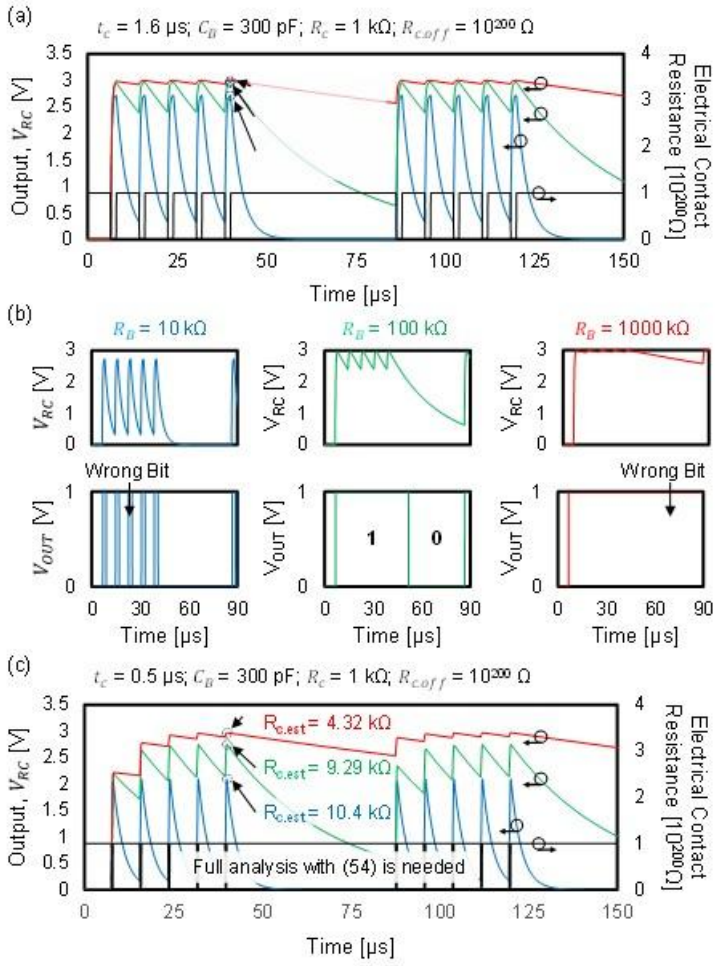


Figure 3-10: (a) Simulated hot-switching voltage at the back-end RC circuit for a contact duration of 1.6 μs. The black pulse waveform represents the contact resistance profile. The blue, green, and red curves depict the output voltage for bleeding resistances of 10, 100, and 1000 kΩ, respectively. (b) Output signals after processing through the comparator. (c) Simulated hot-switching voltage for a short contact duration of 0.4 μs. The contact resistance values, extracted using (61), are indicated in both (a) and (c), showing that poor estimation of contact resistance occurs in cases of short contact duration where the RC time constant significantly exceeds the contact duration. Reproduced with permission of [316] Copyright of © 2025 IEEE.

where $L = (\pi^2\, k_B^2)/(3q^2) = 2.4435 \times 10^{-8}\ [V^2/K^2]$ signifies the Lorentz number characteristic of ideal conductors [391], while $k_B = 1.380649 \times 10^{-23}$ [J/K] and $q = -1.602 \times 10^{-19}$ [C] correspond to the Boltzmann constant and the elementary

doi:10.6342/NTU202600018

electron charge, respectively. T_0 indicates the ambient room temperature. The terms R_M and R_S reiterate the resistances associated with contamination and constriction films, respectively. It is significant to observe that the peak temperature developed within a metallic constriction remains largely invariant with respect to specific geometries or materials, a phenomenon attributed to the highly confined (i.e., localized) nature of the heating at the a-spot [392, 393].

Typically, the implementation of a substantial bleeding resistance R_B is preferable, as it facilitates a reduction in the contact voltage. Consequently, under the condition where $R_B \gg R_c$, the time constant governing the ON state is approximated as $\tau_{on} \approx C_B R_c$. Premised on the condition that the contact duration significantly exceeds the ON-state time constant (specifically, $t_c \gg \tau_{on}$), the ultimate output magnitude during the ON state may be estimated by

$$V_C = I_c R_c \approx \left(\frac{V_S}{R_B + R_C}\right) R_C \tag{3-61}$$

Figure 3-10 (a) depicts the output switching waveforms associated with several bleeding resistance values, given a contact duration of 1.6 μs (approximately $4\tau_{on}$). In this simulation, the ON and OFF resistances are fixed at 1 kΩ and 10^{200} Ω, respectively, with a zero-transition interval. As demonstrated in Figure 3-10 (a), the peak magnitude of the switching waveforms aligns with the predictions of (3-61). Figure 3-10 (b) presents the comparator output waveforms across the three bleeding resistance variants, revealing that specific time constant values may induce bit errors. Conversely, Figure 3-10 (c) displays a scenario characterized by an abbreviated contact duration of 0.4 μs (approximately τ_{on}) relative to Figure 3-10 (a) ; in this instance, the maximum amplitude corresponds to (3-57) rather than (3-61). It is imperative to acknowledge that the ON/OFF contact resistances utilized in this simulation are presumed invariant, featuring a transition time of zero. In physical systems, the actual contact force and resistance may exhibit variability. Nonetheless, the simulations in Figure 3-10 provide critical perspective regarding how the component parameters of the RC back-end

doi:10.6342/NTU202600018

circuits influence the switching output.

Concluding this section, [394] posits that the magnitude of the Joule heating current constitutes the primary determinant of RF switch lifetime. The introduction of external inductance serves to attenuate the severity of current spikes. This measure is crucial for diminishing thermal effects and preventing the contact temperature from arising to levels that induce softening of the contact material. Should the temperature become uncontrolled, material properties may be compromised, thereby elevating the risk of micro-welding. Although it might be contended that material softening could augment the contact area and consequently reduce contact resistance, this phenomenon does not necessarily equate to an enhancement in device lifetime.

3.4 Theoretical Analysis of Resoswitches

This section delineates the simulation of resoswitch operation within both time and frequency domains, grounded in the device parameters and modeling frameworks elaborated in Section 3.2 and 3.3. Specifically, MATLAB and Simulink are utilized as the numerical tools to acquire time-domain transient responses, frequency responses, and the steady-state repulsive force. Complementing this, analytical derivations relying on the method of averaging, such as equation (3-44), are applied to compute the frequency responses and steady-state repulsive force.

Beyond the mechanical and electrical attributes, TABLE 3-4 incorporates the Hamaker constant, tip radius, and Poisson's ratio for the TiN contact material, sourced from reported values in the literature. Furthermore, the mechanical and electrical nonlinear stiffnesses, $k_{3.m}$ and $k_{3.e}$ are calculated via (3-42). The nonlinear damping coefficient b_3 and the viscoelastic contact damping coefficient b_c are established through measurement results.

3.4.1 Numerical simulation Set-up

As previously indicated, MATLAB and Simulink are employed in this study to ascertain the tapping mode frequency and time-transient responses, adhering to the methodology delineated in [229]. Figure 3-11 depicts the block diagram representing

doi:10.6342/NTU202600018

the Simulink model: panel (a) displays the primary framework, which incorporates a forced 1-DOF lumped mechanical model alongside two subsidiary modules for the contact interaction force and electrical contact resistance, while panels (b) and (c) detail these respective sub-models.

Although the feedthrough path is conventionally characterized by a parasitic capacitance C_p, a series parasitic resistance R_p and inductance L_p integrated into the numerical simulation to preclude singularity. Absent these components, the simulation risks generating non-finite output values and encountering convergence difficulties. Consequently, the transfer function defining the feedthrough path assumes the following structure

$$H_p = \frac{C_p s}{L_p C_p s^2 + R_p C_p s + 1} \tag{3-62}$$

Nevertheless, the magnitudes assigned to R_p and L_p require prudent selection to ensure they exert negligible impact on the system dynamics.

A MATLAB script governs the overarching simulation protocol, encompassing the initialization of device parameters and the execution of preliminary computations requisite for Simulink. The time-marching process is regulated via the integrated error-controlled variable-step Runge-Kutta Dormand-Prince (RKDP) algorithm (specifically, the *ode45* solver in MATLAB).

In experimental characterizations, it is standard practice to acquire both frequency responses—facilitated by network analyzers performing frequency sweeps—and time-transient responses via function generators operating at single driving frequencies. During the measurement phase, the rate of frequency sweeping must be sufficiently gradual. Excessive sweep speeds prevent the system from attaining a steady-state condition at individual frequency increments, thereby yielding non-stationary responses [53, 395].

To replicate this phenomenon computationally, the simulated frequency response is derived at every discrete frequency coordinate by generating the time-domain

doi:10.6342/NTU202600018

waveform and subsequently extracting the steady-state peak amplitude. At the inception of the simulation process, the initial parameters—specifically displacement, velocity, and phase difference (measured between the driving signal and the displacement maxima)—are initialized to zero, denoted as $(x_1, x_1', \emptyset_{d,1}) = (0,0,0)$. For ensuing successive frequency data points, the initial conditions are established using the steady-state terminal values from the preceding frequency step, such that $(x_i, x_i', \emptyset_{d,i}) = (x_{max,i-1}, 0, \emptyset_{d,i-1} + 90°)$. Given that this study employs a sinusoidal wave function within Simulink to model the driving signal, and recognizing that the phase difference is computed relative to the signal's peak, the excitation for the subsequent frequency interval must commence at a phase of $\emptyset_{d,i-1} + 90°$. This methodology guarantees seamless amplitude transitions across frequency steps, effectively mimicking the continuity of the actual driving signal observed during measurements.

doi:10.6342/NTU202600018

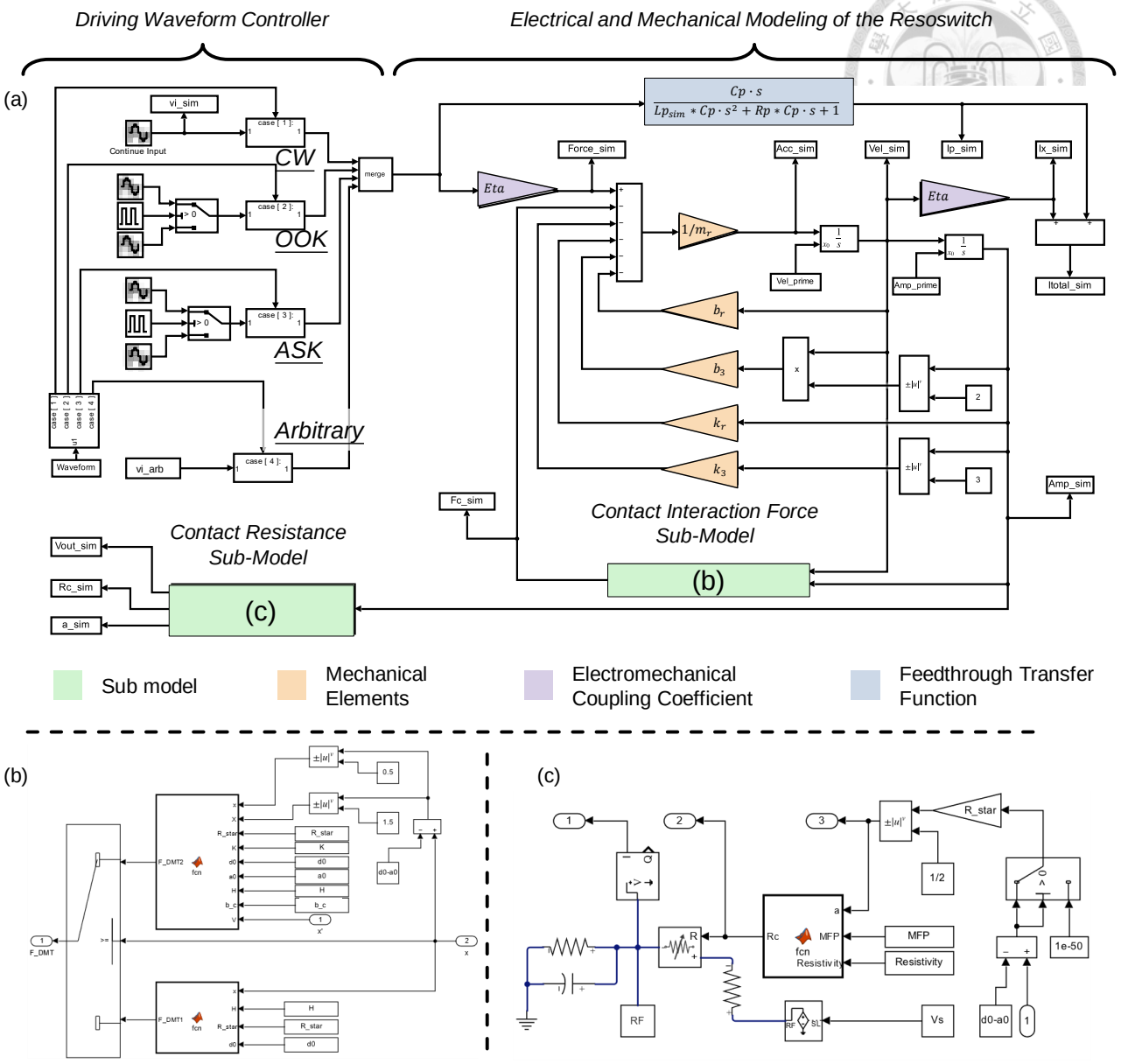


Figure 3-11: (a) Systematic block diagram of the resoswitch and its sub-model for (b) surface interaction force modeling and (c) electrical contact resistance modeling. The "MATLAB function" blocks in (b) and (c) are (3-40) and (3-55), respectively. Reproduced with permission of [316] Copyright of © 2025 IEEE.

Furthermore, the frequency interval characterized by two co-existing stable solutions (specifically, the bistable region or hysteresis region) can be ascertained by employing forward and backward sweeping schemes. It is imperative to refrain from initializing the simulation within this region containing coexisting stable solutions; otherwise, the simulated device response may fail to breach the tapping region and

doi:10.6342/NTU202600018

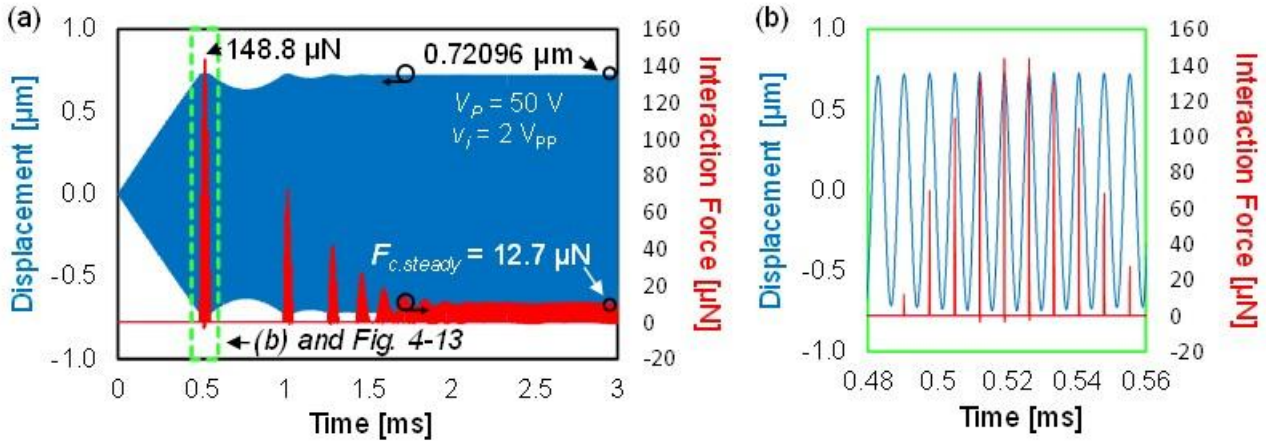


Figure 3-12: (a) Simulated displacement and interaction force time history with continuous driving at linear resonance frequency. (b) Zoom-in view of the boxed region in (a). Reproduced with permission of [316] Copyright of © 2025 IEEE.

instead converge to the lower amplitude solution. To mitigate this risk, the starting frequency ought to be situated significantly outside the bistable region delimited by the grazing frequencies, adhering to the expression

$$\begin{cases} f_{start,forward} = f_{GR,1} - f_a \\ f_{start,backward} = f_{GR,2} + f_a \end{cases} \tag{3-63}$$

wherein the initial terms $f_{GR,i=1,2}$ represent the grazing frequencies described in (3-16), and the subsequent term f_a denotes the offset frequency. Regarding data acquisition, the sampling rate for every block is fixed at 400 points per period of the linear resonant frequency, which guarantees adequate resolution to accurately resolve the phase difference.

3.4.2 Force-Distance Plot

Figure 3-12 (a) illustrates the simulated time-transient response initiating from a rest position, while (b) presents a magnified perspective of the area enclosed within the box in (a). As demonstrated in Figure 3-12 (a), the peak contact force sustained during the transient state is approximately 12-fold higher than the magnitude observed in the steady state. This suggests that within the transient state, resonance effects are

doi:10.6342/NTU202600018

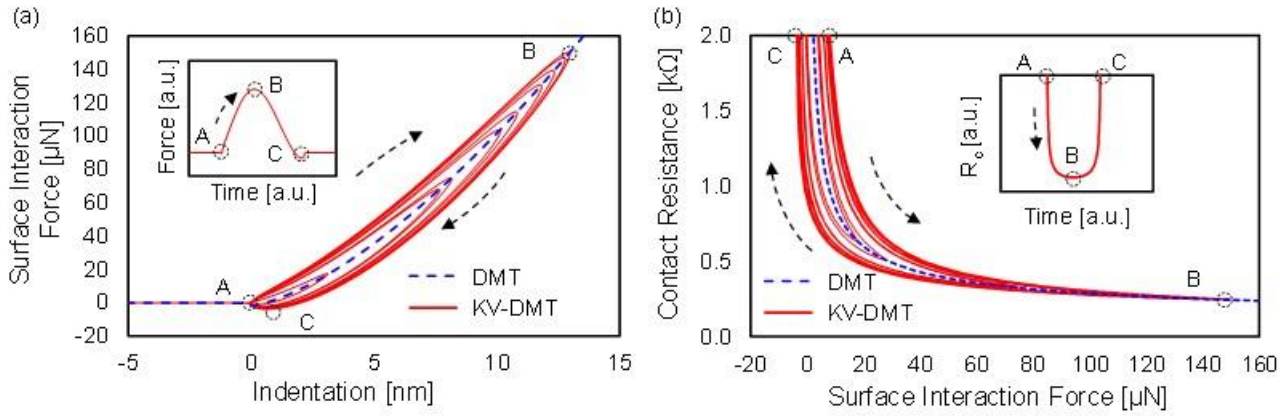


Figure 3-13: (a) Force-indentation plot for the boxed region in Figure 3-12 (a) along with the DMT prediction based on (3-36) and (b) Contact resistance versus surface interaction force plot for the boxed region. The insert figures in (a) and (b) shows the simulated time domain surface interaction force profiles and simulated time-domain contact resistance for one cycle from A to B and back to C, respectively. Reproduced with permission of [316] Copyright of © 2025 IEEE.

preserved alongside an overshooting phenomenon; conversely, in the steady state, these effects attenuate owing to alterations in resonance conditions. As a result, the contact force declines should the operational duration surpass a specific limit. These findings indicate that the resoswitch operates most effectively within the transient state, yielding superior contact force and enhanced signal sensitivity.

3.4.3 Hot Switching Responses

Figure 3-13 (a) and (b) depict the force-indentation plot and the contact resistance versus force plot, respectively, derived via the proposed Simulink model. The illustrated hysteresis loop correlates to the response isolated from the highlighted area in Figure 3-12 (a). Furthermore, the inset diagram displays the simulated time-domain response corresponding to each physical quantity.

The back-end RC circuit, comprising the resistive R_b and capacitive components C_b, is dictated by the applied load resistance, the parasitic capacitance of the cables, and the input resistance and capacitance inherent to the oscilloscope. Based on the equipment datasheet and characterization of the experimental setup, these values of R_b and C_b were determined to are found to be 90 kΩ and 300 pF, respectively. The 90-kΩ

doi:10.6342/NTU202600018

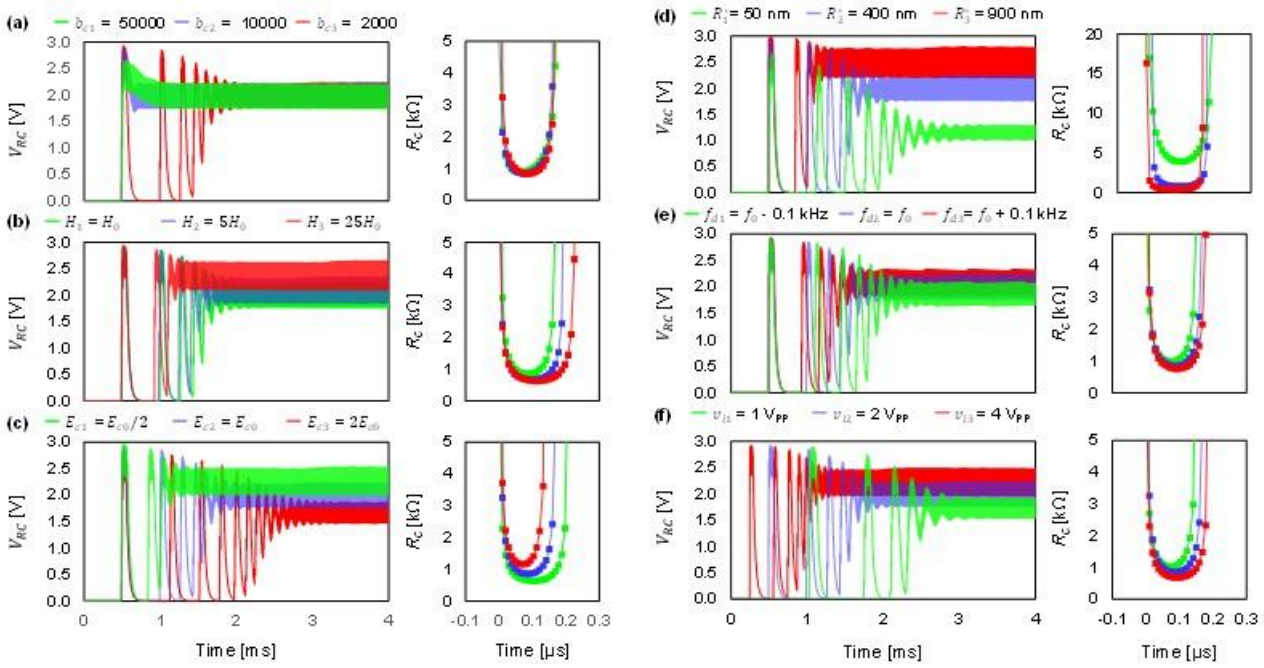


Figure 3-14: Time-domain hot switching responses with zoom-in to the one-cycle steady-state contact resistance history using the Simulink model. The parametric studies on aspects of (a) viscoelastic contact damping, (b) Hamaker contact, (c) Young's modulus of contact material, (d) tip radius, (e) driving frequency, and (f) driving voltage. Reproduced with permission of [316] Copyright of © 2025 IEEE.

resistance value is derived from the parallel combination of a 100-kΩ load resistance and the oscilloscope's 1-MΩ input resistance.

The additional energy provided by adhesion, which augments the contact force, is in agreement with the outcomes of the simulation. Specifically, Figure 3-14 (a) and (b) delineate the influence of viscoelastic contact damping and adhesion force (modulated via distinct Hamaker constant values), respectively. As demonstrated, elevated levels of viscoelastic contact damping and a stronger adhesion force (represented by the Hamaker constant) result in a curtailment of the transient time. Furthermore, an intensification of the adhesion force correlates with an escalation in contact force. It is observed that increased contact force enhances viscoelastic contact damping, a phenomenon ascribed to the rate-dependent hardness inherent in viscoelastic properties. Nevertheless, this elevated contact force does not translate into deeper indentation; consequently, the hot switching voltage output remains largely unaffected.

doi:10.6342/NTU202600018

Additionally, transient times reaching as high as 50 ms are noted when the viscoelastic contact damping is tenuous (specifically, $b_c < 200$).

Figure 3-14 (c) and (d) underscore the influence exerted by the Young's modulus of the contact material and the contact tip radius. While an elevated Young's modulus augments the peak repulsive force, it concurrently diminishes indentation owing to the heightened material stiffness. This attenuation in deformation subsequently compromises both contact damping and adhesion force. Conversely, an expanded asperity radius of curvature bolsters not only the effective contact stiffness but also adhesion and damping. This enhancement stems from the enlarged contact area, which facilitates more adhesive interactions and greater energy dissipation.

Figure 3-14 (e) depicts the impact of driving frequency, wherein the maximal contact force sustained during the transient state scales with the driving frequency, paralleling the behavior observed in the steady-state response. Given that a defining characteristic of resonance is the absence of the overshooting phenomenon [396, 397] , the duration of the transient time decreases as the driving frequency converges upon the nonlinear resonance frequency. Lastly, Figure 3-14 (f) elucidates the consequences of driving voltage; specifically, an increment in driving voltage precipitates a decline in switching time alongside an elevation in the hot switching voltage.

The time integration approach applied to (3-1) produces dependable solutions, contingent upon the minimization of errors stemming from the integration procedure itself. Consequently, the principal challenge resides in the model reduction characterizing (3-1). While the inclusion of additional modes might refine the approximation of the physical system, the present simplified lumped model yields significant insights that demonstrate strong concordance with experimental findings. In this study, simulations were executed on a personal computer equipped with an i7-8700 processor and 32 GB of RAM. Computing a 100-ms simulation requires approximately 2.5 minutes at a high sampling rate. By lowering the sampling rate, the computational duration can be curtailed to 40 seconds, all while preserving accuracy

doi:10.6342/NTU202600018

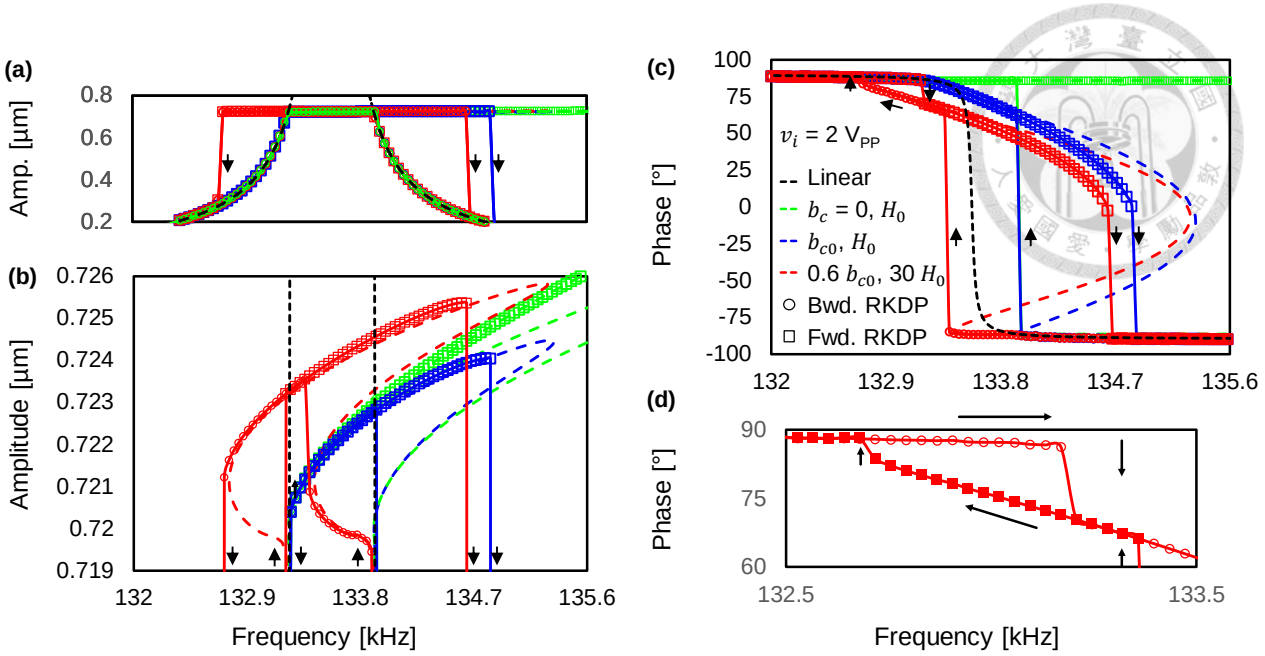


Figure 3-15: (a) Simulated frequency responses and (b) the zoomed-in to the indentation region. (c) the corresponding phase difference responses and (d) the zoomed-in to the left bifurcation region. Several cases with varying viscoelastic contact damping, Hamaker constant, nonlinear stiffness and damping are conducted. The dashed lines show the results by the method of averaging. The solid line with rectangle and circle represents the response simulated by the RKDP method with forward and backward sweeping, respectively. Reproduced with permission of [316] Copyright of © 2025 IEEE.

within permissible tolerances. This degree of simulation efficiency is analogous to the methodology described in [15].

3.4.4 Frequency Responses

The frequency response of the resoswitch is determinable by resolving (3-1) utilizing either the RKDP algorithm or the analytical formulation provided in (3-44). Figure 3-15 depicts the steady-state frequency response regarding displacement amplitude alongside the corresponding phase difference relative to the forcing term. One can discern that the steady-state indentation manifested at the nonlinear resonant frequency is roughly double the magnitude observed at the linear resonant frequency. As demonstrated in Figure 3-15, owing to inherent nonlinearities, the application of a single-tone frequency input within the tapping region of the forward sweep does not invariably excite the device into the tapping mode, a consequence of the presence of

doi:10.6342/NTU202600018

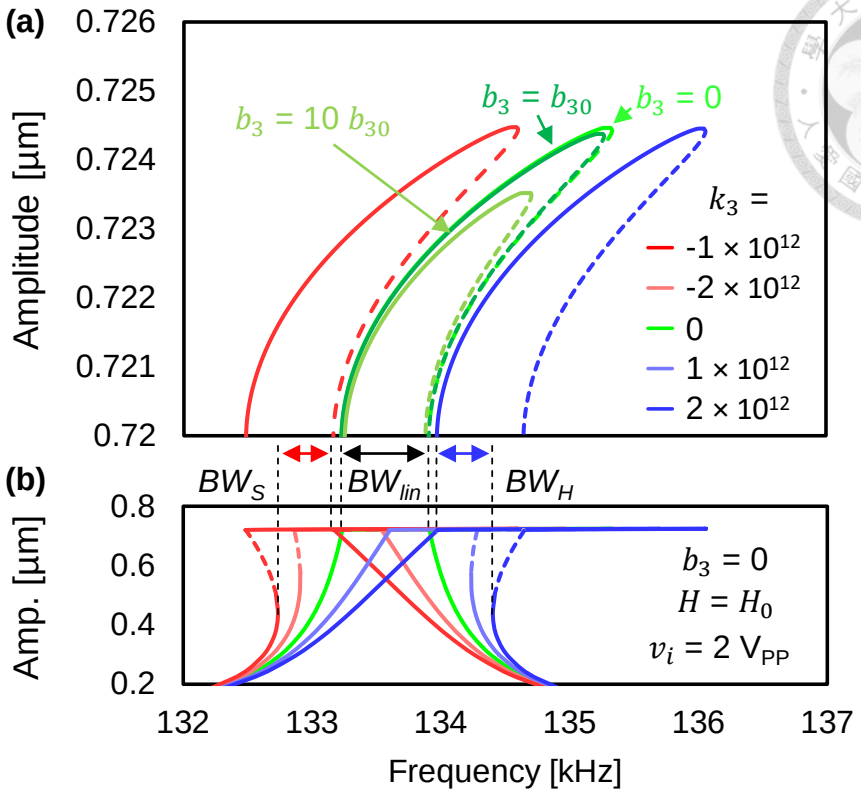


Figure 3-16: Simulated frequency responses with nonlinear stiffness i.e., the Duffing term, of (a) zoom-in to the indentation region and (b) the whole span. (a) also compares varying nonlinear damping, i.e., the van der Pol term. Reproduced with permission of [316] Copyright of © 2025 IEEE.

multiple coexisting solutions. Rather, the effective operating bandwidth wherein the device can be reliably actuated into tapping via a single frequency input is restricted to the overlapping tapping region shared by forward and backward sweeps, a frequency interval characterized by the existence of a unique solution. The grazing condition predicted by (3-16) where $x_l = d_0$, exhibits strong alignment with the nonlinear equation, notwithstanding its derivation from linear theory. This alignment holds true provided that both the attractive force and the Duffing term are maintained at negligible levels.

It is noteworthy that not every analytical solution possesses a numerical counterpart; specifically, analytical solutions unattainable via numerical methods correspond to unstable solutions. Furthermore, as illustrated in Figure 3-15 (a), the incorporation of nonlinear damping displaces the nonlinear resonant frequency and attenuates the

doi:10.6342/NTU202600018

amplitude. Nevertheless, it exerts minimal influence on the vibration amplitude (specifically, the indentation value) within the overlapped region.

Figure 3-16 portrays the frequency response of a generalized nonlinear system, accounting for stiffness and damping nonlinearities arising from Duffing and van der Pol terms. Stability analysis is executed through the evaluation of the Jacobian matrix eigenvalues at equilibrium points, following the treatment detailed in [376]. In Figure 3-16 dashed lines denote the unstable solutions. The additional positive and negative stiffness derived from the Duffing term induces frequency shifts within the system yet impacts the contact force negligibly when the stiffness is weak [53]. Spring softening (or hardening) augments (or diminishes) the contact force at the linear resonance frequency primarily by virtue of the resonance frequency shift, rather than alterations in stiffness itself. Moreover, nonlinear stiffness displaces the overlapped region distally from the linear resonance frequency. Concentrating exclusively on the Duffing term, the jump-up frequency may be solved by equating the derivative of the amplitude in (3-44) to zero, as exemplified in [398]

$$\omega_{D.JU} = \omega_n \left(1 + sign \frac{1}{2} \left(\frac{3}{2} \right)^{\frac{4}{3}} \times \left(\frac{|k_3|}{k_r^3} F_d^2 \right)^{\frac{1}{3}} \right) \tag{3-64}$$

wherein $sign = +1$ applies to a hardening system and $sign = -1$ relates to a softening system. In specific instances, the overlapped tapping region may contract or entirely disappear at particular driving voltages owing to the manifestation of jump-up bifurcation. Such a scenario could preclude the device from accessing the tapping mode operation when subjected to a higher single frequency driving voltage.

The method of averaging permits both amplitude and phase to fluctuate over time, predicated on the premise that the phase remains substantially constant within a specified period. Consequently, phase calculations derived from the time difference between peak or zero crossing points might diverge from those acquired through method of averaging. This discrepancy occurs because, in systems exhibiting sufficient

doi:10.6342/NTU202600018

nonlinearity, the phase evolves slowly over time.

As demonstrated in Figure 3-15, the frequency responses generated via the method of averaging exhibit marked discrepancies when compared to the numerical results. This deviation stems from disparities between the approximated contact force utilized in the averaging method and the original force model of KV-DMT of (3-40). The approximation demonstrates superior fidelity in the region of gentle contact, where indentation is minimal, potentially yielding reduced deviations within that range [376]. Furthermore, within the time domain, the fundamental harmonic may be impacted by the superposition of higher harmonics. This phenomenon, compounded by the constraints of numerical time resolution, can induce calculation inaccuracies [399]. Regarding nonlinear systems, the degree of nonlinearity depicted in Figure 3-15 constitutes a near-critical scenario for first-order approximation. In this context, the free-air vibration amplitude is approximately 2.4 times the magnitude of the gap clearance. This ratio precipitates significant errors and imprecise characterization, although the general trend maintains consistency as nonlinearity or amplitude escalates further. To enhance precision, future investigations should integrate higher-order terms.

For devices functioning in the vicinity of linear resonance, the proposed time constant equation for the back-end RC circuit exhibits strong corroboration with time integration simulations (virtually overlapping, though not graphically presented). However, the nonlinear switching time formula remains intractable via perturbation theory—whether through the method of averaging or the method of multiple scales—to the best of the author's current knowledge.

3.4.5 Steady-State Peak Repulsive Force

It is advantageous to establish a closed-form analytical expression regarding the peak repulsive force for a device actuated by a single-frequency input in the vicinity of the linear resonance frequency. By neglecting the influence of surface interaction force, (3-44) may be simplified to the following representation

doi:10.6342/NTU202600018

$$x_{vD.f} = \frac{A_d \cos(\omega_d t - \phi)}{m_r \sqrt{\bar{\bar{A}}^2 + \bar{\bar{B}}^2}} \tag{3-65}$$

wherein the parameters $\bar{\bar{A}}$ and $\bar{\bar{B}}$ are defined as

$$\bar{\bar{A}} = (1 + K_D)\omega_n^2 - \omega_d^2 \tag{3-66}$$

$$\bar{\bar{B}} = \omega_n(2\xi + C_{vdP})\omega_d \tag{3-67}$$

As previously noted, nonconservative surface interaction forces become insignificant when the device operates in proximity to the linear resonance frequency. Adopting the derivation methodology presented in [376], wherein the DMT model is approximated via a Taylor series expansion, the peak repulsive force is expressed as

$$F_{vD.DMT} = 2^{\frac{1}{8}} 3^{-\frac{1}{4}} \pi^{\frac{3}{4}} E^{*\frac{1}{4}} R^{*\frac{1}{8}} A_{ratio}^{\frac{9}{8}} A_0^{\frac{9}{8}} k_r^{\frac{3}{4}} Q_{eff}^{-\frac{3}{4}} \chi_{vD}^{\frac{3}{4}} + \frac{F_{ad}}{2} \tag{3-68}$$

in which A_{ratio} is defined and simplified as

$$A_{ratio}^2 = \left(\frac{x_{T.f}}{x_{vD.f}}\right)^2 = \frac{\bar{\bar{A}}^2 + \bar{\bar{B}}^2}{\hat{A}^2 + \hat{B}^2} \approx \frac{A_0}{d_0} \tag{3-69}$$

and the frequency response function χ_{vD} is provided by

$$\chi_{vD} = Q_{eff}\left(\Omega_d^2 - \Omega_{eff.D}^2\right) + \sqrt{\frac{1}{A_{ratio}^2}\left[\Omega_d^2 + Q_{eff}\left(\Omega_{eff.D}^2 - \Omega_d^2\right)^2\right] - \Omega_d^2} \tag{3-70}$$

F_{ad} denotes the adhesion force, formulated as

$$F_{ad} = \frac{HR^*}{6a_0^2} \tag{3-71}$$

Q_{eff} signifies the effective quality factor, represented by

$$Q_{eff} = \left(2\xi + \frac{1}{4}\frac{b_3 d_0^2}{m_r \omega_n}\right)^{-1} \tag{3-72}$$

doi:10.6342/NTU202600018

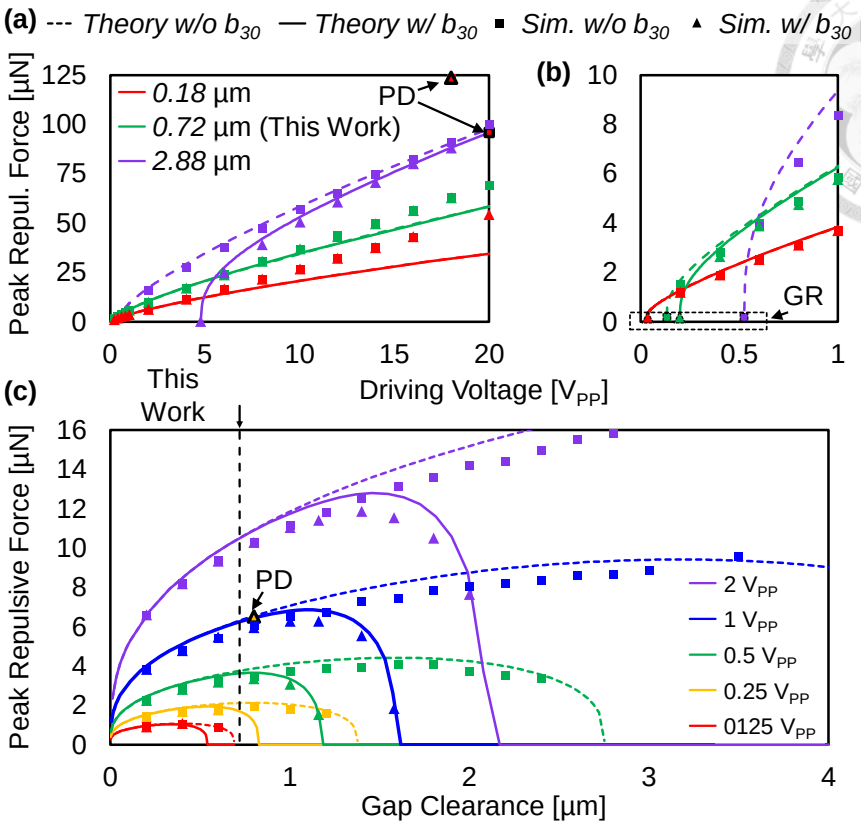


Figure 3-17: Simulated peak repulsive force map as a function of (a) driving voltage, (b) zoom-in to the small driving voltage region from (a), and (c) gap clearance. Reproduced with permission of [316] Copyright of © 2020 IEEE.

Under conditions where the device is actuated at the center frequency of the Duffing backbone curve (i.e., $\omega_d = \omega_n[1 - 3k_3 d_0^2/(8k_r)]$), χ_{vD} can be reduced as

$$\chi_{vD} = \sqrt{\frac{1}{A_{ratio}^2} - 1} \tag{3-73}$$

By differentiating (3-68) with respect d_0 while operating at the center frequency, it is established that an optimal value for gap clearance exists which results in a maximum contact force, representing the form

$$d_{0.op} = 3^{-\frac{1}{2}} A_0 \approx 0.5773 A_0 \tag{3-74}$$

Upon substituting (3-74) into (3-68), the maximal contact force corresponding to a

doi:10.6342/NTU202600018

specific driving force at the center frequency is determined to be

$$F_{vD.DMT.op} = 2^{\frac{1}{8}}\pi^{\frac{3}{4}}\left(3^{-\frac{7}{6}} - 3^{-\frac{13}{6}}\right)^{\frac{3}{8}} E^{*\frac{1}{4}} R^{*\frac{1}{8}} k_r^{\frac{3}{4}} Q^{-\frac{3}{4}} A_0^{\frac{9}{8}} + \frac{F_{ad}}{2} \tag{3-75}$$

Alternatively, if the frequency shifting attributed to the Duffing term is disregarded,(3-70) allows for simplification in the form of

$$\chi_{vD} = Q_{eff}(\Omega_d^2 - 1) + \sqrt{\frac{1}{A_{ratio}^2}\left[\Omega_d^2 + Q_{eff}(1 - \Omega_d^2)^2\right] - \Omega_d^2} \tag{3-76}$$

When operating at the linear resonance frequency, the frequency response function χ_{vD} simplifies to the form presented in (3-73) , predicated on the assumption that the influence of the Duffing term regarding amplitude is negligible.

Figure 3-17 collocate the analytical steady-state contact force derived from (3-68) against the results obtained through simulation. In this context, the driving frequency is fixed at the center frequency of the Duffing backbone curve. Figure 3-17 (a) illustrates the peak repulsive force across a range of driving voltages for distinct gap spacings, while Figure 3-17 (b) offers a magnified perspective of the low driving voltage region. Both scenarios—those incorporating van der Pol damping and those excluding it—are examined. As observed in Figure 3-17 (b), the initial voltage point exhibiting a contact force equivalent to the adhesion force defines the grazing voltage. Devices subject to van der Pol damping demonstrate elevated grazing voltages. Although a reduced gap clearance produces a higher contact force at low driving voltages, an increased gap clearance exhibits superior contact force immediately upon exceeding its specific grazing voltage. These findings diverge somewhat from previous investigations [310, 400] regarding contact force, which consistently advocated for minimized clearance.

Figure 3-17 (c) further elucidates the influence of gap clearance, indicating that the maximal contact force is realized at approximately 0.58× the free vibration amplitude when the van der Pol term is neglected. Conversely, with the inclusion of van der Pol

doi:10.6342/NTU202600018

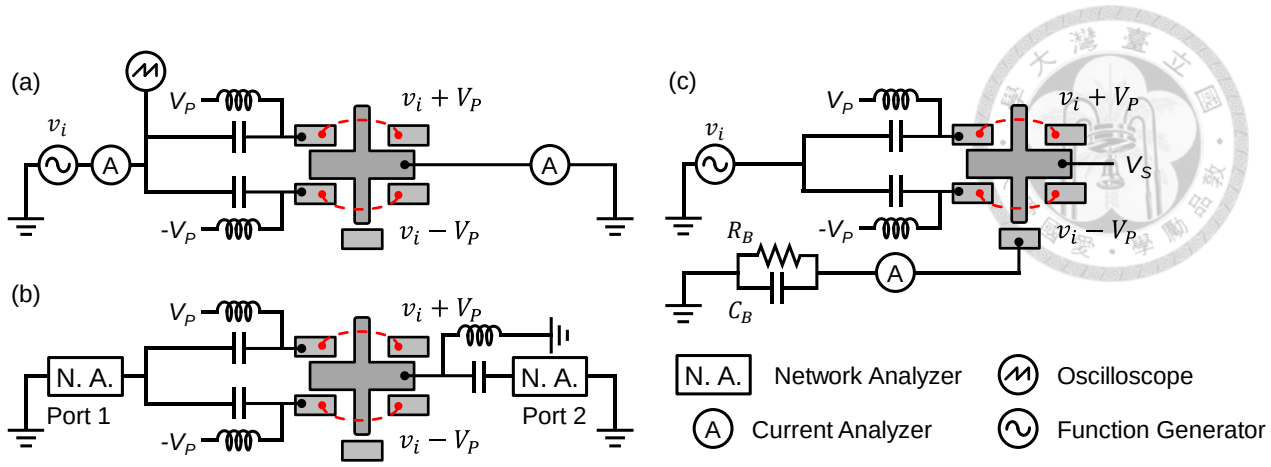


Figure 3-18: Measurement set-up for (a) time-domain motional current, (b) electrical frequency response, and (c) hot switching operation, respectively. Reproduced with permission of [316] Copyright of © 2025 IEEE.

damping, the peak contact force shifts to a lower vibration amplitude; this is attributed to the reduction in effective Q as the vibration amplitude escalates. In certain instances, significantly higher peak contact forces are detected within the simulation, stemming from the onset of period-doubling bifurcation [107]. The oscillation amplitude associated with period-doubling bifurcation modulates at a low frequency; this causes a corresponding fluctuation in contact force, thereby making the peak contact force greater than theoretical predictions.

3.5 Device Characterization

This section delineates the characterization of resoswitches, encompassing frequency responses alongside time-domain responses observed during ring-down, forced vibration, and hot switching. The data collected is utilized to extract key parameters from the fabricated devices. Subsequently, post-simulations founded upon these derived parameters are conducted to provide a comparative analysis against the measured results.

3.5.1 Measurement Set-up

Figure 3-18 (a) depicts the experimental configuration for non-hot-switching (or tapping/cold switching) time-domain motional current acquisition, utilizing a function generator alongside a current waveform analyzer. Subsequently, Figure 3-18 (b)

doi:10.6342/NTU202600018

presents the arrangement for frequency transmission quantification employing a network analyzer. For the tapping mode assessments in both Figure 3-18 (a) and (b), the output electrode remains floating, while the structure is held at zero bias. Differential biasing is applied to the input electrodes using a polarization bias $\pm V_P$, wherein the driving voltage v_i is merged with the bias voltage via bias-tees. Conversely, Figure 3-18 (c) details the schematic for hot switching measurements; here, the output electrode is coupled to a load/bleeding resistance, and the resonant structure undergoes biasing at V_S. All experimental procedures were executed within a vacuum probe station maintained at a pressure of 10^{-5} Torr.

Given that the resoswitch input exhibits high input impedance relative to the signal source (either the network analyzer or function generator)—which inherently possesses a 50-Ω source impedance—the device theoretically receives a driving voltage double that of the power level configured on the source instrument. For instance, a source power setting of 10 dBm yields a driving voltage of 2 V_{PP} across a 50 Ω load, but translates to 4 VPP across a high-impedance load. Nevertheless, the bias-tees employed in this study, characterized by a lower cut-off frequency of 10 MHz (ZFBT-282-1.5A+, Mini-Circuits), induce signal attenuation in the ac signal, corresponding to a factor of 0.69 based on empirical measurements. Consequently, the effective driving voltage delivered to the high-impedance input port is approximately 2.76 V_{PP} when the signal source (with 50-Ω impedance) is adjusted to 10 dBm.

Regarding the time-transient characterizations referenced in Figure 3-18 (a), device actuation is facilitated by a function generator (33600A, Keysight). To mitigate signal loss, the device output is directly coupled to a current waveform analyzer (CWA, CX3300A equipped with a CX1103A sensor head, Keysight), bypassing the use of a bias-tee. A power supply (E3647A, Keysight) furnishes the DC polarization bias. For the acquisition of phase data regarding the driving signal, the input signal originating from the function generator is monitored concurrently (CX3300A with CX1101A sensor head, Keysight) and routed to a high-impedance terminal oscilloscope

doi:10.6342/NTU202600018

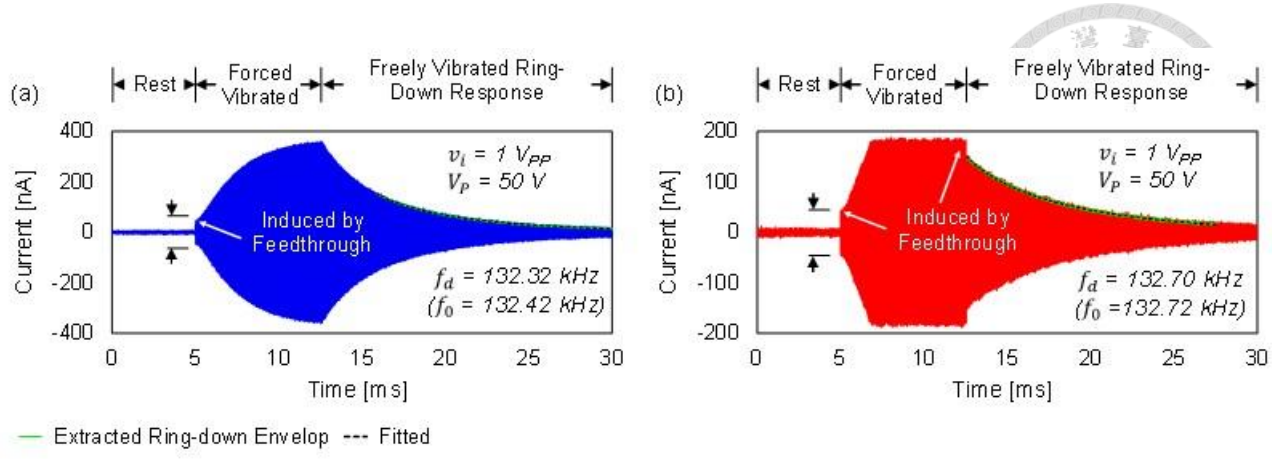


Figure 3-19: Measured motional current output responses of (a) a resonator (without stoppers) and (b) a resoswitch for the ring-down test. Reproduced with permission of [316] Copyright of © 2025 IEEE.

(DSOX2004A, Keysight). In the context of frequency response characterization as shown in Figure 3-18 (b), the ac driving signal is sourced from a network analyzer (E5080A, Keysight). The sweep speed underwent meticulous calibration to avert non-stationary responses [53, 129] and to regulate the cold switching cycle. Specifically, the configuration utilized an IF bandwidth of 20 Hz and 1601 frequency points, with the frequency span tailored to the specific region of interest. Finally, for hot switching characterization, the resulting output switching waveforms are recorded via the oscilloscope (DSOX2004A, Keysight).

In this section, three specific characterization protocols for the tapping operation are executed: the time-transient ring-down response, the forced time-transient response, and the frequency response. The time-transient ring-down responses serve as the basis for isolating the parameters of the nonlinear damping b_3 and the electromechanical coupling coefficient η. Subsequently, frequency transmission measurements are undertaken to derive the equivalent electrical model of the resonator, the nonlinear stiffness k_3, and the viscoelastic contact damping b_c. Conversely, the hot switching responses are utilized to determine the viscoelastic contact damping, the effective radius of curvature, and the electrical properties of the contact a-spot under hot switching conditions.

doi:10.6342/NTU202600018

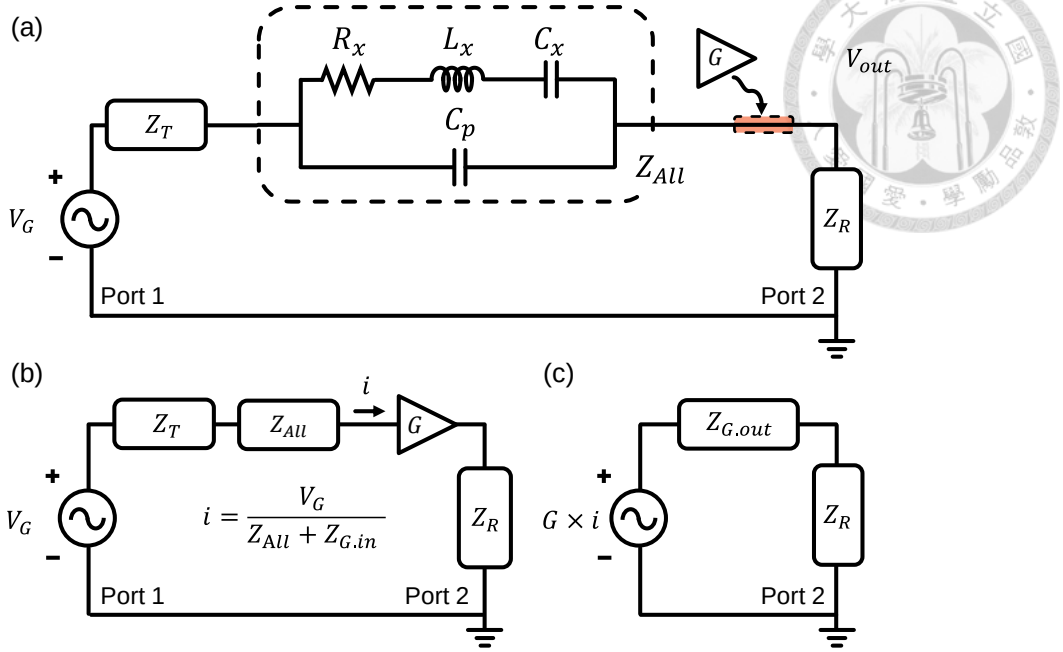


Figure 3-20: (a) Equivalent circuit for the experimental set-up of frequency response measurement using the network analyzer. (b) The equivalent circuit when using a transimpedance amplifier. (c) The simplified equivalent circuit for (b). Reproduced with permission of [316] Copyright of © 2025 IEEE.

3.5.2 Ring-Down Responses

Figure 3-19 (a) and (b) graph the device response transitioning from a rest state to forced vibration—in the absence and presence of stoppers, respectively—and subsequently entering the ring-down phase. In particular, Figure 3-19 (b) captures the tapping response manifesting between the structure and the stopper during the period of forced vibration. The electromechanical coupling coefficient may be determined experimentally by utilizing the gap spacing visualized in SEM micrographs $d_{0.SEM} = 0.72\ \mu m$ alongside the measured motional current I^* at the onset of the ring-down sequence, as follows

$$\eta = \frac{I^*}{x'} \approx \frac{I^*}{\omega_d d_{0.SEM}} = \frac{154\ nA}{2\pi \times 132.4\ kHz \times 0.72\ \mu m} = 2.5711 \times 10^{-7}\ A/m \tag{3-77}$$

wherein the driving frequency is aligned with the linear resonance frequency. TABLE 3-4 presents a comparative summary of the extracted parameters relative to their

doi:10.6342/NTU202600018

theoretical counterparts. Furthermore, the nonlinear damping is determined via curve fitting techniques applied to the ring-down responses. Drawing upon the work presented in [401], which characterizes free vibration as governed by the van der Pol-Duffing equation, the dimensionless vibration amplitude derived via the method of averaging is formulated as

$$\hat{x}(t) = \frac{e^{-\xi t}}{\sqrt{1 + \frac{B_3}{8\xi}(1 - e^{-2\xi t})}} \tag{3-78}$$

wherein the dimensionless displacement amplitude is characterized by $\hat{x} = x/x_0^*$ and the dimensionless van der Pol damping is defined as $B_3 = b_3 {x_0^*}^2/(m_r \omega_0)$; notably, this formulation exhibits a minor deviation from the definition previously applied to forced vibration. In this context, $d_{0.SEM}$ functions concurrently as the reference dimension x_0^* and as the initial gap spacing governing the ring-down sequence. The Q factor extracted for the linear region, characterized by minimal vibration amplitudes, is denoted as $Q_{time} \approx 3020$ whereas the extracted nonlinear damping values are tabulated in TABLE 3-4.

3.5.3 Frequency Domain Response and Electrical Model

Figure 3-20 (a) depicts the equivalent circuit corresponding to the experimental configuration for frequency response acquisition, employing a network analyzer in conjunction with an optional transimpedance amplifier (TIA, HF2TA, Zurich Instruments). Specifically, Figure 3-20 (b) and (c) illustrate simplified equivalent circuit models derived from (a); in these schematics, the current signal undergoes preliminary amplification via a transimpedance amplifier (TIA) characterized by a gain G (measured in units of resistance) prior to being directed to Port 2 of the network analyzer. The TIA operates as a voltage source delivering $G \times i$ to Port 2 of the network analyzer. In this framework, the input and output resistances of the amplifier, as well as the terminal resistances associated with the input and output ports (designated as $Z_{G.in}$, $Z_{G.out}$, Z_T, and Z_R, respectively, are uniformly defined as $Z_0 =$

doi:10.6342/NTU202600018

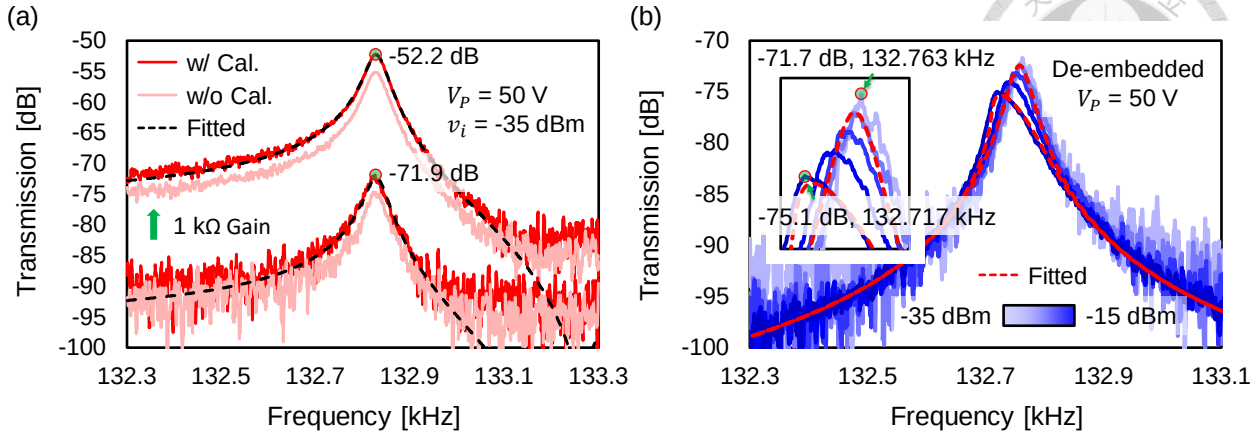


Figure 3-21: (a) Measured transmissions of the resonator with and without the transimpedance amplifier and calibration. (b) Measured transmissions of the resonator with varying driving power level. In (b), the transmission peak is banded to the left due to negative Duffing term and the transmission level decreases as the driving power increases due to the present of the van der Pol term. Reproduced with permission of [316] Copyright of © 2025 IEEE.

50 Ω). Additionally, v_G denotes the voltage source originating from the instrument. Consequently, the transmission coefficients, determined both in the absence and presence of the TIA, are expressed as [402-404]

$$S_{21} = 20\,log_{10}\left(\frac{v_{out}}{\frac{1}{2}v_G}\right) = 20\,log_{10}\left(\frac{2Z_R}{Z_T + Z_{All} + Z_R}\right) = 20\,log_{10}\left(\frac{2Z_0}{Z_{All} + 2Z_0}\right) \tag{3-79}$$

$$S_{21.Gain} = 20\,log_{10}\left(\frac{v_{out}}{\frac{1}{2}v_G}\right) = 20\,log_{10}\left(\frac{2Gi\frac{Z_R}{Z_{G.out}+Z_R}}{Z_T + Z_{All} + Z_{G.in}}\right) = 20\,log_{10}\left(\frac{Gi}{Z_{All} + 2Z_0}\right) \tag{3-80}$$

where v_{out} is the voltage at the receiving end. Based on (3-79) and (3-80), the equivalent circuit elements, R_x, L_x, C_x, and C_p are extracted using least squares fitting.

Figure 3-21 (a) displays the measured linear frequency response of a resonator, contrasting the results obtained with calibration against those acquired without. This resonator is analogous to the resoswitch, distinguished primarily by the exclusion of

doi:10.6342/NTU202600018

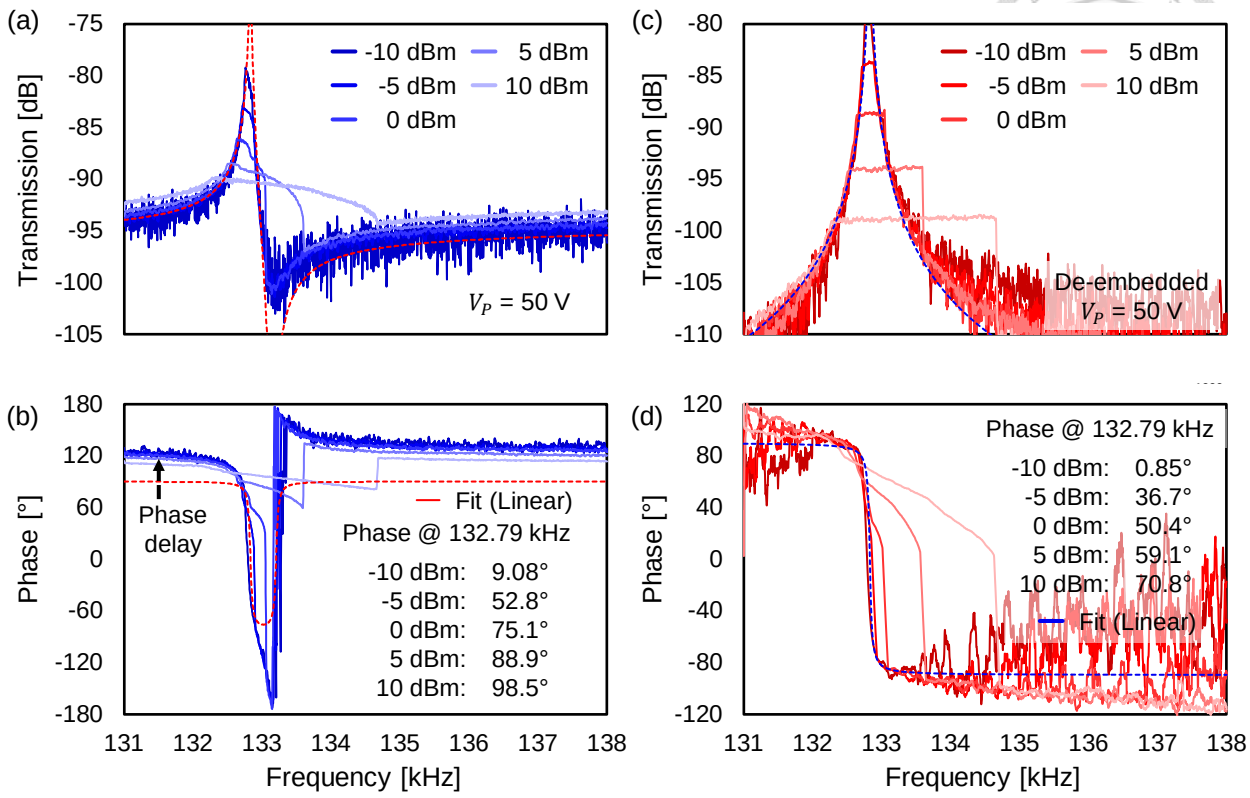


Figure 3-22: Measured responses of the resoswitch from the linear to tapping mode. (a) and (b) are the responses before de-embedding, and (c) and (d) are the responses after de-embedding. In (b), the feedthrough screens the actual phase features of the device while in (d), the phase difference at the linear resonant frequency approaches 90° as the driving power increases. Reproduced with permission of [316] Copyright of © 2025 IEEE.

the output electrode/stopper, a modification that facilitates the isolated characterization of the resonator's performance. As demonstrated, the integration of a TIA with a 1-kΩ gain augments the signal-to-noise ratio, thereby contributing to the refined accuracy of parameter extraction. By synthesizing (3-12)-(3-14) and (3-77), the linear mechanical model of the resonator is derived. The quality factor determined via the extracted RLC parameters is $Q_{freq} \approx 2930$, a value that aligns closely with the result obtained from the ring-down method ($Q_{time} \approx 3020$).

Subsequently, the nonlinear frequency responses of the resonator are utilized to quantify the device's nonlinear stiffness k_3. As documented in [405] and [406], feedthrough capacitance has the potential to obscure the genuine response of the

doi:10.6342/NTU202600018

resonator, leading to erroneous estimations of both the quality factor and the mechanical resonant frequency. Furthermore, the superposition of Duffing nonlinearity and feedthrough capacitance can induce an anomalous frequency response morphology characterized by inverse distortion [407]. Consequently, to mitigate the influence of feedthrough capacitance, a de-embedding technique is implemented during the extraction of nonlinear stiffness [408-410].

Figure 3-21 (b) depicts the de-embedded transmission responses obtained from a resonator subjected to modulating driving power throughout a backward frequency sweep. As illustrated, both the transmission amplitude and the resonance frequency exhibit fluctuations concomitant with escalating driving power, thereby signifying the presence of nonlinear stiffness and damping within the device. Specifically, the nonlinear stiffness induces a frequency shift of approximately 300 ppm and an amplitude attenuation of roughly 3.5 dB across a driving range spanning -35 dBm to -15 dBm. Predicated on the previously established linear model, a driving input of -15 dBm corresponds to a displacement of 0.88 μm. Nevertheless, owing to nonlinear damping, the actual displacement is diminished to 0.59 μm, as inferred from the measured transmission amplitude.

While stiffness and damping nonlinearities are extractable from empirical frequency responses via curve-fitting algorithms [410, 411], such an approach necessitates a significantly larger volume of measurement data and involves labor-intensive processing to disentangle and isolate these dual effects. In this study, the extraction of nonlinear damping b_3 is decoupled from the nonlinear stiffness by employing the time-domain ring-down method delineated in the preceding subsection [401]. Utilizing the derived value of b_3, the nonlinear Duffing term k_3 is readily determined via the resonance frequency shift (*cf.* Figure 3-21 (b)) from (3-53). The resulting value for k_3 is tabulated in TABLE 3-4.

Beyond expediting parameter extraction, de-embedding serves to retrieve the genuine signal indicative of device motion, devoid of interference from electrical

doi:10.6342/NTU202600018

feedthrough. Figure 3-22 (a)-(b) and (c)-(d) juxtapose the frequency responses of the resoswitch in the absence and presence of de-embedding. As demonstrated, the tapping bandwidth broadens with increasing driving power, a consequence of the highly nonlinear hardening effect induced by impact during the forward sweeping operation. Figure 3-22 (b) exhibits a global phase shift relative to the model defined by (3-16), revealing that the measurement setup imparts a phase delay along the signal path. As observed in Figure 3-22 (a) and (b), the feedthrough induces an anti-resonance, causing distortion in both amplitude and phase. Following de-embedding, Figure 3-22 (c) and (d) reveal the responses originating from the actual mechanical motion. Specifically, the amplitude transmission in Figure 3-22 (c) exhibits a relatively uniform response across the tapping region; concurrently, as depicted in Figure 3-22 (d), the phase response evolves progressively from 90° to 0°, demonstrating a more gradual phase transition than that observed in the linear case.

doi:10.6342/NTU202600018

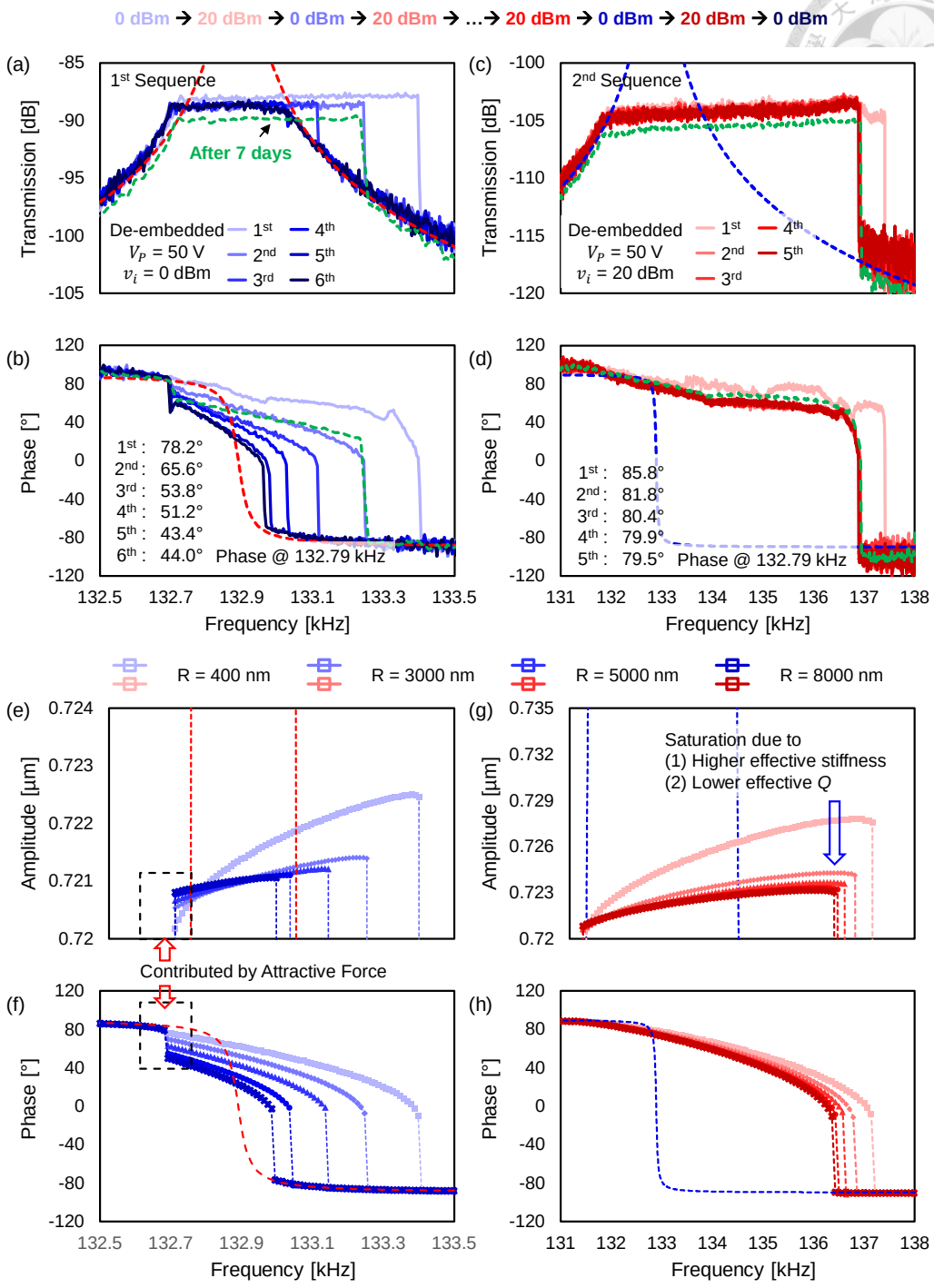


Figure 3-23: Measured and simulated frequency responses with the input power cycling between 0 dBm and 20 dBm. (a) and (b) show the transmission and phase measurement results at 0 dBm for each run, respectively, while (c) and (d) show the transmission and phase measurement results at 20 dBm for each run. (e), (f), (g), and (h) represent simulations based on curve fitting of the effective tip radius. Reproduced with permission of [316] Copyright of © 2025 IEEE.

doi:10.6342/NTU202600018

Conversely, this study notes that the effective tip radius of the contact surface undergoes evolution driven by impact and material tribological properties. By modulating the driving power between 0 and 20 dBm applied to a resoswitch immediately following release, Figure 3-23 (a)-(b) delineates the amplitude and phase responses across the initial alternating cycles. As demonstrated, during the primary cycle at 0 dBm, the phase response exhibits significant fluctuation; conversely, the 20-dBm scenario exhibits a downward jump prior to attaining resonance (specifically, the 0° phase shift). This behavior implies that the contact surface condition lacks stability, causing the system dynamics to undergo specific perturbations during operation.

Furthermore, the tapping bandwidth associated with the 0-dBm instances (*cf.* Figure 3-23 (a)) contracts and progressively converges toward a constant magnitude following each exposure to large contact force induced by the preceding 20-dBm drive. In contrast, regarding the 20-dBm scenarios in Figure 3-23 (c), the tapping bandwidth remains virtually unaltered, a consequence of the pronounced hardening effect and viscoelastic damping present under the comparatively higher driving force. Given that these measurements are conducted on the device immediately post-release, the observed variation in tapping bandwidth is attributed more plausibly to plastic deformation or stress relaxation [358, 359, 411] as opposed to superficial oxide breakdown [412]. Nevertheless, the green dashed line in Figure 3-23 (a)-(d) depicts the response of the identical device after a seven-day interval. Here, the tapping bandwidth under 0-dBm driving reverts to a broader range, indicating an alteration in surface condition likely stemming from oxidation.

To validate the aforementioned empirical results, Figure 3-23 (e)-(h) presents the simulated amplitude and phase, incorporating a specific viscoelastic contact damping and a variable tip radius derived via curve fitting to the measured data in Figure 3-23 (a)-(d). The fitting protocol commences with the initial cycle for both 0 dBm and 20 dBm. It is established that a tip radius of 400 nm combined with a viscoelastic contact damping of $b_c = 50000$ N•s/m2 yields tapping bandwidths and phases that exhibit the

doi:10.6342/NTU202600018

optimal fit with the experimental outcomes for the initial cycles at both power levels. For every subsequent cycle, the effective contact radius is estimated utilizing the measured tapping bandwidth and phase from the 0-dBm instances. As illustrated in Figure 3-23 (g)-(h), the tapping bandwidths corresponding to the 20-dBm cases display relative insensitivity to the contact radius, a finding consistent with the empirical data in Figure 3-23 (c)-(d). The frequency saturation observed in the 20-dBm scenarios represents the cumulative impact of augmented contact stiffness and viscoelastic damping within the region dominated by repulsive force. Conversely, for the 0-dBm cases, the attractive force escalates more rapidly than the repulsive force as the contact radius expands, precipitating a shift in the nonlinear resonant frequency toward a lower value.

Furthermore, the preceding measurements suggest that the resoswitch undergoes plastic deformation during the frequency sweep, culminating in an enlarged contact area and diminished contact pressure. Additionally, since the contact surface is susceptible to oxidation and contamination [349], the decline in contact pressure may impede the resoswitches from penetrating the contact surface oxide. This, in turn, prevents the devices from executing normal hot switching when operating as a receiver under standard single-frequency driving. Indeed, the majority of devices in this investigation fail, exhibiting high-impedance contact resistances attributable to surface oxidation and reduced contact pressure.

3.5.4 Forced Time-Transient Responses

Figure 3-24 displays the time transients of the received current and phase evolution for a 1000-cycle sinusoidal input applied to (a) a standard resonator (lacking output electrodes/stoppers) and (b) a resoswitch. During the initial duration of approximately 1 ms, both phase responses adhere to the behavior of a typical linear system, converging toward a ~0° phase shift. The phase shift is characterized and computed based on the signal peaks detected between the input driving signal and the output current signal (*cf*. Figure 3-24 (a)). It is noteworthy that the measured current comprises

doi:10.6342/NTU202600018

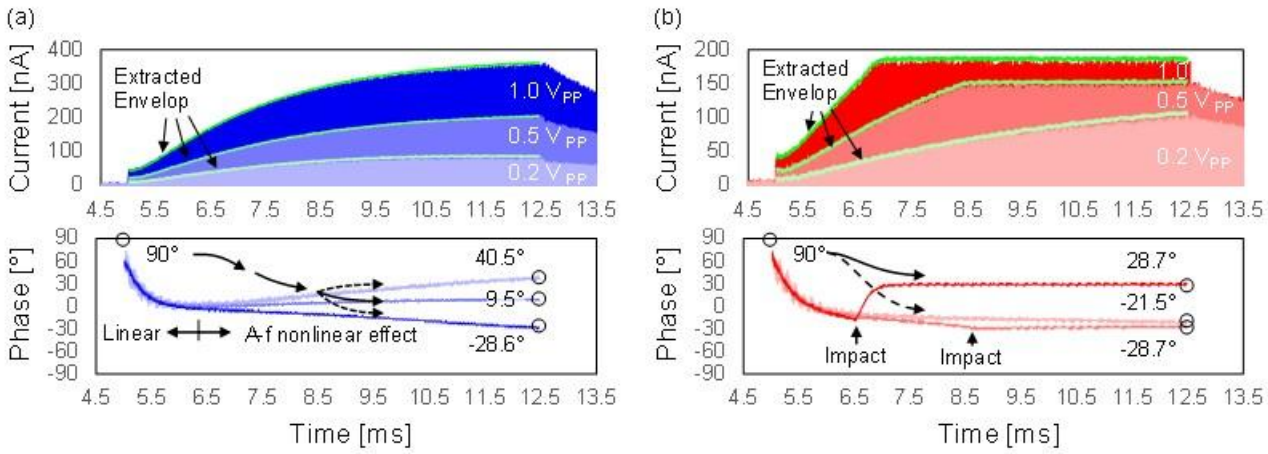


Figure 3-24: Measured motional current output responses of (a) a resonator (without stoppers) and (b) a resoswitch for forced vibration test with varying driving voltage. The results illustrate the effect of nonlinearities under different driving levels. Reproduced with permission of [316] Copyright of © 2025 IEEE.

two distinct components: the feedthrough current and the motional current. Initially, the feedthrough current dominates; however, the motional current progressively intensifies and eventually supersedes the feedthrough component. As depicted in Figure 3-24 (a), the phase responses corresponding to various driving amplitudes incrementally stabilize at distinct phase levels, a result of the amplitude-frequency effect. In juxtaposition, Figure 3-24 (b) demonstrates that at a driving level of 1 V_{PP}, the resoswitch traverses the linear resonance condition before rapidly shifting to an alternative phase level upon the incidence of impact, owing to contact damping. At the 1 V_{PP} driving level, the repulsive force governs the system, thereby elevating the resulting resonance frequency above the linear resonance frequency. Consequently, the phase response stabilizes at ~28.7°, a value significantly divergent from that of the 0.2-V_{PP} instance, which serves as a reference for the non-tapping, albeit nonlinear, condition. Conversely, for the 0.5-V_{PP} driving level, the attractive force dominates during impact, yielding a resonance frequency inferior to the linear resonance frequency. Thus, the phase response in this scenario converges to a value marginally lower than that of the 0.2-V_{PP} case.

doi:10.6342/NTU202600018

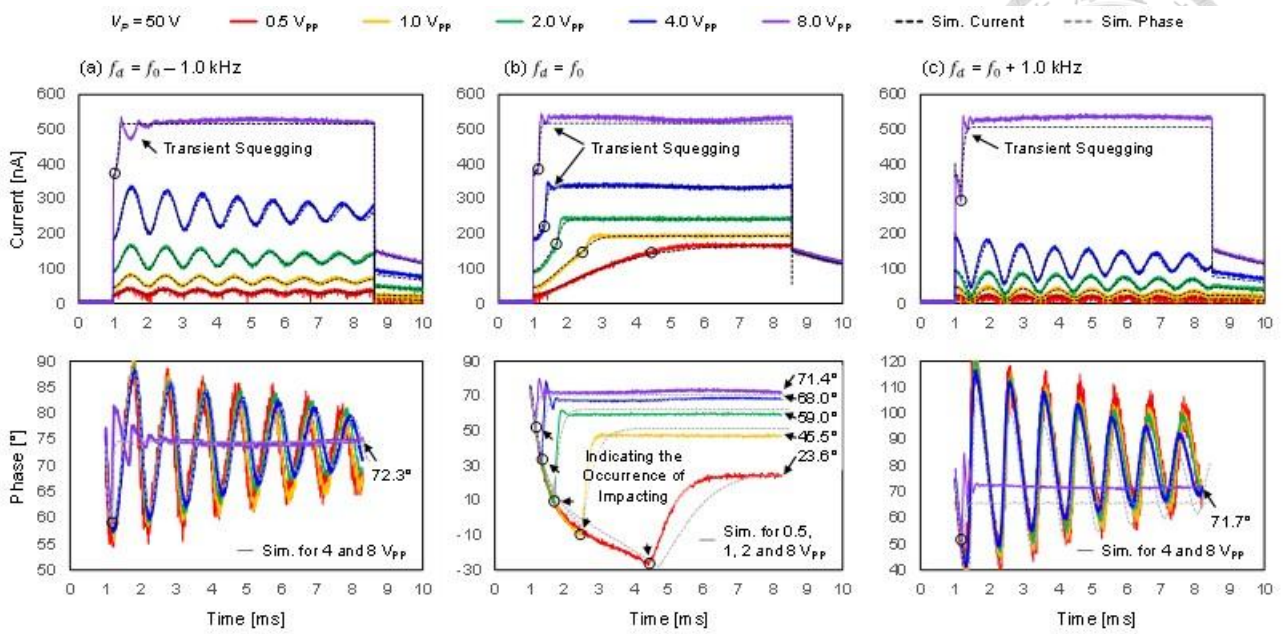


Figure 3-25: Measured current output responses and associated phase responses for signal peak envelope when driving the resoswitch at (a) $f_0 - 1$ kHz, (b) f_0, and (c) $f_0 + 1$ kHz. Significant overshooting and beating phenomenon can be observed when the device is driven at off-resonance condition in the non-tapping region. The overshooting can also be seen in the tapping region especially for large driving voltage. The overshooting in the tapping region is referred to transient squegging in this work. Reproduced with permission of [316] Copyright of © 2025 IEEE.

It is further noted that impact induces additional damping, which precipitates a condensed settling time for the device relative to non-impact conditions. A systematic examination is presented in Figure 3-25 (a)-(c), wherein the curves represent the envelopes and phases of the current signal for varying driving amplitudes at the linear resonance frequency in (b) and offset by 1 kHz in (a) and (c). The applied driving signal consists of a 1000-cycle burst sinusoidal signal. As illustrated in Figure 3-25 (b), the current signal associated with each driving amplitude ascends and stabilizes at a specific level. The circles denote the instant the device initiates the tapping mode, at which point the corresponding phase exhibits an abrupt transition signaling the occurrence of impacting. Additionally, for the two comparatively higher driving levels of 4 V_{PP} and 8 V_{PP}, overshooting within the current amplitude is detected. This behavior is characterized here as a *transient squegging phenomenon*, referring to the scenario

doi:10.6342/NTU202600018

where the device response oscillates slowly around its steady-state value during the transition from the non-tapping mode to the tapping mode.

Conversely, regarding the scenarios depicted in Figure 3-25 (a) and (c), with the exception of the maximum excitation amplitude of 8 V_{PP}—which continues to generate transient squegging—the remaining drive levels are inadequate for initiating the tapping mode. Rather, the resonator exhibits beating oscillation arising from the interplay between the actuation signal and the device's inherent resonance. As demonstrated, the settling time associated with transient squegging responses is significantly abbreviated compared to that of the beating oscillation, implying that impact events introduce additional damping.

It is important to highlight that the presented simulation results incorporate the KV-DMT model (specifically, accounting for viscoelastic contact damping b_c) alongside nonlinearities stemming from Duffing and van der Pol phenomena, which account for nonlinear stiffness k_3 and damping b_3, respectively. In the absence of these nonlinear terms, the computational outcomes would fail to correlate with the experimental observations (although, for the sake of brevity, the comparative analysis between including and excluding these terms is omitted). As previously elucidated, the phase response within the non-tapping mode is governed by the resultant system stiffness, which may exhibit hardening, softening, or a hybrid behavior. A positive phase shift is observed when the overall stiffness ($K_D + K_{vdW} + K_H$) yields a positive value, whereas a negative shift occurs when the overall stiffness becomes negative. Furthermore, the van der Pol term b_{vdP} and viscoelastic contact damping b_{vis}—both of which dictate the effective quality factor and nonlinear resonant frequency—significantly influence the ultimate phase values as well as the profile of the phase transition.

3.5.5 Hot Switching Output

Figure 3-26 depicts the simulated and experimental hot switching output signals resulting from a 1000-cycle sinusoidal input administered with diverse input driving amplitudes, employing (a) a 0.1-MΩ bleeding resistor and (b) a 1-MΩ bleeding resistor.

doi:10.6342/NTU202600018

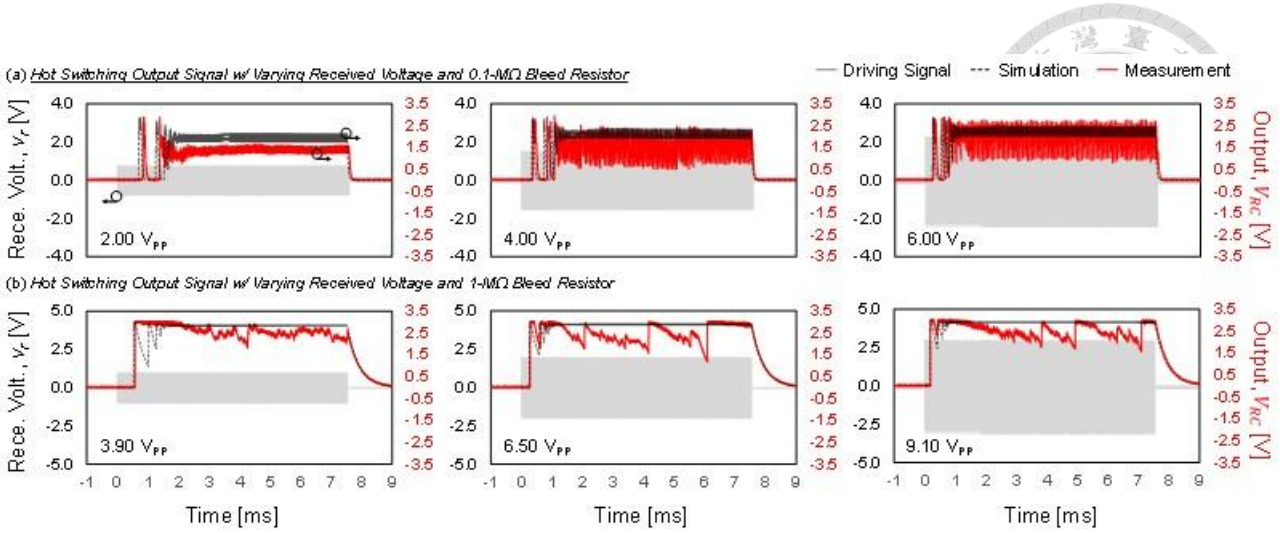


Figure 3-26: Measured hot switching output with a bleeding resistance of (a) 0.1 MΩ and (b) 1 MΩ at varying driving voltage. As illustrated in (b), a larger bleeding resistance results in a longer discharging time and higher hot switching output. Reproduced with permission of [316] Copyright of © 2025 IEEE.

The actuation OOK signal reflects the actual driving voltage received, V_r as acquired by the oscilloscope, which accounts for voltage attenuation stemming from the bias-tee. As evident in Figure 3-26 (a), the escalation in steady-state output voltage commensurate with the rise in driving voltage signifies a diminution in contact resistance, a behavior that aligns with the model's predictions. Furthermore, an elevated output voltage magnitude is discernible during the transient squegging state at the onset of the resoswitch activation. Regarding the scenario presented in Figure 3-26 (b), the experiments involved resoswitches that had undergone prior sustained operation; consequently, the contact property is inferior to that of a fresh device. As illustrated, the output voltage exhibits erratic fluctuations, inasmuch as surface degradation renders the electrical contact resistance volatile.

Nevertheless, the comparatively more significant contact occurring in the transient state facilitates the generation of a stable output, notwithstanding these adverse conditions. Figure 3-27 exemplifies this phenomenon by modulating the input driving signal to OOK with distinct duty cycles. The duty cycle is characterized as

doi:10.6342/NTU202600018

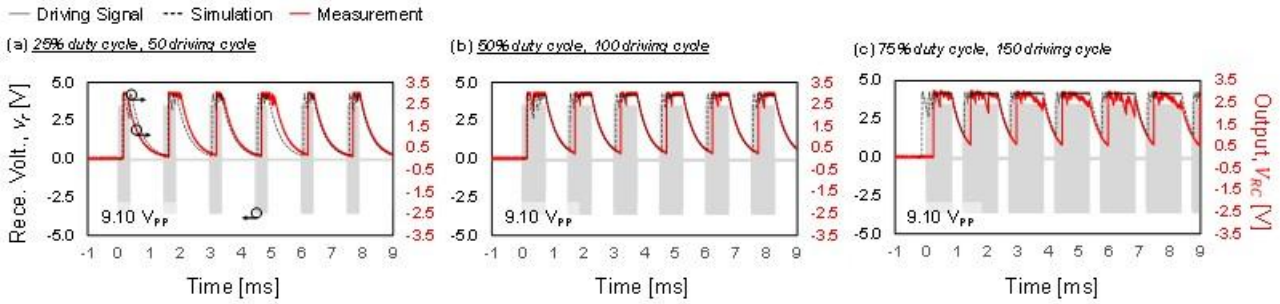


Figure 3-27: Measured hot switching output with the input duty cycle of (a) 25%, (b) 50%, and (c) 75%. For the largest duty cycle of (c), the output exhibits unstable response due to reduced contact force similar to that observed in Figure 3-26. Reproduced with permission of [316] Copyright of © 2025 IEEE.

$$D_d = \frac{T_{on}}{T_{on} + T_{off}} \tag{3-81}$$

The findings indicate that transient squegging facilitates superior contact conditions, attributable to impact forces that exceed those observed during the steady state. A comparative analysis of the transient squegging behaviors depicted in Figure 3-25 and Figure 3-26 reveals that the transient squegging phase persists for a longer duration under the hot switching condition. This discrepancy may be ascribed to thermal effects arising from electrical conduction, which induce expansion of the contact tip and consequently modify the contact force. Specifically, prior investigations regarding RF switches have established that Joule heating causes localized deformation and alters surface parameters [379, 392, 413-415]. Material softening induced by thermal loads leads to increased plastic deformation or topological modifications of the contact surface. Moreover, the surface force, influencing both mechanical and electrical attributes, exhibits temperature dependence. To account for this phenomenon, a reduced viscoelastic contact damping value of 2000—as opposed to the 50,000 employed in the non-hot-switching tapping mode—is selected, predicated on curve fitting applied to the empirical hot switching waveforms.

Thermal effects engendered by hot switching may further modulate the device dynamical behavior during active operation. Figure 3-28 illustrates the switching

doi:10.6342/NTU202600018

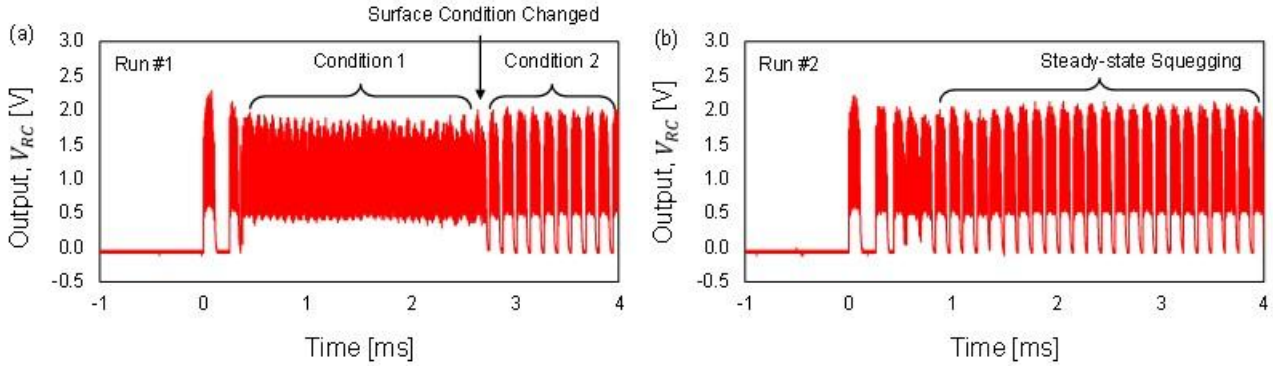


Figure 3-28: Measured hot switching outputs showing (a) changed re-sponse during operation and (b) the response measured again after (a). The measurement is performed using a single-sided configuration with a bias voltage of 60 V and input voltage of 8 VPP at its linear resonant frequency. The structure bias is 2 V and the bleeding resistance is 1 kΩ. Reproduced with permission of [316] Copyright of © 2025 IEEE.

waveforms from two sequential measurements utilizing an identical setup, wherein the hot switching waveform undergoes a radical transformation during operation. The period-doubling phenomenon emerges during operation (*cf.* Figure 3-28 (a)) attributable to alterations in the contact surface, which compel the system into the period-doubling region [304, 416, 417], yielding a persistent periodic pattern in the subsequent measurement (*cf.* Figure 3-28). The period-doubling phenomenon is characterized as steady-state squegging oscillation accompanied by a periodic loss of contact [304, 389, 417]. Subsequent research is necessary to improve the impacts resulting from time varying surface conditions.

Ultimately, Figure 3-29 displays the measured switching time derived from Figure 3-26, Figure 3-27 and supplementary measurements, presented alongside simulations grounded in (3-35) and (3-43). The application of curve fitting to the empirical data via a power law is depicted, demonstrating that the switching time declines as the driving voltage escalates, consistent with the estimation provided by (3-35). Notably, the nonlinear simulation accurately reproduces the observed outcomes, whereas the linear model results in an underestimation of the switching time.

doi:10.6342/NTU202600018

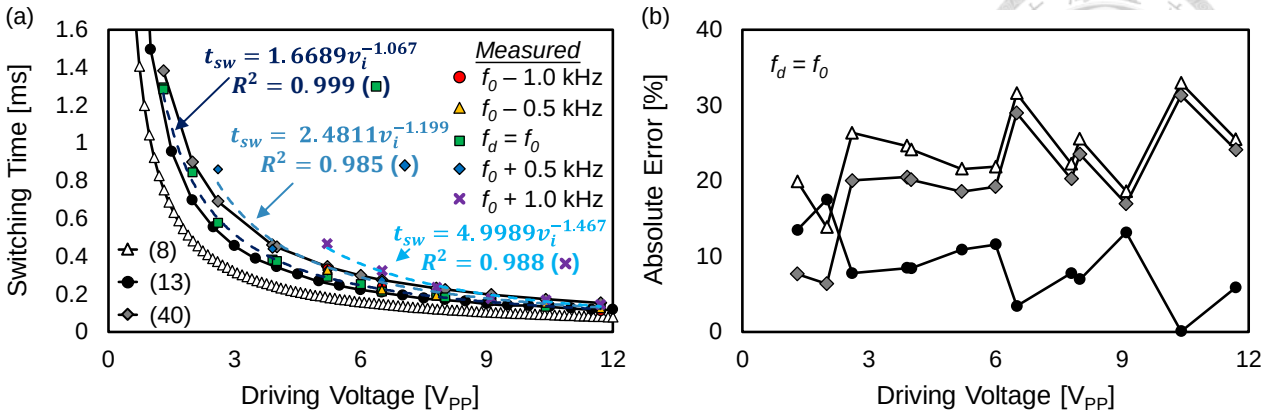


Figure 3-29: (a) Measured and simulated switching time. The theoretical formula from the linear model (i.e., (3-35)), nonlinear simulation (i.e., (3-43) with numerical integration) and the approximated solution shown in (3-83) are compared against the measurement results at $f_d = f_0$. (b) the absolute error between models and measurement results along varying driving voltages. The averaged errors are about 23.8, 8.9 and 19.8% for (3-35), (3-43) and (3-83), respectively. Reproduced with permission of [316] Copyright of © 2025 IEEE.

3.6 Discussion

In light of the analytical assessments and empirical observations detailed within this study, multiple critical insights concerning the operational behavior of CMOS-MEMS comb-driven resoswitches have been derived.

3.6.1 Influence of Effective Q on Contact Force and Switching Behavior

The effective Q governs the level of contact force principally within the grazing region. Nevertheless, regarding greater indentation depths extending outside this domain, the contact force proves to be invariant with respect to Q. Specifically, provided the free vibration amplitude adheres to the condition $A_0 = QA_d/k_r \gg d_0$ (i.e., $d_0 A_d^2 \gg k_r^2 d_0^3 Q^{-2}$), the peak repulsive force formulation in (3-68) solves to

$$F_{DMT.peak} = 2^{\frac{1}{8}} 3^{-\frac{1}{4}} \pi^{\frac{3}{4}} E^{*\frac{1}{4}} R^{*\frac{1}{8}} d_0^{\frac{3}{8}} A_d^{\frac{3}{4}} + \frac{F_{ad}}{2} \tag{3-82}$$

Figure 3-30 (a) delineates this tendency through two exemplary contact materials, each displaying divergent contact force thresholds. Material A demonstrates negligible

doi:10.6342/NTU202600018

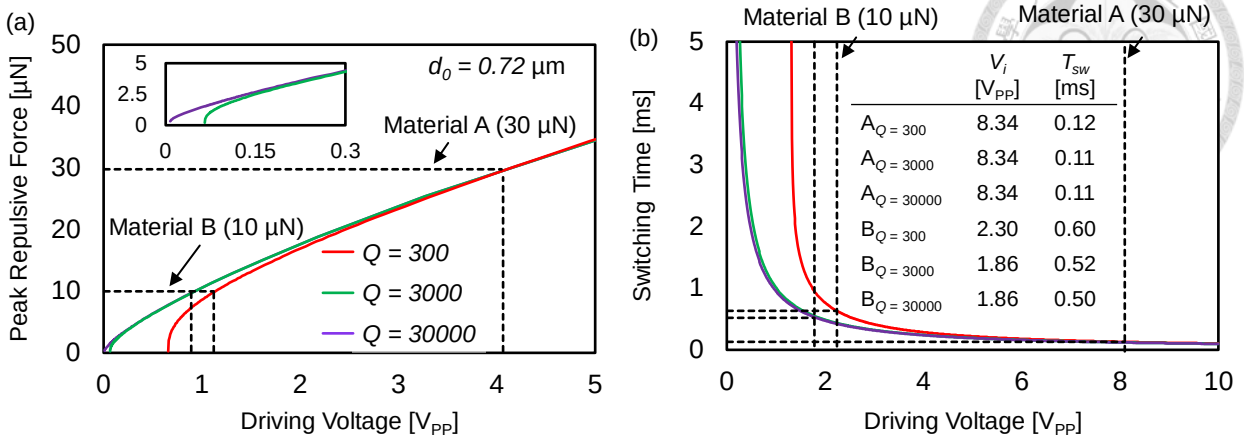


Figure 3-30: Simulated (a) peak repulsive force and (b) switching time with varying effective Q. The comparison of Material A and B il-lustrates how the material property, specifically minimum contact force required for electrical conduction, determines sensitivity and corresponding switching time. Reproduced with permission of [316] Copyright of © 2025 IEEE.

enhancement in sensitivity relative to an elevated Q, whereas Material B derives significant advantage from a higher Q, thereby attaining superior sensitivity. Contingent upon the device parameters employed within this study, the entirety of the tested materials classify as Material A, implying that an augmented Q confers only marginal augmentation to sensitivity.

Furthermore, Figure 3-30 (b) plots the switching time as a function of the driving voltage across a spectrum of linear Q values. This trajectory reflects the behavior observed in the contact force, which reaches saturation exceeding a specific driving voltage threshold, independent of Q. Developing an expansion of (3-35) using a Taylor series relative to the damping ratio results in

$$t_{sw} \approx \frac{2d_0\sqrt{m_r k_r}}{F_d} \tag{3-83}$$

Fundamentally, this expression corresponds to the solution outlined in (3-1), wherein the damping term b_r, the nonlinear terms k_3 and b_3, and the contact interaction force F_c excluded [354]. The relationship defined by (3-83) implies that subsequent optimization of the switching time necessitates the alteration of intrinsic physical

doi:10.6342/NTU202600018

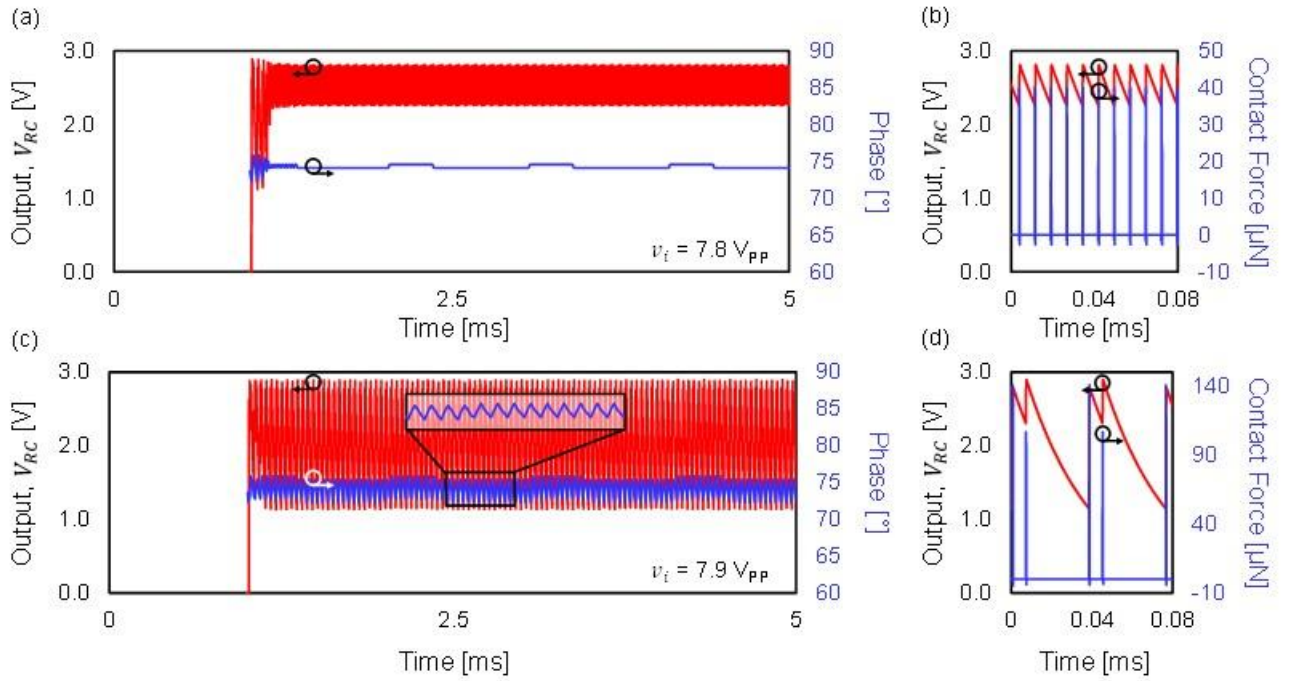


Figure 3-31: Simulated hot switching output (a, c) and zoom-in to the steady state (b, d) with driving level of 7.8 VPP and 7.9 VPP. The phase and contact force are also plotted as the second y-axis, where (d) exhibits the period-doubled response. The driving voltage is near the bifurcation boundary so a small change on the driving voltage changes the response on contact force therefore significantly altering the hot switching output. Reproduced with permission of [316] Copyright of © 2025 IEEE.

parameters—specifically, diminishing the gap clearance, reducing mass, augmenting stiffness, or elevating the driving force—as opposed to merely amplifying *Q*.

3.6.2 Impact of Period-Doubling on Contact Force and Switching Voltage

The period-doubling steady-state *squegging* phenomenon induces elevated contact forces when contrasted with continuous switching. Figure 3-31 delineates simulation results that juxtapose the output switching voltage and contact force, differentiating scenarios characterized by the presence versus the absence of the period-doubling effect. Within the period-doubled regime represented in Figure 3-31 (c) and (d), the peak repulsive forces manifest periodic fluctuations and surpass the magnitudes recorded during the continuous switching instance shown in Figure 3-31 (a) and (b). The detected 2/6 motion—wherein two impacts transpire within a span of six cycles—induces amplified variance within the output switching signal relative to the continuous

doi:10.6342/NTU202600018

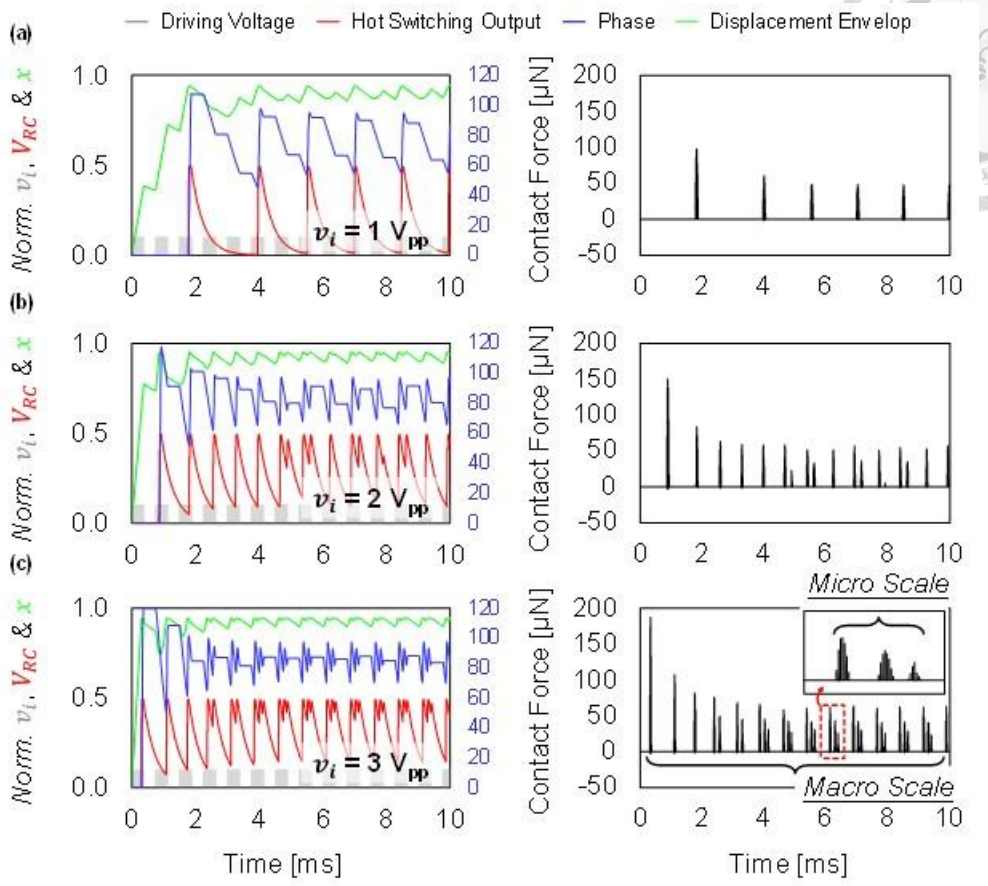


Figure 3-32: Simulated (a) peak repulsive force and (b) switching time with varying effective Q. The comparison of Material A and B il-lustrates how the material property, specifically minimum contact force required for electrical conduction, determines sensitivity and corresponding switching time. Reproduced with permission of [316] Copyright of © 2025 IEEE.

switching condition.

While antecedent research presented in [123] and [274] established a high degree of concordance between simulated and empirical contact dynamics, the force model applied within this context does not comprehensively reproduce the experimental findings observed in the period-doubling regime, a limitation arising from the inherent complexity of hot switching. Notwithstanding this discrepancy, the formulated dynamic model effectively elucidates this phenomenon from a qualitative perspective.

3.6.3 Resoswitch Modulation Techniques for Communication Applications

Within the context of communication receiver applications, the pre-energization

doi:10.6342/NTU202600018

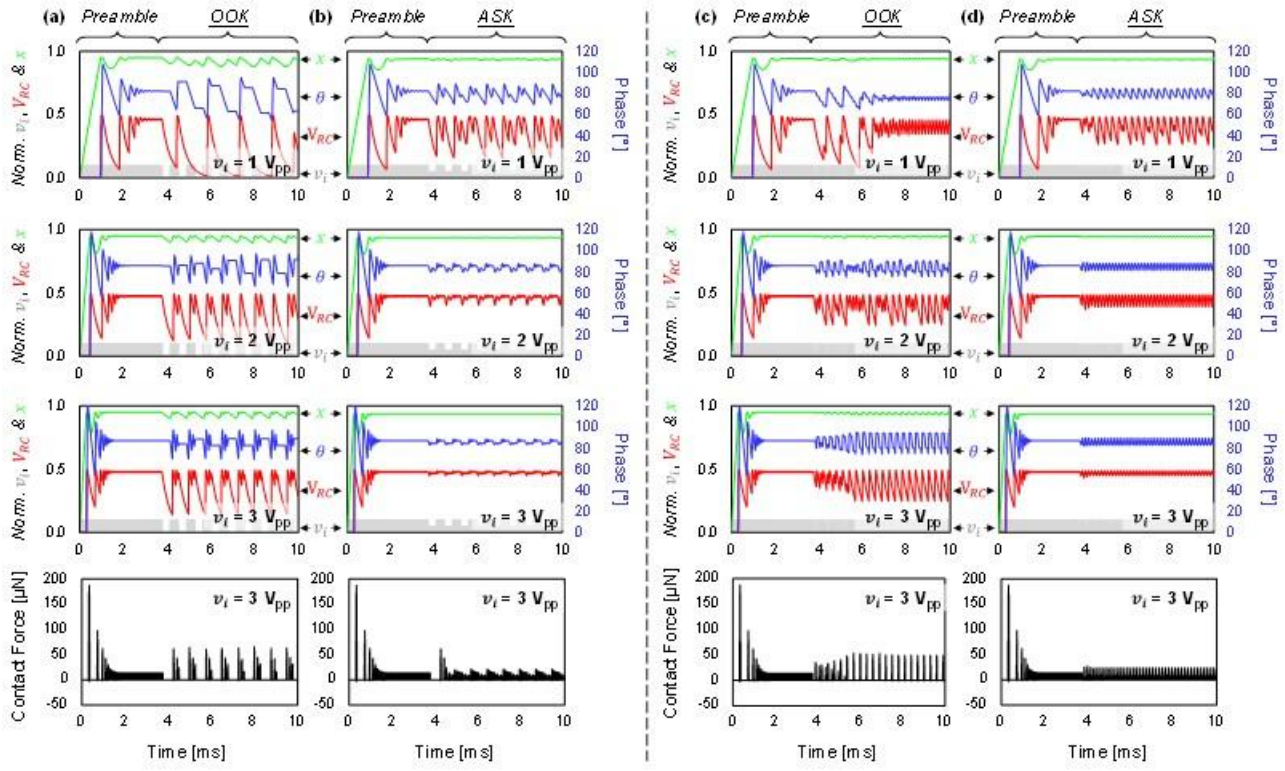


Figure 3-33: Simulated responses for two different bit rates with varying driving voltage. (a) and (b) represent a 1.3-kbps bit rate (50 cycle per message packet), while (c) and (d) correspond to a 6.7-kbps bit rate (10 cycle per message packet). The pre-amble signal is around 3.76 ms long (500 cycle) for all simulation while the modulation factor and duty cycle are 0.33 and 0.5, respectively, for ASK modulated signal. The bit rates are chosen to illustrate the effect of pre-amble, pre-energization and driving level. Reproduced with permission of [316] Copyright of © 2025 IEEE.

technique serves to curtail the transient switching time, thereby facilitating elevated bit rates [311, 418]. This strategy conserves vibration energy while in the OFF state through the transmission of a pre-amble sequence antecedent to the actual data stream, or alternatively, by implementing amplitude-shift keying (ASK) modulation rather than on-off keying (OOK). Under this pre-energizing scheme, the modulation factor M_d and duty cycle B_d pertaining to the ASK wave are characterized by:

$$M_d = \frac{v_{i.max} - v_{i.min}}{v_{i.max} + v_{i.min}} \tag{3-84}$$

$$B_d = \frac{2}{T_{on} + T_{off}} \tag{3-85}$$

doi:10.6342/NTU202600018

Figure 3-32 delineates the simulated displacement x, hot switching output voltage v_{RC}, phase, and contact force under resulting from varying driving voltages v_i applied to an OOK input signal operating at 1.3 kbps. Under conditions of low driving voltages, the prolonged transient time precipitates missing bits, a phenomenon notably prevalent at the inception of each message packet. Furthermore, every scenario displays elevated contact forces throughout the initial OOK cycles. Even within the duration of a single bit (specifically where v_i = 3 V_{PP}), the contact force manifests transient responses characterized by heightened magnitude at the onset, a behavior that correlates with the transient responses documented in Figure 3-12. Both macro-scale and micro-scale transient responses may be ameliorated through the application of pre-energization. Specifically, the macro switching time is subject to reduction via the intercalation of a pre-amble sequence preceding the OOK signals, whereas the micro switching time can be addressed through the employment of ASK modulation.

Figure 3-33 provides a comparative analysis of the simulated responses arising from distinct modulation schemes at both 1.3-kbps (low-bit rate) and 6.7 kbps (high-bit rate). The findings indicate that the inclusion of a pre-amble abbreviates the macro transient time and suppresses the occurrence of missing bits at low driving voltages. Conversely, in the context of high-bit rate OOK signals, relying solely on pre-ambles proves inadequate, as evidenced in Figure 3-33 (c). Alternatively, ASK modulation successfully curtails transient time within the high-bit rate case (*cf.* Figure 3-33 (d)). Nonetheless, at low-bit rates, ASK signals may induce the resoswitches to persist in the ON state (*cf.* Figure 3-33 (b)), thereby necessitating precise modulation factor tuning.

Notably, the contact force observed in Figure 3-33 (d) regarding the high-bit rate ASK signal is demonstrably lower than that depicted in Figure 3-33 (a) for the low-bit rate OOK signal. This implies that pre-energization utilizing waveform modulation techniques such as ASK leads to a diminution of sensitivity attributable to the decreased state difference, and consequently, the trade-off between bit-rate and

doi:10.6342/NTU202600018

sensitivity persists as a fundamental design constraint [311, 418].

3.6.4 The Role of Viscoelastic Damping in Phase Response

Throughout the progression from static to steady tapping (referencing Figure 3-24 (b) and Figure 3-25), the phase undergoes a preliminary negative deviation prior to reverting to a positive magnitude coincident with impact. A plurality of determinants governs this characteristic response, specifically viscoelastic damping, contact stiffness, and the driving force. As detailed in Section 4.3.3, the exclusion of nonlinear viscoelastic contact damping leads to inordinately protracted transients, thereby causing earlier investigations to inaccurately portray the authentic system dynamics. Moreover, when the system is actuated via modulated signals, viscoelastic damping fundamentally dictates the transient behavior, influencing the phase at the culmination of each excitation cycle and consequently modifying the system's reaction in the succeeding period. This observation compels further detailed examination.

3.6.5 Contact Material Considerations

It is widely acknowledged that metals possessing high conductivity—specifically silver, copper, gold, and aluminum—demonstrate lower hardness relative to barrier or undercoating materials such as nickel, tungsten, chromium, and zinc. By virtue of this inherent malleability, these metals exhibit a greater susceptibility to plastic deformation, a characteristic that facilitates the reduction of electrical contact resistance (ECR). For example, numerous investigations have substantiated the efficacy of employing noble and highly conductive contact materials to minimize contact resistance and prolong the operational lifespan of relays [349, 419-424]. Nevertheless, although these materials provide exceptional conductivity, their elevated adhesion force and expanded contact area may precipitate stiction failure within micro relays.

Conversely, harder materials are prone to manifesting higher ECR and an increased vulnerability to oxidation, which may culminate in high resistance failure. Consequently, the selection of contact material for resoswitches necessitates

doi:10.6342/NTU202600018

meticulous evaluation contingent upon the desired bit rate and sensitivity prerequisites. The resonant operation characterizing resoswitches intrinsically alleviates stiction failure, a prevalent deficiency in conventional MEMS relays. Accordingly, soft noble metals like gold, silver, and platinum are typically favored, particularly for high-bit rate applications, inasmuch as they necessitate a lower contact force to initiate conduction and possess superior resilience against corrosion and oxidation.

Furthermore, material engineering strategies, such as the amalgamation of distinct materials, can augment the performance and reliability of MEMS relays. To illustrate, the implementation of alloys and layered structures has been examined in both macro relays [425-428] and their MEMS counterparts [420, 429]. Moreover, hybrid contact designs—which integrate a hard-to-soft contact material interface—have been proven to extend the lifetime of MEMS relays [430]. Within the specific framework of CMOS-MEMS platforms, research detailed in [310] and [311] indicates that electroless nickel plating enhances the reliability of resoswitches direct VIA-to-VIA contacts. This observation concurs with established data regarding macro relays, wherein nickel coating has been demonstrated to ameliorate corrosion fatigue and bolster durability [340].

3.7 Conclusion

This dissertation elucidates the comprehensive development of CMOS-MEMS comb-driven resoswitches, spanning the domains of design, modeling, and characterization. The influence of distinct design and operating parameters upon the dynamic response of the device has been rigorously examined via a tripartite methodology integrating experimental, theoretical, and numerical investigations. The generalized nonlinear equations of motion were solved utilizing the method of averaging, complemented by numerical simulations executed within MATLAB and Simulink. Concordant outcomes from both experimental and computational analyses disclose several critical insights. Specifically, the peak contact force observed during the transient state surpasses that of the steady state; conversely, the peak repulsive force

doi:10.6342/NTU202600018

can be amplified through the introduction of adhesion forces, spring softening, or by functioning within the period-doubling region. The effective Q exerts a dominant influence on switching time and peak repulsive force, primarily within the near-grazing region, whereas fluctuations in surface conditions possess the capacity to substantially modify the device's dynamic properties. Furthermore, input waveform engineering—specifically via the pre-energization technique—has been demonstrated to ameliorate transient time and contact force, thereby preserving the balance between bit rate and sensitivity.

These observations delineate prospective avenues for future inquiry regarding CMOS-MEMS resoswitches. For example, phenomena typically regarded as deleterious, such as Duffing nonlinearity and surface adhesion forces, might be strategically leveraged to augment device performance. Moreover, the enhancement of contact resistance and device lifetime may be realized through sophisticated contact material engineering, exemplified by electroless nickel immersion gold (ENIG) coatings [431, 432] or ultra-high adhesion force structure [433]. Furthermore, the period-doubled hot switching output recorded in this investigation is not comprehensively elucidated by the constructed theoretical model, a discrepancy potentially attributable to the inherent constraints of the one-mode approximation [201, 206, 434] or imprecise formulations of the surface interaction force. The development of a more robust surface interaction model, coupled with the precise characterization of actual contact material properties and geometry, is requisite for subsequent refinement. Upon the determination of either the material properties or the effective contact radius, the remaining variable may be deduced via curve fitting [435-439].

doi:10.6342/NTU202600018

4 Developments on MEMS All-mechanical Circuits

4.1 Resoswitch-embedded Wake-up Receiver

The present work introduces a 125-kHz zero quiescent power OOK/FSK communication receiver integrated with a micromechanical resoswitch, engineered via a CMOS-MEMS fabrication platform specifically for low-frequency (LF) active RFID standby receiver applications. In contrast to antecedent receivers that utilized a CMOS-incompatible Au fabrication process [82], the present work leverages a standard 0.35-μm CMOS process to construct a folded-beam comb-driven resoswitch incorporating a digital decoder. This pivotal resoswitch component enables the receiver to execute on-chip signal filtering, power amplification, and demodulation, necessitating an average power consumption of 10.46 μW during the processing of a "1" bit, while maintaining near zero power usage for "0" bits and standby states. Such an implementation validates the efficacy of cost-effective, high-fidelity CMOS processes for the realization of all-mechanical resoswitch-based RF applications.

4.1.1 Introduction

Commercial active RFID tags, exemplified by those deployed in passive keyless entry (PKE) systems, extensively employ low-frequency (LF) communication within the 125 kHz spectral band. Such applications necessitate those receivers perpetually monitor for transmissions emanating from transmitter modules situated in locations including automobiles or building access points. To guarantee extended battery longevity, it is imperative that such standby receivers function with negligible power expenditure. Although a battery replacement interval of 2-3 years is deemed permissible for a standard PKE key fob, a receiver exhibiting substantially reduced standby power drain could enable a broader array of wireless sensor applications, specifically in inaccessible environments where battery maintenance presents logistical difficulties.

To realize this objective, contemporary progressions in MEMS technology have

doi:10.6342/NTU202600018

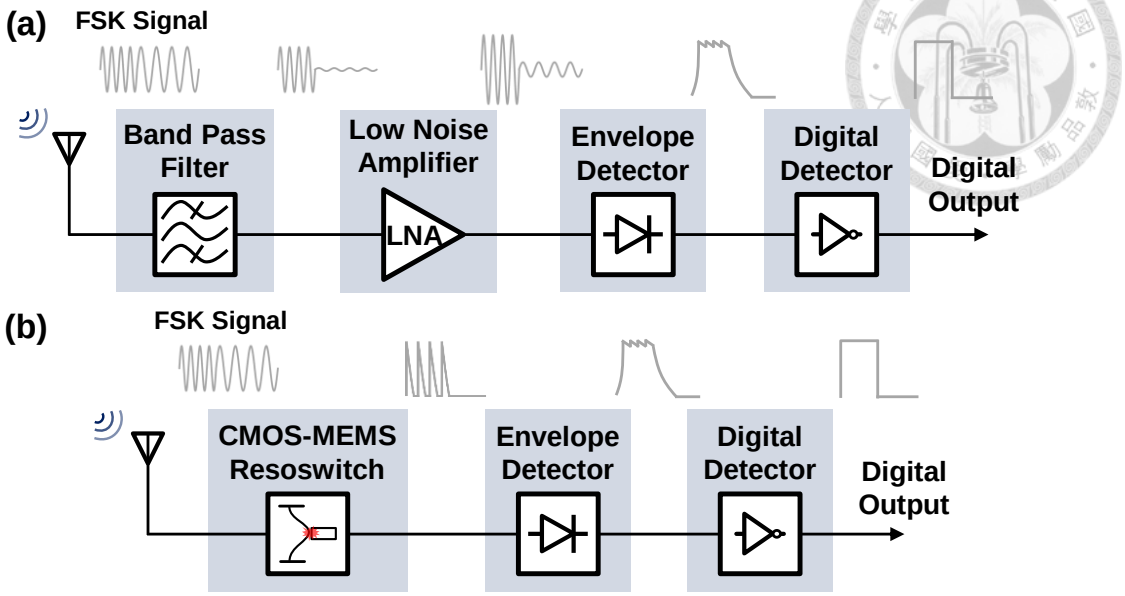


Figure 4-1: A comparison of FSK receiver architectures, showing (a) a conventional RF front-end utilizing a filter and LNA, and (b) an alternative design based on a CMOS-MEMS resoswitch. Reproduced with permission of [89], Copyright of © 2020 IEEE.

facilitated novel communication paradigms, permitting the receiver front-end to maintain an active state and monitor incoming interrogation signals while incurring minimal or theoretically zero power dissipation [82, 83, 440]. These methodologies are broadly classified into two distinct categories: piezoelectric and capacitive actuation schemes. While the piezoelectric-based technique provides superior impedance matching between the antenna and the front-end circuitry, it necessitates the inclusion of transistor readout circuits that draw a finite standby current to perceive the incoming RF signal [441]. In contrast, the capacitive-driven resoswitch strategy obviates the requirement for standby current, thereby accomplishing signal filtering, amplification, and demodulation in the absence of power consumption [82].

Thus far, communication receivers utilizing resoswitch technology have effectively substantiated OOK reception capabilities within the LF band. Nevertheless, these systems depend upon constituent materials such as Au [82] or polycide [83] for the resoswitch structures; such materials either necessitate high-temperature processing steps that are incompatible with CMOS or impede direct integration with CMOS digital

doi:10.6342/NTU202600018

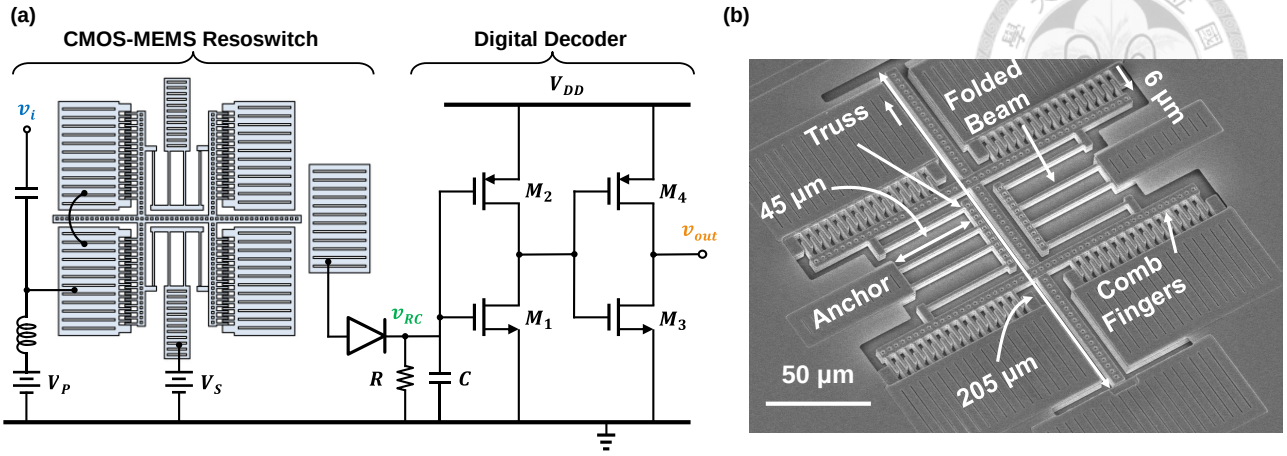


Figure 4-2: (a) The circuit diagram for a zero-quiescent power OOK/FSK receiver, which is based on a CMOS-MEMS folded-beam comb-driven resoswitch and a digital decoder. (b) An SEM image of the fabricated resoswitch after release. Reproduced with permission of [89], Copyright of © 2020 IEEE.

processing circuitry. To surmount this obstacle, [265] utilized a CMOS-compatible all-metal Al process to fabricate a slotted-disk resoswitch. Furthermore, [87] and [336] leveraged a standard 0.35-µm CMOS process to engineer CC-beam resoswitches. Expanding upon this identical CMOS platform, the present research advances the state of the art by implementing a comprehensive OOK/FSK communication receiver that incorporates a folded-beam comb-driven resoswitch and an on-chip digital decoder tailored for 125-kHz active RFID tag applications. By way of illustration, within an operational context wherein data processing occurs for a duration of one minute (assuming a 50% of bit "1") per hour, the empirical power consumption—registering approximately 0 µW during standby (lower than the environment noise level and unmeasurable) and 10.46 µW during the processing of bit "1"—yields a reduction in the receiver's aggregate energy expenditure by a factor exceeding 110 relative to a standard commercial low-power tag [442], which typically exhibits a standby power draw of 10 µW.

4.1.2 Resonant Switch as a Filtering Amplifier

Figure 4-1 (a) delineates a traditional OOK/FSK receiver framework wherein the

doi:10.6342/NTU202600018

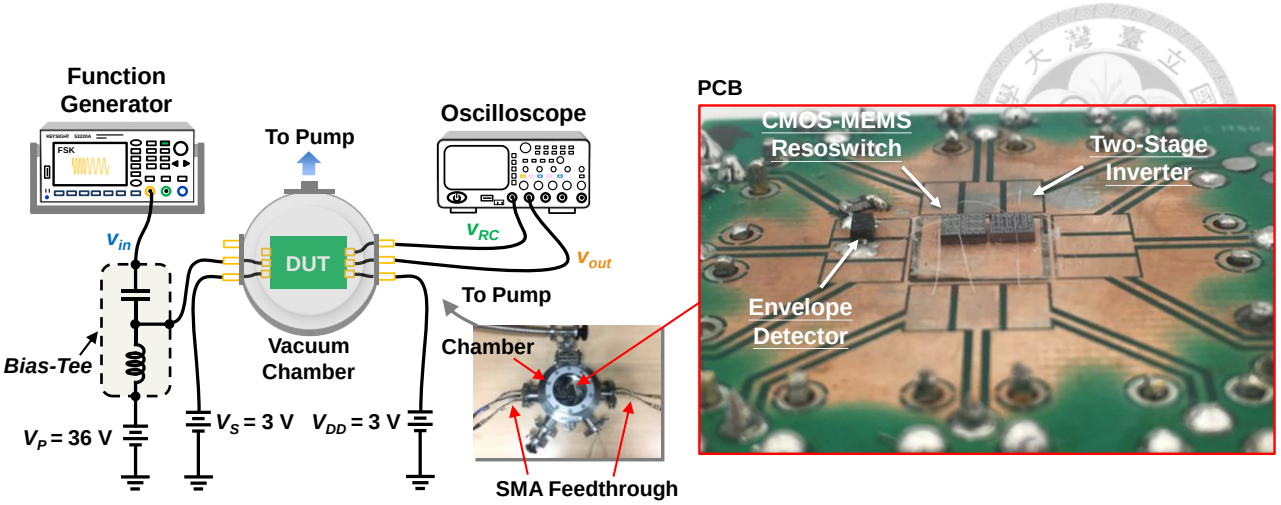


Figure 4-3: The measurement setup for the OOK/FSK receiver. The inset on the right shows an optical photograph of the PCB, which holds the two bonded dies for the digital decoder circuit and the resoswitch. Reproduced with permission of [89], Copyright of © 2020 IEEE.

front-end low noise amplifier (LNA) necessitates a continuous standby current to discern the interrogation signal. This quiescent current constitutes a substantial portion of the power expenditure during the listening state, thereby mandating frequent battery upkeep. In contrast, Figure 4-1 (b) portrays an adapted configuration in which micromechanical resoswitches supplant both the front-end filter and the amplifier. This alteration effectively eradicates the standby power draw associated with the amplifier, presenting the potential to drastically prolong battery lifetime. Furthermore, the intrinsic resonance characteristics of the resoswitch confer an inherent channel-selectivity filtering capability, which serves to mitigate false alarms and precludes superfluous baseband power dissipation arising from repetitive signal pattern verification triggered by interference.

4.1.3 Structure and Operation

Figure 4-2 (a) presents the comprehensive circuit schematic of the receiver, inclusive of the actuation and biasing configurations. The polarization bias V_P and the actuation signal v_i—which functions as the RF input signal in practical scenarios—are amalgamated via a bias-tee network and subsequently impressed upon the input electrode. To enable hot switching, a DC bias voltage V_S is supplied to the resonator

doi:10.6342/NTU202600018

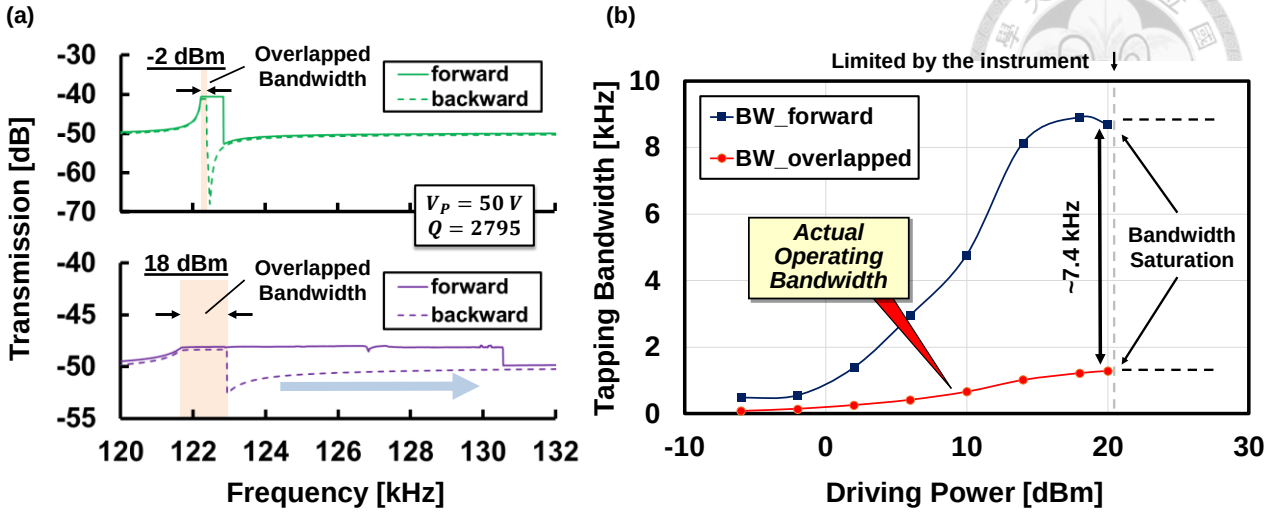


Figure 4-4: (a) Measured frequency responses for the receiver, showing both forward and backward sweeps at different input power levels. (b) A plot of the extracted forward and overlapped bandwidths, highlighting the actual operating bandwidth available for single-frequency driving.

structure. At the output electrode, a diode paired with an RC circuit functions to rectify and attenuate the transient spikes generated by hot switching; concurrently, the digital decoder, comprised of a dual-inverter assembly, buffers the signal to yield a square wave output. While the present implementation houses the resoswitch and the digital decoder on discrete chips, monolithic integration into a singular die remains a natural option. Within the context of the CMOS process, TiN/Ti is selected as the contact material for the VIA layers interfacing with the Aluminum metal; this selection is predicated on TiN/Ti's high hardness and excellent wear resistance, thereby enhancing reliability despite the associated penalty of increased contact resistances as mentioned in Chapter 3. Although elevated contact resistances can detrimentally impact the power gain and bandwidth of the front-end receiver, resistance values spanning from tens to hundreds of kΩ are deemed permissible for the specific operating frequency utilized in this research.

4.1.4 Experimental Results

The fabrication protocol for the resoswitch adheres to the methodology delineated in Section 3.2. The primary fabrication phase employs a 0.35-μm CMOS process,

doi:10.6342/NTU202600018

integrating continuous VIA barriers to shield the intermediate oxide (IMD) layers from etchant attack during the release step. This approach facilitates the construction of a robust metal-rich architecture accomplished by laminating successive metal and VIA/IMD strata. Following this, wet etching in an Al-compatible HF solution yields the cross-sectional profile depicted in. Figure 4-2 (b) exhibits SEM micrographs of the resoswitch, wherein a magnified view of the contact interface unveils the protrusion of ARC layers. Such protrusion manifests inherently owing to process artifacts, resulting from the alignment of VIA and metal layer boundaries within the layout. Figure 4-3 provides an optical image showing the two wire-bonded dies—specifically the digital decoder and the resoswitch—mounted upon the printed circuit board. Also, Figure 4-3 delineates the experimental configuration utilized for the OOK/FSK receiver characterization. A function generator (Keysight 53220A) is employed to emulate the OOK/FSK waveform, while an oscilloscope (Keysight DSOX2002A) records the transient responses at both the resoswitch output and the decoder output. The test printed circuit board is housed within a bespoke vacuum enclosure, which is evacuated to pressures inferior to 10^{-5} Torr via a turbo pump.

Figure 4-4 (a) presents the measured forward and backward frequency responses of the resoswitch, indicating that the effective operating bandwidth corresponds to the single-valued overlapping region. Furthermore, Figure 4-4 (b) illustrates the bandwidth extracted from these measurements, demonstrating the channel-selection capability of the resoswitch. Figure 4-5 (a) displays the measured OOK reception signals, wherein an input driving voltage of 1.5 V equates to 1.25 μW at the device input, yielding an equivalent sensitivity of -29 dBm assuming a match to 50 Ω. This actuation voltage is comparatively elevated relative to commercial transistor-based receivers and necessitates reduction. A plausible remediation involves migrating the device to advanced fabrication nodes that permit reduced gap dimensions, consequently diminishing the actuation voltage via enhanced transduction efficacy. Furthermore, Figure 4-5 (b) exemplifies the acquisition of an FSK signal ("1" at 125 kHz and "0" at

doi:10.6342/NTU202600018

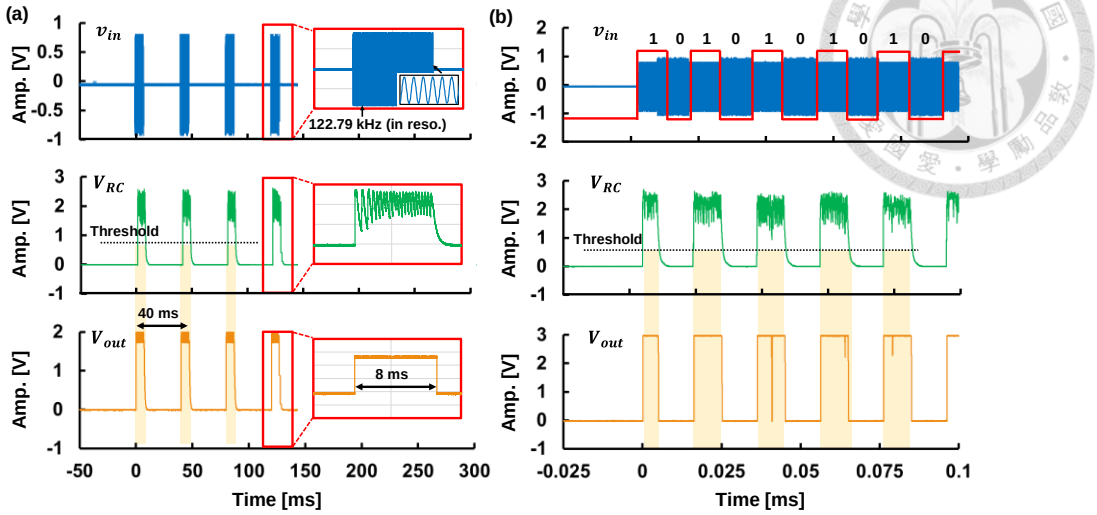


Figure 4-5: Oscilloscope waveforms captured during receiver operation, showing the demodulation of (a) an OOK input signal and (b) an FSK input signal. The resoswitch's filtering capability enables it to distinguish the in-channel signal from the out-of-channel signal. Reproduced with permission of [89], Copyright of © 2020 IEEE.

10 kHz), validating the apparatus's capacity to differentiate between in-channel and out-of-channel signals.

Figure 4-6 illustrates the quantified energy and power consumption of the resoswitch and decoder during OOK operation, as determined via a current waveform analyzer (Keysight CX3324A). The receiver dissipates 20.37 nJ for the resoswitch and 3.18 nJ for the decoder while processing a bit "1" over a 2 ms duration, culminating in an average power consumption of 11.78 µW during operation and approximately 0 W during standby. It is pertinent to highlight that the digital decoder draws a supplementary 1.31 µW attributable to the 1-MΩ load resistance of the oscilloscope. This extraneous power dissipation is obviated upon connection to a high-impedance digital gate in practical applications, lowering the aggregate projected power consumption to 10.47 µW. This metric is commensurate with that of a standard 125-kHz active RFID tag receiver in sleep mode; however, the resoswitch-embedded receiver dissipates energy exclusively during data processing intervals, whereas standard receivers perpetually deplete battery reserves.

doi:10.6342/NTU202600018

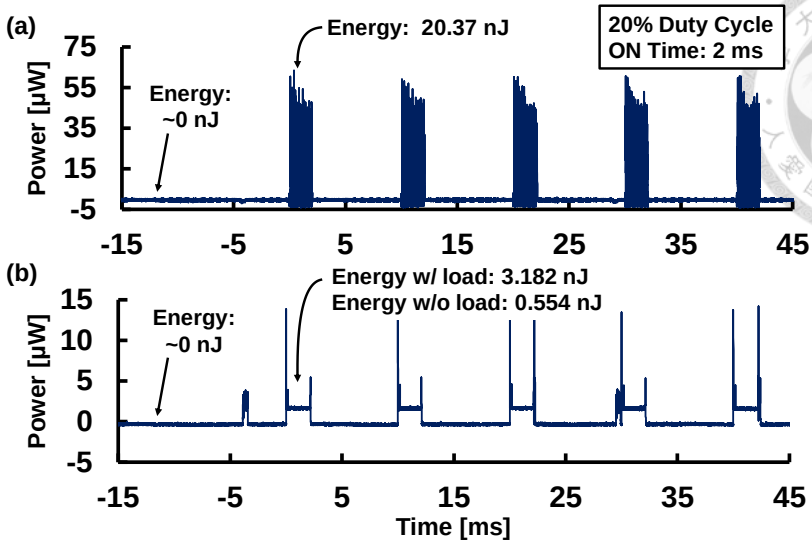


Figure 4-6: Measured power consumption during switching for (a) the resoswitch and (b) the inverter decoder. The static power drawn by the decoder is primarily due to the oscilloscope's load resistance. Reproduced with permission of [89], Copyright of © 2020 IEEE.

4.1.5 Conclusions

This dissertation substantiated the functionality of a 125-kHz OOK/FSK receiver predicated on a CMOS-MEMS folded-beam comb-driven resoswitch, engineered to eradicate the quiescent power draw inherent to traditional RF front-end architectures. Through the exploitation of the resonance and nonlinear impacting characteristics of the resoswitch, this system obviates the requirement for both the front-end filter and the energy-intensive LNA conventionally present in standard receiver frameworks. Consequently, the device attains analogous signal filtering and amplification capabilities while maintaining zero quiescent power dissipation. Such technological progress holds the potential to substantially prolong the operational lifespan of standard active RFID tags and facilitate novel applications, specifically within environments where battery replacement poses logistical challenges.

TABLE 4-1 provides a comparative analysis contrasting this study against commercially available solutions and previously documented OOK/FSK receivers. The implemented receiver functions with a power expenditure of 10.46 µW, a metric commensurate with alternative receiver systems. Nevertheless, the current receiver

doi:10.6342/NTU202600018

TABLE 4-1 COMPARISON OF RECEIVER SPECIFICATIONS. REPRODUCED WITH PERMISSION OF [89], COPYRIGHT OF © 2020 IEEE.

	[443]	[442]	[444]	[445]	[446]	This work
Power Consumption (Standby) (μW)	7.2	3.8	9.72	*NA*	*NA*	0
Power Consumption (Active) (μW)	36	7.9	29.9	20.8	13.8	10.46
Sensitivity (V_{pp})	1 m	1.414 m	0.141 m	0.5 m	0.4 m	[a]1
Carrier Frequency (kHz)	125	125	110-150	125+5%	125+10%	125+3%
Data Rate (kbps)	10	4	0.5-4	3.9+3%	3.9+3%	0.5

[a]: The lowest measured actuation voltage for continuous hot switching.

sensitivity, quantified at 1 V_{PP}, remains comparatively elevated relative to competing systems, thereby diminishing the immediate prominence of this technology. Enhancing sensitivity is paramount, and the most efficacious strategy involves the reduction of the gap spacing. Prospective remediation strategies encompass the adoption of more sophisticated fabrication processes or the utilization of post-process additive materials to constrict the gap dimensions.

doi:10.6342/NTU202600018

4.2 Pulse Density Modulator

This work presents the inaugural realization of frequency-to-pulse density modulation (PDM) capabilities within micromechanical resoswitches, achieved through the exploitation of the period-doubling bifurcation mechanism. In contradistinction to the antecedent resoswitch-based squegging clock generator detailed in [84], which functions in a low-frequency squegging oscillation regime dictated by contact structural or material stiffness, the present study demonstrates intricate nonlinear dynamical switching behaviors. These dynamical responses are regulated by the period-doubling (PD) bifurcation cascade alongside the driving frequency within the tapping region, culminating in diverse *M/N* impact/motion configurations (defined as *M* impacts occurring within *N* motions). Realized via a CMOS-MEMS folded-beam comb-driven resoswitch, the *M/N* impact/motion

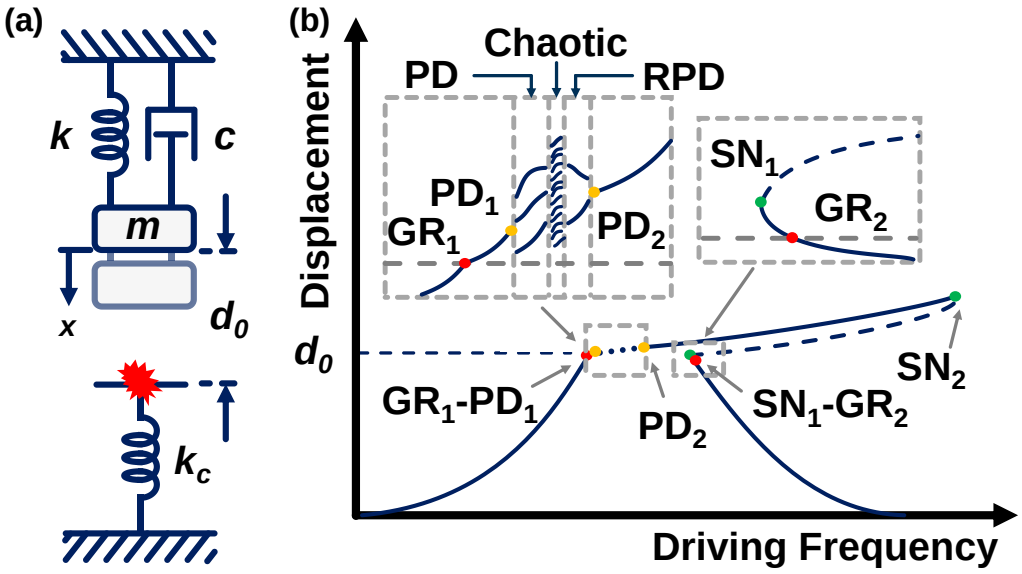


Figure 4-7: (a) A 1-DOF mechanical model of a vibro-impact resonator. (b) An illustrative frequency response for a nonlinear tapping-mode vibro-impact resonator. The plot highlights key dynamic features: grazing bifurcations (GR_1-PD_1 and SN_1-GR_2), the period-doubling and reverse period-doubling region (PD_1 to PD_2), and saddle-node bifurcations (SN_1 and SN_2). The labels GR_1-PD_1 and SN_1-GR_2 are used because, in typical cases with significant stopper stiffness and contact force, the grazing points (GR) are nearly coincident with the first period-doubling (PD_1) and second saddle-node (SN_2) bifurcations. Reproduced with permission of [237], Copyright of © 2022 IEEE.

doi:10.6342/NTU202600018

phenomena derived from period-doubling bifurcation are converted directly into sequential pulse trains, wherein the pulse density is established by the *M/N* ratio. Consequently, this research not only validates the nonlinear period-doubled operation within micromechanical resoswitches but also establishes novel avenues for the engineering of resoswitch-based communication receivers utilizing advanced modulation schemes predicated on frequency-controlled PDM, supplementing existing FSK/OOK protocols [89].

4.2.1 Introduction

Contemporary developments in MEMS resoswitches have yielded all-mechanical RF receivers functioning at low-frequency bands, characterized by minimal standby leakage currents. These innovations encompass Au-electroplated FSK receivers [82], polycided soft-impacting AM receivers [83], and CMOS-compatible OOK/FSK receivers [89]. Nevertheless, such resoswitch configurations frequently exhibit a detrimental squegging effect arising from nonlinear dynamics, precipitating instability in oscillation amplitudes. This squegging effect, as substantiated in [263], [87], and [146], can engender critical interruptions in output signals, thereby mandating corrective interventions for its suppression [146].

Conversely, [84] innovatively harnesses the squegging oscillation within resoswitches for the purpose of clock generation. This regime of low-frequency ringing facilitates the synthesis of a clock signal even while the component is subjected to continuous high-frequency wave excitation. As delineated in [84], precise modulation of the clock frequency is attainable via manipulation of the resonator's quality factor, variation of the stopper structure stiffness, or adjustment of material loss characteristics.

Although designated by distinct terminologies, this low-frequency amplitude ringing effect is observable across a diverse array of systems. For example, the squegging phenomenon, induced by period-doubling (PD) bifurcations, is classified as chattering within machining contexts [448], and quenching in super-regenerative receivers [449]. Period-doubling bifurcation may manifest owing to individual or

doi:10.6342/NTU202600018

amalgamated factors, comprising regenerative excitation [448], intrinsic feedback loops, parametric excitation, or modal coupling interaction [112].

4.2.2 Period-Doubling Bifurcation

A resoswitch, or more comprehensively defined as a vibro-impact resonator (refer to Figure 4-7 (a)), incorporates displacement-constraining stoppers that establish a characteristic piecewise smooth configuration—wherein the system stiffness undergoes a transition pre- and post-contact. This architectural configuration precipitates grazing bifurcation (defined as zero-relative-velocity contact) followed by a sequential cascade of PD bifurcations [112, 117] (consult Figure 4-7 (b)). In particular, the discontinuity at the boundary induces an abrupt alteration in velocity over a momentary interval, culminating in additional energy dissipation [146], phase delay [117, 450], and impulsive restoring forces that stimulate modes spanning a broad frequency spectrum [94]. As depicted in Figure 4-7 (b), these phenomena can engender

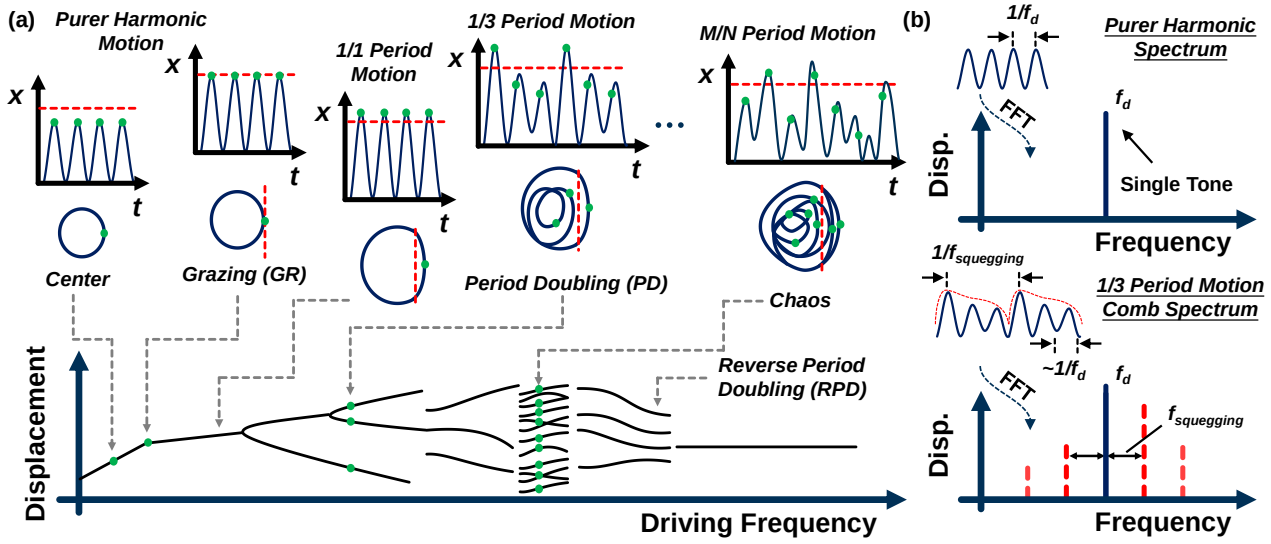


Figure 4-8: (a) A depiction of the system's dynamics across various regions of the frequency response, including time-domain waveforms, phase portraits, and Poincaré maps (indicated by green dots). The phase portraits display the system's trajectories, including the discontinuity boundary, while the Poincaré maps reveal the motion's state at specific phase conditions, showing a complex fractal pattern when chaos is present. (b) An illustration comparing the FFT spectra for continuous motion versus motion induced by period-doubling. Reproduced with permission of [237], Copyright of © 2022 IEEE.

doi:10.6342/NTU202600018

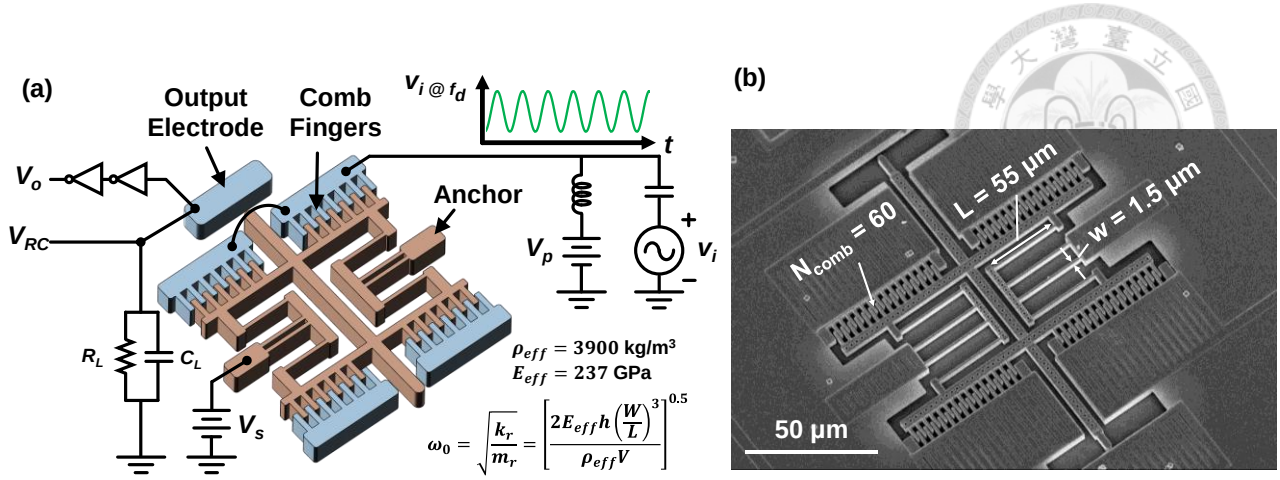


Figure 4-9: (a) A schematic diagram of the CMOS-MEMS comb-driven resoswitch, including its testing setup. (b) SEM images of the fabricated and released resoswitch. Reproduced with permission of [237], Copyright of © 2022 IEEE.

a progression of intricate dynamic motions during impact events within the tapping region, encompassing initial grazing (GR_1), period doubling (PD), chaotic regimes, reverse period doubling (RPD), and saddle-node bifurcations (SN). This observation suggests that the squegging frequency is governed not merely by the resonator's quality factor, the stiffness of the stopper structure, or material damping characteristics [84], but is also significantly modulated by the driving conditions.

The capacity to tune PD through the manipulation of driving parameters, such as excitation voltage and frequency, offers substantially superior flexibility and practical utility compared to mechanical structural modifications. Figure 4-8 (a) presents the associated time-domain waveforms, phase portraits, and Poincaré maps across diverse nonlinear states, substantiating that the switching output manifests as either continuous or period-doubled waveforms contingent upon the specific driving frequency. Figure 4-8 (b) elucidates the disparities observed in the frequency spectrums when comparing a continuous signal against a period-doubled switching signal. It is imperative to acknowledge that the physical attributes of the device, such as gap spacing, retain a determining influence over the PD bifurcation.

doi:10.6342/NTU202600018

4.2.3 Structure and Operation

Figure 4-9 (a) depicts the architectural schematic corresponding to a resoswitch-integrated PDM circuit. Excitation of the resoswitch is achieved by superimposing the polarization bias V_P and input signal v_i onto the driving electrode; concurrently, the structural body is energized at V_S, a potential that is conducted to the output electrode during contact events. A pair of cascaded inverters operates in the capacity of digital comparators, serving to square the switching waveforms and transmit pulse trains to the output terminal.

4.2.4 Experimental Results

Figure 4-9 (b) exhibits SEM micrographs capturing a released device, inclusive of a magnified perspective focusing on the contact region. Analogous to the methodology delineated in Section 3.2, device fabrication utilizes a standard 0.35-μm CMOS process, incorporating a wet release process performed within an aluminum-compatible HF-based Silox Vapox III at ambient temperature for a duration of roughly 70 minutes. The architecture of the folded-beam comb-driven resoswitch incorporates composite metal stacks spanning from METAL1 to METAL4, wherein peripheral VIAs are implemented to shield the intermediate oxide layers.

Figure 4-10 shows the experimental setup and the frequency responses acquired via conventional bidirectional frequency sweeps (forward and reverse) under diverse excitation magnitudes within a one-port testing configuration. These spectral responses are derived utilizing the integrated sweep capability of a lock-in amplifier, configured to execute 800 discrete increments spanning the designated frequency interval. Analysis of the output frequency spectrums is conducted via a spectrum analyzer operating with a 100-Hz resolution bandwidth; concurrently, the modulated signal output is recorded by an oscilloscope interfacing through an RC network and a digital decoder possessing a temporal resolution of 0.2-μs.

doi:10.6342/NTU202600018

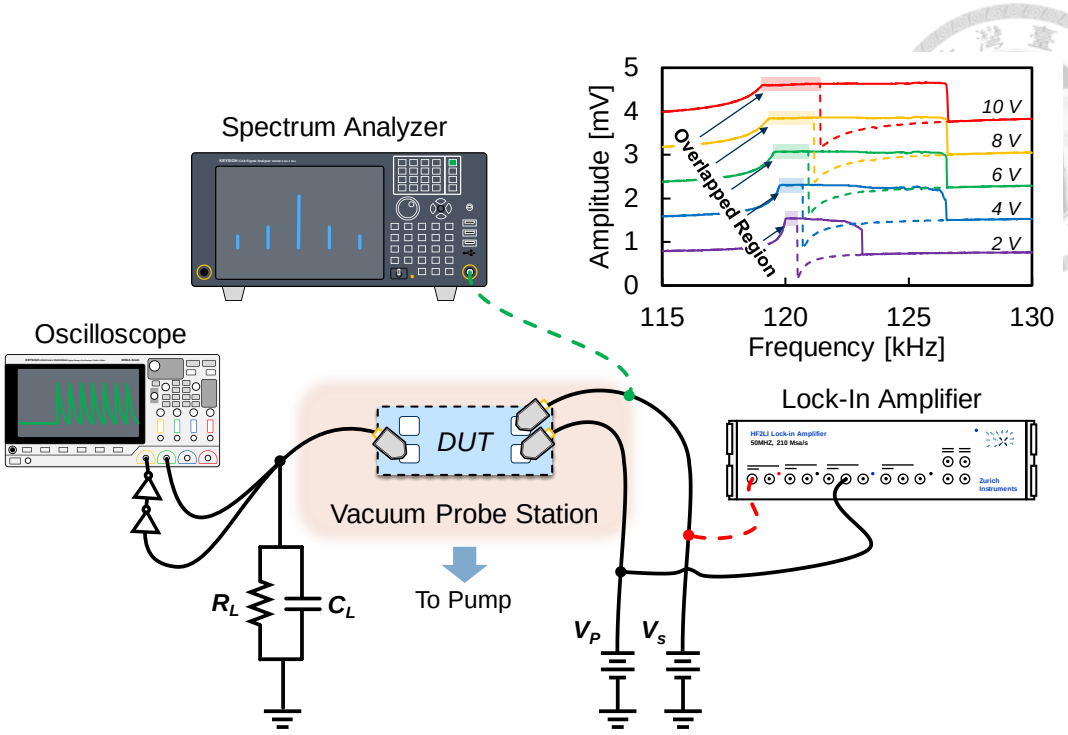


Figure 4-10: The experimental setup for measuring frequency transmission, the output frequency spectrum, and the modulated signal output. The inset displays the measured frequency transmission curves for several different driving voltages. Reproduced with permission of [237], Copyright of © 2022 IEEE.

For the implementation of a single-frequency driving scheme, it is imperative to verify that the excitation frequency lies within the single-valued region. Failing this condition, the device exhibits a propensity to settle into the lower energy state associated with the reverse sweep trajectory, as demarcated by the dashed traces in Figure 4-11.

Figure 4-11 (a) presents the measured frequency response characteristics of a 120-kHz folded-beam comb-driven resoswitch, exhibiting an overlapped frequency band spanning 1.88 kHz. Encompassed within this bandwidth, Figure 4-11 (b)-(d) delineate the hot switching signals V_{RC}, the output pulse signals V_O, and the associated spectral content derived via fast Fourier transform at five distinct frequency coordinates. These plots elucidate diverse *M/N* motion configurations, characterized by squegging frequencies extending from 8.5 kHz up to 12.7 kHz. Figure 4-11 (e) expands the analysis to frequency comb generation by sweeping the driving signal from 119.003

doi:10.6342/NTU202600018

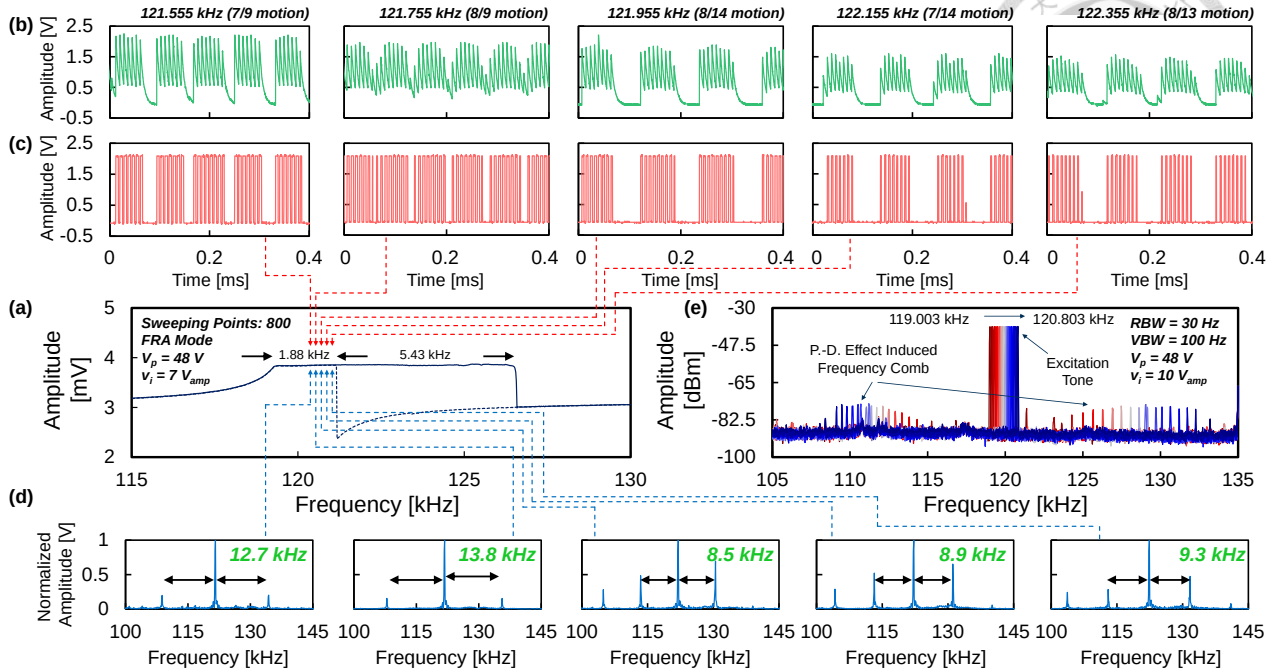


Figure 4-11: A collection of measured data for the resoswitch. (a) The frequency transmission response under specified conditions. (b) Time-domain waveforms of the hot-switching signals (V_{RC}). (c) The corresponding PDM output signal waveforms (V_O). (d) The frequency spectra of the hot-switching signals at five points within the period-doubling region. (e) A plot of the frequency combs across a range of driving frequencies in the reverse period-doubling region, demonstrating an increase in the squegging frequency as the driving frequency is increased. Reproduced with permission of [237], Copyright of © 2022 IEEE.

kHz to 120.803 kHz in precise 0.1-kHz steps; this examination uncovers an elevation in squegging frequencies—signifying wider intervals, reduced periods, or a diminution in period-doubling states—throughout the examined spectral range. These findings imply that the operational frequency range of the device under test principally encompasses the reverse period-doubling region.

4.2.5 Conclusions

This work has substantiated the realization of frequency-to-pulse density modulation (PDM) via a CMOS-MEMS folded-beam comb-driven resoswitch. The observed results underscore the feasibility of implementing post-fabrication tuning within resoswitch-embedded clock generators. Moreover, the PDM capability holds

doi:10.6342/NTU202600018

promise for facilitating sophisticated modulation schemes applicable to resoswitch-based communication receivers. Nevertheless, the efficacious utilization and design of this functionality necessitates precise modeling of the fundamental nonlinear dynamical motion behavior and period-doubling bifurcation.

doi:10.6342/NTU202600018

5 Developments on MEMS Attractor Exchangers

5.1 Gap-Continuation Based Attractor Exchanger

This study presents the inaugural realization of a micromechanical *attractor exchanger*, facilitating the transition of attractors across the high- and low-energy branches situated in the hysteresis region of a nonlinear resonator. Diverging from the traditional usage of the frequency sweeping method to access the high-energy branch attractor, the proposed technique leverages gap-spacing continuation to shift stable operation from the lower-energy attractor to the higher-energy one using a single-frequency drive. This methodology establishes a novel operation scheme that obviates the requirement for circuitry capable of producing frequency sweeping signals. Consequently, the approach is highly advantageous for implementations relying on the open-loop operation of nonlinear resonators.

5.1.1 Introduction

In recent years, the nonlinear phenomenon and dynamical behaviors intrinsic to MEMS devices have been the subject of comprehensive investigation. Operating in the nonlinear regime has proven advantageous for optimizing the signal-to-noise ratio and frequency stability within devices such as gyroscopes and oscillators. Additionally, this operational mode augments the capture of small signal sensing in various applications, including AFM and mass determination [9, 179, 246, 451, 452]. Furthermore, the hysteresis region, engendered by nonlinearity within the frequency response, poses distinct difficulties. This region, characterized by the manifestation of dual response states during forward and backward frequency sweeps, renders the manipulation of such devices more intricate. To be precise, when the system is excited by a single frequency from a state of rest, the resulting motion predominantly converges to the low-energy state.

doi:10.6342/NTU202600018

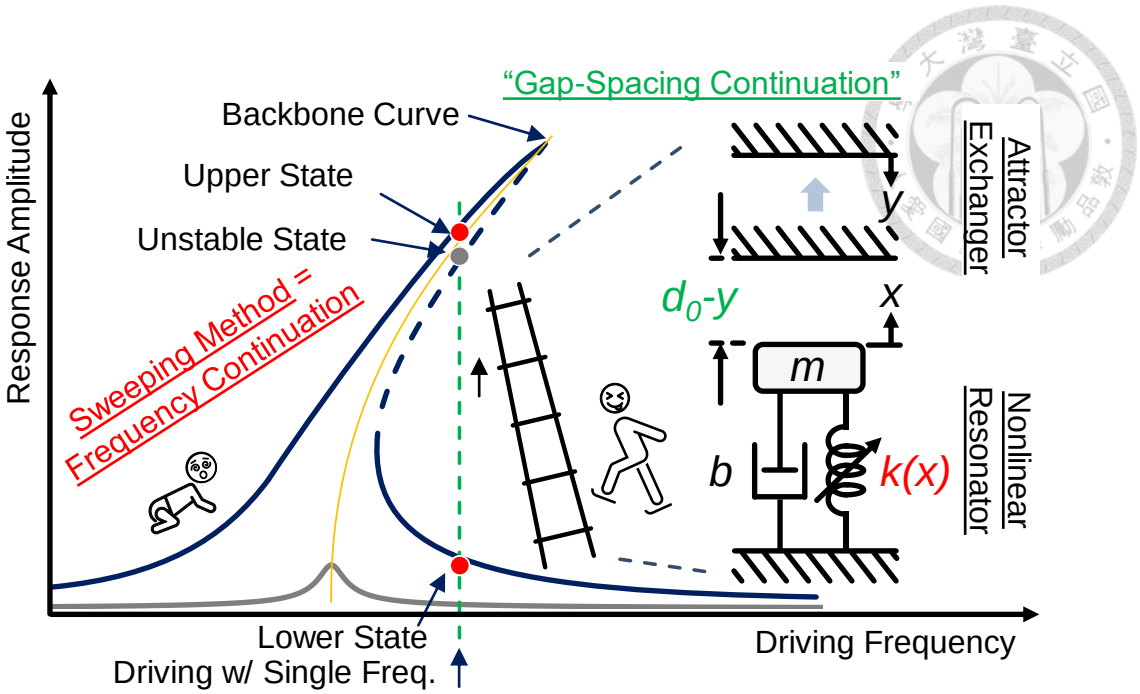


Figure 5-1: A conceptual illustration of the gap-spacing continuation technique, shown with its corresponding mechanical model for an attractor exchanger integrated with a nonlinear device. Reproduced with permission of [273], Copyright of © 2023 IEEE.

An experimental technique known as control-based continuation (CBC) has been established to pinpoint the unstable orbits inherent in nonlinear devices at the macro scale. This approach has been utilized to access distinct states or to investigate device bifurcations [453-455]. The methodology entails the concurrent regulation of multiple parameters of a nonlinear device, including the driving force, displacement, or phase. For the effective identification of the system's orbits, the controller is required to be non-invasive; this implies that any feedback or constraint exertion must dissipate once the system aligns with the orbit (specifically, the feedback gain must fall to zero subsequent to stabilization) [453]. Consequently, the determination of the supplementary controlled parameter is of critical significance in CBC.

Although this method is applicable at the micro scale—utilizing a phase shifter to designate the operating point of nonlinear resonators by governing the I/O phase difference—it remains restricted to the nonlinear oscillator subset. In alternative scenarios, such as surface condition monitoring utilizing a vibro-impact resonator

doi:10.6342/NTU202600018

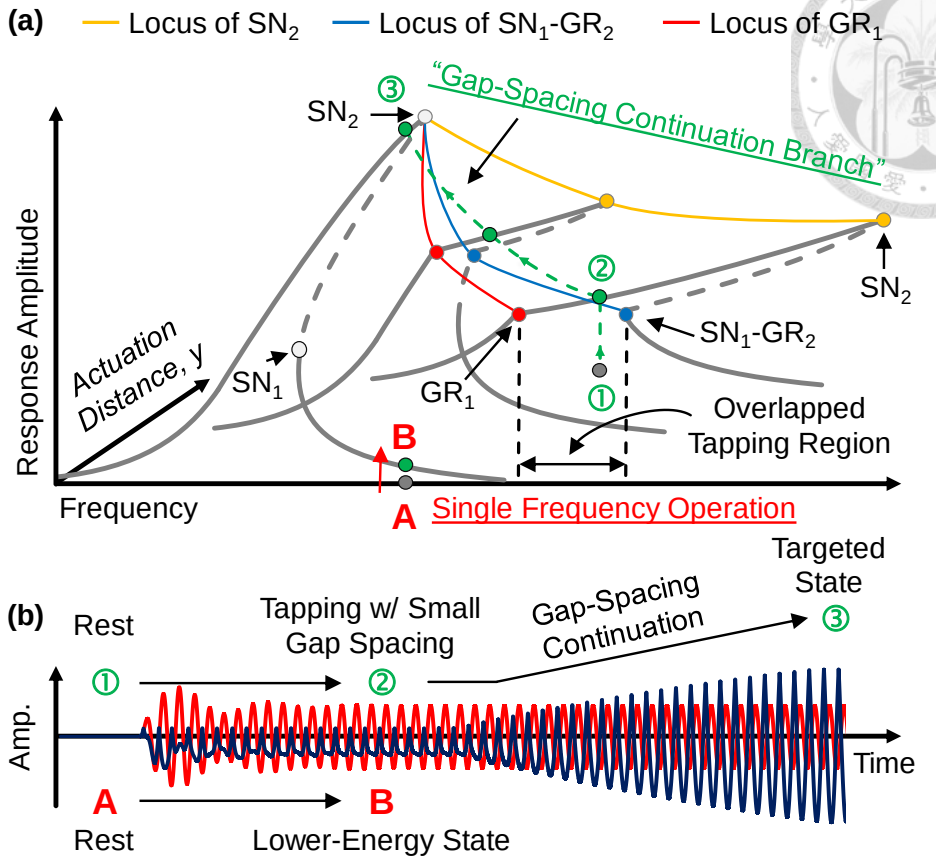


Figure 5-2: (a) A diagram illustrating the gap-spacing continuation technique, which displays the frequency response curves of a Duffing resonator under varying gap spacing and reveals a new, smooth gap-spacing continuation branch. (b) A simulated time-domain plot showing the evolution of a Duffing oscillator's displacement amplitude during the gap-spacing continuation process. (Note: SN_i and GR_i denote the saddle-node and grazing bifurcations, respectively, while SN_1-GR_2 indicates a point where these two bifurcations are very close). Reproduced with permission of [273], Copyright of © 2023 IEEE.

[191], open-loop frequency sweeping is customarily necessitated to attain specific orbits or periodic solutions. Nonetheless, the frequency sweeping scheme necessitates the inclusion of complex control circuits for frequency synthesis and data flow regulation, thereby rendering it less amenable to practical circuit integration.

5.1.2 Gap-spacing Sweeping Technique

The conceptual framework of the gap-spacing continuation technique is illustrated in Figure 5-1, deriving inspiration from the CBC technique alongside closed-loop

doi:10.6342/NTU202600018

operation protocols. By employing variable gap spacing as an additional parameter, this approach regulates the system state, thereby eliminating the necessity for feedback loops or frequency sweeping generators. In contrast to the conventional frequency sweeping method—analogous to an infant *crawling uphill*—the gap-spacing continuation technique offers a divergent trajectory within the gap-spacing space, akin to *climbing a ladder* to attain the objective.

The elucidation of the gap-spacing continuation method is provided in Figure 5-1. The attractor exchanger initiates the process by diminishing the gap spacing, an action that widens the overlapped-tapping region. This enables the device to sustain excitation via a single frequency, thereby engaging tapping-mode operation, comparable to ascending the initial rung of a ladder (refer to ① to ② in Figure 5-2 (a)). Subsequently, the attractor exchanger gradually expands the gap spacing, altering the device's orbit in a manner parallel to frequency sweeping, yet confined within the gap-spacing space (refer to ② to ③ in Figure 5-2 (a)). As the gap spacing varies, the device tracks a novel attractor in proximity to the existing one, persistently steering the response until convergence with the high-energy attractor is achieved. Figure 5-2 (b), displays the qualitative numerical simulation conducted utilizing MATLAB and Simulink. This illustration highlights the evolution of the time-domain displacement amplitude from

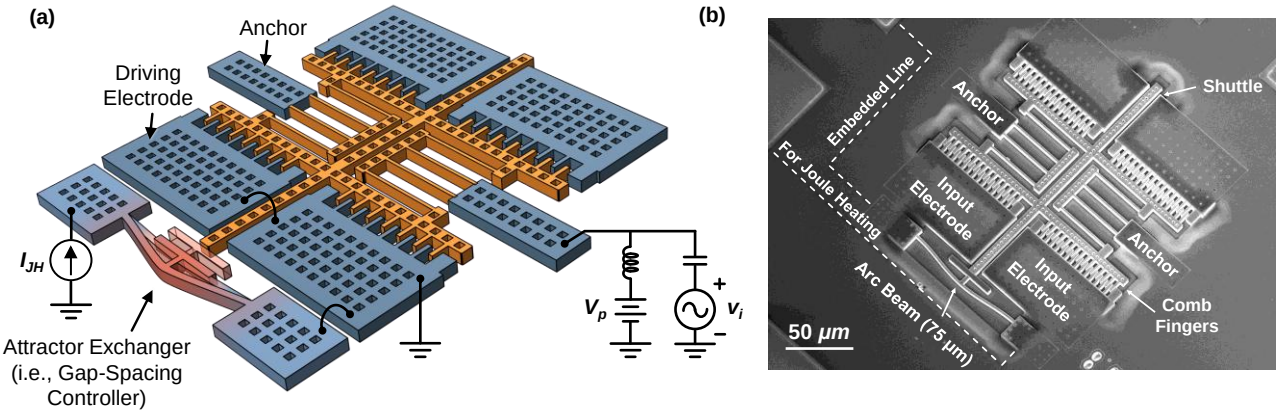


Figure 5-3: (a) A schematic of the attractor exchanger, which consists of an arc-beam thermal actuator driven by a Joule-heating current (I_{JH}), shown with the comb-driven resonator and its experimental setup. (b) An SEM image of the released arc-beam thermal actuator integrated with the comb-driven vibro-impact resonator. Reproduced with permission of [273], Copyright of © 2023 IEEE.

doi:10.6342/NTU202600018

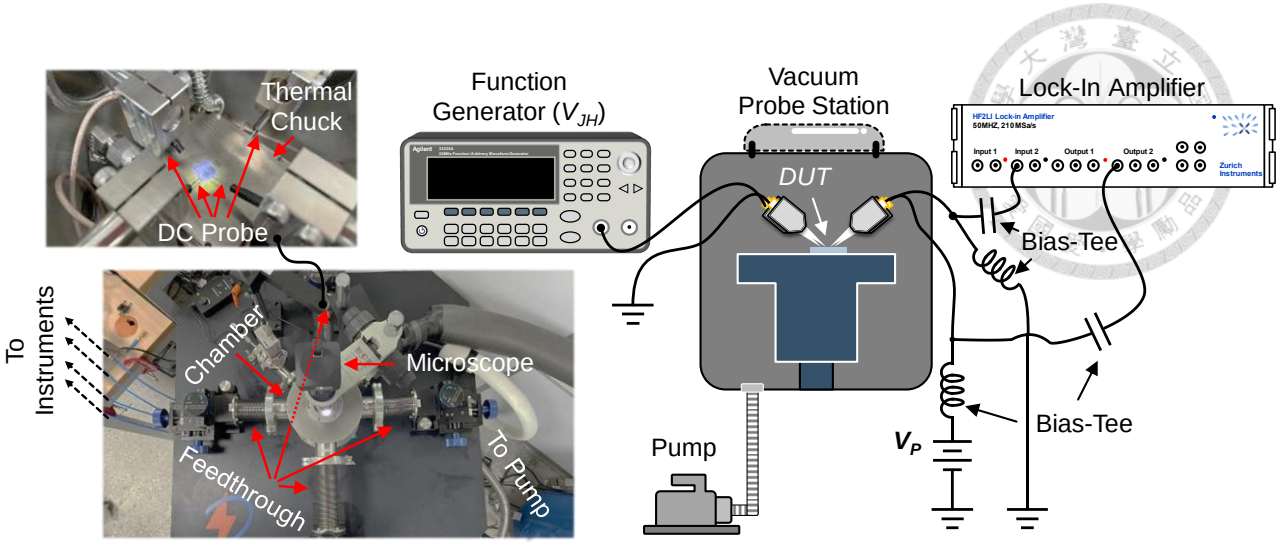


Figure 5-4: The measurement setup used for characterizing the frequency transmission and validating the functionality of the gap-spacing continuation. The inset provides photographs of the probe station, its associated feedthrough, and a detailed view of the DC probe. Reproduced with permission of [273], Copyright of © 2023 IEEE.

① to ② to ③ realized via the gap-spacing continuation technique, in juxtaposition with the single-frequency drive applied to the original device configuration (A to B).

5.1.3 Structure and Operation

Figure 5-3 illustrates the configuration of an arc-beam thermal actuator functioning as the attractor exchanger for the gap-spacing controllable stopper embedded within a CMOS-MEMS comb-driven vibro-impact resonator. Excitation of the resonator is accomplished via an AC signal v_i, while a polarization bias V_P is imposed upon the driving electrode. The administration of a Joule heating current I_{JH} induces deformation in the attractor exchanger, thereby facilitating continuous regulation and modulation of the gap spacing during operation.

5.1.4 Experimental Results

In accordance with the post-fabrication process detailed in Section 3.2, the device is constructed utilizing a standard 0.35-μm CMOS process platform and subsequently released employing an Al-compatible HF-based Silox Vapox III at room temperature for a duration of approximately 60 minutes. The device schematic representation is

doi:10.6342/NTU202600018

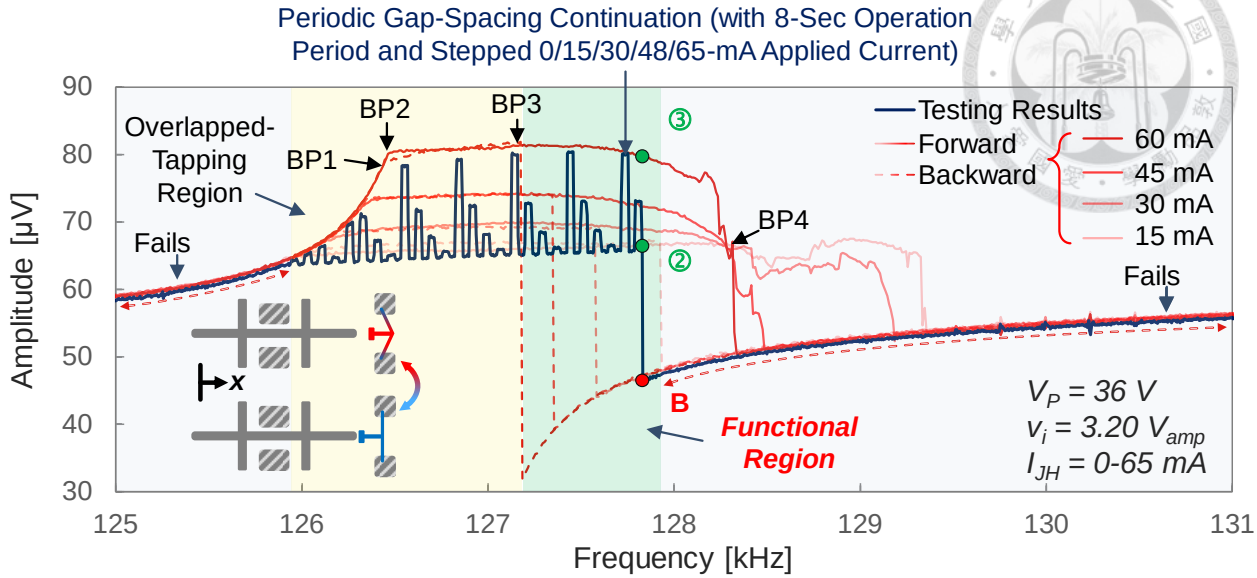


Figure 5-5: A plot demonstrating the functionality of the gap-spacing continuation technique, measured using the sweeper function of a lock-in amplifier. The frequency transmission of the vibro-impact resonator is shown for applied currents of 0, 15, 30, 48, and 65 mA (gradual red lines), with solid and dashed lines indicating forward and backward sweeps, respectively. The system's operating state is shown to switch from the lowest attractor to higher ones in response to pulsed Joule-heating currents. Reproduced with permission of [273], Copyright of © 2023 IEEE.

depicted in Figure 5-3 (a) , whereas Figure 5-3 (b) presents the SEM micrograph of the released device. Figure 5-4 displays photographs of the experimental measurement apparatus. The die is positioned within a custom-engineered vacuum probe station, which is evacuated to a pressure inferior to 5 $\times 10^{-3}$ Torr. An arbitrary waveform generator (33220A, Agilent Technologies, USA) administers the DC or modulated pulse signal to the attractor exchanger, while a lock-in amplifier (HF2LI, Zurich Instruments, Switzerland) characterizes the frequency response via the conventional frequency sweeping method. Owing to inherent instrument constraints, the functionality is substantiated indirectly within the frequency domain. Specifically, 1200 distinct increments are designated across the frequency region of interest, with the period of the modulated pulse signal established at 8 seconds (corresponding to a 1-second hold time per step).

doi:10.6342/NTU202600018

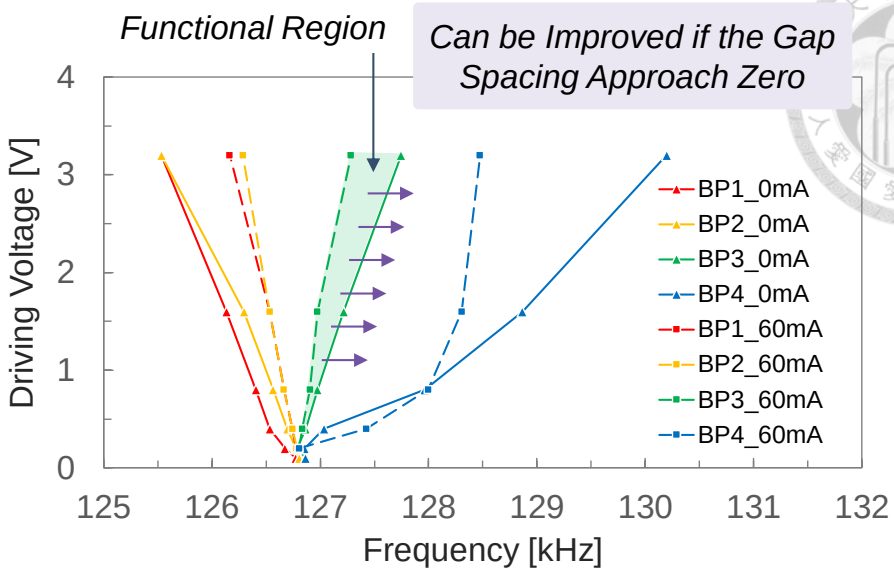


Figure 5-6: The measured bifurcation set for the vibro-impact resonator, plotting driving voltage against the frequency locations of the bifurcation points (BP), both with and without an applied current of 60 mA. This plot provides a detailed view of the functional region for attractor exchange. Reproduced with permission of [273], Copyright of © 2023 IEEE.

The frequency response of the vibro-impact resonator, subject to varying levels of Joule-heating current applied to the attractor exchanger, is illustrated in Figure 5-5. An elevated transmission level correlates to an increased gap spacing. The critical bifurcation points are designated as BP1 through BP4. To validate the efficacy of the attractor exchanger, the component is actuated with an alternating Joule-heating current throughout the frequency sweeping measurement. The data indicates that the exchanger functions exclusively within the functional region and the overlapped-tapping region, as illustrated in Figure 5-5, and confirms that the device response is capable of transitioning between the low-energy and high-energy attractors.

In Figure 5-6, the driving voltage relative to the BP locations—defined as the bifurcation set—is plotted for the comb-driven vibro-impact resonator under applied currents of 0 and 60 mA. For each individual attractor, the overlapped-tapping region is situated between BP2 and BP3. The attractor exchange functional region is positioned between the BP3 coordinates of the respective states.

doi:10.6342/NTU202600018

5.1.5 Conclusions

This research has substantiated the attractor exchange functionality through the implementation of a fundamental CMOS-MEMS arc-beam thermal actuator, thereby facilitating transitions between the high- and low-energy attractors residing within the hysteresis region of a nonlinear resonator during open-loop operation. Moreover, gap continuation is leveraged as an alternate parameter space, enabling the migration of stable operation across attractors via a single-frequency drive. This approach establishes a novel operational scheme, which obviates the necessity for circuits designed to synthesize frequency sweeping signals in applications predicated on the open-loop operation of nonlinear resonators. Nonetheless, the precise modeling of the intrinsic nonlinear dynamical motion remains imperative for the optimal design and exploitation of this functionality within nonlinear devices.

doi:10.6342/NTU202600018

5.2 Vibro-Impact Perturbation-Based Attractor Exchanger

This study presents a novel technique for toggling the behavior of a nonlinear micromechanical resonator amidst two co-existing attractors through the employment of vibro-impact perturbation. Such a protocol permits the nonlinear resonator to exchange between attractors under a single-frequency drive, thereby circumventing the conventional requirement for frequency sweeping. The resonator responsible for striking the target nonlinear device—designated herein as an *attractor exchanger*—induces perturbations throughout the system. Through precise modulation of the driving signal's phase and duration, consistent exchange between attractors is realized. Consequently, this mechanism obviates the need for frequency sweeping circuits or the closure of a phase control loop, establishing a distinct operation scheme for nonlinear resonators. This strategy offers significant potential for specific applications, notably fast start-up oscillators and mechanical computation.

5.2.1 Introduction

MEMS resonant devices frequently incorporate diverse nonlinear sources and manifest complex nonlinear dynamical behaviors [9, 456, 457]. Although nonlinearity can enhance capabilities or be exploited in sensing applications [9, 451], it simultaneously engenders a multi-valued region within the frequency response of resonators, wherein various motion solutions exist concurrently. This intricacy complicates the identification of an optimal operating point. To illustrate, energy harvesters typically require functioning within the large motion orbit to optimize energy output, whereas vibration reduction applications may favor the smaller motion orbit to mitigate oscillations.

Consequently, researchers have formulated various control-based continuation (CBC) methods to identify and regulate the stable and unstable orbits of nonlinear resonators across both macro- and microscale systems. These strategies encompass time-delayed feedback control [458] and phase-locked loops [459]. Moreover, numerous perturbation-based control laws have been engineered to manipulate stable

doi:10.6342/NTU202600018

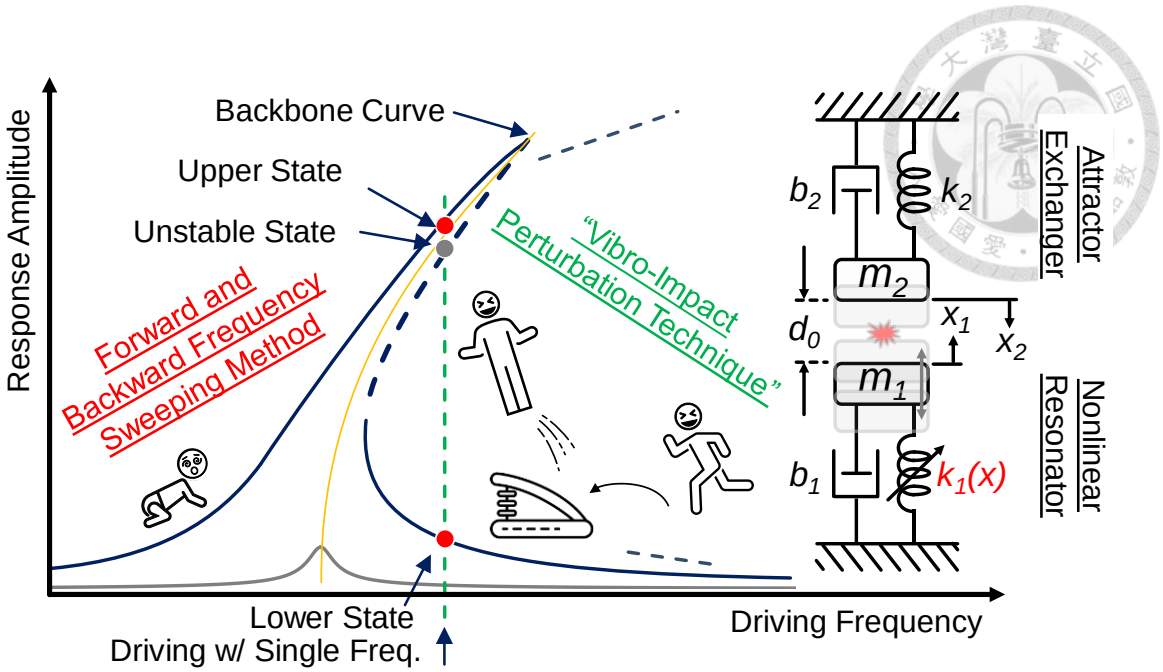


Figure 5-7: A conceptual illustration of the vibro-impact perturbation technique, shown with its corresponding mechanical model for an attractor exchanger integrated with a general nonlinear device. Reproduced with permission of [306], Copyright of © 2023 IEEE.

co-existing attractors in open-loop systems. Prominent instances include intermittent control [460], sweeping parameters [461], and the linear augmentation method [462]. Recently, [273] employed a thermal actuator to establish a novel gap-spacing space in a nonlinear resonator, thereby facilitating attractor exchange in microscale resonators. Regarding all open-loop control laws, a specific control approach is requisite to drive or steer the system from the current attractor to the target attractor, guaranteeing that the trajectory satisfies a proximity constraint within the basin of attraction of the desired attractor.

Governance of the system is achievable via methods such as precise driving waveforms or by sweeping certain parameters during excitation. Nevertheless, these methodologies are often constrained regarding the operating range and present significant hurdles for practical implementation. To circumvent these impediments, this research employs a vibro-impact perturbation technique. This methodology facilitates a substantially broader operating range and affords superior flexibility for the target resonator.

doi:10.6342/NTU202600018

5.2.2 Vibro-impact Perturbation Technique

Drawing inspiration from the perturbative characteristics of the previously illustrated methodologies, this work advances a vibro-impact perturbation technique designed to facilitate transitions between attractors within MEMS resonators. In contrast to the frequency sweeping method depicted in Figure 5-7, the vibro-impact perturbation affords an immediate switch—analogous to *jumping on a springboard*—propelling the system from a low-energy attractor toward the desired high-energy one. To corroborate the efficacy of the attractor exchanger, a vibro-impact nonlinear resonator is employed, owing to its wider multi-valued range.

Figure 5-8 (a) delineates the 2-DOF model characterizing the nonlinear resonator integrated with the attractor exchanger. To mitigate potential interference between the paired resonators, the attractor exchanger is situated at a separation from the target resonator that exceeds the gap existing between the target resonator and its stopper. The governing coupled equation of motion is expressed as follows

$$\begin{cases} m_1 x_1'' + b_1 x_1' + k_1 x_1 + k_{c1}(x_1 - d_1)H(x_1 - d_1) \\ +k_{c2}(x_2 - x_1 - d_2)H(x_2 - x_1 - d_2) = A_{d1}cos(\omega_{d-1}t) \\ \\ m_2 x_2'' + b_2 x_2' + k_2 x_2 \\ +k_{c2}(x_2 - x_1 - d_2)H(x_2 - x_1 - d_2) = A_{d2}cos(\omega_{d-2}t) \end{cases} \tag{5-1}$$

and parameter values used are summarized in the caption.

A qualitative simulation rooted in (5-1) was executed employing the protocols detailed in [192]; however, the model incorporated an elevated damping coefficient (Q of 100) alongside a reduced frequency to curtail computation time, thereby prioritizing the observation of the vibro-impact perturbation and the consequent transient motions. To approximate the interaction force arising between the resonator and the stopper, a linear spring model was utilized, effectively replicating the tapping-mode frequency response as well as the time-domain motion characteristic of the vibro-impact resonator.

Figure 5-8(b) depicts the modeled multi-valued frequency response exhibited by the vibro-impact resonator. Subsequently, Figure 5-8 (c) presents the steady-state time

doi:10.6342/NTU202600018

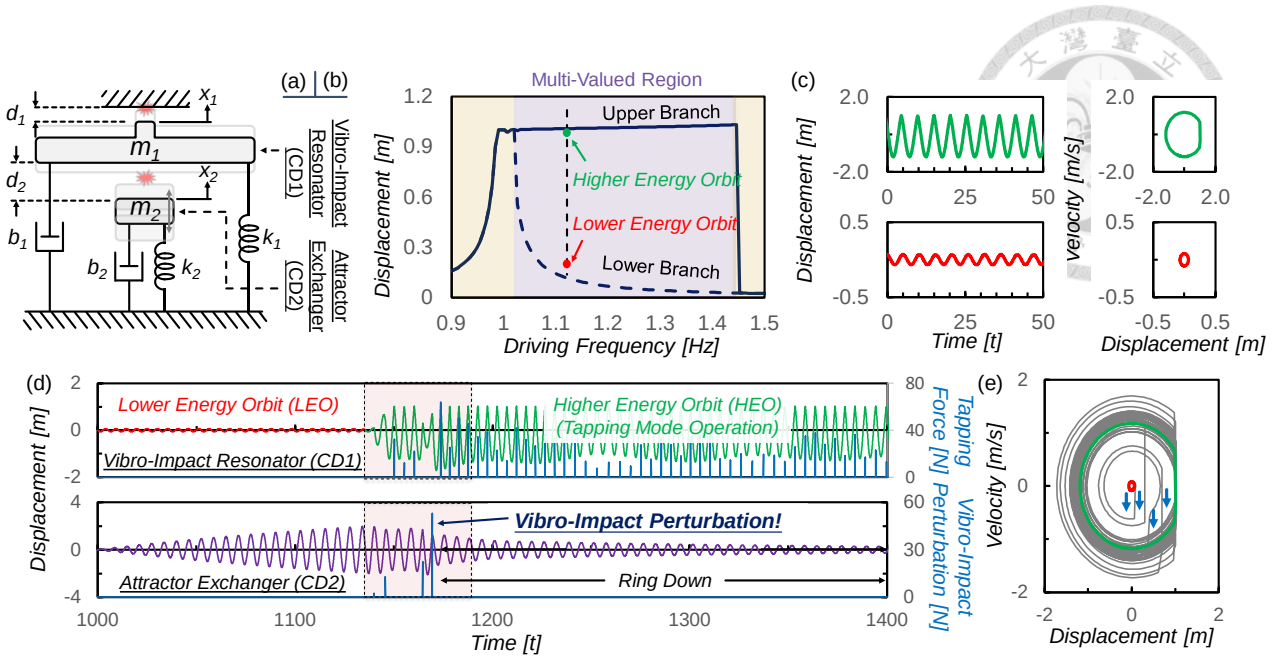


Figure 5-8: (a) A 2-DOF model of the vibro-impact resonator with the proposed attractor exchanger. (b) The general frequency response of a vibro-impact resonator, illustrating the hysteresis and multi-valued region. (c) Time-domain histories and phase portraits for the higher and lower energy orbits indicated in (b). (d) The time-domain response of the resonator and exchanger during the orbit exchange. (e) The phase portrait showing the two orbits and the transient trajectory connecting them. Reproduced with permission of [306], Copyright of © 2023 IEEE. Parameters used for the numerical simulations are: $m_{i=1,2} = 1$ (kg), $b_{i=1,2} = 0.01$ (N•s/m), $k_{i=1,2} = 1$ (N/m), $k_{c,1} = 2500$ (N/m), $k_{c,2} = 1$ (N/m), $A_1 = 3$ (N), $A_2 = 4$ (N), $d_1 = 1$ (m) and $d_2 = 2$ (m).

history and phase portrait corresponding to the coexisting high and low energy attractors identified within Figure 5-8 (b). The fundamental principle of the vibro-impact perturbation technique involves initiating a sequence of periodic impacts designed to agitate the target device, compelling a transition from one stable attractor to an alternative one. Figure 5-8 (d) delineates the displacement versus time for both resonators at the specific frequency point highlighted in Figure 5-8 (b); this visualization confirms that the target resonator sustains multiple impacts, resulting in an abrupt alteration in velocity, as evidenced by the associated phase portrait in Figure 5-8 (e).

The simulation results elucidate that the successful implementation of the vibro-impact perturbation technique necessitates: (1) a comprehensive characterization of the

doi:10.6342/NTU202600018

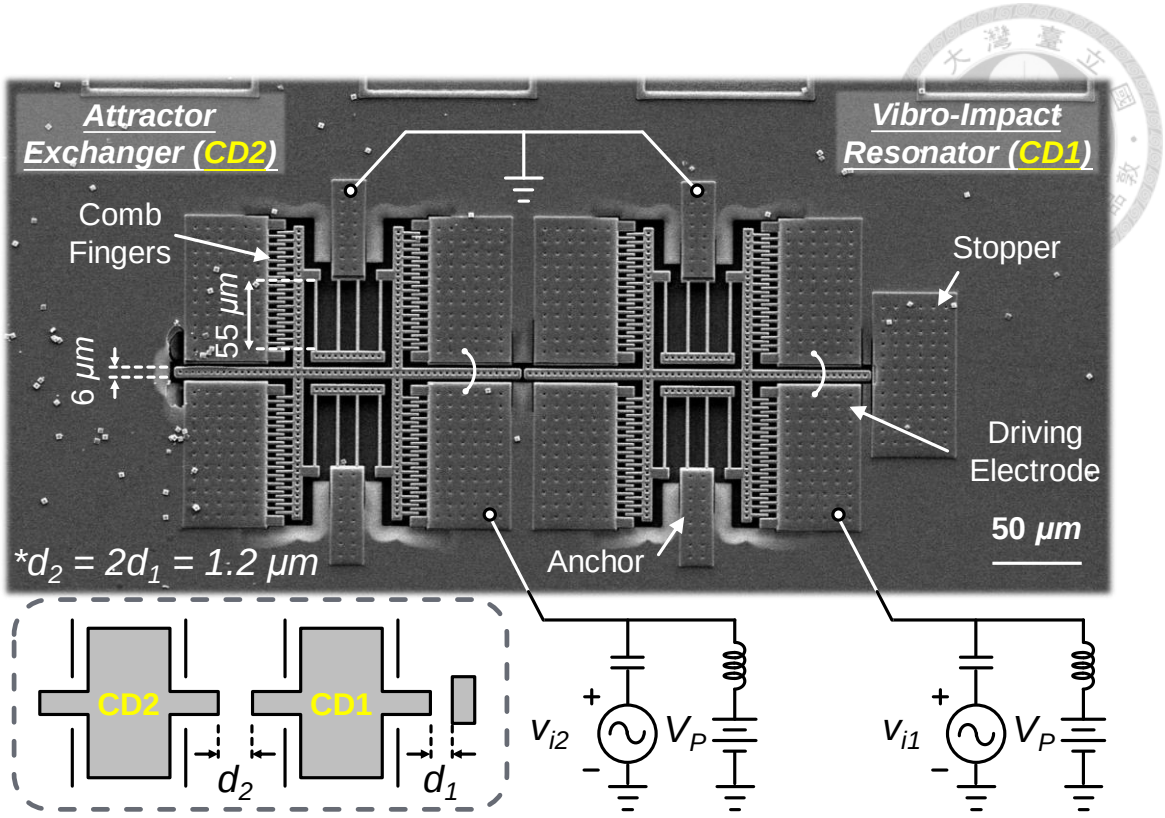


Figure 5-9: An SEM image of the released comb-driven vibro-impact resonator with an integrated attractor exchanger. The device structure is composed of the entire metal layer stack from METAL1 to METAL4 of the 0.35-μm CMOS process. Reproduced with permission of [306], Copyright of © 2023 IEEE.

system's basin of attraction, (2) the magnitude of the control (specifically, vibro-impacting), and (3) the precise timing of the control application.

5.2.3 Structure and Operation

For experimental validation, the study employs two CMOS-MEMS comb-driven resonators, designated as the vibro-impact resonator (CD1) and the attractor exchanger resonator (CD2), as identified in Figure 5-9. Adhering to the fabrication method delineated in Section 3.2, the device is fabricated via a standard 0.35-μm CMOS-MEMS process platform, succeeded by in-house post-CMOS processing utilizing a commercial buffered oxide etchant, Silox Vapox III (Transene Company, Inc.), at 20°C for a duration of approximately 60 minutes. Figure 5-9 exhibits the SEM image of the released structures alongside the corresponding testing circuit. Actuation of both resonators is effectuated by alternating current signals v_{i1} and v_{i2}, with a DC

doi:10.6342/NTU202600018

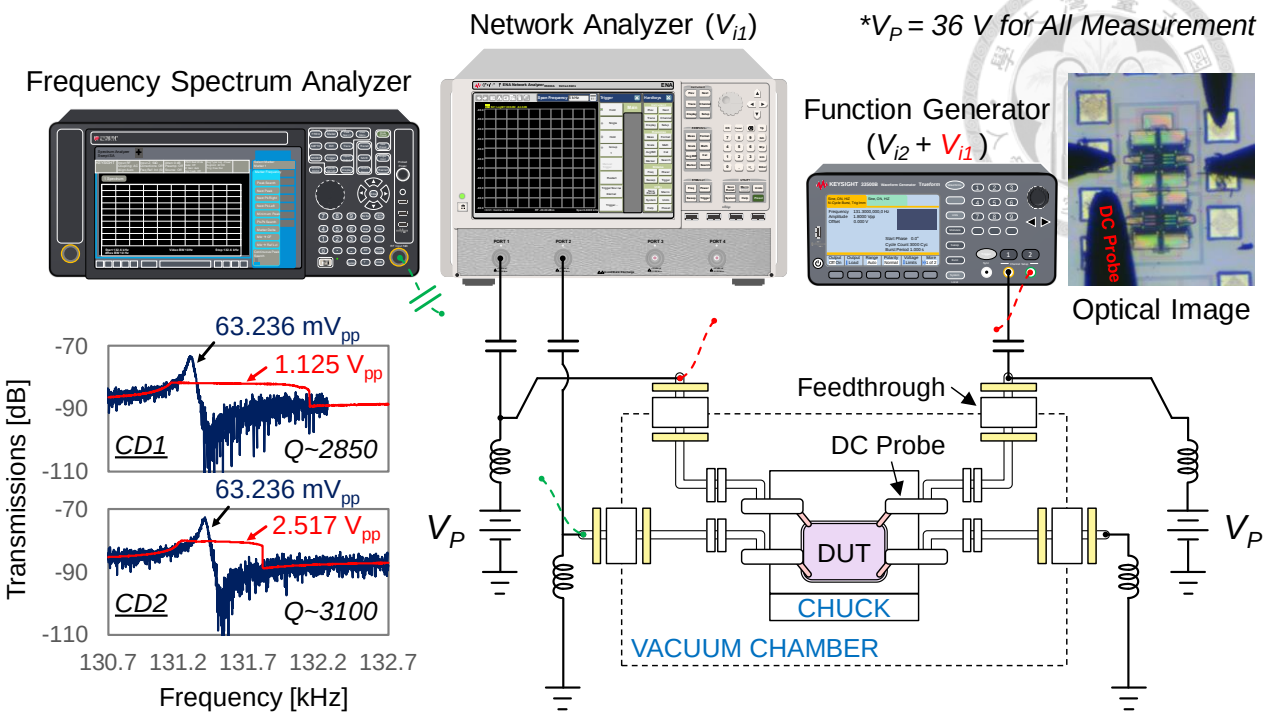


Figure 5-10: The measurement setup for characterizing the frequency transmission and validating the vibro-impact perturbation technique. The inset on the right provides an optical image of the DUT under test. The insets on the left display the measured frequency responses for the two resonators in both linear and tapping-mode operation. Reproduced with permission of [306], Copyright of © 2023 IEEE.

polarization bias voltage V_P applied across the driving electrodes. To avert interference as previously established, the design features a gap of 0.6 μm between the vibro-impact resonator and the stopper, and a gap of 1.2 μm separating the two resonators.

5.2.4 Experimental Results

Figure 5-10 delineates the experimental configuration implemented for the assessment of the devices. The specimen is secured within a custom-built vacuum probe station, where the environment is depressurized to a level exceeding 5×10^{-3} Torr. Determination of the vibro-impact resonator's frequency response is executed via a network analyzer (E5080A, Keysight Technologies, USA) employing a conventional frequency sweeping method.

The insets positioned on the left of Figure 5-10 exhibit the linear and tapping responses corresponding to the two resonators. The grazing condition (zero-velocity

doi:10.6342/NTU202600018

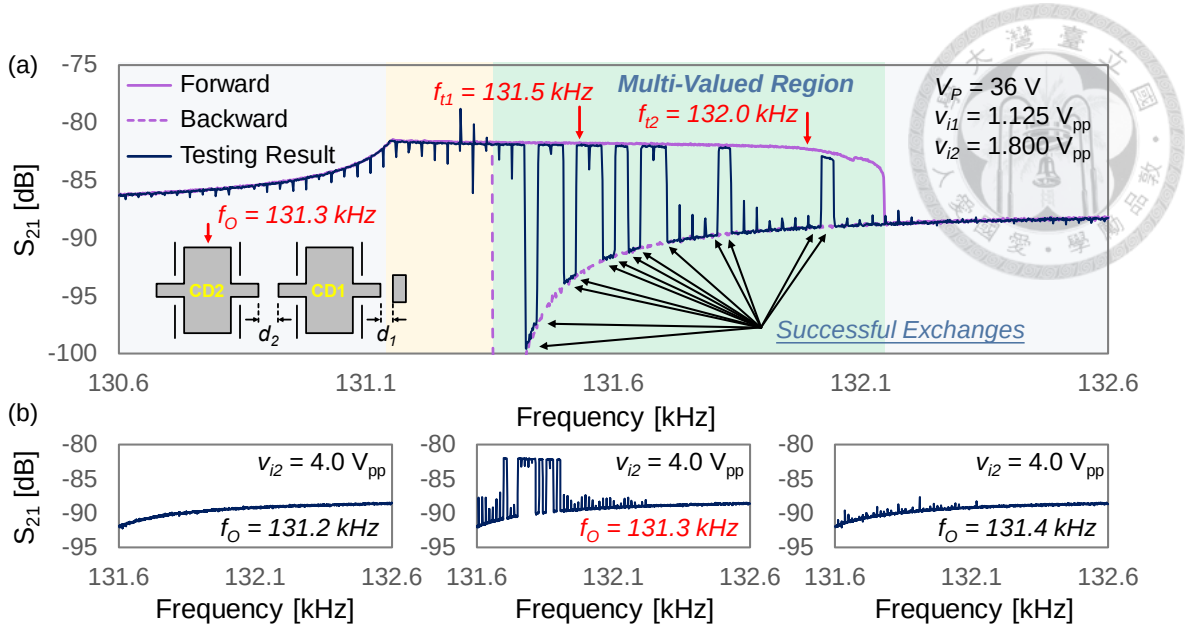


Figure 5-11: (a) A plot validating the vibro-impact perturbation technique, measured using a standard frequency sweep. The resonator's orbit is shown to successfully switch between the upper and lower branches when the exchanger is driven by a 3000-cycle, 1-Hz burst signal at 131.3 kHz. (b) Measured backward-sweeping transmission responses of the vibro-impact resonator with the exchanger driven at different frequencies, demonstrating that the attractor exchange is only effective when the exchanger operates at its resonance frequency. Reproduced with permission of [306], Copyright of © 2023 IEEE.

impact) occurring at the resonance frequency of each resonator is established utilizing drive levels of -3 dBm (~0.45 V_{PP}) and 5 dBm (~1.125 V_{PP}), respectively. Regarding acquisition parameters, the E5080A is configured to capture 1601 points with a 20-Hz IF bandwidth spanning a specific 2-kHz frequency range, whereas a 36-V polarization bias is maintained by a power supply (E3647A, Keysight Technologies, USA). To induce the requisite vibro-impact perturbation, an arbitrary waveform generator (33500B, Keysight Technologies, USA) transmits a burst signal to the attractor exchanger. Because of specific instrument limitations, validation is conducted via a signal analyzer (N9000B, Keysight Technologies, USA); this involves employing a 3000-cycle 1-Hz burst signal throughout the frequency sweeping measurement for illustrative intent, followed by the application of a solitary 3000-cycle burst signal to explicitly verify the vibro-impact perturbation technique.

doi:10.6342/NTU202600018

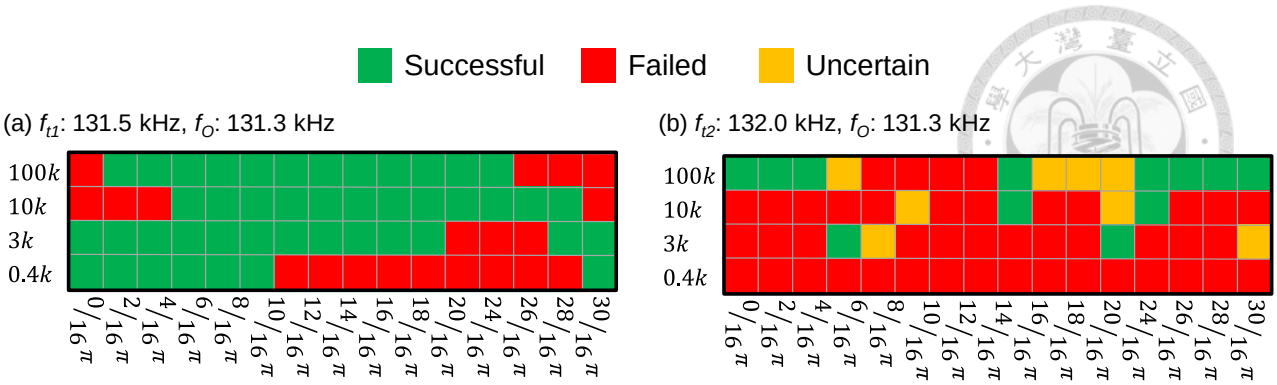


Figure 5-12: A map detailing the success of attractor exchange as a function of the number of burst cycles and the initial phase difference between the driving signals of the target resonator and the exchanger. The results are compared for two different target resonator frequencies: (a) 131.5 kHz and (b) 132.0 kHz. Reproduced with permission of [306], Copyright of © 2023 IEEE.

Figure 5-11 (a) depicts the acquired frequency response, wherein the exchanger is stimulated by a 3000-cycle 1-Hz burst signal precisely at its resonance frequency of 131.3 kHz. As evidenced in Figure 5-11 (b), the operation of the exchanger is strictly confined to its resonance frequency. To ascertain the optimal driving frequency for the attractor exchanger, the forward sweeping method is employed.

Figure 5-12 delineates a mapping of the conditions under which attractor exchange transpires, specifically correlating varying burst cycles and phase shifts—defined here as the phase difference existing between the excitation signals of the paired resonators—across two separate target frequencies. Effectuating the exchange at 132.0 kHz presents increased difficulty, attributed to the substantially more pronounced energy gap separating the attractors.

5.2.5 Conclusions

The present study successfully validates a vibro-impact perturbation-based attractor exchanger, establishing a novel approach for regulating the dynamics of nonlinear resonator devices. This methodology facilitates switching between the high and low energy branches inherent to the hysteresis region of the devices. Crucially, the vibro-impact perturbation technique permits the commutation between attractors via single-frequency operation. Experimental findings reveal that the quantity of perturbation cycles exerts a profound influence on the efficacy of the attractor exchange, thereby

doi:10.6342/NTU202600018

illuminating potential trajectories for subsequent investigation.



doi:10.6342/NTU202600018

6 Conclusions and Remarks

6.1 Results Summary

This dissertation focuses on the development of modeling of vibro-impact resonator incorporating with other nonlinearities and electrical hot switching operation, resulting in a more general governing equation and nonlinear dynamics of vibro-impact resonators that can predict the responses quantitatively. With the developed model, the dissertation not only explores the resoswitch's dynamics, including both steady and transient phase, but also demonstrates the resoswitch and attractor exchanger technology for wake-up receiver, pulse-density modulator and open-loop control of multi-stable device by administer the nonlinear dynamics. The contact force prediction based on the MOA and the MATLAB & SIMULINK system-level simulation platforms are developed. Additionally, the dissertation presents the fully characterization and analysis of the devices based on CMOS platform that is helpful for monolithic integration of next-generation MEMS application.

6.2 Future Research Directions

Although this dissertation demonstrated and analyzed vibro-impact resonator with two types of all-mechanical circuits and two types of attractor exchangers, enhancing the understanding of these devices, significant fundamental challenges remain regarding electromechanical reliability. Before these devices can transition into practical RF components, the intrinsic limits of contact physics must be addressed—specifically, the degradation of contact surfaces due to mechanical wear and the accelerated erosion caused by RF hot-switching. Below are potential future research directions aimed at overcoming these tribological limits to ensure sufficient device lifetime and stable signal integrity in real-world applications.

doi:10.6342/NTU202600018

6.2.1 Model and Simulation Capability Improvement

6.2.1.1 Material Properties Investigation

The modeling approach presented here heavily relies on curve fitting procedures, such as for the nonlinear damping coefficient and nonlinear contact damping. Additionally, to accurately capture the frequency response with both tapping and nonlinear softening features, the Hamaker constant is modified to leave some space, and the conductivity of the contact material is determined based on curve fitting with an initial guess. Although these applied values are based on a broad survey of the literature, they still stem from insufficient investigation into the material properties of the fabrication platform. To address this, extracting mechanical and electrical properties through Atomic Force Microscopy (AFM), frequency response testing of simple beam elements and conductivity determinization from four-point measurement of electrical routing can provide more reliable data, eliminating the need for extensive correction procedures and offering a solid foundation for modeling. This approach would improve the accuracy and reliability of the models, making them more robust and dependable for practical applications. With clear material properties, one might overcome the need of several curve fitting and the issues that the work cannot predicates the responses with period-doubling bifurcation and its locations.

6.2.1.2 Modal Analysis and Optimization for the Resoswitch

The devices of the presented comb-driven resoswitch are not optimized. [263] states that the contacting position can influence the output hot switching response. It might properly origin form the lower contact force caused by modal interaction. As presented in [40], the mode engineering of the device could provide lower contact force and improve the sensitivity of an AFM. One could optimize the resoswitch through modal analysis and maximum the contact force. This kind of mode frequency optimization is already published in [38, 39] for optimization of nonlinear MEMS gyroscopes.

On the other hand, the contact dynamic modeling considering N mode for $N > 1$ are common to improve the accuracy for medium-Q device such as RF switch and AFM

doi:10.6342/NTU202600018

in liquid environment. It might overcome the issues for predicating the responses with period-doubling bifurcation and its locations.

6.2.1.3 Surface Roughness and Time-Dependent Contact Physics

Although the simplified contact model incorporating the Duffing-van der Pol equation offers a closed-form solution for initial design guidelines, it does not fully capture the period-doubling dynamics and long-term reliability limitations of the resoswitch. Establishing a safety margin for end-of-life contact force and consistent contact dynamics requires expanding the experimental and modeling framework to include surface roughness and time-dependent interface evolution. This is critical because contact resistance evolves under the complex interplay of material hardening, visco-elasto-plastic deformation, and Joule heating.

To address this, future efforts must integrate coupled electro-thermo-mechanical behaviors, even a simplified version, to predict resistance evolution, potentially using power-law relations. Furthermore, incorporating a three-dimensional fractal representation of surface roughness, such as the Weierstrass-Mandelbrot function, would be valuable for accurately describing the multiscale nature of contact asperities [358, 359, 463, 464].

6.2.1.4 Prediction of the Maximum Peak Repulsive Force in the Transient State

Previously, [465, 466] employed the principle of energy conservation to estimate the transient state peak repulsive force experienced by an AFM probe encountering a sudden topographical change. These works assumed that the probe's kinetic energy is fully converted into indentation energy, with the impact velocity estimated from the product of oscillation amplitude and frequency, scaled by the topography difference. However, this approach is not applicable to the resoswitch, as accurately predicting the impact velocity is challenging in this context.

Additionally, [467, 468] addressed the periodically forced Duffing equation using the method of averaging, revealing a transient response characterized by an overshoot

doi:10.6342/NTU202600018

phenomenon. In the undamped case, the overshoot is shown to depend on the driving frequency, force amplitude, and the strength of Duffing nonlinearity.

These findings suggest the potential to identify how system parameters influence the transient-state peak repulsive force in a resoswitch, which would enhance modeling efficient, understanding and contribute to the improvement of the device sensitivity.

6.2.2 Reliability and Sensitivity Improvements

Another critical aspect is contact reliability. Historically, mechanical switches have struggled with switching reliability, and resoswitches are no exception. While resoswitches experience less contact stiction, they still suffer from contact degradation over time. The reliability is significantly influenced by the contact material used, contact force level and backend bleeding circuit.

6.2.2.1 Contact Material Engineering

[261] has demonstrated that electroless nickel plating can extend the lifetime of CMOS-MEMS resoswitches from approximately 3×10^6 to 2.2×10^7 cycles. However, unlike RF switches that operate in a static mode, resoswitches function at high operating frequencies, which lead to a significantly higher contact degradation rate. To transmit the same amount of data, the required lifespan of a resoswitch must be approximately 10^2 to 10^5 times longer, depending on the application and technology, than the ~10^9 switching cycles typically required for RF switches. Therefore, further research is needed from both fabrication process, post-fabrication treatment, packaging and measurement characterization perspectives to comprehensively evaluate and improve the reliability of resoswitches.

It is believed that based on previous results and analyses, the implementation of high-performance surface finishes processes same as what PCB industry did—such as electroless nickel immersion gold (ENIG), electroless nickel immersion silver (ENImAg), or electroless nickel electroless palladium immersion gold (ENEPIG)—could overcome current limitations in lifetime and sensitivity. Since resoswitches do not suffer from stiction failures due to high adhesion forces, the ultra-low contact

doi:10.6342/NTU202600018

resistance achieved by noble metals with a hard underlying nickel layer presents a promising solution for enhancing both reliability and sensitivity.

6.2.2.2 Optimized Bleeding Circuit and Time Constant

The output bleeding circuit can be further optimized. In typical resoswitch designs, an RC tank is implemented because the series resistance is necessary for signal reception, and parasitic capacitances are inevitable in practice. As noted earlier, no additional capacitance is manually introduced in this dissertation; instead, a parasitic capacitance of approximately 300–400 pF arises from cables and measurement equipment, which constrains the design space.

Regarding the switching scheme, using a higher-value bleeding resistor in combination with a lower capacitance is preferred, as it reduces the hot-switching current, minimizes the voltage drop at the contact point, and thereby improves device reliability.

Alternatively, a push-pull operation scheme was innovatively proposed in [469], where two resoswitches with different resonance frequencies are connected in parallel, one biased and the other grounded. This configuration theoretically achieves an infinite bleeding resistance in the ON state and near-zero bleeding resistance in the OFF state. However, this topology necessitates two resoswitches and limits its applicability to frequency-dependent modulation schemes.

These observations suggest that CMOS-based resistors, with their high resistance and negligible capacitance, could be viable candidates for further optimization. Additionally, active circuit components may offer another path for improvement, though considerations such as power consumption, device footprint, and the net performance benefits, similar to those addressed in energy harvester developments, must be carefully evaluated.

6.2.2.3 Mechanical Engineering on the Output Electrode

As previously mentioned, typically undesirable effects such as Duffing nonlinearity and surface adhesion forces can be intentionally harnessed to improve performance of

doi:10.6342/NTU202600018

resoswitches. For example, [433] introduces a novel MEMS relay that leverages a high-adhesion contact structure to achieve ultra-low contact resistance at low actuation voltages. By incorporating a large contact area and a spring-assisted detachment mechanism, the relay ensures stable operation across multiple switching cycles. Given the significantly higher structural stiffness of the resoswitch, this suggests that a contact surface with ultra-high adhesion force may not pose a limitation such as stiction if properly engineered. Moreover, it opens up additional design space for batter sensitivity that warrants further exploration.

In parallel, metamaterials have been employed in RF switches to mitigate stiction issues and enhance overall performance [281-283], while soft-impact structures have been implemented to suppress squegging phenomena [83, 312]. Future performance improvements for resoswitches may be realized by optimizing output electrodes in terms of stiffness, damping coefficient, mass, resonance frequency, quality factor, and adhesion force. It is worth noting that, as demonstrated in vibro-impact perturbation based attractor exchangers, It is believed that the system should be generally modeled with at least two DOF like impulsively coupled oscillator [470, 471]. After that, considering more DOF for accuracy improvement or treating output electrode with pulse or quasistatic situation for system model simplification could be implemented. Accordingly, structural interactions, particularly those involving frequency detuning, quality factor, and stiffness, must be carefully analyzed and integrated into the design process.

Furthermore, [83] stated that soft-contact electrode suppresses the squegging phenomenon, improve the sensitivity and lower the slop of the input voltage to contact resistance transfer function, making resoswitch possible for AM receiver applications. However, according to our investigation, soft-contact electrode is expected to lower the contact force and therefore lower the sensitivity. Besides, [470] numerically investigate the synchronization phenomenon and nonlinear oscillations of two mechanical oscillators coupled by impacts, including symmetry periodic solutions,

doi:10.6342/NTU202600018

asymmetry periodic solutions, quasi-periodic solutions and even chaotic solutions. Noted, the numerical simulation is based on the coefficient of restitution which cannot present the contact force and revel the effect of material properties in detail. The surveyed results indicate that the mechanism of the soft-contact electrode is still not very clear. The further work is needed to revel the universal truth.

6.2.3 Packaging and Integration

So far, demonstrations of zero-quiescent wake-up receivers and pulse-density modulator have been limited to the component level. The technology would be more promising and convincing if integrated with transistor circuits and discrete components for front-end and back-end processing, extending its relevance beyond MEMS applications. This dissertation initially demonstrates a two-chip bonding integration with CMOS circuits, where optimizing both components is more straightforward.

Although this work demonstrated the potential for monolithic integration and prior work of [246] introduced a ferrite-rod antenna for short-range wireless reception, a complete system-level integration has not yet been achieved.

6.2.4 On-Chip Vibro-impact Perturbation-based Stiction Solver

Surface forces, such as van der Waals forces, capillary forces, and electrostatic forces, are the primary mechanisms causing stiction in MEMS [472-474]. Over the past decade, solutions to the stiction issue have commonly involved replacing materials, adding contact spacer, applying surface coatings/treatments, special etching process [475], employing supercritical drying techniques [476], and redesigning structures with smaller possible contact area. During the 1990s, laser treatment emerged as a new technique, relying on external force-induced movement [477, 478]. Unlike the early strategies of modifying MEMS structures to reduce contact areas or the need for additional equipment in laser treatment, new mechanical engineering solutions began to appear around the 2000s. Innovations such as moveable resonant stopper [479] and initially stiffness structure [480] were developed.

Moreover, a vibro-impact resonator offers an alternative solution for solving

doi:10.6342/NTU202600018

stiction. This device remains completely detached from the main structure and eliminate the need for extra equipment. The vibro-impact perturbation-based stiction solver operates similarly to the vibro-impact perturbation-based attractor exchanger. As a result, it can be monolithically integrated with the main structure, delivering specifically chosen periodic impacts to excite and release the main structure once stiction occurs.

doi:10.6342/NTU202600018

Appendix A: Time and Frequency Domain Responses of Single-DOF m-b-k Systems

This appendix derivate some formular to explore some basic characterization of linear m-b-k system, including switching time, frequency response, ring-down response and beating phenomenon. The basic idea on the dynamic of a periodically excited resonator will be conducted. In the following, symbol "→" represents some mathematical operations and provides some detail on the derivation.

According to the lumped system of a linear resonator, the 1-DOF equation of motion can be read as

$$m_r x'' + b_r x' + k_r x = A_d \cos(\omega_d t) \tag{A-1}$$

In certain cases, the periodic forcing term is expressed as an exponential term of

$$m_r x'' + b_r x' + k_r x = A_d \mathrm{e}^{\omega_d t} \tag{A-2}$$

and the final solution on amplitude is obtained by taking the real part operation of the solved general solution while phase is obtained by dividing imaginary part over the real part. The details will be shown.

To capture the general forced response, sometimes we will see the equation of motion in the form

$$m_r x'' + b_r x' + k_r x = A_d(\tau) * \delta(t - \tau) \tag{A-3}$$

where $\delta_p(t-\tau) = \begin{cases} 1; t = \tau \\ 0; t \neq \tau \end{cases}$ is unit impulse function, also called the Dirac delta function, obeying $\mathcal{L}[\delta(t-\tau)] = 1$ in which $\mathcal{L}[\cdot]$ is Laplace transform operator. $F_d(\tau)$ is arbitrary forcing function including periodic excitation as presented and $*$ indicate the convolution operator. The physical insight of convolution operation is that if we know the pulse response, the response of any arbitrary forced response can be obtained by summing all the responses due to the elementary impulses acting at all times. Mathematically, $\mathcal{L}[F_d(\tau) * \delta(t-\tau)] = \mathcal{L}[F_d(\tau)]\mathcal{L}[\delta(t-\tau)]$ is easy to treat at

doi:10.6342/NTU202600018

Laplace domain, providing some unique properties on solving equation.

A.1 Linear Frequency Response

Considering (A-1), the steady-state solution (or called particular solution) can be treated to be harmonic and can be assumed in the form [354]

$$x_{l.f} = x_{l.f}(t) = a_{p.l}cos(\omega_d t - \phi) \tag{A-4}$$

The first and second derivative of the steady-state solution are given as

$$x'_{l.f} = -a_{p.l}\omega_d sin(\omega_d t - \phi) \tag{A-5}$$

$$x''_{l.f} = -a_{p.l}\omega_d^2 cos(\omega_d t - \phi) \tag{A-6}$$

where $a_{p.l}$ and ϕ are constants to be determined, indicating the amplitude and phase difference of the response, respectively. By substituting (A-4)-(A-6) into (A-1), we obtain

$$a_{p.l}[(k_r - m_r\omega_d^2)\cos(\omega_d t - \phi) - b_r\omega_d \sin(\omega_d t - \phi)] = A_d \cos(\omega_d t) \tag{A-7}$$

Using the trigonometric relations of

$$cos(\omega_d t - \phi) = cos(\omega_d t)\, cos(\phi) + sin(\omega_d t) sin(\phi) \tag{A-8}$$

$$sin(\omega_d t - \phi) = sin(\omega_d t)\, cos(\phi) - cos(\omega_d t) sin(\phi) \tag{A-9}$$

and equating the coefficients of $cos(\omega_d t)$ and $sin(\omega_d t)$ on both sides of (A-7), we obtain

$$(k_r - m_r\omega_d^2)\cos(\phi) + b_r\omega_d \sin(\phi) = A_d / a_{p.l} \tag{A-10}$$

$$(k_r - m_r\omega_d^2)\sin(\phi) - b_r\omega_d \cos(\phi) = 0 \tag{A-11}$$

Solution of (A-10) and (A-11) for two known variables $sin(\phi)$ and $\cos(\phi)$ are given as

$$\sin(\phi) = \frac{b_r\omega_d A_d}{a_{p.l}[(k_r - m_r\omega_d^2)^2 + (b_r\omega_d)^2]} \tag{A-12}$$

doi:10.6342/NTU202600018

$$\cos(\phi) = \frac{(-m_r\omega_d^2 + k_r)A_d}{a_{p.l}[(k_r - m_r\omega_d^2)^2 + (b_r\omega_d)^2]} \tag{A-13}$$

Thus, the displacement amplitude and phase difference are obtained as

$$a_{p.l} = a_{p.l}[\sin^2(\phi) + cos^2(\phi)] = \frac{A_d}{\sqrt{(k_r - m_r\omega_d^2)^2 + (b_r\omega_d)^2}} \equiv \frac{A_d}{m_r\sqrt{\bar{A}^2 + \bar{B}^2}} \tag{A-14}$$

and

$$\frac{\sin(\phi)}{\cos(\phi)} = \tan(\phi) \rightarrow \phi = \tan^{-1}\left(\frac{\bar{B}}{\bar{A}}\right) \tag{A-15}$$

where

$$\bar{A} = \omega_n^2 - \omega_d^2 \tag{A-16}$$

$$\bar{B} = \omega_n\omega_d/Q = \omega_n\xi\omega_d \tag{A-17}$$

and $\omega_n = \sqrt{k_r/m_r}$ and $\xi = 1/Q$.

Substituting (A-14) into (A-4), we have

$$x_{l.f}(t) = a_{p.l}cos(\omega_d t - \phi) = \frac{A_d cos(\omega_d t - \phi)}{m_r\sqrt{\bar{A}^2 + \bar{B}^2}} \tag{A-18}$$

If the driving frequency is equal to the natural frequency, $\omega_d = \omega_n$, the amplitude will become

$$a_{p.l.n} = \frac{A_d}{m_r\omega_n^2\xi} = Q\frac{A_d}{k_r} \equiv A_0 \tag{A-19}$$

It can be seen that the displacement would be amplified Q times if operated at the natural frequency compared to that in the static force case (i.e., A_d/k_r).

Alternatively, we can assume the particular solution in the beginning with the form $x_{l.f}(t) = C_1\cos(\omega_d t) + C_2\sin(\omega_d t)$ and the final results will be the same.

On the other hand, if solve the frequency response with Laplace transformation, it

doi:10.6342/NTU202600018

is familiar to take (A-3). By doing Laplace transforms of both sides, we get [481]

$$\begin{aligned} & m_r\mathcal{L}[x''] + b_r\mathcal{L}[x'] + k_r\mathcal{L}[x] = \mathcal{L}[F_d\delta(t)] \\ \rightarrow\ & m_r[s^2X(s) - sx(0) - x'(0)] + b_r[sX(s) - x(0)] + k_rX(s) \\ & = \mathcal{F}_d[1] \end{aligned} \tag{A-20}$$

where $\mathcal{F}_d$ denotes the Laplace transformed arbitrary forcing function.

Since initial condition (I.C.) will not affect the steady-state solution, $x(t \to \infty)$, in linear system, the transfer function of the system can be obtained by setting $x(0) = x'(0) = 0$

$$(m_rs^2 + b_rs + k_r)X(s) \equiv H(s)X(s) = \mathcal{F}_d(s) \tag{A-21}$$

Rearranging above equation yields the so-called transfer function $H(s)$

$$H(s) = \frac{X(s)}{\mathcal{F}_d(s)} = \frac{1}{m_rs^2 + b_rs + k_r} = \frac{1/m_r}{s^2 + b_r/m_rs + k_r/m_r} \tag{A-22}$$

Substituting $s = j\omega_d$, where j is the root of $x^2 = -1$, and rearranging with definition of $\omega_n = \sqrt{k_r/m_r}$, $b_r = \sqrt{k_rm_r}/Q$ and $\xi = 1/Q$ yields

$$\begin{aligned} H(s) &= \frac{1/m_r}{(j\omega_d)^2 + \omega_n\xi(j\omega_d) + \omega_n^2} = \frac{1/m_r}{(\omega_n^2 - \omega_d^2) + j\omega_n\omega_d\xi} \\ &= \frac{(\omega_n^2 - \omega_d^2)/m_r}{(\omega_n^2 - \omega_d^2)^2 - (\omega_n\omega_d\xi)^2} + j\frac{(j\omega_n\omega_d\xi)/m_r}{(\omega_n^2 - \omega_d^2)^2 - (\omega_n\omega_d\xi)^2} \end{aligned} \tag{A-23}$$

The inverse Laplace transformation of $X(s)$ will be $\mathcal{L}^{-1}[X(s)] = x_p = \mathcal{L}^{-1}[\mathcal{F}_d(s)/\hbar(s)] = \mathcal{L}^{-1}[\mathcal{F}_d(s)] * \mathcal{L}^{-1}[1/\hbar(s)] = A_d(t) * (1/h(t))$, where $*$ denotes the convolution operation and $h(t)$ represents the homogenous solution in time domain. Noted, the zero initial condition, $x(0) = x'(0) = 0$, are assumed here. See [481] and [482] for details. Additionally, although the s is complex variable in the Laplace transform, when examining the system's response to a periodic excitation, the Laplace transform simplifies to the Fourier transform along the imaginary axis. This reduction represents the periodic oscillation component without the decaying feature

doi:10.6342/NTU202600018

associated with the real part of s.

The transfer function shown above is called compliance and, in fact, there are some other measures that are frequency used, namely mobility and accelerance, dynamic stiffness, mechanical impedance and dynamic mass. The dynamic stiffness, mechanical impedance and dynamic mass are the reciprocal of compliance, mobility and accelerance, respectively.

Taking the derivative in time domain means multiplying s in complex domain, thus, the mobility which represent the relation between velocity and force is given by

$$\frac{V(s)}{\mathcal{F}_d(s)} = \frac{sX(s)}{\mathcal{F}_d(s)} = \frac{j\omega_d/m_r}{(\omega_n^2 - \omega_d^2) + j\omega_n\omega_d\xi} \tag{A-24}$$

and the accelerance which represent the relation between acceleration and force is given by

$$\frac{A(s)}{\mathcal{F}_d(s)} = \frac{s^2X(s)}{\mathcal{F}_d(s)} = \frac{-\omega_d^2/m_r}{(\omega_n^2 - \omega_d^2) + j\omega_n\omega_d\xi} \tag{A-25}$$

Figure A-1 show the transfer function of these six kinds of measures.

In summary, the displacement amplitude and phase derivate by Laplace transform are same as (A-14) and (A-15), given by

$$a_{l.p} = \sqrt{Im[H(s)]^2 + Re[H(s)]^2} = \frac{A_d}{m_r\sqrt{\bar{A}^2 + \bar{B}^2}} \tag{A-26}$$

$$\phi = tan^{-1}\left\{\frac{Im[H(s)]}{Re[H(s)]}\right\} = tan^{-1}\left(\frac{\bar{B}}{\bar{A}}\right) \tag{A-27}$$

where $\bar{A}$ and $\bar{B}$ are defined in (A-16) and (A-17).

Furthermore, taking the derivative to the (A-14) (or (A-26)), one can find maximum amplitude occurs with zero numerator at

doi:10.6342/NTU202600018

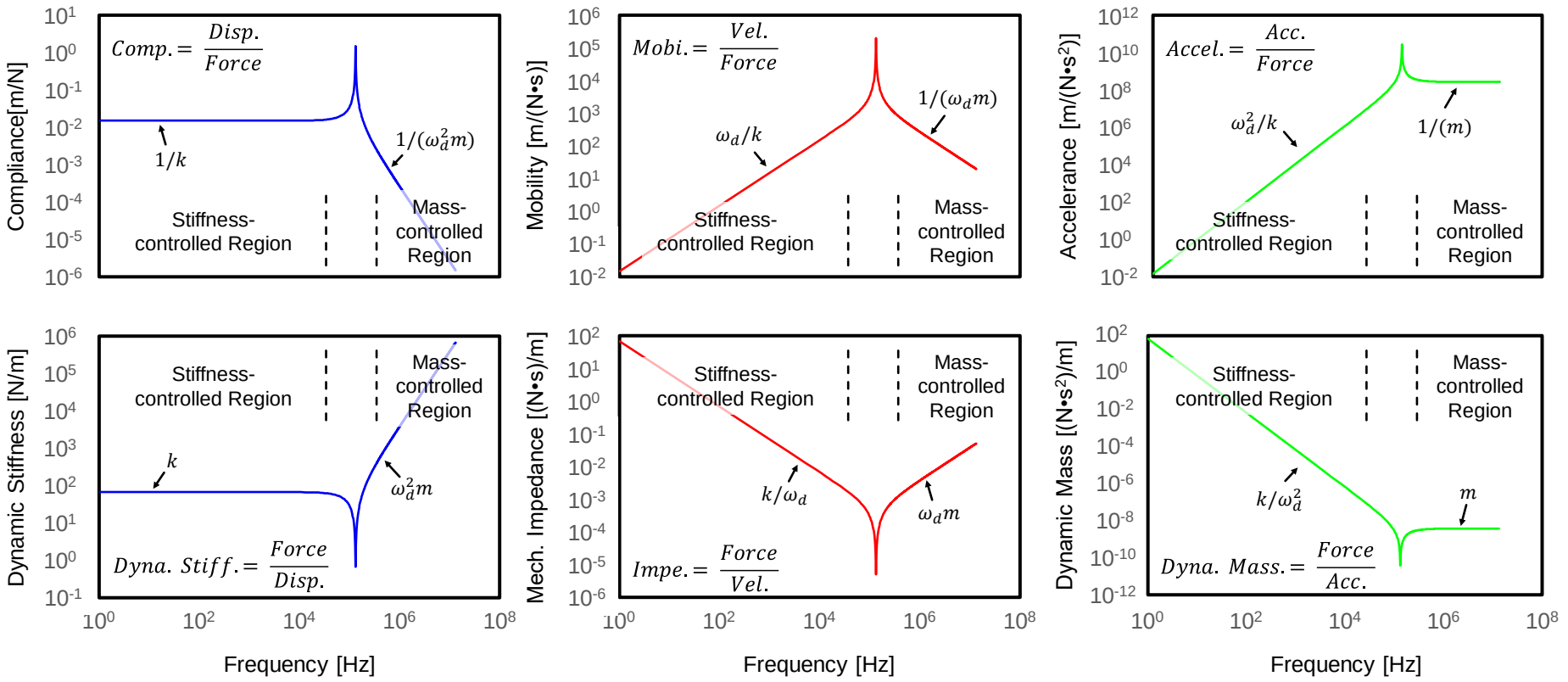


Figure A-1: Transfer function of compliance, mobility, accelerance, dynamic stiffness, mechanical impedance and dynamic mass, representing a system with different input and output variable.

doi:10.6342/NTU202600018

$$\frac{da_{p.l}}{d\omega_d} = \left[\frac{A_d}{\sqrt{(k_r - m_r\omega_d^2)^2 + (b_r\omega_d)^2}}\right]' = 0$$

$$\rightarrow -\frac{4m_r^2\omega_d^3 + 2(b_r^2 - 2k_rm_r)\omega_d}{[(-m_r\omega_d^2 + k_r)^2 + (b_r\omega_d)^2]^2}A_d = 0$$

$$\rightarrow 4m_r^2\omega_d^3 + 2(b_r^2 - 2k_rm_r)\omega_d = 0 \tag{A-28}$$

$$\rightarrow \omega_{d.max} \equiv \sqrt{\frac{k_r}{m_r} - \frac{b_r^2}{2m_r^2}} = \omega_n\sqrt{1 - \frac{1}{2Q^2}} = \omega_n\sqrt{1 - \frac{\xi^2}{2}}$$

Noted, the negative value of $\omega_{d.max}$ are unreasonable thus drop out.

The maximum amplitude is given by substituting $\omega_{d.max}$ into (A-14) (or (A-26))

$$a_{p.l.0} \equiv A_{0.max}$$

$$= \frac{2A_d}{k_r}Q\sqrt{\frac{1}{4 - \xi^2}} = \frac{2A_d}{k_r}Q\sqrt{\frac{Q^2}{4Q^2 - 1}} = \frac{A_d}{k_r}Q\sqrt{\frac{1}{1 - \frac{1}{4Q^2}}} \tag{A-29}$$

and can be reduced as $A_{0.max} \approx A_0 \equiv QA_d/k_r$ for high Q devices.

Therefore, ω_n and ω_0 indicate maximum amplitude without and with considering of damping, known as natural frequency and resonance frequency, respectively. If $Q \gg 1$ than $\omega_n \approx \omega_0$.

According to (A-14) (or (A-26)), finding the frequency positions of $A_{0.max}/\sqrt{2}$ yields [354]

$$\frac{A_{0.max}}{\sqrt{2}} = \frac{\sqrt{2}A_d}{k_r}Q\sqrt{\frac{Q^2}{4Q^2 - 1}} = \frac{A_d}{m_r\sqrt{(\omega_n^2 - \omega_{3dB}^2)^2 + (\omega_n\xi\omega_{3dB})^2}} \tag{A-30}$$

doi:10.6342/NTU202600018

$$\rightarrow \sqrt{\frac{2Q^4}{4Q^2-1}} \approx \frac{Q}{\sqrt{2}} = \frac{1}{\sqrt{\left(1-\frac{\omega_{3dB}^2}{\omega_n^2}\right)^2 + \left(\xi\frac{\omega_{3dB}}{\omega_n}\right)^2}}$$

$$\rightarrow \left(\frac{\omega_{3dB}}{\omega_n}\right)^2 = 1 - \frac{1}{2Q^2} \pm \frac{1}{Q}\sqrt{1+\frac{1}{4Q^2}}$$

Ignore the high order term, the square of upper and lower 3dB frequency ratio (i.e., ω_d/ω_n) can be approximated as

$$\left(\frac{\omega_{3dB}}{\omega_n}\right)^2 \approx 1 - \frac{1}{2Q^2} \pm \left(\frac{1}{Q} + \frac{1}{8Q^3}\right) \approx 1 \pm \frac{1}{Q} \tag{A-31}$$

Form (A-31), we can find

$$\omega_{3dB.2}^2 - \omega_{3dB.1}^2 = \left(\frac{2}{Q}\right)\omega_n^2 \tag{A-32}$$

and

$$\begin{aligned}&(\omega_{3dB.2} + \omega_{3dB.1})(\omega_{3dB.2} - \omega_{3dB.1})\\ &= (2\omega_n)(\omega_{3dB.2} - \omega_{3dB.1}) = \left(\frac{2}{Q}\right)\omega_n^2\\ &\rightarrow \omega_{3dB.2} - \omega_{3dB.1} = \frac{\omega_n}{Q}\end{aligned} \tag{A-33}$$

Therefore, the well-known 3-dB formular can be obtain as

$$Q = \frac{\omega_n}{\omega_{3dB.2} - \omega_{3dB.1}} = \frac{f_n}{\Delta f_{3dB}} \tag{A-34}$$

Which means the kinetic power at $\frac{A_{0.max}}{\sqrt{2}}$ is smaller than at peak by 3 dB ($KE_{peak} = \frac{1}{2}k(A_{0.max})^2$, $KE_{half} = \frac{1}{2}k\left(A_{0.max}/\sqrt{2}\right)^2 = KE_{peak}/2$ and $KE_{half.dB} = 10 \times \log\left(KE_{half}/KE_{peak}\right) = 10 \times \log(1/2) = -3.01 \approx -3$ dB). Thus, the peak frequency divided by the 3 dB frequency bandwidth of the peak equal to the quality

doi:10.6342/NTU202600018

factor.

On the other hand, (A-27) also suggests that the quality factor can be measured from the phase response. Linearizing around resonance frequency with $\tan(\phi) = -\cot(\phi) = 1/\phi$, the zero-crossing phase slope, $\frac{d\phi}{d\omega_d}\Big|_{\omega_d=\omega_n}$, and the quality factor can be given and extracted by

$$tan(\phi) = \frac{\bar{B}}{\bar{A}} = \frac{\omega_n \omega_d}{Q(\omega_n^2 - \omega_d^2)} \approx \frac{1}{\phi} \rightarrow \frac{d\phi}{d\omega_d}\Big|_{\omega_d=\omega_n} = \frac{Q}{2\omega_n} \tag{A-35}$$

$$Q = \frac{\omega_n}{2}\frac{d\phi}{d\omega_d}\Big|_{\omega_d=\omega_n} \tag{A-36}$$

As shown, the slope of the phase response near resonance is large when Q is large.

Noted, the frequency domain Q estimation derived here is valid for linear system with $Q \gg 1$, said $Q > 10$ as described in [354]. See generalized frequency-domain Q estimation formular in [483] for systems with nonlinear stiffness. Noted, the fractional-power formular with not only half power but any values of power drop are also introduced in [483]. The Q estimation for system with nonlinear damping are more suitable by extracting on time domain with ring-down method because recently developed frequency-domain method for systems with nonlinear damping is typically based on manually modified/corrected the 3-dB frequency points. See [103, 401, 484-491] for recent development and investigation for Q estimation of the nonlinearly damped systems.

A.2 Linear Time Response and Switching Time

Since (A-1) is non-homogeneous (i.e., forced), its general solution $x = x(t)$ is given by the sum of homogeneous solution, $x_h(t)$, and the particular solution, $x_p(t)$. Ignore the forcing term $A_d\cos(\omega t)$, the homogenous solution in general can be written as

doi:10.6342/NTU202600018

$$x = Ce^{\lambda t} \tag{A-37}$$

Substitute into (A-1), we have

$$m_r\left[C\lambda^2 e^{\lambda t}\right] + b_r\left[C\lambda e^{\lambda t}\right] + k_r[Ce^{\lambda t}] = 0 \tag{A-38}$$

The equation is a second order algebraic equation, known as characteristic equation, and the solution respect to eigenvalue, λ, are

$$\lambda_{1,2} = \frac{-b_r \pm \sqrt{b_r^2 - 4m_r k_r}}{2m_r} = Re(\lambda_{1,2}) \pm Im(\lambda_{1,2}) \equiv \lambda_r \pm i\lambda_i \tag{A-39}$$

where m_r, b_r and k_r are positive, therefore, the eigenvalues are complex conjugate.

The particular solution with two un-known coefficient that will be determined by the I.C. is then given by

$$x_h = C_1 e^{\lambda_1 t} + C_2 e^{\lambda_2 t} = C_1 e^{\lambda_r t} e^{i\lambda_i t} + C_2 e^{\lambda_r t} e^{-i\lambda_i t} \tag{A-40}$$

As we can see, $\lambda_r = -b_r/(2m_r)$ and $\lambda_i = \sqrt{4m_r k_r - b_r^2}/(2m_r) = \sqrt{k_r/m_r - [(b_r/2m_r)]^2}$ represent the decay/growing rate of the system and characteristic frequency of the system, respectively. It should be noted that a nondimensional coefficient called the damping ratio, ξ, represents the characteristic frequency related decay rate and is indicated as

$$\xi = -\frac{2Re(\lambda_{1,2})}{|Im(\lambda_{1,2})|} = -\frac{2\lambda_r}{\lambda_i} = \frac{2b_r}{\sqrt{4m_r k_r - b_r^2}} \tag{A-41}$$

For low damping system ($b_r \ll 1$, $\sqrt{4m_r k_r - b_r^2} \approx \sqrt{4m_r k_r}$ or $\sqrt{k_r/m_r - [(b_r/2m_r)]^2}) \approx \sqrt{k_r/m_r}$, the damping ratio can be reduced to

$$\xi \approx \frac{2b_r}{\sqrt{4m_r k_r}} = \frac{b_r}{\sqrt{m_r k_r}} \tag{A-42}$$

The damping ratio represents a meaningful measure for the system. It is frequently used in time domain characterization, while its reciprocal, called quality factor, Q, is

doi:10.6342/NTU202600018

commonly used in frequency domain characterization, defined as

$$Q = \frac{1}{\xi} = -\frac{\lambda_i}{2\lambda_r} = \frac{\sqrt{4m_r k_r - b_r^2}}{2b_r} \approx \frac{\sqrt{m_r k_r}}{b_r} \tag{A-43}$$

Since the forcing function is harmonic, we assume the particular solution is also in harmonic and take the form

$$x = Asin(\omega_d t) + Bcos(\omega_d t) \tag{A-44}$$

The first and second derivative are given as

$$x' = A\omega_d cos(\omega_d t) - B\omega_d sin(\omega_d t) \tag{A-45}$$

$$x'' = -A\omega_d^2 sin(\omega_d t) - B\omega_d^2 cos(\omega_d t) \tag{A-46}$$

Substitute (A-44)-(A-46) into (A-1), we get

$$\begin{aligned} &m_r[-A\omega_d^2 sin(\omega_d t) - B\omega_d^2 \cos(\omega_d t)] \\ &+b_r[A\omega_d cos(\omega_d t) - B\omega_d sin(\omega_d t)] \\ &+k_r[Asin(\omega_d t) + Bcos(\omega_d t)] = A_d \cos(\omega_d t) \end{aligned} \tag{A-47}$$

Equating the coefficients of $cos(\omega_d t)$ and $sin(\omega_d t)$ on both sides, we obtain

$$-m_r B\omega_d^2 + b_r A\omega_d + Bk_r = A_d \tag{A-48}$$

$$-m_r A\omega_d^2 - b_r B\omega_d + Ak_r = 0 \tag{A-49}$$

Divide (A-48) by B and subtract (A-49) divided by A, we arrive at

$$\left(\frac{A}{B} + \frac{B}{A}\right)\omega_d b_r = \frac{A_d}{B} \tag{A-50}$$

Multiplying the (A-50) with AB gives

$$(A^2 + B^2)\omega_d b_r = AF_d \rightarrow (A^2 + B^2) = \frac{AA_d}{\omega_d b_r} \tag{A-51}$$

On the other hand, making the sum of (A-48) multiplied B and (A-49) multiplied A, we arrive at

doi:10.6342/NTU202600018

$$(A^2+B^2)k_r-(A^2+B^2)m_r\omega_d^2=A_dB \tag{A-52}$$

Substituting (A-51) into (A-52) gives

$$B=A\left(\frac{k_r}{\omega_d b_r}-\frac{\omega_d m_r}{b_r}\right) \tag{A-53}$$

and substituting (A-53) into (A-51) gives

$$\left(A^2+\left[A\left(\frac{k_r}{\omega_d b_r}-\frac{\omega_d m_r}{b_r}\right)\right]^2\right)=\frac{AA_d}{\omega_d b_r}$$

$$\rightarrow A\left[1+\left(\frac{k_r}{\omega_d b_r}-\frac{\omega_d m_r}{b_r}\right)^2\right]=\frac{A_d}{\omega_d b_r} \tag{A-54}$$

$$\rightarrow A=\frac{A_d}{\omega_d b_r}\left[1+\left(\frac{k_r}{\omega_d b_r}-\frac{\omega_d m_r}{b_r}\right)^2\right]^{-1}$$

Combining (A-53) and (A-51), we obtain

$$B=\frac{A_d}{\omega_d b_r}\left[1+\left(\frac{k_r}{\omega_d b_r}-\frac{\omega_d m_r}{b_r}\right)^2\right]^{-1}\left(\frac{k_r}{\omega_d b_r}-\frac{\omega_d m_r}{b_r}\right) \tag{A-55}$$

Therefore, the general solution and its first derivative is given by

$$x=C_1e^{\lambda_1 t}+C_2e^{\lambda_2 t}+Asin(\omega_d t)+Bcos(\omega_d t) \tag{A-56}$$

$$x'=C_1\lambda_1e^{\lambda_1 t}+C_2\lambda_2e^{\lambda_2 t}+A\omega_d cos(\omega_d t)-B\omega_d sin(\omega_d t) \tag{A-57}$$

Considering the I.C. with $x(0)=x_0$ and $x'(0)=v_0$, we have

$$x_0=C_1+C_2+B$$

$$\rightarrow C_1=x_0-C_2-B \tag{A-58}$$

$$v_0=C_1\lambda_1+C_2\lambda_2+A\omega_d$$

$$=(x_0-C_2-B)\lambda_1+C_2\lambda_2+A\omega_d \tag{A-59}$$

$$\rightarrow C_2=(\lambda_2-\lambda_1)^{-1}[v_0-(x_0-B)\lambda_1-A\omega_d]$$

doi:10.6342/NTU202600018

In summary, four coefficients of A, B, C_1 and C_2 are determined with (A-54), (A-55), (A-58) and (A-59).

If driving the device near the resonance frequency, $\omega_d \approx \omega_n = \sqrt{k_r/m_r}$, or said $k_r \approx m_r\omega_d^2$, the coefficients of A, B, C_1 and C_2 can be reduced as

$$A = \frac{A_d}{b_r\omega_d}\left[1 + \left(\frac{k_r - m_r\omega_d^2}{b_r\omega_d}\right)\right]^{-1} \rightarrow A = \frac{A_d}{b_r\omega_d} = \frac{A_d}{k_r}Q = A_0 \tag{A-60}$$

$$B = A\left[\frac{k_r - m_r\omega_d^2}{b_r\omega_d}\right] \rightarrow B = 0 \tag{A-61}$$

$$C_1 = x_0 - B - C_2 \rightarrow C_1 = x_0 - C_2 \tag{A-62}$$

$$C_2 = \frac{v_0 - x_0\lambda_1 - A\omega_d + B\lambda_1}{\lambda_2 - \lambda_1} \rightarrow C_2 = \frac{v_0 - x_0\lambda_1 - A_d/b_r}{\lambda_2 - \lambda_1} \tag{A-63}$$

Taking look on the eigenvalue λ_1 and λ_2, in which, the term on the square root can be treat as $\sqrt{b_r^2 - 4m_rk_r} = i\sqrt{4m_rk_r - b_r^2} \approx i\sqrt{4m_rk_r}$ sine the b_r is typically small for high Q device, i.e., $b_r \ll 4m_rk_r$, we then have

$$Re(\lambda_1) = Re(\lambda_2) = -b_r/(2m_r) \tag{A-64}$$

$$Im(\lambda_1) = -Im(\lambda_2) = \sqrt{4m_rk_r}/(2m_r) = \sqrt{k_r/m_r} = \omega_n \tag{A-65}$$

and

$$\lambda_2 - \lambda_1 = -2\sqrt{k_r/m_r}\, i = -2\omega_n i \tag{A-66}$$

where $Re(\cdot)$ and $Im(\cdot)$ is real and imaginary operator, respectively.

The coefficient C_1 and C_2 then reduced as

$$C_2 = \frac{v_0 - x_0\left(-\frac{b_r}{2m_r} + \omega_n i\right) - \frac{A_d}{b_r}}{-2\omega_n i} = \frac{x_0}{2} + \left(\frac{v_0}{2\omega_n} + \frac{b_r x_0}{4m_r\omega_n} - \frac{A_d}{2\omega_n b_r}\right)i \tag{A-67}$$

doi:10.6342/NTU202600018

$$C_1 = \frac{x_0}{2} - \left(\frac{v_0}{2\omega_n} + \frac{b_r x_0}{4m_r\omega_n} - \frac{A_d}{2\omega_n b_r}\right) i \tag{A-68}$$

Similar to eigenvalues, one can conclude

$$Re(C_1) = Re(C_2) = \frac{x_0}{2} \tag{A-69}$$

$$-Im(C_1) = Im(C_2) = \frac{v_0}{2\omega_n} + \frac{b_r x_0}{4m_r\omega_n} - \frac{A_d}{2\omega_n b_r} \tag{A-70}$$

Because the initial displacement will change the initial phase difference that are not taken in the derivation, letting $x_0 = 0$ gives

$$-C_1 = C_2 = \left(\frac{v_0}{2\omega_n} - \frac{A_d}{2\omega_n b_r}\right) i \tag{A-71}$$

and the general solution reduced as

$$\begin{aligned} x &= C_1 e^{Re(\lambda_1)t} e^{iIm(\lambda_1)t} + C_2 e^{Re(\lambda_1)t} e^{-iIm(\lambda_1)t} + Asin(\omega_n t) \\ &= C_1 e^{\lambda_r t} e^{i\lambda_i t} + C_2 e^{\lambda_r t} e^{-i\lambda_i t} + Asin(\omega_n t) \\ &= e^{\lambda_r t} C_1 \left[e^{i\lambda_i t} - e^{-i\lambda_i t}\right] + \frac{A_d}{\omega_n b_r} sin(\omega_n t) \end{aligned} \tag{A-72}$$

Moreover, with the Euler's formula, $e^{i\lambda t} = \cos(\lambda t) + isin(\lambda t)$ and $e^{-i\lambda t} = \cos(\lambda t) - isin(\lambda t)$, the general solution can then be obtained as

$$x_{l.t} = e^{\lambda_r t}\left(\frac{v_0}{2\omega_n} - \frac{A_d}{2\omega_n b_r}\right)[2\sin(\omega_n t)] + \frac{A_d}{\omega_n b_r} sin(\omega_n t) \tag{A-73}$$

Ignoring the fast oscillation term, $sin(\omega_n t)$, the upper envelope curve could be treated as

$$x_{en} = e^{\lambda_r t}\left(\frac{v_0}{\omega_n} - \frac{A_d}{\omega_n b_r}\right) + \frac{A_d}{\omega_n b_r} \tag{A-74}$$

Further, considering both zero initial displacement and velocity, the upper envelope curve could be reduced as

doi:10.6342/NTU202600018

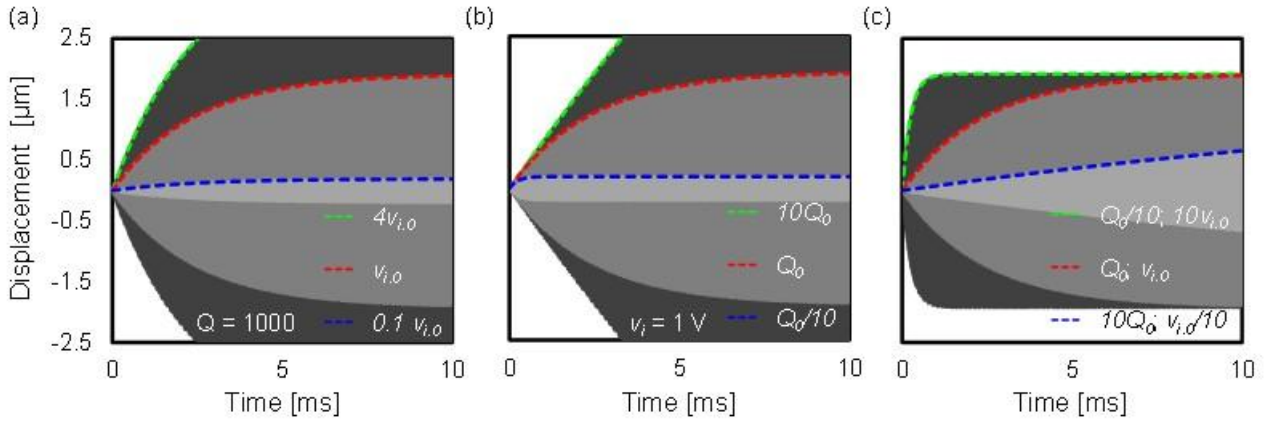


Figure A-2 Time history simulation results of (A-73) and (A-76) for a resonator starting from rest, showing comparisons for (a) varying driving voltage levels, (b) varying quality factors, and (c) three combinations with the same voltage-quality factor product.

$$x_{en} = e^{\lambda_r t}\left(-\frac{A_d}{\omega_n b_r}\right) + \frac{A_d}{\omega_n b_r} \tag{A-75}$$

Thus, the switching time shown in Section 3.2.3 can be estimated by setting x_{en} equal to d_0 in (A-75), yielding the following expression

$$t_{sw} = \ln\left[1 - \frac{d_0 b_r \omega_d}{A_d}\right] / \lambda_r \tag{A-76}$$

Figure A-2 shows the simulation results of (A-73) and (A-76) with varying conditions. Regarding on the consideration of vibro-impact operation, a careful observation reveals that the growing rate is linear proportional to time in the beginning where the damping effect is ignorable.

Expanding (A-76) via a Taylor series with respect to the damping ratio yields

$$t_{sw} \approx \frac{2d_0\sqrt{m_r k_r}}{A_d} \tag{A-77}$$

A.3 Ring-down Response

Considering the (A-1) without forcing term

doi:10.6342/NTU202600018

$$m_r x'' + b_r x' + k_r x = 0 \tag{A-78}$$

and take the I.C. as $x(0) = x_0^*$ and $x'(0) = 0$

Recalling (A-40) as

$$x_{RD} = C_1 e^{\lambda_1 t} + C_2 e^{\lambda_2 t} \tag{A-79}$$

where C_1 and C_2 in (A-58) and (A-59) reduce as

$$C_1 = x_0 - C_2 = (x_0^* \lambda_2)/(\lambda_2 - \lambda_1) \tag{A-80}$$

$$C_2 = (-x_0^* \lambda_1)/(\lambda_2 - \lambda_1) \tag{A-81}$$

and the eigenvalues are recalled from (A-39) and written as

$$\lambda_{1,2} = \frac{-b_r \pm \sqrt{b_r^2 - 4m_r k_r}}{2m_r} = -\frac{\omega_n}{2Q} \pm i\omega_n \sqrt{1 - \frac{1}{4Q^2}} \tag{A-82}$$

$$= Re(\lambda_{1,2}) \pm Im(\lambda_{1,2}) \equiv \lambda_r \pm i\lambda_i$$

Then, the ring-down response can be represented as

$$x_{RD} = \frac{x_0^* \lambda_2}{\lambda_2 - \lambda_1} e^{\lambda_1 t} + \frac{-x_0^* \lambda_1}{\lambda_2 - \lambda_1} e^{\lambda_2 t}$$

$$= \frac{x_0^* \lambda_2}{\lambda_2 - \lambda_1} e^{(\lambda_r + i\lambda_i)t} + \frac{-x_0^* \lambda_1}{\lambda_2 - \lambda_1} e^{(\lambda_r - i\lambda_i)t}$$

$$= \frac{x_0^*}{\lambda_2 - \lambda_1} e^{(\lambda_r)t} \left[\lambda_2 e^{(i\lambda_i)t} - \lambda_1 e^{(-i\lambda_i)t}\right] \tag{A-83}$$

$$= \frac{x_0^*}{(-2i\lambda_i)} e^{(\lambda_r)t} \{(\lambda_r - i\lambda_i)[\cos(\lambda_i t) + i\sin(\lambda_i t)]$$

$$- (\lambda_r + i\lambda_i)[\cos(\lambda_i t) - i\sin(\lambda_i t)]\}$$

$$= \frac{x_0^*}{(-2i\lambda_i)} e^{(\lambda_r)t} \{-2i\lambda_i \cos(\lambda_i t) + 2\lambda_r i\sin(\lambda_i t)\}$$

doi:10.6342/NTU202600018

$$= x_0^* e^{(\lambda_r)t}\left\{\cos(\lambda_i t) - \frac{\lambda_r}{\lambda_i} sin(\lambda_i t)\right\}$$

$$= x_0^* e^{(\lambda_r)t}\left\{\cos(\lambda_i t) + \frac{b_r}{\sqrt{4m_r k_r - b_r^2}} sin(\lambda_i t)\right\}$$

$$= x_0^* e^{(\lambda_r)t}\left\{\cos(\lambda_i t) + \frac{1}{\sqrt{4Q^2 - 1}} \sin(\lambda_i t)\right\}$$

If ϕ_λ representing the angle between ω_0 and ω_n as shown in Figure A-3 (a), the ring-down response can be simplified as

$$x_{RD} = x_0^* e^{(\lambda_r)t}\left\{\cos(\lambda_i t) + \frac{1}{\sqrt{4Q^2 - 1}} \sin(\lambda_i t)\right\}$$

$$= x_0^* \frac{\omega_n}{\lambda_i} e^{(\lambda_r)t}\left\{\frac{\lambda_i}{\omega_n}\cos(\lambda_i t) - \frac{\lambda_r}{\omega_n}\sin(\lambda_i t)\right\}$$

$$= x_0^* \frac{\omega_n}{\omega_0} e^{(\lambda_r)t}\{\cos(\phi_\lambda)\cos(\lambda_i t) - \sin(\phi_\lambda)\sin(\lambda_i t)\} \quad \text{(A-84)}$$

$$= x_0^* \frac{\omega_n}{\omega_0} e^{-\frac{b_r}{2m_r}t} \cos\left[\left(\omega_n\sqrt{1 - \frac{1}{4Q^2}}\right)t + \phi_\lambda\right]$$

$$\approx x_0^* e^{-\frac{b_r}{2m_r}t} \cos[\omega_n t + \phi_\lambda] \;\; if \; Q \gg 1$$

where $\cos(\phi_\lambda) = \sqrt{1 - 1/4Q^2}$ and $\sin(\phi_\lambda) = 1/(2Q)$, respectively, and the envelope of the ring-down response can be obtained as [354]

$$x_{RD.en} = x_0^* e^{-\frac{\omega_n}{2Q}t} \quad \text{(A-85)}$$

Figure A-3 (b) shows the responses of (A-84) and(A-85).

Finding the ring-down cycle M_c with amplitude that is N_c time lower the initial displacement (i.e., x_0^*/N_c) yields

doi:10.6342/NTU202600018

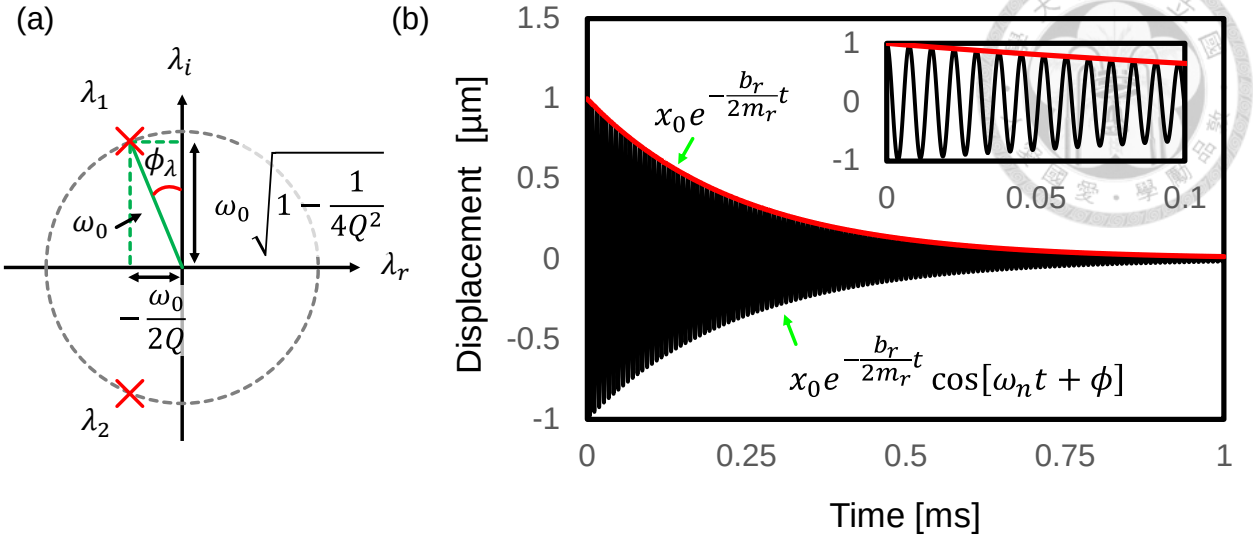


Figure A-3: (a) A graphic representation of the transformation used in (A-84). (b) simulation results of (A-84) and (A-85), representing the ring-down response and its corresponding envelope for a resonator with an initial displacement of 1 μm.

$$\frac{x_0^*}{N_c} = x_0^* e^{-\frac{\omega_n}{2Q}t}$$

$$\rightarrow Q = -\frac{\pi f_n t}{\ln\left(\frac{1}{N_c}\right)} \tag{A-86}$$

$$\rightarrow Q = \frac{\pi M_c}{ln(N_c)}$$

As shown on Figure A-4 (a), researchers choose half of the initial displacement (i.e., $N_c = 2$) as a standard frequently, thus, the Q is function of number of the cycles as

$$Q = \frac{\pi M_c}{ln(2)} \approx 4.53 \times M_c \approx 4.53 \times 22 = 99.66 \tag{A-87}$$

and, of course, it can be estimated by a fixed value of count as shown in the Figure A-4 (b) and estimated by the displacement drop ratio

$$Q = \frac{\pi M_c}{ln(1/0.9386)} \approx 49.5786 \times 2 = 99.157 \tag{A-88}$$

Noted, the (A-85) is valid for underdamped system where $Q \gg 1$. For critically

doi:10.6342/NTU202600018

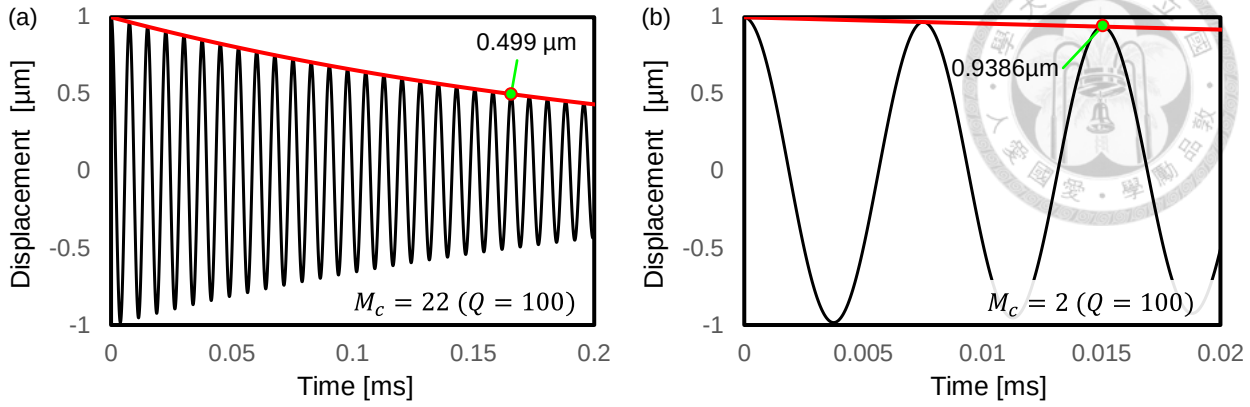


Figure A-4: (a) An illustration of Q factor extraction methods, showing (a) extraction based on a fixed amplitude ratio and (b) extraction based on a fixed number of ring-down cycles.

damped and overdamped system, there is no oscillation during ring down, the estimation requires the information such as reflection point and curvature of the ring-down curve. See [492] and [493] for details and see Appendix B.8 for the Q factor and the resonance frequency extraction of multiple modes response through the application of FFT and curve fitting.

A.4 Beating Phenomenon and Transient Response

The phenomenon known as beating can occur when the forcing frequency is nearly, but not exactly, equal to the system's natural frequency. In this type of vibration, the amplitude increases and then decreases in a consistent pattern. Inspired by (A-57), one can simplify the problem by consider a waveform of the sum of two unit-amplitude sinusoidal response as [354]

$$x_{beat}(t) = [\cos(\omega_d t) - \cos(\omega_n t)] \tag{A-89}$$

The equation states that the system naturally vibration at resonance frequency, however, perturbated by the driving frequency. Using the trigonometric identity

$$\cos(u) - \cos(v) = 2\sin\left(\frac{v-u}{2}\right)\sin\left(\frac{v+u}{2}\right) \tag{A-90}$$

(A-89) becomes

doi:10.6342/NTU202600018

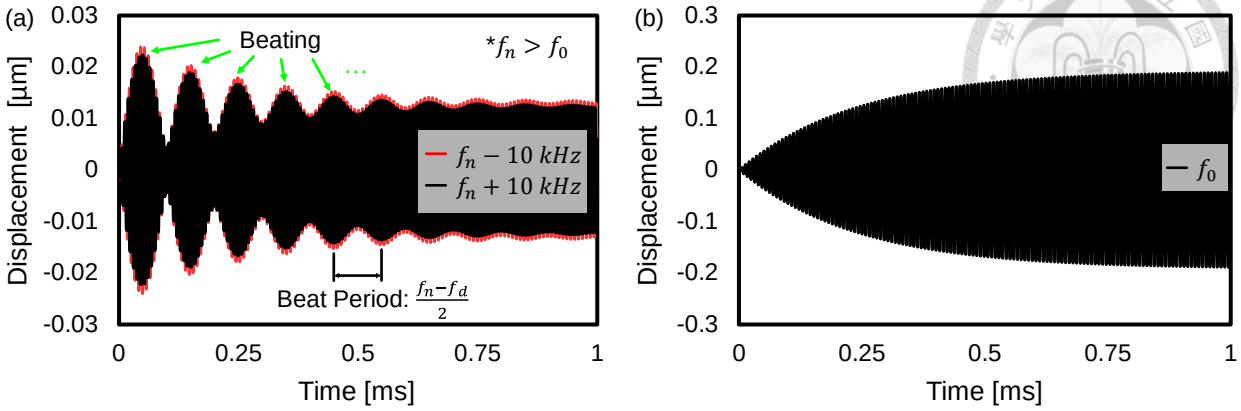


Figure A-5: A displacement-time history plot for a resonator, illustrating (a) the beating phenomenon when driven near resonance and (b) the fast-growing response when driven exactly at resonance.

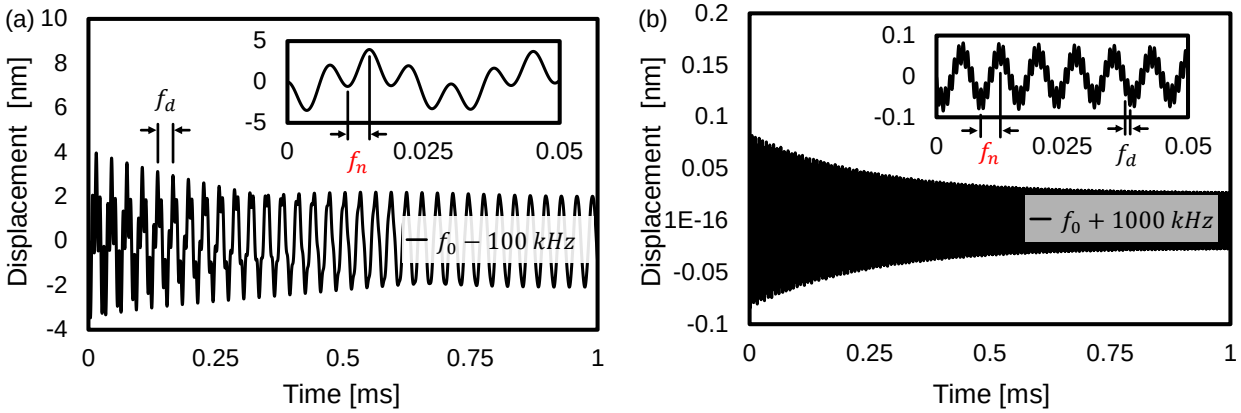


Figure A-6: Additional examples of the beating phenomenon for a resonator driven at frequencies significantly (a) lower and (b) higher than its resonance frequency. The inset provides a detailed view of the initial interaction between the homogenous and particular solutions.

$$x_{beat}(t) = \left[2\sin\left(\frac{\omega_n - \omega_d}{2}t\right)\sin\left(\frac{\omega_n + \omega_d}{2}t\right)\right] \tag{A-91}$$

Since the value of $(\omega_n - \omega_d)$ is small and $(\omega_n + \omega_d)$ is large because $\omega_d \approx \omega_n$, the term $\sin[(\omega_n - \omega_d)t/2]$ oscillates with a much longer period than the term $\sin[(\omega_n + \omega_d)t/2]$. This causes a rapid oscillation with a slowly changing amplitude, known as a beat. Figure A-5 illustrates the numerical simulation of (A-1) for driving

doi:10.6342/NTU202600018

frequencies slightly lower (*c.f.* Figure A-5 (a)), exactly at (*c.f.* Figure A-5 (b)), and slightly higher than the resonance frequency(*c.f.* Figure A-5 (a)). The system is a standard 1-DOF system that includes the effects of damping. As observed, the motion starts from zero displacement and reaches a constant oscillation amplitude, transitioning from a static state to a constant oscillation state. Additionally, Figure A-6 (a) and (b) show the cases where the driving frequencies significantly lower and higher than the resonance frequency. As presented, the resonance behavior will appear in the transient region as the systems are perturbated, however, die out as they approach the steady state since the systems are forced by certain frequencies. For more details on the beating phenomenon of linear systems, refer to [354] and [482].

Although there is no direct relationship between the beating phenomenon in linear systems and certain characteristics of nonlinear systems, here provides an imagination/feeling of nonlinear vibration through the concept of beating. The primary cause of beating is the slight discrepancy between the resonance frequency and the driving frequency. This transient response features a change in the system state from one condition to another with long period oscillation. In a nonlinear system, as the displacement increases, properties like stiffness may change, potentially resulting in beating characteristics due to the mismatch between resonance frequency (i.e., $\sqrt{k_r/m_r}$) at linear region (i.e., $k_r = k_1 + \Delta k_n(x) \approx k_1$) and nonlinear region (i.e., $k_r = k_1 + \Delta k_n(x)$). As discussed in the previous section, a linear system requires Q oscillations to transform from one state to another, whereas a nonlinear system may require more or fewer oscillations depending on the sign of the stiffness change (i.e., $\Delta k_r(x) > 0$ or $\Delta k_r(x) < 0$) affecting the nonlinear resonance frequency. It is also important to note that nonlinear damping can influence the settling time, which is directly related to Q.

A.5 Stability of 1-DOF Linear and Nonlinear Systems

To determine the stability of 1-DOF linear systems, it requires analyzing the homogeneous equation's characteristic equation (i.e., (A-39)). There are three main

doi:10.6342/NTU202600018

cases for system's stability, determined by the sign of the real part of the eigenvalues, namely asymptoticly stable, marginally stable and unstable.

For an asymptoticly stable system, the system returns to its equilibrium state over time. This happens when the real parts of all eigenvalues are negative ($Re(\lambda_1) < 0$ and $Re(\lambda_2) < 0$). This results in decaying exponential terms in the solution, causing the motion to die out. Physically, this corresponds to a damped system ($b > 0$ for (A-1)) that dissipates energy, like a pendulum eventually stopping due to air resistance.

For a marginally stable system, the system's response remains bounded but does not return to its equilibrium. This occurs when the real parts of the eigenvalues are zero ($Re(\lambda_1) = 0$ and $Re(\lambda_2) = 0$), and the imaginary parts are non-zero. The system oscillates indefinitely with a constant amplitude. This represents an undamped system ($b = 0$ for (A-1)) where energy is conserved, such as an ideal spring-mass system oscillating forever.

For an unstable system, the system's response grows unbounded and moves away from equilibrium. This happens when at least one eigenvalue has a positive real part ($Re(\lambda_1) > 0$ and/or $Re(\lambda_2) > 0$). This results in exponentially growing terms in the solution. This can occur in systems with negative damping, causing the displacement to increase indefinitely until the system breaks or saturates.

As a brief summary, the stability of a 1-DOF linear system is a direct consequence of the physical properties (i.e., mass, damping, and stiffness in mechanical system). Analyzing the roots of the characteristic equation predict whether a system will return to equilibrium, oscillate, or grow unstable. The principles of stability analysis extend beyond linear dynamic systems, they are also applicable to static problems and can be adapted for both static and dynamic nonlinear problems through the use of linearization techniques. TABLE A-1 shows how to use eigenvalues to determine the behavior of solution in phase plane (i.e., $x - x'$ space). Although, the table shows the stability classification of 1-DOF systems, it can be extended to higher DOF system. In addition, the stability of a vibro-impact resonator characterized within this dissertation is

doi:10.6342/NTU202600018

TABLE A-1: THE CLASSIFICATION OF THE STABILITY AND PHASE PORTRAIT OF 1-DOF SYSTEMS.

Behavior	Stability	Eigenvalue and Symbolic Description	Note
Source/ Unstable Node	Unstable	$\lambda_1, \lambda_2 \in \mathbb{R}; \lambda_1, \lambda_2 > 0$	Both real and positive
Sink/ Stable Node	Stable	$\lambda_1, \lambda_2 \in \mathbb{R}; \lambda_1, \lambda_2 < 0$	Both real and negative
Saddle Point	Unstable	$\lambda_1, \lambda_2 \in \mathbb{R}; \lambda_1 > 0, \lambda_2 < 0$ or $\lambda_1 < 0, \lambda_2 > 0$	One real negative, one real positive
Center	Stable	$\lambda_{1,2} = \pm bi; b \in \mathbb{R}; b > 0$	Complex conjugate with zero real parts
Spiral Source	Unstable	$\lambda_{1,2} = a \pm bi; a, b \in \mathbb{R}; a, b > 0$	Complex conjugate with positive real part
Spiral Sink	Stable	$\lambda_{1,2} = -a \pm bi; a, b \in \mathbb{R}; a, b > 0$	Complex conjugate with negative real part

analyzed as a representative example of a dynamic nonlinear stability problem in Appendix E.5. For a more comprehensive understanding of the stability theory, including the classification of Poincaré maps for linear autonomous systems (e.g., node, saddle, spiral source, spiral sink, center as briefly shown), the types of instability (i.e., divergent, flutter), stability analysis of nonlinear systems, and the study of bifurcations (e.g., Hopf, saddle-node, transcritical, pitchfork), a review of the literature [494-498] and the reference citated in the Section 2.2 are recommended.

doi:10.6342/NTU202600018

Appendix B:Equivalent Circuit, Two-Port Networks, Transmission, and Parameter Extraction

The characterization of electrostatic MEMS device typically needs the background of the two-port network and the operation principle of network analyzer (i.e., the device response detector). Network analyzers, typically contain two-port network, are used to measure the frequency response of a circuit based on transmission line theory. The fundamental theory of two-port network and transmission line are already developed for a long time [402, 403, 499]. The equivalent circuit representation of MEMS device is also developed for a while, [351, 352, 500] provide great content on the equivalent circuit of MEMS systems.

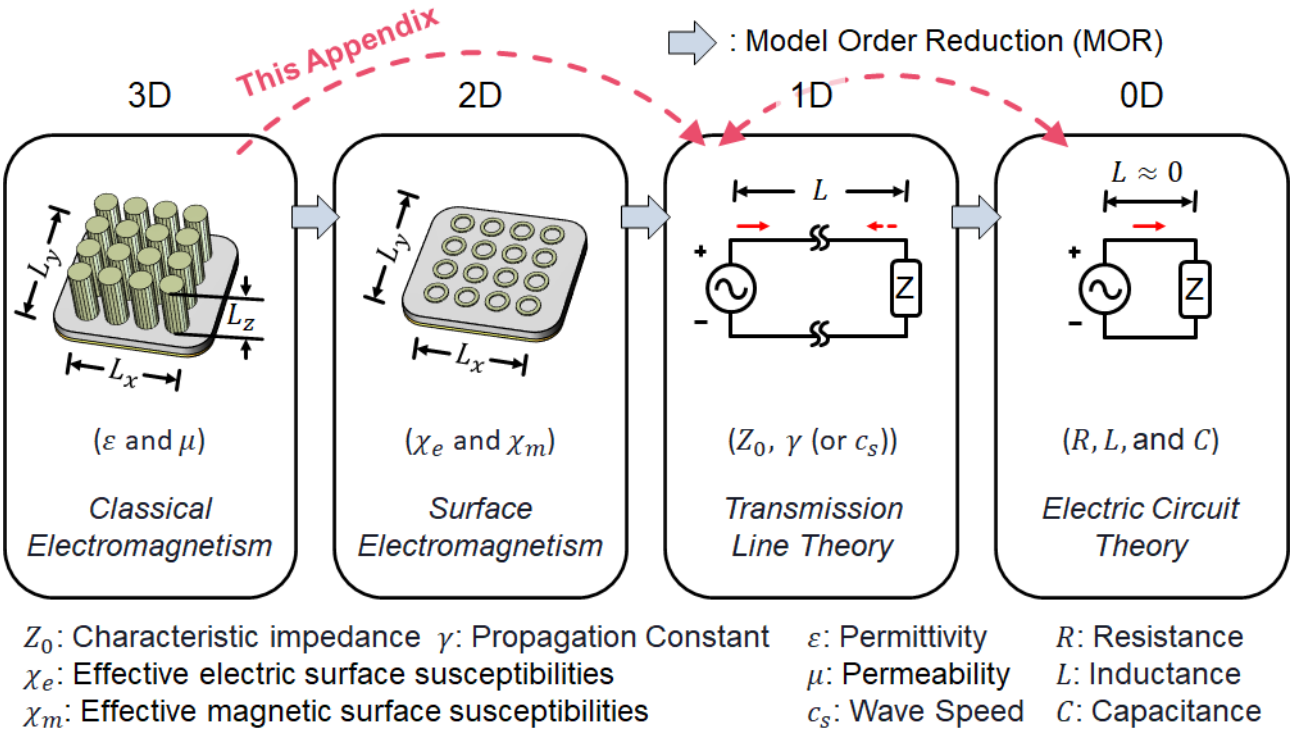


Figure B-1: The relationship between distributed-parameter modeling and the lumped-parameter modeling approach, illustrating the connection between the electromagnetic wave and the equivalent circuit model. Also, the goal of this appendix is marked.

doi:10.6342/NTU202600018

In this appendix, we focus on building the foundation of the parameter extraction for the electrostatic MEMS resonator, including wave analogy of electromagnetic wave, transmission line, equivalent circuit of the MEMS resonator, calibration technology and parameter extraction algorithm.

As shown on Figure B-1, this appendix provides the connection between the electromagnetic wave (i.e., distributed model) and equivalent model (i.e., lumped model). It finally arrives to the simple electric circuit since the operating frequency of MEMS devices studied in this dissertation are low and the calibration is applied. More importantly, this appendix builds the connection between mechanical wave to other type of waves. This is important to the development of this dissertation because it connect main objects for MEMS that are related to electrical part, mechanical part, the device itself and the interaction from external environment. Early-career MEMS researchers coming from the field of mechanical engineering often lack familiarity with these concepts. This unfamiliarity creates a barrier, preventing the adoption of interesting ideas from other disciplines.

Appendix B.6 is the main content for parameter extraction, reading only that is recommended for reader who are familiar with the background or not interesting to the origin. In the following, symbol "→" represents some mathematical operations and provides some detail on the derivation.

The first paragraph will introduce the background on the transmission line from wave analogy, including the physical meaning as well as the concept of distributed-parameter approach and lumped-parameter approach. It assumes that the background of the reader is mechanical engineering, thus it first covers the brief introduction for wave propagation in elastic medium then build the analogy between mechanical wave and electromagnetic wave. The second part will introduce the general modeling method for a two-port network based on scattering coefficients and ABCD matrix. The followed section will introduce the modeling method of a capacitive MEMS resonator associated with lumped-parameter approach. The link between the mechanical lumped

doi:10.6342/NTU202600018

model and equivalent electrical circuit will be built in this section. Finally, the calibration method, de-embedding technology and the parameter extraction procedure will be conducted. Sine this appendix is not going to cover all of the things related, the drawing of the physical meaning (i.e., graphical representation and context) along the field is focused. However, the equations are helpful for deeper understanding. The key equations are summarized, and the reference are given for further reading.

B.1 Wave Analogy for Few Types of Energy

Basically, the waves can be divided into mechanical and non-mechanical waves [501]. Mechanical waves require a medium for propagation while non-mechanical waves, such as light, do not require any medium for propagation. As shown in the Figure B-2, take mechanical waves as an example, the waves can be classified as longitudinal wave, transverse wave or surface wave based on the propagating structure. For instance, the particles of the medium vibrate up and down perpendicular (back and forth parallel) to the direction of the wave for transverse (longitudinal) wave. The most common examples of mechanical waves are water waves (can be along surface or in the body), sound waves (can be in air, water or solid), and seismic waves (in Earth). The sound waves can be further classified as infrasound (< 20 Hz), audible sound (20 Hz to 20 kHz) and ultrasound (>20 kHz) wave while seismic waves can be primary

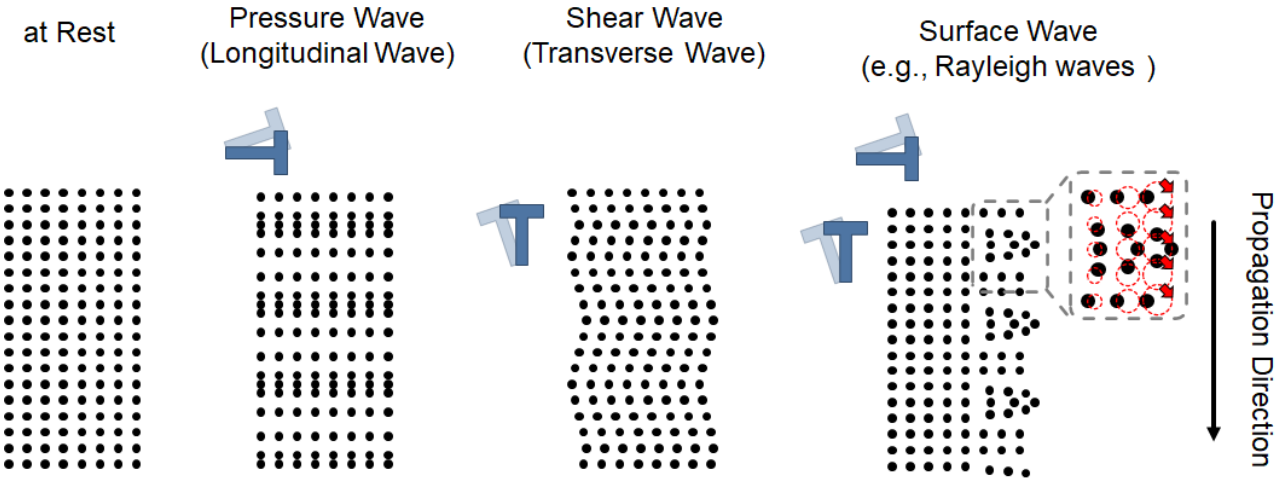


Figure B-2: A conceptual illustration of material particle movement for a longitudinal, transverse, and Rayleigh wave, respectively.

doi:10.6342/NTU202600018

classified as pressure and shear waves (the combination of these two waves are called body waves that propagates through the body of an object), and Love and Rayleigh waves (the combination of these two waves are called surface waves that propagates along the interface between differing media). Rayleigh waves are a combination of transverse and longitudinal waves (*cf.* Figure B-2), thus, the particles of the medium vibrate both up and down and back and forth, so they end up moving in a circle shape along the surface. Love wave is moving with horizontal shifting along the surface. The seismic waves can be generalized as bulk wave for which the waves propagate in certain object not only Earth. One should keep in mind is that the waves are propagated along certain direction with specific shape of energy field and as seems, they are classified by distinct characteristics, fields of application and frequency range, and the classifications are somewhat not clear and occasionally overlapped.

Additionally, light comes under the category of transverse non-mechanical wave, particularly, the electromagnetic wave. As shown on the Figure B-3, the classifications of electromagnetic wave are described by frequency, wavelength, wavenumber or energy and, they are interchangeable. The scientific convention of these four measures allows the convenient use of units that have numbers that are neither too large nor too small. According to the frequency band (or other measure), application and the name suggested, again, they can divide into many disciplines such as microwave, radio frequency, laser, visible light, and so on. Non-mechanical longitudinal waves are not common in daily life, the longitudinal modes of a laser cavity can be an example for which the wave traveling back and forth, certain wavelengths within the gain bandwidth of the laser tend to be more enhanced than others.

Noted, the reason of such complex classification in both mechanical and non-mechanical waves is mainly due to industry interesting (i.e., application), different research purposes (i.e., fundamental or easy-to-use theory), development of the measurement instruments (i.e., scale, precision and new finding of science), and more importantly, they are kind of different. As said by P. W. Anderson, *the more is different*,

doi:10.6342/NTU202600018

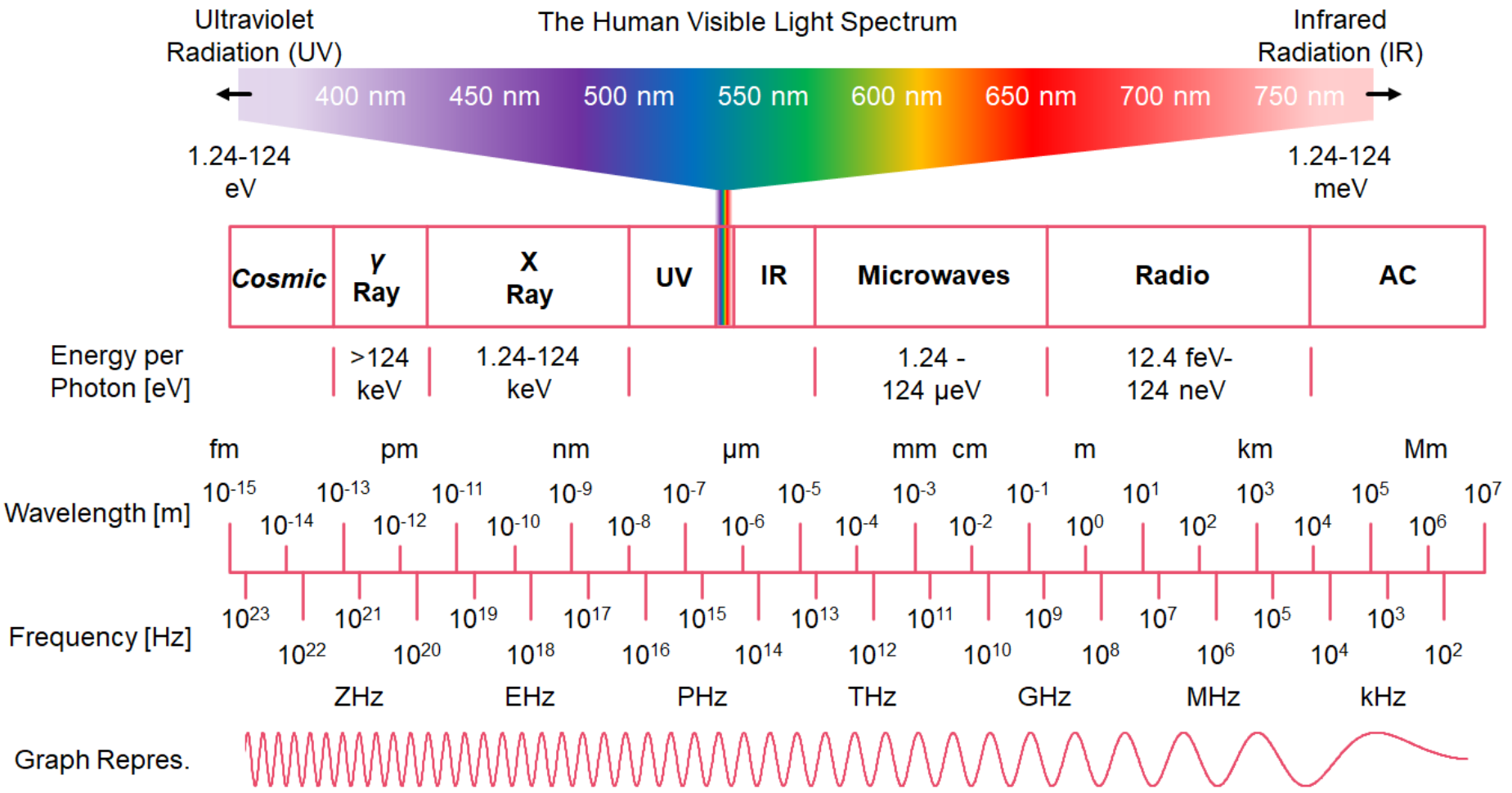


Figure B-3: A summary of useful properties for an electromagnetic wave.

doi:10.6342/NTU202600018

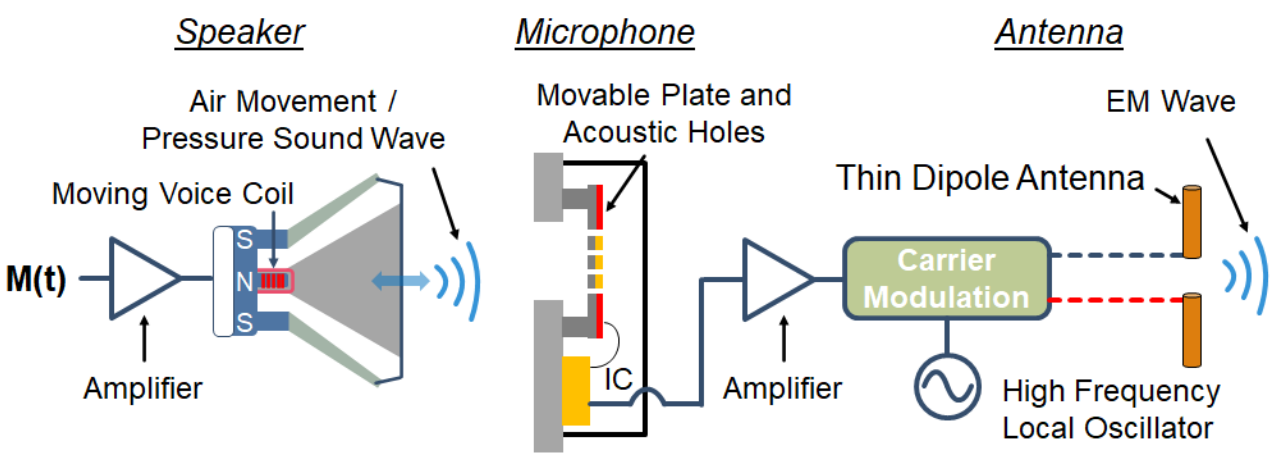


Figure B-4: A diagram of the energy transduction path, showing the energy transfer from an electrical signal to an electromagnetic (EM) wave through electrical-mechanical, piezoelectric, and electromagnetic transduction mechanisms.

meaning that complex physical systems may exhibit behaviour that cannot be understood only in terms of the laws governing their microscopic constituents [502].

For example, the reflection and refraction and the location or interface that the propagating direction change are focused on geometrical optics, but the wave properties (i.e., displacement field change in time and space) are not interested; although the material properties are determined by strength of the atomic bonds and the mass of each atomic, the density and Young's modulus are of important in mechanics of materials and provides deeper understanding for the mechanical engineering.

Before going into detail, Figure B-4 shows a schematic for electrical-mechanical-piezoelectric-electromagnetic transduction path that convert energy from electrical signal to electromagnetic wave through several mechanisms. On should note that the energy can be transfer from one to any other if the transduction mechanism presented. Therefore, certain characteristics must be exactly the same no matter what field or the energy type they propagate/transfer.

[503, 504] provides the detail discussion of the dispersion and damping effect for mechanical wave while [505] for electromagnetic wave. The analogy of mechanical

doi:10.6342/NTU202600018

wave and electromagnetic wave can also be found in [506]. In following, the dispersion and damping effect are ignored for simplicity. Some keywords will be mentioned to facilitate reader's search and learning.

B.1.1 Introduction to the Mechanical Wave

As Figure B-5 (a) shows, considering an infinitesimal segment of a rod, the force balance equation from Newton's second law is given by

$$\begin{gathered} -A\sigma_x + \left(A + \frac{\partial A}{\partial x}dx\right)\left(\sigma_x + \frac{\partial \sigma_x}{\partial x}dx\right) = \rho\left\{\frac{1}{2}\left(A + A + \frac{\partial A}{\partial x}dx\right)\right\}(dx)\frac{\partial^2 u}{\partial t^2} + c.c. \\ \rightarrow \frac{\partial}{\partial x}(A\sigma_x) = \rho A\frac{\partial^2 u}{\partial t^2} \end{gathered} \tag{B-1}$$

where $c.c.$ represent the ignored higher order terms.

For 1-D cases, the strain and stress are linear dependent on Young's modulus ($\sigma_x = E\varepsilon_x = E\frac{\partial u}{\partial x}$), we obtain

$$\begin{gathered} \frac{\partial}{\partial x}\left(AE\frac{\partial u}{\partial x}\right) = \rho A\frac{\partial^2 u}{\partial t^2} \\ \rightarrow \frac{\partial^2 u}{\partial x^2} = \frac{1}{c_l^2}\frac{\partial^2 u}{\partial t^2} \end{gathered} \tag{B-2}$$

where u indicate the x-component of displacement and $c_{l.r} = \sqrt{E/\rho}$ is longitudinal wave speed of the rod. The above equation is true if the problem obeys (1) small deformation, (2) the negligible transverse effects (Poisson's effect, lateral inertia, bending, etc.), (3) thin rod where the wavelength is much longer than thickness of rod and (4) the rod is uniform ($A(x) = contstant$) and homogeneous rod ($E(x) = contstant$). Noted, the Young's modulus is only considered constitutive equation here.

doi:10.6342/NTU202600018

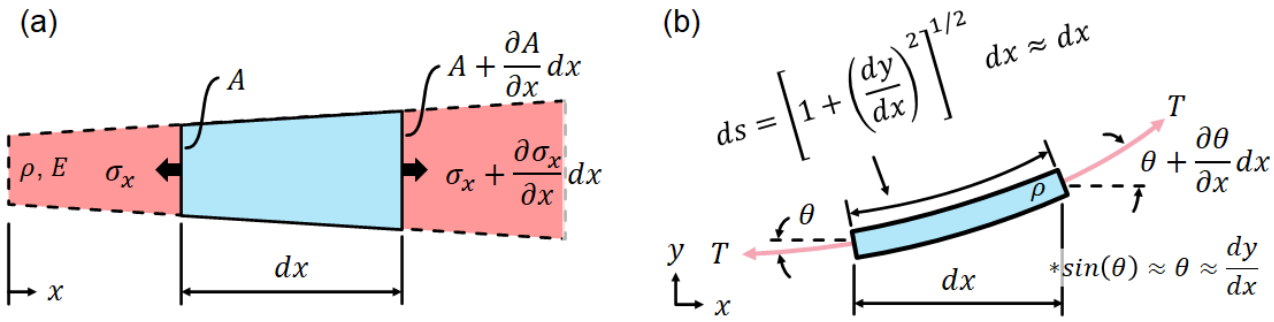


Figure B-5: Free body diagram of (a) a rod and (b) a wire.

In addition, there are one-dimensional structural members similar to rods. For example, the transverse wave equation of a string (*cf.* Figure B-5 (b)) or the energy propagation through a medium such as air (i.e., acoustic wave) can be found in similar procedure. Those standard 1-D wave problems take a general form as

$$\frac{\partial^2 u}{\partial x^2} = \frac{1}{c^2}\frac{\partial^2 u}{\partial t^2} \tag{B-3}$$

where c is the wave speed of the problems. The transverse wave speed of string is given by $c = c_t = \sqrt{T/\rho}$ where T is the tension in the string, while longitudinal wave speed of media such as gas or liquid is given by $c = c_{l.m} = \sqrt{K/\rho}$ where K is modulus of bulk elasticity for the media.

Letting two new offset variables as $\xi = x + ct$ and $\eta = x + ct$, the 1st and 2nd derivative of displacement with respect to x and t become

$$\frac{\partial u}{\partial x} = \frac{\partial u}{\partial \xi}\frac{\partial \xi}{\partial x} + \frac{\partial u}{\partial \eta}\frac{\partial \eta}{\partial x} = \frac{\partial u}{\partial \xi} + \frac{\partial u}{\partial \eta} \tag{B-4}$$

$$\frac{\partial u}{\partial t} = \frac{\partial u}{\partial \xi}\frac{\partial \xi}{\partial t} + \frac{\partial u}{\partial \eta}\frac{\partial \eta}{\partial t} = c\frac{\partial u}{\partial \xi} - c\frac{\partial u}{\partial \eta} \tag{B-5}$$

$$\frac{\partial^2 u}{\partial x^2} = \frac{\partial}{\partial \xi}\left(\frac{\partial u}{\partial x}\right)\frac{\partial \xi}{\partial x} + \frac{\partial}{\partial \eta}\left(\frac{\partial u}{\partial x}\right)\frac{\partial \eta}{\partial x} = \frac{\partial^2 u}{\partial \xi^2} + 2\frac{\partial^2 u}{\partial \xi \partial \eta} + \frac{\partial^2 u}{\partial \eta^2} \tag{B-6}$$

doi:10.6342/NTU202600018

$$\frac{\partial^2 u}{\partial t^2} = \frac{\partial}{\partial \xi}\left(\frac{\partial u}{\partial t}\right)\frac{\partial \xi}{\partial t} + \frac{\partial}{\partial \eta}\left(\frac{\partial u}{\partial t}\right)\frac{\partial \eta}{\partial t} = c^2\left(\frac{\partial^2 u}{\partial \xi^2} - 2\frac{\partial^2 u}{\partial \xi \partial \eta} + \frac{\partial^2 u}{\partial \eta^2}\right) \quad \text{(B-7)}$$

Substituting (B-6) and (B-7) into (B-3) yields

$$\frac{\partial^2 u}{\partial \xi \partial \eta} = 0 \rightarrow \frac{\partial u}{\partial \eta} = f_1(\xi) \rightarrow u = f_1(\xi) + f_2(\eta) \quad \text{(B-8)}$$

The final simple equation of (B-8) turns out that the solution for (B-3) are always in the form

$$u(x,t) = f_1(\xi) + f_2(\eta) = f_1(x+ct) + f_2(x-ct) \quad \text{(B-9)}$$

where $f_1(x+ct)$ and $f_2(x+ct)$ is to be determined by initial and boundary conditions. The (B-9) is called d´Alembert's formula, meaning that the general solution of 1-D wave equation can always be expressed as a sum of two arbitrary functions with arguments $x+ct$ and $x-ct$.

Moreover, considering a problem on an infinite rod involving the standard 1-D transverse wave equation with initial displacement $h(x)$ and initial velocity $v(x)$, applying the Fourier transform to (B-3) yields

$$\begin{gathered}\int_{-\infty}^{\infty}\left(\frac{\partial^2 u}{\partial x^2}\right)e^{-ikx}dx = \frac{1}{c_t^2}\int_{-\infty}^{\infty}\left(\frac{\partial^2 u}{\partial t^2}\right)e^{-ikx}dx \\ \rightarrow (ik)^2\hat{u} - \frac{1}{c_t^2}\frac{\partial^2 \hat{u}}{\partial t^2} = 0\end{gathered} \quad \text{(B-10)}$$

where $\hat{u} = \hat{u}(k,t)$ represent the displacement field after Fourier transform.

The general solution of this second order homogenous differential equation is given by

$$\hat{u} = A(k)e^{ikct} + B(k)e^{-ikct} \quad \text{(B-11)}$$

From I.C., we obtain

$$A(k) + B(k) = \hat{h}(x) \quad \text{(B-12)}$$

doi:10.6342/NTU202600018

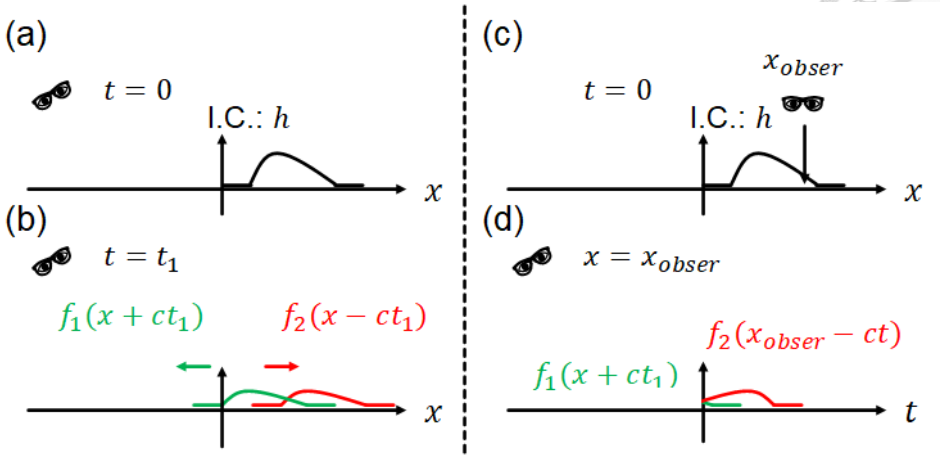


Figure B-6: An illustration of wave propagation, showing the spatial evolution from (a) an initial state to (b) a later time, and the temporal evolution at a fixed observation point from (c) an initial state to (d) a later time.

$$ikc[A(k) - B(k)] = \hat{v}(x) \tag{B-13}$$

Thus, the unknown coefficients are determined as

$$A(k) = \frac{1}{2}\left[\hat{h}(x) + \frac{\hat{v}(x)}{ikc}\right] \tag{B-14}$$

$$B(k) = \frac{1}{2}\left[\hat{h}(x) - \frac{\hat{v}(x)}{ikc}\right] \tag{B-15}$$

By doing reverse Fourier transform to (B-11), we obtain

$$\begin{aligned} &\hat{u} = \frac{1}{2}\hat{h}(x)\left(e^{ikct} + e^{-ikct}\right) + \frac{\hat{v}(x)}{2ikc}\left(e^{ikct} + e^{-ikct}\right) \\ &\rightarrow u(x,t) = \frac{1}{2}[h(x + c_t t) + h(x - c_t t)] + \frac{1}{2c_t}\int_{x-c_t t}^{x+c_t t} v(y)dy \end{aligned} \tag{B-16}$$

where y is the dummy variable, it will disappear after integration.

Figure B-6 shows the schematic of disturbance propagation for which the initial velocity is zero (i.e., $v(x) = 0$ and $(x,t) = [h(x + c_t t) + h(x - c_t t)]/2$). As Figure B-6 (a) and (b) show, the initial disturbance is split into two equal parts, propagating

doi:10.6342/NTU202600018

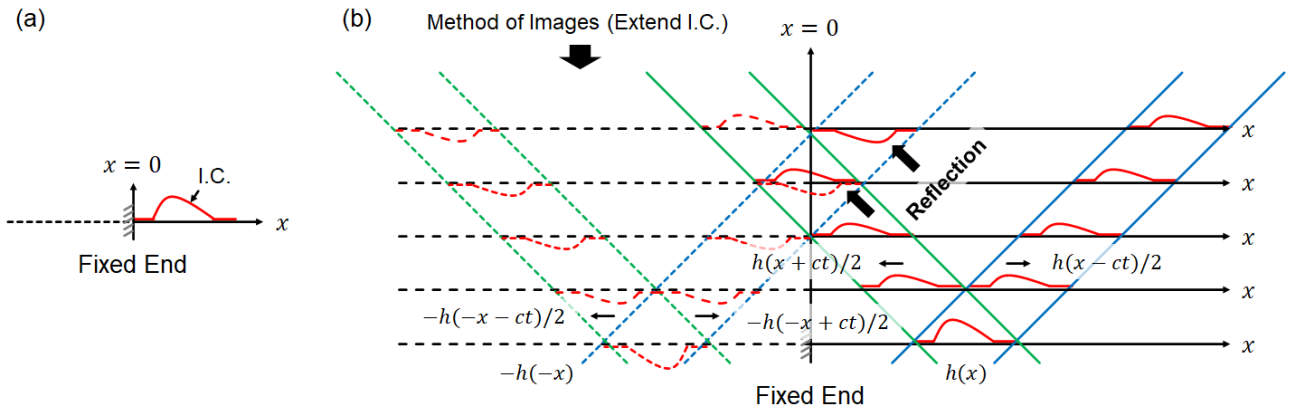


Figure B-7: (a) The initial disturbance at $t = 0$. (b) The time evolution of the disturbance up to time t, determined using the method of images to model the fixed end by introducing an extended, inverted initial condition.

in opposite directions with constant speed c. The $f_1(x+ct) = h(x+c_t t)/2$ indicate the disturbance propagates to the direction of positive x axis and $f_2(x-ct) = h(x-c_t t)/2$ the disturbance propagates to the direction of negative x axis. The shape of the disturbance $f_1(x+ct)$ and $f_2(x-ct)$ remains unchanged and equal to shape of initial displacements with half magnitude. The dissipation is not included thus this kind of wave are called non-dispersive wave. Figure B-6 (c) and (d) show the time history plot at a specific observation point. Differing from rigid body motion, the concept of wave propagation is that the motion takes time to reach a certain point. Noted, there is no contribution of the boundary condition sine the rod is infinite long.

Considering a semi-infinite rod fixed at left hand side end with zero initial velocity field as shown in Figure B-7 (a), we will obtain same results as (B-16), representing

$$u(x,t) = \frac{1}{2}[h(x+c_t t) + h(x-c_t t)] \tag{B-17}$$

However, the B.C. should contribute something, thus, considering additional B.C., we obtain

$$u(0,t) = 0 = \frac{1}{2}[h(c_t t) + h(-c_t t)] \tag{B-18}$$

doi:10.6342/NTU202600018

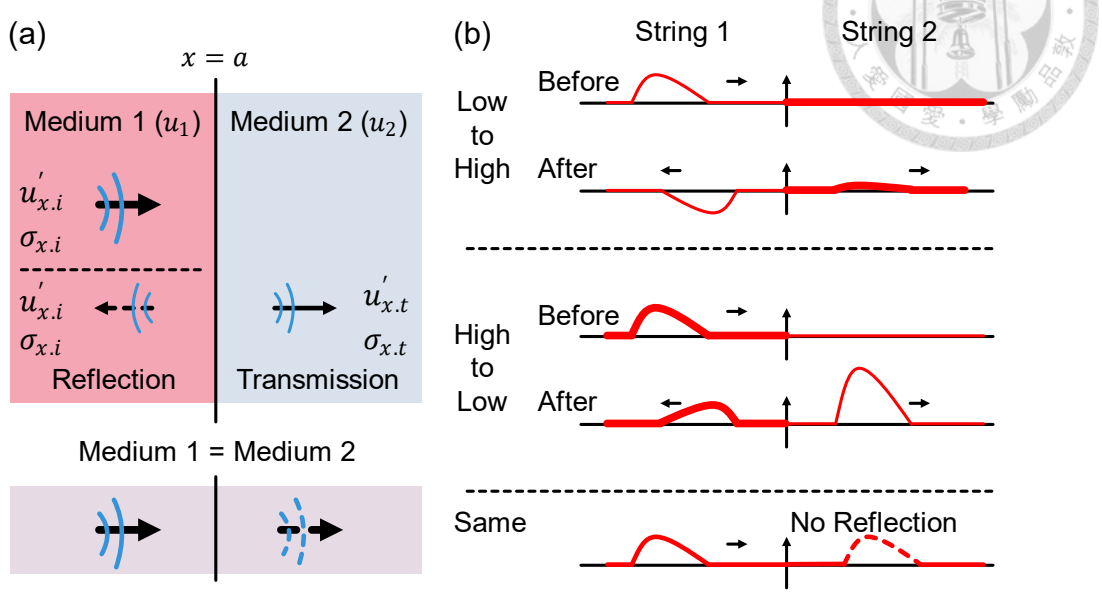


Figure B-8: An illustration of the effect of impedance on wave reflection and transmission. (a) A general case of a wave propagating between two media. (b) Wave behavior on a string with varying densities: (i) from low to high density, (ii) from high to low density, and (iii) a control case with uniform density

$$\rightarrow -h(c_t t) = h(-c_t t)$$

Since the term with $x + c_t t$ are always positive, considering only the terms of $x - c_t t$, it turns out

$$x - c_t t > 0: u(x,t) = \frac{1}{2}[h(x + c_t t) + h(x - c_t t)] \tag{B-19}$$

$$x - c_t t < 0: u(x,t) = \frac{1}{2}[h(x + c_t t) - h(x - c_t t)] \tag{B-20}$$

It is clear and match to daily experience, as shown in Figure B-7 (b), the wave propagating to the fixed end will turn around and change the sign. The odd function property of fixed end B.C. is equivalent to add appropriate images of $h(x + c_t t)$ and $h(x - c_t t)$ on the negative x axis in order to satisfy B.C. The rules are called *method of images*. The method of images for free end B.C. will also follow the odd function

doi:10.6342/NTU202600018

however the sign will not change [504].

Moreover, considering 1-D velocity wave incident from one media to another media at $x = a$ as shown in Figure B-8 (a), the governing equations in medias and interface B.C. for both stress and velocity are given as

$$\frac{\partial^2 u_1}{\partial x^2} = \frac{1}{c_1^2}\frac{\partial^2 u_1}{\partial t^2} \tag{B-21}$$

$$\frac{\partial^2 u_2}{\partial x^2} = \frac{1}{c_2^2}\frac{\partial^2 u_2}{\partial t^2} \tag{B-22}$$

$$\sigma_{x.i} + \sigma_{x.r} = \sigma_{x.t} \tag{B-23}$$

$$u'_{x.i} + u'_{x.r} = u'_{x.t} \tag{B-24}$$

where the subscript i, r and t represent the incident, reflected and transmitted wave, respectively. $u'_{x.i}$, $u'_{x.r}$ and $u'_{x.t}$ represent the velocity wave field.

Using the D'Alembert's formular yields

$$u'_{x.i} = f_i(t - x/c_1) \tag{B-25}$$

$$u'_{x.r} = f_r(t + x/c_1) \tag{B-26}$$

$$u'_{x.t} = f_t(t - x/c_2) \tag{B-27}$$

With interface B.C., we obtain

$$-\rho_1 c_1 f_i(t - a/c_1) + \rho_1 c_1 f_r(t + a/c_1) = -\rho_2 c_2 f_t(t - a/c_2) \tag{B-28}$$

$$f_i(t - a/c_1) + f_r(t + a/c_1) = f_t(t - a/c_2) \tag{B-29}$$

Rearrange the (B-28)-(B-29), we obtain the relation of reflection and transmission to the known incident velocity wave as

$$f_r(t + a/c_1) = \Gamma_{11} f_i(t - a/c_1) \tag{B-30}$$

$$f_t(t - a/c_2) = \Gamma_{21} f_i(t - a/c_1) \tag{B-31}$$

doi:10.6342/NTU202600018

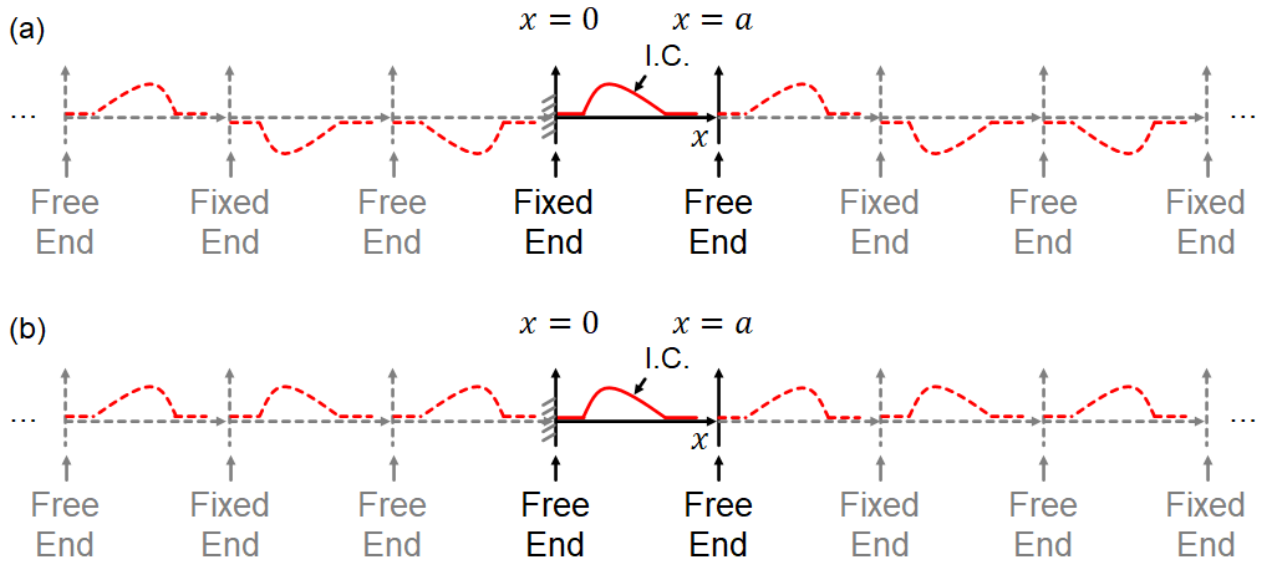


Figure B-9: An illustration of wave propagation with (a) fixed-free and (b) free-free boundary conditions, showing the infinite set of extended initial conditions created by the method of images at $t = 0$.

where $\Gamma_{11} = \frac{\rho_1 c_1 - \rho_2 c_2}{\rho_1 c_1 + \rho_2 c_2}$ and $\Gamma_{21} = \frac{2\rho_1 c_1}{\rho_1 c_1 + \rho_2 c_2}$ are refection coefficient and transmission coefficient for the propagating waves, respectively. If the product of $\rho_1 c_1$ equal to $\rho_2 c_2$, the case reduces to same media case thus there is no reflection (i.e., $\Gamma_{11} = 0$ and $\Gamma_{21} = 1$, *cf.* Figure B-8 (b)). It becomes fixed end B.C. and totally reflected if $\rho_2 c_2 \gg \rho_1 c_1$ (i.e., $\Gamma_{11} = -1$ and $\Gamma_{21} = 0$). The specific case is that if $\rho_2 c_2 \ll \rho_1 c_1$, the transmitted velocity doubled (i.e., $\Gamma_{11} = 1$ and $\Gamma_{21} = 2$).

Figure B-8 (c) presents an alternative perspective, illustrating the wave's propagation through a string. The wave moves from a region of low density to one of high density, or vice versa. This movement results in varying transmission and reflection, as previously mentioned. When the wave travels from a low-density to a high-density region, its shape is inverted. This inversion occurs because the high-density string behaves like a fixed boundary. Conversely, when the wave moves from high density to low density, it encounters a free boundary, and the shape sign are not inverted.

Considering a finite string subjected to an initial disturbance and assuming the string

doi:10.6342/NTU202600018

ends are fixed-free (*cf.* Figure B-9 (a)) or free-free (*cf.* Figure B-9 (b)), the field of image waves required to satisfy the boundary condition is illustrated for $t = 0$. It is essential to construct an infinite set of image strings to describe the response over time. In addition, the D'Alembert's formular is applicable to simple B.C. and is mainly provide the quantitative understanding for such problem because the infinite series approximation is unrealistic. It is inefficient for general analysis.

In fact, although the motion can be described by propagating waves even if system is bounded (i.e., finite length with certain boundaries), the projection-based method (e.g. method of separation variables, method of normal mode or Galerkin method) is more useful because the problem become so-called eigenvalue problem in which description on the specific vibration shape and specific frequencies are meaningful than infinite series approximation that solved by D'Alembert's solution with method of images. These specific vibration shape and frequencies are known as normal mode (or standing wave) and natural frequencies, respectively.

B.1.2 Introduction to the Electromagnetic Wave

People often link the *light* with *visible light* and consider the radio wave (3 Hz to 30 MHz), microwave (300 MHz to 30 GHz), infrared wave (300 GHz to 400 THz), ionizing radiation (3 PHz to 300 EHz) as other things. As mentioned in the beginning of this appendix, the truth is that they are all electromagnetic wave and sometimes called radiation. They are a kind of propagating power wave classified with different operation frequency band and contain different level of energy.

Before talking about the physic through mathematical treatment, here first review some matrix operators as listed bellow

$$\text{Partial derivatives operator: } \vec{\nabla} = \frac{\partial}{\partial x}\hat{x} + \frac{\partial}{\partial y}\hat{y} + \frac{\partial}{\partial z}\hat{z} \tag{B-32}$$

$$\text{Gradient of a scaler: } \vec{\nabla}\emptyset = \frac{\partial \emptyset}{\partial x}\hat{x} + \frac{\partial \emptyset}{\partial y}\hat{y} + \frac{\partial \emptyset}{\partial z}\hat{z} \tag{B-33}$$

doi:10.6342/NTU202600018



$$\text{Divergence of a vector: } \vec{\nabla}\cdot\vec{A} = \frac{\partial A_x}{\partial x} + \frac{\partial A_y}{\partial y} + \frac{\partial A_z}{\partial z} \tag{B-34}$$

$$\text{Curl of a vector: } \vec{\nabla}\times\vec{A} = \begin{vmatrix} \hat{x} & \hat{y} & \hat{z} \\ \frac{\partial}{\partial x} & \frac{\partial}{\partial y} & \frac{\partial}{\partial z} \\ A_x & A_y & A_z \end{vmatrix} \tag{B-35}$$

$$= \left(\frac{\partial A_z}{\partial y} - \frac{\partial A_y}{\partial z}\right)\hat{x} + \left(\frac{\partial A_x}{\partial z} - \frac{\partial A_z}{\partial x}\right)\hat{y} + \left(\frac{\partial A_y}{\partial x} - \frac{\partial A_x}{\partial y}\right)\hat{z}$$

$$\text{Laplacian of a vector: } \vec{\nabla}^2\,\vec{A} = \left(\vec{\nabla}\cdot\vec{\nabla}\right)\vec{A} = \frac{\partial^2\vec{A}}{\partial x^2} + \frac{\partial^2\vec{A}}{\partial y^2} + \frac{\partial^2\vec{A}}{\partial z^2} \tag{B-36}$$

$$\text{Curl of curl of a vector: } \vec{\nabla}\times\left(\vec{\nabla}\times\vec{A}\right) = \vec{\nabla}\left(\vec{\nabla}\cdot\vec{A}\right) - \left(\vec{\nabla}\cdot\vec{\nabla}\right)\vec{A} \tag{B-37}$$

, the second derivative terms in (B-36) are

$$\frac{\partial^2\vec{A}}{\partial x^2} = \frac{\partial^2}{\partial x^2}\left(A_x\hat{x} + A_y\hat{y} + A_z\hat{z}\right) \tag{B-38}$$

$$\frac{\partial^2\vec{A}}{\partial y^2} = \frac{\partial^2}{\partial y^2}\left(A_x\hat{x} + A_y\hat{y} + A_z\hat{z}\right) \tag{B-39}$$

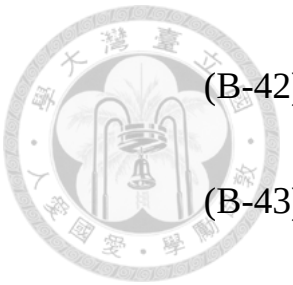
$$\frac{\partial^2\vec{A}}{\partial z^2} = \frac{\partial^2}{\partial z^2}\left(A_x\hat{x} + A_y\hat{y} + A_z\hat{z}\right) \tag{B-40}$$

where the $\emptyset$ and $\vec{A}$ is a scaler and a vector, respectively.

Maxwell's equations, in electromagnetism, form a set of coupled partial differential equations. They lay the foundation for understanding how electric and magnetic fields are produced by charges, currents, and variations in the fields. The Maxwell's equations with constitutive relation (i.e., material effect from ε and μ) in differential form can be given as [505]

$$\text{Gauss's law for electricity: } \vec{\nabla}\cdot\vec{E} = \frac{\rho_c}{\varepsilon_0} \tag{B-41}$$

doi:10.6342/NTU202600018



Gauss's law for magnetism: $\vec{\nabla} \cdot \vec{B} = 0$ (B-42)

Faraday's law of induction: $\vec{\nabla} \times \vec{E} = -\frac{\partial \vec{B}}{\partial t}$ (B-43)

Ampere's circuital law: $\vec{\nabla} \times \vec{B} = \mu_0 \vec{J} + \varepsilon_0 \mu_0 \frac{\partial \vec{E}}{\partial t}$ (B-44)

where $\vec{E}$, $\vec{B}$ and $\vec{J}$ are electric field, magnetic field and current density, respectively. The ρ_c, $\mu_0 = 4\pi \times 10^{-7}$ (H/m) and $\varepsilon_0 = 8.854188 \times 10^{-12}$ (F/m) are charge density, magnetic permeability of free space and permittivity of free space, respectively.

Considering a source-free system without charge, electric current or any dielectric medium (i.e., in vacuum), then Maxwell's equations are reduced as

$$\vec{\nabla} \cdot \vec{E} = 0 \tag{B-45}$$

$$\vec{\nabla} \cdot \vec{B} = 0 \tag{B-46}$$

$$\vec{\nabla} \times \vec{E} = -\frac{\partial \vec{B}}{\partial t} \tag{B-47}$$

$$\vec{\nabla} \times \vec{B} = \frac{1}{{c_{light}}^2} \frac{\partial \vec{E}}{\partial t} \tag{B-48}$$

where $c_{light} = 1/\sqrt{\varepsilon_0 \mu_0} = 299792458 \approx 3 \times 10^8$ (m/s) is speed of light (i.e., propagating velocity of electromagnetic wave).

The electromagnetic wave equation can be obtained by taking the curl of Faraday's law or Ampere's law as

$$\text{LHS: } \vec{\nabla} \times \left(\vec{\nabla} \times \vec{E}\right) = \vec{\nabla}\left(\vec{\nabla} \cdot \vec{E}\right) - \left(\vec{\nabla} \cdot \vec{\nabla}\right)\vec{E} = -\vec{\nabla}^2 \vec{E}$$

$$\text{RHS: } -\frac{\partial}{\partial t}\left(\vec{\nabla} \times \vec{B}\right) = -\frac{\partial}{\partial t}\left(\frac{1}{{c_{light}}^2} \frac{\partial \vec{E}}{\partial t}\right) \tag{B-49}$$

$$\text{LHS = RHS: } \vec{\nabla}^2 \vec{E} = \frac{\partial}{\partial t}\left(\frac{1}{{c_{light}}^2} \frac{\partial \vec{E}}{\partial t}\right)$$

doi:10.6342/NTU202600018

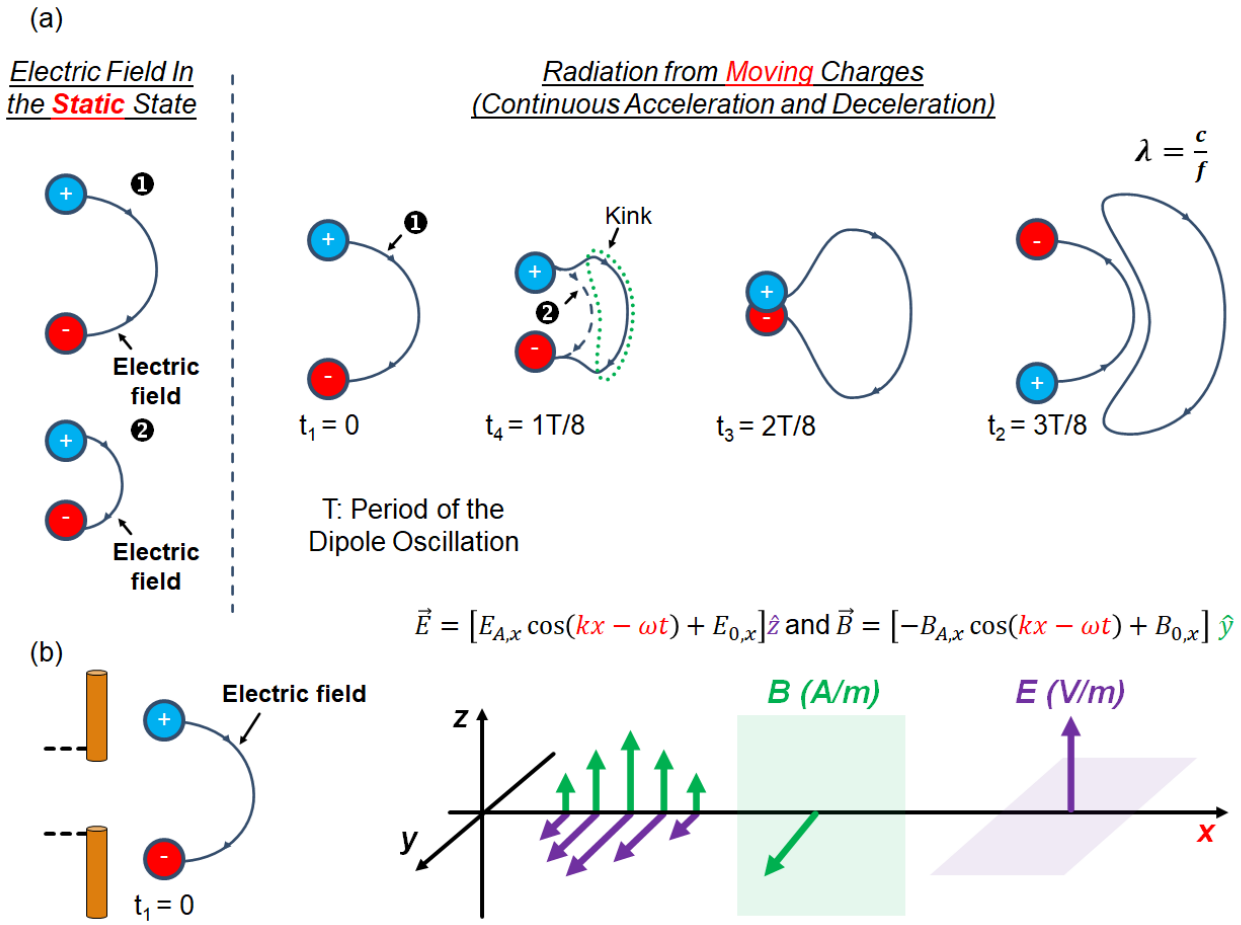


Figure B-10: (a) A comparison between a static dipole's electric field and the principle of radiation generation from an oscillating dipole. (b) An illustration of a continuous electromagnetic wave generated by a dipole antenna, where an applied RF signal forces charges to accelerate and decelerate periodically, in turn generating the wave. Noted, the EM wave and electric field on the left-hand side have been omitted for clarity of representation.

$$\text{LHS: } \vec{\nabla} \times \left(\vec{\nabla} \times \vec{B}\right) = \vec{\nabla}\left(\vec{\nabla} \cdot \vec{B}\right) - \left(\vec{\nabla} \cdot \vec{\nabla}\right)\vec{B} = -\vec{\nabla}^2\vec{B}$$

$$\text{RHS: } \frac{1}{{c_{light}}^2}\frac{\partial}{\partial t}\left(\vec{\nabla} \times \vec{E}\right) = \frac{1}{{c_{light}}^2}\frac{\partial}{\partial t}\left(-\frac{\partial \vec{B}}{\partial t}\right) \tag{B-50}$$

$$\text{LHS = RHS: } \vec{\nabla}^2\vec{B} = \frac{1}{{c_{light}}^2}\frac{\partial}{\partial t}\left(-\frac{\partial \vec{B}}{\partial t}\right)$$

where the left-hand side (LHS) and right-hand side (RHS) of equations are labelled for clarity, representing LHS = RHS practically.

Looking back to the (B-47)-(B-50), it is not hard to find that both electrical field

doi:10.6342/NTU202600018

and magnetic field behavior as a wave while generate each other simultaneously. A changing magnetic field will induce a changing electric field and vice-versa. In fact, they are a linked energy wave called electromagnetic wave, exiting as one kind of propagating energy naturally. They are perpendicular to each other and perpendicular to the propagating direction. On the other word, if there is a progressive EM wave in vacuum, we can find them if and only if the electric and a magnetic field exist simultaneously.

Although the creation of the EM propagation from the transition field known as a *Kink* is out of the scope, however, one might be summarized as that *moving charges* with the moving speed less than speed of the light will cause the discontinues field and generate the radiation. Figure B-10 (a) illustrate the generating process of the radiation and please see [507-509] for details.

As shown in Figure B-10 (b), if the electromagnetic wave, generated by a dipole antenna, propagating along x direction and facing to z direction, the 1-D version of electromagnetic wave equation for electrical field becomes

$$\frac{\partial^2 \vec{E}}{\partial x^2} = \frac{1}{{c_{light}}^2}\frac{\partial^2 \vec{E}}{\partial t^2} \tag{B-51}$$

One of the solutions of (B-51) is given by

$$\vec{E} = \left[E_{A.x}\, cos(kx - \omega t) + E_{0,x}\right]\hat{z} \tag{B-52}$$

where $k = 2\pi/\lambda = \omega/c_{light}$ is the wave number and $E_{0,z}$ is constant to be determined through I.C.

As the solution for electrical field presented, one can find out the magnetic field with the Faraday's law as

$$-\frac{\partial \vec{B}}{\partial t} = \vec{\nabla} \times \vec{E} = \begin{vmatrix} \hat{x} & \hat{y} & \hat{z} \\ \frac{\partial}{\partial x} & \frac{\partial}{\partial y} & \frac{\partial}{\partial z} \\ E_x & E_y & E_z \end{vmatrix} = \frac{\partial E_z}{\partial x}\hat{y} \tag{B-53}$$

doi:10.6342/NTU202600018

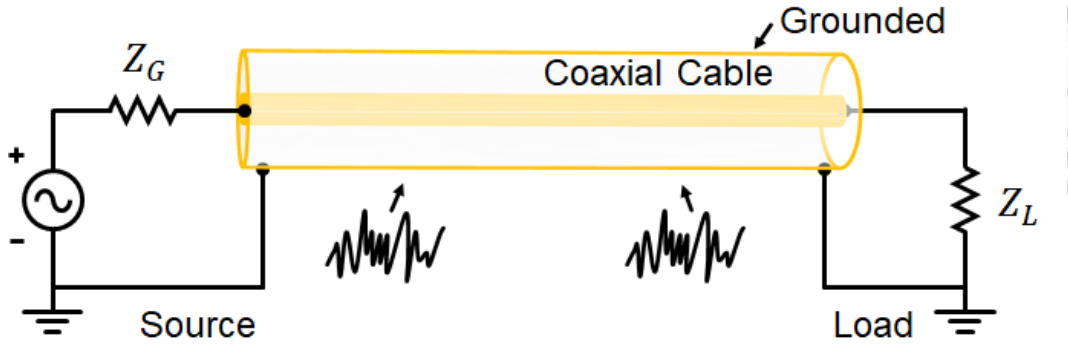


Figure B-11: A schematic of a basic 1-port network, with the coaxial cable situated between a source and a load.

$$= E_{A.x} k \, sin(kx - \omega t) \, \hat{y}$$

Taking the integration, the magnetic field could be obtained as

$$\vec{B} = \left[-\frac{E_{A.x} k}{\omega} cos(kx - \omega t) + B_{0,x} \right] \hat{y} = \left[-B_{A.x} \, cos(kx - \omega t) + B_{0,x} \right] \hat{y} \quad \text{(B-54)}$$

where $B_{0,x}$ is constant to be determined through I.C. According to (B-52) and (B-54), as mentioned, the progressive EM wave in vacuum exist simultaneously. They are perpendicular to each other and perpendicular to the propagating direction.

B.1.3 Transverse Electromagnetic Transmission Line

Energy can be transmitted not only by radiation of free electromagnetic waves but also can be varied in various conductor arrangement known as transmission line. Transmission lines usually transmit electrical signals and power efficiently between different points along various paths and can serve as circuit elements.

In the majority of transmission lines, the electric and magnetic fields are oriented purely transverse to the direction of propagation. These waves are known as transverse electromagnetic (TEM) waves, and the corresponding transmission lines are referred to as TEM transmission lines. Transmission lines often display frequency-dependent behavior in communication systems. Therefore, complex notation is frequently employed. The transmission line theory discussed in this appendix focus on those used for characterizing electrostatic MEMS devices.

doi:10.6342/NTU202600018

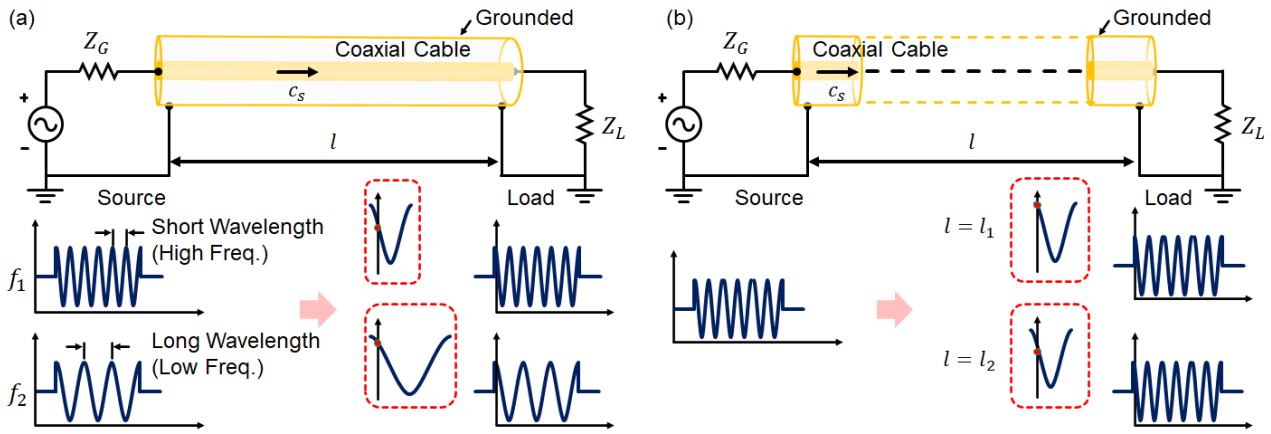


Figure B-12: An illustration of the effects on phase delay and voltage change at the load end, considering (a) the signal's wavelength and (b) the cable's length.

Figure B-11 shows a 1-port transmission line system, the RF energy is transmitted from source to load through a coaxial cable in order to lower the effect of noise form external environment (e.g., the electromagnetic wave generated from surrounding devices, instruments or antennas). If any external RF energy strikes the cable, it reaches the grounded conductor and is shielded from the core. In other words, any noisy electromagnetic energy is grounded by the outer conductor without reaching the inner one. This ensures that any unwanted external RF signal cannot affect the signal being carried along the coaxial cable.

The effect of the cable is ignored in the electric circuit theory, treating problem in 0-D domain where the effect of cable length is ignored. However, the effect of the cable cannot be always ignored because the transmitting speed of the electrical signal is finite. To give an imagination, Figure B-12 illustrate the idea on effect of the frequency/wavelength of the propagating electrical power. Considering the voltage provided by port 1 delayed by l/c_s, the received voltage at port 2 is qualitatively represented as

$$V_2 = V_1 \cos\left[2\pi f\left(t - \frac{l}{c_s}\right)\right] = V_1 \cos[2\pi f t - \phi_s] \qquad \text{(B-55)}$$

where $\phi_s = 2\pi f l/c_s = 2\pi l/\lambda_s$ represents the phase delay and $\lambda_s = c_s/f$ (m) is

doi:10.6342/NTU202600018

wavelength.

Considering the case of Figure B-12 (a) where the cable length is $l = 10^4$ (m) and comparing two operating frequencies of (1) $f_1 = 2 \times 10^1$ (Hz) and (2) $f_2 = 2 \times 10^3$ (Hz) (the corresponding wavelength are (1) $\lambda_{s1} = 2 \times 10^8 / 2 \times 10^1 = 10^7$ and (2) $\lambda_{s2} = 2 \times 10^8 / 2 \times 10^3 = 10^5$ (m), respectively), if the voltage wave is transmitting in a standard cable (e.g., RG-58 cable), with a given value of wave speed $c_s \approx 2/3 \times c_{light} = 2 \times 10^8$ (m/s), the received voltage at $t = 0$ is given by

$$(1): V_{2.1} = V_1 \cos\left[-2\pi \frac{l}{\lambda_{s1}}\right] = 0.99998 V_1 \tag{B-56}$$

$$(2): V_{2.2} = V_1 \cos\left[-2\pi \frac{l}{\lambda_{s2}}\right] = 0.80901 V_1 \tag{B-57}$$

On the other hand, considering the case of Figure B-12 (b) where the operating frequency is $f = 2 \times 10^3$ (Hz) and comparing cable length of (3) $l_2 = 10^3$ and (4) $l_3 = 5 \times 10^4$ (m), the received voltage at $t = 0$ is given by

$$(3): V_{2.3} = V_1 \cos\left[-2\pi \frac{l_2}{\lambda_{s2}}\right] = 0.99803 V_1 \tag{B-58}$$

$$(4): V_{2.4} = V_1 \cos\left[-2\pi \frac{l_3}{\lambda_{s2}}\right] = -1.00000 V_1 \tag{B-59}$$

doi:10.6342/NTU202600018

These examples illustrate that the effect of transmission line can be ignored if the cable length is totally short than wavelength. However, it cannot be ignored if the wavelength is comparable to, or even less than, the cable length. By rule of thumb, $l/\lambda_s < 0.1$ is a threshold. Assuming the wave speed is $c_s = 2 \times 10^8$, that means, for a 10-MHz/1-GHz signal (i.e., $\lambda_{s.10M} = 20$ (m)/ $\lambda_{s.1G} = 0.2$ (m)), if the transmission line/interconnecting wire is longer than 2/0.02 meters, the effects of transmission line must be considered. As will be presented, in fact, it is necessary to account not only the phase delay but also for the presence of reflected signals that may have been bounced back toward the transmitting end by the receiving end load impedance. In analogy to mechanical waves, it is essential that the motion takes time to reach a certain point (i.e., phase delay due to finite propagating speed) and reflected due to the material properties mismatch (i.e., load impedance mismatch) as shown in Figure B-8 (c) and Figure B-8 (d).

Figure B-13 (a) shows the schematic of a coaxial cable in detail and Figure B-13 (b) shows the pattern of electric field and magnetic field of an ideal coaxial cable in TEM mode. Although the transmission line can also carry the transverse electric (TE) and transverse magnetic (TM) modes, one might conclude that TEM mode dominated the

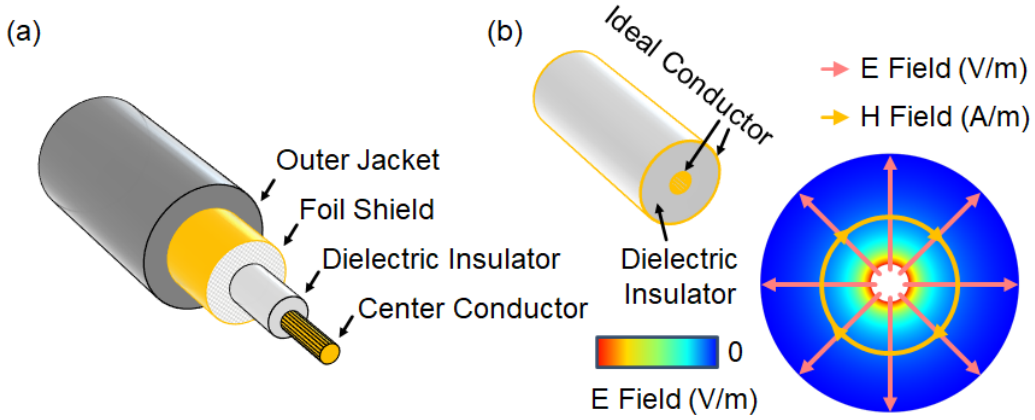


Figure B-13: (a) A schematic diagram of a coaxial cable. (b) A cross-sectional view illustrating the electric (E) and magnetic (H) fields in the transverse electromagnetic (TEM) mode.

doi:10.6342/NTU202600018

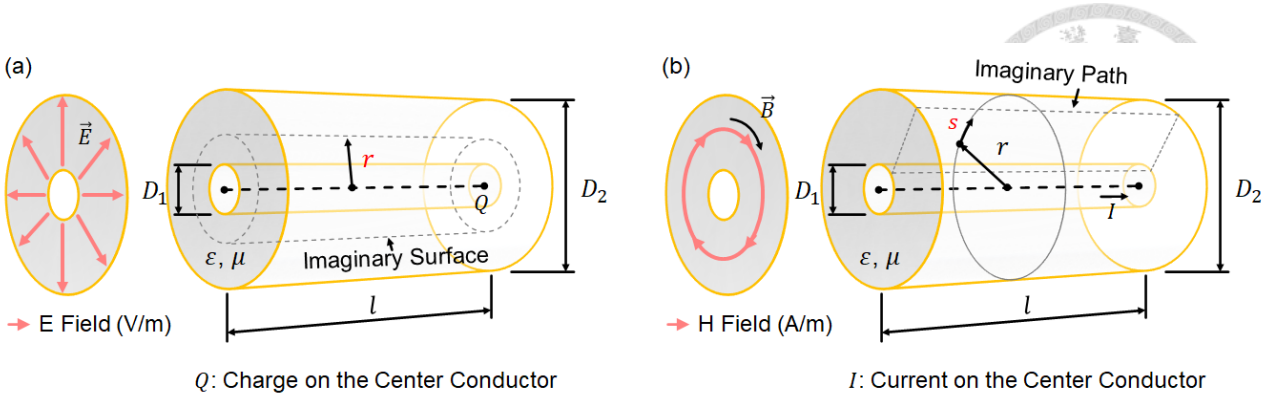


Figure B-14: Diagrams showing the integration paths used to calculate the electrical properties of a coaxial cable, for (a) the electric field and (b) the magnetic field.

behavior in typical transmission line. Therefore, modeling a 2D cross section is suffices to compute the fields and the impedance.

As presented, it is convenient to treat it as 1-D problem as the fields in radius coordinate is steady. Considering a small portion of coaxial cable as shown in Figure B-14 (a), using Gauss' law and an *imaginary surface*, the voltage in the cylinder can be obtained through the integral of electric field as

$$\int \vec{E} d\vec{A} = \frac{Q_c}{\varepsilon} \rightarrow E 2\pi r l = \frac{Q_c}{\varepsilon} \rightarrow E = \frac{Q_c}{\varepsilon 2\pi r l} \tag{B-60}$$

The voltage difference is the integral of the electric field, take the form

$$V = \int_{r_1}^{r_2} E dr = \frac{Q_c}{\varepsilon 2\pi l} \int_{D_1}^{D_2} \frac{1}{r} dr = \frac{Q_c}{\varepsilon 2\pi l} \left[\ln\left(\frac{D_2}{2}\right) - \ln\left(\frac{D_1}{2}\right) \right] = \frac{Q_c}{\varepsilon 2\pi l} \ln\left(\frac{D_2}{D_1}\right) \tag{B-61}$$

Therefore, the effective capacitance per unit length can be obtained as

$$Q_c = CV \rightarrow C = \frac{Q_c}{V} = \frac{\varepsilon 2\pi l}{\ln\left(\frac{D_2}{D_1}\right)} \rightarrow \bar{C} = \frac{C}{l} = \frac{\varepsilon 2\pi}{\ln\left(\frac{D_2}{D_1}\right)} \tag{B-62}$$

Similarly, using Ampere' law and an *imaginary path* as shown in Figure B-14 (b), the current in the cylinder can be obtained through the integral of magnetic field as

doi:10.6342/NTU202600018

$$\oint \vec{B}d\vec{s} = \mu I \rightarrow B2\pi r = \mu I \rightarrow B = \frac{\mu I}{2\pi r} \tag{B-63}$$

Determining the flux through the imaginary loop yields

$$\phi = \int_{D_1}^{D_2} \vec{B}d\vec{A} = \frac{\mu I}{2\pi}\int_{D_1}^{D_2} \frac{1}{r} l dr = \frac{\mu I}{2\pi} l \ln\left(\frac{D_2}{D_1}\right) \tag{B-64}$$

With that, the inductance per unit length can be obtained by calculating the time derivative of flux as

$$\begin{aligned} V = \frac{d\phi}{dt} = \frac{\mu}{2\pi} l \ln\left(\frac{D_2}{D_1}\right)\frac{dI}{dt} = L\frac{dI}{dt} \rightarrow L = \frac{\mu}{2\pi} l \ln\left(\frac{D_2}{D_1}\right) \\ \rightarrow \bar{L} = \frac{L}{l} = \frac{\mu}{2\pi}\ln\left(\frac{D_2}{D_1}\right) \end{aligned} \tag{B-65}$$

Therefore, the voltage and current difference between the small piece of cable for the generic equivalent circuit represented in Figure B-15 is given by

$$-\{V(x+\Delta x,t) - V(x,t)\} = \bar{L}\Delta x\frac{\partial I(x,t)}{\partial t} + \bar{R}\Delta x I(x,t) \tag{B-66}$$

$$-\{I(x+\Delta x,t) - I(x,t)\} = \bar{C}\Delta x\frac{\partial V(x+\Delta x,t)}{\partial t} + \bar{G}\Delta x V(x,t) \tag{B-67}$$

where $\bar{R}$ and $\bar{G}$ are equivalent resistance and conductance per unit length, representing the non-ideal effect of $\bar{L}$ and $\bar{C}$.

Dividing all terms by discrete distance, rearranging them and treating in limit as $\Delta x \rightarrow 0$ yields the well-known telegrapher's equation of

$$-\frac{\partial V(x,t)}{\partial x} = \bar{L}\frac{\partial I(x,t)}{\partial t} + \bar{R}I(x,t) \tag{B-68}$$

$$-\frac{\partial I(x,t)}{\partial x} = \bar{C}\frac{\partial V(x,t)}{\partial t} + \bar{G}V(x,t) \tag{B-69}$$

doi:10.6342/NTU202600018

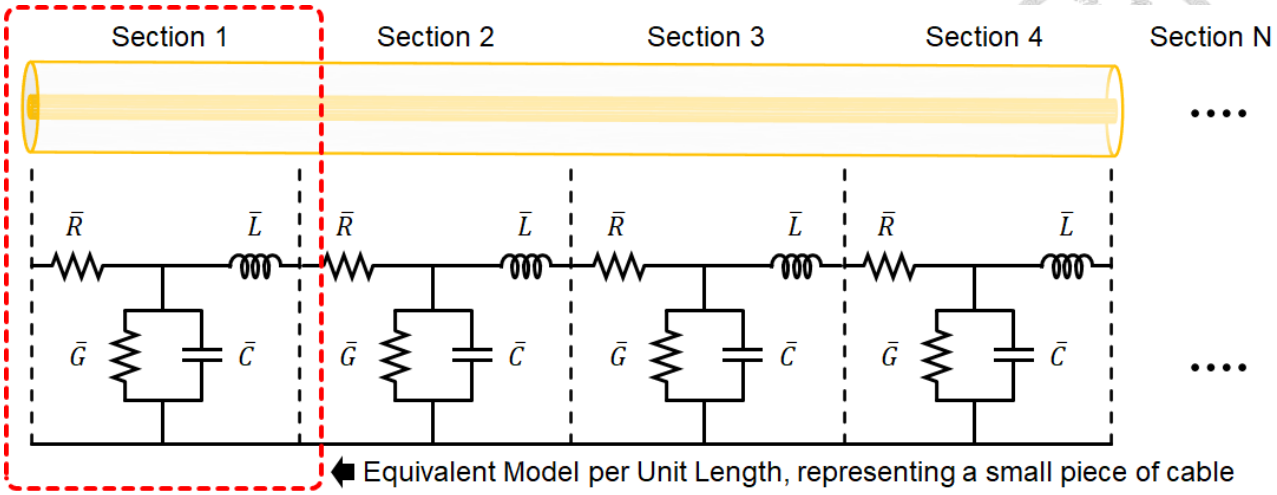


Figure B-15: A schematic illustrating the lumped-parameter modeling approach for a transmission line, where the continuous line is represented by a series of discrete equivalent circuits.

Focusing on sinusoidal steady-state conditions, utilizing phasor representation (or phasor transformation) can greatly simplify the solving process. Similar to other transformations like the Fourier transform, the equations become easier to solve in their transformed domain and converting them back to the original form is relatively straightforward. Noted, some equations may encounter challenges during the inverse transformation.

For instance, consider a simple phasor transformation with a cosine reference. Introducing $V = Re(\bar{V}e^{j\omega t})$ and $I = Re(\bar{I}e^{j\omega t})$ where $\bar{V}$ and $\bar{I}$ are time-independent phasor, the (B-68) and (B-69) become

$$-\frac{\partial \bar{V}(x)}{\partial x} = (j\omega\bar{L} + \bar{R})\,\bar{I}(x) \tag{B-70}$$

$$-\frac{\partial \bar{I}(x)}{\partial x} = (j\omega\bar{C} + \bar{G})\,\bar{V}(x) \tag{B-71}$$

These two first-order coupled equation can be combined to give two second-order uncoupled wave equation in term of current or voltage. Differentiating both sides of (B-70) and (B-71) with respect to x yields

doi:10.6342/NTU202600018

$$-\frac{\partial^2 \bar{V}(x)}{\partial x^2} = (j\omega\bar{L} + \bar{R})\frac{\partial \bar{I}(x)}{\partial x} \tag{B-72}$$

$$-\frac{\partial^2 \bar{I}(x)}{\partial x^2} = (j\omega\bar{C} + \bar{G})\frac{\partial \bar{V}(x)}{\partial x} \tag{B-73}$$

Replacing the first-order differential term by using (B-70) and (B-71) yields the wave equation of

$$\frac{\partial^2 \bar{V}(x)}{\partial x^2} - \frac{1}{c_s^2}\bar{V} = 0 \tag{B-74}$$

$$\frac{\partial^2 \bar{I}(x)}{\partial x^2} - \frac{1}{c_s^2}\bar{I} = 0 \tag{B-75}$$

where $c_s = 1/\sqrt{(j\omega\bar{L} + \bar{R})(j\omega\bar{C} + \bar{G})}$ is essentially the wave speed of electron in a transmission line. However, the wave speed of electron is frequently replaced by so-called complex propagation constant, $\gamma = 1/c_s$ sine the time dependence is not important in steady state.

In a lossless dielectric, the velocity of electromagnetic waves differs from that in a vacuum and is determined by the properties of the material as

$$c_s = \frac{1}{\sqrt{\bar{L}\bar{C}}} = \frac{1}{\sqrt{\left[\frac{\mu}{2\pi}\ln\left(\frac{D_2}{D_1}\right)\right]\left[\frac{\varepsilon 2\pi}{\ln\left(\frac{D_2}{D_1}\right)}\right]}} = \frac{1}{\sqrt{\mu_0\mu_r\varepsilon_0\varepsilon_r}} = \frac{c_{light}}{\sqrt{\mu_r\varepsilon_r}} \tag{B-76}$$

where $c_{light} = 299792458 \approx 3 \times 10^8$ (m/s) is speed of light in vacuum, $\varepsilon = \varepsilon_0\varepsilon_r$ and $\mu = \mu_0\mu_r$. ε_0, μ_0, ε_r and μ_r are magnetic permittivity of free space, permeability of free space and relative magnetic permeability of the material and relative permittivity of the material, respectively. The electromagnetic waves travels less than speed of light in vacuum sine there is some resistance from the transmitting medium.

The general solution for (B-74) and (B-75) are given by

doi:10.6342/NTU202600018

$$\bar{V}(x) = V_0^+ e^{-\gamma x} + V_0^- e^{\gamma x} \tag{B-77}$$

$$\bar{I}(x) = I_0^+ e^{-\gamma x} + I_0^- e^{\gamma x} \tag{B-78}$$

Substituting (B-77) and (B-78) into (B-72) or (B-73), we obtain

$$\bar{I}(x) = \frac{\gamma}{j\omega\bar{L} + \bar{R}}[V_0^+ e^{-\gamma x} - V_0^- e^{\gamma x}] = \frac{V_0^+}{Z_0} e^{-\gamma x} - \frac{V_0^-}{Z_0} e^{-\gamma x} \tag{B-79}$$

Comparing (B-78) and (B-79), we found

$$\frac{V_0^+}{I_0^+} = -\frac{V_0^-}{I_0^+} = Z_0 \tag{B-80}$$

where $Z_0 = (j\omega\bar{L} + \bar{R})/\gamma = \sqrt{(j\omega\bar{L} + \bar{R})/(j\omega\bar{C} + \bar{G})}$ is called the characteristic impedance of the transmission line. In lossless system, the complex propagation constant reduced as $\gamma = \sqrt{\bar{L}\bar{C}}$ and characteristic impedance reduced as $Z_0 = \sqrt{\bar{L}/\bar{C}}$. Noted, Z_0 is not a function of the cable length.

In conclusion, the above equations are actually similar with mechanical wave shown in Appendix B.1. 1.. The mismatch on *impedance* present same quantity in both fields where some wave reflected, and some wave transmitted. The energy can totally transmitted with no reflection if the impedance/material properties is matched. The two infinite mismatch cases on impedance are called open (fixed) and short (free) end B.C. in field of electromagnetism (mechanical wave).

Figure B-16 shows a simple simulation based on LTspice with 5 cascaded lumped model of the transmission line. Comparing each curve shown in Figure B-16, one can found that the delay induced by transmission line become more and more significant as it moves along the line. Besides the presented simple structure, the π or T network or even cascaded network are used to capture the real behavior of power wave propagation in medium and long transmission. Noted, people sometimes confuse on the characteristic impedance of a transmission line with the properties of a resistor. The characteristic impedance refers to the ratio between the voltage and current of a

doi:10.6342/NTU202600018

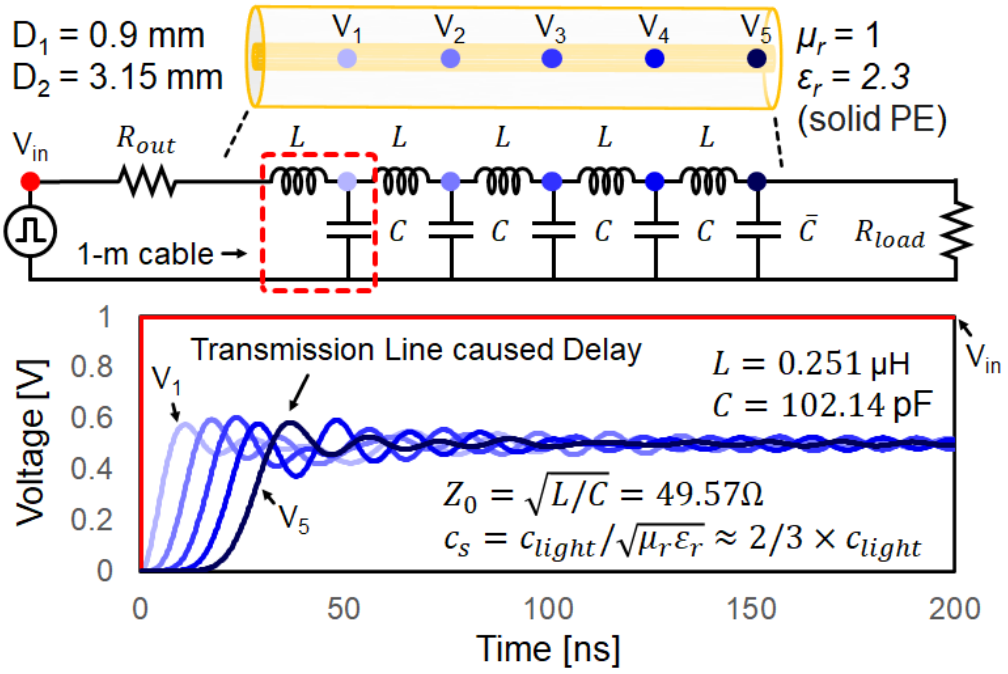


Figure B-16: Simulation results from LTspice for a 1-meter coaxial cable modeled by five cascaded lumped elements, showing the propagation of a unit step function and the resulting signal delay along the cable.

traveling wave on the line (*cf.* (B-80)). Although this ratio shares the same units as impedance, it doesn't result in power loss from the circuit as a resistor does. In fact, it causes phase difference between voltage and current.

The above derivation and discussion focus on the TEM modes. Within a transmission line theory, the wave is linked to electric currents flowing along a *pair* of conductors. These conductors force the currents to remain parallel to the line. As a result, the magnetic and electric components of the electromagnetic field are oriented perpendicularly to the direction of the propagation. TEM mode is unique because it must not have any electric or magnetic field in the direction of the propagation and there is no spatial variation of the fields along the radius direction if considering in case of co-axial transmission line.

Non-TEM transmission lines are commonly called waveguides. A significant distinction in the functioning of waveguide, compared to transmission line designs, lies

doi:10.6342/NTU202600018

in the method of transmission of the electromagnetic wave that carries the signal (i.e., mode shape). In some situation, such as microwave oven or antenna, a *hollow* or *solid* structure with only one conductor is common, supporting an infinite number of modes (but the TEM mode is not included among them) and providing higher capability for high frequency signal than transmission lines because of low loss feature. In addition, silicon ridge waveguides are a fundamental component in photonic integrated circuits (PICs), leveraging the high refractive index contrast between silicon and its surrounding materials, such as silicon dioxide, to confine and guide light efficiently at the micro scale. These waveguides are created by etching a raised *ridge* on a silicon substrate, where the light is confined within the ridge due to internal reflection.

Additionally, TE modes have no electric field in the direction of propagation while TM modes have no magnetic field in the direction of propagation. The cut-off frequency for each mode is important consideration in waveguide design, however, it is beyond the scope of this appendix.

B.2 Introduction to the Network Analyzer

The network analyzer (NA) is designed to measure the magnitude and/or phase of the transmitted and reflected waves from the circuit network of interesting. NA is also known as electrical network analyzer (ENA) where scalar network analyzer (SNA) measuring amplitude properties only while vector network analyzer (VNA) measuring both amplitude and phase properties.

Figure B-17 (a) shows the simplified block diagram of a NA. During operation, RF source is typically configured to sweep across a specified bandwidth. The transmitted (e.g., S_{21} and S_{12}) and reflected (e.g., S_{11} and S_{22}) RF waves are sampled by a detector (i.e., reflectometer), which uses a switch to allow the network to be driven from either port 1 or port 2. These signals are then converted to 100-kHz IF frequencies (it can be lower or higher determined by the setting) via four dual-conversion channels, detected, and digitized. Figure B-17 (b) shows the working principle of frequency-down convertor. Basically, the frequency-down convertor converts the high frequency signal

doi:10.6342/NTU202600018

to a lower frequency band in which a high-performance bandpass filter is easy to achieve. A build-in computer processes this data to calculate and display the magnitude and phase of scattering parameters, as well as other quantities such as standing wave ratio (SWR), return loss, group delay, and impedance. Figure B-17 (c) shows a schematic of a modern network analyzer and Figure B-17 (d) illustrates a possible NA-measured result for a MEMS resonator.

The network analyzer can compute the time-domain response of the characterized network by performing the inverse Fourier transform of the frequency-domain data, providing a detailed analysis of the system's behavior. Moreover, one significant advantage of the NA is the accuracy enhancement achieved through error-correcting software. This software addresses errors arising from non-ideal effect in practice, such as directional coupler mismatch, imperfect directivity, loss, and frequency response variations in the analyzer system, more importantly, lower the effective transmission line length of the test fixture needed for the measurement, utilizing an 8/12-term error model typically and a calibration procedure. The detail will be introduced in the following.

Although N-port network is possible in actual situation, the two-port network is common in characterization of MEMS resonators. Figure B-18 (a) represent the schematic of a regular two-port network. The device under test (DUT) with electrical path (i.e., cable) is placed in between the terminations and the switches exchange the functionality of each port. The NA record the voltage and current in each port with setup of case 1 or case 2, where a_i and b_i are voltage and current related quantity, representing the normalized transmitting and reflecting power waves, respectively. Figure B-18 (b) shows an ideal case for DUT characterization while Figure B-18 (c) shows a case where the cable and connection/junction affect the measurement results thus should be considered.

doi:10.6342/NTU202600018

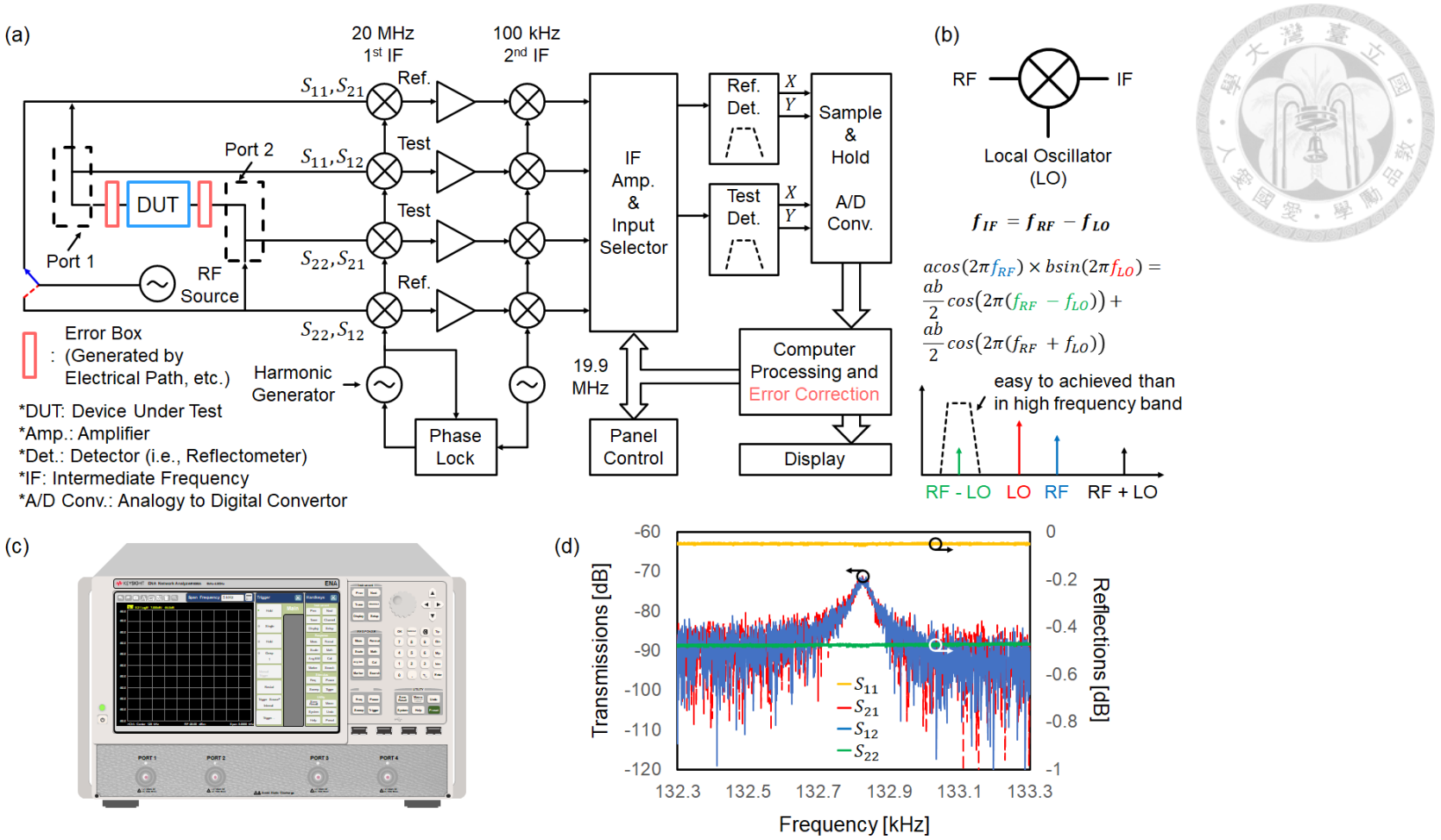


Figure B-17: An overview of a vector network analyzer (VNA), including (a) a simplified block diagram, (b) a representation of the frequency-down conversion function of a mixer, (c) a photograph of a Keysight E5080A VNA, and (d) a sample S-parameter measurement of a MEMS resonator.

doi:10.6342/NTU202600018

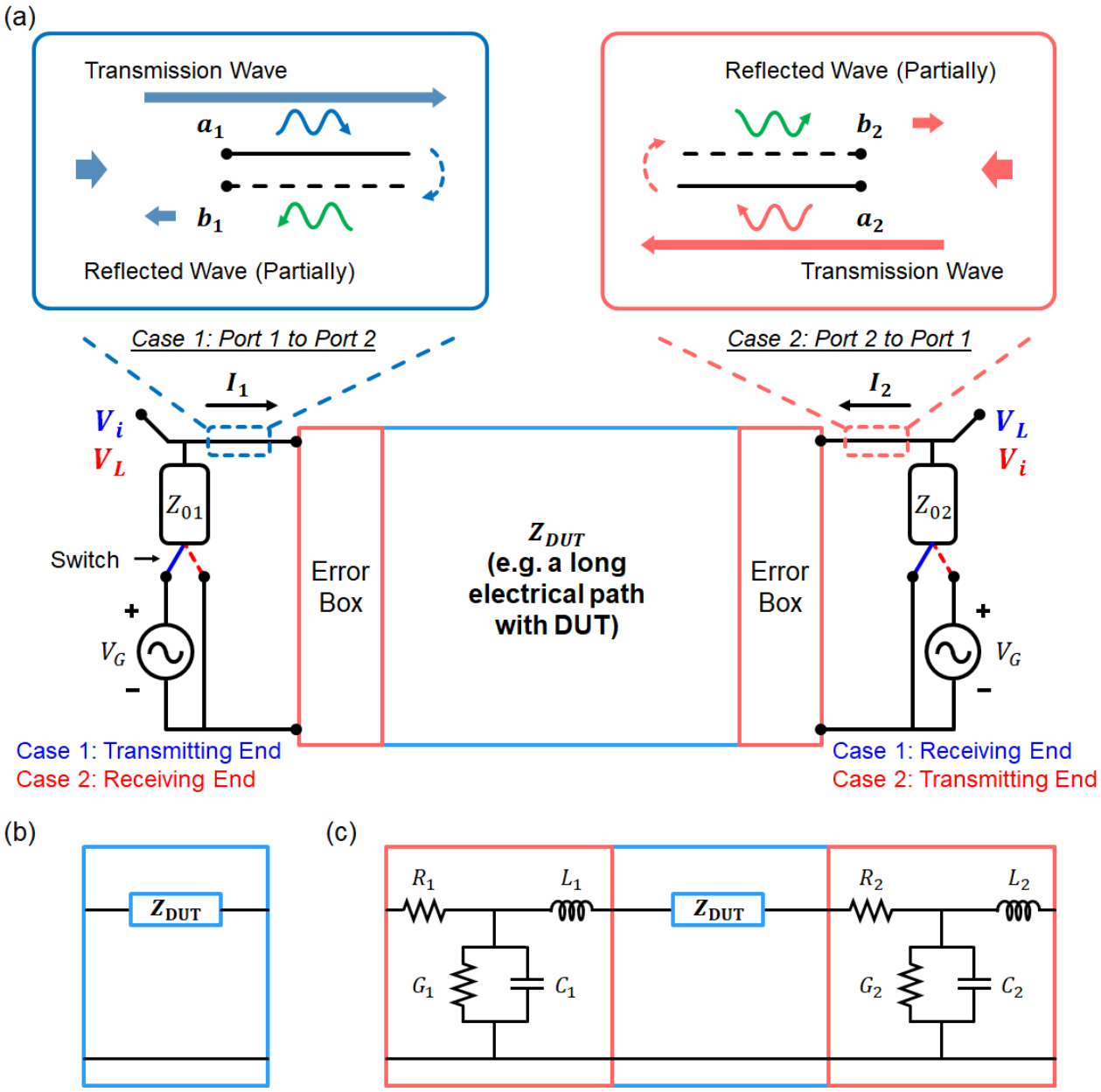


Figure B-18: (a) A general schematic of a two-port network. (b) The ideal setup for device characterization. (c) A more realistic representation of a measurement setup, including the effects of cables and connections.

doi:10.6342/NTU202600018

B.3 Matrix Representation of the Electrical Power Wave

B.3.1 Scattering Parameters, or S Parameter

Figure B-19 (a) shows the schematic of a simple one-port network, considering the lossless transmission line, output impedance from the instrument Z_G and a load Z_L. It is typically to make the characteristic impedance of cable, input and output impedance of the instrument as 50 (Ω), meaning $Z_G = Z_0$. In the following, it will be proved that the maximum power delivered if the load impedance match to the output impedance of the instrument and the characteristic impedance. On the other hand, it is convenient to represent the circuit of Figure B-19 (a) as Figure B-19 (b), and focus on the component of interesting. Noted, the impedances of the terminations are labeled if it is not Z_0 in common sense.

As mentioned, the electrical power wave propagating in the cable contains both transmission part and reflection part (*cf.* Figure B-18 (a)). Recalling the (B-77) and introducing the traveling waves as

$$V_0^+(x) = V_0^+ e^{-j\gamma x} \tag{B-81}$$

$$V_0^-(x) = V_0^- e^{j\gamma x} \tag{B-82}$$

The voltage and current at the load end, $x = 0$, are then represented as

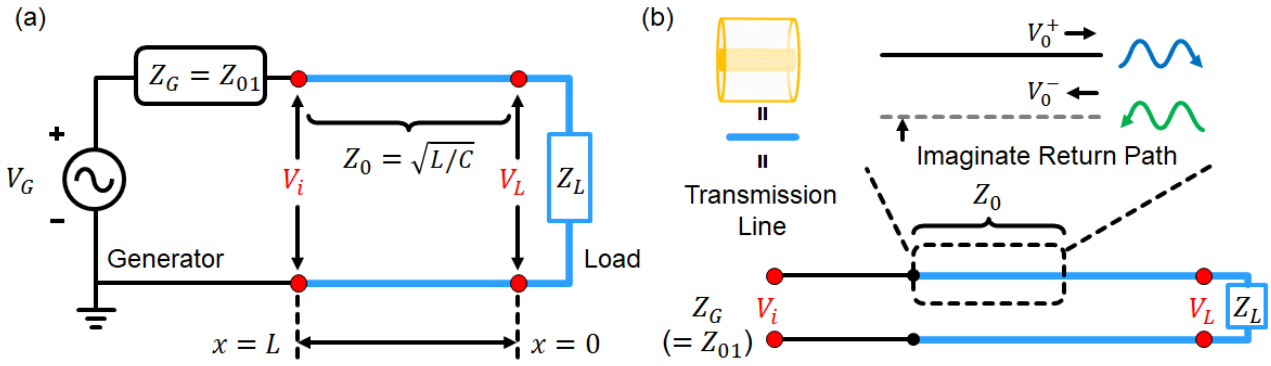


Figure B-19: (a) A schematic diagram of a simple one-port network. (b) Its simplified equivalent circuit representation.

doi:10.6342/NTU202600018

$$V_L = V(x=0) = V_0^+ + V_0^- \tag{B-83}$$

$$I_L = I(x=0) = \frac{V_0^+ - V_0^-}{Z_0} \tag{B-84}$$

The impedance at load can be given by

$$Z_L = \frac{V_L}{I_L} = \frac{V_0^+ + V_0^-}{V_0^+ - V_0^-} Z_0 = \frac{1 + V_0^-/V_0^+}{1 - V_0^-/V_0^+} Z_0 \tag{B-85}$$

With proper moving of terms and finding the equation in term of V_0^-/V_0^+ at one side, the reflection coefficient is obtained as

$$\Gamma = \frac{V_0^-}{V_0^+} = \frac{Z_L - Z_0}{Z_L + Z_0} = \frac{z_L - 1}{z_L + 1} \tag{B-86}$$

where $z_L \equiv Z_L/Z_0$ is moralized load impedance.

Then the transmission coefficient is given by

$$S \equiv 1 - \Gamma = \frac{2Z_0}{Z_L + Z_0} = \frac{2}{z_L + 1} \tag{B-87}$$

One should mention, only the reflection coefficient is measurable in one-port scheme in practice since there is one termination with meter, another is grounded.

On the other hand, the averaged power delivered to the load can be expressed as

$$P_L = I_L V_L = \frac{V_L^2}{Z_L} = \frac{(V_0^+)^2 - (V_0^-)^2}{Z_L} \tag{B-88}$$

Considering the case with maximum transmission, $S = 1$, (i.e., no reflection), the load impedance should be match to the characteristic impedance, $Z_L = Z_0$ (*cf.* (B-87)). If $Z_G = Z_L = Z_0$, the averaged transmitting power is given by

$$P_L = \frac{(V_0^+)^2}{Z_L} = \frac{(V_i)^2}{Z_L} = \frac{\left(\frac{1}{2}V_G\right)^2}{Z_L} = \frac{1}{4}\frac{V_G^2}{Z_L} = \frac{1}{8}\frac{V_{G.rms}^2}{Z_L} \tag{B-89}$$

where $V_{G.rms} = 2V_{i.rms} = \sqrt{\int_0^T (V_G \cos(\omega t))^2 dt\,/T} = V_G/\sqrt{2}$ is valid if the signal is a

doi:10.6342/NTU202600018

cosine wave, representing the root mean square voltage. The (B-86) and (B-87) show the basic idea of reflection and transmission through voltage viewpoint. As mentioned in the beginning, the analysis is based on lossless transmission line and the characteristic impedance represented as $Z_0 = \sqrt{\bar{L}/\bar{C}}$. It provides phase difference between voltage and current and there is no voltage drop caused by the transmission line.

Regarding the averaged power formula, a new set of incident and reflected power waves can be defined. These waves offer useful properties, quantifying power directly rather than voltage or current, which is beneficial when analyzing power transfer between ports where voltage and current exhibit a phase difference. Considering a simplified two-port network as shown in Figure B-20 in which the DUT are placed between one transmitting end (labeled as Port 1) and one receiving end (labeled as Port 2) with known output and input impedance. Because the corresponding wavelength for the operating frequency of our device is totally less than the transmission line. The effect of transmission line is ignored here. As mentioned, $Z_{01} = Z_{02} = Z_0 = 50\ (\Omega)$ is common. This kind of setup make the system symmetric, reciprocal, and easy to analysis. Similar to one-port system (*cf.*, Figure B-19), it is convenient to represent the circuit of Figure B-20 (a) as (b). In the following, the formulas are derived in a general case (i.e., $Z_{01} \neq Z_{02}$), however, it will be simplified to regular case in the end (i.e., $Z_{01} = Z_{02} = Z_0$).

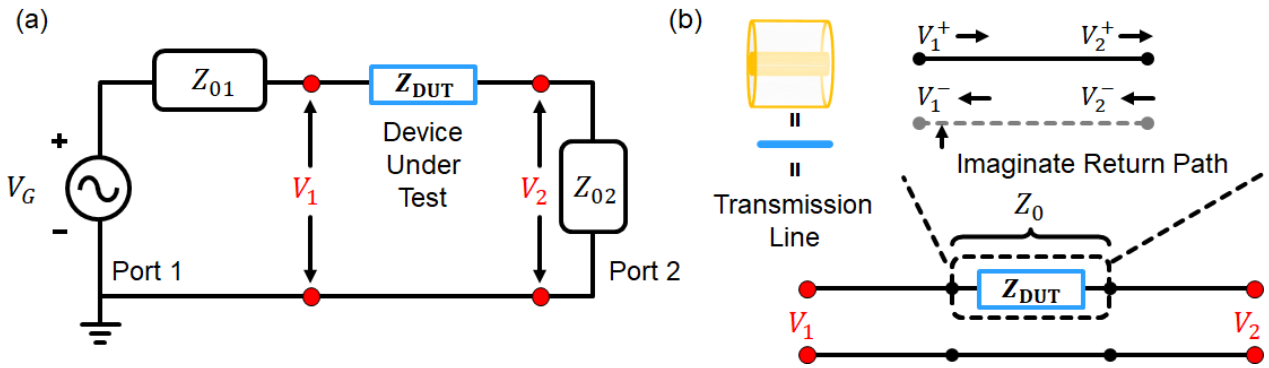


Figure B-20: (a) A schematic diagram of a simple two-port network. (b) Its simplified equivalent circuit representation.

doi:10.6342/NTU202600018

Introducing the normalized from on current and voltage [402]

$$a_i = \frac{V_i^+}{\sqrt{Z_{0i}}} = I_i^+\sqrt{Z_{0i}}; i = 1\ or\ 2 \tag{B-90}$$

$$b_i = \frac{V_i^-}{\sqrt{Z_{0i}}} = I_i^-\sqrt{Z_{0i}}; i = 1\ or\ 2 \tag{B-91}$$

and extending the (B-83) and (B-84) in general yields voltage and current at specific port as

$$V_i = V_i^+ + V_i^-; i = 1\ or\ 2 \tag{B-92}$$

$$I_i = I_i^+ + I_i^- = \frac{V_i^+}{Z_{0i}} - \frac{V_i^-}{Z_{0i}}; i = 1\ or\ 2 \tag{B-93}$$

We can find that, combing the (B-90)-(B-91) and (B-92)-(B-93), the power wave can be represented in term of V_i and I_i as

$$a_i = \frac{(V_i + I_i Z_{0i})/2}{\sqrt{Z_{0i}}} \tag{B-94}$$

$$b_i = \frac{(V_i - I_i Z_{0i})/2}{\sqrt{Z_{0i}}} \tag{B-95}$$

By definition, the so-called scattering parameters are given as

$$S_{11} = \frac{b_1}{a_1}|_{a_2=0}\text{: input reflection/return loss} \tag{B-96}$$

$$S_{21} = \frac{b_2}{a_1}|_{a_2=0}\text{: gain from forward transmission} \tag{B-97}$$

$$S_{12} = \frac{b_1}{a_2}|_{a_1=0}\text{: gain from reverse transmission} \tag{B-98}$$

$$S_{22} = \frac{b_2}{a_2}|_{a_1=0}\text{: output reflection/return loss} \tag{B-99}$$

Instead of the scattering parameter shown in the one-port system, the scattering parameter of the two-port network can be generalized and written in matrix form as

doi:10.6342/NTU202600018

$$\begin{bmatrix} b_1 \\ b_2 \end{bmatrix} = \begin{bmatrix} S_{11} & S_{22} \\ S_{21} & S_{22} \end{bmatrix} \begin{bmatrix} a_1 \\ a_2 \end{bmatrix} \tag{B-100}$$

On the other hand, the square of the transmission from port 1 to port 2, known as transducer power gain, G_T, can be written as

$$G_T = S_{21}^2 = \frac{Power\ delivered\ to\ the\ load}{Power\ available\ from\ the\ source} = \frac{P_{load}}{P_{source}} = \frac{b_2^2}{a_1^2} \tag{B-101}$$

As a quick remind, $P_{rms} = I_{rms}V_{rms} = IV/2 = V^2/2Z$, thus the P_{load} can be written as

$$P_{load} = \frac{\left(\frac{Z_{02}V_G}{Z_{01}+Z_{02}+Z_{DUT}}\right)^2}{2Z_{02}} \tag{B-102}$$

Besides, because $V_G = V_1 + I_1 Z_{01}$, (B-94) can be written as

$$a_1 = \frac{(V_1 + I_1 Z_{01})/2}{\sqrt{Z_{01}}} = \frac{V_G/2}{\sqrt{Z_{01}}} \tag{B-103}$$

It also turns out that the source provides the available power of

$$P_{source} = P_1^+ = \frac{1}{2}\frac{V_1^+}{Z_{01}} = \frac{1}{2}a_1^2 = \frac{1}{8}\frac{V_G^2}{Z_{01}} \tag{B-104}$$

According to (B-94)-(B-95), (B-101)-(B-102) and (B-104), the forward transmission coefficient can be read as

$$S_{21} = \frac{b_2}{a_1}\Big|_{a_2=0} = \frac{\frac{V_2 - I_2 Z_{02}}{2}}{\frac{V_1 + I_1 Z_{01}}{2}} = \frac{\frac{(V_2 + V_2)}{2}}{\frac{V_G}{2}} \tag{B-105}$$

$$= 2\frac{V_2}{V_G} = \frac{2Z_{02}}{Z_{01}+Z_{02}+Z_{DUT}} = \frac{2Z_0}{2Z_0 + Z_{DUT}}$$

or

doi:10.6342/NTU202600018

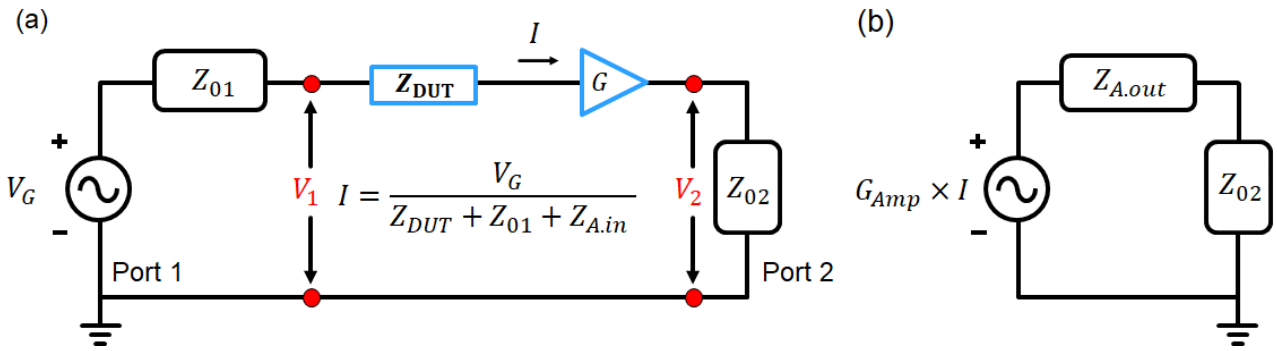


Figure B-21: (a) A schematic of a two-port network where the DUT's output signal is amplified by a gain stage (G). (b) The equivalent circuit representation from the amplifier's output to Port 2.

$$S_{21} = \sqrt{\frac{P_{load}}{P_{source}}} = \sqrt{\frac{\left(\frac{Z_{02}V_G}{Z_{01}+Z_{02}+Z_{DUT}}\right)^2}{\frac{2Z_{02}}{\frac{1}{8}\frac{V_G^2}{Z_{01}}}}} \tag{B-106}$$

$$= \frac{Z_{02}}{Z_{01}+Z_{02}+Z_{DUT}} = \frac{2Z_0}{2Z_0+Z_{DUT}}$$

where $V_2 = -I_2 Z_{02}$ and $V_G = V_1 + I_1 Z_{01}$ are applied. If assume $Z_{DUT} = 0$ and $Z_{01} = Z_{02} = Z_0$ then (B-105) indicate that $S_{21} = 2V_2/V_G = 1$. The outcome implies that $V_2 = V_G/2$, which is so-called matched condition and the problem reduced to 1-port network as mentioned early (*cf.* (B-87)).

Looking into the set-up with amplifier for improving signal-to-noise ratio and making the signal become strong, the derivation of forward transmission coefficient with amplifier is necessary. Considering the set-up as shown in Figure B-21 (a) where the motional current flow into the amplifier and transform to the voltage at output. As presented in Figure B-21 (b), treating the output of the amplifier as a voltage source of $G_{Amp} \times I$ yields the forward transmission coefficient of entire circuit as (*cf.* (B-105) and (B-106))

doi:10.6342/NTU202600018

$$S_{21.Amp} = 2\frac{V_2}{V_G} = 2\frac{(IG_{Amp})\dfrac{Z_{02}}{Z_{02}+Z_{A.out}}}{V_G} \tag{B-107}$$

$$= \frac{2G_{Amp}Z_{02}}{(Z_{DUT}+Z_{01}+Z_{A.in})(Z_{02}+Z_{A.out})} = \frac{G_{Amp}}{Z_{DUT}+Z_0+Z_{A.in}}$$

or

$$S_{21.Amp} = \sqrt{\frac{\left(\frac{1}{2}G_{Amp}\dfrac{V_G}{Z_{DUT}+Z_{01}+Z_{A.in}}\right)^2}{\dfrac{2Z_{02}}{\frac{1}{8}\dfrac{V_G^2}{Z_{01}}}}} \tag{B-108}$$

$$= \sqrt{\frac{Z_{01}}{Z_{02}}}\frac{G_{Amp}}{Z_{DUT}+Z_{01}+Z_{A.in}} = \frac{G_{Amp}}{Z_{DUT}+Z_0+Z_{A.in}}$$

As illustrated in Figure B-22, the transmission line and other error factors must be considered if they have a significant impact on the DUT characterization. However, as will be demonstrated, calibration and de-embedding techniques are applied during device characterization, making the error boxes unnecessary for this dissertation. After calibration, the effective length of the transmission line (~1 m) is much shorter than the wavelength of the operating frequency (~1600 m at 125 kHz) used here. Furthermore, any remaining transmission line and possible errors are minimized in NA-based measurements after calibration or de-embedding. It is only true for linear

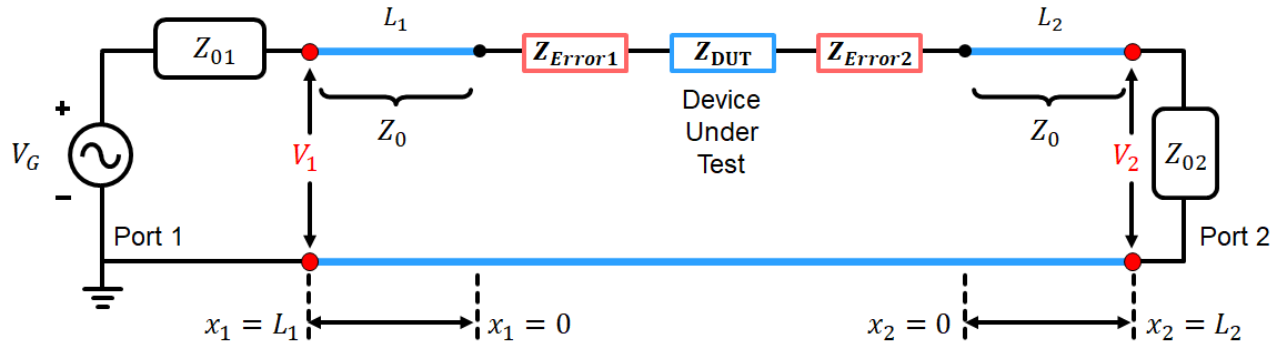


Figure B-22: A representation of a real-world measurement scenario, illustrating the error boxes that account for non-ideal effects in the test fixture and cables.

doi:10.6342/NTU202600018

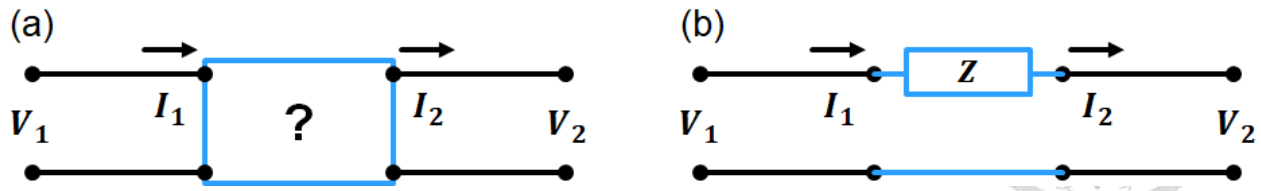


Figure B-23: (a) A schematic illustrating the input and output variables for a generic two-port network. (b) An example circuit diagram showing a series impedance (Z) configured as a two-port network.

devices and calibrated measurements. For nonlinear devices or no-calibration measurements, extra error terms and effects of the transmission line alter the actual received voltage, affecting the responses.

B.3.2 Chain Parameter, or ABCD Parameter and Others

ABCD parameter represent the relationship of the input voltage and currents to the output voltage and currents in other perspective. The S parameter analysis shown in previous section provides the foundation for the circuit network analysis, however, it is recommended for reader to enter transmission line theory through ABCD parameter in the beginning in which the Kirchhoff's current and voltage law are enough to analyze basic circuits. As will be shown, ABCD parameter can be easily convert to S parameter.

Considering the schematic shown in Figure B-23 (a), it takes the form

$$\begin{bmatrix} V_1 \\ I_1 \end{bmatrix} = \begin{bmatrix} A & B \\ C & D \end{bmatrix} \begin{bmatrix} V_2 \\ I_2 \end{bmatrix} \tag{B-109}$$

while the ABCD parameter of Figure B-24 (b) is given by $\begin{bmatrix} 1 & Z \\ 0 & 1 \end{bmatrix}$ because $V_1 = AV_2 + BI_2 = V_2 + ZI_2$ and $I_1 = CV_2 + DI_2 = 0V_2 + 1I_2$.

The physical meaning of ABCD parameter can be given by the short-circuited and open-circuited condition as

$$I_2 = 0 \rightarrow \begin{cases} A = V_1/V_2\text{: voltage ratio} \\ C = I_1/V_2\text{: short circuited resistance} \end{cases} \tag{B-110}$$

doi:10.6342/NTU202600018

$$V_2 = 0 \rightarrow \begin{cases} B = V_1/I_2\text{: open circuited conductance} \\ D = I_1/I_2\text{: current ratio} \end{cases} \quad \text{(B-111)}$$

TABLE B-1 summarize the ABCD parameter representation of basic circuits, including common circuit units, transmission line, controlled sources and idea transformer. Noted, matrix operation can be applied for ABCD parameter therefore the T and π network circuit units can be represented by the series-shut-serries (i.e., $\begin{bmatrix} 1 & Z_1 \\ 0 & 1 \end{bmatrix}\begin{bmatrix} 1 & 0 \\ 1/Z_2 & 1 \end{bmatrix}\begin{bmatrix} 1 & Z_3 \\ 0 & 1 \end{bmatrix}$) and shunt-series-shunt (i.e., $\begin{bmatrix} 1 & Z_1 \\ 0 & 1 \end{bmatrix}\begin{bmatrix} 1 & 0 \\ 1/Z_2 & 1 \end{bmatrix}\begin{bmatrix} 1 & Z_3 \\ 0 & 1 \end{bmatrix}$) impedance network, respectively.

In addition, the defined current flow direction in Z parameter and ABCD parameter are in opposite direction, with the Z parameter being defined as

$$\begin{bmatrix} V_1 \\ V_2 \end{bmatrix} = \begin{bmatrix} Z_{11} & -Z_{12} \\ Z_{21} & -Z_{22} \end{bmatrix}\begin{bmatrix} I_1 \\ I_2 \end{bmatrix} \quad \text{(B-112)}$$

Z-parameters are also known as open-circuit impedance parameters because they are calculated under open-circuit conditions. The physical meaning of a Z-parameters can be given by the open-circuited condition, which differs slightly from that of the ABCD parameter as

$$I_2 = 0 \rightarrow \begin{cases} Z_{11} = V_1/I_2 \\ Z_{21} = V_2/I_1 \end{cases} \quad \text{(B-113)}$$

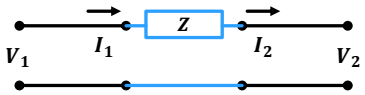
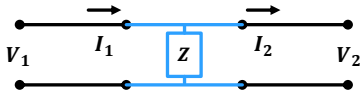
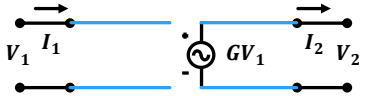
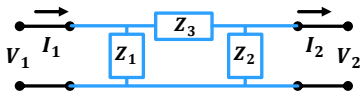
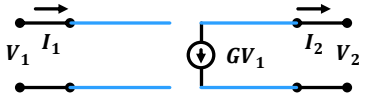
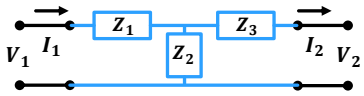
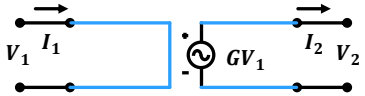
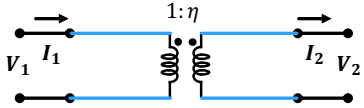
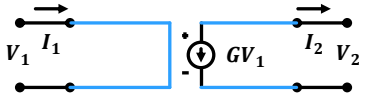
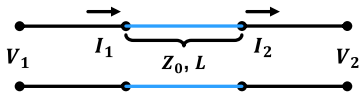
$$I_1 = 0 \rightarrow \begin{cases} Z_{22} = V_2/I_2 \\ Z_{12} = V_1/I_2 \end{cases} \quad \text{(B-114)}$$

Comparing (B-110)-(B-111) and (B-113)-(B-114) yield

$$A = V_1/V_2|_{I_2=0} = (Z_{11}I_1)/(Z_{21}I_1) = Z_{11}/Z_{21} \quad \text{(B-115)}$$

doi:10.6342/NTU202600018

TABLE B-1 THE SUMMARY OF COMMON CIRCUITS' ABCD MATRIX.

Circuit Representation	Name/ABCD Matrix	Circuit Representation	ABCD Matrix
	Series Impedance $\begin{bmatrix} 1 & Z \\ 0 & 1 \end{bmatrix}$		Shunt Impedance $\begin{bmatrix} 1 & 0 \\ 1/Z & 1 \end{bmatrix}$
	Voltage-controlled Voltage Source $\begin{bmatrix} 1/G & 0 \\ 0 & 0 \end{bmatrix}$		π Network $\begin{bmatrix} 1+\frac{Z_3}{Z_2} & Z_3 \\ \frac{1}{Z_1}+\frac{1}{Z_2}+\frac{Z_3}{Z_1Z_2} & 1+\frac{Z_3}{Z_1} \end{bmatrix}$
	Voltage-controlled Current Source $\begin{bmatrix} 0 & 1/G \\ 0 & 0 \end{bmatrix}$		T Network $\begin{bmatrix} 1+\frac{Z_1}{Z_2} & Z_1+Z_3+\frac{Z_1Z_3}{Z_2} \\ \frac{1}{Z_2} & 1+\frac{Z_3}{Z_2} \end{bmatrix}$
	Current-controlled Voltage Source $\begin{bmatrix} 0 & 0 \\ 1/G & 0 \end{bmatrix}$		Idea Transformer $\begin{bmatrix} 1/\eta & 0 \\ 0 & \eta \end{bmatrix}$
	Current-controlled Current Source $\begin{bmatrix} 0 & 0 \\ 0 & 1/G \end{bmatrix}$		Transmission Line $\begin{bmatrix} cos\gamma L & jZ_0 sin\gamma L \\ jY_0 sin\gamma L & cos\gamma L \end{bmatrix}$

doi:10.6342/NTU202600018

$$B = V_1/I_2|_{V_2=0} = (Z_{11}I_1 - Z_{12}I_2)/(I_2)$$
$$= \left(Z_{11}I_1 - Z_{12}\frac{Z_{21}}{Z_{22}}I_1\right)\Big/\left(\frac{Z_{21}}{Z_{22}}I_1\right) \quad \text{(B-116)}$$
$$= (Z_{22}Z_{11} - Z_{12}Z_{21})/Z_{21}$$

$$C = I_1/V_2|_{I_2=0} = I_1/(Z_{21}I_1) = 1/Z_{21} \quad \text{(B-117)}$$

$$D = I_1/I_2|_{V_2=0} = (Z_{21}/Z_{22})I_2/I_2 = Z_{21}/Z_{22} \quad \text{(B-118)}$$

The (B-115)-(B-118) represent the transformation of Z to ABCD parameter and, in fact, it is convenient to convert the circuit between several forms.

TABLE B-2 copy the results from [402, 403, 510], showing the summary of conversion between the four common parameter forms with the condition of $Z_{01} = Z_{02} = Z_0$. For the general case of $Z_{01} \neq Z_{02}$, please see [510]. Y parameter represent the admittance matrix of the circuit of interesting. Noted, admittance, Y, is the reciprocal of the impedance, Z, (i.e., $Y = 1/Z$). It is sometimes easy to analyze, depending on the circuit . (B-119) and (B-120) compare the formular of serial and parallel RLC circuit with these two forms

$$\text{Serial RLC: } \begin{cases} Z = B = \frac{|Z|}{Z_{21}} \rightarrow Z_{sRLC} = R + \frac{1}{j\omega C} + j\omega L \\ Y = \frac{-1}{Y_{21}} \rightarrow Y_{sRLC} = \left(R + \frac{1}{j\omega C} + j\omega L\right)^{-1} \end{cases} \quad \text{(B-119)}$$

$$\text{Parallel RLC: } \begin{cases} Z = \frac{|Z|}{Z_{21}} \rightarrow Z_{pRLC} = \left(R + \frac{1}{j\omega C} + j\omega L\right)^{-1} \\ Y = \frac{-1}{Y_{21}} \rightarrow Y_{pRLC} = R + \frac{1}{j\omega C} + j\omega L \end{cases} \quad \text{(B-120)}$$

doi:10.6342/NTU202600018

TABLE B-2 SUMMARY FOR THE CONVERSION EQUATION, ASSUMING PORT IMPEDANCES ARE MATCHED TO CHARACTERISTIC IMPEDANCE $Z_{01} = Z_{02} = Z_0$.

	S	Z	Y	$ABCD$
S_{11}	S_{11}	$\frac{(Z_{11}-Z_0)(Z_{22}+Z_0)-Z_{12}Z_{21}}{(Z_{11}+Z_0)(Z_{22}+Z_0)-Z_{12}Z_{21}}$	$\frac{(Y_0-Y_{11})(Y_0+Y_{22})+Y_{12}Y_{21}}{(Y_{11}+Y_0)(Y_{22}+Y_0)-Y_{12}Y_{21}}$	$\frac{AZ_0+B-CZ_0^2-DZ_0}{AZ_0+B+CZ_0^2+DZ_o}$
S_{12}	S_{12}	$\frac{2Z_{12}Z_0}{(Z_{11}+Z_0)(Z_{22}+Z_0)-Z_{12}Z_{21}}$	$\frac{-2Y_{12}Y_0}{(Y_{11}+Y_0)(Y_{22}+Y_0)-Y_{12}Y_{21}}$	$\frac{2Z_0(AD-BC)}{AZ_0+B+CZ_0^2+DZ_0}$
S_{21}	S_{21}	$\frac{2Z_{21}Z_0}{(Z_{11}+Z_0)(Z_{22}+Z_0)-Z_{12}Z_{21}}$	$\frac{-2Y_{21}Y_0}{(Y_{11}+Y_0)(Y_{22}+Y_0)-Y_{12}Y_{21}}$	$\frac{2Z_0}{AZ_0+B+CZ_0^2+DZ_0}$
S_{22}	S_{22}	$\frac{(Z_{11}+Z_0)(Z_{22}-Z_0)-Z_{12}Z_{21}}{(Z_{11}+Z_0)(Z_{22}+Z_0)-Z_{12}Z_{21}}$	$\frac{(Y_0+Y_{11})(Y_0-Y_{22})+Y_{12}Y_{21}}{(Y_{11}+Y_0)(Y_{22}+Y_0)-Y_{12}Y_{21}}$	$\frac{-AZ_0+B-CZ_0^2+DZ_0}{AZ_0+B+CZ_0^2+DZ_0}$
Z_{11}	$Z_0\frac{(1+S_{11})(1-S_{22})+S_{12}S_{21}}{(1-S_{11})(1-S_{22})-S_{12}S_{21}}$	Z_{11}	$\frac{Y_{22}}{Y_{11}Y_{22}-Y_{12}Y_{21}}$	$\frac{A}{C}$
Z_{12}	$Z_0\frac{2S_{12}}{(1-S_{11})(1-S_{22})-S_{12}S_{21}}$	Z_{12}	$\frac{-Y_{12}}{Y_{11}Y_{22}-Y_{12}Y_{21}}$	$\frac{AD-BC}{C}$
Z_{21}	$Z_0\frac{2S_{21}}{(1-S_{11})(1-S_{22})-S_{12}S_{21}}$	Z_{21}	$\frac{-Y_{21}}{Y_{11}Y_{22}-Y_{12}Y_{21}}$	$\frac{1}{C}$
Z_{22}	$Z_0\frac{(1-S_{11})(1+S_{22})+S_{12}S_{21}}{(1-S_{11})(1-S_{22})-S_{12}S_{21}}$	Z_{22}	$\frac{Y_{11}}{Y_{11}Y_{22}-Y_{12}Y_{21}}$	$\frac{D}{C}$
Y_{11}	$Y_0\frac{(1-S_{11})(1+S_{22})+S_{12}S_{21}}{(1+S_{11})(1+S_{22})-S_{12}S_{21}}$	$\frac{Z_{22}}{Z_{11}Z_{22}-Z_{12}Z_{21}}$	Y_{11}	$\frac{D}{B}$
Y_{12}	$Y_0\frac{-2S_{12}}{(1+S_{11})(1+S_{22})-S_{12}S_{21}}$	$\frac{-Z_{12}}{Z_{11}Z_{22}-Z_{12}Z_{21}}$	Y_{12}	$\frac{BC-AD}{B}$
Y_{21}	$Y_0\frac{-2S_{21}}{(1+S_{11})(1+S_{22})-S_{12}S_{21}}$	$\frac{-Z_{21}}{Z_{11}Z_{22}-Z_{12}Z_{21}}$	Y_{21}	$\frac{-1}{B}$
Y_{22}	$Y_0\frac{(1+S_{11})(1-S_{22})+S_{12}S_{21}}{(1+S_{11})(1+S_{22})-S_{12}S_{21}}$	$\frac{Z_{11}}{Z_{11}Z_{22}-Z_{12}Z_{21}}$	Y_{22}	$\frac{A}{B}$
A	$\frac{(1+S_{11})(1-S_{22})+S_{12}S_{21}}{2S_{21}}$	$\frac{Z_{11}}{Z_{21}}$	$\frac{-Y_{22}}{Y_{21}}$	A
B	$Z_0\frac{(1+S_{11})(1+S_{22})-S_{12}S_{21}}{2S_{21}}$	$\frac{Z_{11}Z_{22}-Z_{12}Z_{21}}{Z_{21}}$	$\frac{-1}{Y_{21}}$	B
C	$Z_0\frac{(1-S_{11})(1-S_{22})-S_{12}S_{21}}{2S_{21}}$	$\frac{1}{Z_{21}}$	$\frac{(Y_{11}+Y_0)(Y_{22}+Y_0)-Y_{12}Y_{21}}{Y_{21}}$	C
D	$\frac{(1-S_{11})(1+S_{22})+S_{12}S_{21}}{2S_{21}}$	$\frac{Z_{22}}{Z_{21}}$	$\frac{-Y_{11}}{Y_{21}}$	D

doi:10.6342/NTU202600018

The perspective of impedance is easy to analysis if elements are in serial while perspective of admittance is easy to analysis if elements are in parallel. Although Z and Y are different than Z and Y parameters/matrix. The reasons for the development may be similar.

Considering a regular DUT analysis presented in previous section, the ABCD parameter can be given as

$$\begin{bmatrix} A & B \\ C & D \end{bmatrix} = \begin{bmatrix} 1 & Z_{DUT} \\ 0 & 1 \end{bmatrix} \tag{B-121}$$

According to [510], the S parameter of this DUT with different impedance of ports (i.e., $Z_{01} \neq Z_{02}$) can be given by

$$S_{11} = \frac{AZ_{02} + B - CZ_{01}Z_{02} - DZ_{01}}{AZ_{02} + B + CZ_{01}Z_{02} + DZ_{01}} = \frac{-Z_{01} + Z_{02} + Z_{DUT}}{Z_{01} + Z_{02} + Z_{DUT}} \tag{B-122}$$

$$S_{21} = \frac{2(AD - BC)\sqrt{Z_{01}Z_{02}}}{AZ_{02} + B + CZ_{01}Z_{02} + DZ_{01}} = \frac{2\sqrt{Z_{01}Z_{02}}}{Z_{01} + Z_{02} + Z_{DUT}} \tag{B-123}$$

$$S_{12} = \frac{2\sqrt{Z_{01}Z_{02}}}{AZ_{02} + B + CZ_{01}Z_{02} + DZ_{01}} = \frac{2\sqrt{Z_{01}Z_{02}}}{Z_{01} + Z_{02} + Z_{DUT}} \tag{B-124}$$

$$S_{22} = \frac{-AZ_{02} + B - CZ_{01}Z_{02} + DZ_{01}}{AZ_{02} + B + CZ_{01}Z_{02} + DZ_{01}} = \frac{Z_{01} - Z_{02} + Z_{DUT}}{Z_{01} + Z_{02} + Z_{DUT}} \tag{B-125}$$

and, if $Z_{01} = Z_{02} = Z_0$, they can be simplified as (*cf.* TABLE B-2)

$$S_{11} = \frac{AZ_0 + B - CZ_0^2 - DZ_0}{AZ_0 + B + CZ_0^2 + DZ_0} = \frac{Z_{DUT}}{2Z_0 + Z_{DUT}} \tag{B-126}$$

$$S_{21} = \frac{2Z_o}{AZ_0 + B + CZ_0^2 + DZ_0} = \frac{2Z_0}{2Z_0 + Z_{DUT}} \tag{B-127}$$

$$S_{12} = \frac{2Z_0(AD - BC)}{AZ_0 + B + CZ_0^2 + DZ_0} = \frac{2Z_0}{2Z_0 + Z_{DUT}} \tag{B-128}$$

doi:10.6342/NTU202600018

$$S_{22} = \frac{-AZ_0 + B - CZ_0^2 + DZ_0}{AZ_0 + B + CZ_0^2 + DZ_0} = \frac{Z_{DUT}}{2Z_0 + Z_{DUT}} \tag{B-129}$$

Moreover, TABLE B-3 shows the cases with varying device impedance and corresponding S parameter for reference.

In addition, considering the forward transmission coefficient of the DUT with amplifier that analyzed in previous section. As shown in Figure B-21, it can be also derived by the ABCD parameter first and then covert to S parameter. The ABCD parameter for the equivalent circuit follows the train rule, namely

$$\begin{aligned}\begin{bmatrix} A & B \\ C & D \end{bmatrix} &= \begin{bmatrix} 1 & Z_{DUT} + Z_{A.in} \\ 0 & 1 \end{bmatrix} \begin{bmatrix} 0 & 0 \\ G_{Amp} & 0 \end{bmatrix} \begin{bmatrix} 1 & Z_{A.out} \\ 0 & 1 \end{bmatrix} \\ &= \frac{1}{G_{Amp}} \begin{bmatrix} Z_{DUT} + Z_{A.in} & (Z_{DUT} + Z_{G.in})Z_{A.out} \\ 1 & Z_{A.out} \end{bmatrix}\end{aligned} \tag{B-130}$$

Following the formula in TABLE B-2 yields

$$\begin{aligned} S_{21.Amp} &= \frac{2\sqrt{Z_{01}Z_{02}}}{AZ_{02} + B + CZ_{01}Z_{02} + DZ_{01}} \\ &= \frac{2\sqrt{Z_{01}Z_{02}}G_{Amp}}{(Z_{DUT} + Z_{A.in})Z_{02} + [(Z_{DUT} + Z_{A.in})Z_{G.out}] + Z_{01}Z_{02} + Z_{A.out}Z_{01}} \\ &= \frac{2\sqrt{Z_{01}Z_{02}}G_{Amp}}{(Z_{DUT} + Z_{01} + Z_{A.in})(Z_{02} + Z_{A.out})} \end{aligned} \tag{B-131}$$

In regular network analyzer, $Z_{01} = Z_{02} = Z_0 = 50\ (\Omega)$, the (B-131) reduces as

$$S_{21.Amp} = \frac{G_{Amp}}{Z_{DUT} + Z_0 + Z_{A.in}} \tag{B-132}$$

Comparing (B-107), (B-108) and (B-131), it is found that the forward transmission coefficient can be expressed in several ways, namely

$$S_{21.Amp} = \frac{2G_{Amp}Z_{02}}{(Z_{DUT} + Z_{01} + Z_{A.in})(Z_{02} + Z_{A.out})} \tag{B-133}$$

doi:10.6342/NTU202600018

TABLE B-3: A SUMMARY OF S-PARAMETER VALUES FOR DIFFERENT DEVICE UNDER TEST (DUT) IMPEDANCES, RANGING FROM A SHORT (0 Ω) TO AN OPEN (∞ Ω) CIRCUIT.

Z_{DUT}	S Parameter			
	$S_{11} = S_{22}$	$S_{11.dB} = S_{22.dB}$	$S_{21} = S_{12}$	$S_{21.dB} = S_{12.dB}$
0	0	$-Inf.$	1	0
7	0.0654	−23.6857	0.9346	−0.5877
50	0.3333	−9.5424	0.6667	−3.5218
350	0.7778	−2.1829	0.2222	−13.0642
500	0.8333	−1.5836	0.1667	−15.5630
1000	0.9090	−0.8278	0.0909	−20.8278
1000000	0.9999	−0.0087	9.999×10^{-5}	−90.0009
∞	1	0	0	$-Inf.$

$$= \sqrt{\frac{Z_{01}}{Z_{02}}} \frac{G_{Amp}}{Z_{DUT} + Z_{01} + Z_{A.in}} = \frac{2\sqrt{Z_{01}Z_{02}}G_{Amp}}{(Z_{DUT} + Z_{01} + Z_{A.in})(Z_{02} + Z_{A.out})}$$

and it implies

$$\frac{2Z_{02}}{Z_{02} + Z_{A.out}} = \sqrt{\frac{Z_{01}}{Z_{02}}} = \frac{2\sqrt{Z_{01}Z_{02}}}{Z_{02} + Z_{A.out}} \quad \text{(B-134)}$$

Even though the results are identical when $Z_{01} = Z_{02} = Z_{A.out} = Z_0$. Additional analysis on (B-134) will be required if each of impedance are not equal.

It is worth to noting that, with 20-Hz IF bandwidth and -20 dBm driving power, the noise floor of one network analyzer (E5061B, Keysight) used in this dissertation is about -80 dB, corresponding the effective resistance of 10^6 (Ω); the noise floor of another network analyzer (E5080A, Keysight) used in this dissertation is about -100 dB, corresponding the effective resistance of 10^7 (Ω). The equivalent resistance including gain over the values cannot be measured.

The HF2TA (50-MHz current amplifier, Zurich Instruments) and the SR570 (1-MHZ current amplifier, Stanford Research Systems) are two frequently used amplifier in this dissertation. The input impedance of the HF2TA is varying with gain value. The

doi:10.6342/NTU202600018

input impedance is 50 (Ω) with 10^2-10^4 V/A gain and is larger when the gain larger than 10^5 V/A (100, 300, 1.6k and 70k Ω for 10^5, 10^6, 10^7, 10^8 V/A, respectively) [511]. The input impedance of SR570 is 1, 100, 10k and 1M (Ω) for gain of 10^3-10^4, 10^5-10^6, 10^7-10^8, 10^9-10^{12}, V/A respectively [512]. The SR570 is design to drive high impedance loads where the instrument's gain is calibrated for high impedance loads, therefore, the voltage gain of the amplifier is reduced by a factor of two when driving a 50 (Ω) load [512]. Besides, there is no further calibration for HF2TA, thus, the provided gain value will not affected by the output load.

B.4 Practice, Error Source and Correction

B.4.1 SOLT Calibration Method

No test equipment, including a network analyzer, is perfect. However, employing a set of special operations—calibration can minimize measurement errors [513, 514]. These operations improve the laboratory measurement data, providing a more accurate representation of the DUT. Calibration technology can be considered as a pre-

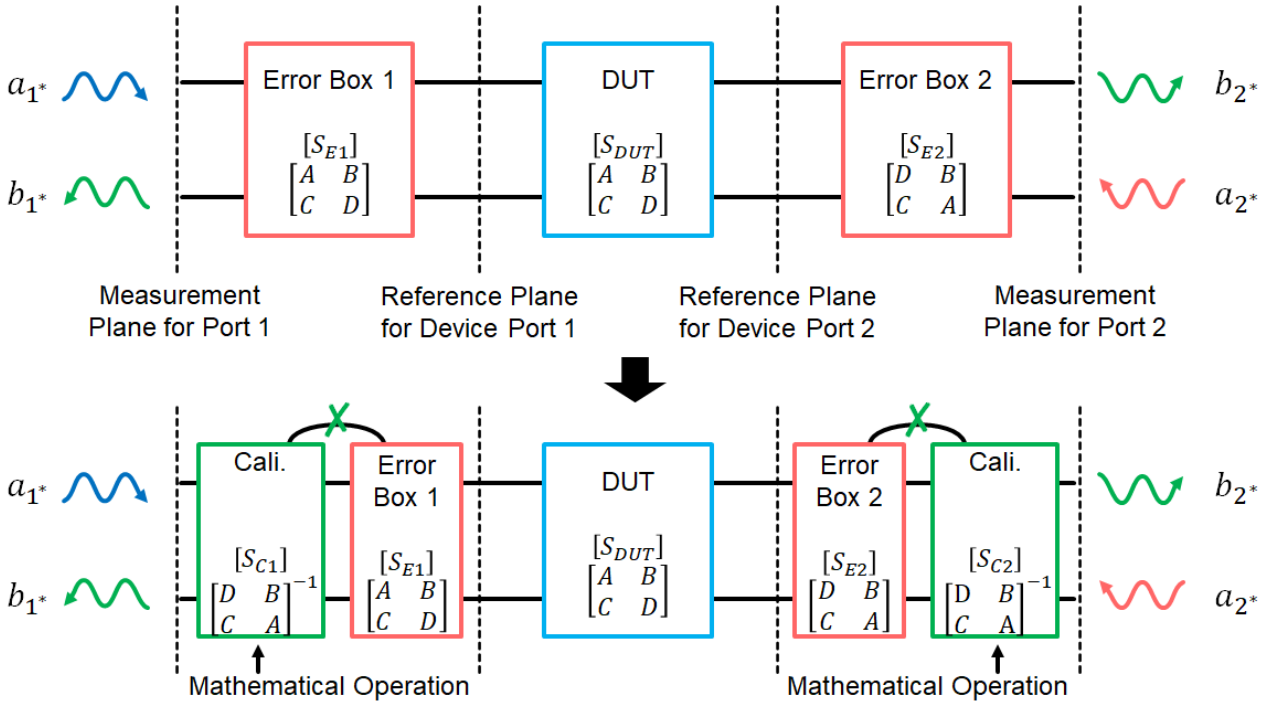


Figure B-24: (a) A diagram showing the placement of error boxes relative to a device under test (DUT) in a two-port network. (b) The block diagram for the 8-term error model, which highlights the calibration error terms for each port.

doi:10.6342/NTU202600018

measurement error correction procedure. As illustrated in Figure B-24, the primary objective of calibration is to eliminate the error box caused by factors such as wire bonding, bond pad probing contact resistance, adapter connections, cables, or feedthroughs. The feedthrough mentioned here is a conductor that carries a signal through an enclosure. The actual response of DUT in an error-exist environment can be collected after calibration, namely

$$[\boldsymbol{S}]_{\boldsymbol{DUT}} = [\boldsymbol{S}]_{\boldsymbol{C1}}^{-\boldsymbol{1}}\{[\boldsymbol{S}]_{\boldsymbol{E1}}[\boldsymbol{S}]_{\boldsymbol{DUT}}[\boldsymbol{S}]_{\boldsymbol{E2}}\}[\boldsymbol{S}]_{\boldsymbol{C2}}^{-\boldsymbol{1}} \tag{B-135}$$

or

$$\begin{bmatrix} A & B \\ C & D \end{bmatrix}_{DUT} = \begin{bmatrix} A & B \\ C & D \end{bmatrix}_{C1}^{-1} \left\{ \begin{bmatrix} A & B \\ C & D \end{bmatrix}_{E1} \begin{bmatrix} A & B \\ C & D \end{bmatrix}_{DUT} \begin{bmatrix} D & B \\ C & A \end{bmatrix}_{E2} \right\} \begin{bmatrix} D & B \\ C & A \end{bmatrix}_{C2}^{-1} \tag{B-136}$$

Noted, the characteristics of the DUT can be completely captured when the calibration matrix exactly matches the error box (i.e., $[\boldsymbol{S}]_{\boldsymbol{C1}}^{-\boldsymbol{1}}[\boldsymbol{S}]_{\boldsymbol{E1}} = [\boldsymbol{S}]_{\boldsymbol{E2}}[\boldsymbol{S}]_{\boldsymbol{C2}}^{-\boldsymbol{1}} = \boldsymbol{I}$). However, if they differ, the remaining error may still affect the DUT. This is why it is recommended to perform the calibration procedure as close to the DUT as possible, moving the reference plane as near to the DUT as feasible in order to lower the error.

Figure B-25 shows the commonly used three-term error model for one-port calibration. The measured reflection coefficient with three terms model can be shown as

$$\Gamma_M = \frac{b_0^*}{a_0^*} = \frac{E_{00} - \Delta_e \Gamma}{1 - E_{11}\Gamma}$$

Or

$$\Gamma_M = E_{00} - \Delta_e \Gamma + E_{11}\Gamma_M \Gamma \tag{B-137}$$

where $\Delta_e = [E_{00}E_{11} - E_{10}E_{01}]$.

One should emphasize that with three known error described in ABCD parameter form, implying that three-independent measurement, i.e., measurement of three known components, should be used in order to get the value of known terms (i.e., E_{00}, E_{11} and $E_{10}E_{01}$). With this, the actual reflection coefficient can be represented as

doi:10.6342/NTU202600018

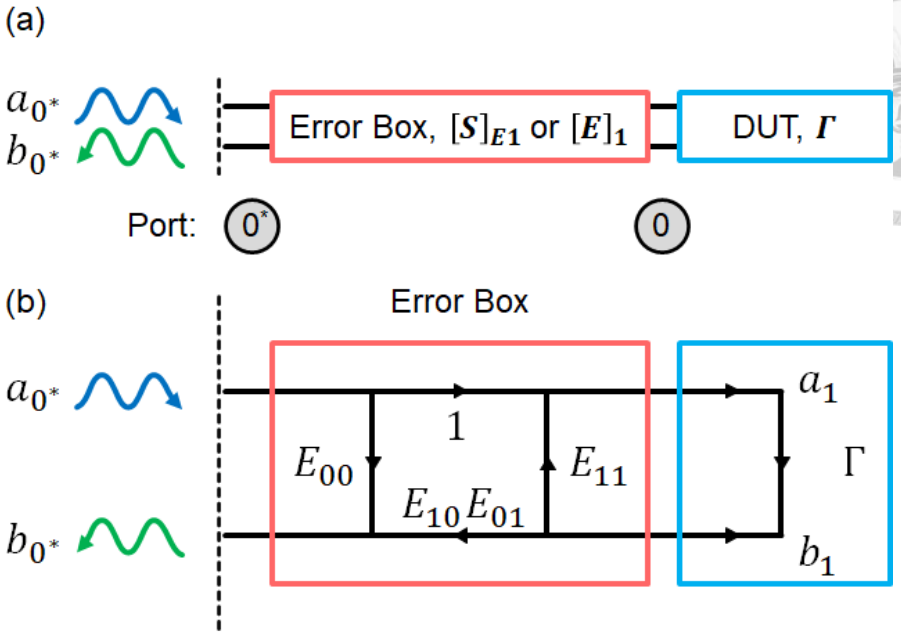


Figure B-25: (a) The three-term error model for a one-port network is depicted as a block diagram. (b) A schematic view of the error box that is associated with a one-port network measurement.

$$\Gamma = \frac{\Gamma_M - E_{00}}{E_{11}\Gamma_M - \Delta_e} \tag{B-138}$$

The two-port case can be modeled in the same manner as shown in Figure B-26. This error adapter contains the six-error terms for the forward direction and another six-error terms for the backward direction, known as 12-term error model. In the real procedure, the one-port calibration will be conducted first with three known components as described previously. Connecting the two port and measuring the full S parameter with *isolation* (i.e., connected to matched load with $S_{21} = 0$ condition) and *through* condition (i.e., connected port 1 to port 2 directly with $S_{21} = S_{12} = 1$ and $S_{11} = S_{22} = 0$ condition) can deliver twenty error terms with measured S parameter of

$$\text{Forward: } \begin{cases} S_{11.M} = \frac{b_1^*}{a_1^*} = E_{1^*1^*} + E_{11^*}E_{1^*1}\frac{S_{11} - E_{22}\Delta_S}{1 - E_{11}S_{11} - E_{22}S_{22} + E_{11}E_{22}\Delta_S} \\ S_{21.M} = \frac{b_2^*}{a_1^*} = E_{1^*2^*} + E_{11^*}E_{1^*1}\frac{S_{21}}{1 - E_{11}S_{11} - E_{22}S_{22} + E_{11}E_{22}\Delta_S} \end{cases} \tag{B-139}$$

doi:10.6342/NTU202600018

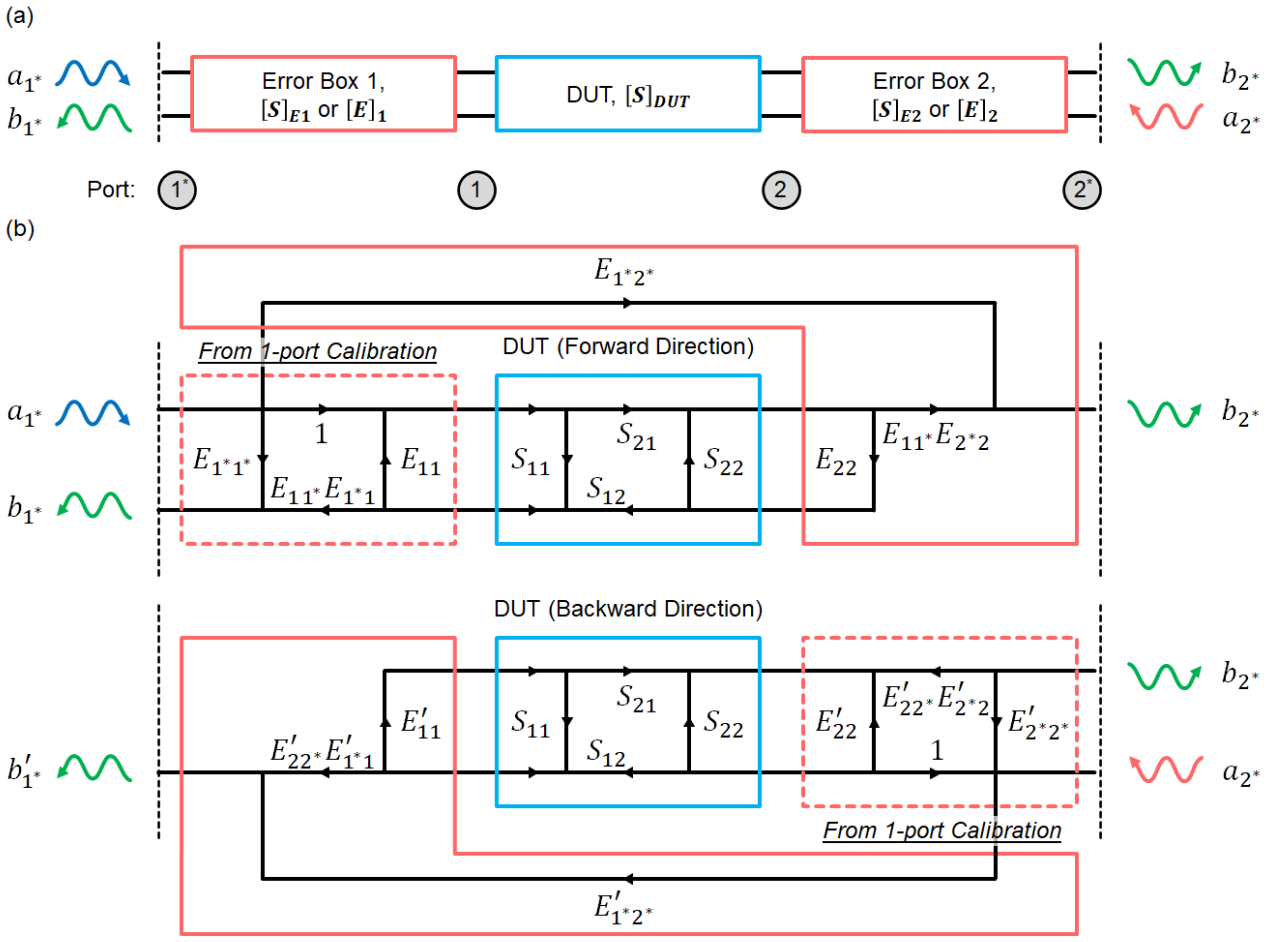


Figure B-26: (a) A block diagram of the 12-term error model for a two-port network, illustrating the forward and backward error adapters that account for measurement system imperfections when characterizing a device under test (DUT). (b) A schematic representation of the error boxes associated with the two-port network measurement.

$$\text{Backward: } \begin{cases} S_{22.M} = \dfrac{b_2^*}{a_2^*} = E'_{2^*2^*} + E'_{22^*}E'_{2^*2}\dfrac{S_{22}-E'_{11}\Delta_S}{1-E'_{11}S_{11}-E'_{22}S_{22}+E'_{11}E'_{22}\Delta_S} \\ S_{12.M} = \dfrac{b_1^*}{a_2^*} = E'_{1^*2^*} + E'_{22^*}E'_{1^*1}\dfrac{S_{12}}{1-E'_{11}S_{11}-E'_{22}S_{22}+E'_{11}E'_{22}\Delta_S} \end{cases} \quad \text{(B-140)}$$

where $\Delta_S = S_{11}S_{22} - S_{21}S_{12}$ and, E_{22}, $E_{11^*}E_{2^*2}$, E'_{11} and $E'_{22^*}E'_{1^*1}$ are four knowns.

With similar procedure, the actual reflection coefficient can be represented as

$$S_{11} = \frac{\left(\dfrac{S_{11.M} - E_{1^*1^*}}{E_{11^*}E_{1^*1}}\right)\left[1 + \left(\dfrac{S_{22.M} - E'_{2^*2^*}}{E'_{22^*}E'_{2^*2}}\right)E'_{22}\right] - E_{22}D_2}{D_1} \quad \text{(B-141)}$$

doi:10.6342/NTU202600018

$$S_{21} = \frac{\left(\frac{S_{21.M} - E_{2^*1^*}}{E_{11^*}E_{2^*2}}\right)\left[1 + \left(\frac{S_{22.M} - E'_{2^*2^*}}{E'_{22^*}E'_{2^*2}}\right)(E'_{22} - E_{22})\right]}{D_1} \quad \text{(B-142)}$$

$$S_{22} = \frac{\left(\frac{S_{22.M} - E'_{2^*2^*}}{E'_{22^*}E'_{2^*2}}\right)\left[1 + \left(\frac{S_{11.M} - E_{1^*1^*}}{E_{11^*}E_{1^*1}}\right)E_{11}\right] - E'_{11}D_2}{D_1} \quad \text{(B-143)}$$

$$S_{12} = \frac{\left(\frac{S_{12.M} - E'_{1^*2^*}}{E'_{22^*}E'_{1^*1}}\right)\left[1 + \left(\frac{S_{11.M} - E_{1^*1^*}}{E_{11^*}E_{1^*1}}\right)(E_{11} - E'_{11})\right]}{D_1} \quad \text{(B-144)}$$

where $D_1 = \left[1 + \left(\frac{S_{11.M} - E_{1^*1^*}}{E_{11^*}E_{1^*1}}\right)E_{11}\right]\left[1 + \left(\frac{S_{22.M} - E'_{2^*2^*}}{E'_{22^*}E'_{2^*2}}\right)E'_{22}\right] - D_2$ and $D_2 = \left(\frac{S_{21.M} - E_{2^*1^*}}{E_{11^*}E_{2^*2}}\right)\left(\frac{S_{12.M} - E'_{1^*2^*}}{E'_{22^*}E'_{1^*1}}\right)$.

In fact, the calibration extracts all leakage, crosstalk, match errors of the network analyzer along with the cables, connectors, or probes that connect to DUT. Although, there exit several calibration methods, such as normalization, unknown thru, thru-reflect-line (TRL), line-reflect-match (LRM). The standard short-open-load-thru (SOLT, 85033E calibration kit, Keysight) is selected to enhance accuracy due to its widespread availability and ease of access in this dissertation.

B.4.2 De-embedding Technology

Although calibration can be performed using a commercial network analyzer and minimizes the error arise by the feedthrough, de-embedding measured data is sometimes necessary for precise measurements. De-embedding technology can be considered a post-measurement error correction and can also be done with a commercial network analyzer. Calibration is a pre-measurement step that minimizes errors relative to a reference plane. However, the most critical operation for isolating the DUT's behavior is de-embedding, which mathematically removes the effects of associated fixturing that changed time by time.

doi:10.6342/NTU202600018

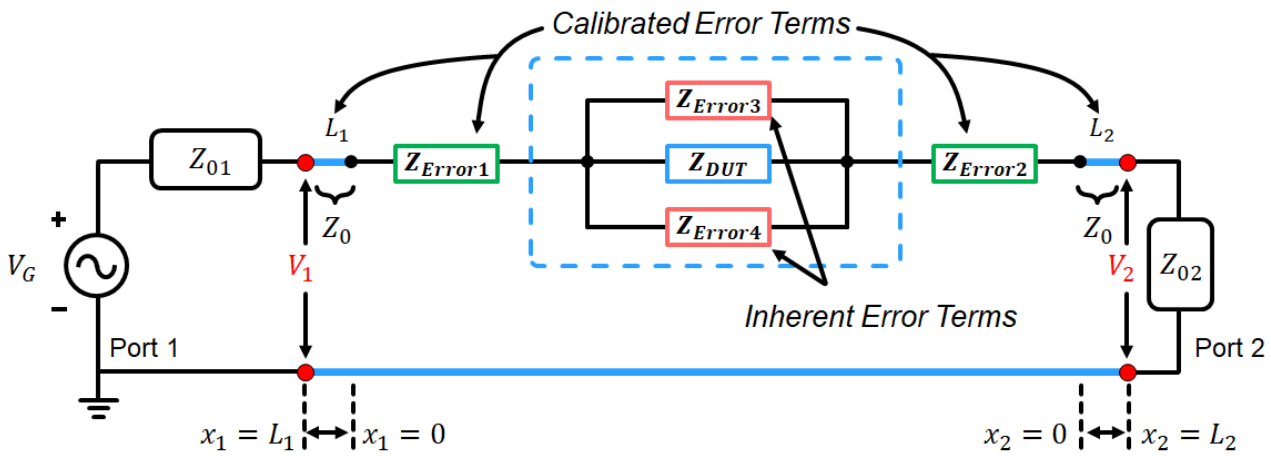


Figure B-27: This schematic shows a measurement setup with a DUT placed in a test fixture. It highlights the fixture's inherent parasitic elements, which are not removed by calibration and must be corrected through de-embedding for accurate results.

Imagine that there is a cable that is moved/twisted after a person finish a part of testing. The error contributed by parasitic capacitance, conductance and resistance of the cable may be different, and the system has changed. At this point, calibration may not be a straightforward method to improve data accuracy. For electrostatic MEMS resonators, calibration can be performed as close to the DUT as possible. However, it cannot eliminate unwanted parasitic effects inherent to the device (*cf.* Figure B-27), such as its static capacitance of a MEMS component. Unlike the feedthrough, the test fixture mentioned here is positioned slightly away from the calibrated reference plane, close to the device. It is used to consistently test the DUT, such as with a probe station or a testing socket board.

The de-embedding needs full 2-port S parameter measurement (i.e., four S parameter along the interested bandwidth), it firstly covert the amplitude and phase of measured S parameters form phasor domain to time domain as

$$\vec{\boldsymbol{S}} = \begin{bmatrix} \vec{\boldsymbol{S}}_{11.i} & \vec{\boldsymbol{S}}_{12.i} \\ \vec{\boldsymbol{S}}_{21.i} & \vec{\boldsymbol{S}}_{22.i} \end{bmatrix} \tag{B-145}$$

where

doi:10.6342/NTU202600018

$$\vec{S}_{11.i} = S_{11.i}e^{j\phi_{11.i}} = S_{11.i}\,cos(\phi_{11.i}) + jS_{11.i}sin\,(\phi_{11.i}) \quad \text{(B-146)}$$

$$\vec{S}_{12.i} = S_{12.i}e^{j\phi_{12.i}} = S_{12.i}\,cos(\phi_{12.i}) + jS_{12.i}sin\,(\phi_{12.i}) \quad \text{(B-147)}$$

$$\vec{S}_{21.i} = S_{21.i}e^{j\phi_{21.i}} = S_{21.i}\,cos(\phi_{21.i}) + jS_{21.i}sin\,(\phi_{21.i}) \quad \text{(B-148)}$$

$$\vec{S}_{22.i} = S_{22.i}e^{j\phi_{11.i}} = S_{22.i}\,cos(\phi_{22.i}) + jS_{22.i}sin\,(\phi_{22.i}) \quad \text{(B-149)}$$

$S_{pk.i}$ and $\phi_{pk.i}$ indicate the amplitude and phase of S parameter provided by NA, the subscript $i = 1$ and 2 represent the needed individual measurement where the error components with and without DUT, respectively. The amplitude and phase of S parameter are a matrix containing the information along the measured frequency span.

The data analysis can be started by read the ".s2p" file by "`sparameters`" function with MATLAB. Remined that the equivalent circuit represented by Y parameter is easy to perform de-embedding operation, the S parameter is then converted to Y parameter through TABLE B-2. This operation can be achieved by "`s2y`" function with MATLAB. Next, the Y parameter of the DUT itself, $\vec{Y}_{DUT}$, can be extracted as

$$\vec{Y}_{DUT} = \vec{Y}_{i=1} - \vec{Y}_{i=2} \quad \text{(B-150)}$$

Finally, converting $\vec{Y}_{DUT}$ to S parameter yields $\vec{S}_{DUT}$, which can be done by "`y2s`" function with MATLAB**.** Noted, all error within the measurement that are not removable by the calibration kit are minimized now, providing the almost best accuracy of device performance along all error correction technology to the best of the author's knowledge.

B.4.3 Loss Term of the Bias-tee and Demonstration

To demonstrate calibration and de-embedding techniques, Figure B-28 (a) presents a real image of the calibration kit alongside the SMA and RP-SMA adapters. Figure B-28 (b) illustrates the calibration procedure of a network analyzer (E5080A, Keysight). Figure B-29 displays the measurement results using various setups and DUTs, under

doi:10.6342/NTU202600018

both calibrated and non-calibrated conditions. Before the reference plane, a pair of bias-tees are connected (not shown).

Figure B-29 (a) firstly depicts the measurement results of *through* condition (i.e., without DUT), showing that the measurement system is initially non-reciprocal, where $S_{12} \neq S_{21}$ and $S_{11} \neq S_{22}$. A 1-kΩ resistor serves as the DUT, while another 1-kΩ resistor mimics the feedthrough path for the following example. Figure B-29 (b) and (c) show real pictures and the measurement results of a manually embedded resistance feedthrough and DUT with the feedthrough. As shown, the measurement results with calibration are much closed to the theoretical values (*cf.* TABLE B-3) while a ~2 dB loss is generated by the needed test fixtures (i.e., bias-tee and cables here). Figure B-29 (d) illustrates the cases using de-embedding technology. Notably, the calibrated and de-embedded responses are nearly identical, indicating that de-embedding is unnecessary for DUTs in a calibrated measurement setup, and vise versa, as the inherent error terms are negligible in this case.

doi:10.6342/NTU202600018

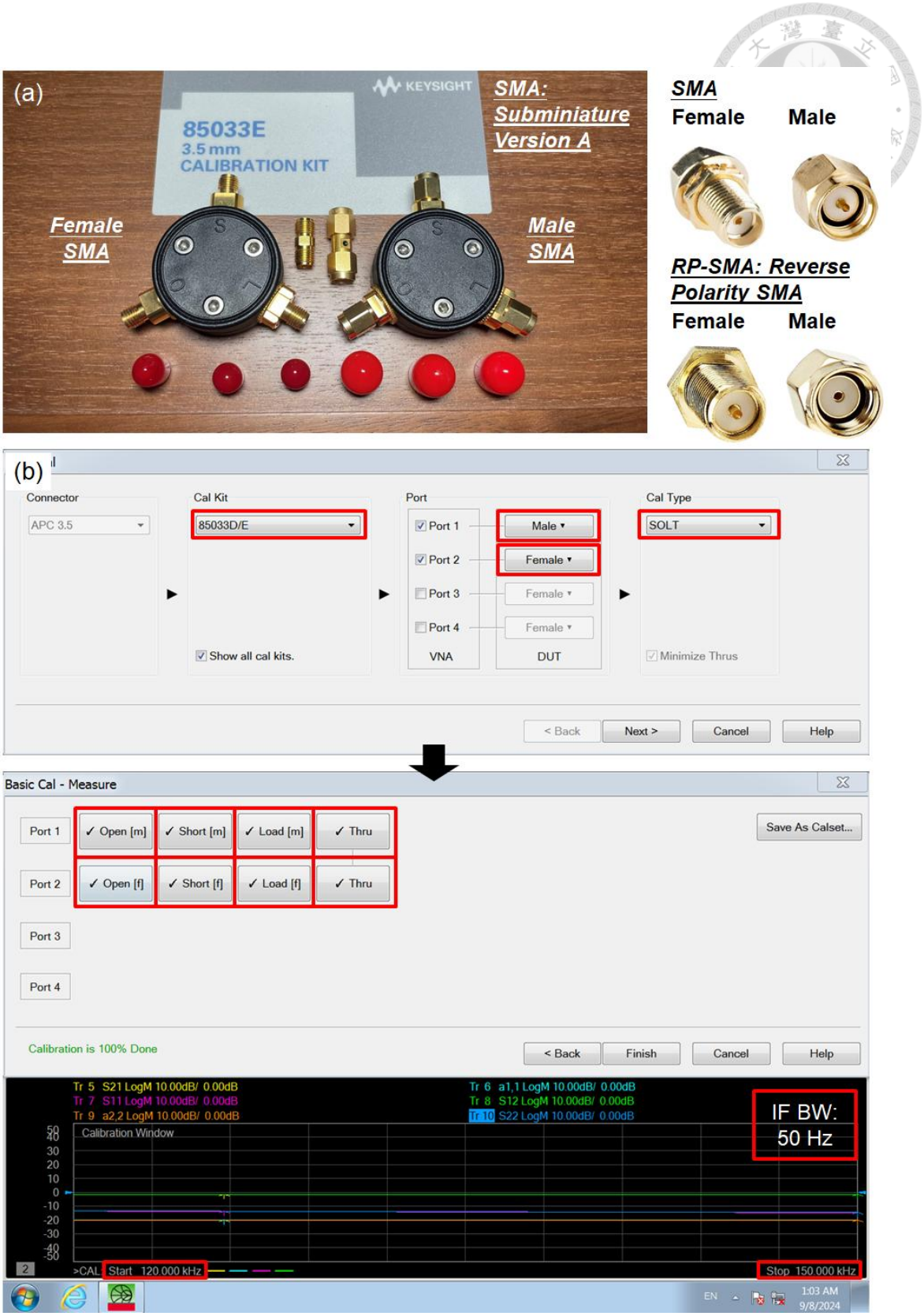


Figure B-28: (a) A photograph of a Keysight Technology 85033E calibration kit used for network analyzer measurements. (b) A screenshot of the software interface on the network analyzer during a Short-Open-Load-Thru (SOLT) calibration.

doi:10.6342/NTU202600018

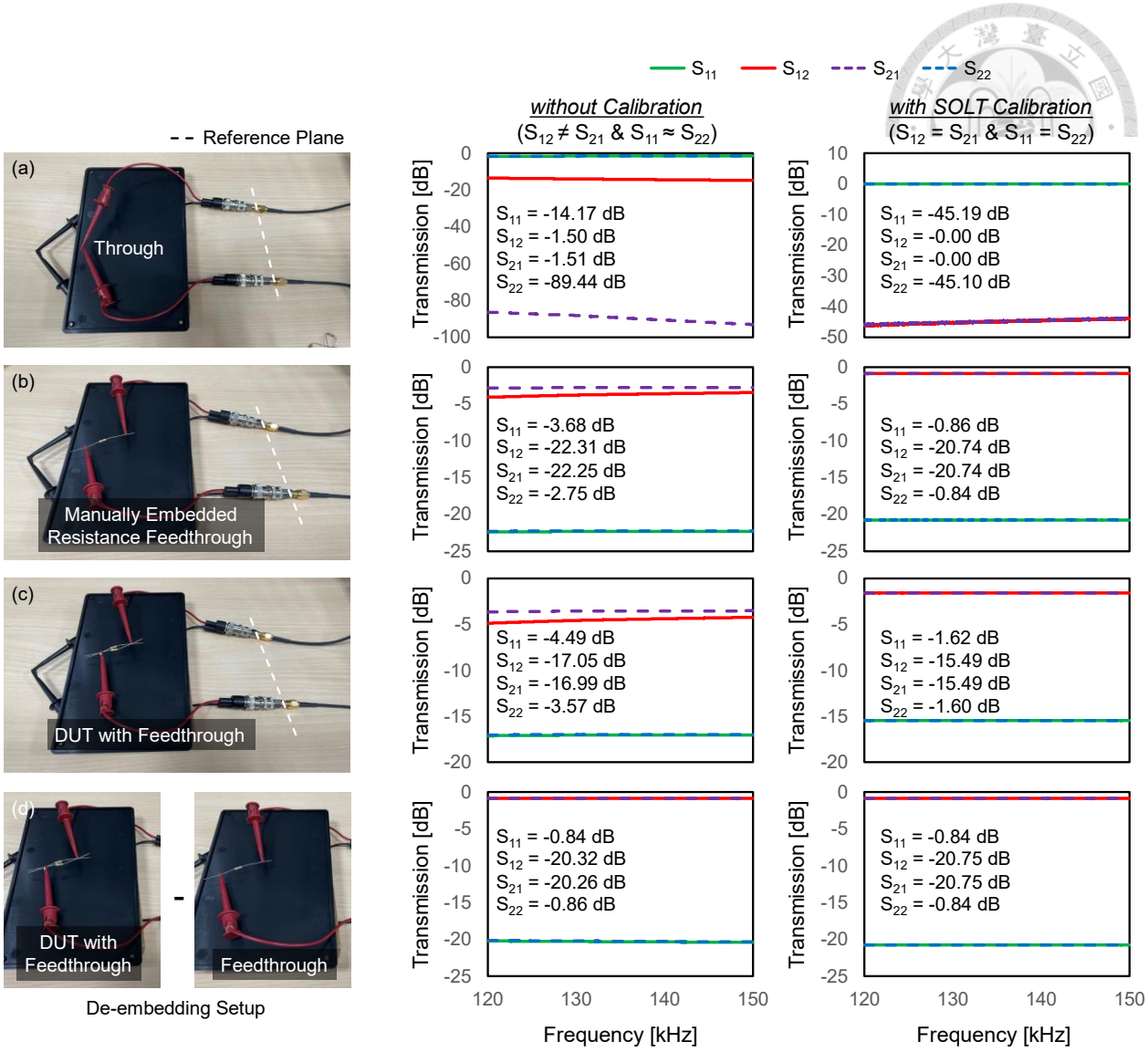


Figure B-29: Measurement results demonstrating the effectiveness of calibration and de-embedding techniques on a two-port network. The techniques are evaluated using several device under test (DUT) configurations, including (a) a through connection, (b) a 1-kΩ DUT, and (c) a 1-kΩ DUT with a parallel 1-kΩ feedthrough resistor. Part (d) illustrates the results after the de-embedding process has been applied, confirming the successful removal of measurement errors.

In addition, Figure B-30 presents real photos of the bias-tee (ZFBT-282-1.5A+, Mini-Circuit Inc.) utilized in this dissertation. Figure B-30 (a) provides a front-side view, while Figure B-30 (b) and (c) reveal the unboxed front and back views of the bias-tee's PCB. To obtain a flat-band frequency response with minimal insertion loss and high isolation, bias-tees are typically built with intricate R-L-C circuits, as shown.

doi:10.6342/NTU202600018

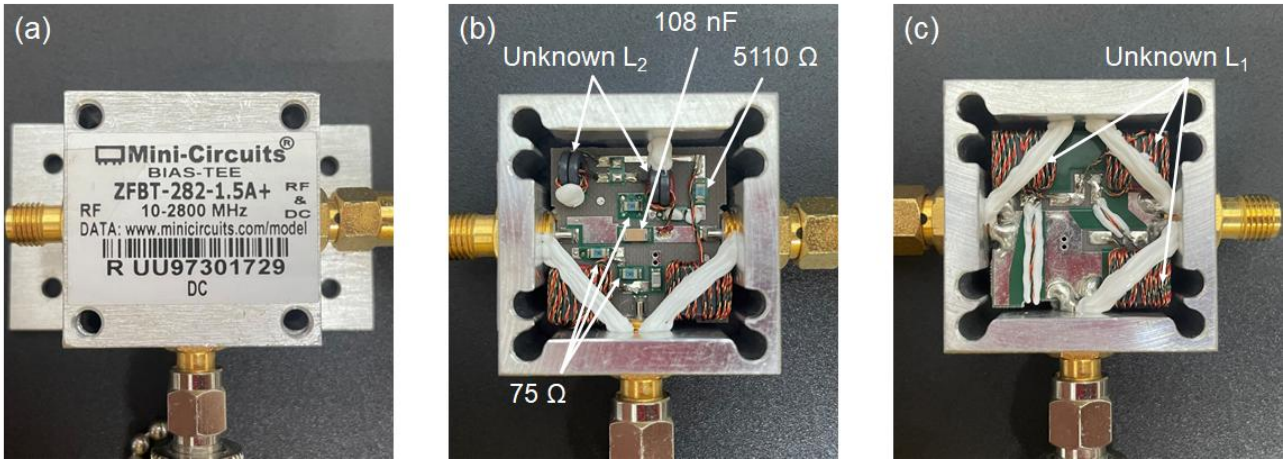


Figure B-30: Photographs showing the Mini-Circuit ZFBT-282-1.5A+ bias-tee used in the experiments. View (a) displays the device's exterior from the front, while views (b) and (c) show the internal printed circuit board (PCB) from the front and back, respectively.

However, since this bias-tee was originally designed for the 10-2800 MHz range, it introduces additional loss in the lower frequency range in our investigation.

Both the NA-based setup and the function generator-oscilloscope setup were employed to validate this effect on the path from the RF port to the RF+DC port. Figure B-31 (a) and (b) display the characterization results from the NA. It was observed that the voltage losses are approximately 0.94 and 0.91 when the terminal resistance at the DC port is GND and High-Z, respectively. The transmission coefficients are nearly flat across the relevant band, suggesting that the equivalent model might be represented by a shunt resistance connected to the DC port. By calculating the ABCD matrix based on the average forward transmission coefficient, a shunt impedance of approximately 390 and 250 Ω for both conditions are obtained, respectively.

However, in practice, port 2 is connected to a high-impedance device, as the effective impedance for our device is around 500~1000 kΩ. Therefore, the function generator and oscilloscope pair were used to validate the extracted shunt impedance. As shown in Figure B-32 (a), due to the oscilloscope's 1 MΩ input impedance, the voltage loss differs slightly from the NA-based setup. The measured shunt impedance

doi:10.6342/NTU202600018

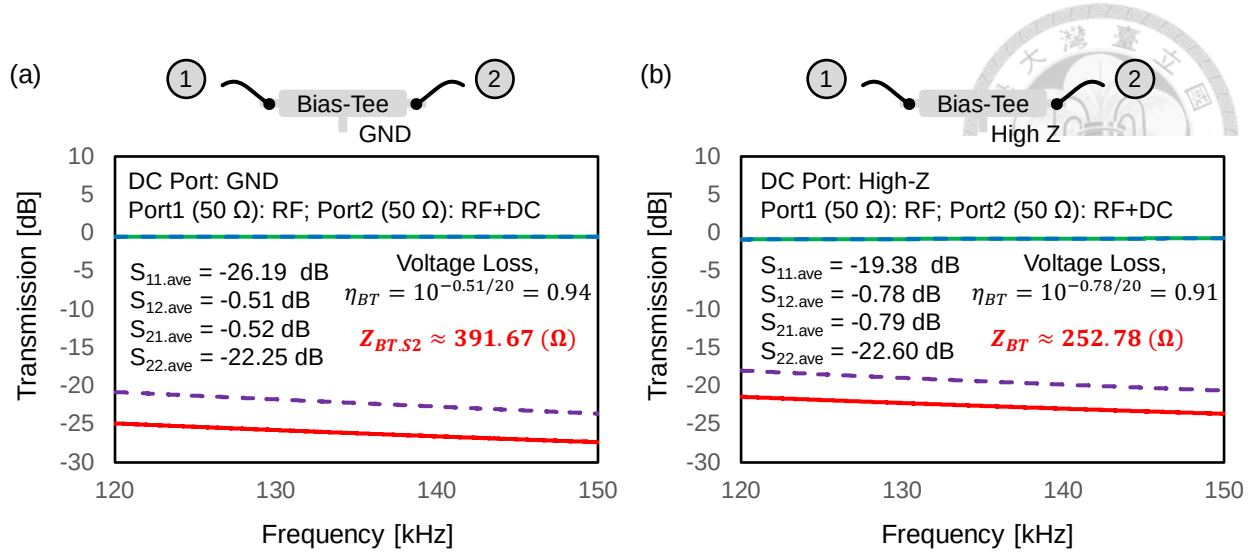


Figure B-31: Characterization of the bias tee insertion loss, measured as the forward transmission coefficient (S_{21}) using a network analyzer, under two distinct DC port termination conditions: (a) connection to ground (GND) and (b) termination with a high-impedance (High-Z) load.

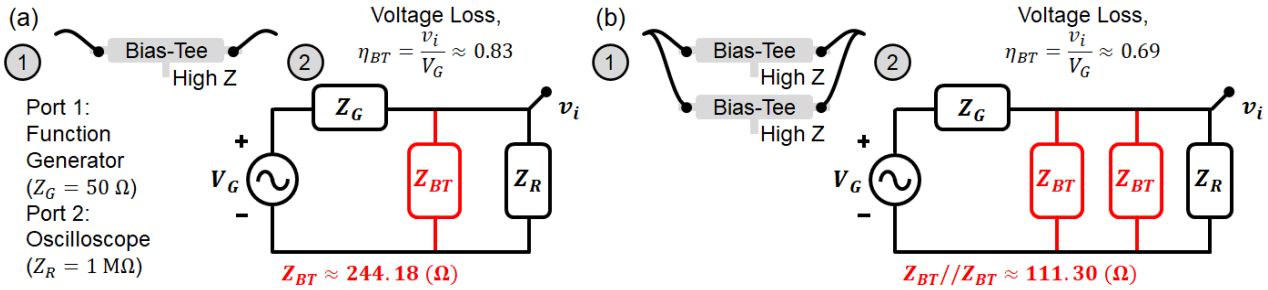


Figure B-32: Validation of the bias tee insertion loss using a function generator and oscilloscope, showing the measured voltage loss and extracted shunt impedance for two configurations: (a) a single bias tee connected to the high-impedance oscilloscope input, and (b) two bias tees connected in parallel at the driving input.

is quite close to the NA-based setup, at around 245 Ω. Moreover, Figure B-32 (b) depicts a scenario where two bias-tees are connected in parallel at the input driving end. This is the actual configuration used in Chapter 3, where the double-side driven setup results in a voltage loss of approximately 0.69 (0.83^2), indicating a shunt impedance of around 110 Ω.

doi:10.6342/NTU202600018

B.5 Equivalent Circuit of Linear Electrostatic MEMS Resonators

The governing equation of an electrical series R-L-C resonator and a lumped mechanical m-b-k resonator can be given by

$$L_x Q'' + R_x Q' + \frac{1}{C_x} Q = V_d \cos(\omega t) \tag{B-151}$$

and

$$m_r x'' + b_r x' + k_r x = A_d \cos(\omega t) \tag{B-152}$$

It is clear that the form of equations are the same. The physical meaning of each element is equivalent. The analogy between electrical and mechanical quantities are listed in TABLE B-4. As presented in the previous section (*cf.* Figure B-4), no matter the energy is transmitting in electrical domain or mechanical domain (even in acoustic domain, optical domain, and others), they are propagating or standing waves in specific medium with certain special shapes. Once transduction mechanism is found, it can be transformed from one domain to another easily and there is almost no different mathematically.

In electrostatic transduction, the voltage induced charge ($Q = CV$) can be similarly represented by mechanical force induced displacement ($x = F/k$). As an example, Figure B-33 (a) shows the equivalent circuit of an electrostatically driven MEMS resonator, where the two-coil multiple winding transformer represents the transduction mechanism of a pair of conductive units that convert the voltage varying to the electrostatic force into the device. Since the device motional velocity (x') can be convert to motional current ($Q' = I$), it can be represented totally by a circuit as Figure B-33 (b) shown. Following provides the details.

doi:10.6342/NTU202600018

TABLE B-4: THE ANALOGY BETWEEN KEY QUANTITIES IN MECHANICAL TRANSLATIONAL SYSTEMS AND ELECTRICAL CIRCUIT SYSTEMS.

Energy Domain	**Effort**	**Displacement**	**Flow**	**Derivative of Flow**
Mechanical Translation	Force F	Position x	Velocity x'	Rate of Change of Velocity (Acceleration) x''
Electric Circuit	Voltage V	Charge Q	Current I	Rate of Change of Current $Q'' = I'$
Energy Domain	**Potential Energy**	**Kinetic Energy**	**Circuit Representation**	**Dissipation Factor**
Mechanical Translation	$\frac{1}{2}kx^2 = \frac{1}{2}\frac{1}{(1/k)}x^2$	$\frac{1}{2}mx'^2$	k *and* m	$Q = \frac{1}{b}\sqrt{mk}$
Electric Circuit	$\frac{1}{2}CV^2 = \frac{1}{2}\frac{1}{C}Q^2$	$\frac{1}{2}LI^2$	$\frac{1}{C}$ *and* L	$Q = \frac{1}{R}\sqrt{\frac{L}{C}}$

doi:10.6342/NTU202600018

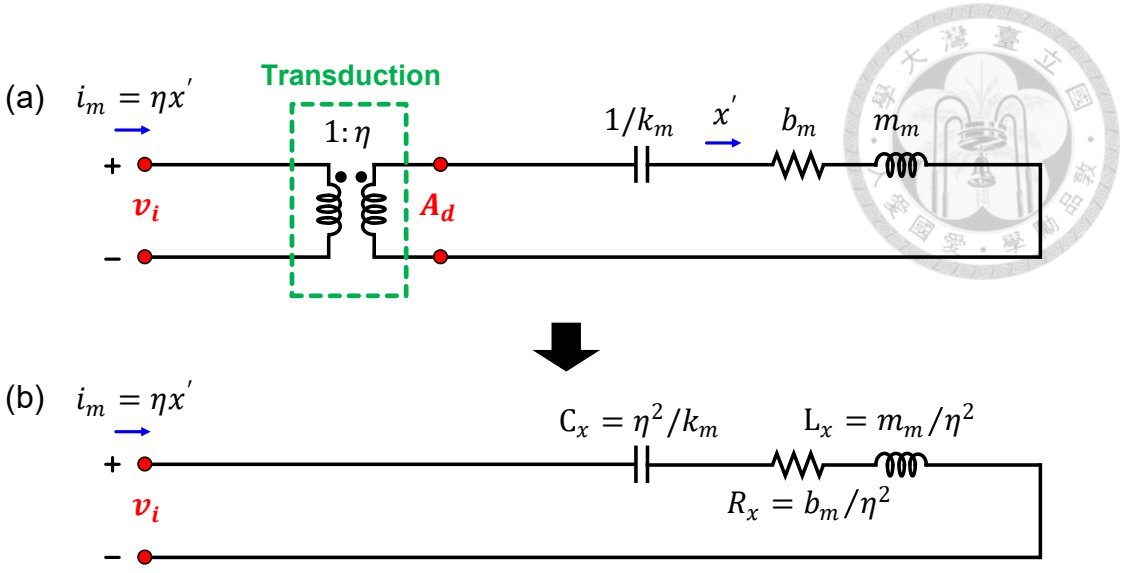


Figure B-33: (a) An equivalent circuit diagram of a one-port electrostatic MEMS resonator, representing the electromechanical transduction mechanism as a transformer. (b) The simplified Butterworth-Van Dyke (BVD) equivalent circuit model for the resonator.

The electrostatic transducer that converts energy from electrical domain to mechanical one can be analogized to a transformer converting voltage from one level to another. As shown in the Figure B-34 (a), by applying the Faraday's law of induction, it arrives

$$V_P = -N_P \frac{d\Phi}{dt} \tag{B-153}$$

and

$$V_S = -N_S \frac{d\Phi}{dt} \tag{B-154}$$

The power at each side should be the same if transformer is lossless, namely

$$P = I_P V_P = I_S V_S \tag{B-155}$$

Combing (B-152)-(B-155), the transformation identity in voltage and current is given by

doi:10.6342/NTU202600018

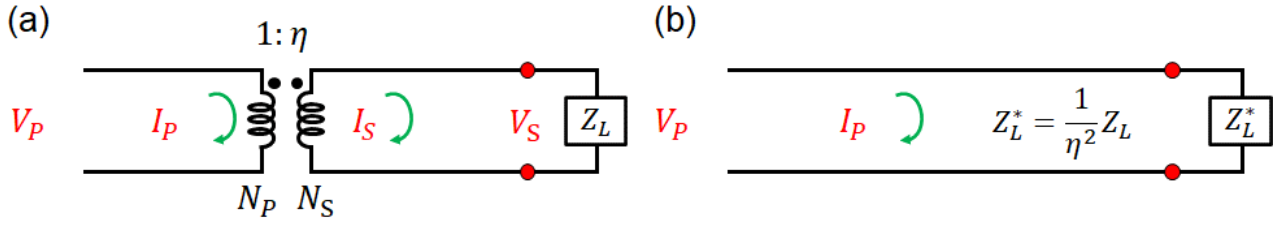


Figure B-34: (a) A diagram of an ideal transformer, illustrating the relationship between its primary and secondary circuits. (b) The equivalent circuit demonstrates how a load impedance (Z_L) on the secondary side is reflected to the primary side, appearing as an equivalent impedance (Z_L^*).

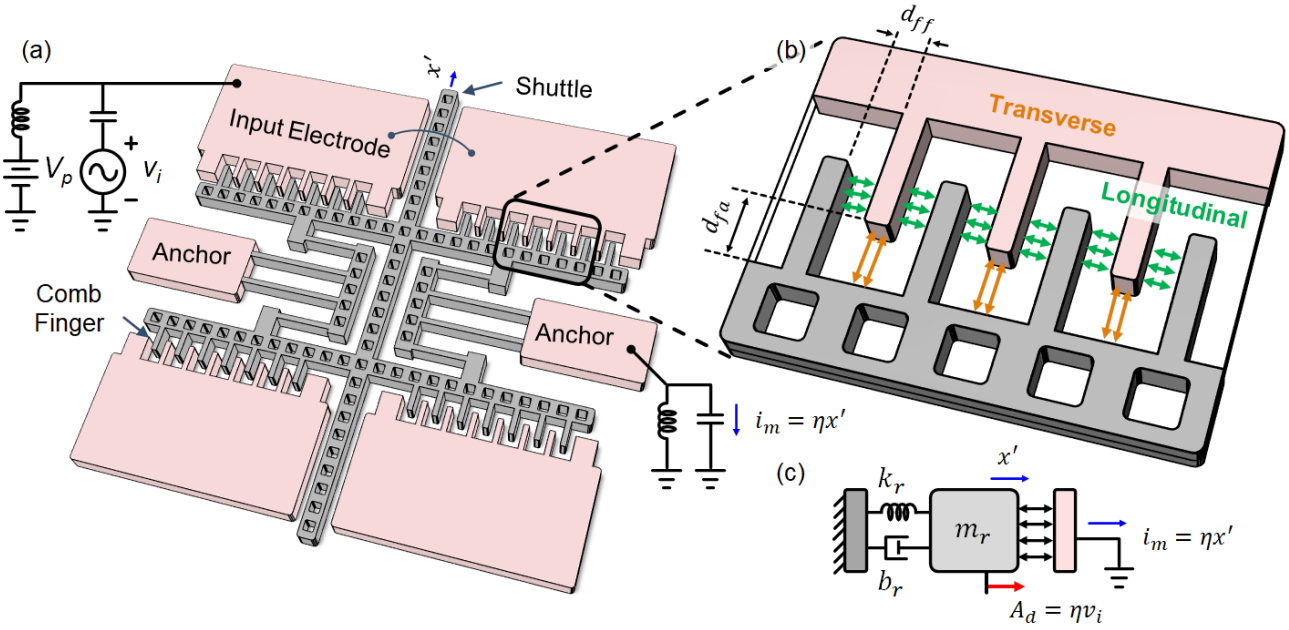


Figure B-35: (a) A schematic representation of the comb-driven resonator frequently featured in this dissertation. (b) A detailed view of the interdigitated comb fingers. (c) The lumped-parameter model representing the resonator's mechanical components.

$$\frac{V_P}{V_S} = \frac{I_S}{I_P} = \frac{N_P}{N_S} \equiv \frac{1}{\eta} \tag{B-156}$$

By generalized Ohm's law, the circuit of Figure B-34 (a) can be equivalently represented as Figure B-34 (b), namely

$$Z_L^* = \frac{V_P}{I_P} = \frac{V_S/\eta}{\eta I_S} = \frac{1}{\eta^2}\frac{V_S}{I_S} = \frac{1}{\eta^2} Z_L \tag{B-157}$$

doi:10.6342/NTU202600018

where $Z_L = V_S/I_S$, thus it will be said that the impedance looking from the primary circuit into the slave circuit are Z_L^*.

Figure B-35 (a) shows the schematic of a comb-driven resonator frequently used in this dissertation. Figure B-35 (b) shows the zoom-in to the comb fingers and Figure B-35 (c) shows the lumped model, in which the mechanical parts are discussed previously. If the bias polarization is much larger than the amplitude of the periodic driving signal, $V_P \gg v_i$, the electrostatic force of electrostatically driven MEMS resonators can be approximated by

$$A_d = \frac{\partial E}{\partial x} = \frac{1}{2}\frac{dC_d}{dx}(V_P + v_i)^2 \approx \frac{dC_d}{dx}V_P v_i = \eta v_i \tag{B-158}$$

where η is the electromechanical coupling coefficient. See [515] for more discussion on the driving force approximation.

Applying (B-157), the equivalent electrical components in terms of mechanical components and transduction (*cf.* Figure B-33) can be represented as

$$R_x = \frac{1}{\eta^2}b_r \tag{B-159}$$

$$L_x = \frac{1}{\eta^2}m_r \tag{B-160}$$

$$C_x = \frac{\eta^2}{k_r} \tag{B-161}$$

According to the viewpoint on analogy of potential energy, the value of the equivalent capacitance is at denominator but the value of the stiffness is at numerator, i.e., $Z_L^* = 1/\eta^2 \times Z_L \rightarrow 1/(sC_x) = 1/\eta^2 \times (k/s)$. Thus, it is actually more convenient to analogize the capacitance to the reciprocal of stiffness, called compliance, as $1/(sC_x) = 1/\eta^2\,[1/s(1/k)]$. Noted, the (B-159)-(B-161) shows the case for Figure B-33 as that derived by so-called one-port configuration (i.e., one transduction mechanism presented).

doi:10.6342/NTU202600018

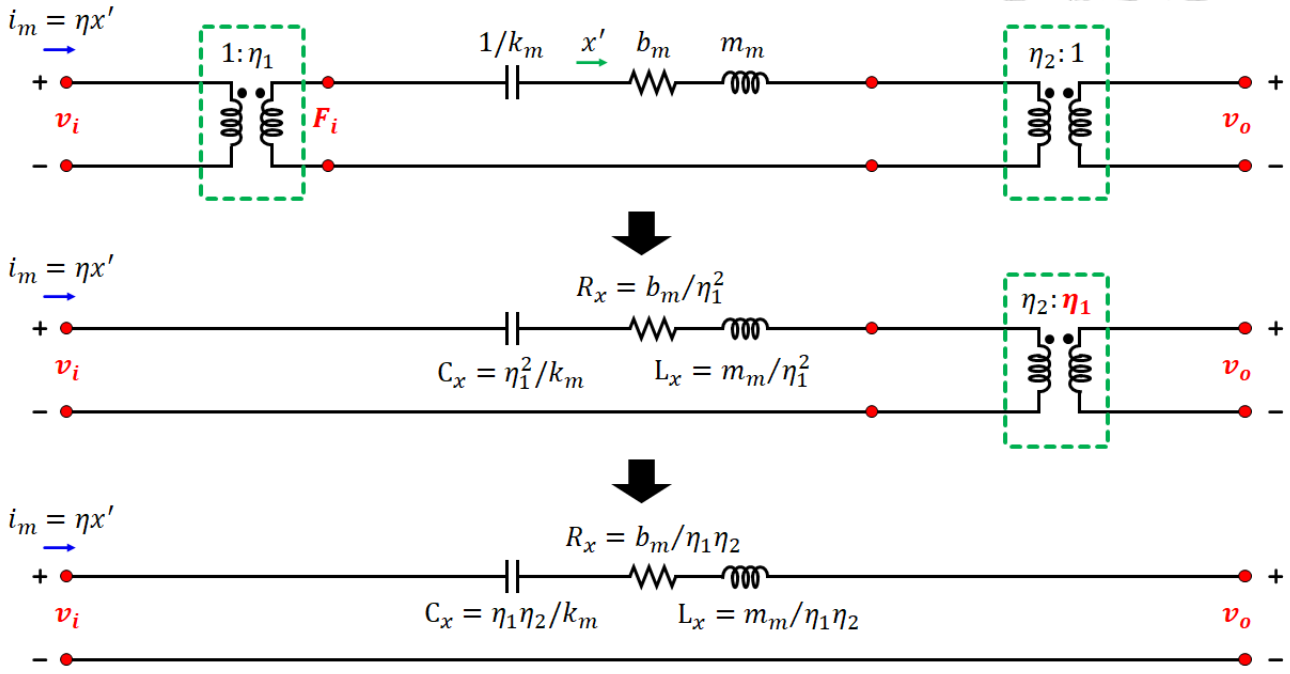


Figure B-36: A two-port MEMS resonator configuration is illustrated, which features distinct transduction mechanisms for actuation at Port 1 (η_1) and sensing at Port 2 (η_2).

Figure B-36 shows the case for the two-port configuration (i.e., two transductions presented), where the electromechanical coupling coefficient at first and second port are represented by η_1 and η_2. The equivalent electrical components can be similarly obtained as

$$R_x = \frac{1}{\eta_1\eta_2} b_r \tag{B-162}$$

$$L_x = \frac{1}{\eta_1\eta_2} m_r \tag{B-163}$$

$$C_x = \frac{\eta_1\eta_2}{k_r} \tag{B-164}$$

Thus, the impedance of the resonator itself can be obtained as

$$Z_r = R_x + j\omega L_x + \frac{1}{j\omega C_x} = R_x - \frac{1-\omega^2/\omega_s^2}{\omega C_x} \tag{B-165}$$

doi:10.6342/NTU202600018

where $\omega_s = 1/\sqrt{L_x C_x} = \sqrt{k_r/m_r}$ is the natural frequency (or called series resonance frequency), which is considered as the resonance frequency if the device's Q is high enough. Noted, the resonance represents a phenomenon where the system loss less during oscillation. It provides largest peak displacement in mechanical domain and, here, deliver biggest motional current in electrical domain.

The equivalent circuit in reality is inherently more complex. Each connection point can introduce additional unwanted non-ideal terms due to factors such as feedthrough, or even the device itself due to its structural nature or the equivalent circuit of other modes. Sometimes the value of those parasitic terms is not significant compared to the MEMS resonator or contributes less effect in the interesting frequency band. For instance, if ignore the effect on the transverse part of comb finger capacitance sine comb fingertip to electrode spacing is big in design, the static capacitance and inductance for a comb-driven resonator can be estimated as

$$C_0 = N\frac{\varepsilon_0 A_f}{d_{ff}} = 60\frac{8.854\times10^{-12}\times(5.87\times10^{-6}\times10^{-5})}{10^{-6}} = 31.18\times10^{-15} \quad \text{(B-166)}$$

$$L_0 = N\frac{\mu_0 d_{ff} l_f}{h_f} = 60\frac{(4\pi\times10^{-7})\times10^{-6}\times10^{-5}}{5.87\times10^{-6}} = 128.45\times10^{-12} \quad \text{(B-167)}$$

where N, ε and μ are number of comb finger pair, permittivity of free space and permeability of free space, respectively. A_f, d_{ff}, l_f and h_f represent the plate area, separation between fingers, length of fingers and height of fingers, respectively. The additional parasitic capacitance and inductance contributed by the coaxial BNC cable can be estimated for about 80-100 (pF) and 0.1-0.3 (μH) per meter, respectively. The layout size of the metal bond pad for wire bonding in 0.35-μm CMOS process is specified as 100 square meters, which contributes a parasitic capacitance of 300~700 (pF) regularly. On the other hand, the contact resistance created by connection of cable,

doi:10.6342/NTU202600018

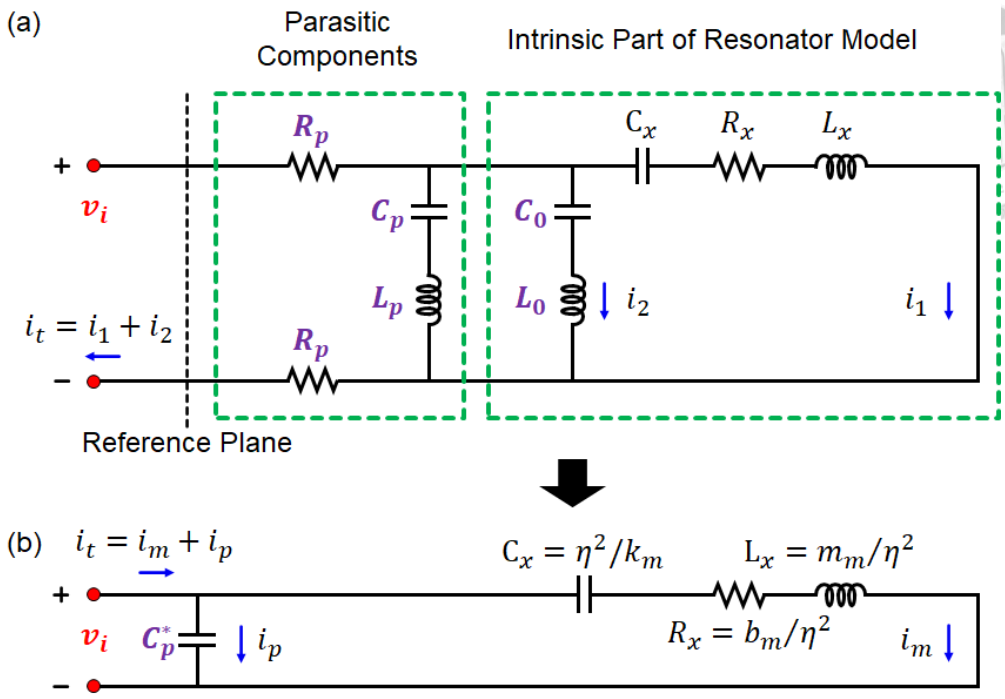


Figure B-37: Equivalent circuit models for a one-port electrostatic MEMS resonator, illustrating two common representations. The first one (a) is a comprehensive model that includes the resonator's motional (i.e., R_x, L_x, C_x) and static (C_0, L_0) components, along with external parasitic resistance (R_p), inductance (L_p,), and capacitance (C_p). The second one (b) is the simplified and widely used model, which represents the core resonator elements in parallel with a single lumped parasitic capacitance (C_p^*).

bond pad probing or wire bonding can be over the range of single digit to about one hundred ohms. It turns out that the measuring cable contributes much effort to the device responses if there is no calibration.

Figure B-37 displays a 1-port equivalent circuit of a MEMS resonator where a parasitic inductance, L_p, and capacitance, C_p, are connected in parallel, while a parasitic resistance, R_p, is placed in series with the MEMS resonator. In additional, the circuit includes both static capacitance, C_0, and inductance, L_0, from device itself. The parasitic resistance on L_p-C_p (i.e., feedthrough and cable resistance) or L_0-C_0 (i.e., substrate resistance) path is ignored [500, 516]. Noted, these errors factors presented

doi:10.6342/NTU202600018

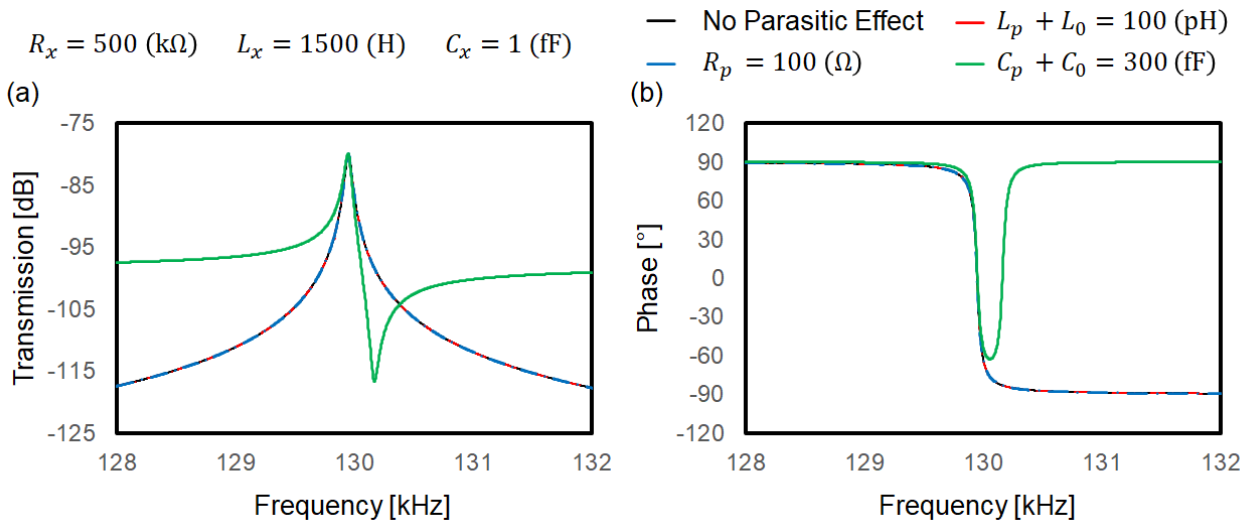


Figure B-38: Simulated frequency response of a MEMS resonator illustrating the impact of various parasitic elements. The plots compare the (a) transmission (S_{21}) and (b) phase responses of an ideal resonator against those incorporating parasitic resistance (R_p), inductance (L_p), or capacitance (C_p). These results demonstrate that parasitic capacitance exerts the most significant influence on the overall device characteristics.

are the errors possibly appeared after the reference plane which the errors before this reference plane are calibrated. Although the calibrated error terms introduce influence on the actual received voltage and therefore the signal to noise ratio, it typically does not affect the characterization results if device is linearly operated in NA-based setup.

Recalling the result derived in Appendix B.3.1 (*cf.* (B-106)), assuming $Z_{01} = Z_{02} = Z_0$ and replacing Z_{DUT} as Z_{total} (*cf.* (B-169)), the transmission (in dB) of an electrostatically driven MEMS resonator considering the parasitic capacitance are given by

$$S_{21} = 20\,log_{10}\left(\frac{v_{out}}{v_i}\right) = 20\,log_{10}\left(\frac{2Z_0}{Z_{total} + 2Z_0}\right) \tag{B-168}$$

With this, Figure B-38 (a) and (b) show the simulation results of transmission and phase from LTspice, comparing common values of real situation for parasitic terms by

doi:10.6342/NTU202600018

keep other terms to zero. One can conclude that the parasitic capacitance contributes highest effect to the MEMS resonator. Therefore, for most case of 1-DOF electrostatically driven MEMS resonator, the equivalent circuit are represented by the device impedance with the parasitic capacitance as Figure B-37 (b) shown, namely

$$Z_{total} = \left(\frac{1}{R_x + j\omega L_x + \frac{1}{j\omega C_x}} + j\omega C_p^* \right)^{-1} = \frac{1}{\omega C_0} \frac{(\omega_s^2 - \omega^2) + j\omega \frac{R_x}{L_x}}{-\omega \frac{R_x}{L_x} + j(\omega_p^2 - \omega^2)} \quad \text{(B-169)}$$

where $C_p^* = C_p + C_0$ represent the lumped parasitic capacitance, which reduces to C_p in some devices. $\omega_s = 1/\sqrt{L_x C_x}$ and $\omega_p = \sqrt{(C_x + C_p^*)/(L_x C_x C_p^*)} = \omega_s \sqrt{1 + C_x/C_p^*} > \omega_s$ are series resonance frequency and parallel resonance frequency, respectively. They are commonly called resonance frequency and anti-resonance frequency in MEMS field, representing the frequency with smallest and biggest resistance values, respectively. In the field of piezoelectric materials, this equivalent circuit is called Butterworth-Van Dyke (BVD) model [517]. Moreover, the modified BVD (mBVD) and π-shaped BVD (PiBVD) model are used when the parallel resistance, capacitance and to-ground parasitic terms exist and are unignorable [518, 519]. In summary, Figure B-39 (a) and (b) show the equivalent circuit of electrostatic MEMS resonator under 1-port and 2-port configurations, respectively.

Considering the impedance of the resonator and the driving voltage, from the definition of capacitance, $Q = CV$, the motional current of the resonator can be presented by

$$\begin{aligned} i(t) &= \frac{d(CV)}{dt} = C\frac{dV}{dt} + V\frac{dC}{dt} \\ \rightarrow i_m(t) + i_p(t) &\approx C_p \frac{dv_i}{dt} + V_P \frac{dC_d}{dx}\frac{dx}{dt} = C_p \frac{dv_i}{dt} + \eta \frac{dx}{dt} = \frac{v_i}{Z_r} \end{aligned} \quad \text{(B-170)}$$

doi:10.6342/NTU202600018

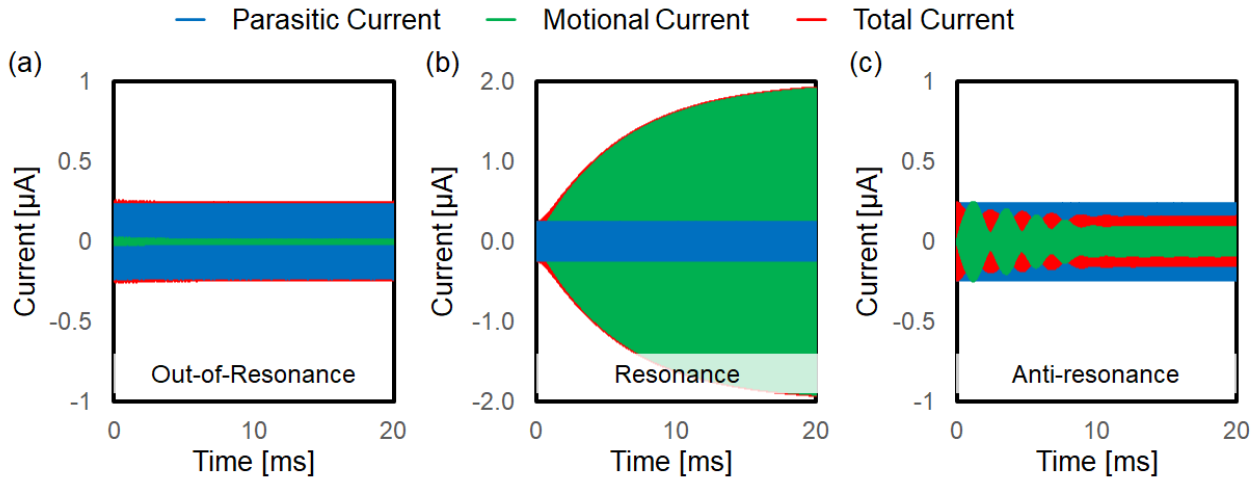


Figure B-40: Comparison of the motional, feedthrough, and total currents in a MEMS resonator at three distinct operating frequencies: (a) below resonance, (b) at resonance, and (c) at anti-resonance.

Figure B-39: Equivalent circuit models representing an electrostatic MEMS resonator configured as (a) a one-port device and (b) a two-port device.

Take a look to the current flow on the path of the resonator and the parasitic capacitance, instead of describing the antiresonance as a kind of resonance that the energy alternating back and forth between L_x and C_0. It is more accurate to say that the antiresonance is the result of the cancelation of the motional current by the parasitic current due to phase difference caused interference. Differing from the usage of antiresonance in coupled oscillators, there is no direct coupling or electrical resonance. Figure B-40 (a) shows the case where the operating frequency is much lower than resonance frequency, showing that the parasitic current dominated the total response. Figure B-40 (b) shows the currents if operating device at resonance where the motional current dominated response while Figure B-40 (c) shows the case that operating device at antiresonance where the parasitic current cancels the motional current.

Figure B-41 shows the comparison on the effect of parasitic capacitance. As the level of parasitic capacitance increases, the anti-resonance frequency will be closed to the resonance frequency and distort the shape of the peak. This effect will make the quality factor extraction failed. The -3 dB points didn't exist possibly as the red curve shown in the inserts of Figure B-41 (a). Besides, the phase does not pass the 0° at resonance sine the response is dominated by parasitic current so the phase is more and

doi:10.6342/NTU202600018

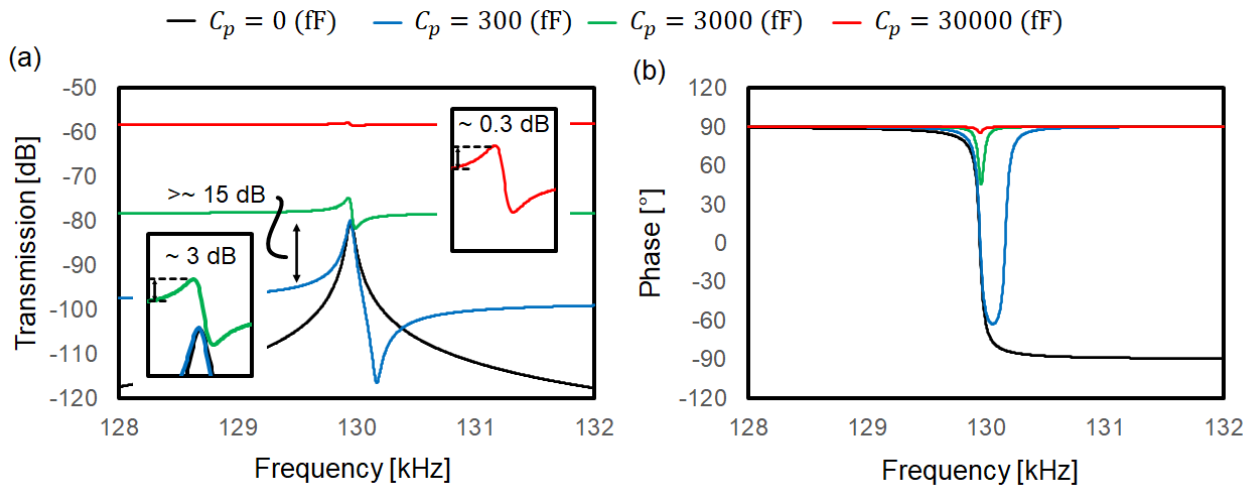


Figure B-41: An illustration of the effects of parasitic capacitance on the frequency response of a MEMS resonator, detailing the (a) transmission (S_{21}) and (b) phase response. As parasitic capacitance increases, the anti-resonance frequency shifts closer to the resonance frequency, causing significant distortion of the peak shape. The inset in (a) demonstrates how this effect can impede the extraction of the quality factor (Q-factor) using the -3 dB method. Concurrently, the phase response is altered, with the phase angle at resonance shifting toward 90° as the parasitic capacitance increases.

more closed to 90° as parasitic capacitance increases (*cf.* Figure B-41 (b)). Furthermore, Figure B-42 shows an illustration for second situation where the -3 dB points exist, however, the frequency response is distorted and the Q factor extraction fails.

If there is an amplifier, then the forward transmission coefficient of (B-106) is modified as (*cf.* (B-108) and (B-133))

$$S_{21.A} = 20\,log_{10}\left(\frac{G \times I}{v_i}\right) = 20\,log_{10}\left(\frac{Z_0 G}{(Z_{total} + Z_0 + Z_{A.in})(Z_0 + Z_{A.\text{out}})}\right) \qquad \text{(B-171)}$$

According to (B-171), Figure B-43 shows the responses comparison on the effect of gain values. As mentioned early, the noise floor defined the measurable signal level in practice, therefore, the higher gain values could increase SNR. Imaging that the noise floor is about -80 dB in certain environment, the received signal lower than this value cannot be measured, as shown in Figure B-43 (a). As the gain value increase, the SNR ratio become batter, however, it then dominated by the feedthrough signal and saturated to a certain value. On the other hand, if the amplifier is non-inverting type, the phase

doi:10.6342/NTU202600018

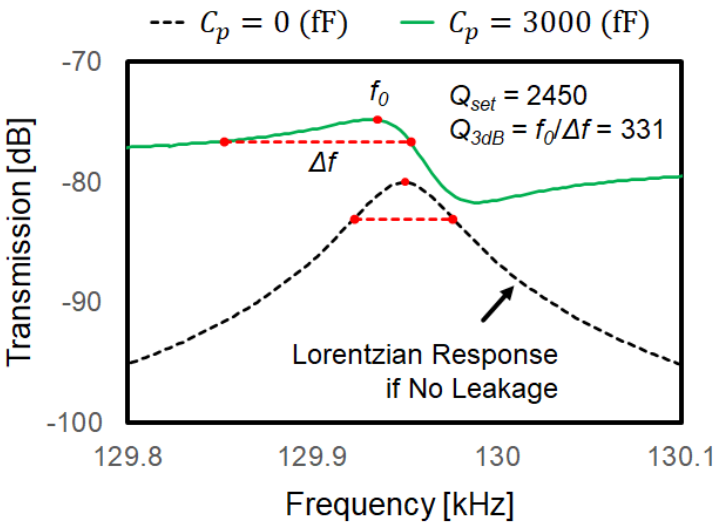


Figure B-42: Demonstration of an inaccurate quality factor extraction resulting from a frequency response distorted by parasitic capacitance. Although the -3 dB points are identifiable in this scenario, the non-ideal shape of the resonance peak invalidates the assumptions of the extraction method, leading to an erroneous calculation.

response will not change if the bandwidth of the amplifier is larger enough (*cf.* Figure B-43 (b)).

It should be noted, the network analyzer typically has an input and output impedance of 50 (Ω). When configuring the analyzer, the transmitted energy refers to the energy received by the component under impedance-matched conditions. Therefore, for devices with high impedance, the received voltage will be doubled. [351, 352, 520] are recommended for more details and perspective on equivalent circuit of MEMS devices.

doi:10.6342/NTU202600018

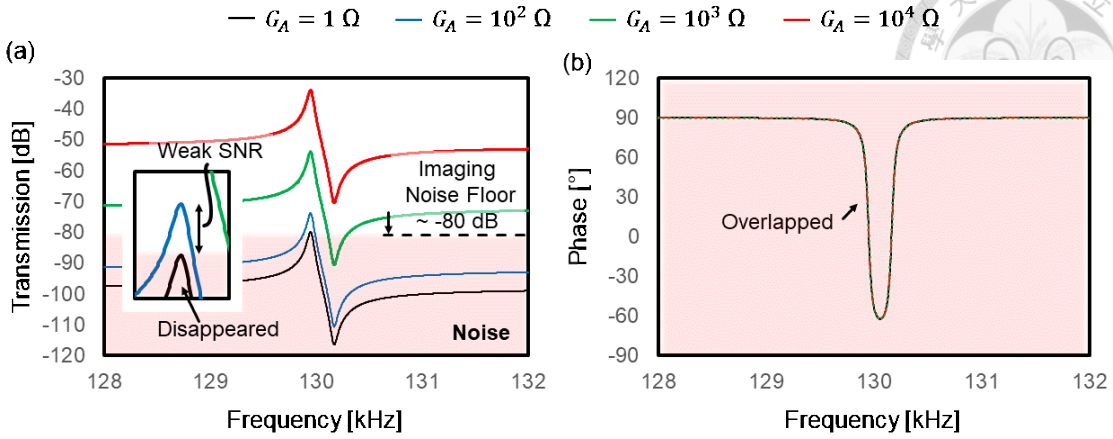


Figure B-43: The influence of amplifier gain on the measured frequency response. (a) The transmission (S_{21}) plot demonstrates that higher gain improves the signal-to-noise ratio (SNR) and reveals signals previously obscured by the noise floor. (b) The noisy output could make the phase response unreliable and therefore correlated to the SNR of the transmission. See Figure 3-22 for real measurement results.

B.6 Parameter Extraction and Initial Guess

According to (B-169), the number of unknown lumped elements in practice can be deliver to two situations. The first situation is that the system with ignorable parasitic capacitance and unobservable anti-resonance (i.e., there is no observable transmission dip because it immerses into noise floor), or the response are calibrated or de-embedded where the feedthrough is limited, then there are three unknown parameters, R_x, L_x, and C_x. The second situation is that the feedthrough is big enough and the distorted resonance peak and anti-resonance are present, then there are four unknown parameters, R_x, L_x, C_x, and C_0.

According to (B-168)-(B-171), the initial guess for resistance is reasonable to choose at resonance peak. Approximating the impedance at resonance condition by ignore the parasitic capacitance yields

$$Z_{total@\omega_s} = R_x \parallel Z_{c_0} \approx R_x = \begin{cases} (2Z_0 - Z_0 S_{21.max})/S_{21.max}; \text{w/o TIA} \\ G - (Z_0 + Z_{in})/S_{21.max}; \text{w/ TIA} \end{cases} \quad \text{(B-172)}$$

Besides, the resonance frequency and the anti-resonance frequency are another

doi:10.6342/NTU202600018

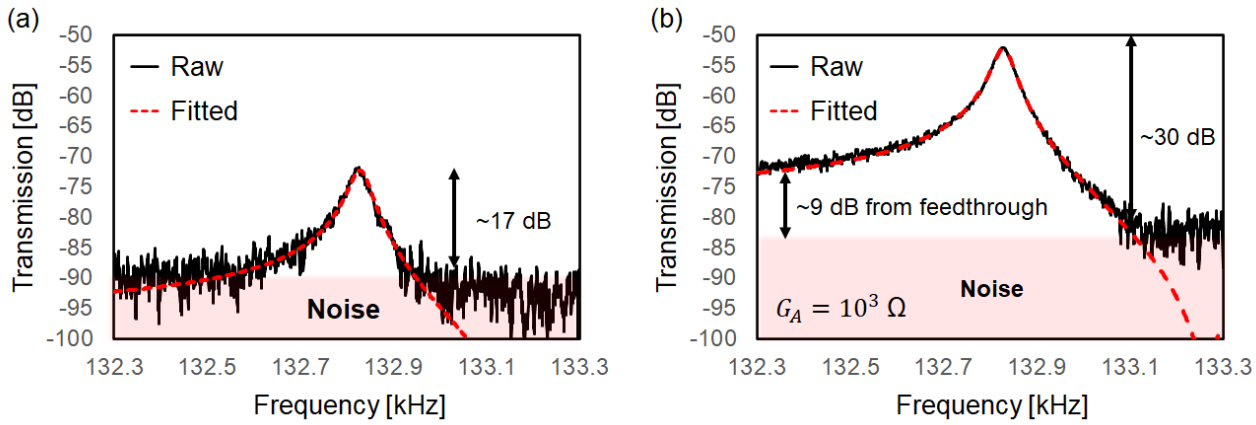


Figure B-44: Measured frequency response and corresponding successful curve fit for a resonator characterized by low parasitic capacitance. The data is presented for two distinct measurement configurations: (a) without a transimpedance amplifier (TIA) and (b) with a TIA.

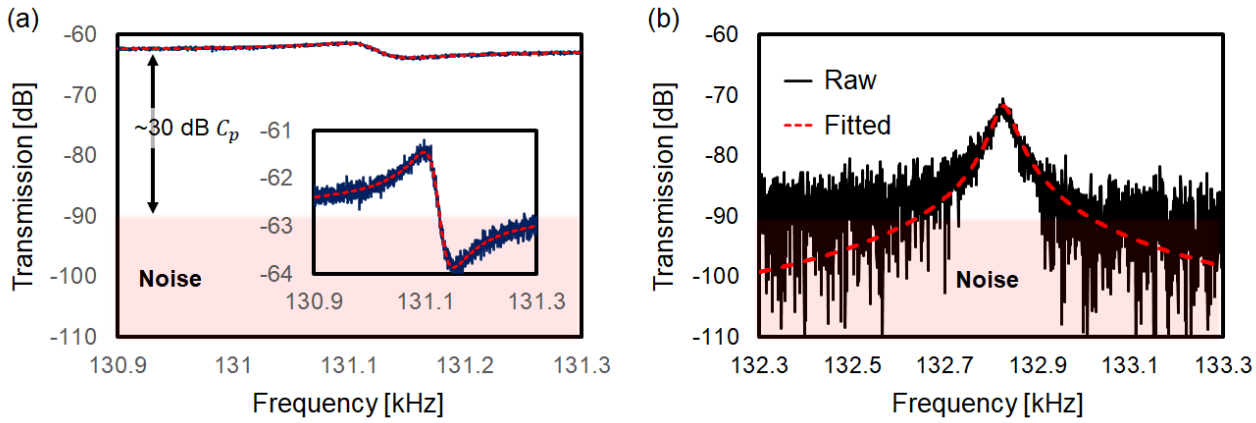


Figure B-45: (a) An illustration of a measured frequency response of a resonator with high parasitic capacitance, a condition that necessitates an improved initial guess for a successful curve fit. (b) An example illustration demonstrates that a more accurate parameter extraction can be achieved by limiting the fit to a narrow bandwidth around the resonance peak, as the algorithm is able to detect the distorted peak shape even when the anti-resonance is not apparent.

valuable indicator for precise fitting and lowering the computational cost. Finding the resonance frequency and extracting the quality factor with 3-dB bandwidth method yields next approximation of

$$Q \approx \frac{f_n}{\Delta f_{3dB}} \approx \frac{1}{R_x}\sqrt{\frac{L_x}{C_x}} = \frac{1}{R_x}\sqrt{\frac{1}{C_x^2\omega_s^2}} \rightarrow C_x = \frac{1}{QR_x\omega_s} \tag{B-173}$$

doi:10.6342/NTU202600018

and the equivalent conductance is obtained as

$$\omega_s^2 = \frac{1}{L_x C_x} \rightarrow L_x = \frac{1}{C_x \omega_s^2} \tag{B-174}$$

The initial guess value of parasitic capacitance is then estimated by

$$\omega_p^2 = \frac{C_x + C_0}{L_x C_x C_0} \rightarrow C_0 = \frac{C_x}{\omega_p^2 C_x L_x - 1} \tag{B-175}$$

The concern on this initial guessing comes from the first (*cf.* (B-172)) and second approximation (*cf.* (B-173)) where the parasitic capacitance is ignored, thus, the initial guess become poor for case who parasitic capacitance is huge. Since the anti-resonance frequency will be clearly observable if parasitic capacitance is huge in most of cases, one might fit the response in two steps to avoid this trouble. According to (B-169), it is found that there are only two variables if set $C_{RL} = R_x/L_x$. Fitting C_{RL} and C_0 in first run can improved the initial guess, then the new approximation of equivalent resistance can be approached as

$$R_{x.new} = R_x - \frac{1}{\omega_s C_0} \tag{B-176}$$

To illustrate, Figure B-44 (a) and (b) shows measured responses with low parasitic capacitance before and after amplifier, showing the success fitting. Figure B-45 (a) shows a measured response with high parasitic capacitance which needs an improved initial guess to success fit the response. Manually adjusting the initial guess of parasitic capacitance to address this issue is acceptable, while gradient descent or Newton's method can be used for initial guess optimization if the above one-step improved estimation fails.

On the other hand, as shown in Figure B-45 (b), sometimes fitting the response with a small bandwidth around the resonance peak yields batter extraction results since the effect of out-of-band noise floor can be minimized, and algorithm can detect and extract the distorted peak shape associated with the parasitic capacitance even if the

doi:10.6342/NTU202600018

anti-resonance peak is absent. According to Appendix B.4 to B.6, it is recommended for further reading on [409, 520-522] and book of [402, 403]. The parameter extraction on Duffing term and van der Pol term are presented in the Section E.6 and E.7 in detail.

doi:10.6342/NTU202600018

B.7 Multiple Ports, Multiple DOF and Coupled Systems

As a part of the equivalent circuit model of electrostatic MEMS devices, this subsection provides a very brief introduction and illustration on the multiple ports system, coupled systems and the system represented with multiple modes.

To manipulate the system performance and achieve compensation of un-wanted interference, multiple ports could be implemented. Figure B-46 (a) and (b) show the example schematic and equivalent circuit representation of a multiple ports system, respectively. The device is constructed with three comb finger electrodes, as shown in Figure B-46 (a), port 1 and port 2 are used for actuation of the 1st in-plane vibration mode while port 3 is the sensing electrode. The resultant actuation force from these two ports is summing or cancelling each other dependence on the phase of the input voltage. See [351, 352, 523, 524] for details on the design consideration and the applications of multiple ports.

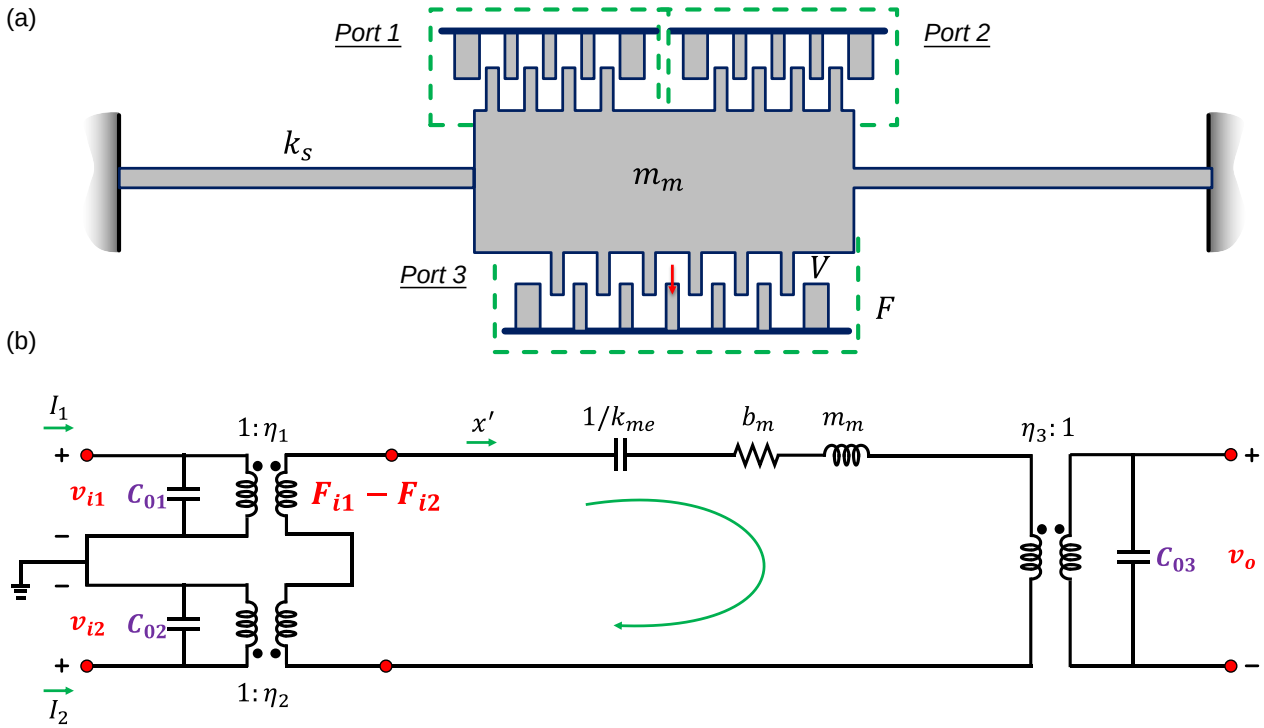


Figure B-46: (a) A example schematic of a multi-port MEMS resonator and (b) its equivalent lumped-element circuit model. The terms v_{i1} and v_{i2} represent the input ac signal, v_0 is the output voltage at port 3 and C_{0i} represent the rest capacitance of port i.

doi:10.6342/NTU202600018

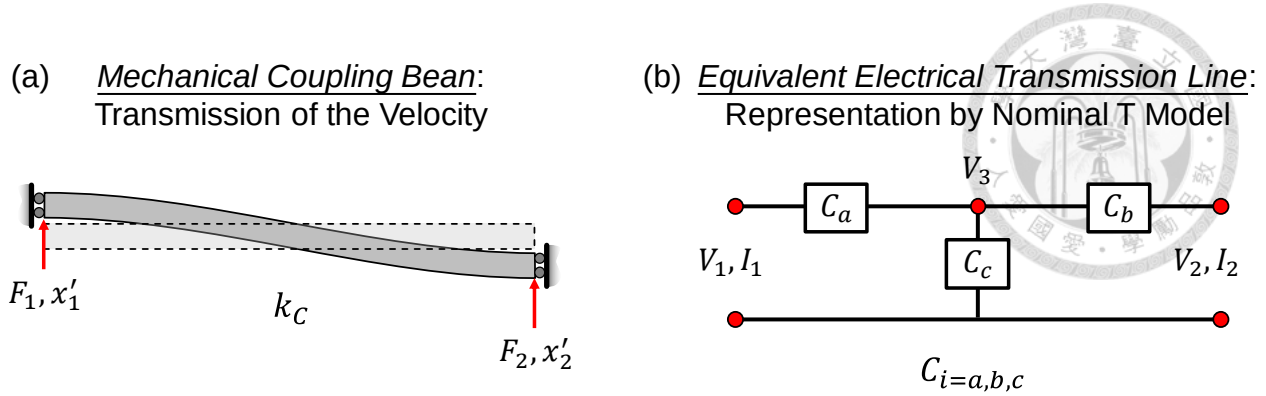


Figure B-47: (a) A mechanical coupling beam and (b) its equivalent circuit representation. The diagram illustrates the analogy between the mechanical domain (force, velocity) and the electrical domain (voltage, current).

To achieve the sharp frequency roll-offs and high signal rejection required in many communication applications, filters need to be of a higher order. In the context of MEMS filters, the order is directly related to the number of resonators used in the filter's construction. To create these necessary higher-order filters, multiple individual MEMS resonators must be linked together. One could accomplish this through the use of coupling beams, as shown in Figure B-47 (a), which are essentially tiny mechanical springs that connect the resonators. The coupling beam dimensions yielding specific impedance values can be obtained through consideration of the impedance matrix as shown in Figure B-47 (b) for this flexural mode beam under sliding/guiding support boundary conditions (*cf.* Figure B-47 (a)). When resonators are coupled (*cf.* Figure B-48 (a)), the entire system can vibrate in several distinct modes, each at a slightly different frequency. These different vibrational modes correspond to the passband of the filter—the range of frequencies that are allowed to pass through as illustrated in Figure B-48 (b). See [408, 525-529] for the foundation and valuable achievements.

The last thing would like to mention is that, in the presence, the systems are typically lumped as a 1-DOF system and being considered to be coupled and to be a higher DOF system. However, the systems are with infinity DOF in reality. As a general example, the linearized equation of motion governing the transverse deflections $w(x,t)$ of a prismatic beam with a rectangular cross-section as a function of the longitudinal

doi:10.6342/NTU202600018

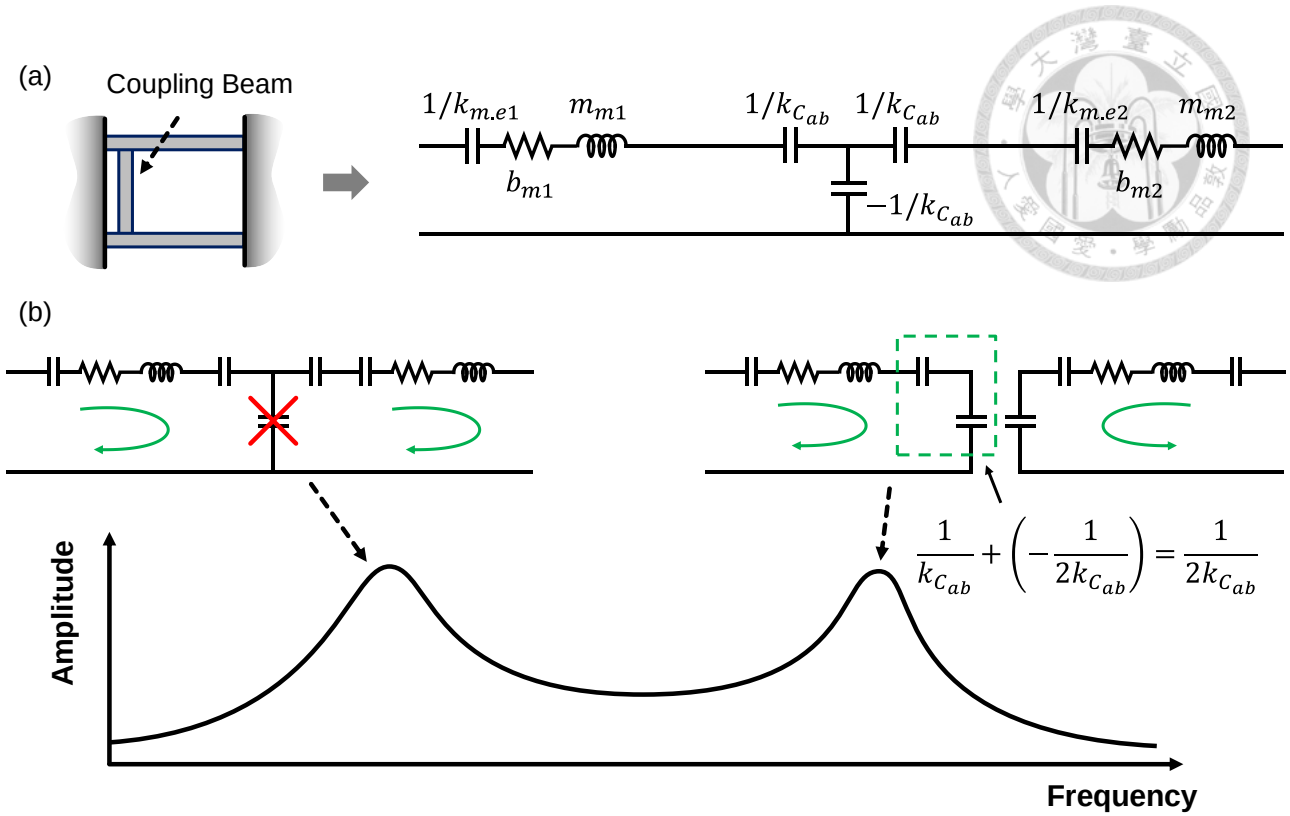


Figure B-48: (a) A lumped-element model of a second-order coupled resonator. (b) Its frequency response, showing the split resonance peaks corresponding to the in-phase and anti-phase modes, with current flows illustrated.

coordinate x and the time t can be expressed as

$$EI\frac{\partial^4 w}{\partial x^4} - N\frac{\partial^2 w}{\partial x^2} + c\frac{\partial w}{\partial t} + \rho bh\frac{\partial^2 w}{\partial t^2} = q(x,t) \tag{B-177}$$

where E is the Young's modulus of the beam material, $I = bh^3/12$ is the second moment of inertia of the beam cross section, N is an applied axial force. ρ denotes the specific mass of the beam material, b and h are the width and thickness of the beam, respectively, c is the viscous drag parameter (drag force per unit length and unit velocity), $q(x,t)$ denotes a transverse force per unit length and represents all externally applied mechanical forces.

Using modal analysis techniques and separation of variable, it can be shown that the solution to (B-184) can be written as follows

doi:10.6342/NTU202600018

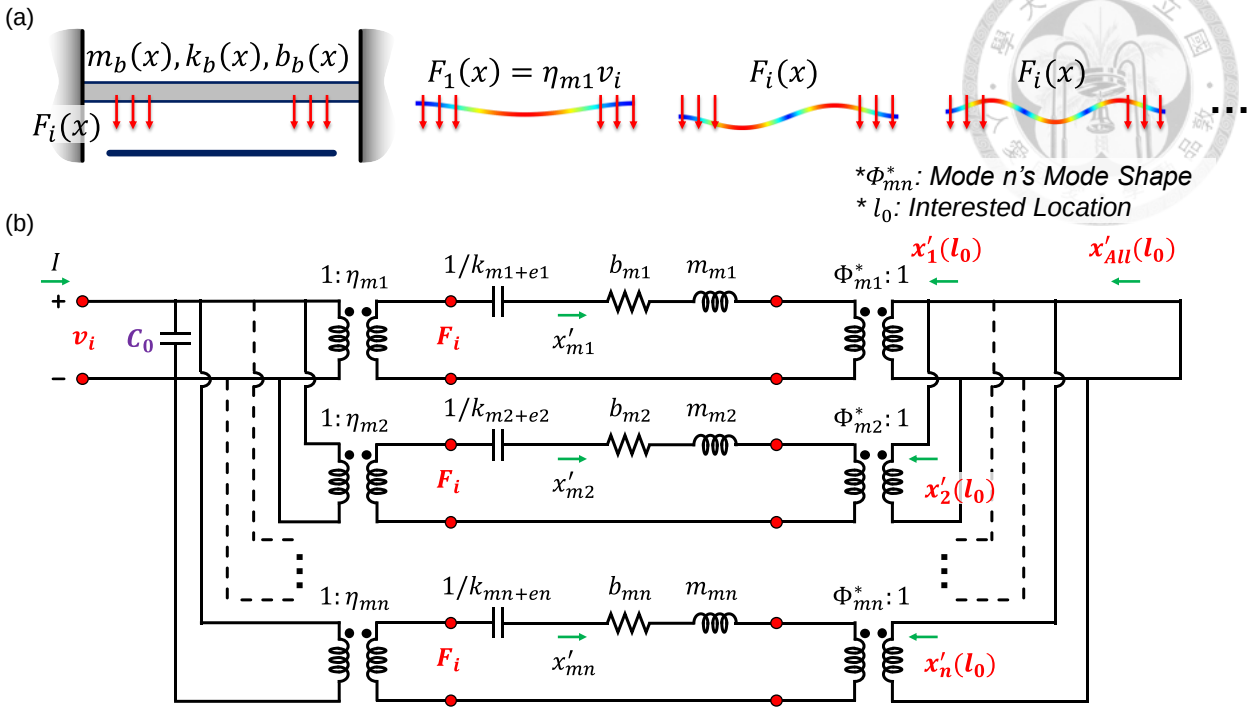


Figure B-49: (a) A example schematic of a CC-beam MEMS resonator considering several modes. (b) Equivalent circuit representations of (a).

$$w(x,t) = \sum_{n=1}^{\infty} \phi_n(x) A_n(t) \tag{B-178}$$

where $\phi_n(x)$ are the normalized mode shapes and $A_n(t)$ are the generalized coordinates. Introducing the series expansion given above into the equation of motion (B-177) and next multiplying each term by a normal mode ϕ_m, integrating along the beam length and calling upon the orthogonality property of the mode shapes leads to

$$M_n A_n''(t) + B_n A_n'(t) + K_n A_n(t) = P_n(t) \tag{B-179}$$

with generalized mass, stiffness, damping and external load, all corresponding to position with maximum amplitude of mode n as

$$M_n = \int_0^l \rho b h \phi_n^2(x) dx \tag{B-180}$$

$$B_n = \int_0^l c \phi_n^2(x) dx \tag{B-181}$$

doi:10.6342/NTU202600018

$$K_n = \int_0^l \phi_n(x) \left[EI \frac{\partial^4 w}{\partial x^4} - N \frac{\partial^2 w}{\partial x^2} \right] dx = \omega_n^2 M_n \tag{B-182}$$

$$P_n(t) = \int_0^l q(x) \phi_n(x) dx \tag{B-183}$$

Figure B-49 shows the equivalent circuit representation of the system considering multiple eigen-modes. Using the clampled-clampled resonator as an example as shown in Figure B-49 (a), by using the mode-superposition principle as expressed by (B-179), leads to an infinite number of ordinary differential equations. Each represent a eigen-mode of the device, and, it is clear that the turn ratio of a constructed device-electrode pair would be related to the mode shape. [18, 351, 352, 530, 531] are suggested for more details.

doi:10.6342/NTU202600018

B.8 Lorentzian Response and Application of FFT

The ring-down response is advantageous for single DOF systems because its output is free of feedthrough current, making it suitable for extracting both linear and nonlinear damping coefficients. In multiple DOF systems, however, the response becomes complex, as the interaction of motional currents from different modes can create a modulated waveform. Furthermore, calculating the Q factor from a discrete frequency response using the half-power bandwidth method (A-34) is prone to inaccuracies, particularly with noisy data, high feedthrough current and low frequency resolution.

Although the procedure in Appendix B.6 allows for modal parameter extraction even when limited feedthrough or noise is present, this chapter presents alternative perspectives. Specifically, it details methods for (i) obtaining a frequency response function from ring-down data [532], and (ii) extracting Q factors and resonance frequencies of MDOF systems by applying a Fast Fourier Transform (FFT) to the ring-down response data and Lorentzian response fitting [533, 534].

B.8.1 Frequency Responses from Ring-down Response

Recalling the ring-down response equation of (A-84) with the application of transformation $\cos(\omega_n t + \phi_\lambda) = \left[e^{i(\omega_n t+\phi_\lambda)} + e^{-i(\omega_n t+\phi_\lambda)}\right]/2$

$$x(t) = \frac{x_0^*}{2}\left[e^{i\phi_\lambda}e^{\left(-\frac{b_r}{2m_r}+i\omega_n\right)t} + e^{-i\phi_\lambda}e^{\left(-\frac{b_r}{2m_r}-i\omega_n\right)t}\right] \tag{B-184}$$

The Fourier transform of (B-184) can be obtained as

$$X(\omega_d) = \frac{x_0^*}{2}\left[\frac{e^{i\phi_\lambda}}{\frac{b_r}{2m_r}+i(\omega_d-\omega_n)} + \frac{e^{-i\phi_\lambda}}{\frac{b_r}{2m_r}+i(\omega_d+\omega_n)}\right] \tag{B-185}$$

where the first term and second term centered at ω_n and $-\omega_n$, respectively.

B.8.2 Lorentzian Response and Parameter Extraction

According to (A-14), the output power of a resonator in mechanical domain is proportional to the square of the displacement as

doi:10.6342/NTU202600018

$$P_m = \frac{C_{m.peak}}{(\omega_n^2 - \omega_d^2)^2 + \left(\frac{\omega_n \omega_d}{Q}\right)^2} \tag{B-186}$$

where $C_{m.peak}$ is a constant.

As frequency near the resonance, it can be approximated as

$$\begin{aligned} P_m &= \frac{C_{m.peak}}{[(\omega_n + \omega_d)(\omega_n - \omega_d)]^2 + \left(\frac{\omega_n \omega_d}{Q}\right)^2} \\ &\approx \frac{C_{m.peak}}{[2\omega_n(\omega_n - \omega_d)]^2 + \left(\frac{\omega_n^2}{Q}\right)^2} \end{aligned} \tag{B-187}$$

which is the same as calculated through the positive frequency part of (B-185).

Similarity, if ignore the effect of parasitic (because no driving signal applied in the ring-down duration, *cf.* Figure 3-19 and Figure B-50), the output power of a resonator in electrical domain is proportional to the square of the voltage also and represented with similar form of

$$P_e \approx \frac{C_{e.peak}}{[2\omega_n(\omega_n - \omega_d)]^2 + \left(\frac{\omega_n^2}{Q}\right)^2} \tag{B-188}$$

As shown, (B-186) and (B-188) do not represent the dependent variable (i.e., P_m or P_e) as a linear combination of the independent variable (i.e., ω_d). In order to full fill the requirement of fitting the frequency response to extract the frequency and quality factor with least squares procedure. The reverse power spectrum function, in general, is introduced

$$\begin{aligned} \frac{1}{P} &\approx \hat{C}\left\{\omega_n^2 - 2\omega_n\omega_d + \omega_d^2 + \frac{1}{4Q^2}\right\} \\ &\equiv \hat{C}\{\omega_d^2 + a\omega_d + b\} \end{aligned} \tag{B-189}$$

where $a = -2\omega_n$, , $b = \omega_n^2 + \frac{1}{4Q^2}$ and $\hat{C}$ is a constant.

doi:10.6342/NTU202600018

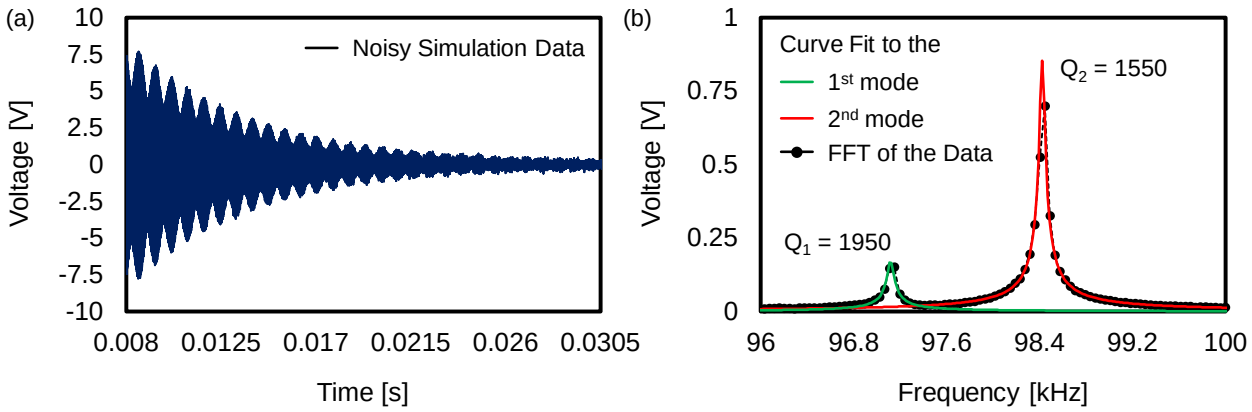


Figure B-50: (a) Time-domain simulation of a two-mode ring-down response. (b) The corresponding frequency spectrum obtained via FFT (black dots), showing the fitted resonance peaks for the first (red) and second (green) modes according to (B-189).

A plot of $\frac{1}{P}$ against ω_d should therefore be a parabola. Fitting a second-order polynomial to values of $\frac{1}{P}$ and ω_d determine the Q-factor and the resonant frequency from

$$\omega_n = -\frac{a}{2} \tag{B-190}$$

$$Q = (4b - a^2)^{-\frac{1}{2}} \tag{B-191}$$

Figure B-50 (b) shows the application of FFT to the output of a two-mode system and implementation of Lorentzian response fitting for the extraction of Q and resonance frequencies.

doi:10.6342/NTU202600018

Appendix C: Introduction to the Surface Interaction Forces

To make sure this dissertation self-sustained. This paragraph focuses on given some basic physical imagination on the surface interaction forces not on the resultant formular but some detailed physical imagination and source that are not presented in the main Chapter, especially Chapter 2. The content for attractive force formulation is referenced to [535] and [139]. For reader who want to know the DLVO theory (named after Boris Derjaguin and Lev Landau, Evert Verwey and Theodoor Overbeek), i.e., description of van der Waals attraction and electric double-layer repulsion as a function of interparticle distance, it is recommended to have a read to [535] and [139]. These forces play a vital role in the daily life and there are many interesting *chemical phenomenon* can be explained with *force* viewpoint (how interesting it is! they are all physics!). For instance, the effect of vinegar on the soy milk and the demonstrated video are shown in [535] and its supplementary.

Scientifically speaking, the DLVO theory, explain how a change on pH value can lead to immediate coagulation in an initially stable dispersion. However, it will not fully explain in this appendix since this appendix focuses on the physical imagination

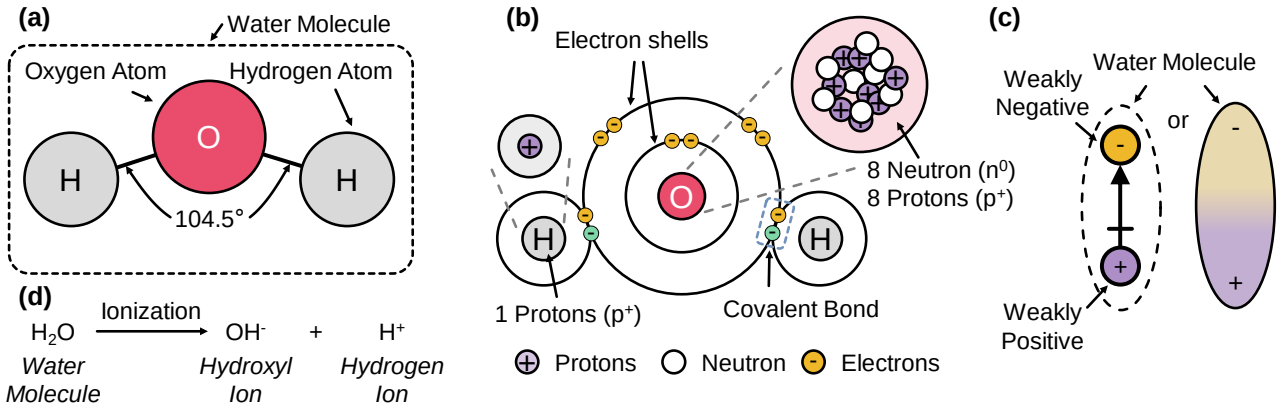


Figure C-1: Illustrations of a water molecule, showing (a) its structural formula, (b) a schematic of the molecule and its atoms, (c) its resulting dipole moment, and (d) its ionization process.

doi:10.6342/NTU202600018

of surface force for some equations in the main content.

The origin of all interactions lies in the four fundamental forces of nature (i.e., the basis for all interaction), namely weak force, strong force, gravitation and electromagnetism, in which the gravitation and electromagnetism are well known and easy to imagine since they are daily observable and in macro scale. Among these forces, electromagnetism is the most significant in explaining chemical processes and *surface interaction force*, however, do not become a common sense for most of mechanical engineers.

Essentially, all interactions between atoms and molecules stem from electromagnetic forces. The presence of condensed phases, such as liquid and solid states, is solely due to the electromagnetic force acting upon molecules and atoms. Figure C-1 (a) shows structural formular of a water molecule and Figure C-1 (b) shows the breakdown schematic of molecules and atom, and corresponding physical quantity. As shown, the atoms (and therefore molecules) are composed of protons (positively charged), neutron (neutral) and electrons (negatively charged). With this configuration, the top and bottom side of the water molecule become weakly negative and positive charged, respectively. Two illustrations describing the dipole moment that arises in a water molecule is provided in Figure C-1 (c). Additionally, Figure C-1 (d) present the ionization process of the water, as shown, when a molecule or atom loses or gains one or more electrons, it acquires a charge and becomes an ion.

As shown in Figure C-2 (a), the interaction energy W_{ion} between ions in a medium, at separation r much larger than their respective radius, can be described by Coulomb's law

$$W_{ion}(r) = k\frac{q_1 q_2}{r^2} = \left(\frac{1}{4\pi\varepsilon_r\varepsilon_0}\right)\frac{z_1 z_2 e^2}{r^2} \tag{C-1}$$

where $k = 1/(4\pi\varepsilon_r\varepsilon_0)$ is a constant representing the effect of the surrounding medium and $q_{i=1,2}$ represent the charge of the ions. z_1 and z_2 are the valences of the interacting ions, respectively. $e = 1.602 \times 10^{-19}$ (C) is the elementary charge, $\varepsilon_0 = 8.854 \times$

doi:10.6342/NTU202600018

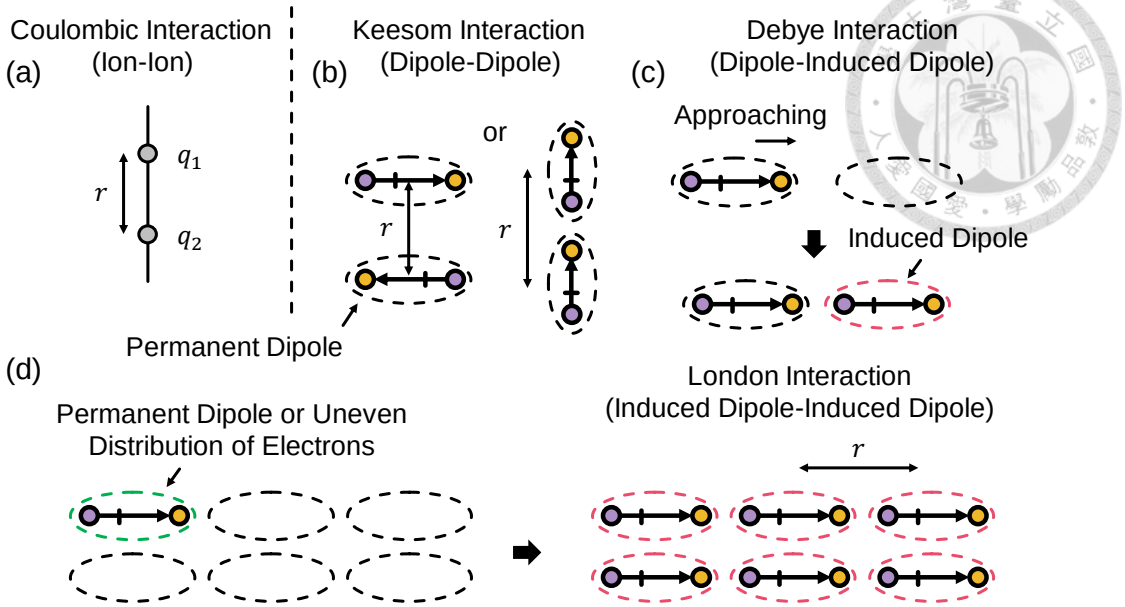


Figure C-2: A depiction of various intermolecular and ionic interactions, including (a) Coulombic, (b) Keesom, (c) Debye, and (d) London dispersion forces.

10^{-12} (f/m) is permittivity of vacuum and ε_r is the relative permittivity of the medium.

Furthermore, van der Waals forces are the grouped force from Keesom, Debye and London interaction. Figure C-2 (b-d) show the schematic of these three mechanisms. First, considering the interaction between polar molecules, which have a permanent dipole moment. As shown in Figure C-2 (b), the positive end of one dipole attracts the negative end of another. If dipoles can rotate freely, such as in gas or liquid phases, they tend to align in a way that maximizes this attraction (i.e., lower energy state). Consequently, the negative end of one dipole is oriented primarily toward the positive end of another dipole, creating a net electrostatic attraction between non-charged polar molecules. This type of interaction is known as the Keesom interaction, which diminishes with the sixth power of the distance between molecules, making it significantly shorter in range compared to ionic interactions. As shown in Figure C-2 (c), polar molecules and ions can influence the electron cloud of another molecule, inducing a dipole moment. This results in a net electrostatic attraction, even between polar and non-polar molecules. This type of interaction is known as the Debye interaction, and it also diminishes with the sixth power of the distance between the

doi:10.6342/NTU202600018

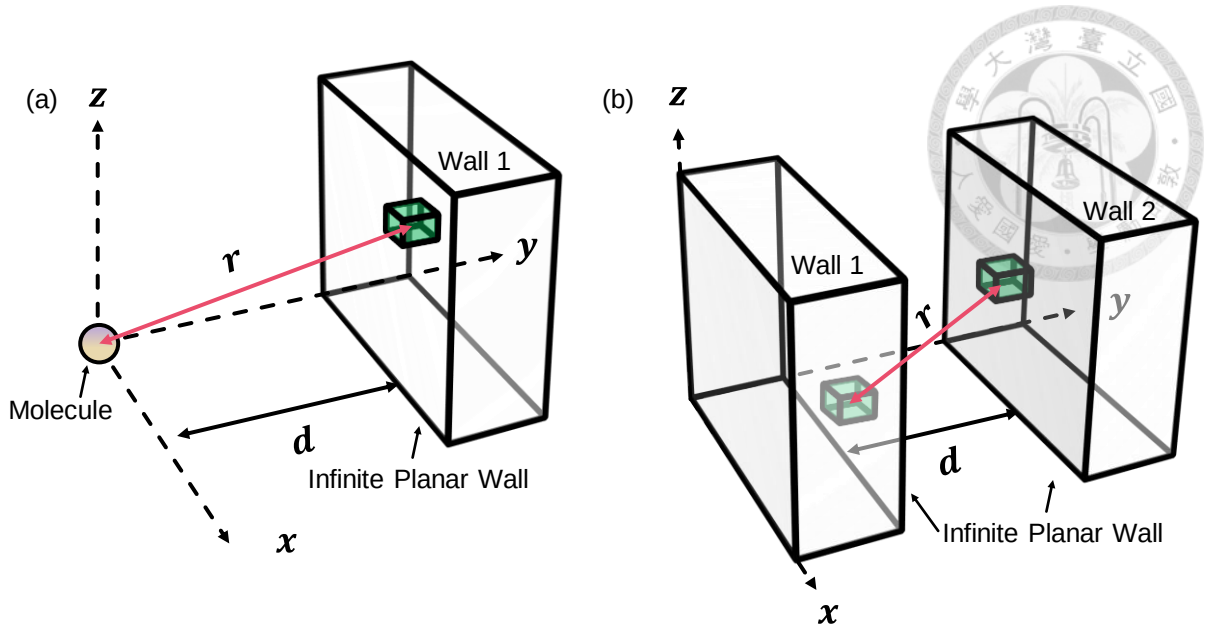


Figure C-3: Schematic diagrams illustrating the interaction forces between (a) a single molecule and an infinite planar surface, and (b) two parallel infinite planar surfaces.

molecules. Finally, due to the constant motion of the electron clouds surrounding all molecules and atoms, an uneven distribution of electrons can occur at any moment. When this happens, the molecule or atom temporarily gains a dipole moment, which can then induce a dipole in a nearby molecule, resulting in an attractive force between them. Of course, this attractive force can be induced by a permanent dipole. This type of force, called the dispersion force or London force, is present between all molecules. Dispersion forces allow elements like helium to condense into a liquid phase. Similar to the Keesom and Debye interactions, this force decreases with the sixth power of the distance between the molecules.

These forces between individual molecules are predominantly electromagnetic and their strength rapidly decreases with distance in power of six, thus they are combined as one commonly known name—van der Waals force. These forces are named after Dutch physicist *Johannes Diderik van der Waals* because he first described the forces in the late 19th century. The van der Waals interaction between two molecules in vacuum takes the form

doi:10.6342/NTU202600018

$$W_{vdW}(r) = -\frac{C_{vdW}}{r^6} \tag{C-2}$$

where the coefficient C_{vdW} includes the contribution from all the interaction and is thus dependent on the permanent dipol moment, polarizability and the first ionization energy of the molecules interacting. In vacuum, C_{vdW} is always positive, indicating that the van der Waals interaction in vacuum is always attractive. Unlike the long-range ion-ion interaction described by (C-1), van der Waals interactions between molecules have a very limited range. Consequently, these attractive forces are only significant when the molecules are in very close proximity.

Consider that there is one molecule away with an infinite planar wall with a given distance of d in the y-axis as shown in Figure C-3 (a), the energy of van der Waals interaction between that single molecule and all molecules within the wall can be approximated as the sum of all interactions as

$$\begin{aligned} W_{vdW(r)} &= \iiint -\rho_{m.1}\frac{C_{vdW}}{r^6}dV \\ &= \int_{-\infty}^{\infty}\int_{d}^{\infty}\int_{-\infty}^{\infty} -\rho_{m.1}\frac{C_{vdW}}{(x^2+y^2+z^2)^3}dxdydz = -\pi\frac{\rho_{m.1}C_{vdW}}{6d^3} \end{aligned} \tag{C-3}$$

where $\rho_{m.1}$ is the density of molecules per volume unit for the wall 1 and $r = \sqrt{x^2+y^2+z^2}$ is the separation between that single molecule and all molecules within the wall. A notable result of (C-3) is that the interaction strength decreases with d^{-3}, as opposed to the d^{-6} dependence seen between individual molecules. This means that the van der Waals interaction between a molecule and an infinite wall extends much farther than the interaction between individual molecules. Consequently, the influence of a wall on a molecule is felt over a greater distance compared to the interaction range between two separate molecules.

Furthermore, applying similar analysis, the energy of total van der Waals interaction between two infinite planar walls as depicted in Figure C-3 (b) can be given as

doi:10.6342/NTU202600018

$$W_{vdW}(r) = \int_{-\infty}^{0}\int_{-\infty}^{\infty}\int_{d}^{\infty}\int_{-\infty}^{\infty} F_{walls}\,dy_1\,dx\,dy_2\,d_z$$
$$= -\pi\frac{\rho_{m.1}\rho_{m.2}C_{vdW}}{12d^2} = -\frac{H_{12}}{12\pi d^2} \quad \text{(C-4)}$$

where $F_{walls} = \frac{C_{vdW}\rho_{m.1}\rho_{m.2}}{[r^2]^3} = \frac{C_{vdW}\rho_1\rho_2}{[(x_2-x_1)^2+(y_2-y_1)^2+(z_2-z_1)^2]^3}$ and $r = \sqrt{(x_2-x_1)^2+(y_2-y_1)^2+(z_2-z_1)^2}$ is the separation of volume differentials. $H_{12} = \pi^2\rho_1\rho_2C_{vdW}$ is the Hamaker constant escribing the interaction between the two walls. This suggests that the van der Waals interaction between planar surfaces extends much farther than it does between individual molecules, as its strength decreases with the square of the distance between them. As a result, the short-range van der Waals forces that act between molecules can generate long-range forces between larger macroscopic objects.

Although, the above statement and equation provide good quantity, the interaction between objects are typically with finite geometries. The particular interesting is to describe the interaction between two spherical objects in common situation. A highly useful relationship for determining the force $F(d)$ between two spheres is given by the Derjaguin approximation. According to this approximation, the force is proportional to the interaction energy $W_{vdW}(d)$ between two planar surfaces, provided that the separation d between the spheres is less than their radius

$$F_{vdW}(d) = \frac{2\pi W_{vdW}(d)}{(1/R_1)+(1/R_2)} \quad \text{(C-5)}$$

whereR_1 and R_2 are radius of the two interacting spheres. If the radius of two spheres is same, the equation reduced as

$$F_{vdW}(d) = \pi R^* W_{vdW}(d) \quad \text{(C-6)}$$

where $R^* = (1/R_1 + 1/R_2)^{-1} = R_1$

The Derjaguin approximation is applicable to various types of interactions, making it extremely valuable for extrapolating results from infinite planar surfaces to finite

doi:10.6342/NTU202600018

spherical ones. This means that the interaction energy between two spheres can be calculated based on the interaction energy between two infinite surfaces, allowing for accurate predictions in practical scenarios. For two spheres with finite size, the energy of van der Waals is given by

$$W_{vdW} = -\int_{\infty}^{d} F(x)dx \tag{C-7}$$

where x is the dummy variable of the separation.

Thus, the energy of van der Waals interaction between two spheres with radius R_1 and R_2 are presented as

$$W_{vdW} = -\frac{H_{12}}{12\pi d} \tag{C-8}$$

It is remarkable that the van der Waals interaction between spherical particles decays linearly with the inverse of the separation distance, much like the Coulomb interaction between ions (*cf.* (C-3)). It becomes evident that the geometry of the interacting objects significantly influences the distance dependence of van der Waals interactions. As a result, spherical particles exhibit a much longer interaction range compared to planar surfaces and other geometrical configurations.

Noted, the Hamaker coefficient H_{12} for the interaction between two different media 1 and 2 can be estimated using the Hamaker coefficients H_{11} and H_{22}, which represent the interactions of each medium with itself. This relationship can be approximately described as $H_{12} \approx \sqrt{H_{11}H_{22}}$ if the environment is vacuum. When media 1 and 2 interact across a space filled with a third medium, medium 3, the resulting Hamaker coefficient can be approximated by $H_{132} \approx \sqrt{H_{131}H_{232}}$ where $H_{i3i} \approx H_{ii} + H_{33} - 2H_{i3} \approx \left(\sqrt{H_{ii}} - \sqrt{H_{33}}\right)^2$ and $i = 1$ and 2. Thus, relationship can be approximately described as $H_{132} \approx \left(\sqrt{H_{11}} - \sqrt{H_{33}}\right)\left(\sqrt{H_{22}} - \sqrt{H_{33}}\right)$. Those expressions illustrate what are known as combining relations. These approximations provide reasonable accuracy, within roughly 10~20%, as long as dispersion forces are the predominant

doi:10.6342/NTU202600018

component of the van der Waals interaction and the dielectric constants are not excessively high [139]. Typically, the Hamaker coefficient for most solid or liquid condensed phases in a vacuum range from 0.4×10^{-19} to 4×10^{-19} J. Also, [139] introduced more precise formulas for calculating Hamaker coefficients based on Lifshitz theory. It is worth pointing out that the term retarded and non-retarded Hamaker constants refer to different approaches in calculating dispersion forces between particles. The non-retarded Hamaker constant gives a simpler, straightforward estimation of the van der Waals forces between particles. The retarded Hamaker constant provides a more accurate description of dispersion forces over longer distances where the Retardation effect is considered [56, 139].

There are several different interatomic potentials that can be combined with energy potential of attractive interaction to model the real situation. In atomic scale, the repulsive force of objects (i.e., atoms) is originally from Pauli repulsion. The resultant force formular describing both attractive and repulsive force commonly take the form of

$$v_{LJ,12-6} = 4\epsilon\left[\left(\frac{\sigma}{r}\right)^{12} - \left(\frac{\sigma}{r}\right)^{6}\right] \tag{C-9}$$

This energy formula, known as the Lennard-Jones potential, is one of the most straightforward to understand and is widely used as the physical basis for molecular mechanics and molecular dynamics simulations. It is extensively applied in computational chemistry, computational physics, and computational materials science to explain and predict material properties, providing a link between molecular-scale phenomena, micro- and macro-scale properties. Please see the content in Chapter 2 for a discussion of different operating situations as described in (2-38) and (2-39).

For larger objects, the discussion shifts to the field of contact mechanics, where the Hertz model, derived from mechanics of materials and continuum mechanics, is the most commonly used formula. Please see the content in Chapter 2 for a discussion for micro and macro-scale situation as described in (2-23) to (2-33). Detailed formulations

doi:10.6342/NTU202600018

for Hertz model can be found in [138], where both qualitative and rigorous treatments offer valuable physical insights.



doi:10.6342/NTU202600018

Appendix D: Characteristic of Vibro-impact Resonators

D.1 Parametrically Numerical Investigations

The time- and frequency-domain responses of a periodically excited vibro-impact resonator with single-sided stopper has been numerically analyzed. Although the choose quality factor is much lower than the real MEMS device, it keep system parameters similar to the main content, and the unique features with varying parameters are carefully presented. This lower quality factor allows for a substantial reduction in simulation time and makes the system easier to analyze without compromising the generality of the results. In particular, parameters such as the forcing amplitude, Hamaker constant (i.e., the measure of attractive force), Young's modules (i.e., the measure of repulsive force), contact viscoelastic damping, gap distance show strong influences on the responses. The resulting tendency of responses on contact force/indentation and nonlinear resonance frequency provides the guidance for the development of theoretical modeling and resoswitch performance optimization.

D.1.1 Introduction

Nonlinear process in mechanical system often occurs though the repeated impact that known as vibro-impact [536], in which the displacement of device is limited and create a strongly nonlinear behavior (i.e., non-smooth stiffness). Traditional macro-scale application of vibro-impact system includes percussion technologies used for penetration, forging, punching etc. [536] and, new applications include machining [537, 538] and vibration protection [292, 539]. Not only that, nonlinear vibro-impact dynamics has been apply to various micro-scale devices recently, including atomic force microscopy [143, 154, 196], vibration energy harvesters [74, 75], communication receiver and surface condition monitoring device [257]. Such devices are one of most challenging subjects in the nonlinear dynamics and have significant influence on engineering. Previously, [156] shows the frequency response with a simple linear

doi:10.6342/NTU202600018

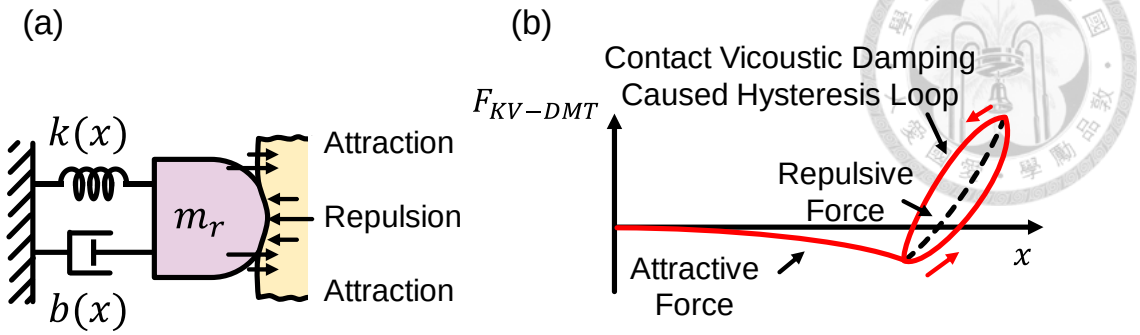


Figure D-1: (a) The 1-DOF lumped mechanical model for the vibro-impact resonators being analyzed. (b) An illustration of the contact model, which incorporates attractive, repulsive, and contact viscoelastic forces.

contact force formulation, [191] shows the effect of the adhesion coefficient—Hamaker constant on displacement frequency response, and [192] shows the influence of double-side stopper configuration on frequency response. However, the effect of the operation conditions such as gap spacing, driving frequency, and driving voltage and material properties on motion behavior is not very clear. As a result, the main purpose in this section is to numerically investigate the steady-state nonlinear motion behavior of the vibro-impact resonators that practically similar to a resoswitch without the electrical influence, including both time and frequency domain responses. Parametrically exploring the system response will help the development of analytic expression and creation of assumptions for a clear mathematical representation of the system.

D.1.2 Modeling Method

The physical model of the forced 1-DOF vibro-impact resonators investigated in this section is shown in Figure D-1 (a). The equation of motion takes the form

$$m_r x'' + (b_r + b_3 x^2)x' + (k_r + k_3 x^2)x = F_d - F_c \qquad \text{(D-1)}$$

where x is displacement. m_r, $b_r = \sqrt{m_r k_r}/Q$, and k_r represent equivalent mass, damper, and stiffness, respectively. Q is quality factor. $F_d = A_d \cos(\omega_d t) = \eta v_i \cos(\omega_d t)$ and F_C are the external driving force and the nonlinear surface interaction

doi:10.6342/NTU202600018

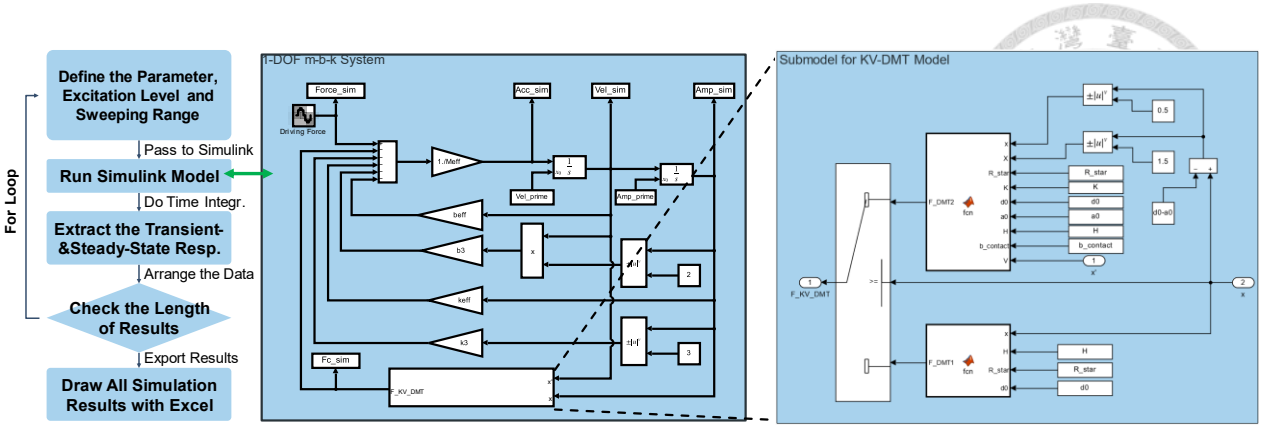


Figure D-2: The simulation workflow is depicted alongside its implementation as a Simulink block diagram. The KV-DMT model is computed within a dedicated block that is based on a *MATLAB* function.

forces.

As shown in Figure D-1 (b), although the device can assume linear contact stiffness in most situation for macro-scale devices for small indentation, the interaction force in micro-scale is much complicated. Because of the increased ratio of surface-to-volume force, the nonlinear repulsive and long-/short-term attractive surface interaction force must take into account to represent the real situation [141]. To be general, the contact induced energy loss is also take into account [313, 314]. As a result, the Kelvin-Voigt DMT (KV-DMT) contact model is chosen

$$F_c = F_{KV-DMT} = -\begin{cases} -\dfrac{HR^*}{6(d_0 - x)^2}; x < d_0 - a_0 \\ -\dfrac{HR^*}{6a_0^2} + K(\delta)^{\frac{3}{2}} + b_c\sqrt{R^*}(\delta)^{\frac{1}{2}}x'; x \geq d_0 - a_0 \end{cases} \quad \text{(D-2)}$$

where R^*, a_0, d_0 and H are the effective radius of curvature of the contact interface, the intermolecular interaction distance, the gap spacing and the Hamaker constant, respectively. $E^* = (1 - v_1^2/E_1 + 1 - v_2^2/E_2)$ is the effective Young's modulus of the contact materials. This model is suitable to investigate the effect of contact materials' mechanical properties.

The above equations were then used in numerical simulation based on MATLAB and Simulink to obtain the tapping mode frequency responses and displacement time

doi:10.6342/NTU202600018

TABLE D-1 SUMMARY OF THE USED PARAMETERS FOR THE SIMULATIONS.

Parameter	Value	Unit
Contact Clearance, d_0	0.72	μm
Quality Factor, Q_0	100	-
Lumped Mass, m_r	0.96×10^{-10}	kg
Lumped Stiffness, k_r	66.91	N/m
Nonlinear Stiffness, k_3	-1.2×10^{11}	N/m^3
Lumped Damper, b_{r0}	2.74×10^{-8}	N•s/m
Nonlinear Damper, b_{30}	1.09×10^{5}	$N•s/m^3$
Linear Resonant Frequency, f_0	132.80	kHz
Electromechanical Coupling Coefficient, η	2.5711×10^{-7}	N/V
Driving Voltage, v_{i0}	30	V
Hamaker Constant in Vacuum, H_0	$20\times15.73\times10^{-20}$	J
Interatomic Spacing, a_0	0.165	nm
Poisson's Ratio, $v_{i=1,2}$	0.2	-
Young's Modulus, $E_{i=1,2}$	224.54	GPa
Effective Youngs's Modulus, E_{c0}	119.75	GPa
Effective Tip Radius, R^*	400	nm
Contact-stiffness Parameter, K_0	1.01×10^{8}	$N/m^{3/2}$
Viscoelastic Contact Damping, b_c	10^4	$N•s/m^2$

history as well as contact force time history. Figure D-2 summarizes the simulation flow and Simulink block diagram used in this study. Simulink will perform the simulation of a particular excitation frequency with build-in time integration function based on Runge-Kutta Dormand-Prince (RKDP) method (i.e., *ode45* in MATLAB. After simulation, the contact force and displacement time histories are extracted.

To mimic the standard frequency sweeping measurement method, each of the frequency steps requires the information of amplitude, velocity, and phase of the previous frequency point as the initial conditions. The information extracted based on the time-domain waveforms of the last 50 stable cycles of the previous step obtained in Simulink is first passed to MATLAB for computing the simulation conditions, i.e., amplitude, velocity, and phase, all of which then return to Simulink to perform the time-domain simulation of the particular frequency point, simultaneously, the phase

doi:10.6342/NTU202600018

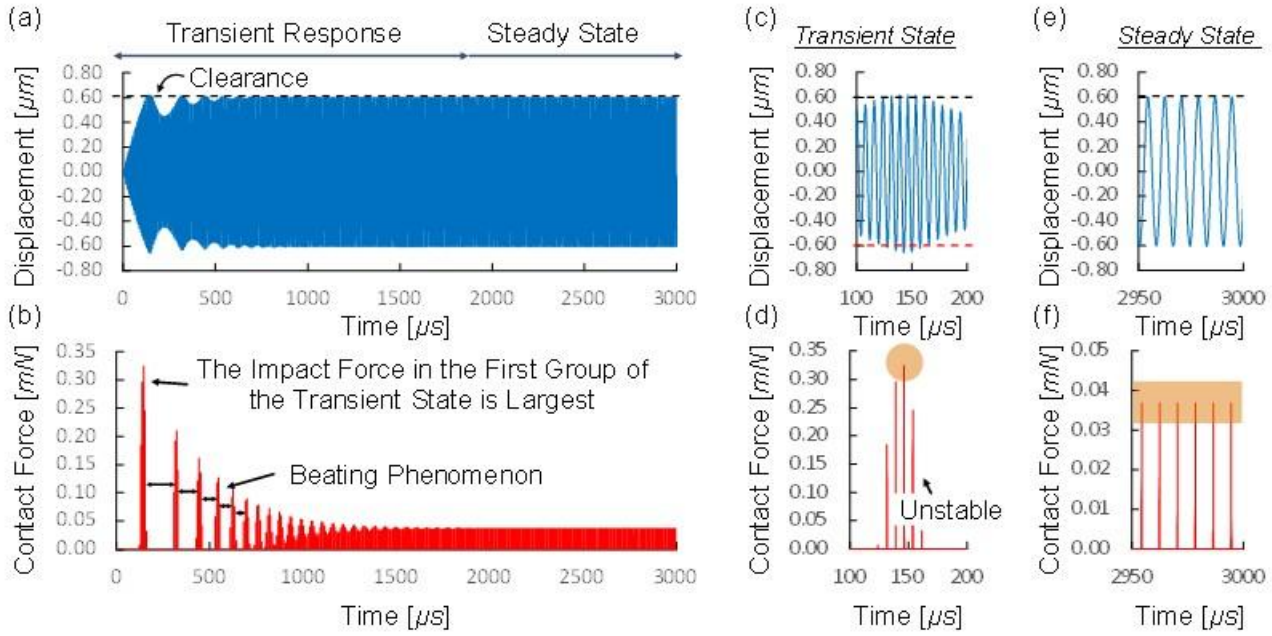


Figure D-3: Simulated time-domain responses for a vibro-impact resonator that is driven at its resonance frequency, starting from rest. The complete time histories for (a) displacement and (b) the corresponding contact force are presented. A comparison between the transient and steady-state phases is provided through detailed views: (c) and (d) highlight the initial transient behavior, which features a significant overshoot, while (e) and (f) show the stable, lower-amplitude response in the steady state.

portrait and contact force are extracted. Repeating this procedure for points across the frequency range of interest finally arrives the numerically simulated frequency response and time response of the vibro-impact resonators. It is worth noting that, the initial conditions at each frequency step affect the response significantly [156]. Each of parameters shown in (D-1) and (D-2) has been studied separately by keeping the other parameters fixed or variedly. The standard values of simulation parameters are listed in TABLE D-1 and the parameters used in following parametric study are labeled in the figures.

D.1.3 Time-domain Response Features

For illustration, Figure D-3 shows the general response for time-domain motion. Clearly, due to the damping caused constructive intervention, the largest contact force

doi:10.6342/NTU202600018

is found in transient state, and both displacement and contact force settle down to steady state with lower value after certain duration. In transient state, the beating phenomenon is found due to non-resonance but near-resonance condition. As marked, the maximum contact force is much larger than the steady-state contact force, and it will be investigated in next sub-section in detail. On the other hand, it should be noted that the contact force in transient is very unstable, it might be the source of squegging phenomenon in on-off keying (OOK) or frequency-shift keying (FSK) operation for resoswitch-based receiver. See Chapter 3 for detail.

D.1.4 Frequency-domain Response Features

Figure D-4 shows the simulated displacement amplitude frequency response for structural nonlinearity and electrostatic nonlinearity. Figure D-4 (a) shows the response with varying value of van der Pol damping. As shown, the van der Pol damping lower the overall quality factor and thus lower the amplitude in high amplitude level, however, the effect is weak for displacement amplitude lower than a certain value. Figure D-4 (b) shows three combinations of linear quality factor and driving voltage while keep the product of driving-voltage and quality factor constant. As shown, the maximum amplitude is the same, indicating that the effect of van der Pol damping is amplitude dependent. The small divergences come from the insufficient frequency resolution. Figure D-4 (c) shows the frequency responses with varying value of Duffing stiffness. The amplitude become higher and lower with negative Duffing stiffness and positive Duffing stiffness, respectively. However, the value of Duffing stiffness and the amplitude is quite large here, and it is shown in [398] that the frequency change is observable even if the amplitude change is ignoble as the nonlinearity is weak enough. Figure D-4 (d) shows the frequency response with four combination of linear quality factor and driving voltage while keep the product of driving-voltage and quality factor constant again. As shown, the frequency changes are related to the amplitude like what occurs in the cases for van der Pol damping.

doi:10.6342/NTU202600018

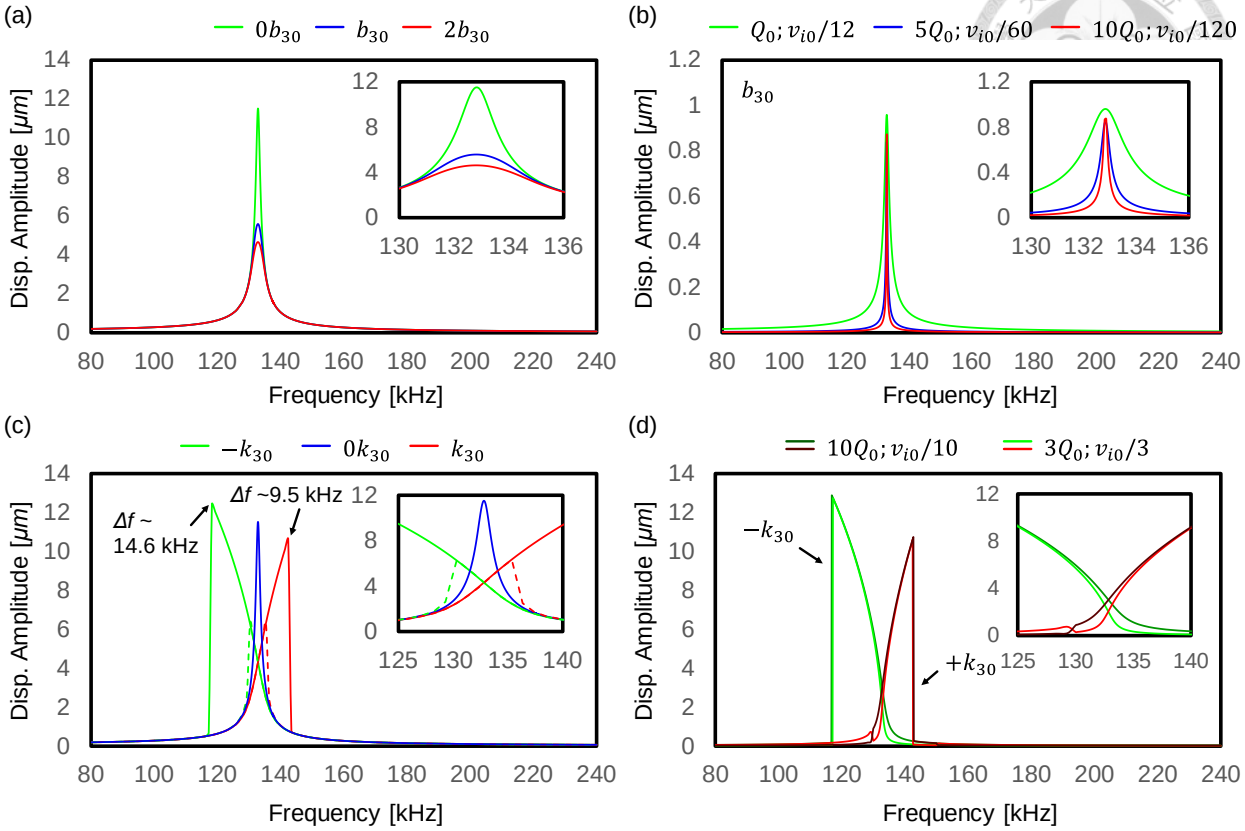


Figure D-4: Computed frequency responses for the resonator, demonstrating the effects of intrinsic nonlinearities. (a) The response is shown for different levels of nonlinear damping while excluding nonlinear stiffness. (b) The amplitude-dependent characteristic of the damping is illustrated by maintaining a constant product of the quality factor and driving voltage. (c) The influence of varying both positive and negative nonlinear (Duffing) stiffness is displayed. (d) A similar analysis with a constant product of quality factor and driving voltage is performed, this time including the nonlinear stiffness effects.

doi:10.6342/NTU202600018

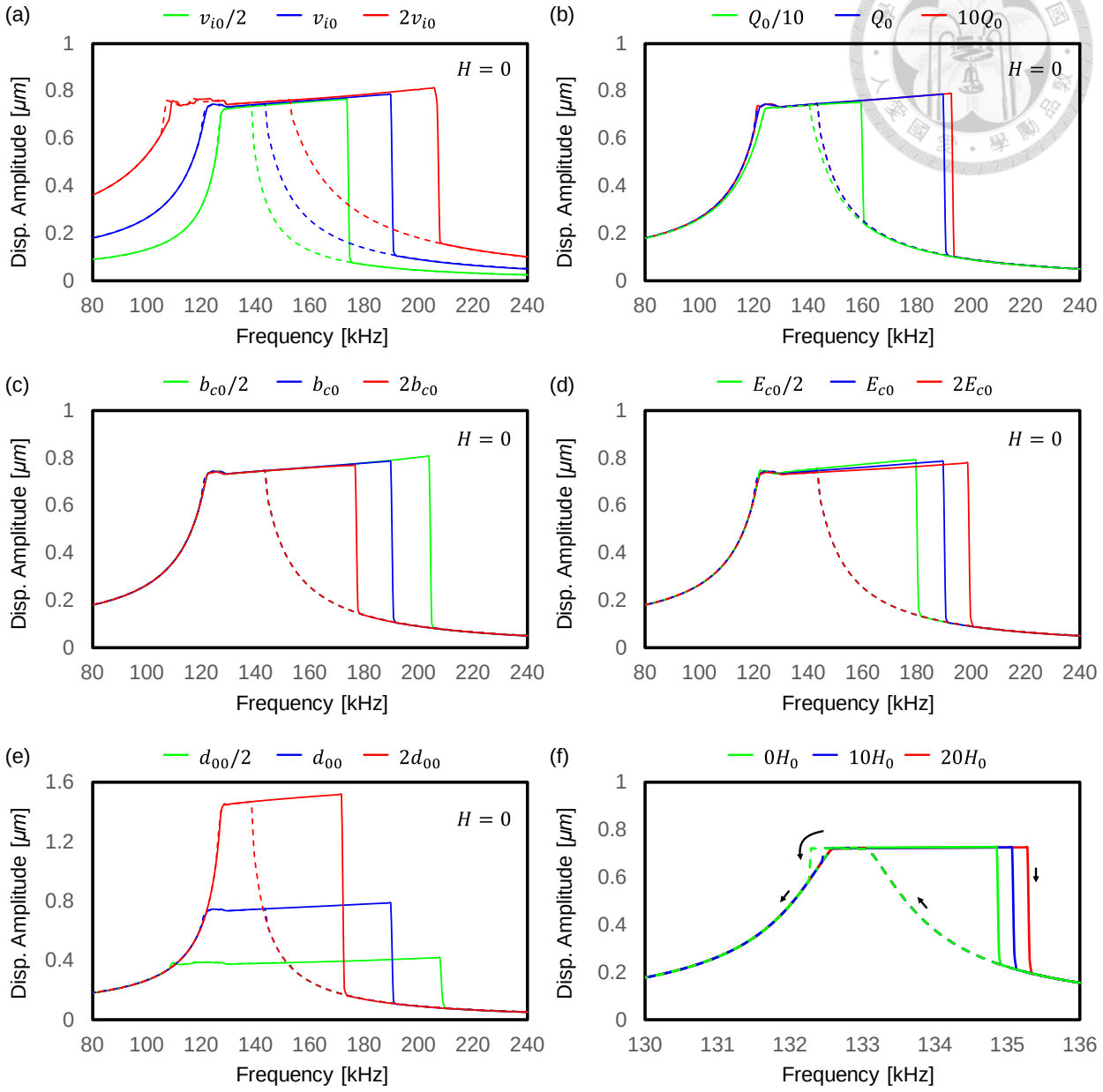


Figure D-5: Numerically generated frequency responses for the vibro-impact resonator, illustrating a parametric study of the system's behavior. The individual plots show the effects of varying (a) driving voltage, (b) quality factor, (c) contact viscoelastic damping, (d) Young's modulus of the contact material, (e) gap spacing, and (f) Hamaker constant.

doi:10.6342/NTU202600018

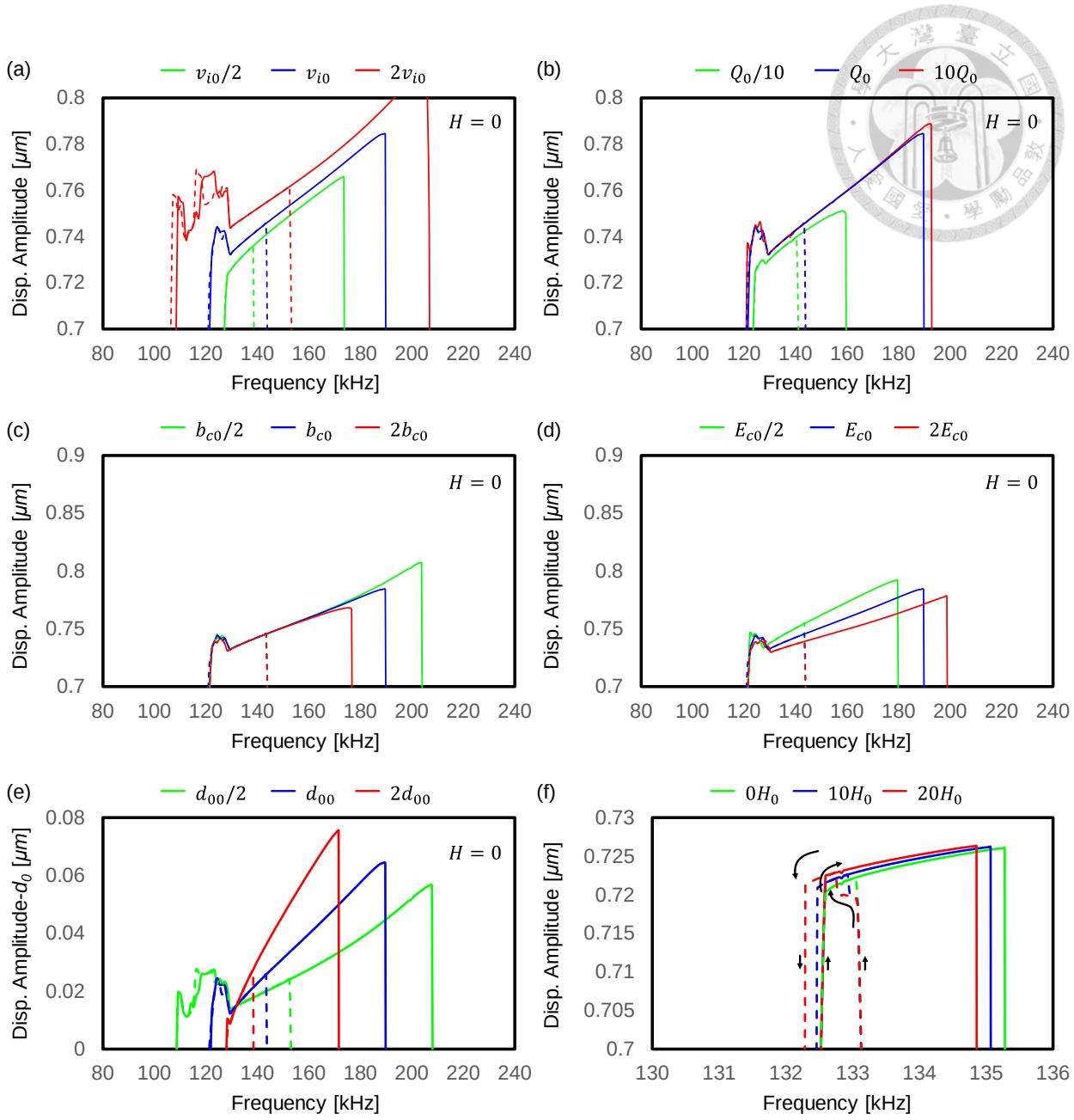


Figure D-6: Magnified views of the tapping responses from Figure D-5. These plots offer a closer look at the complex dynamics near the onset of impact, including the period-doubling bifurcations that are difficult to see in the full-scale plots.

doi:10.6342/NTU202600018

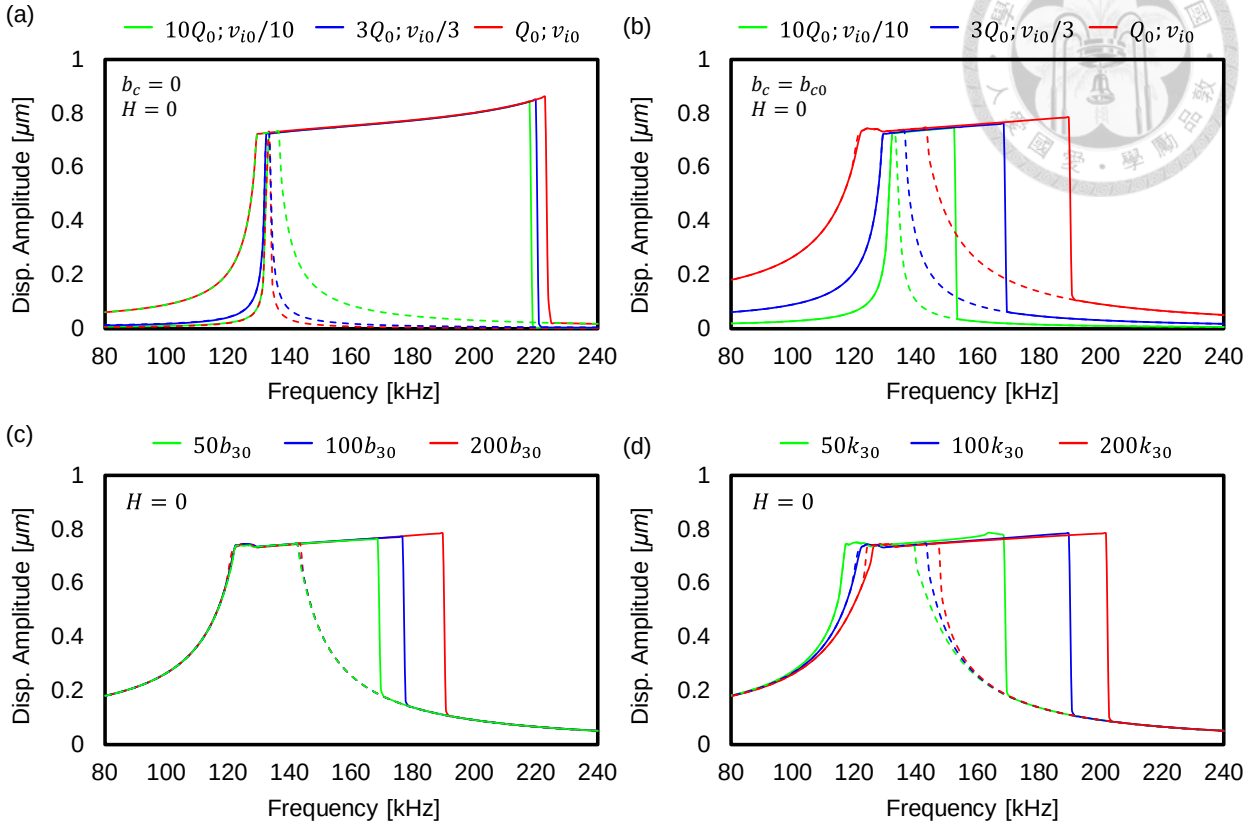


Figure D-7: A comparison of simulated frequency responses for the vibro-impact resonator under different conditions. (a) The effect of varying the product of driving voltage and quality factor is shown for a system without contact viscoelastic damping. (b) The same analysis is repeated for a system that includes contact viscoelastic damping. (c) The impact of varying nonlinear damping is illustrated. (d) The influence of varying nonlinear stiffness on the frequency response is presented.

As shown in Figure D-5 and Figure D-7 and the zoom-in to the near contact region of Figure D-6 and Figure D-8, each of these parameters has been studied. Please see the figures pair simultaneously for deep understanding. It is noteworthy, the strange response near the first grazing point are the responses with period-doubling bifurcation, they will be discussed in next sub-section. Figure D-5 (a) and (b) and Figure D-6 (a) and (b) show that, the tapping bandwidth increases as the driving voltage or quality factor increases. The indentation at linear resonance frequency increases as the driving

doi:10.6342/NTU202600018

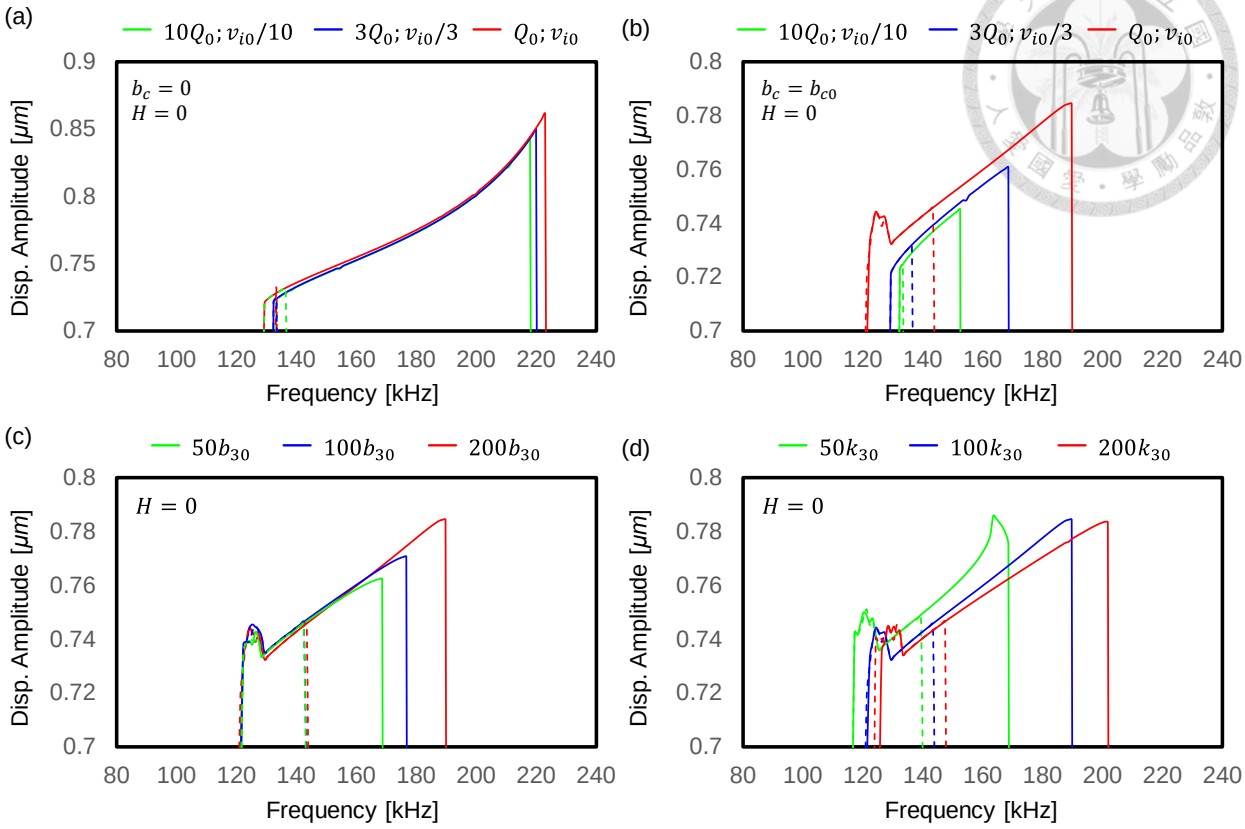


Figure D-8: Magnified views of the tapping responses from Figure D-7. These plots offer a more detailed look at the complex dynamics occurring near the contact region.

voltage increase but the increment of indentation at linear resonance frequency as the quality factor increased is ignorable after certain value. This is because that the nonlinear resonance frequency becomes too high and the benefit of the quality factor loosed (i.e., out-of-resonance). Noted, the tapping bandwidth increasing with increased driving voltage are due to not only the increased nonlinear resonance frequency but also the lower grazing frequency. As illustrated in Figure D-6 (b), The change of grazing frequency for higher quality factor is ignorable because the grazing frequency becomes too far away to the linear resonance frequency thus the responses for different quality factor are almost same as the grazing frequency is located at non-resonance region where again the benefit of the quality factor loosed.

In Figure D-5 (c) and Figure D-6 (c), the contact damping present negative effect for high indentation situation where the effective quality factor decreases and the

doi:10.6342/NTU202600018

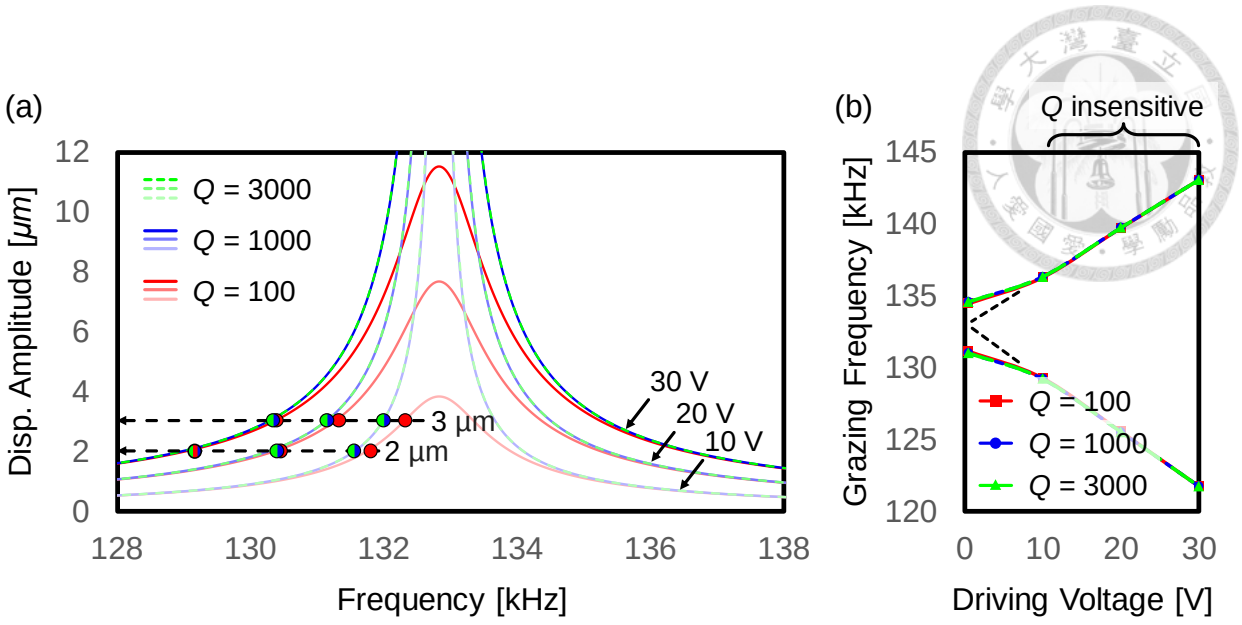


Figure D-9: (a) The simulated frequency response of the linear system is shown for a range of driving voltages and quality factors. (b) The corresponding grazing frequencies, extracted from the response curves in (a), are plotted to illustrate their dependence on driving voltage.

nonlinear resonance frequency decreases as the effect of contact damping increases. However, the contact damping present weak effect for indentation near linear resonance frequency, indicating that the nonlinear damping is ignorable for small indentation. Moreover, this also indicate that a lower contact damping is necessary to realize a wider frequency bandwidth. However, in a limited parameter space, this study does not find benefit of a lower contact damping for indentation or contact force at near linear resonance frequency region. Besides, as the stiffness of the contact material increases (*cf*. Figure D-5 (d) and Figure D-6 (d)), the indentation decreases for each frequency in the tapping region, and the nonlinear resonance becomes higher.

The frequency response with various gap spacing is shown in Figure D-5 (e) and Figure D-6 (e). As can be seen, a shorter gap distance results in a wider frequency bandwidth at the expense of a reduction in the relative indentation. The adhesion force provides effectively negative stiffness for the system and effectively lower the nonlinear resonance frequency and increase the indentation as presented in Figure D-5

doi:10.6342/NTU202600018

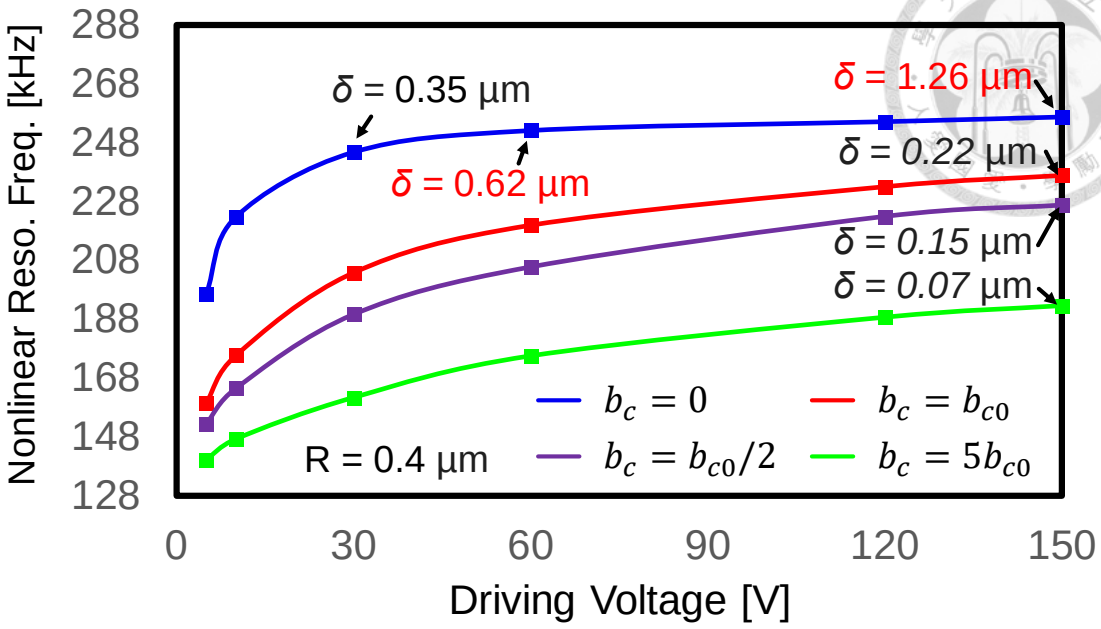


Figure D-10: A plot of the extracted nonlinear resonance frequency versus the driving voltage for a vibro-impact resonator, illustrating the effect of varying contact viscoelastic damping. The curves show that the resonance frequency undergoes an initial development, followed by rapid growth, and eventual saturation as the driving voltage is increased.

(f).

Figure D-7 (a) and (b) and its zoom-in to the contact region of Figure D-8 (a) and (b) present the frequency response with different combinations of driving voltage and quality factor. Combining the observation from Figure D-5 (b) and Figure D-6 (b), one can conclude that the change of resonance frequency from surface interaction force is also amplitude dependent and the effect of quality factor contribute less if it is high enough (i.e., $Q \gg 1$). Figure D-7 (c) and Figure D-8 (c) show the frequency responses for varying van der Pol damping, the contributions are similar to nonlinear contact damping. Figure D-7 (d) and Figure D-8 (d) show the frequency responses for varying Duffing stiffness, the contributions are similar to attractive and repulsive force represented by Hamaker constant and Young's modulus as shown in Figure D-5 (f) and Figure D-5 (d). In Figure D-8 (d), the period-doubling bifurcation is observed near the nonlinear resonance frequency, again, it will be discussed in next sub-section in

doi:10.6342/NTU202600018

detail.

Figure D-9 (a) presents the linear frequency response of the system under varying driving voltages and quality factors. Two illustrative lines indicating the collision gap are marked on the graph, and their intersections with the frequency response curves denote the grazing frequency points predicted by linear theory. Figure D-9 (b) shows the extracted plot of driving voltage versus grazing frequency, revealing that beyond a certain driving voltage, the grazing frequency becomes insensitive to the quality factor and exhibits a linear relationship with the driving voltage.

As shown in Figure D-10 for nonlinear resonance frequency verses driving voltage, the second Saddle-node bifurcation (i.e., the jump point in the forward sweeping operation) experience initial development, rapid growing and finally saturated at certain frequency for varying contact viscoelastic damping. For cases with contact damping, it is found that the nonlinear resonance frequency approach certain value because the effective quality factor becomes smaller, representing no increment of indentation. For no contact damping case, it is found that the nonlinear resonance frequency approach certain value if the indentation approaches the effective contact radius. One might explain this by that the overall effective stiffness become so large that the indentation can not be increases as the driving voltage increases even at resonance condition.

D.1.5 Stability and Basin of Attraction

In order to unveil the detail for the device feature and the importance of the initial condition for the device response. As marked in Figure D-11 (a), a frequency point of 170 kHz within the bistable region is chosen as the illustrative example where the frequency response is copied from Figure D-5 (a). In bistable region, there are two possible solutions for a frequency value and the final steady-state response are determined by the initial condition if driven by a single tone frequency. Figure D-11 (b) shows the time-history plot from two closed I.C.s in the beginning and the steady state, respectively. Figure D-11 (c) shows the phase portrait in both states and the

doi:10.6342/NTU202600018

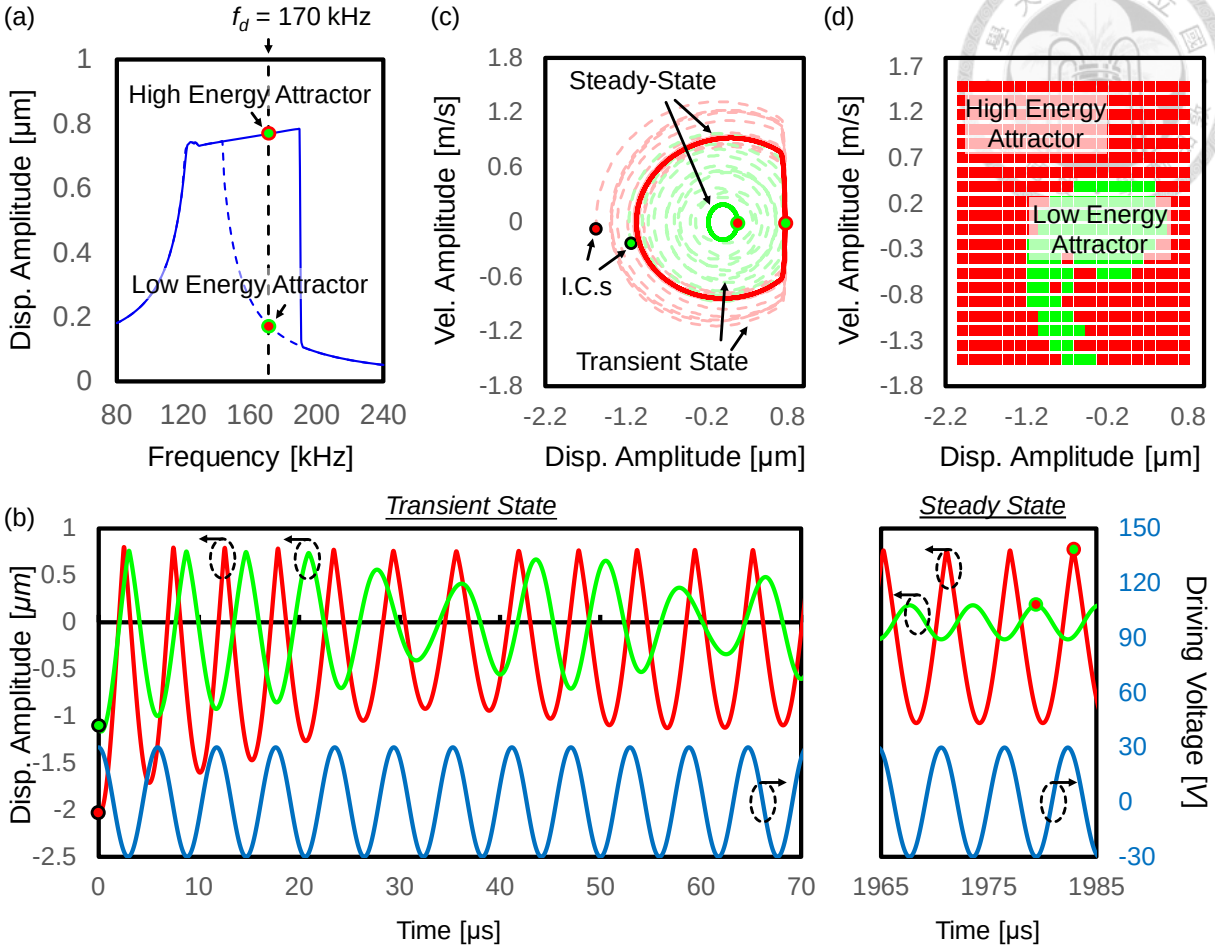


Figure D-11: An analysis of the system's bistable behavior, demonstrating how initial conditions determine the final steady-state motion. (a) The frequency response from Figure D-5 (a) is reproduced to identify the bistable region where high- and low-energy attractors coexist. (b) Time-domain simulations starting from two different initial conditions, $(x, x') = (-1\ \mu m, 0)$ and $(x, x') = (-2\ \mu m, 0)$ show that the system evolving to two distinct steady-state responses. (c) The complete trajectories are visualized in a phase portrait, which displays the initial conditions (I.C.s), the transient phase, and the final steady-state solutions. (d) A basin of attraction map, calculated for a driving frequency of 170 kHz, illustrates the sets of initial conditions that converge to each of the two stable attractors.

Poincaré map at steady state of the Figure D-11 (b). By searching the response over a parameter space with intervals $-2 \times 10^{-6} \leq x \leq 0.75 \times 10^{-6}$ (m) and $-1.5 \leq x' \leq 1.5$ (m/s), one can find the basin of attraction as shown in Figure D-11 (d). This basin of attraction map reveals the effect of I.C. to the final state of the system.

doi:10.6342/NTU202600018

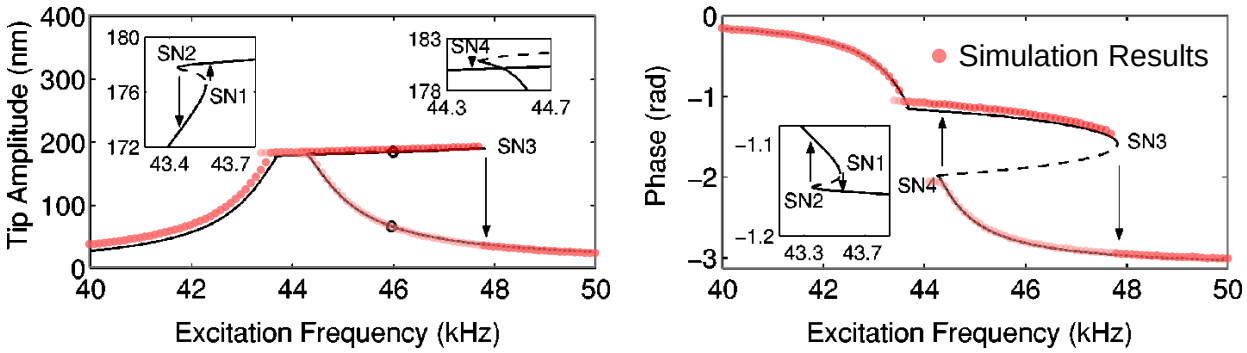


Figure D-12: A validation of the simulation platform is presented by comparing its output to the results from [58]. The excellent agreement between the simulation and the previously published data confirms the accuracy and reliability of the developed model. Reproduced with permission of [58], Copyright © 2002 by American Physical Society.

D.1.6 Remarks for Simulation Conditions

In the numerical simulation, there are some important simulation parameters, including frequency step size, sampling rate and simulation time. They affect the simulation results significantly. Although, the sampling rate will not affect the response too much because the response will be stable and satisfy the tolerance with the MATLAB build-in Newton iteration. The lower the sampling rate the lower the phase and steady state (i.e., displacement and velocity) resolution, thus it will in term affect the stability of the response for next simulation run. In this work, at least 100 points per cycle is chosen (i.e., $t_{sample} \geq 1/(100f_0)$) and sometime it will be larger than 400 points per cycle (i.e., $t_{sample} \geq 1/(400f_0)$). On the other hand, the simulation time is at lease larger than Q time oscillation (i.e., $t_{sim} \geq Q/f_0$) in this work even the state difference between each simulation frequency is small. A small to medium frequency step size of ~0.5 kHz is the standard value for the frequency response simulation. Noted, the resonance condition (i.e., 90° phase shift) at nonlinear resonance frequency is check every single simulation run to ensure the correction of simulation. Also, the simulation platform is checked with [58] as shown on Figure D-12.

D.1.7 Conclusions

This work yields several time and frequency domain responses of a single-side

doi:10.6342/NTU202600018

vibro-impact resonator and investigate the system behaviors with different material properties, device parameters and excitation frequencies comprehensively, providing a helpful understanding for vibro-impact resonators.

doi:10.6342/NTU202600018

D.2 Periodic-Doubling Bifurcation and Comb Generation

Both experimental and numerical investigations on the frequency comb generation of the CMOS-MEMS vibro-impact resonators are studied. In particular, the mechanism of frequency comb generation via the period-doubling bifurcation are presented numerically. The frequency comb generation of two devices, namely folded-beam comb-driven and clamped-clamped beam resonator, are experimentally studied. Both symmetric and asymmetric frequency comb generation based on the vibro-impact resonators are reported. In addition, the spectrums with chaotic motion created by vibro-impact operation are presented.

D.2.1 Introduction

Recently, mechanical frequency combs have been extensively studied due to their promising potential in enhancing the performance of various applications. For instance, frequency combs have been utilized to improve energy extraction in energy harvesting [540, 541] and demonstrated as a ranging sensor [542]. Besides, the theoretical development [27, 34, 543] and experimental investigation [544, 545], to name a few, with more and more new phenomenon and observation are attractive for the researchers on the application of frequency combs recently.

In CMOS-MEMS platform, the internal resonance-based frequency comb was first reported by [546] with one-to-six ratio and has been applied as temperature sensors [547, 548], random number generator [549, 550], binary phase shift keying demodulator [551] and physical unclonable functions [552] with stepped beam structures. [553] reports the output frequency comb at not only near the fundamental tone but also higher harmonic tones for a nonlinearly driven CMOS-MEMS wide-width beam resonator recently.

As best what author can tracked, the frequency comb generation showing with comb spectrum on MEMS vibro-impact resonator was presented by [123] for the first time while presented with time-domain period-doubled pattern in [554] for the first time. Recently, [274] and [555] generate internal resonance through impacting and achieved

doi:10.6342/NTU202600018

frequency comb with detailed analysis. In this study, the early investigation for the frequency comb generation of the CMOS-MEMS vibro-impact resonators is reported. This is essentially the base for the study presented in Section 4.2.

D.2.2 Theoretical Analysis through Numerical Simulation

Figure D-13 displays the schematic of the vibro-impact resonator's period-doubling route. It is commonly understood that routes to chaos are sequences of intermediate states a system undergoes while transitioning from a stable to a chaotic state due to parameter changes. The period-doubling route, where the oscillation period doubles repeatedly until it becomes infinite, indicating chaos, is the most commonly observed route. Additional routes, such as the disintegration of a quasiperiodic torus [52] also exist in MEMS field. As depicted, after grazing occurs, period-doubling bifurcation takes place, typically near the grazing bifurcation with a saddle-node type discontinuous feature as outlined in Chapter 2, indicating that period-doublings do not develop smoothly. The physical model of the forced 1-DOF vibro-impact resonator investigated in this work and the simulation method are same as presented in Appendix D.1 (*cf.* Figure D-2). The used parameters values are shown in TABLE D-1.

Figure D-14 (a)-(c) illustrate the frequency responses at three different driving voltages of 30, 60, and 120 V. The maximum displacement amplitudes are shown with solid lines, and the minimum with dashed lines. It is evident that the vibration displacement becomes asymmetric and increases as the frequency approaches the nonlinear resonance frequency due to the stopper restricting motion in the positive direction. Notably, displacement enlarges in certain regions even away from the nonlinear resonance frequency. To clearly demonstrate this, Figure D-14 (d) and (e) depict the bifurcation diagrams (*cf.* Section 2.2.2 and 2.2.3) near the first grazing point for Figure D-14 (b) and (c), showing that these particular events are due to period-doubling bifurcations.

doi:10.6342/NTU202600018

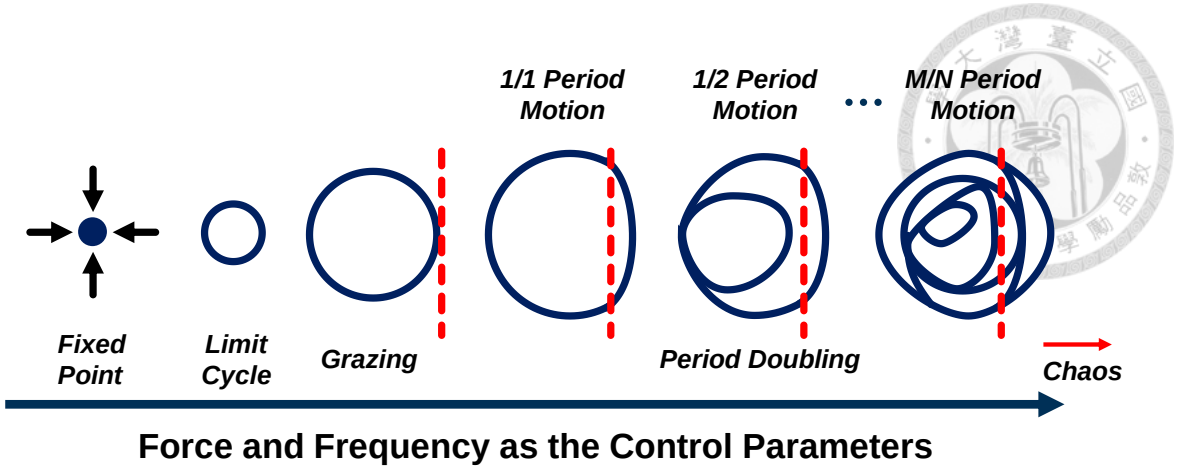


Figure D-13: A diagrammatic representation of the period-doubling route to chaos in a nonlinear system. As control parameters such as force and frequency are adjusted, the system's motion evolves from a stable fixed point to a limit cycle, followed by a grazing impact, and then progresses through a cascade of period-doubling motions, ultimately leading to chaos.

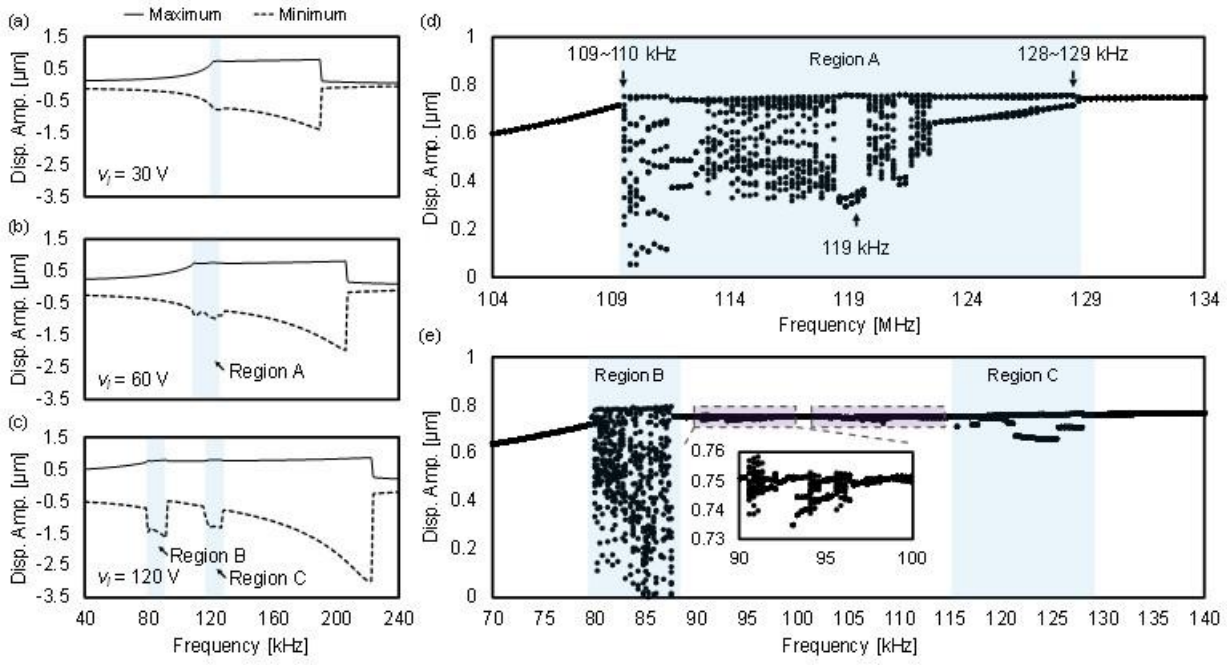


Figure D-14: A comparison of the system's frequency response at driving voltages of (a) 30 V, (b) 60 V, and (c) 120 V. To further analyze the dynamics, bifurcation diagrams corresponding to the 60 V and 120 V cases are presented in (d) and (e), respectively. These diagrams were derived using a stroboscopic Poincaré section taken at the maximum displacement.

doi:10.6342/NTU202600018

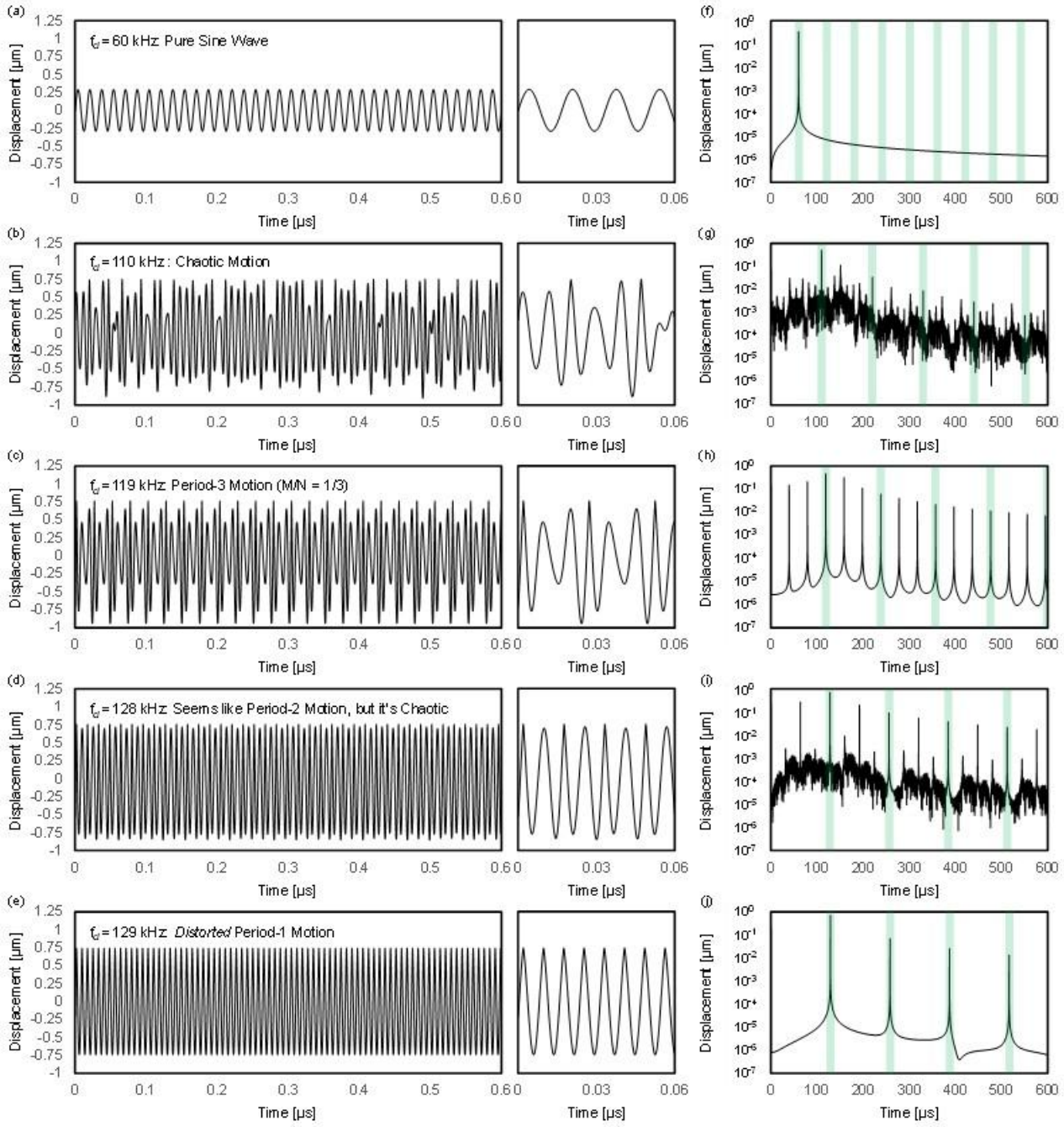


Figure D-15: The time-domain steady-state motion of the system at five distinct driving frequencies, along with their associated FFT spectra. The waveforms are shown for (a) 60 kHz, (b) 110 kHz, (c) 119 kHz, (d) 128 kHz, and (e) 129 kHz. The corresponding frequency spectra for each case are displayed in (f-j).

doi:10.6342/NTU202600018

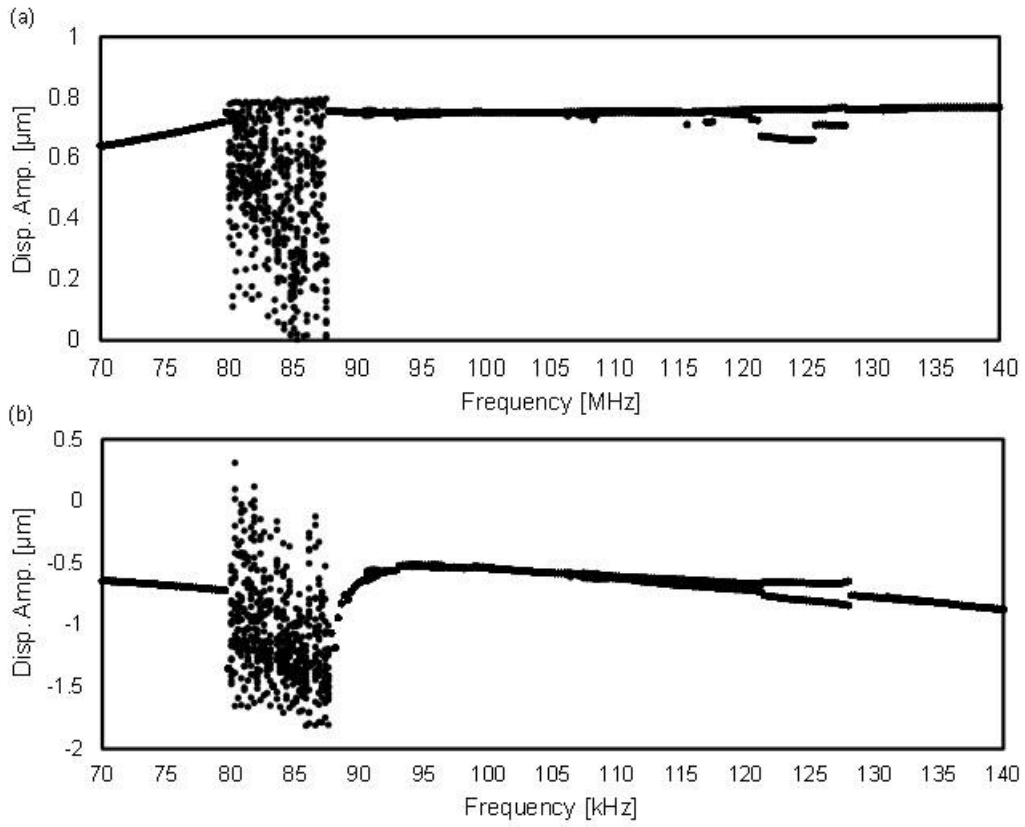


Figure D-16: The bifurcation plot from Figure D-14 (e) is displayed again, this time representing the system's motion by plotting both (a) the maximum and (b) the minimum displacement of the periodic orbits.

Additionally, Figure D-15 displays the time-domain motion and its fast Fourier transform (FFT) spectrum for five specific frequencies under a 60-V driving voltage, demonstrating five basic types of responses. Figure D-15 (a) presents a pure sine wave response without impact, far from the tapping region, hence the FFT spectrum shows a single peak. Figure D-15 (b) to (e) depict responses with impacts from low to high frequency. Comparing (a) and (e), it is observed that the distorted waveform generates higher-order harmonics, with the frequency of the nth harmonic being n times the frequency of the fundamental frequency (i.e., driving frequency). Moreover, Figure D-15 (c) portrays the period-3 motion response with a low-frequency envelope that is three times lower than the driving frequency, which then represents frequency combs in the frequency domain with three-times lower frequency spacing.

doi:10.6342/NTU202600018

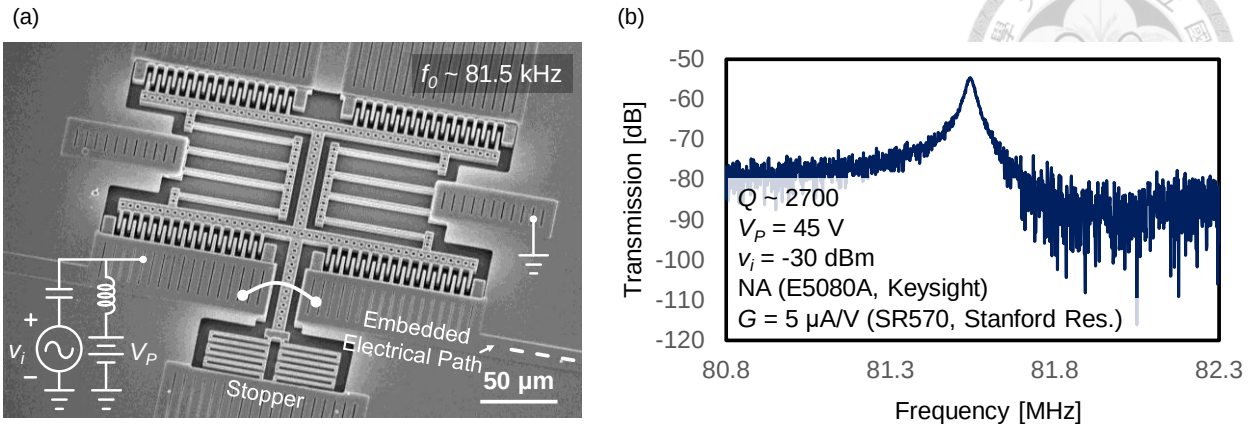


Figure D-17: (a) An SEM photograph of the 80-kHz comb-driven folded-beam resonator is displayed, along with the experimental setup. (b) The device's linear frequency response is presented, which was measured using a network analyzer and indicates a quality factor of approximately 2700.

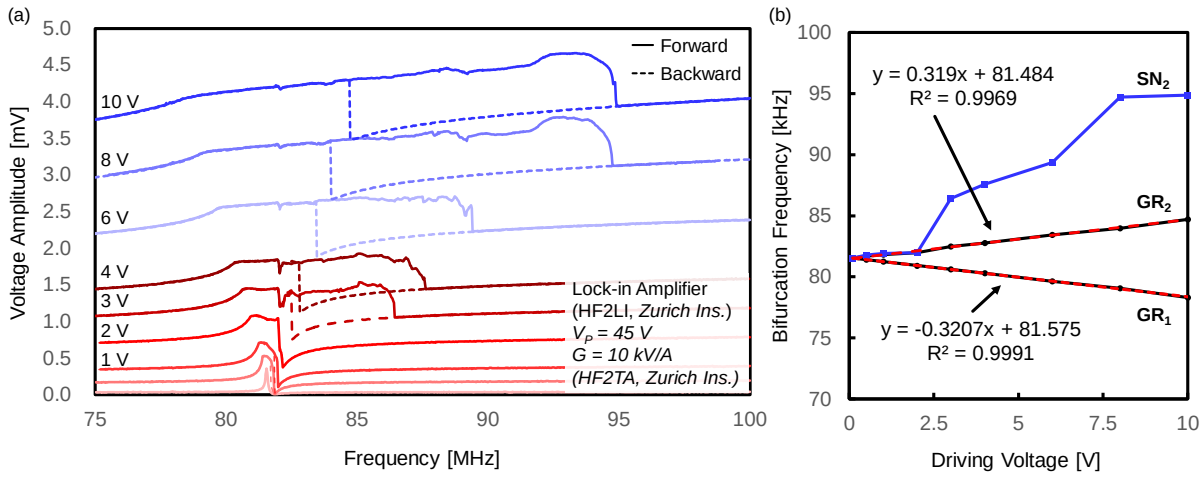


Figure D-18: (a) The measured tapping responses of the resonator are presented for several driving voltages, using both forward and backward frequency sweeps. (b) The bifurcation frequencies derived from the data in (a) are plotted as a function of the driving voltage.

Finally, Figure D-15 (b) and (d) display responses with chaotic motion, featuring very long repeating periods and thus complex and wide-band FFT spectrum. Notably, although Figure D-15 (d) appears to show period-2 motion in the time domain, it is actually a chaotic motion since the displacement amplitude varying in the negative direction with a long repeating period similar to that seen in Figure D-15 (b). Noted, this kind of chaotic motion and resultant frequency comb spectrum might not be observable due to environment noise and classified as period-2 motion in reality. Last

doi:10.6342/NTU202600018

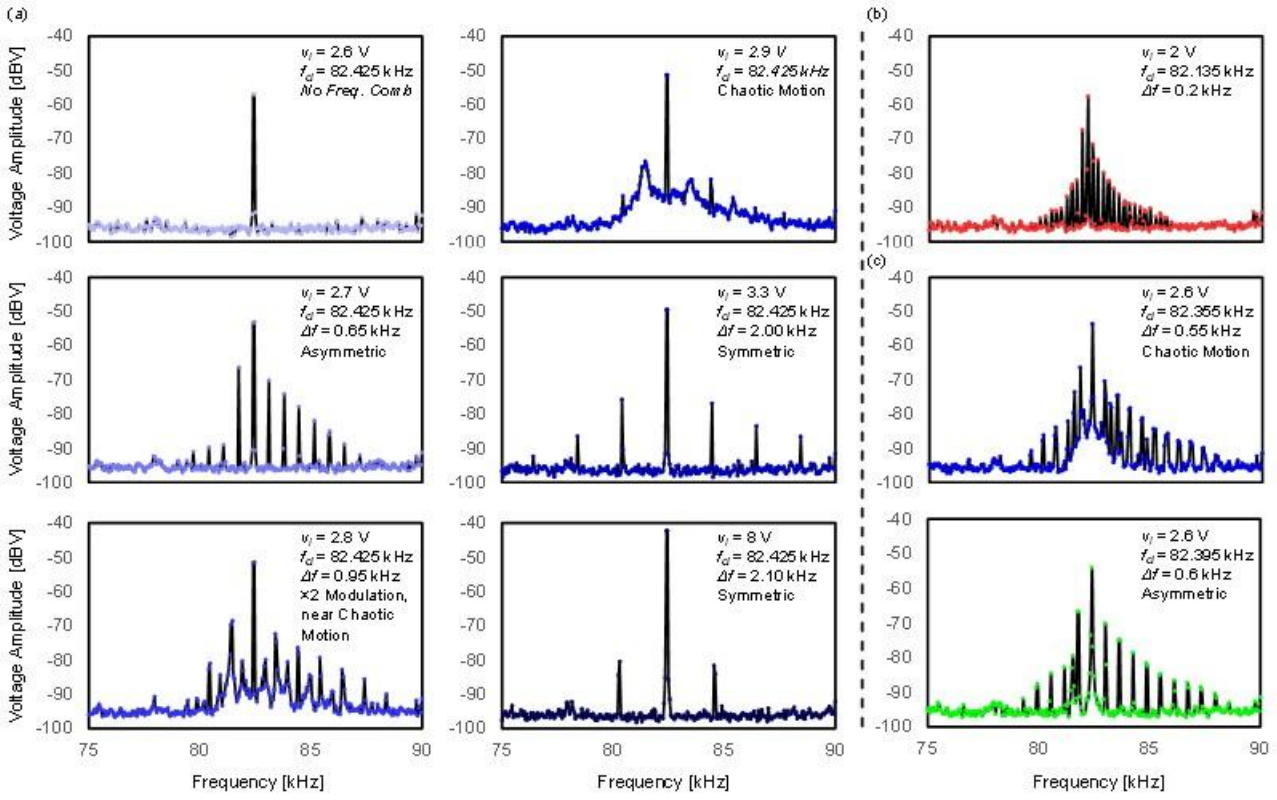


Figure D-19: Experimentally observed frequency comb spectra are presented for the resonator under various operating parameters. (a) The spectral evolution is detailed for an increasing driving voltage, which induces a progression through several dynamic regimes, including asymmetric, chaotic, and symmetric patterns. (b) A distinct frequency comb that was generated under a lower driving voltage is also shown. (c) The sensitivity of the comb structure to the driving frequency is demonstrated, highlighting the resulting shifts between chaotic and asymmetric responses.

but not least, Figure D-16 (a) and (b) present bifurcation plots extracted using the stroboscopic Poincaré section at the points of maximum and minimum displacement, respectively. Although the extracted bifurcation points differ between the two plots, both effectively capture the same characteristics of the system's periodic orbits in a reduced, one-dimensional representation.

D.2.3 Comb-driven Folded-beam Vibro-impact Resonator

Structure and Operation

Figure D-17 (a) presents the SEM image of the investigated device with set-up. The

doi:10.6342/NTU202600018

resonator is driven by a combination of polarization bias V_P and input signal v_i on the driving electrode. The device's motion is constrained in one direction by the stopper, in which the stopper is made by a folded beam structure and the designed stopper's stiffness is about five times lower than the resonator. Figure D-17 (b) shows the measured frequency response in linear region by a network analyzer, representing the quality factor of the device around 2700 and a resonance frequency around 81.5 kHz.

Experimental Results

Figure D-18 (a) shows the tapping mode frequency response with varying driving voltage measured by a lock-in amplifier. Figure D-18 (b) shows the extracted bifurcation frequencies. As presented in Section 3.1, the 1st and 2nd grazing frequency present linear relation between driving voltage and the frequencies. Note that a softer stopper, featuring merely five times the stiffness, is expected to allow the resonator to vibrate with greater displacement at the nonlinear resonance frequency. However, the response is like to impact with a hard stopper (i.e., anchor), where the output voltage remains constant. Consequently, we believe that releasing output stopper cannot happen before the resonator fails. Additionally, the second Saddle-node bifurcation (i.e., the jump-point near nonlinear resonance frequency) experience initial development, rapid growing and finally saturated at certain frequency. It is believed this feature is caused by the nonlinear contact damping.

Figure D-19 shows the observed frequency comb spectrums. In this device, we only found one period-doublings region around 82.1~82.4 kHz that higher than the overlapped tapping region a little bit. Figure D-19 (a) shows the frequency comb spectrum with varying driving voltage. As observed, symmetric pattern, asymmetric pattern, and complex pattern from chaotic motion are found. Figure D-19 (b) shows a frequency comb spectrum found in 2-V driving voltage. In this driving level of 2 V, we didn't find other period-doubling region, this might resultant from too tiny frequency band. Figure D-19 (c) shows two additional measurement results at 2.6-V driving voltage where the driving frequency are different than the measurement results

doi:10.6342/NTU202600018

in Figure D-19 (a). As shown, the frequency comb spacing are varying as the parameters, such as driving voltage or driving frequency, varying. In particular, the extra comb fingers with lower amplitude appeared in 2.8 V (*c.f.* Figure D-19 (d)) are attributed to an additional signal period caused by additional period-doubling phenomenon. This effect naturally results in a double modulation of the time-domain envelope without any additional input [556].

D.2.4 Clamped-Clamped Beam Vibro-impact Resonator

Structure and Operation

Figure D-20 (a) presents the SEM image of the investigated device with set-up. The resonator is driven by a combination of polarization bias V_P and input signal v_i on the driving electrode. The device's motion is constrained in one direction by the stopper, in which the stopper is made by a hard stopper (i.e., an anchor). Figure D-20 (b) shows the measured frequency response in linear region by a network analyzer, representing the quality factor of the device around 670 and a resonance frequency around 2.2 MHz.

Experimental Results

Figure D-21 (a) shows the tapping mode frequency response with varying driving

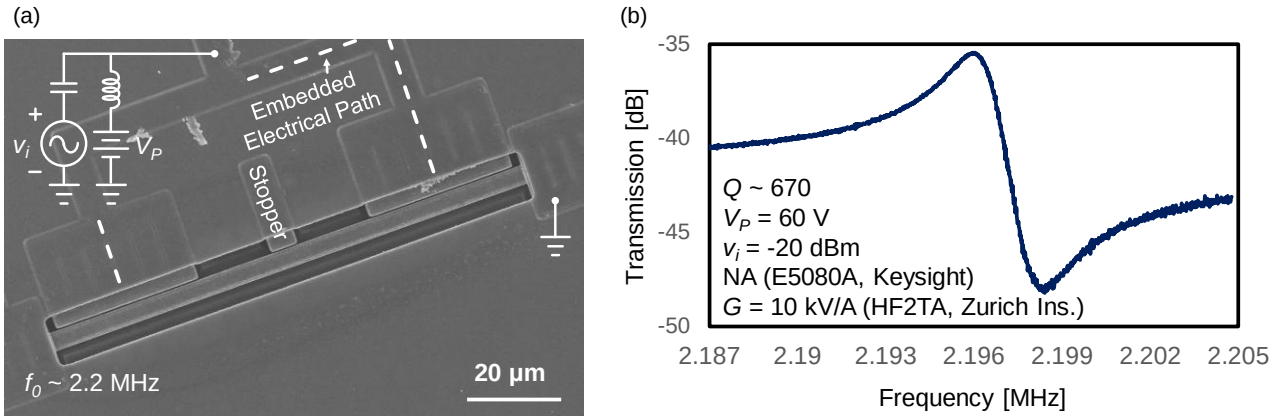


Figure D-20: (a) An SEM image of the 2.2-MHz clamped-clamped (CC) beam resonator is shown, including its experimental setup. (b) The device's linear frequency response, measured with a network analyzer.

doi:10.6342/NTU202600018

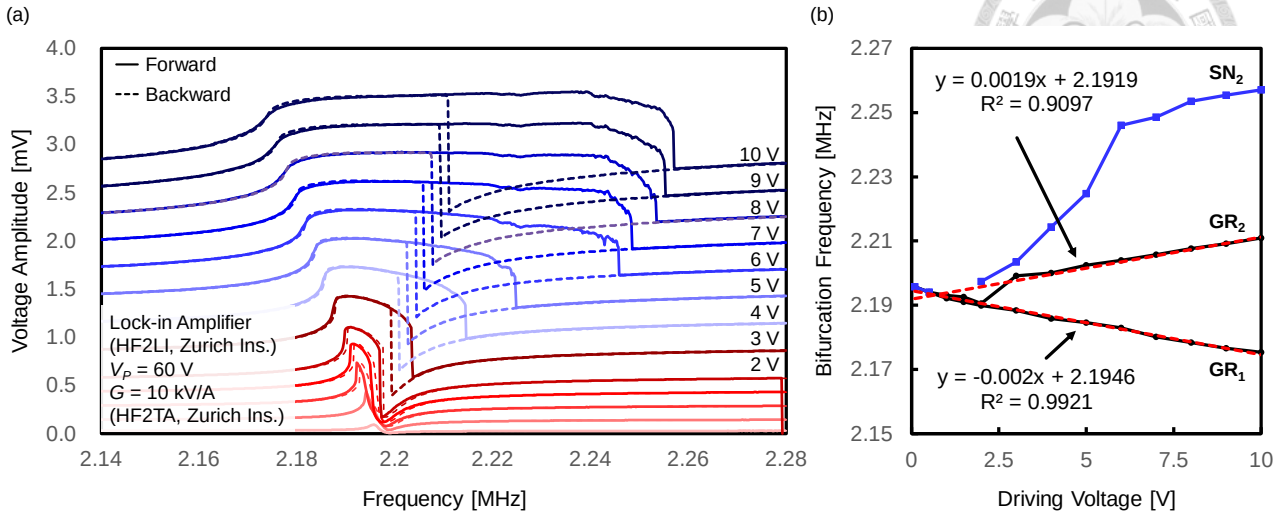


Figure D-21: (a) The measured tapping responses of the CC-beam resonator are shown for various driving voltages, using both forward and backward frequency sweeps. (b) The bifurcation frequencies, extracted from the data in (a), are plotted as a function of driving voltage, revealing the evolution of the grazing (GR) and saddle-node (SN) points.

voltage measured by a lock-in amplifier. Figure D-21 (b) shows the extracted bifurcation frequencies. Similarly, the 1st and 2nd grazing frequency present linear relation between driving voltage and the frequencies and the second Saddle-node bifurcation experience three phases and finally saturated at certain frequency as discussed in previous sections. Figure D-22 shows the occurrence map of frequency comb in this device, where two regions are found if driving voltage higher than 5.2 V and one region is found under 4.2-V driving voltage. Figure D-23 shows the measured frequency comb spectrums in detail. Figure D-23 (a) shows the measured frequency comb spectrums under 4.2-V driving voltage and Figure D-23 (b) and (c) show the frequency comb spectrums under 5.2-V and 6.2-V driving voltage, respectively. Differing than the frequency comb generated by the comb-driven folded-beam vibro-impact resonator, the comb spectrum shown here are all symmetric.

D.2.5 Conclusions

The work presents the both numerical and experimental investigation on the frequency comb generation of vibro-impact resonators. The effect of distorted

doi:10.6342/NTU202600018

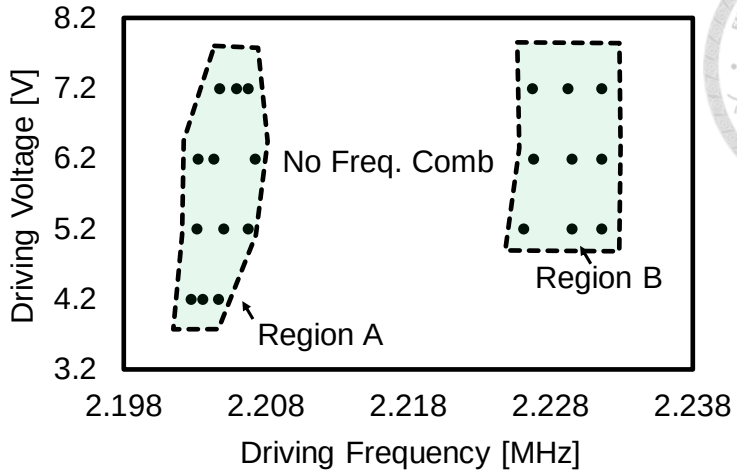


Figure D-22: An experimentally derived map illustrating the occurrence of frequency combs. The shaded green areas indicate the specific driving voltage and frequency ranges where frequency comb generation was observed.

waveform and low-frequency oscillation on envelop for the frequency comb spectrum are explained. The symmetric, asymmetric spectrums and the spectrums with chaotic motion are found experimentally. Differing than the frequency comb generated by internal resonance with smoothly varying spacing, the frequency comb is changed smoothly or suddenly due to the occurrence of discontinuous bifurcation in the vibro-impact resonator. It is believed that the frequency comb generation based on vibro-impact mechanism could provide higher tunability on the patten of frequency comb spectrum. The results could open-up new possibility for signal processing and sensing applications.

doi:10.6342/NTU202600018

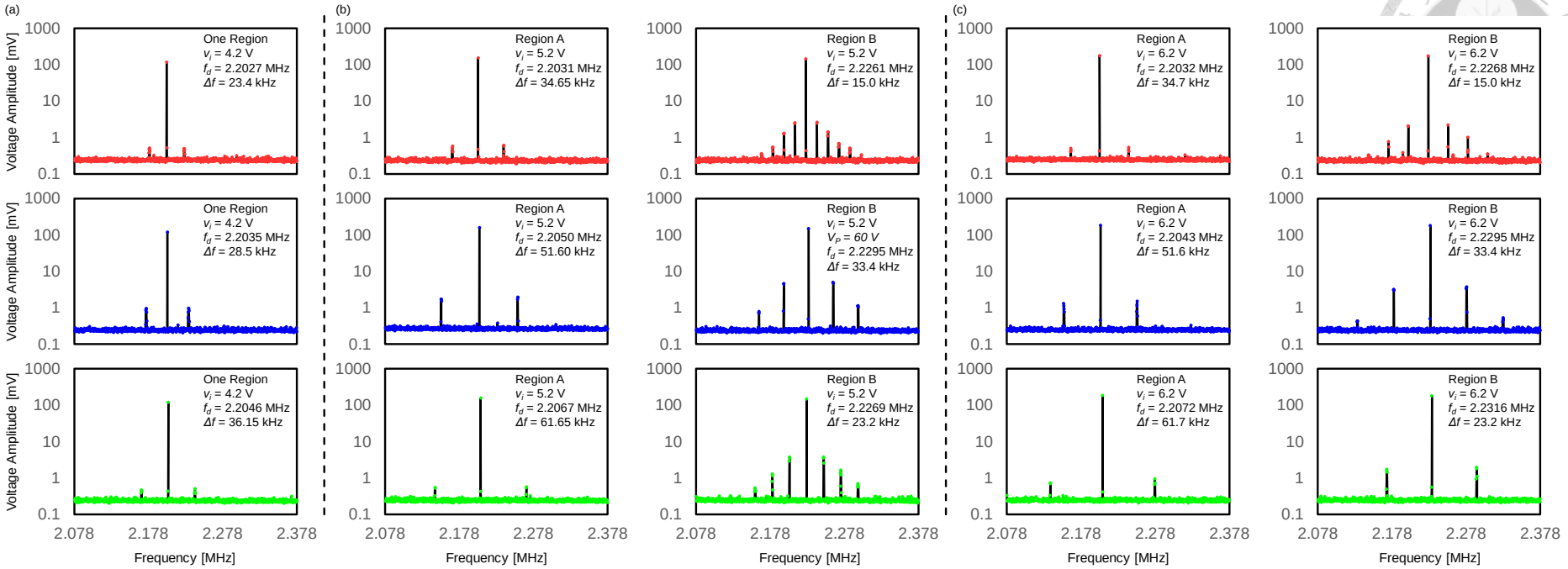


Figure D-23: A collection of measured frequency comb spectra for the CC-beam resonator under different operating conditions. The plots show the symmetric comb patterns generated at driving voltages of (a) 4.2 V, (b) 5.2 V, and (c) 6.2 V, corresponding to the different operational regions identified in Figure D-22.

doi:10.6342/NTU202600018

D.3 Double-sided Vibro-Impact Resonator

A CMOS-MEMS based vibro-impact resonator with double-sided stopper structures has been demonstrated to exhibit a tapping bandwidth up to 2.3 times wider than its conventional single-sided counterpart. Specifically, a folded-beam capacitive-comb transduced resonator, fabricated using a 0.35-μm CMOS process, impacts the stopper structures on either side of the shuttle, with an air gap ranging from 0.6 to 0.7 μm. This results in a flat region in the frequency transmission response, where tapping occurs, around the resonance frequency of 125 kHz. The system's effective stiffness, and thus the resonance frequency, abruptly increase during tapping, leading to bend-to-right transmission response curves at higher frequencies. Conceptually, the additional stopper in the double-sided impacting resonator causes extra stiffness hardening, further increasing the impact-induced resonance frequency. A numerical model established here confirms the trend of bandwidth widening in structures with double-sided stoppers.

D.3.1 Introduction

Recently, nonlinear vibro-impact dynamics has proven beneficial in various devices and applications, ranging from vibration energy harvesters [76, 252, 471, 557] to wireless communication receivers [82, 87, 89] and surface condition monitoring [191, 303]. In particular, vibration energy harvesters achieve higher efficiency and broader bandwidth by incorporating stoppers into the resonance structures. Meanwhile, resoswitches utilize impact dynamics for RF signal filtering and amplification. The properties of the contact surface, such as roughness, interaction force, and hardness, influence the tapping bandwidth of the frequency responses in impacting resonators. This capability presents a unique potential for in situ on-chip surface condition monitoring.

doi:10.6342/NTU202600018

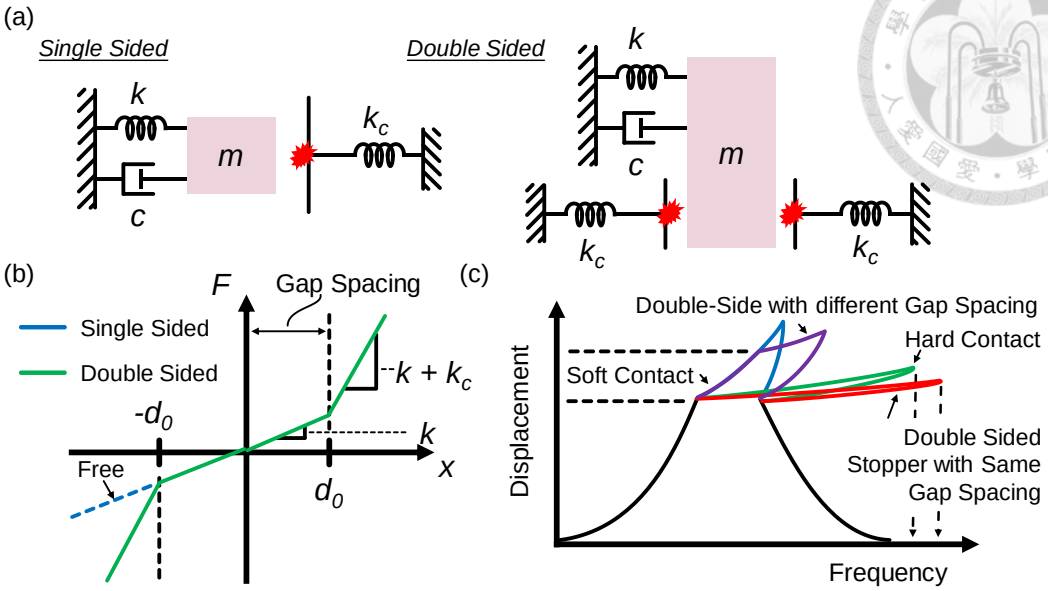


Figure D-24: A comparison of resonator models using 1-DOF lumped diagrams for (a) a single-sided stopper and (b) a double-sided stopper. (c) A force-displacement plot showing the resulting piecewise-linear system stiffness. (d) A comparison of frequency responses for resonators with soft contact, hard contact, and double-sided hard contacts. Reproduced with permission of [192], Copyright of © 2021 IEEE.

Additionally, more sophisticated stopper structures, such as double-sided stoppers, have been demonstrated in vibration energy harvesters to further extend the device's operational bandwidth [471, 557]. This work explores the use of double-sided stopper structures in micromechanical resonators to validate their effectiveness for bandwidth widening in microscale vibro-impact resonators/oscillators, which are crucial components of resoswitch-based receivers and on-chip surface condition monitoring devices. It is noteworthy that the devices used in [82] already exhibit double-sided impacting outputs; however, their characteristics and comparisons to single-sided versions have not been reported.

D.3.2 Comparison on the Configurations

Figure D-24 illustrates the lumped models for (a) a regular single-sided impacting resonator and (b) a double-sided one. Figure D-24 (c) shows the force experienced by the vibro-impact structure as a function of displacement, indicating varied stiffness

doi:10.6342/NTU202600018

depending on whether the structure is in contact with the stoppers or not. Ignoring the spring softening effect for simplicity

Figure D-24 (d) plots the frequency responses of the impacting resonator. There are two distinct regions separated by the gap spacing: the resonator exhibits regular frequency responses when the displacement is below the gap spacing and enters tapping responses at a higher resonance frequency once the displacement exceeds the gap spacing. As illustrated, the gap spacing of the two stopper might be different thus the response could further separate with three regions. The resonator can move into the stoppers with a certain indentation, which depends on the contact materials. Generally, soft contacts result in larger indentation and smaller tapping bandwidth compared to hard contacts and double-sided hard contacts and additional stoppers could contribute more hardening effect.

D.3.3 Structure and Operation

Figure D-25 shows the schematic of a comb-driven folded-beam double-sided vibro-impact resonator along with the setup configuration for frequency response measurement using a network analyzer. The structure includes a stack of layers from METAL1 to METAL4 of the CMOS process. The release step was conducted in-house using an HF-based etchant (Silox Vapox III by Transene Company, Inc.). During operation, device is put in in a vacuum chamber to lower the damping, two DC biases V_P with opposite polarities are applied on either side of the comb fingers, generating a differential driving force with double the strength compared to a single bias. The transmission frequency response, denoted as S_{21}, is measured by connecting Port 1 of the network analyzer to the structure and Port 2 to one of the finger comb sets to pick up the motional current due to resonance.

doi:10.6342/NTU202600018

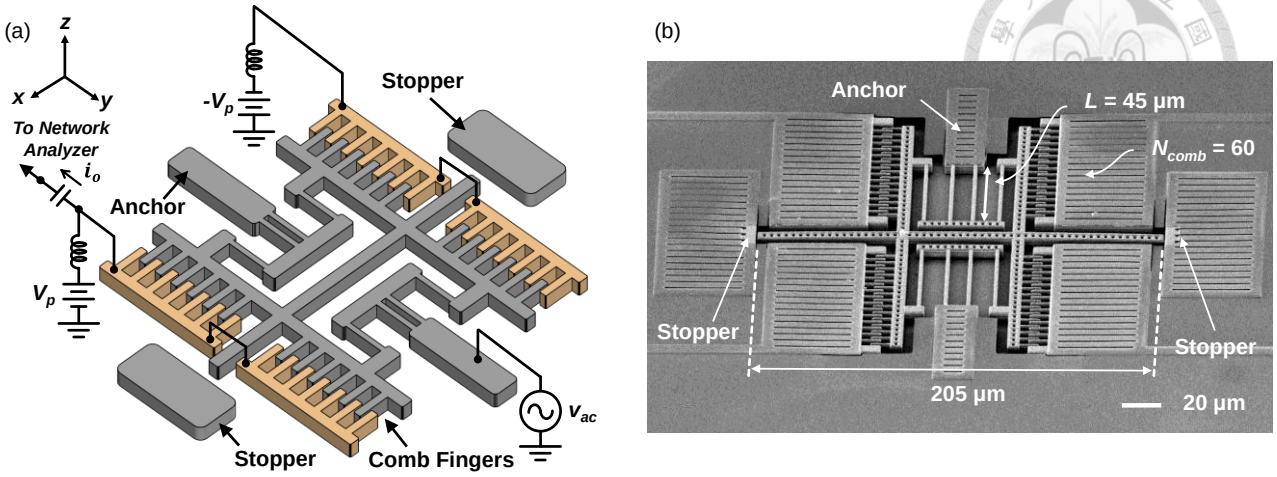


Figure D-25: (a) A schematic diagram and (b) an SEM image of the fabricated comb-driven folded-beam micromechanical vibro-impact resonator, featuring symmetrical double-sided stoppers. Reproduced with permission of [192], Copyright of © 2021 IEEE.

While macroscale devices can assume linear contact stiffness of k_c of Figure D-24 (c), in micro/nanoscale devices, however, the interaction forces between the structure and stoppers become far complicated. Plus, a previous study of [79] indicates that contact occurs only in few asperities. On the other hand, the long-range attractive force would also affect the tapping behavior in the micro/nanoscale. As a result, DMT contact model that includes the attractive forces into the classic Hertz model is chosen [191, 218].

The equation of motion for the forced 1-DOF vibro-impact resonator takes the form

$$m_r x'' + b_r x' + k_r x = A_d \cos(\omega_d t) - F_C \tag{D-3}$$

where x denotes displacement, and m_r, b_r, and k_r represent equivalent mass, damping, and stiffness, respectively. The derivations for these parameters are provided in [523]. F_d and F_{cont} indicate the external driving force and the piecewise nonlinear forces that combine the repulsive and attractive interactions between contact surfaces. The combined interaction force for a double-sided vibro-impact resonator is shown in (D-4) and can be simplified to (D-5) for single-sided scenarios.

$$F_{C.DS} = F_{DS.DMT} = F_{rep} + F_{att} \tag{D-4}$$

doi:10.6342/NTU202600018

$$= \begin{cases} \frac{4}{3}E^*\sqrt{R^*}(x-d_0+a_0)^{1.5} + \left(\frac{HR^*}{6a_0^2} - \frac{HR^*}{6(d_0+x)^2}\right), x \geq d_0 - a_0 \\ \left[\frac{HR^*}{6(d_0-x)^2} - \frac{HR^*}{6(d_0+x)^2}\right], \quad -d_0 + a_0 < x < d_0 - a_0 \\ -\frac{4}{3}E^*\sqrt{R^*}(-x-d_0+a_0)^{1.5} - \left(\frac{HR^*}{6a_0^2} + \frac{HR^*}{6(d_0-x)^2}\right), x \leq -d_0 + a_0 \end{cases}$$

$$F_{C.SS} = F_{DMT} = \begin{cases} \frac{4}{3}E^*\sqrt{R^*}(x-d_0+a_0)^{1.5} - \left(\frac{HR^*}{6a_0^2}\right), x \geq d_0 - a_0 \\ -\frac{HR^*}{6(d_0+x)^2}, x < d_0 - a_0 \end{cases} \quad \text{(D-5)}$$

where R^*, a_0, d_0 and H a represent the effective radius of curvature of the contact interface, the intermolecular interaction distance, the gap spacing, and the Hamaker constant, respectively. The effective Young's modulus of the contact materials, denoted as E^*, is expressed as

$$E^* = \left(\frac{1-v_1^2}{E_1} + \frac{1-v_2^2}{E_2}\right)^{-1} \quad \text{(D-6)}$$

The driving force F_d for the setup shown in Figure D-25 is given by

$$A_d = \frac{1}{2}\frac{\partial C_{long}}{\partial x}[(2V_P v_{ac}) - (-2V_P v_{ac})] = 2\frac{\partial C_{long}}{\partial x}V_P v_{ac} = \eta v_{ac} \quad \text{(D-7)}$$

doi:10.6342/NTU202600018

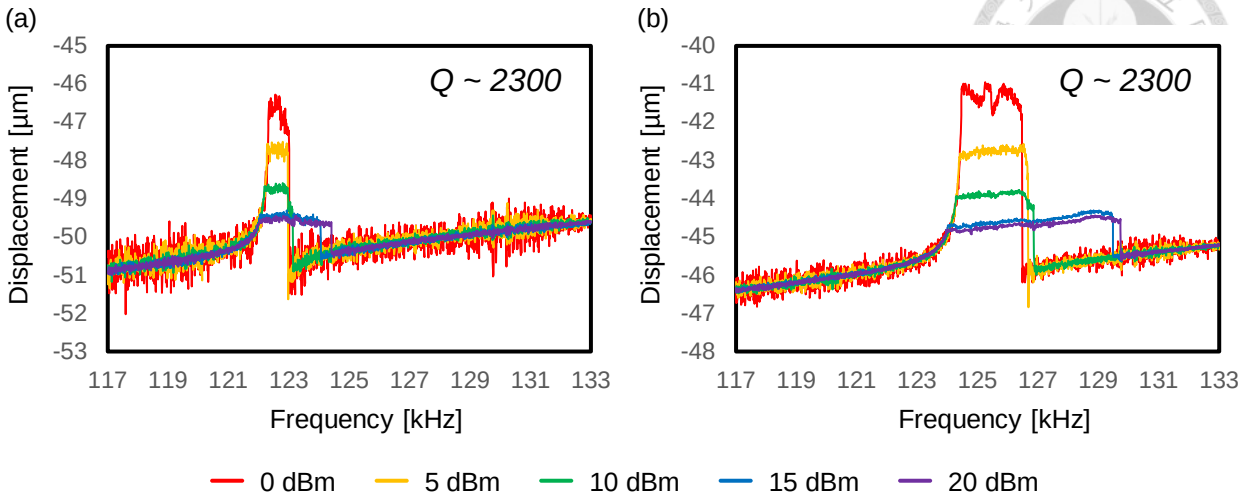


Figure D-26: Measured frequency responses for vibro-impact resonators with a polarization voltage of 36 V and driving signal levels from 0 dBm to 20 dBm, comparing (a) a single-sided stopper configuration with (b) a double-sided stopper configuration. Reproduced with permission of [192], Copyright of © 2021 IEEE.

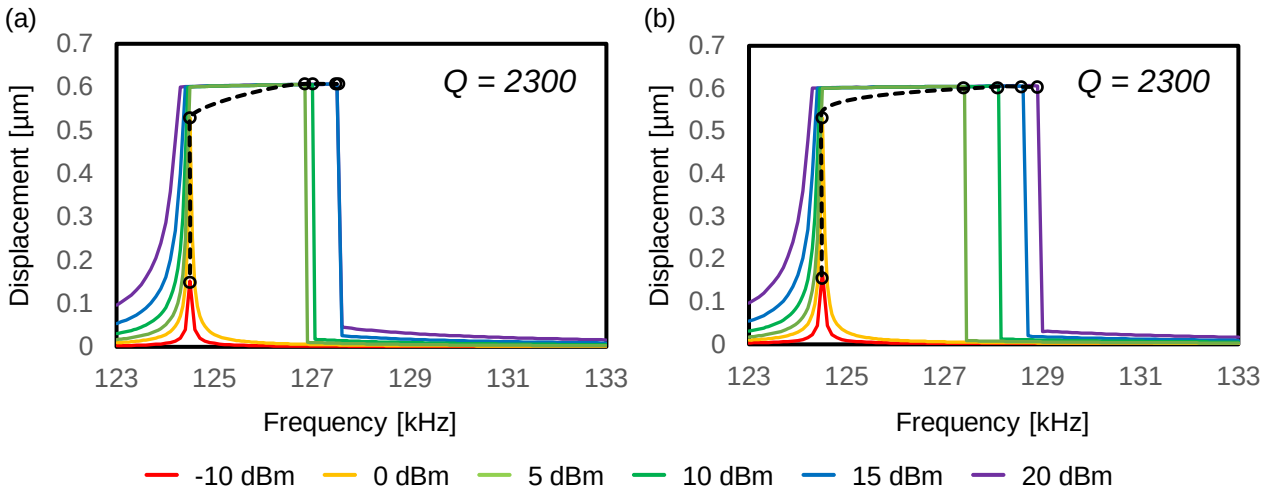


Figure D-27: Simulated nonlinear tapping-mode frequency responses for (a) a single-sided and (b) a double-sided stopper structure, with driving power levels from -10 dBm to 20 dBm. Reproduced with permission of [192], Copyright of © 2021 IEEE.

where $C_{long}(x) = [N\varepsilon h(l_{ff} + x)]/d$ represents the total capacitance of the comb fingers, V_P is the DC bias, v_{ac} is the AC driving signal, and η is the overall electro-mechanical coupling coefficient.

The aforementioned equations were utilized in a numerical simulation using

doi:10.6342/NTU202600018

TABLE D-2: SUMMARY OF THE USED PARAMETERS FOR THE SIMULATIONS

Parameter	Value	Unit
Contact Clearance, d_0	0.6	μm
Lumped Mass, m_r	1.536×10^{-10}	kg
Lumped Stiffness, k_r	94	N/m
Lumped Damper, b_r	5.224×10^{-8}	N•s/m
Linear Resonant Frequency, f_0	124.5	kHz
Electromechanical Coupling Coefficient, η	6.8596×10^{-8}	N/V
Hamaker Constant in Vacuum, H	40×10^{-20}	J
Interatomic Spacing, a_0	0.38	nm
Effective Youngs's Modulus, E_c	183	GPa
Effective Tip Radius, R^*	200	nm

MATLAB and Simulink to determine the tapping mode frequency responses. It is important to note that phase shift significantly influences the response during highly nonlinear operations [229]. To emulate the frequency sweeping measurement, each frequency step requires the amplitude, velocity, and phase information from the previous frequency point as initial conditions. Specifically, the data extracted from the time-domain waveforms of the last 50 stable cycles of the previous step obtained in Simulink are first transferred to MATLAB to compute the simulation conditions, including amplitude, velocity, and phase. These conditions are then fed back into Simulink to perform the time-domain simulation for the specific frequency point. By repeating this process across the frequency range of interest, the numerically simulated frequency response of the vibro-impact resonator is obtained. Considering the quality factor and resonance frequency, the simulated time period for each frequency is approximately 0.8 seconds to ensure steady-state conditions.

According to (D-4), the dynamic responses of the vibro-impact resonator depend on various contact material parameters and the equivalent mechanical parameters of the device (i.e., m, b, and k). In this context, the contact-interface effective radius of curvature R is the only fitting parameter used to match the measured results, while the other parameters are based on the reported data [191].

doi:10.6342/NTU202600018

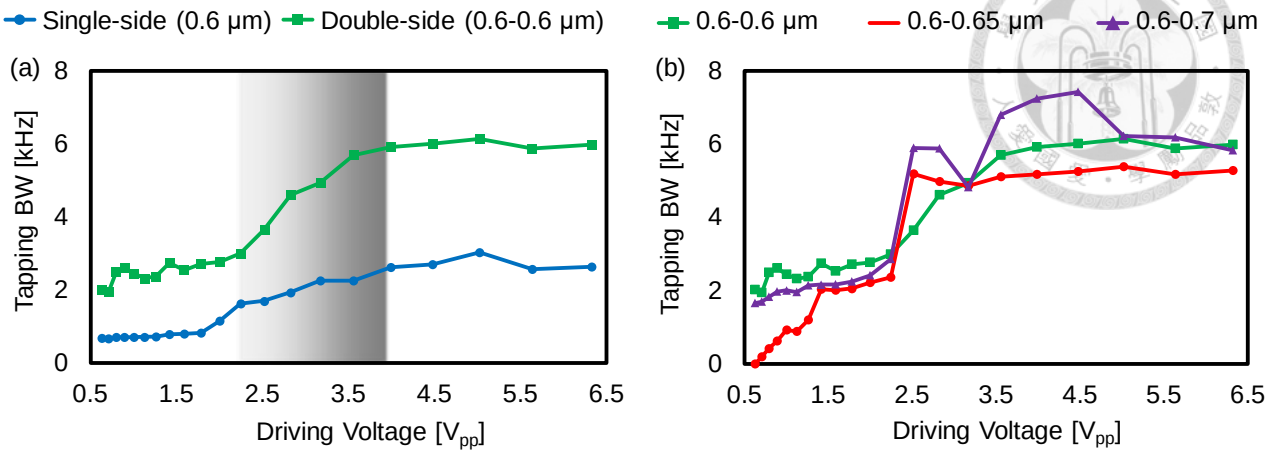


Figure D-28: (a) A plot comparing the measured tapping bandwidth versus driving voltage for single-sided and double-sided vibro-impact resonators. (b) An analysis of measured tapping bandwidth versus driving voltage for double-sided resonators with different gap spacing configurations. Reproduced with permission of [192], Copyright of © 2021 IEEE.

D.3.4 Experimental Results

Figure D-25 displays the SEM photo of a released double-sided vibro-impact resonator, showcasing its symmetrical structure. Figure D-26 presents the measured frequency responses for (a) single-sided and (b) double-sided stopper structures, confirming that the double-sided configuration has a wider tapping bandwidth. Figure D-28 (a) illustrates the measured tapping bandwidth versus driving voltage in V_{pp} with finer increments. It is noteworthy that the shaded area, where the tapping bandwidth exhibits a steeper transition, defines the boundary where the dominant contact force shifts from attractive to repulsive and finally saturated to certain frequency due to nonlinear contact damping. Figure D-28 (b) illustrates other cases with different gap spacing configuration, although the tapping bandwidth widening is clear for symmetric double-side vibro-impact resonator, we do not find out the difference for asymmetric cases. These results might suffer from the effect of plastic deformation and surface degradation and also the influence of the quality factor between devices. The further study is needed.

doi:10.6342/NTU202600018

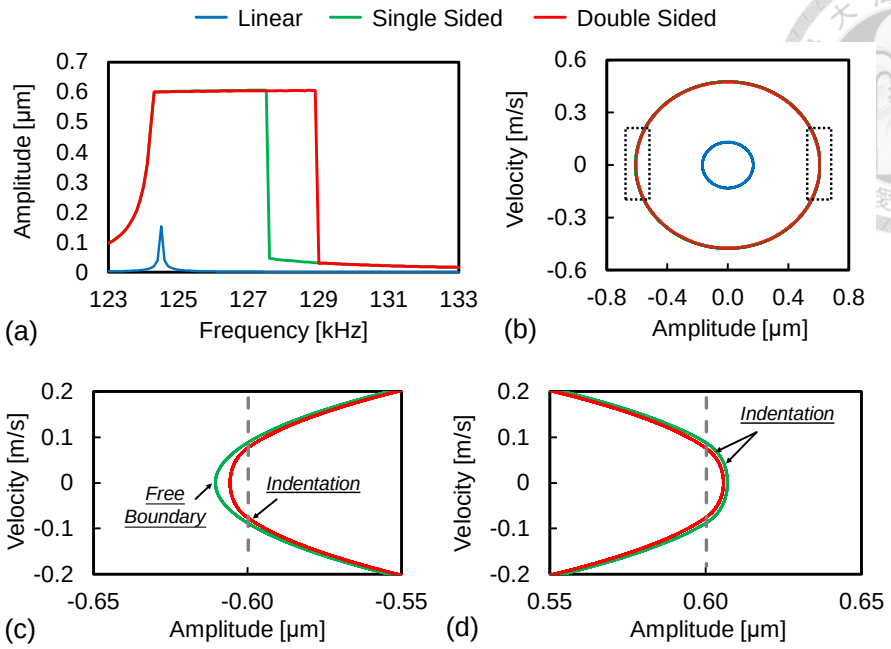


Figure D-29: A comparison of numerically simulated responses for linear, single-sided, and double-sided impact configurations, showing (a) the frequency responses and (b) the phase portraits. Detailed views of the phase portraits at the stopper locations are provided in (c) and (d). Reproduced with permission of [192], Copyright of © 2021 IEEE.

By inputting the parameter values into the previously described numerical simulation platform, we can obtain simulated frequency responses. Figure D-27 (a) and (b) show these responses based on the parameter values summarized in TABLE D-2, illustrating the backbone of the resonance peaks as the driving power increases. This simulation echoes the wider tapping bandwidth for double-sided stoppers shown in Figure D-26 (b). It should be noted that the bandwidth enlargement in the simulation is not as significant as the measured >2× increase. This discrepancy might be due to actual material properties and device dimensions differing from those used in the simulation. More accurate values for some parameters could be derived through various experimental designs. For example, gap variation experiments could determine the actual gap spacing, and stopper spring variation experiments could determine the effective Young's modulus. Additionally, zero contact damping and small contact radios contribute large error in high driving force level as mentioned in Appendix D.1.

doi:10.6342/NTU202600018

In order to understand the underlying mechanism clearly, further study is preferred and will be presented in Chapter 3.

Figure D-29 (a) shows the simulated frequency responses for linear, single-sided, and double-sided configurations, where the only nonlinearity arises from impact-induced hardening. Consequently, the left edge of the tapping frequency responses follows the linear response with increased amplitudes. Figure D-29 (b) presents the phase portraits for the three conditions. Zoomed-in views of the stopper portion on either end are shown in (c) and (d), revealing distorted curvatures due to indentation when the structure moves beyond the gap displacement of +0.6 μm. In contrast, the single-sided case has an unaltered curve for the free boundary on the other side at -0.6 μm.

D.3.5 Conclusions

This study confirms that the double-sided stopper structure significantly enlarges the tapping bandwidth of vibro-impact resonators at the microscale. An analytical analysis is applied to capture the feature qualitatively. A CMOS-MEMS based folded-beam comb-driven vibro-impact resonator was used as a test vehicle, demonstrating a wider tapping bandwidth compared to single-sided designs. These findings could enhance the performance of micromechanical vibro-impact resonator-based applications. For instance, this topology can be applied to increase the bandwidth of micromechanical resoswitches and improve the sensitivity and resolution of vibro-impact resonator-based on-chip surface monitoring. Additionally, the developed numerical model can be utilized to investigate the nonlinear dynamical behaviors of impacting resonators, opening up interesting avenues for future research.

doi:10.6342/NTU202600018

Appendix E: Introduction to Perturbation Theory

The goal of this appendix is to reduce the gap to know the dynamic feature of nonlinear problems with the help of mathematics and provides the detail of derivation on the problem conducted in the main text. In the following, symbol "→" represents some mathematical operations and provides some detail on the derivation.

Generally speaking, analyzing non-linear dynamic problems is challenging due to the absence of universal methods for their solution, as they depend on various factors such as the problem's nature, the type of nonlinearity, and the desired solution. While certain methods are suitable for weak nonlinearities, others are more effective for strong nonlinearities. Among those, perturbation theory comprises methods for finding an approximate solution of a weakly nonlinear equation by starting from the exact solution of a related and simpler equation—typically start from unperturbed equation (i.e., letting nonlinear function to be zero), and continuously improving a previously obtained approximate solution by correction terms.

In first place, this appendix will introduce the idea of perturbation theory with an illustrative example from asymptotic analysis. Secondly, the general procedure on the nondimensionalization technique will be introduced. The technique can simplify and parameterize problems where measured units are involved, making the equation scale-independent and universal. The followed sections introduce the popular methods with different benefit regarding to solving capability, including the method of multiple scale (MMS) and method of averaging (MOA). Those methods are applicable to system of the form

$$x' = \varepsilon F_{nl}(x, t)$$

or (E-1)

$$x'' + x = \varepsilon F_{nl}(x, x', t)$$

where ε is a small dimensionless parameter.

doi:10.6342/NTU202600018

It is worth to mention that the *method* is somewhat referred as *analysis*, therefore, the perturbation *analysis* is sometime used to reduce the original problem to a new *approximated* problems and solve by another perturbation *method* for a desired solution. For example, an equation with quadratic and cubic nonlinear stiffness can be approximated to an equation with only cubic nonlinear stiffness through MMS, and the approximated equation can be than solved by MOA in a convenient way.

According to what *N. David Mermin* said, it is convenient to say that the perturbation theory is a mathematical technique to reduce original problem and represent with an approximated solution. There are some physically meaningless procedures, thus, let's "*shut up and calculate.*" [558]

E.1 Illustrative Example based on Asymptotic Analysis

The case of interest involves a system where nonlinearity is minor, resulting in behavior that closely approximates the linearly reduced version. The requirement is to find the solution to the linear version and, most critically, the correction terms.

Let's consider a simple example coming from the prediction of motion time history of flying trajectory of an object, x, projected upward the sky from the floor as shown in Figure E-1. The gravitational force is dependent on the distance between the object and the Earth's barycenter, the equation of motion takes the from [559]

$$\frac{d^2x}{dt^2} = -g_x = -g_0\left(\frac{R_E}{R_E + x}\right)^2 \tag{E-2}$$

where $g_0 = 9.81$ (m/s^2) is standard gravitational acceleration, $R_E \approx 6371000$ (m) is the radius of the Earth. Here assume that the initial conditions (I.C.) as $x(0) = 0$ and $x'(0) = v_0 > 0$.

doi:10.6342/NTU202600018

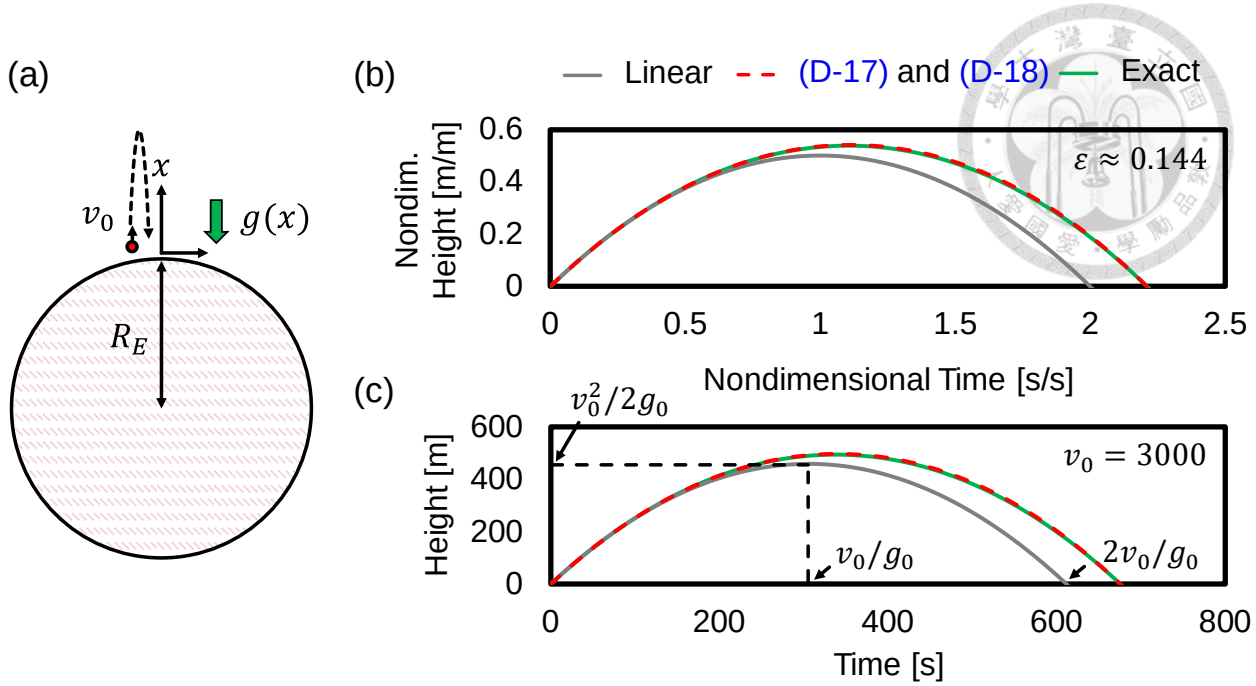


Figure E-1: (a) A diagram of the projectile motion problem, showing the trajectory over time. (b) The corresponding simulation results are presented in both nondimensional and dimensional forms.

It may be assumed that the motion is tiny compared to the radius of the Earth, i.e., $R_E \gg x$ and thus $R_E + x \approx R_E$. Under this assumption, the equation reduced to the simple equation typically taught in introductory physics

$$\frac{d^2x}{dt^2} = -g_0 \tag{E-3}$$

Solving the linearized equation with two-times integration and I.C. yields

$$x(t) = v_0 t - \frac{1}{2} g_0 t^2 \tag{E-4}$$

and

$$x'(t) = v_0 - g_0 t \tag{E-5}$$

One can find that the object reaches a maximum height of $x_{max} = v_0^2/(2g_0)$ at $t_{max} = v_0/g_0$ and get back to the floor when $t_{back} = 2v_0/g_0$. However, this reduction totally ignores the nonlinear term and loss the features.

A drawback of this reduction is the ambiguous objective for finding the correction

doi:10.6342/NTU202600018

to the approximated solution. For a systematic and behaviorally accurate reduction, it is essential to scale the variables and solve with perturbation theory instead of modifying the governing equation, meaning

$$\hat{t} = \frac{t}{t_s} \tag{E-6}$$

and

$$\hat{x} = \frac{x}{x_s} \tag{E-7}$$

where t_s and x_s are scaling factors to time and displacement, respectively. Significant freedom exists in the choice of these scaling factors. However, they must be representative of the final solution. This is commonly achieved by selecting the scaling factors based on the characteristics of the linear counterpart. Based on previous discussion on linear behavior, the choice of $x_s = 2x_{max}$ and $t_s = t_{max}$, transforms the problem as follows

$$\frac{d^2(2x_{max}\hat{x})}{d(t_{max}\hat{t})^2} = -g_0\left(\frac{R_E}{R_E + 2x_{max}\hat{x}}\right)^2 = -g_0\left(\frac{1}{1 + \frac{2x_{max}}{R_E}\hat{x}}\right)^2 \tag{E-8}$$

$$\rightarrow \frac{d^2\hat{x}}{d\hat{t}^2} = -\left(\frac{1}{1 + \varepsilon\hat{x}}\right)^2$$

where $\varepsilon = 2x_{max}/R_E$ is a *small* dimensionless parameter, if $R_E << x_{max}$, that measures the ratio of the object's achieved height to the Earth's radius. The system equation is thus simplified, retaining only a measure, ε, of the physical problem in its form. This resulting form is known as the perturbed equation, and the version where $\varepsilon = 0$ is called the unperturbed equation. The I.C. become $\hat{x}(0) = 0$ and $\hat{x}'(0) = 1$.

Furthermore, despite not knowing the true solution of the full nonlinear equation, a series expansion technique can be employed. Similar to how a Taylor series expansion approximates a nonlinear function, this method can be used to linearize the nonlinear

doi:10.6342/NTU202600018

equation around a specific point and find an approximate solution. In other words, for small ε, the solution can be assumed to be in the form of a ε-power series, as follows

$$\hat{x} \approx \hat{x}_0(\hat{t}) + \varepsilon\hat{x}_1(\hat{t}) + \varepsilon^2\hat{x}_2(\hat{t}) + \cdots \tag{E-9}$$

where the first term or said first-order approximation ($\hat{x}_0$) in this expansion is the scaled version of the solution solved in (E-4) and second term are its first order correction ($\hat{x}_1$). For infinite terms, the series solution is exact solution of the nonlinear equation, however, it is typically approximated with just few terms and the solution with few terms are called *perturbation solution*. The expansion used here is call *asymptotic expansion* and can be manually designed to make solving procedure easy.

Substituting (E-9) into (E-8) yields

$$\frac{d^2\hat{x}_0}{d\hat{t}^2} + \varepsilon\frac{d^2\hat{x}_1}{d\hat{t}^2} + \cdots = \left\{\frac{1}{1 + \varepsilon[\hat{x}_0(\hat{t}) + \varepsilon\hat{x}_1(\hat{t}) + \cdots]}\right\}^2 \tag{E-10}$$

To simplify the differential equation further, based on Tayer series expansion of $(1 + \varepsilon y)^n \approx 1 + n\varepsilon y$ for small εy is used, which transforms (E-10) into

$$\frac{d^2\hat{x}_0}{d\hat{t}^2} + \varepsilon\frac{d^2\hat{x}_1}{d\hat{t}^2} + \cdots = -1 + 2\varepsilon[\hat{x}_0(\hat{t}) + \varepsilon\hat{x}_1(\hat{t}) + \cdots] \tag{E-11}$$

The method for identifying the terms in the expansion mirrors the approach used to solve algebraic equations. By matching similar powers of ε up to 1, it derive the following problems

$$O(\varepsilon^0 = 1): \frac{d^2\hat{x}_0}{d\hat{t}^2} = -1 \tag{E-12}$$

and

$$O(\varepsilon^1): \frac{d^2\hat{x}_1}{d\hat{t}^2} = 2\hat{x}_0(\hat{t}) \tag{E-13}$$

where the I.C. becomes $\hat{x}(0) = \hat{x}_0(0) + \varepsilon\hat{x}_1(0) + \cdots = 0$ and $\hat{x}'(0) = \hat{x}_0(0) + \varepsilon\hat{x}_1(0) + \cdots = 1$, therefore, they are $\hat{x}_0(0) = \hat{x}_1(0) = \hat{x}_1'(0) = 0$ and $\hat{x}_0'(0) = 1$ for (E-12) and (E-13), respectively. The $O(\varepsilon^n)$ represent the nth order of ε.

doi:10.6342/NTU202600018

Solving the (E-12) with two-times integration and I.C. yields

$$O(\varepsilon^0 = 1): \hat{x}_0 = \hat{t} - \frac{1}{2}\hat{t}^2 \tag{E-14}$$

Substituting to (E-13) yields

$$O(\varepsilon^1): \frac{d^2\hat{x}_1}{d\hat{t}^2} = 2\hat{t} - \hat{t}^2 \tag{E-15}$$

Doing the similar procedure, it arrivals

$$O(\varepsilon^1): \hat{x}_1 = \frac{1}{3}\hat{t}^3 - \frac{1}{12}\hat{t}^4 \tag{E-16}$$

Therefore, the approximate solution with one-term correction shows

$$\hat{x} \approx \hat{t} - \frac{1}{2}\hat{t}^2 + \varepsilon\left(\frac{1}{3}\hat{t}^3 - \frac{1}{12}\hat{t}^4\right) \tag{E-17}$$

Using the definition of the nondimensionalized quantity, a transformation can be made to convert the equation back to one using physical variables

$$x \approx v_0 t - \frac{1}{2}g_0 t^2 + \frac{v_0^2}{R_E g_0}\left(\frac{1}{3}\frac{g_0^2}{v_0}t^3 - \frac{1}{12}\frac{g_0^3}{v_0^2}t^4\right) \tag{E-18}$$

where the first two term solved by zero-power order of ε is exactly the linear counterpart and the following terms are the correction terms. Figure E-1 show the comparison on the solution of linear counterpart, two-terms asymptotic expansion with exact solution from numerical integration.

Noted, (E-4) could captures the behavior of the system with extremely small initial velocity, the two-term asymptotic expansion solution of (E-18) captures the behavior as the nonlinearity in the weak region, however, more terms are needed if the system is with high initial velocity (i.e., strong nonlinearity). The capability of the perturbation theory is okay for the weakly nonlinear systems, i.e., $\varepsilon \ll 1$. For strongly nonlinear systems, the higher order term up to N on the expansion should be considered to maintain the accuracy, namely $\varepsilon^N \ll 1$. The equations will be much longer and become

doi:10.6342/NTU202600018

calculation expansive.

Besides, the perturbation theory conducts not only the approximation and transformation on the solution but also on the equation itself, such as homogenization [559]. In the following, nondimensionalization technique and few important perturbation methods for the nonlinear mechanical oscillator used in main text will be introduced.

E.2 Nondimensionalization Technique

E.2.1 Equation of Motion with KV-DMT model and Nonlinearities

The nondimensionalization technique is typically used to simplify and parameterize an equation to a full or partial dimensionless form. This technique makes it easier to analyze the equation and also allows the comparison for systems with different spatial or time scales. In order to convert the dimensional variables to dimensionless variables, the goal of the technique is to define new coordinates for time and/or space and find out dimensionless variables in terms of intrinsic parameters (e.g., m, b, k), meaning

$$\hat{x} = \frac{x - x_r}{x_s} \tag{E-19}$$

and

$$\hat{t} = \frac{t - t_r}{t_s} \tag{E-20}$$

where, $\hat{x}$ and $\hat{t}$ are dimensionless variables, x_s and t_s are the scaling factors, and x_r and t_r are the reference values.

If the reference values of the position and time are chosen as $x_r = t_r = 0$, the derivatives of the displacement and velocity become

$$\frac{dx}{dt} = \frac{d\hat{x}x_s}{d\hat{t}t_s} = \frac{x_s}{t_s}\frac{d\hat{x}}{d\hat{t}} \tag{E-21}$$

and

$$\frac{d^2x}{dt^2} = \frac{d}{d(\hat{t}t_s)}\frac{d\hat{x}x_s}{d\hat{t}t_s} = \frac{x_s}{t_s^2}\frac{d^2\hat{x}}{d\hat{t}^2} \tag{E-22}$$

doi:10.6342/NTU202600018

Considering the equation of motion with KV-DMT model and nonlinearities used in the main content (i.e., (3-40)), the equation of motion for the 1-DOF vibro-impact resonator is recalled as

$$m_r x'' + b_r x' + k_r x + b_3 x^2 x' + k_3 x^3 = A_d \cos(\omega_d t) + F_{KV-DMT}(x) \tag{E-23}$$

where the KV-DMT model is given by

$$F_{KV-DMT}(x) = -\begin{cases} -\dfrac{HR^*}{6(d_0 - x)^2}; x < d_0 - a_0 \\ -\dfrac{HR^*}{6a_0^2} + K(x - d_0 + a_0)^{\frac{3}{2}} + b_c\sqrt{R^*}(x - d_0 + a_0)^{\frac{1}{2}}x'; x \geq d_0 - a_0 \end{cases} \tag{E-24}$$

To simplify the expression on discontinuity, the KV-DMT model is read as

$$F_{KV-DMT}(x) = \frac{HR^*}{6(d_0 - x)_{D_{a_0}}^2} - K(x - d_0 + a_0)_{D_0}^{\frac{3}{2}} - b_c\sqrt{R^*}(x - d_0 + a_0)_{D_0}^{\frac{1}{2}}x' \tag{E-25}$$

where the discontinuity function expression is defined as $(a)_{D_b} = \begin{cases} a; & a > b \\ b; & a \leq b \end{cases}$. In detail, the discontinuity function in first and second term of (E-25) can be express as

$$(d_0 - x)_{D_{a_0}}^2 = \begin{cases} d_0 - x; d_0 - x \geq a_0 \\ a_0; d_0 - x < a_0 \end{cases} = \begin{cases} d_0 - x; x < d_0 - a_0 \\ a_0; x \geq d_0 - a_0 \end{cases} \tag{E-26}$$

and

$$(x - d_0 + a_0)_{D_0}^{3/2} = \begin{cases} x - d_0 + a_0 \ ; \ x \geq d_0 - a_0 \\ 0 \ ; \ x < d_0 - a_0 \end{cases} \tag{E-27}$$

Substituting (E-19)-(E-22) into (E-23) yields

$$\begin{aligned} &\frac{x_s}{t_s^2} m_r \hat{x}'' + b_r \frac{x_s}{t_s} \hat{x}' + k_r x_s \hat{x} + b_3 x_s^2 \hat{x}^2 \frac{x_s}{t_s} \hat{x}' + k_3 x_s^3 \hat{x}^3 = A_d sin(\omega_d t_s \hat{t}) + \\ &\frac{HR^*}{6(d_0 - x_s\hat{x})_{D_{a_0}}^2} - K(x_s\hat{x} - d_0 + a_0)_{D_0}^{\frac{3}{2}} - b_c\sqrt{R^*}(x_s\hat{x} - d_0 + a_0)_{D_0}^{\frac{1}{2}} \frac{x_s}{t_s} \hat{x}' \end{aligned} \tag{E-28}$$

doi:10.6342/NTU202600018

Multiplying $\frac{t_s^2}{m_r x_s}$ yields

$$\hat{x}'' + \frac{b_r t_s}{m_r}\hat{x}' + \frac{k_r t_s^2}{m_r}\hat{x} + \frac{b_3 x_s^2}{m_r t_s}\hat{x}^2\hat{x}' + \frac{k_3 x_s^2 t_s^2}{m_r}\hat{x}^3 =$$

$$\frac{A_d t_s^2}{m_r x_s} sin(\omega_d t_s \hat{t}) + \frac{t_s^2}{m_r x_s}\frac{HR^*}{6(d_0 - x_s\hat{x})_{D_{a_0}}^2} \quad \text{(E-29)}$$

$$-K\frac{t_s^2}{m_r x_s}(x_s\hat{x} - d_0 + a_0)_{D_0}^{\frac{3}{2}} - b_c\sqrt{R^*}(x_s\hat{x} - d_0 + a_0)_{D_0}^{\frac{1}{2}}\frac{t_s}{m_r}\hat{x}'$$

Two scaling quantities are chosen as

$$\frac{k_r t_s^2}{m_r} = 1 \rightarrow t_s = \sqrt{\frac{m_r}{k_r}} = \frac{1}{\omega_n} \quad \text{(E-30)}$$

$$Q\frac{A_d t_s^2}{m_r x_s} = 1 \rightarrow x_s = Q\frac{A_d}{k_r} \equiv A_0 \quad \text{(E-31)}$$

Substituting (E-30) and (E-31) to (E-29) obtains

$$\hat{x}'' + \xi\hat{x}' + \hat{x} + B_3\hat{x}^2\hat{x}' + K_3\hat{x}^3 =$$

$$\widehat{A_d} cos(\Omega_d \hat{t}) + \frac{\alpha}{\left(\widehat{d_0} - \hat{x}\right)_{D_{\widehat{a_0}}}^2} - \beta\left(\hat{x} - \widehat{d_0} + \widehat{a_0}\right)_{D_0}^{\frac{3}{2}} - \gamma\left(\hat{x} - \widehat{d_0} + \widehat{a_0}\right)_{D_0}^{\frac{1}{2}}\hat{x}' \quad \text{(E-32)}$$

where the coefficients are defined as

$$\xi = 1/Q = b_r/\sqrt{m_r k_r} \quad \text{(E-33)}$$

$$B_3 = b_3 A_0^2/\sqrt{m_r k_r} \quad \text{(E-34)}$$

$$K_3 = k_3 A_0^2/k_r \quad \text{(E-35)}$$

$$\alpha = HR^*/(6k_r A_0^3) \quad \text{(E-36)}$$

doi:10.6342/NTU202600018

$$\beta = \frac{KA_0^{\frac{1}{2}}}{k_r} = \frac{4}{3}E^*\sqrt{R^*A_0}/k_r \tag{E-37}$$

$$\gamma = b_c\sqrt{R^*A_0}/\sqrt{m_r k_r} \tag{E-38}$$

$$\widehat{d_0} = d_0/A_0 \tag{E-39}$$

$$\widehat{a_0} = a_0/A_0 \tag{E-40}$$

$$\widehat{A_d} = \frac{A_d}{k_r A_0} = \frac{1}{Q} = \xi \tag{E-41}$$

$$\Omega_d = \omega_d/\omega_n \tag{E-42}$$

Noted, the nondimensionalization of contact viscoelastic damping, γ, used in [314, 466] might have little mistaken.

E.2.2 Equation of Motion with Linear Contact Stiffness

Here is another example. Recalling the equation of motion from (2-1) in the main content

$$m_r x'' + b_r x' + k_r x - k_c(x - d_0)H(x - d_0) = A_d \sin(\omega_d t) \tag{E-43}$$

and substituting same scaling factor defined in (E-30) and (E-31) yields

$$\begin{aligned} &\hat{x}'' + \frac{b_r t_s}{m_r}\hat{x}' + \frac{k_r t_s^2}{m_r}\hat{x} + k_c\frac{t_s^2}{m_r x_s}(x_s\hat{x} - d_0) = \frac{A_d t_s^2}{m_r x_s} sin(\omega_d t_s \hat{t}) \\ &\rightarrow \hat{x}'' + \xi\hat{x}' + \hat{x} + \beta_l\left(\hat{x} - \widehat{d_0}\right)_{D_0} = \widehat{A_d}\cos(\Omega_d t) \end{aligned} \tag{E-44}$$

where $\beta_l = k_c/k_r$ is stiffness ratio.

E.3 Method of Multiple Scale

To provide context for nonlinear motion and '*multiple scale*' analysis, this section begins by recalling a Duffing oscillator, which takes the form

doi:10.6342/NTU202600018

$$m_r x'' + b_r x' + k_r x + k_3 x^3 = A_d \cos(\omega_d t)$$

or

$$m_r x'' + b_r x' + (k_r + k_3 x^2) x = A_d \cos(\omega_d t) \quad \text{(E-45)}$$

describing an oscillator that has a cubic stiffness term. Assuming $k_3 > 0$ ($k_3 < 0$), one can conclude that (1) the equivalent resonance frequency will increase (decrease) as the displacement amplitude increases since the stiffness is function of the amplitude indicated by $k_r + k_3 x^2$; (2) the motion is no longer a sinusoidal wave but modified at large amplitude.

Besides, the slowly varying envelop on the forcing period is clearly observed in the most nonlinear systems at larger displacement amplitude. In fact, the slowly varying behavior is a kind of features for nonlinear oscillator and can be found in many real systems, including vibro-impact system as shown in Figure 2-2 and Figure D-15 of the main content. Thus, the term *multiple scale* means that the scale of time coordinate in the system contain one fast (i.e., forcing term induced motion) and one or many slower (i.e., the motion envelope fluctuation induced by nonlinearities). Noted, as previously introduced concept, perturbation theory is trying to find out the approximate solution from unperturbed equation and improve the accuracy by correction terms. The natural observation to *fast* and *slow* motion are meaningfully introduced by the method of multiple scale as a fast variable and slow variables.

Differing from the straightforward expansion method that is not valid when the time over a threshold, $\tau > O(1/\varepsilon)$, due to the presence of *secular terms* [560]. The Poincaré–Lindstedt method improve the solving capability by using a *strained* time coordinate transformation to cancel the secular terms and construct periodic solutions [560]. Moreover, the method of multiple scale is a more general approach in which they introduce one or more new *slow* time variables for each time scale of interest in the problems. It requires that the solution is a periodic function of the *fast* variable but there is no constraint on slow time scale. The mathematical meaning of secular term

doi:10.6342/NTU202600018

will be introduced thereafter.

This paragraph is going to down convert the equation of motion of a van der Pol-Duffing oscillator as a slowly varying equation (or called reduced equation) and compared to the result derived by MOA presented in the Appendix E.5. The resultant slow varying equation will be solved to extract the nonlinear damping term. Noted, differencing than asymptotic analysis, there are two main steps for MMS. First one is to introduce multiple scale on both time and frequency coordinates and second step is to expand displacement with ε-power series form.

Ignoring the unwanted terms in (E-32) and recalling the dimensionless equation of motion for van der Pol-Duffing oscillator yields

$$\hat{x}'' + \xi\hat{x}' + \hat{x} + B_3\hat{x}^2\hat{x}' + K_3\hat{x}^3 = \widehat{A_d}cos(\Omega_d\hat{t}) \tag{E-46}$$

In the form of perturbation equation, it read as

$$\hat{x}'' + \hat{x} = \varepsilon\left(-\hat{x}' - B_3^*\hat{x}^2\hat{x}' - K_3^*\hat{x}^3 + \widehat{A_d}^*cos(\Omega_d\hat{t})\right) \tag{E-47}$$

where $\varepsilon = \xi \ll 1$, $B_3^* = B_3/\xi$, $K_3^* = K_3/\xi$ and $\widehat{A_d}^* = \widehat{A_d}/\xi$.

Assume that the solution function is in two scale, namely $T_0 = \hat{t}$ and $T_1 = \varepsilon\hat{t}$, the ε-power series expansion of the displacement can be given as

$$\hat{x}(\hat{t}) = \hat{x}(T_0, T_1) = \hat{x}_0(T_0, T_1) + \varepsilon\hat{x}_1(T_0, T_1) + \cdots \tag{E-48}$$

Associated ε-power series expansion on nonlinear resonance frequency can be represented as

$$\Omega_d = 1 + \varepsilon\Omega_1 + \cdots = 1 + \varepsilon\Omega_1 + \cdots \tag{E-49}$$

The 1st order and 2nd order derivative to time becomes

$$\frac{d}{d\hat{t}} = \frac{\partial T_0}{d\hat{t}}\frac{\partial}{dT_0} + \frac{\partial T_1}{d\hat{t}}\frac{\partial}{dT_1} = \frac{\partial}{dT_0} + \varepsilon\frac{\partial}{dT_1} \equiv D_0 + \varepsilon D_1 \tag{E-50}$$

$$\frac{d^2}{d\hat{t}^2} = \frac{d}{d\hat{t}}\left(\frac{d}{d\hat{t}}\right) = (D_0 + \varepsilon D_1)^2 = D_0^2 + 2\varepsilon D_0 D_1 + \varepsilon^2 D_1^2 \tag{E-51}$$

doi:10.6342/NTU202600018

where D_i represent the derivative to T_i and $i = 0$ and 1.

Therefore, considering first two terms of (E-48), the 1st order and 2nd order time derivatives of displacement amplitude, can be written as

$$\frac{d\hat{x}}{d\hat{t}} = (D_0 + \varepsilon D_1)(\hat{x}_0 + \varepsilon\hat{x}_1) = D_0 + \varepsilon(D_0\hat{x}_1 + D_1\hat{x}_0) + \varepsilon^2 D_1\hat{x}_1 \tag{E-52}$$

$$\begin{aligned}\frac{d^2\hat{x}}{d\hat{t}^2} &= (D_0^2 + 2\varepsilon D_0 D_1 + \varepsilon^2 D_1^2)(\hat{x}_0 + \varepsilon\hat{x}_1) \\ &= D_0^2\hat{x}_0 + \varepsilon(D_0^2\hat{x}_1 + 2D_0D_1\hat{x}_0) + \varepsilon^2(D_1^2\hat{x}_0 + 2D_0D_1\hat{x}_1) + \varepsilon^3\hat{x}_1\end{aligned} \tag{E-53}$$

Substituting (E-52) and (E-53) into (E-47) yields

$$\begin{aligned}&\{D_0^2\hat{x}_0 + \varepsilon(D_0^2\hat{x}_1 + 2D_0D_1\hat{x}_0) + \varepsilon^2(D_1^2\hat{x}_0 + 2D_0D_1\hat{x}_1) + \varepsilon^3\hat{x}_1\} \\ &\quad + \{\hat{x}_0 + \varepsilon\hat{x}_1\} = -\varepsilon\{D_0 + \varepsilon(D_0\hat{x}_1 + D_1\hat{x}_0) + \varepsilon^2 D_1\hat{x}_1\} \\ &-\varepsilon B_3^*\{\hat{x}_0 + \varepsilon\hat{x}_1\}^2\{D_0 + \varepsilon(D_0\hat{x}_1 + D_1\hat{x}_0) + \varepsilon^2 D_1\hat{x}_1\} \\ &\quad -\varepsilon K_3^*\{\hat{x}_0 + \varepsilon\hat{x}_1\}^3 + \varepsilon\widehat{A_d}^* cos(\hat{t} + \varepsilon\Omega_1\hat{t})\end{aligned} \tag{E-54}$$

where the angle of forcing term $[1 + \varepsilon\Omega_1]\hat{t} = \hat{t} + \varepsilon\Omega_1\hat{t}$ can be denoted as $T_0 + \Omega_1 T_1$.

Collecting $O(\varepsilon^0)$ and $O(\varepsilon^1)$ obtains

$$O(\varepsilon^0): D_0^2\hat{x}_0 + \hat{x}_0 = 0 \tag{E-55}$$

and

$$\begin{aligned}O(\varepsilon^1): D_0^2\hat{x}_1 + 2D_0D_1\hat{x}_0 + \hat{x}_1 &= -D_0\hat{x}_0 - B_3^*\hat{x}_0^2(D_0\hat{x}_0) \\ &\quad -K_3^*\hat{x}_0^3 + \widehat{A_d}^* cos(T_0 + \Omega_1 T_1)\end{aligned} \tag{E-56}$$

Let the solution of (E-55) as $\hat{x}_0 = Ce^{\lambda\hat{t}}$ and substitute into the equation, the characteristic equation and eigenvalues are given by

$$\lambda_{1,2} = i \text{ and } -i \text{ for } \lambda^2 + 1 = 0 \tag{E-57}$$

and the general solution are found as

doi:10.6342/NTU202600018

$$\hat{x}_0(T_0,T_1) = C_1(\varepsilon\hat{t})e^{i\hat{t}} + C_2(\varepsilon\hat{t})e^{-i\hat{t}} = C_1(T_1)e^{iT_0} + C_2(T_1)e^{-iT_0} \quad \text{(E-58)}$$

Substituting (E-58) into the (E-56) yields:

$$D_0^2\hat{x}_1 + \hat{x}_1 = -D_0\left[C_1e^{iT_0} + C_2e^{-iT_0}\right]$$
$$-B_3^*\left[C_1e^{iT_0} + C_2e^{-iT_0}\right]^2\left\{D_0\left[C_1e^{iT_0} + C_2e^{-iT_0}\right]\right\} - K_3^*\left[C_1e^{iT_0} + C_2e^{-iT_0}\right]^3 \quad \text{(E-59)}$$
$$+\widehat{A_d}^*cos(T_0 + \Omega_1T_1) - 2D_0D_1\left[C_1e^{iT_0} + C_2e^{-iT_0}\right]$$

Each term at RHS of (E-59) can be expanded and arranged as:

$$-D_0\left[C_1e^{iT_0} + C_2e^{-iT_0}\right] = -\left(C_1ie^{iT_0} + C_2e^{-iT_0}\right) \quad \text{(E-60)}$$

$$-B_3^*\left[C_1e^{iT_0} + C_2e^{-iT_0}\right]^2\left\{D_0\left[C_1e^{iT_0} + C_2e^{-iT_0}\right]\right\} =$$
$$-B_3^*\left\{C_1^3ie^{i3T_0} - C_2^3ie^{-i3T_0} + C_1^2C_2ie^{iT_0} - C_1C_2^2ie^{-iT_0}\right\} \quad \text{(E-61)}$$

$$-K_3^*\left[C_1e^{iT_0} + C_2e^{-iT_0}\right]^3$$
$$= -K_3^*\left\{C_1^3e^{i3T_0} + C_2^3e^{-i3T_0} + 3C_1^2C_2e^{iT_0} + 3C_1C_2^2e^{-iT_0}\right\} \quad \text{(E-62)}$$

$$\widehat{A_d}^*cos(T_0 + \Omega_1T_1) = \frac{1}{2}\widehat{A_d}^*\left[e^{i(T_0+\Omega_1T_1)} + e^{-i(T_0+\Omega_1T_1)}\right] \quad \text{(E-63)}$$

$$-2D_0D_1\left[C_1e^{iT_0} + C_2e^{-iT_0}\right] = -2\left(\frac{\partial C_1}{\partial T_1}e^{iT_0} - \frac{\partial C_2}{\partial T_1}ie^{-iT_0}\right) \quad \text{(E-64)}$$

where

$$\left[C_1e^{iT_0} + C_2e^{-iT_0}\right]^2 = C_1^2e^{i2T_0} + C_2^2e^{-i2T_0} + 2C_1C_2 \quad \text{(E-65)}$$

Examining (E-56), it was noted that if a term on the RHS is an eigenfunction of the differential operator on the LHS, secular growth will occur in the solution. Such terms must be eliminated and commonly known as secular term. These terms cause the mathematically valid solution to become unbounded over long periods of time.

To have no secular terms, it requires coefficient of e^{iT_0} and e^{-iT_0} at RHS of (E-59)

doi:10.6342/NTU202600018

to be zero, namely

$$e^{iT_0}: -K_3^* 3C_1^2 C_2 + \frac{1}{2}\widehat{A_d}^* e^{i\Omega_1 T_1} + i\left(-C_1 - B_3^* C_1^2 C_2 - 2\frac{\partial C_1}{\partial T_1}\right) = 0 \quad \text{(E-66)}$$

$$e^{-iT_0}: -K_3^* 3C_1 C_2^2 + \frac{1}{2}\widehat{A_d}^* e^{-i\Omega_1 T_1} + i\left(C_2 - B_3^* C_1 C_2^2 - 2\frac{\partial C_2}{\partial T_1}\right) = 0 \quad \text{(E-67)}$$

It was noted that the solution in slowing oscillation term might be follow the form $A\cos(\theta t) = \frac{1}{2}A\left[\mathrm{e}^{i\theta t} + \mathrm{e}^{-i\theta t}\right]$. Thus, assuming

$$C_1 = \frac{1}{2}\widehat{a_{vD}}(T_1)e^{i\phi(T_1)} \quad \text{(E-68)}$$

$$C_2 = \frac{1}{2}\widehat{a_{vD}}(T_1)e^{-i\phi(T_1)} \quad \text{(E-69)}$$

yields

$$\frac{\partial C_1}{\partial T_1} = \frac{\partial}{\partial T_1}\left(\frac{1}{2}\widehat{a_{vD}}e^{i\phi}\right) = \frac{1}{2}\left(\frac{\partial \widehat{a_{vD}}}{\partial T_1} + i\widehat{a_{vD}}\frac{\partial \phi}{\partial T_1}\right)e^{i\phi} \quad \text{(E-70)}$$

$$\frac{\partial C_2}{\partial T_1} = \frac{\partial}{\partial T_1}\left(\frac{1}{2}\widehat{a_{vD}}e^{-i\phi}\right) = \frac{1}{2}\left(\frac{\partial \widehat{a_{vD}}}{\partial T_1} - i\widehat{a_{vD}}\frac{\partial \phi}{\partial T_1}\right)e^{-i\phi} \quad \text{(E-71)}$$

Substituting (E-68)-(E-71) into (E-66) and (E-67), it arrives

$$\begin{aligned}\text{(E-66)} \rightarrow & -K_3^* 3\left[\frac{1}{4}\widehat{a_{vD}}^2 e^{i2\phi}\right]\left[\frac{1}{2}\widehat{a_{vD}}e^{-i\phi}\right] + \frac{1}{2}\widehat{A_d}^* e^{i\Omega_1 T_1} \\ & + i\left(-\frac{1}{2}\widehat{a_{vD}}e^{i\phi} - B_3^*\left[\frac{1}{4}\widehat{a_{vD}}^2 e^{i2\phi}\right]\left[\frac{1}{2}\widehat{a_{vD}}e^{-i\phi}\right]\right. \\ & \left. - 2\left[\frac{1}{2}\left(\frac{\partial \widehat{a_{vD}}}{\partial T_1} + i\widehat{a_{vD}}\frac{\partial \phi}{\partial T_1}\right)e^{i\phi}\right]\right) = 0 \end{aligned} \quad \text{(E-72)}$$

$$\rightarrow -K_3^*\frac{3}{8}\widehat{a_{vD}}^3 + \frac{1}{2}\widehat{A_d}^* e^{i(\Omega_1 T_1 - \phi)} + \widehat{a_{vD}}\frac{\partial \phi}{\partial T_1}$$

$$+ i\left[-\frac{1}{2}\widehat{a_{vD}} - B_3^*\frac{1}{8}\widehat{a_{vD}}^3 - \frac{\partial \widehat{a_{vD}}}{\partial T_1}\right] = 0$$

doi:10.6342/NTU202600018

(E-67) → $-K_3^* 3\left[\frac{1}{2}\widehat{a_{vD}}e^{i\phi}\right]\left[\frac{1}{4}\widehat{a_{vD}}^2 e^{-i2\phi}\right]+\frac{1}{2}\widehat{A_d}^* e^{i\Omega_1 T_1}$

$$+i\left(-\frac{1}{2}\widehat{a_{vD}}e^{i\phi}-B_3^*\left[\frac{1}{2}\widehat{a_{vD}}e^{i\phi}\right]\left[\frac{1}{4}\widehat{a_{vD}}^2 e^{-i2\phi}\right]\right.$$

$$\left.+2\left[\frac{1}{2}\left(\frac{\partial\widehat{a_{vD}}}{\partial T_1}-i\widehat{a_{vD}}\frac{\partial\phi}{\partial T_1}\right)e^{-i\phi}\right]\right)=0 \quad \text{(E-73)}$$

$$\rightarrow -K_3^*\frac{3}{8}\widehat{a_{vD}}^3+\frac{1}{2}\widehat{A_d}^* e^{-i(\Omega_1 T_1+\phi)}+\widehat{a_{vD}}\frac{\partial\phi}{\partial T_1}$$

$$+i\left[\frac{1}{2}\widehat{a_{vD}}+B_3^*\frac{1}{8}\widehat{a_{vD}}^3+\frac{\partial\widehat{a_{vD}}}{\partial T_1}\right]=0$$

Because it is known that

$$\widehat{A_d}^* e^{i(\Omega_1 T_1-\phi)}=\widehat{A_d}^*[\cos(\Omega_1 T_1-\phi)+i\sin(\Omega_1 T_1-\phi)]$$
$$=\widehat{A_d}^*[\cos(\theta(T_1))+i\sin(\theta(T_1))] \quad \text{(E-74)}$$

and

$$\widehat{A_d}^* e^{-i(\Omega_1 T_1+\phi)}=\widehat{A_d}^*[\cos(\Omega_1 T_1+\phi)-i\sin(\Omega_1 T_1+\phi)]$$
$$=\widehat{A_d}^*[\cos(\theta(T_1))-i\sin(\theta(T_1))] \quad \text{(E-75)}$$

Separating the real and imaginary parts, it can be found that a pair of resultant equations of (E-76) and (E-77) for $\widehat{a_{vD}}$ and ϕ as

$$\widehat{a_{vD}}\frac{\partial\phi}{\partial T_1}=K_3^*\frac{3}{8}\widehat{a_{vD}}^3-\frac{1}{2}\widehat{A_d}^*\cos(\theta)$$

$$\rightarrow \widehat{a_{vD}}\left[\frac{\partial\theta}{\partial T_1}-\Omega_1\right]=K_3^*\frac{3}{8}\widehat{a_{vD}}^3-\frac{1}{2}\widehat{A_d}^*\cos(\theta) \quad \text{(E-76)}$$

$$\rightarrow \widehat{a_{vD}}\left[\frac{\partial\theta}{\partial T_1}\right]=\widehat{a_{vD}}\Omega_1+K_3^*\frac{3}{8}\widehat{a_{vD}}^3-\frac{1}{2}\widehat{A_d}^*\cos(\theta)$$

$$\frac{\partial\widehat{a_{vD}}}{\partial T_1}=-\frac{1}{2}\widehat{a_{vD}}-B_3^*\frac{1}{8}\widehat{a_{vD}}^3+\frac{1}{2}\widehat{A_d}^*\sin(\theta) \quad \text{(E-77)}$$

doi:10.6342/NTU202600018

In summary, the (E-47) are reduced and transferred to slowly varying equations of (E-76) and (E-77) through method of multiple scale, representing the maximum displacement amplitude or envelop of the oscillation. It firstly expand the dependent variable $\hat{x}$ and excitation frequency Ω_d by a perturbation series and replace the independent variable $\hat{t}$ with a series of new independent variable. The resultant equation can be solved numerically in time domain or analytically for the steady state.

Looking into steady-state solution, the derivatives on the state variable of the (E-76) and (E-77) must equal to zero (i.e., $\frac{\partial \widehat{a_{vD}}}{\partial T_1} = \frac{\partial \phi}{\partial T_1} = 0$), yielding

$$\frac{\widehat{A_d}^*}{\widehat{a_{vD}}}\cos(\theta) = \Omega_1 + K_3^* \frac{3}{4}\widehat{a_{vD}}^2 \tag{E-78}$$

$$\frac{\widehat{A_d}^*}{\widehat{a_{vD}}}\sin(\theta) = 1 + B_3^* \frac{1}{4}\widehat{a_{vD}}^2 \tag{E-79}$$

Combining the square of (E-78) and (E-79), sine $\sin^2(\theta) + \cos^2(\theta) = 1$, one can give the frequency response equation of

$$\frac{\widehat{A_d}^{*2}}{\widehat{a_{vD}}^2} = \left(\Omega_1 + K_3^* \frac{3}{4}\widehat{a_{vD}}^2\right)^2 + \left(1 + \frac{1}{4}B_3^* \widehat{a_{vD}}^2\right)^2 \tag{E-80}$$

Instead of solving this equation by given Ω_d, it is highly recommended to given $\widehat{a_{vD}}$ and solve Ω_d because the equation for $\widehat{a_{vD}}$ is nonlinear function of Ω_d.

E.4 Method of Averaging (MOA)

E.4.1 Equation of Motion with KV-DMT model and Nonlinearities

Method of Averaging (MOA) is a useful tool for analyzing weakly nonlinear *oscillators* that exhibit periodic motion with slowly varying behavior due to nonlinearities. For weakly nonlinear oscillators, one could expect that the solution would be close to that of linear ones but with slowly varying oscillation amplitude and phase due to perturbation of nonlinearities. Suppose that any nonlinear function is periodic, f_{nl}, then it seems natural to average the nonlinear function over a period, $\langle f_{nl} \rangle$,

doi:10.6342/NTU202600018

and consider the averaged system behavior with slow oscillation term (i.e., nonlinear effects) as

$$\langle F_{nl} \rangle = \frac{1}{T}\int_0^T F_{nl}dt = \frac{1}{2\pi}\int_0^{2\pi} F_{nl}d\theta \tag{E-81}$$

That means the system still remain oscillation on a fast time scale as without nonlinearities while the nonlinearities are averaged and added to the linear part to approximate the nonlinear solution and capture the nonlinear behavior.

Recalling the nondimensional equation of motion with lumped nonlinearities and surface interaction force based on KV-DMT model (*cf.* Appendix E.2)

$$\hat{x}'' + \xi\hat{x}' + \hat{x} + B_3\hat{x}^2\hat{x}' + K_3\hat{x}^3 =$$
$$\widehat{A_d}cos(\Omega_d\hat{t}) + \frac{\alpha}{\left(\widehat{d_0} - \hat{x}\right)^2_{D_{\widehat{a_0}}}} - \beta\left(\hat{x} - \widehat{d_0} + \widehat{a_0}\right)^{\frac{3}{2}}_{D_0} - \gamma\left(\hat{x} - \widehat{d_0} + \widehat{a_0}\right)^{\frac{1}{2}}_{D_0}\hat{x}' \tag{E-82}$$

Based on the concept of MOA, the solution to (E-82) would then take the form

$$\hat{x} = \widehat{a_{p.T}}(\hat{t})cos\,(\Omega_d\hat{t} + \phi(\hat{t})) = \widehat{a_{p.T}}cos\,(\Omega_d\hat{t} + \phi) \tag{E-83}$$

along with the following assumption

$$\hat{x}' = -\widehat{a_{p.T}}(\hat{t})\Omega_d sin\,(\Omega_d\hat{t} + \phi(\hat{t})) = -\widehat{a_{p.T}}\Omega_d sin\,(\Omega_d\hat{t} + \phi) \tag{E-84}$$

In order the clearly express the following derivation, here transfer the time coordinate to polar coordinate as

$$\theta = \Omega_d\hat{t} + \phi \tag{E-85}$$

Then, the (E-83) and (E-84) becomes

$$\hat{x} = \widehat{a_{p.T}}cos\,(\theta) \tag{E-86}$$

$$\hat{x}' = -\widehat{a_{p.T}}\Omega_d sin\,(\theta) \tag{E-87}$$

Remember that they are function of time $\hat{t}$ as presented.

Further, taking the time derivative of (E-83) yields

doi:10.6342/NTU202600018

$$\hat{x}' = \widehat{a_{p.T}}'\cos(\Omega_d\hat{t}+\phi) + \widehat{a_{p.T}}[-\sin(\Omega_d\hat{t}+\phi)(\Omega_d+\phi'))]$$
$$= \widehat{a_{p.T}}'\cos(\theta) - \widehat{a_{p.T}}\Omega_d\sin(\theta) - \widehat{a_{p.T}}\phi'\sin(\theta) \quad \text{(E-88)}$$

Comparing (E-84) and (E-88), the assumption of (E-84) implies

$$\widehat{a_{p.T}}'\cos(\theta) - \widehat{a_{p.T}}\phi'\sin(\theta) = 0 \quad \text{(E-89)}$$

Therefore, the derivative of (E-84) takes the form

$$\hat{x}'' = -\widehat{a_{p.T}}'\Omega_d\sin(\Omega_d\hat{t}+\phi) - \widehat{a_{p.T}}\Omega_d\cos(\Omega_d\hat{t}+\phi)(\Omega_d+\phi')$$
$$= -\widehat{a_{p.T}}'\Omega_d\sin(\theta) - \widehat{a_{p.T}}\Omega_d{}^2\cos(\theta) - \widehat{a_{p.T}}\Omega_d\phi'\cos(\theta) \quad \text{(E-90)}$$

Substituting (E-86), (E-87) and (E-90) into (E-82) yields

$$\widehat{a_{p.T}}'\sin(\theta) + \widehat{a_{p.T}}\phi'\cos(\theta) =$$
$$-\Omega_d{}^{-1}\{\widehat{A_d}\cos(\Omega_d\hat{t}) + \alpha\left(\widehat{d_0} - \widehat{a_p}\cos(\theta)\right)_{D_{\widehat{a_0}}}^{-2}$$
$$-\beta\left(\widehat{a_p}\cos(\theta) - \widehat{d_0} + \widehat{a_0}\right)_{D_0}^{3/2}$$
$$-\gamma\left(\widehat{a_{p.T}}\cos(\theta) - \widehat{d_0} + \widehat{a_0}\right)_{D_0}^{1/2}\left[-\widehat{a_{p.T}}\Omega_d\sin(\theta)\right] \quad \text{(E-91)}$$
$$-\widehat{a_{p.T}}\Omega_d{}^2\cos(\theta) - \xi\left[-\widehat{a_{p.T}}\Omega_d\sin(\theta)\right] + \widehat{a_{p.T}}\cos(\theta)$$
$$-B_3\left[\widehat{a_{p.T}}\cos(\theta)\right]^2\left[-\widehat{a_{p.T}}\Omega_d\sin(\theta)\right] - K_3\left[\widehat{a_{p.T}}\cos(\theta)\right]^3\Big\}$$
$$\rightarrow \widehat{a_{p.T}}'\sin(\theta) + \widehat{a_{p.T}}\phi'\cos(\theta) = -\Omega_d{}^{-1}\{\ldots\}$$

The long formular in the curly brackets of right-hand side (after $-\Omega_d{}^{-1}$) are represented as $\{\ldots\}$ for short and are sum of eight terms

The product of (E-91) and $\cos(\theta)$, plus the product of (E-84) and $\sin(\theta)$, yields

$$\widehat{a_{p.T}}'\cos^2(\theta) + \widehat{a_{p.T}}'\sin^2(\theta) = \widehat{a_{p.T}}' = \frac{\sin(\theta)}{-\Omega_d}\{\ldots\} \quad \text{(E-92)}$$

The product of (E-91) and $-\sin(\theta)$, plus the product of (E-84) and $\cos(\theta)$, yields

doi:10.6342/NTU202600018

$$\widehat{a_p}\phi' \sin^2(\theta) + \widehat{a_p}\phi' \cos^2(\theta) = \widehat{a_p}\phi' = \frac{cos(\theta)}{-\Omega_d}\{\dots\} \tag{E-93}$$

Taking the integral over a period for (E-92) and (E-93) in polar coordinate (i.e., $\theta = \theta_c$ to $\theta = 2\pi + \theta_c$ where θ_c is contact phase) instead of time domain (i.e., $\hat{t} = 0$ to $\hat{t} = 2\pi/\Omega$), according to (E-81), shows

$$\begin{aligned} &\int_{\theta_c}^{2\pi+\theta_c} \frac{\widehat{a_{p.T}}'}{\Omega_d} d\theta = 2\pi \frac{\widehat{a_{p.T}}'}{\Omega_d} = \int_{\theta_c}^{2\pi+\theta_c} \frac{\sin(\theta)}{-{\Omega_d}^2}\{\dots\}\, d\theta \\ &\rightarrow 2\pi \widehat{a_{p.T}}' = \int_{\theta_c}^{2\pi+\theta_c} \frac{\sin(\theta)}{-\Omega_d}\{\dots\}\, d\theta \end{aligned} \tag{E-94}$$

$$\begin{aligned} &\int_{\theta_c}^{2\pi+\theta_c} \frac{\widehat{a_{p.T}}'\phi'}{\Omega_d} d\theta = 2\pi \frac{\widehat{a_{p.T}}\phi'}{\Omega_d} = \int_{\theta_c}^{2\pi+\theta_c} \frac{\cos(\theta)}{-{\Omega_d}^2}\{\dots\} d\theta \\ &\rightarrow 2\pi \widehat{a_{p.T}}\phi' = \int_{\theta_c}^{2\pi+\theta_c} \frac{cos(\theta)}{-\Omega_d}\{\dots\} d\theta \end{aligned} \tag{E-95}$$

where $d\hat{t} = d\theta/\Omega$.

Apply the integration rules of trigonometric functions of

$$\int_0^{2\pi} sin(\theta)\, cos^n(\theta)\, d\theta = 0\,; n \in \mathbb{R} \tag{E-96}$$

$$\int_0^{2\pi} \sin^2(\theta)\, cos^2(\Theta)\, d\theta = \frac{\pi}{4} \tag{E-97}$$

$$\int_0^{2\pi} \sin^2(\theta)\, d\theta = \int_0^{2\pi} cos^2(\theta)\, d\theta = \pi \tag{E-98}$$

$$\int_0^{2\pi} cos^4(\theta)\, d\theta = \frac{3\pi}{4} \tag{E-99}$$

and analyzing the trigonometric functions of nonlinear terms in the right-hand side of (E-94) and (E-95) given the following results

doi:10.6342/NTU202600018

$$\widehat{A_d}: \int_{\theta_c}^{2\pi+\theta_c} \sin(\theta)\{\sin(\theta)\cos(\phi) + \cos(\theta)\sin(\phi)\}\, d\theta = \pi\cos(\phi) \quad \text{(E-100)}$$

$$\alpha: \int_{\theta_c}^{2\pi+\theta_c} \sin(\theta)\left\{\left(\widehat{d_0} - \widehat{a_{p.T}}cos(\theta)\right)_{D_{a_0}}^{-2}\right\} d\theta = 0 \quad \text{(E-101)}$$

$$\beta: \int_{\theta_c}^{2\pi+\theta_c} \sin(\theta)\left\{\left(\widehat{a_{p.T}}\cos(\theta) - \widehat{d_0} + \widehat{a_0}\right)_{D_0}^{3/2}\right\} d\theta = 0 \quad \text{(E-102)}$$

$$\gamma: \int_{\theta_c}^{2\pi+\theta_c} \sin(\theta)\left\{\left(\widehat{a_{p.T}}\sin(\theta) - \widehat{d_0} + \widehat{a_0}\right)_{D_0}^{1/2} sin(\Theta)\right\} d\theta \equiv I_1 \text{ (remained)} \quad \text{(E-103)}$$

$$\frac{m_r}{m_r} = 1: \int_{\theta_c}^{2\pi+\theta_c} \sin(\theta)\{\cos(\theta)\}\, d\theta = 0 \quad \text{(E-104)}$$

$$\xi: \int_{\theta_c}^{2\pi+\theta_c} \sin(\theta)\{\sin(\theta)\}\, d\theta = \pi \quad \text{(E-105)}$$

$$\frac{k_r t_s^2}{m_r} = \frac{k_r}{k_r} = 1: \int_{\theta_c}^{2\pi+\theta_c} \sin(\theta)\{\cos(\theta)\}\, d\theta = 0 \quad \text{(E-106)}$$

$$B_3: \int_{\theta_c}^{2\pi+\theta_c} \sin(\theta)\{cos^2(\theta)\, sin(\theta)\}\, d\theta = \frac{\pi}{4} \quad \text{(E-107)}$$

$$K_3: \int_{\theta_c}^{2\pi+\theta_c} \sin(\theta)\{\cos^3(\theta)\}\, d\theta = 0 \quad \text{(E-108)}$$

and

$$\widehat{A_d}: \int_{\theta_c}^{2\pi+\theta_c} cos(\theta)\{\sin(\theta)\cos(\phi) + \cos(\theta)\sin(\phi)\} d\theta = \pi\sin(\phi) \quad \text{(E-109)}$$

$$\alpha: \int_{\theta_c}^{2\pi+\theta_c} cos(\theta)\left\{\left(\widehat{d_0} - \widehat{a_{p.T}}cos(\theta)\right)_{D_{\widehat{a_0}}}^{-2}\right\} d\theta \equiv I_2 \text{ (remained)} \quad \text{(E-110)}$$

doi:10.6342/NTU202600018

$$\beta: \int_{\theta_c}^{2\pi+\theta_c} cos(\theta)\left\{\left(\widehat{a_{p.T}}\cos(\theta) - \widehat{d_0} + \widehat{a_0}\right)_{D_0}^{3/2}\right\} d\theta \equiv I_3 \text{ (remained)} \quad \text{(E-111)}$$

$$\gamma: \int_{\theta_c}^{2\pi+\theta_c} cos(\theta)\left\{\left(\widehat{a_{p.T}}\cos(\theta) - \widehat{d_0} + \widehat{a_0}\right)_{D_0}^{1/2} sin(\theta)\right\} d\theta = 0 \quad \text{(E-112)}$$

$$\frac{m_r}{m_r} = 1: \int_{\theta_c}^{2\pi+\theta_c} cos(\theta)\{\cos(\theta)\} d\theta = \pi \quad \text{(E-113)}$$

$$\xi: \int_{\theta_c}^{2\pi+\theta_c} cos(\theta)\{\sin(\theta)\} d\theta = 0 \quad \text{(E-114)}$$

$$\frac{k_r t_s^2}{m_r} = \frac{k_r}{k_r} = 1: \int_{\theta_c}^{2\pi+\theta_c} \cos(\theta)\{\cos(\theta)\}\, d\theta = \pi \quad \text{(E-115)}$$

$$B_3: \int_{\theta_c}^{2\pi+\theta_c} cos(\theta)\{\cos^2(\theta)\, sin\,(\theta)\} d\theta = 0 \quad \text{(E-116)}$$

$$K_3: \int_{\theta_c}^{2\pi+\theta_c} cos(\theta)\{\cos^3(\theta)\} d\theta = \frac{3\pi}{4} \quad \text{(E-117)}$$

where $cos(\Omega_d \hat{t}) = \cos(\theta - \phi) = \cos(\theta)\cos(\phi) + \sin(\theta)\sin(\phi)$ is used in (E-100) and (E-109). Although some nonlinear coefficients disappeared in nondimensionalization (i.e., it is not explicit express in derivation) the nonlinear coefficient are labeled for clarity.

In summary, the displacement and phase formular for averaged system are given by

$$\widehat{a_{p.T}}' = \frac{1}{2\pi}\int_{\theta_c}^{2\pi+\theta_c} \frac{\sin(\theta)}{-\Omega_d}\{\ldots\}\, d\theta$$
$$= \frac{1}{-2\pi\Omega_d}\left\{\widehat{A_d}\pi\sin(\phi) + \widehat{a_{p.T}}\Omega_d\gamma I_1 + \widehat{a_{p.T}}\Omega_d\pi\xi + \Omega_d B_3 \widehat{a_{p.T}}^3 \frac{\pi}{4}\right\} \quad \text{(E-118)}$$

doi:10.6342/NTU202600018

$$\phi' = \frac{1}{2\pi a}\int_{\theta_c}^{2\pi+\theta_c} \frac{cos(\theta)}{-\Omega_d}\{\dots\}d\theta$$

$$= \frac{1}{-2\pi a\Omega_d}\left\{\widehat{A_d}\pi\cos(\phi) + \alpha I_2 - \beta I_3 + \widehat{a_{p.T}}{\Omega_d}^2\pi - \widehat{a_{p.T}}\pi - K_3\widehat{a_{p.T}}^3\frac{3\pi}{4}\right\} \quad \text{(E-119)}$$

where integration coefficient of I_1, I_2 and I_3 are defined and labelled in (E-103), (E-110) and (E-111), respectively.

To find the steady-state periodic solution, the derivatives on the state variable must equal to zero (i.e., $\widehat{a_{p.T}}' = \phi' = 0$) for (E-118) and (E-119), yielding

$$\frac{1}{-2\pi\Omega_d}\left\{\widehat{A_d}\pi\sin(\phi) + \widehat{a_{p.T}}\Omega_d\gamma I_1 + \widehat{a_{p.T}}\Omega_d\pi\xi + \Omega_d B_3\widehat{a_{p.T}}^3\frac{\pi}{4}\right\} = 0$$

$$\rightarrow \frac{\widehat{A_d}}{\widehat{a_p}}\sin(\phi) = \left[\frac{-\gamma}{\pi}I_1 - \xi - \frac{1}{4}B_3\widehat{a_{p.T}}^2\right]\Omega_d \quad \text{(E-120)}$$

$$\frac{1}{-2\pi\Omega_d}\left\{\widehat{A_d}\pi\cos(\phi) + \alpha I_2 - \beta I_3 + \widehat{a_{p.T}}{\Omega_d}^2\pi - \widehat{a_{p.T}}\pi - K_3\widehat{a_{p.T}}^3\frac{3\pi}{4}\right\} = 0$$

$$\rightarrow \frac{\widehat{A_d}}{\widehat{a_{p.T}}}\cos(\phi) = -\frac{1}{\widehat{a_{p.T}}\pi}\alpha I_2 + \frac{1}{\widehat{a_{p.T}}\pi}\beta I_3 - {\Omega_d}^2 + 1 + \frac{3}{4}K_3\widehat{a_{p.T}}^2 \quad \text{(E-121)}$$

Summing up the square of (E-120) and square of (E-121) obtains

$$\frac{\widehat{A_d}^2}{\widehat{a_{p.T}}^2}\sin^2(\phi) + \frac{\widehat{A_d}^2}{\widehat{a_{p.T}}^2}\cos^2(\phi) = \frac{\widehat{A_d}^2}{\widehat{a_{p.T}}^2} =$$

$$\frac{\widehat{A_d}^2}{\widehat{a_{p.T}}^2} = \left[\frac{-\gamma}{\pi}I_1 - \xi - \frac{1}{4}B_3\widehat{a_{p.T}}^2\right]^2{\Omega_d}^2 + \left[-\frac{\alpha I_2}{\widehat{a_{p.T}}\pi} + \frac{\beta I_3}{\widehat{a_{p.T}}\pi} - {\Omega_d}^2 + 1 + \frac{3}{4}K_3\widehat{a_{p.T}}^2\right]^2 \quad \text{(E-122)}$$

Rearranging the above equation and defining few new variables for simplicity, given

doi:10.6342/NTU202600018

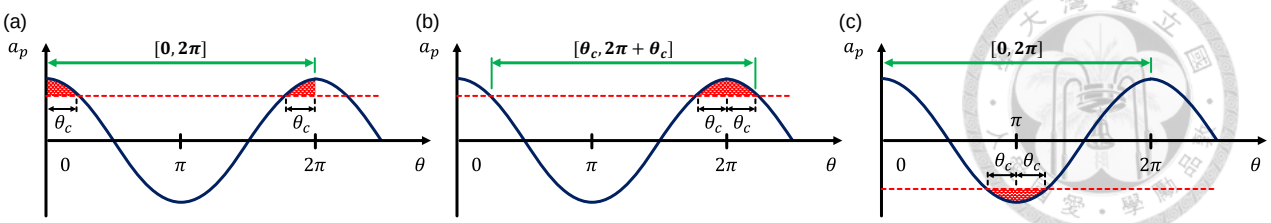


Figure E-2: Three diagrams illustrating one cycle of oscillation for a vibro-impact resonator with a single-sided contact. The representations show different integration paths over the phase angle: (a) from 0 to 2π, (b) from the contact angle θ_c to $2\pi + \theta_c$ and (c) from 0 to 2π with the contact occurring near π instead of 0 or 2π.

$$\frac{\widehat{A_d}^2}{\widehat{a_{p.T}}^2} = [\xi + C_{vis} + C_{vdP}]^2 {\Omega_d}^2 + \left[1 - K_{vdW} + K_H + K_D - {\Omega_d}^2\right]^2 \tag{E-123}$$

and each nonlinear term is defined as

$$C_{vis} = \frac{\gamma}{\pi} I_1 = \frac{\gamma}{\pi} \int_{\theta_c}^{2\pi+\theta_c} \sin(\theta) \left\{ \left(\widehat{a_{p.T}} \cos(\theta) - \widehat{d_0} + \widehat{a_0} \right)_{D_0}^{1/2} sin(\theta) \right\} d\theta \tag{E-124}$$

$$C_{vdP} = \frac{B_3 \widehat{a_{p.T}}^2}{4} \tag{E-125}$$

$$K_{vdW} = \frac{1}{\widehat{a_{p.T}}\pi} \alpha I_2 = \frac{1}{\widehat{a_{p.T}}\pi} \alpha \int_{\theta_c}^{2\pi+\theta_c} cos(\theta) \left\{ \left(\widehat{d_0} - \widehat{a_{p.T}}\, cos\,(\theta) \right)_{D_{\widehat{a_0}}}^{-2} \right\} d\theta \tag{E-126}$$

$$K_H = \frac{1}{\widehat{a_{p.T}}\pi} \beta I_3 = \frac{1}{\widehat{a_{p.T}}\pi} \beta \int_{\theta_c}^{2\pi+\theta_c} cos(\theta) \left\{ \left(\widehat{a_{p.T}}\, cos(\theta) - \widehat{d_0} + \widehat{a_0} \right)_{D_0}^{3/2} \right\} d\theta \tag{E-127}$$

$$K_D = \frac{3}{4} K_3 \widehat{a_{p.T}}^2 \tag{E-128}$$

The (E-123) is essential a quadratic equation in terms of Ω_d that can be used to numerically solve the frequency response of a vibro-impact resonator with KV-DMT model.

In details, as shown in Figure E-2, the piecewise functions in (E-124), (E-126) and

doi:10.6342/NTU202600018

(E-127) can be expanded and represented with physical quantities as with different coordinate definition while, in the case, Figure E-2 (a) is chosen for simplicity, taking the form

$$C_{vis} = \frac{\gamma}{\pi}\left(\frac{a_{p.T}}{A_0}\right)^{\frac{1}{2}}\left\{\int_0^{\theta_c}[\cos(\theta)-\zeta_1+\zeta_2]^{\frac{1}{2}}\sin^2(\theta)\,d\theta + \int_{2\pi-\theta_c}^{2\pi}[\cos(\theta)-\zeta_1+\zeta_2]^{\frac{1}{2}}\sin^2(\theta)\,d\theta\right\} \tag{E-129}$$

$$K_{vdw} = \frac{\alpha}{\pi}\left(\frac{a_p}{A_0}\right)^{-3}\left[\int_0^{\theta_c}\frac{cos(\theta)\,d\theta}{\zeta_2^2} + \int_{\theta_c}^{2\pi-\theta_c}\frac{cos(\theta)\,d\theta}{(\zeta_1-cos(\theta))^2} + \int_{2\pi-\theta_c}^{2\pi}\frac{cos(\theta)\,d\theta}{\zeta_2^2}\right] \tag{E-130}$$

$$K_H = \frac{\beta}{\pi}\left(\frac{a_{p.T}}{A_0}\right)^{\frac{1}{2}}\left\{\int_0^{\theta_c}[\cos(\theta)-\zeta_1+\zeta_2]^{\frac{3}{2}}\cos(\theta)\,d\theta + \int_{2\pi-\theta_c}^{2\pi}[\cos(\theta)-\zeta_1+\zeta_2]^{\frac{3}{2}}\cos(\theta)\,d\theta\right\} \tag{E-131}$$

and the added stiffness and damping of the lumped nonlinearities (*cf.* (E-125) and (E-128)) with physical quantities are represented as

$$C_{vdP} = B_3\frac{\widehat{a_{p.T}}^2}{4} = \frac{b_3A_0^2}{\sqrt{m_rk_r}}\frac{\left(\frac{a_{p.T}}{A_0}\right)^2}{4} = \frac{1}{4}\frac{b_3{a_{p.T}}^2}{m_r\omega_n} \tag{E-132}$$

$$K_D = \frac{3}{4}K_3\widehat{a_{p.T}}^2 = \frac{3}{4}\frac{k_3A_0^2}{k_r}\left(\frac{a_{p.T}}{A_0}\right)^2 = \frac{3}{4}\frac{k_3{a_{p.T}}^2}{k_r} \tag{E-133}$$

where $\zeta_1 = d_0/a_p$ and $\zeta_2 = a_0/a_p$ are amplitude dependent variables, named as gap spacing ratio and interatomic spacing ratio, respectively. Noted, $\theta_c = \cos^{-1}(\zeta_1-\zeta_2)$ and instead of solving this equation by given Ω_d, it is recommended to given $\widehat{a_{p.T}}$ and solve Ω_d because the equation for $\widehat{a_{p.T}}$ is nonlinear function of Ω_d.

doi:10.6342/NTU202600018

Moreover, to link the physical meaning and compared with linear frequency response, taking the square root to (E-123) and expressing the equation in term of nondimensionalized displacement gives

$$\widehat{a_{p.T}} = \frac{\widehat{A_d}}{\sqrt{\bar{\bar{A}}^2 + \bar{\bar{B}}^2}} \tag{E-134}$$

where the coefficient $\bar{\bar{A}}$ and $\bar{\bar{B}}$ are defined as

$$\bar{\bar{A}} = 1 - K_{vdW} + K_H + K_D - {\Omega_d}^2 \tag{E-135}$$

$$\bar{\bar{B}} = (\xi + C_{vis} + C_{vdP})\Omega_d \tag{E-136}$$

Replacing $\widehat{x_{T.f}} = \widehat{a_{p.T}} cos(\Omega_d \hat{t} + \phi) = (a_{p.T}/A_0) cos\,(\omega_d t + \phi)$, $A_0 = QA_d/k_r$, $\widehat{A_d} = A_d/(k_r A_0) = 1/Q$, and $\Omega_d = \omega_d/\omega_n$ yields

$$x_{T.f} = \frac{A_d cos\,(\omega_d t + \phi)}{m_r \sqrt{\hat{A}^{\,2} + B^{\,2}}} \tag{E-137}$$

and

$$\hat{A} = (1 - K_{vdW} + K_H + K_D)\omega_n^2 - \omega_d^2 \tag{E-138}$$

$$\hat{B} = \omega_n(\xi + C_{vis} + C_{vdP})\omega_d \tag{E-139}$$

The equation states that the nonlinear term of K_{vdW}, K_H and K_D affect the resonance frequency and C_{vis} and C_{vdP} contribute additional damping. They are all function of amplitude. In addition, letting $H = \beta = E^* = k_3 = b_3 = 0$ yields the linear frequency response of (A-18), same as the one derivate in Appendix A.1

$$x_{l.f} = \frac{A_d cos\,(\omega_d t + \phi)}{m_r \sqrt{(\omega_n^2 - \omega_d^2)^2 + \omega_n^2 \xi^2 \omega_d^2}} \tag{E-140}$$

Noted, the integration of I_1 shown in [196, 377, 466] might have a mistaken on trigonometric functions which would be $sin^2(\theta)$ instead of $cos(\theta)$.

doi:10.6342/NTU202600018

E.4.2 Equation of Motion with Linear Contact Stiffness

Recalling the nondimensional equation of motion with linear contact stiffness from (E-44)

$$\hat{x}'' + \xi\hat{x}' + \hat{x} + \beta_l\left(\hat{x} - \widehat{d_0}\right)_{D_0} = \widehat{A_d}\cos\left(\Omega_d t\right) \tag{E-141}$$

Following same procedure as presented in Appendix E.1, substituting (E-86), (E-87) and (E-90) into (E-141) yields

$$\begin{aligned} &-\widehat{a_{p.k}}'\Omega_d\, sin(\theta) - \widehat{a_{p.k}}\Omega_d^2\, cos(\theta) - \widehat{a_{p.k}}\Omega_d\phi'\, cos(\theta) \\ &+\xi\left[-\widehat{a_{p.k}}\Omega_d \sin(\theta)\right] + \widehat{a_{p.k}}\cos(\theta) + \beta_l\left[\widehat{a_{p.k}}\cos(\theta) - \widehat{d_0}\right]_{D_0} \\ &= \widehat{A_d}\cos\left(\Omega_d t\right) \end{aligned} \tag{E-142}$$

Solving (E-142) together with (E-89), one can find the slow varying amplitude and phase equation as

$$\begin{aligned} \widehat{a_{p.k}}' = \frac{1}{\Omega_d}\{&-\xi\widehat{a_{p.k}}\Omega_d \sin^2(\theta) - \widehat{a_{p.k}}\Omega_d^2\, cos(\theta)\sin(\theta) \\ &+\widehat{a_{p.k}}\, cos(\theta)\sin(\theta) + sin(\theta)\,\beta_l\left[\widehat{a_{p.k}}\cos(\theta) - \widehat{d_0}\right]_{D_0} \\ &-\widehat{A_d}\sin(\theta)\cos\left(\Omega_d t\right)\} \end{aligned} \tag{E-143}$$

$$\begin{aligned} \phi' = \frac{1}{\widehat{a_{p.k}}\Omega_d}\{&-\xi\widehat{a_{p.k}}\Omega_d \sin(\theta) - \widehat{a_{p.k}}\Omega_d^2\, cos^2(\theta) + \widehat{a_{p.k}}\cos^2(\theta) \\ &+ cos(\theta)\,\beta_l\left[\widehat{a_{p.k}}\cos(\theta) - \widehat{d_0}\right]_{D_0} - \widehat{A_d}\, cos(\theta)\cos\left(\Omega_d t\right)\} \end{aligned} \tag{E-144}$$

Taking the integral over a period for (E-143) and (E-144) in polar coordinate (i.e., $\theta = \theta_c$ to $\theta = 2\pi + \theta_c$ where θ_c is contact phase) gives

$$\widehat{a_{p.k}}' = \frac{1}{2\pi\Omega_d}\{-\xi\widehat{a_{p.k}}\Omega_d\pi - \widehat{A_d}\pi\sin(\phi)\} \tag{E-145}$$

doi:10.6342/NTU202600018

$$\phi' = \frac{1}{2\pi\widehat{a_{p.k}}\Omega_d}\left\{-\widehat{a_{p.k}}\Omega_d^2\pi + \widehat{a_{p.k}}\pi\right.$$
$$\left.+\beta_l\left[\widehat{a_{p.k}}\theta_c + \frac{1}{2}\widehat{a_{p.k}}\sin^2(\theta_c) - 2\widehat{d_0}\sin(\theta_c)\right] - \widehat{A_d}\pi cos\,(\phi)\right\} \quad \text{(E-146)}$$

Looking into steady-state solution, the derivatives on the state variable must equal to zero (i.e., $\widehat{a_{p.T}}' = \phi' = 0$), yielding

$$\widehat{A_d}\sin(\phi) = -\xi\widehat{a_{p.k}}\Omega_d \quad \text{(E-147)}$$

$$\widehat{A_d}\cos(\phi) = -\widehat{a_{p.k}}\Omega_d^2 + \widehat{a_{p.k}}$$
$$+\frac{\beta_l}{\pi}\left[\widehat{a_{p.k}}\theta_{c.k} + \frac{1}{2}\widehat{a_{p.k}}\sin^2(\theta_{c.k}) - 2\widehat{d_0}\sin(\theta_{c.k})\right] \quad \text{(E-148)}$$

Summing up the square of (E-147) and square of (E-148) obtains

$$\widehat{A_d}^2 = \left(-\xi\widehat{a_{p.k}}\Omega_d\right)^2 + \left\{-\widehat{a_{p.k}}\Omega_d^2 + \widehat{a_{p.k}}\right.$$
$$\left.+\frac{\beta_l}{\pi}\left[\widehat{a_{p.k}}\theta_{c.k} + \frac{1}{2}\widehat{a_{p.k}}\sin^2(\theta_{c.k}) - 2\widehat{d_0}\sin(\theta_{c.k})\right]\right\}^2 \quad \text{(E-149)}$$

Rearranging the above equation and defining a new variable for simplicity, one could write

$$\frac{\widehat{A_d}^2}{\widehat{a_{p.k}}^2} = (\xi\Omega_d)^2 + [1 + K_c - \Omega_d^2]^2 \quad \text{(E-150)}$$

where the nonlinear contact stiffness term and contact angle are defined as

$$K_c = \frac{\beta_l}{\widehat{a_{p.k}}^2\pi}\left[\widehat{a_{p.k}}\theta_c + \frac{1}{2}\widehat{a_{p.k}}\sin^2(\theta_c) - 2\widehat{d_0}\sin(\theta_c)\right] \quad \text{(E-151)}$$

$$\theta_{c.k} = \cos^{-1}\left(\frac{\widehat{d_0}}{\widehat{a_{p.k}}}\right) \quad \text{(E-152)}$$

Noted, again, instead of solving this equation by given Ω_d, it is recommended to given $\widehat{a_{p.k}}$ and solve Ω_d because the equation for $\widehat{a_{p.k}}$ is nonlinear function of Ω_d.

Similarity, the frequency response in terms of physical quantity can be given by

doi:10.6342/NTU202600018

$$a_{p.k} = \frac{A_d}{m_r\sqrt{\tilde{A}^2 + \bar{B}^2}} \tag{E-153}$$

and coefficients are presented as

$$\bar{B} = \omega_n \omega_d / Q = \omega_n \xi \omega_d \tag{E-154}$$

$$\tilde{A} = (1 + K_c)\omega_n^2 - \omega_d^2 \tag{E-155}$$

$$K_c = \frac{k_c\, A_0}{k_r a_{p.k} \pi}\left[\theta_{c.k} + \frac{1}{2}\sin^2(\theta_{c.k}) - 2\frac{d_0}{a_{p.k}}\sin(\theta_{c.k})\right] \tag{E-156}$$

E.5 Stability Analysis based on Slowly Varying Equation

Recalling the results in (E-118) and (E-119) (*cf.* Appendix E.4), the vector field of averaged system, $\boldsymbol{F}$, are shown as

$$\boldsymbol{F}(\boldsymbol{x}(\boldsymbol{t}), \boldsymbol{p}) = \begin{bmatrix} \widehat{a_p}' \\ \phi' \end{bmatrix} \tag{E-157}$$

where $\boldsymbol{p}$ indicate the possible control parameters, for instance, forcing level, Hamaker constant, stiffness of system, …, etc. The 1st order time derivative of the displacement and phase (i.e., (E-118) and (E-119)) are given by

$$\widehat{a_{p.T}}' = \frac{1}{-2\pi\Omega}\left\{\widehat{A_d}\pi\cos(\phi) + \widehat{a_{p.T}}\Omega_d\gamma I_1 + \widehat{a_{p.T}}\Omega_d\pi\xi + \Omega_d B_3 \widehat{a_{p.T}}^3 \frac{\pi}{4}\right\} \tag{E-158}$$

$$\begin{aligned}\phi' = \frac{1}{-2\pi\widehat{a_{p.T}}\Omega_d}\Big\{&\widehat{A_d}\pi\sin(\phi) + \alpha I_2 - \beta I_3 + \widehat{a_{p.T}}\Omega_d{}^2\pi - \widehat{a_{p.T}}\pi \\ &- K_3\widehat{a_{p.T}}^3\frac{3\pi}{4}\Big\}\end{aligned} \tag{E-159}$$

The Jacobian matrix of the given vector field can be written as

$$D_x\boldsymbol{F} = \boldsymbol{A} = \begin{bmatrix} \frac{\partial(\widehat{a_{p.T}}')}{\partial a} & \frac{\partial(\widehat{a_{p.T}}')}{\partial \phi} \\ \frac{\partial(\phi')}{\partial a} & \frac{\partial(\phi')}{\partial \phi} \end{bmatrix} = \begin{bmatrix} A_1 & A_2 \\ A_3 & A_4 \end{bmatrix} \tag{E-160}$$

doi:10.6342/NTU202600018

The eigenvalue problem for above vector is given by

$$[\boldsymbol{A}-\lambda\boldsymbol{I}]=\begin{bmatrix}A_1-\lambda & A_2\\ A_3 & A_4-\lambda\end{bmatrix} \tag{E-161}$$

where $\boldsymbol{I}$ is identity matrix of order two.

It seems like this is a homogeneous linearized system, therefore it should have a nontrivial solution if and only if its coefficient determinant is zero, that is

$$\begin{aligned} det[\boldsymbol{A}-\lambda\boldsymbol{I}] &= (A_1-\lambda)(A_4-\lambda)-A_2A_3\\ &= \lambda^2-(A_1+A_4)\lambda+A_1A_4-A_2A_3 \end{aligned} \tag{E-162}$$

where the coefficients are

$$A_1=\frac{1}{-2\pi\Omega_d}\left\{\Omega_d\gamma\left(\widehat{a_{p.T}}I_1\right)'+\Omega_d\pi\xi+\Omega_dB_3{\widehat{a_{p.T}}}^2\frac{\pi}{4}\right\} \tag{E-163}$$

$$A_2=\frac{1}{-2\pi\Omega_d}\left\{-\widehat{A_d}\pi\sin(\phi)\right\} \tag{E-164}$$

$$A_3=\frac{1}{-2\pi\Omega_d}\left\{\frac{\widehat{A_d}\pi\sin(\phi)}{-{\widehat{a_{p.T}}}^2}+\left(\frac{\alpha I_2}{\widehat{a_{p.T}}}\right)'-\left(\frac{\beta I_3}{\widehat{a_{p.T}}}\right)'-K_3\widehat{a_{p.T}}\frac{3\pi}{2}\right\} \tag{E-165}$$

$$A_4=\frac{1}{-2\pi\widehat{a_{p.T}}\Omega_d}\left\{\widehat{A_d}\pi\cos(\phi)\right\} \tag{E-166}$$

where the derivatives on integration function remained and the terms $\sin(\phi)$ and $\cos(\phi)$ are to be determined. Although, the term $1/-2\pi\Omega$ can be dropped out here because all terms have, however, it is deferred and will disappear at next step.

Considering the steady-state equation for (E-158) and (E-159), the relations could be obtained as

$$0=\frac{1}{-2\pi\Omega_d}\left\{\widehat{A_d}\pi\cos(\phi)+\widehat{a_{p.T}}\Omega_d\gamma I_1+\widehat{a_{p.T}}\Omega_d\pi\xi+\Omega_dB_3{\widehat{a_{p.T}}}^3\frac{\pi}{4}\right\} \tag{E-167}$$

doi:10.6342/NTU202600018

$$\rightarrow \cos(\phi) = \frac{1}{\widehat{A_d}}\left[-\frac{\Omega_d \widehat{a_{p.T}} \gamma I_1}{\pi} - \Omega_d \widehat{a_{p.T}} \xi - \frac{\Omega_d B_3 \widehat{a_{p.T}}^3}{4}\right]$$

$$0 = \frac{1}{-2\pi \widehat{a_{p.T}} \Omega_d}\left\{\widehat{A_d}\pi \sin(\phi) + \alpha I_2 - \beta I_3 + \widehat{a_{p.T}} {\Omega_d}^2 \pi - \widehat{a_{p.T}}\pi - K_3 \widehat{a_{p.T}}^3 \frac{3\pi}{4}\right\} \quad \text{(E-168)}$$

$$\rightarrow \sin(\phi) = \frac{1}{\widehat{A_d}}\left[-\frac{\alpha I_2}{\pi} + \frac{\beta I_3}{\pi} - \widehat{a_{p.T}} {\Omega_d}^2 + \widehat{a_{p.T}} + K_3 \widehat{a_{p.T}}^3 \frac{3}{4}\right]$$

Substituting (E-167) and (E-168) into (E-158) and (E-159), the coefficients $A_{i=1,2,3,4}$ can be determined as

$$A_1 = \frac{1}{-2\pi\Omega_d}\left\{\Omega_d \gamma\left[I_1 + \widehat{a_{p.T}} I_4\right] + \Omega_d \pi \xi + \Omega_d B_3 3 \widehat{a_{p.T}}^2 \frac{\pi}{4}\right\} \quad \text{(E-169)}$$

$$A_2 = \frac{1}{2\Omega_d}\left\{-\frac{\alpha I_2}{\pi} + \frac{\beta I_3}{\pi} - \widehat{a_{p.T}} {\Omega_d}^2 + \widehat{a_{p.T}} + K_3 \widehat{a_{p.T}}^3 \frac{3}{4}\right\} \quad \text{(E-170)}$$

$$\begin{aligned} A_3 = \frac{1}{-2\pi\Omega_d}\Bigg\{&\frac{1}{-\widehat{a_p}^2}\left[-\alpha I_2 + \beta I_3 - \widehat{a_{p.T}}\pi {\Omega_d}^2 + \widehat{a_{p.T}}\pi + K_3 \widehat{a_{p.T}}^3 \pi \frac{3}{4}\right] \\ &+\alpha\left(\frac{I_2}{-\widehat{a_{p.T}}^2} + \frac{(I_2)'}{\widehat{a_{p.T}}}\right) - \beta\left(\frac{I_3}{-\widehat{a_{p.T}}^2} + \frac{(I_3)'}{\widehat{a_{p.T}}}\right) - K_3 \widehat{a_{p.T}} \frac{3\pi}{2}\Bigg\} \\ = \frac{1}{-2\pi\Omega_d}&\left\{\frac{\pi {\Omega_d}^2}{\widehat{a_{p.T}}} - \frac{\pi}{\widehat{a_{p.T}}} + \frac{\alpha (I_2)'}{\widehat{a_{p.T}}} - \frac{\beta (I_3)'}{\widehat{a_{p.T}}} - K_3 \widehat{a_{p.T}} \frac{9\pi}{4}\right\} \\ = \frac{1}{-2\pi\Omega_d}&\left\{\frac{\pi {\Omega_d}^2}{\widehat{a_{p.T}}} - \frac{\pi}{\widehat{a_{p.T}}} + \frac{\alpha I_5}{\widehat{a_{p.T}}} - \frac{\beta I_6}{\widehat{a_{p.T}}} - K_3 \widehat{a_{p.T}} \frac{9\pi}{4}\right\} \end{aligned} \quad \text{(E-171)}$$

$$A_4 = \frac{1}{-2\widehat{a_{p.T}}\Omega_d}\left\{-\Omega_d \widehat{a_{p.T}} \gamma I_1 - \Omega_d \widehat{a_{p.T}} \pi \xi - \pi \frac{\Omega_d B_3 \widehat{a_{p.T}}^3}{4}\right\} \quad \text{(E-172)}$$

where the integration functions are given as

doi:10.6342/NTU202600018

$$I_4 = \frac{dI_1}{d\widehat{a_{p.T}}} = \int_{\theta_c}^{2\pi+\theta_c} \left\{ \left(\frac{\widehat{a_{p.T}}}{2}\cos(\theta) - \widehat{d_0} + \widehat{a_0} \right)_{D_0}^{-1/2} \cos(\theta)\, sin^2(\theta) \right\} d\theta \quad \text{(E-173)}$$

$$I_5 = \frac{dI_2}{d\widehat{a_{p.T}}} = \int_{\theta_c}^{2\pi+\theta_c} 2\, cos^2(\theta) \left\{ \left(\widehat{d_0} - \widehat{a_{p.T}} cos\,(\theta) \right)_{D_{a_0}}^{-3} \right\} d\theta \quad \text{(E-174)}$$

$$I_6 = \frac{dI_3}{d\widehat{a_{p.T}}} = \int_{\theta_c}^{2\pi+\theta_c} \frac{3}{2} cos^2(\theta) \left\{ \left(\widehat{a_{p.T}}\cos(\theta) - \widehat{d_0} + \widehat{a_0} \right)_{D_0}^{1/2} \right\} d\theta \quad \text{(E-175)}$$

By solving the characteristic equation of (E-162), one can determine the stability of the system based on the analysis method presented in Appendix E.6. In short, the system is unstable (stable) if the real part of the eigenvalues greater or equal to (less than) zero.

E.6 Nonlinear Ring-down Envelop Equation

On the other hand, in order to extract the nonlinear van der Pol damping term, a analytical solution of the nonlinear ring-down envelop is needed. Considering only the Duffing and van der Pol term (i.e., ignore the effect of relatively strongly surface interaction force in the beginning) and recalling the slow varying equation on amplitude (E-118) presents

$$\widehat{a_{RD.vdP}}' = -\frac{\xi}{2}\widehat{a_{RD.vdp}} - \frac{B_3}{8}\widehat{a_{RD.vdp}}^3 \quad \text{(E-176)}$$

Observably, the Duffing term only affect the frequency thus disappear here (i.e., they are related to the equation with ϕ'). Arranging the equation in the special form and separate the variable a and $\hat{t}$ obtains

$$\frac{d\widehat{a_{RD.vdP}}}{\widehat{a_{RD.vdP}}^3 \left(\frac{B_3}{4\xi} + \widehat{a_{RD.vdP}}^{-2} \right)} = -\frac{\xi}{2} d\hat{t} \quad \text{(E-177)}$$

Defining a transformation of

doi:10.6342/NTU202600018

$$u = \widehat{a_{RD.vdP}}^{-2} \tag{E-178}$$

$$du = -2\widehat{a_{RD.vdP}}^{3} d\widehat{a_{RD.vdP}} \rightarrow d\widehat{a_{RD.vdP}} = -\frac{1}{2}\widehat{a_{RD.vdP}}^{3} du \tag{E-179}$$

And substituting (E-178) and (E-179) into (E-177), the equation becomes

$$\frac{du}{\frac{B_3}{4\xi} + u} = \xi d\hat{t} \tag{E-180}$$

Taking integration and transforming bake to the original variable yields

$$\begin{aligned} &\ln\left(\frac{B_3}{4\xi} + u\right) + C_1 = \xi\hat{t} \\ &\rightarrow \ln\left(\frac{B_3}{4\xi} + \widehat{a_{RD.vdP}}^{-2}\right) + C_1 = \xi\hat{t} \end{aligned} \tag{E-181}$$

If I.C. is $\widehat{a_{RD.vdP}}(0) = \widehat{a_{RD.vdP.0}}$, the unknown coefficient C_1 can be obtained as

$$\begin{aligned} &\ln\left(\frac{B_3}{4\xi} + \widehat{a_{RD.vdP.0}}^{-2}\right) + C_1 = 0 \\ &\rightarrow C_1 = -\ln\left(\frac{B_3}{4\xi} + \widehat{a_{RD.vdP.0}}^{-2}\right) \end{aligned} \tag{E-182}$$

The solution is thus given by

$$\begin{aligned} &\ln\left(\frac{B_3}{4\xi} + \widehat{a_{RD.vdP}}^{-2}\right) - \ln\left(\frac{B_3}{4\xi} + \widehat{a_{RD.vdP.0}}^{-2}\right) \\ &= \ln\left(\frac{\frac{B_3}{4\xi} + \widehat{a_{RD.vdP}}^{-2}}{\frac{B_3}{4\xi} + \widehat{a_{RD.vdP.0}}^{-2}}\right) = \xi\hat{t} \end{aligned} \tag{E-183}$$

Arranging the above equation, one can get

$$\left(\frac{B_3}{4\xi} + \widehat{a_{RD.vdP}}^{-2}\right)/\left(\frac{B_3}{4\xi} + \widehat{a_{RD.vdP.0}}^{-2}\right) = e^{\xi\hat{t}} \tag{E-184}$$

doi:10.6342/NTU202600018

$$\rightarrow \frac{B_3}{4\xi} + \widehat{a_{RD.vdP}}^{-2} = \frac{B_3}{4\xi} + \widehat{a_{RD.vdP.0}}^{-2} e^{\xi\hat{t}}$$

$$\rightarrow \widehat{a_{RD.vdP}}^{-2} = \left(\frac{B_3}{4\xi} + \widehat{a_{RD.vdP.0}}^{-2}\right) e^{\xi\hat{t}} - \frac{B_3}{4\xi}$$

$$= \widehat{a_{RD.vdP.0}}^{-2} e^{\xi\hat{t}} + \frac{B_3}{4\xi}\left(e^{\xi\hat{t}} - 1\right)$$

$$\rightarrow \widehat{a_{RD.vdP}}^{2} = \frac{1}{\left[\widehat{a_{RD.vdP.0}}^{-2} e^{\xi\hat{t}} + \frac{B_3}{4\xi}\left(e^{\xi\hat{t}} - 1\right)\right]}$$

$$\rightarrow \widehat{a_{RD.vdP}}^{2} = \frac{\widehat{a_{RD.vdP.0}}^{2} e^{-\xi\hat{t}}}{1 + \frac{B_3}{4\xi}\widehat{a_{RD.vdP.0}}^{2}\left(1 - e^{\xi\hat{t}}\right)}$$

$$\therefore \widehat{a_{RD.vdP}} = \frac{\widehat{a_{RD.vdP.0}} e^{-\frac{\xi}{2}\hat{t}}}{\sqrt{1 + \frac{B_3}{4\xi}\widehat{a_{RD.vdP.0}}^{2}\left(1 - e^{\xi\hat{t}}\right)}} = \frac{e^{-\frac{\xi}{2}\hat{t}}}{\sqrt{1 + \frac{B_3}{4\xi}\left(1 - e^{\xi\hat{t}}\right)}}$$

where the non-dimensional van der Pol damping is a bit different than the previous subsection, defined as $B_3 = b_3 x_0^{*2}/(m_r\omega_0)$ here. In fact, the $x_m^* = d_{0.SEM}$ is both reference dimension and initial condition during ring down, therefore, $\widehat{a_{RD.vdP.0}} = x_0^*/x_0^* = 1$ sine the definition of dimensionless amplitude are $\widehat{a_{p.vdP}} = a_{p.vdP}/x_0^*$ here.

(E-184) can then represented as

$$x_{RD.en.vdP} = \frac{x_0^* e^{-\frac{\xi}{2}\hat{t}}}{\sqrt{1 + \frac{B_3}{4\xi}\left(1 - e^{\xi\hat{t}}\right)}} \tag{E-185}$$

Noted, the measured data are fist transfer to dimensionless domain then smooth by averaging twenty data and fitted with (E-184). Finally, the $b_3 = B_3 m_r\omega_0/x_0^{*2}$ are calculated.

E.7 Jump-up Frequency of Duffing Oscillators

Recalling the averaged Duffing system from (E-123) as

doi:10.6342/NTU202600018

$$\frac{\widehat{A_d}^2}{\widehat{a_{p.D}}^2} = \xi^2 {\Omega_d}^2 + \left[1 + \frac{3}{4} K_3 \widehat{a_{p.T}}^2 - {\Omega_d}^2\right]^2 \tag{E-186}$$

Following with [398], it is considered that the jump-up frequency is weakly dependent on the damping thus the (E-186) reduces as

$$\begin{aligned} \frac{\widehat{A_d}}{\widehat{a_{p.D^*}}} &= 1 + \frac{3}{4} K_3 \widehat{a_{p.D^*}}^2 - {\Omega_d}^2 \\ \rightarrow \Omega_d &= \left(1 + \frac{3}{4} K_3 \widehat{a_{p.D^*}}^2 + \frac{\widehat{A_d}}{\widehat{a_{p.D^*}}}\right)^{1/2} \end{aligned} \tag{E-187}$$

Taking the derivative with respect to $\widehat{a_{p.D^*}}$ to (E-187) yields

$$\frac{\partial \Omega_d}{\widehat{a_{p.D^*}}} = \frac{\left[\frac{3}{2} K_3 \widehat{a_{p.D^*}} - \frac{\widehat{A_d}}{\widehat{a_{p.D^*}}^2}\right]}{2\left[1 + \frac{3}{4} K_3 \widehat{a_{p.D^*}}^2 + \frac{\widehat{A_d}}{\widehat{a_{p.D^*}}}\right]} \tag{E-188}$$

Solving $\partial \Omega_d / \widehat{a_{p.D^*}} = 0$ for $\widehat{a_{p.D^*}}$ given

$$\begin{aligned} \frac{3}{2} K_3 \widehat{a_{p.D^*}} - \frac{\widehat{A_d}}{\widehat{a_{p.D^*}}^2} &= 0 \\ \rightarrow \widehat{a_{p.D^*.JU}} &= \left(\frac{2}{3}\right)^{\frac{1}{3}} \left(\frac{\widehat{A_d}}{K_3}\right)^{\frac{1}{3}} \end{aligned} \tag{E-189}$$

Substituting into (E-187) yields the jump-up frequency

$$\begin{aligned} \Omega_{D.JU} &= \left(1 + sign\frac{3}{4}|K_3|\left(\frac{2}{3}\right)^{\frac{2}{3}}\left(\frac{\widehat{A_d}}{|K_3|}\right)^{\frac{2}{3}} + sign\widehat{A_d}\left(\frac{2}{3}\right)^{\frac{-1}{3}}\left(\frac{\widehat{A_d}}{|K_3|}\right)^{\frac{-1}{3}}\right)^{\frac{1}{2}} \\ &= \left[1 + sign\left(\frac{3}{2}\right)^{\frac{4}{3}} \widehat{A_d}^{\frac{2}{3}} |K_3|^{\frac{1}{3}}\right]^{1/2} \end{aligned} \tag{E-190}$$

doi:10.6342/NTU202600018

where the $sign$ is $+1$ for hardening system and $sign = -1$ for softening system.

For weak Duffing term (i.e., $K_3 \ll 1$), (E-190) simplifies to

$$\Omega_{D.JU} = 1 + sign\frac{1}{2}\left(\frac{3}{2}\right)^{\frac{4}{3}} \widehat{A_d}^{\frac{2}{3}} |K_3|^{\frac{1}{3}} \tag{E-191}$$

Putting the physical quantity back to the equation yields

$$\omega_{D.JU} = \left[1 + sign\frac{1}{2}\left(\frac{3}{2}\right)^{\frac{4}{3}} |k_3|^{\frac{1}{3}} k_r^{-1} A_d^{\frac{2}{3}}\right] \omega_n \tag{E-192}$$

doi:10.6342/NTU202600018

Appendix F: Derivation of Peak Repulsive Force Formulas and Scaling Laws

The appendix provides the detail of derivation on the peak repulsive force formulars conducted in the main text. Few results are copied and revied from another Chapters firstly. The reason and meaning of results are brief remind to give clear representation. In the following, symbol "→" represents some mathematical operations and provides some detail on the derivation.

The closed form analytical expressions of peak repulsive force formulars for MEMS vibro-impact resonators are not presented in this work for the first time. In fact, the peak repulsive force formulars based on 1-DOF equation of motion are first derived by [376, 561] for the application of the tapping mode AFM, in which the analytical derivation based on a general tip-sample interaction force taking the form of

$$F_c(x) = \begin{cases} -\dfrac{C_{ts}}{x^{\alpha}} \\ -\dfrac{C_{ts}}{a_0^{\alpha}} + D_{ts}(a_0 - x)^{\beta} \end{cases} \tag{F-1}$$

are presented. Three formulars based on pure attractive force, DMT model, and linear contact stiffness model with proper choose of C_{ts}, D_{ts}, α and β is discussed therein. In particular, the derivative formular based on DMT model are compared with several hundred simulated data and the sources of errors are conducted fully. The impressive idea is based on an insightful approximation by changing the integral path for which the nonlinear frequency formular is integrable. In this dissertation, the results are extended further with the limited effect of Duffing term and van der Pol term where the linear quality factor and linear resonance are modified with correction terms that caused by the nonlinearities.

F.1 Governing Equation, Assumptions and Remarks

Here summarize the main results derived in Appendix E.2 and E.4. Recalling the

doi:10.6342/NTU202600018

non-dimensional nonlinear equation of motion of (E-32)

$$\hat{x}'' + \xi\hat{x}' + \hat{x} + B_3\hat{x}^2\hat{x}' + K_3\hat{x}^3 =$$

$$\widehat{A_d}cos(\Omega_d\hat{t}) + \frac{\alpha}{\left(\widehat{d_0} - \hat{x}\right)^2_{D_{\widehat{a_0}}}} - \beta\left(\hat{x} - \widehat{d_0} + \widehat{a_0}\right)^{\frac{3}{2}}_{D_0} - \gamma\left(\hat{x} - \widehat{d_0} + \widehat{a_0}\right)^{\frac{1}{2}}_{D_0}\hat{x}' \quad \text{(F-2)}$$

It is considered with the implementation of method averaging presented in Appendix E.5 where the effect of nonlinearity is investigated with the averaged system. The 1st order derivative of displacement and phase of the averaged system of (E-118) and (E-119) are given by

$$\widehat{a_{p.T}}' = \frac{1}{-2\pi\Omega_d}\left\{\widehat{A_d}\pi\cos(\phi) + \widehat{a_{p.T}}\Omega_d\gamma I_1 + \widehat{a_{p.T}}\Omega_d\pi\xi + \Omega_d B_3\widehat{a_{p.T}}^3\frac{\pi}{4}\right\} \quad \text{(F-3)}$$

$$\phi' = \frac{1}{-2\pi\widehat{a_{p.T}}\Omega_d}\left\{\widehat{A_d}\pi\sin(\phi) + \alpha I_2 - \beta I_3 + \widehat{a_{p.T}}\Omega_d{}^2\pi - \widehat{a_{p.T}}\pi - K_3\widehat{a_{p.T}}^3\frac{3\pi}{4}\right\} \quad \text{(F-4)}$$

These two equations represent the evolution on the slow time scale (i.e., envelope) of the displacement amplitude and phase of the forced vibro-impact oscillator. Looking on the steady-state solution needs that $\widehat{a_{p.T}}' = \phi' = 0$ leading to the equilibrium solution[3] as follows [376]

$$\begin{gathered}\widehat{A_d}\pi\cos(\phi) = -\left\{\widehat{a_{p.T}}\Omega_d\gamma I_1 + \widehat{a_{p.T}}\Omega_d\pi\xi + \Omega_d B_3\widehat{a_{p.T}}^3\frac{\pi}{4}\right\} \\ \rightarrow \widehat{A_d}\cos(\phi) \equiv -\widehat{a_{p.T}}\Omega_d\xi_{eff}\end{gathered} \quad \text{(F-5)}$$

$$\widehat{A_d}\pi\sin(\phi) = -\left\{\alpha I_2 - \beta I_3 + \widehat{a_{p.T}}\Omega_d{}^2\pi - \widehat{a_{p.T}}\pi - K_3\widehat{a_{p.T}}^3\frac{3\pi}{4}\right\}$$

$$\rightarrow \widehat{A_d}\sin(\phi) = \widehat{a_{p.T}}\left\{1 - \frac{\alpha I_2}{\widehat{a_{p.T}}\pi} + \frac{\beta I_3}{\widehat{a_{p.T}}\pi} + K_3\widehat{a_{p.T}}^2\frac{3}{4} - \Omega_d{}^2\right\} \quad \text{(F-6)}$$

$$\rightarrow \widehat{A_d}\sin(\phi) \equiv \widehat{a_{p.T}}\left\{\Omega_{eff}^2 - \Omega_d{}^2\right\}$$

[3] As motioned early, the so-called equilibrium solution represents the amplitude of periodic solution in fast varying coordinate while equilibrium solution in slowly varying coordinate.

doi:10.6342/NTU202600018

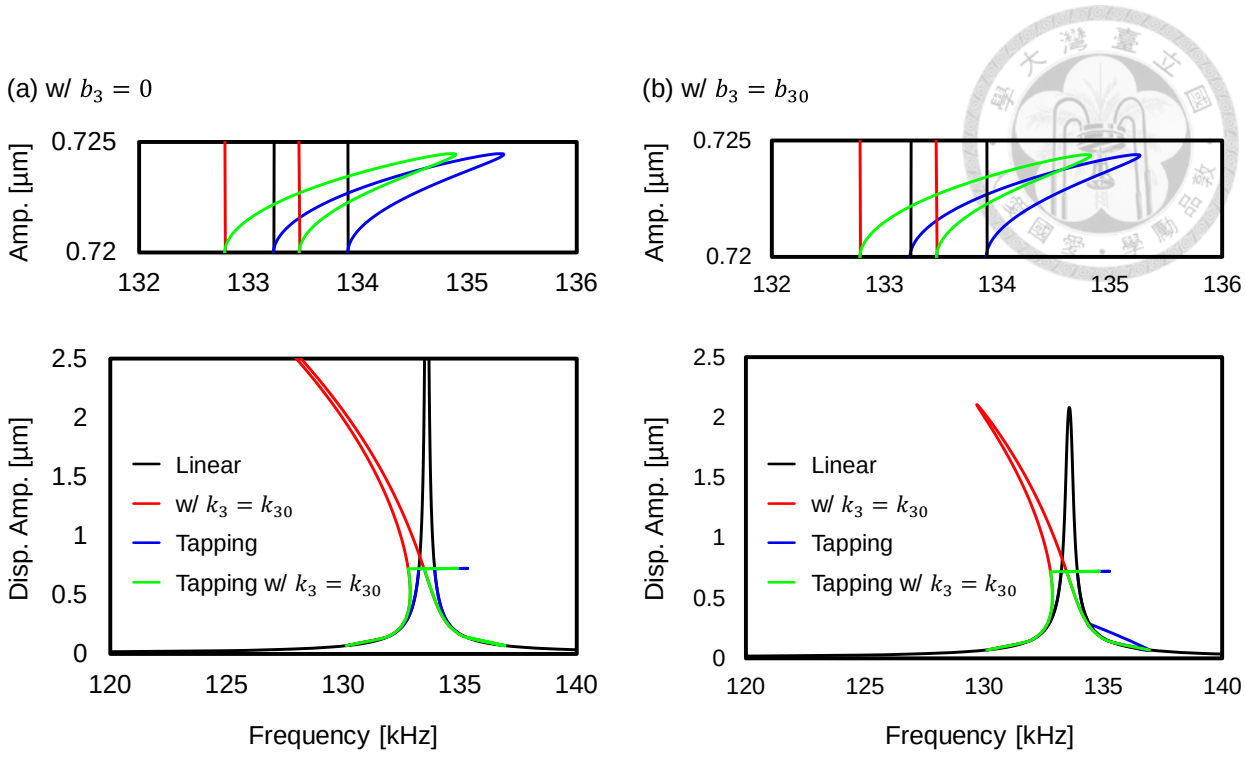


Figure F-1: Simulated frequency responses based on (E-123), comparing systems (a) without the nonlinear damping term $b_3 = 0$ and (b) with the nonlinear damping term $b_3 = b_{30}$.

where the effective damping ratio and effective nonlinear resonance frequency are defined as

$$\xi_{eff} = \xi + \frac{\gamma I_1}{\pi} + B_3 \widehat{a_{p.T}}^2 \frac{\pi}{4} \tag{F-7}$$

$$\Omega_{eff}^2 = \Omega_{n.T}^2 = 1 - \frac{\alpha I_2}{\widehat{a_{p.T}}\pi} + \frac{\beta I_3}{\widehat{a_{p.T}}\pi} + K_3 \widehat{a_{p.T}}^2 \frac{3}{4} \tag{F-8}$$

According to the simulation results shown in Figure F-1, it is reasonable to simplify the (F-7) by ignoring the nonconservative tip-sample interaction forces term if operating frequency is near the linear resonance frequency. Consequently, (F-5)-(F-7) can be simplified as follows

$$\widehat{A_d}\cos(\phi) = -\left\{\widehat{a_{p.vD.D}}\Omega_d\xi + \Omega_d B_3 \widehat{a_{p.vD.D}}^3 \frac{\pi}{4}\right\} = -\widehat{a_{p.vD.D}}\Omega_d\xi_{eff} \tag{F-9}$$

$$\widehat{A_d}\sin(\phi) = \widehat{a_{p.vD.D}}\left\{\Omega_{eff}^2 - \Omega_d{}^2\right\} \tag{F-10}$$

doi:10.6342/NTU202600018

$$\xi_{eff} = \frac{1}{Q_{eff}} = \xi + B_3 \widehat{a_{p.vD.D}}^2 \frac{\pi}{4} = \xi + C_{vdP} \tag{F-11}$$

Combining the square of (F-9) and square of (F-10) yields

$$\begin{aligned} \widehat{A_d}^2 &= \left(-\widehat{a_{p.vD.D}}\Omega_d \xi_{eff.v}\right)^2 + \left[\widehat{a_{p.vD.D}}\left(\Omega_{eff}^2 - {\Omega_d}^2\right)\right]^2 \\ &= \widehat{a_{p.vD.D}}^2 \left[\frac{\Omega_d^2}{Q_{eff.v}^2} + \left(\Omega_{eff}^2 - {\Omega_d}^2\right)^2\right] \end{aligned} \tag{F-12}$$

Therefore, the square of displacement amplitude frequency response can be represented as

$$\widehat{a_{p.vD.D}}^2 = \frac{\widehat{A_d}^2}{\left[\frac{\Omega_d^2}{Q_{eff}^2} + \left(\Omega_{eff}^2 - {\Omega_d}^2\right)^2\right]} \tag{F-13}$$

Putting the physical variable back into the equation, the frequency response function can be represented as

$$x_{vD.D.f} = \frac{A_d cos\left(\omega_d t + \phi\right)}{m_r \sqrt{\bar{\bar{A}}^2 + \bar{\bar{B}}^2}} \tag{F-14}$$

where the coefficients of $\bar{\bar{A}}$ and $\bar{\bar{B}}$ are

$$\hat{A} = (1 - K_{vdW} + K_H + K_D)\omega_n^2 - \omega_d^2 \tag{F-15}$$

$$\hat{B} = \omega_n(\xi + C_{vdP})\,\omega_d \tag{F-16}$$

and

$$C_{vdP} = \frac{B_3 \widehat{a_{p.vD.D}}^2}{4} \tag{F-17}$$

$$K_{vdW} = \frac{1}{\widehat{a_{p.vD.D}}\pi} \alpha I_2 \tag{F-18}$$

doi:10.6342/NTU202600018

$$= \frac{1}{\widehat{a_{p.vD.D}}\pi}\alpha\int_{\theta_c}^{2\pi+\theta_c} cos(\theta)\left\{\left(\widehat{d_0} - \widehat{a_{p.vD.D}}cos\,(\theta)\right)_{D_{\widehat{a_0}}}^{-2}\right\}d\theta$$

$$K_H = \frac{1}{\widehat{a_{p.vD.D}}\pi}\beta I_3 = \tag{F-19}$$

$$\frac{\beta}{\widehat{a_{p.vD.D}}\pi}\int_{\theta_c}^{2\pi+\theta_c} cos(\theta)\left\{\left(\widehat{a_{p.vD.D}}\cos(\theta) - \widehat{d_0} + \widehat{a_0}\right)_{D_0}^{3/2}\right\}d\theta$$

$$K_D = \frac{3}{4}K_3\widehat{a_{p.vD.D}}^2 \tag{F-20}$$

See Appendix E.2 and E.4 for details.

Considering the response without effect of surface interaction force yields the response with effect of Duffing term and van der Pol term as

$$\widehat{a_{p.vD}}^2 = \frac{\widehat{A_d}^2}{\left[\frac{\Omega_d^2}{Q_{eff}^2} + \left(\Omega_{eff.D}^2 - {\Omega_d}^2\right)^2\right]} \tag{F-21}$$

and, as a remark, the coefficient Q_{eff} and $\Omega_{eff.D}^2$ are

$$Q_{eff} = \frac{1}{\xi_{eff}} = \frac{1}{\xi + B_3\widehat{a_{p.vD}}^2\frac{\pi}{4}} \tag{F-22}$$

$$\Omega_{n.D}^2 = 1 + K_3\widehat{a_{p.vD}}^2\frac{3}{4} \tag{F-23}$$

Dividing (F-13) by (F-21) yields the amplitude ratio with respect to system who is nonlinear in non-contact phase

$$A_{ratio}^2 = \left(\frac{a_{p.vD.D}}{a_{p.vD}}\right)^2 = \left(\frac{\widehat{a_{p.vD.D}}}{\widehat{a_{p.vD}}}\right)^2 = \frac{{\Omega_d}^2 + Q_{eff}^2\left(\Omega_{n.D}^2 - {\Omega_d}^2\right)^2}{{\Omega_d}^2 + Q_{eff}^2\left(\Omega_{n.T}^2 - {\Omega_d}^2\right)^2} \tag{F-24}$$

On the other hand, here recall the linear frequency response of

$$\widehat{a_p}^2 = \frac{\widehat{A_d}^2}{\left[\frac{\Omega_d^2}{Q_{eff}^2} + \left(1 - {\Omega_d}^2\right)^2\right]} \tag{F-25}$$

doi:10.6342/NTU202600018

The amplitude ratio with respect to system who is linear in non-contact phase can be determined by divide (F-13) by (F-25) as

$$A_{ratio}^2 = \left(\frac{\widehat{a_{p.vD.D}}}{\widehat{a_p}}\right)^2 = \frac{{\Omega_d}^2 + Q_{eff}^2\left(1 - {\Omega_d}^2\right)^2}{{\Omega_d}^2 + Q_{eff}^2\left(\Omega_{n.T}^2 - {\Omega_d}^2\right)^2} \tag{F-26}$$

On the other hand, one can presents the nonlinear resonance frequency by arrange (F-24) as

$$\Omega_{n.T}^2 = {\Omega_d}^2 \pm \sqrt{\frac{1}{Q_{eff}^2}\left\{\frac{1}{A_{ratio}^2}\left[{\Omega_d}^2 + Q_{eff}^2\left(\Omega_{n.D}^2 - {\Omega_d}^2\right)^2\right] - {\Omega_d}^2\right\}} \tag{F-27}$$

As shown in Figure 3-15, this equation gives two branches over certain frequency (i.e., the hysteresis region). However, the solution with minus sign is an unstable solution while solution with plus sign is a stable solution as discussed in Appendix E.5.

F.2 Main Derivation on Peak Repulsive Force Formulars

One can represent device contact with the stopper in formular as

$$x - d_0 + a_0 = -a_{p.vD.D}cos(\theta) - d_0 + a_0 \le 0 \tag{F-28}$$

and the contact angle can be presented as

$$\theta_c = cos^{-1}\left(\frac{d_0 - a_0}{a_{p.vD.D}}\right) = cos^{-1}\left(\frac{\widehat{d_0} - \widehat{a_0}}{\widehat{a_{p.vD.D}}}\right) \tag{F-29}$$

where $a_{p.vD.D} = A_{ratio}a_{p.vD} = A_{ratio}A_0\frac{Q_{eff}}{Q} \equiv A_{ratio}A_{0.v}$, $\widehat{a_{p.vD.D}} = a_{p.vD.D}/A_{0.v}$ and, be noted, $A_0Q_{eff}/Q = Q_{eff}A_d/k_r \equiv A_{0.v}$ and the contact interval is defined as $\pi - \theta_c < \theta < \pi + \theta_c$ as a minus sign added in (F-28).

doi:10.6342/NTU202600018

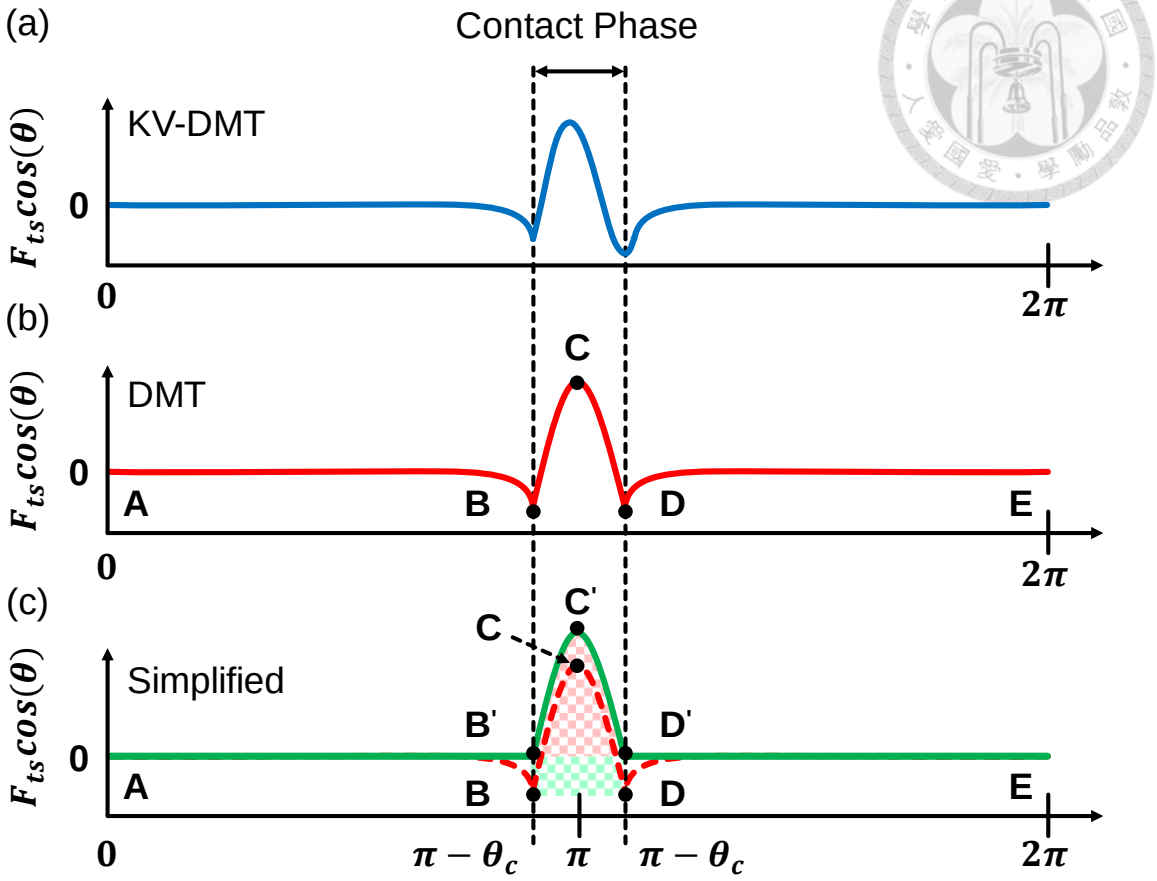


Figure F-2: Integral paths for the nonlinear surface interaction forces over the phase angle θ, shown for the (a) KV-DMT, (b) DMT and (c) simplified model, respectively.

Figure F-2 shows an example of the variation of the integral of nonlinear surface interaction force over θ. The original integral over path A-B-C-D-E (*cf.*, Figure F-2 (b)) is approximated by the integral over path A-B'-C'-D'-E minus integral over path B-B'-D'-D (*cf.*, Figure F-2 (c)). In addition, since the *maximum* indentation (i.e, $\cos(\theta) = 1$) is defined as $\delta = a_{p.vD.D} - d_0 + a_0$ and its non-dimensional form is defined as $\Delta = \delta / a_{p.vD.D} = (a_{p.vD.D} - d_0 + a_0)/a_{p.vD.D} = 1 - \cos(\theta_c)$, the contact angle for small indentation can be approximated[4] as

$$\theta_c = \cos^{-1}\left(\frac{d_0 - a_0}{a_{p.vD.D}}\right) = \cos^{-1}\left(\frac{a_{p.vD.D} - \delta}{a_{p.vD.D}}\right) \approx \sqrt{2\Delta} + O(\Delta^{3/2}) \qquad \text{(F-30)}$$

[4] The Taylor series for the cosine is $\cos(x) = 1 - x^2/2! + x^4/4! + \cdots$. Replacing x by $\sqrt{2y}$ and truncating to first two terms yields $\cos(\sqrt{2y}) \approx 1 - \frac{\sqrt{2y}^2}{2!} = 1 - y$. Therefore, for small value of $\cos^{-1}(1-y)$, it can be approximated as $\sqrt{2y}$.

doi:10.6342/NTU202600018

By performing a series expansion of the integrand of (F-18) and (F-19) around maximum indentation (i.e., $\theta = \pi$) for small indentation and disregarding higher-order terms[5], one can present the analytical expression for nonlinear resonance frequency of (F-8) as

$$
\begin{aligned}
\Omega_{eff}^2 = \Omega_{n.T}^2 &= 1 - \frac{\alpha I_2}{\widehat{a_{p.vD.D}}\pi} + \frac{\beta I_3}{\widehat{a_{p.vD.D}}\pi} + \frac{3}{4}K_3\widehat{a_{p.vD.D}}^2 \\
&= 1 - \frac{\alpha}{\widehat{a_{p.vD.D}}\pi}\left(\int_{\pi-\theta_c}^{\pi+\theta_c} cos(\theta)\left\{\left(\widehat{d_0} + \widehat{a_{p.vD.D}}cos(\theta)\right)_{D_{a_0}}^{-2}\right\}d\theta\right) \\
&\qquad + \frac{3}{4}K_3\widehat{a_{p.vD.D}}^2 \\
&+ \frac{\beta}{\widehat{a_{p.vD.D}}\pi}\left(\int_{\pi-\theta_c}^{\pi+\theta_c} cos(\theta)\left\{\left(-\widehat{a_{p.vD.D}}cos(\theta) - \widehat{d_0} + \widehat{a_0}\right)_{D_0}^{3/2}\right\}d\theta\right) \\
&= 1 - \frac{\alpha}{\widehat{a_{p.vD.D}}\pi}\left(\int_{\pi-\theta_c}^{\pi+\theta_c} \frac{cos(\theta)}{\widehat{a_0}^2}d\theta\right) \qquad \text{(F-31)} \\
&+ \frac{\beta\widehat{a_{p.vD.D}}^{1/2}}{\pi}\left(\int_{\pi-\theta_c}^{\pi+\theta_c}\left\{A^{\frac{3}{2}}\left[-\Delta^{\frac{3}{2}} + \frac{1}{2}\Delta^{\frac{1}{2}}\left(\frac{3}{2}+\Delta\right)(\theta-\pi)^2 + \cdots\right]\right\}d\theta\right) \\
&\qquad + \frac{3}{4}K_3\widehat{a_{p.vD.D}}^2 \\
&= 1 - \frac{\alpha}{\widehat{a_{p.vD.D}}\pi}\left[\frac{2\,sin(\theta_c)}{\widehat{a_0}^2}\right] + \frac{\beta\widehat{a_{p.vD.D}}^{1/2}}{\pi}\left[-2\Delta^{\frac{3}{2}}\theta_c + \frac{1}{3}\Delta^{\frac{1}{2}}\left(\frac{3}{2}+\Delta\right)\theta_c^3\right] \\
&\qquad + \frac{3}{4}K_3\widehat{a_{p.vD.D}}^2
\end{aligned}
$$

[5] The Taylor expansion of $f(\theta) = \left[-\widehat{a_{p.vD.D}}cos(\theta) - \widehat{d_0} + \widehat{a_0}\right]cos(\theta)$ around π is approximated by $f(\theta) = f(\pi) + f'(\pi)(\theta-\pi) + f''(\pi)(\theta-\pi)^2 + \cdots \approx A^{\frac{3}{2}}\left[-2\Delta^{\frac{3}{2}}\theta_c + \frac{1}{3}\Delta^{\frac{1}{2}}\left(\frac{3}{2}+\Delta\right)\theta_c^3\right]$

doi:10.6342/NTU202600018

$$\approx 1-\frac{\alpha}{\widehat{a_{p.vD.D}}\pi}\left[\frac{2\,sin(\theta_c)}{\widehat{a_0}^2}\right]+\frac{\beta\widehat{a_{p.vD.D}}^{1/2}}{\pi}\left[-2\Delta^{\frac{3}{2}}\theta_c+\frac{1}{2}\Delta^{\frac{1}{2}}\theta_c^3\right]$$
$$+\frac{3}{4}K_3\widehat{a_{p.vD.D}}^2$$

$$\approx 1-\frac{2\sqrt{2}\alpha}{\widehat{a_p}\widehat{a_0}^2\pi}\Delta^{\frac{1}{2}}-\sqrt{2}\frac{\beta\widehat{a_{p.vD.D}}^{1/2}}{\pi}\Delta^2+\frac{3}{4}K_3\widehat{a_{p.vD.D}}^2$$

$$=1-\frac{\sqrt{2}HR^*}{3\pi k_r a_0^2 A_{ratio}A_0}\Delta^{\frac{1}{2}}-\frac{4\sqrt{2}}{3}\frac{E^*\sqrt{R^*A_{0.v}A_{ratio}}}{\pi k_r}\Delta^2$$
$$+\frac{3}{4}\frac{k_3}{k_r}A_{0.v}^2A_{ratio}^2$$

where $\left[\widehat{d_0}+\widehat{a_{p.vD.D}}cos(\theta_c)\right]_{D_{a_0}}=\widehat{a_0}$, $\left[-\widehat{d_0}-\widehat{a_{p.vD.D}}cos(\theta_c)+\widehat{a_0}\right]_{D_0}=\widehat{a_{p.vD.D}}-\widehat{d_0}+\widehat{a_0}=\widehat{a_{p.vD.D}}\Delta$, $sin(\pi+\theta_c)=sin\,(\theta_c)\approx\theta_c\approx\sqrt{2\Delta}$ and $sin(\pi-\theta_c)=-sin\,(\theta_c)\approx-\sqrt{2\Delta}$ are used as the device is in the contact regime around π.

Eliminating Ω_{eff} by combining (F-31) and (F-27) gives

$$\Delta^2=\Psi+\Phi\Delta^{1/2}\rightarrow\Delta=\left(\Psi+\Phi\Delta^{1/2}\right)^{1/2}=\Psi^{1/2}\left(1+\frac{\Phi\Delta^{1/2}}{\Psi}\right)^{1/2} \quad \text{(F-32)}$$

where coefficients Ψ and Φ are defined as

$$\Phi\equiv\frac{H\sqrt{R^*}}{4E^*a_0^2(A_{ratio}A_{0.v})^{3/2}} \quad \text{(F-33)}$$

$$\Psi\equiv\frac{3\pi k_r}{4\sqrt{2}E^*\sqrt{R^*A_{0.v}A_{ratio}}Q_{eff}}\chi_D \quad \text{(F-34)}$$

, respectively, and the frequency response function χ_D is defined as

$$\chi_{vD}=Q_{eff}\left(\Omega_d{}^2-\Omega_{n.D}^2\right)+\sqrt{\frac{1}{A_{ratio}^2}\left[\Omega_d{}^2+Q_{eff}\left(\Omega_{n.D}^2-\Omega_d{}^2\right)^2\right]-\Omega_d{}^2} \quad \text{(F-35)}$$

If $\Psi\gg\Phi\Delta^{1/2}$ or $1\gg(\Phi\Delta^{1/2})/\Psi$, (F-32) can be approximated as

doi:10.6342/NTU202600018

$$\Delta \approx \Psi^{1/2}\left(1+\frac{1}{2}\frac{\Phi\Delta^{1/2}}{\Psi}\right)=\Psi^{1/2}+\frac{\Phi\Delta^{1/2}}{2\Psi^{1/2}} \tag{F-36}$$

However, the further simplification is needed because formular still contain Δ in both sides. Looking into the requirement $\Psi \gg \Phi\Delta^{1/2}$, which implies that the term $\Phi\Delta^{1/2}$ is much smaller than Ψ. Therefore, one can treat $\Phi\Delta^{1/2}$ as a perturbation to Ψ. To simplify, here first start by solving the simplified form of the equation

$$\Delta^2 \approx \Psi \rightarrow \Delta \approx \sqrt{\Psi} \tag{F-37}$$

Correcting the simplified equation with perturbation ε, takes the form

$$\Delta \approx \sqrt{\Psi}+\varepsilon \tag{F-38}$$

Substituting back into (F-32) and expanding the terms[6] yields

$$\begin{gathered}\left(\sqrt{\Psi}+\varepsilon\right)^2 \approx \Psi+\Phi(\sqrt{\Psi}+\varepsilon)^{1/2} \\ \rightarrow \Psi+2\sqrt{\Psi}\varepsilon+\varepsilon^2 \approx \Psi+\Phi\Psi^{1/4}\left[1+\varepsilon/(2\sqrt{\Psi})\right] \\ \rightarrow 2\sqrt{\Psi}\varepsilon+\varepsilon^2 \approx \Phi\Psi^{1/4}\left[1+\varepsilon/(2\sqrt{\Psi})\right]\end{gathered} \tag{F-39}$$

Comparing the order, term ε^2 and $\varepsilon/(2\sqrt{\Psi})$ are drop out, and give

$$2\sqrt{\Psi}\varepsilon \approx \Phi\Psi^{1/4} \rightarrow \varepsilon \approx \Phi\Psi^{-1/4}/2 \tag{F-40}$$

and[7]

$$\Delta \approx \sqrt{\Psi}+\varepsilon \approx \Psi^{\frac{1}{2}}+\Phi\Psi^{-1/4}/2=\Psi^{\frac{1}{2}}\left(1+\Phi\Psi^{-3/4}/2\right) \tag{F-41}$$

In addition, substituting (F-37) to the (F-32) for only right-hand side yields

$$\begin{gathered}\Delta^2=\Psi+\Phi\left(\sqrt{\Psi}\right)^{1/2} \\ \rightarrow \Delta=\Psi^{1/2}\left(1+\Phi\Psi^{-3/4}\right)^{1/2} \approx \Psi^{\frac{1}{2}}\left(1+\frac{\Phi\Psi^{-3/4}}{2}\right)=\Psi^{1/2}+\frac{\Phi}{2\Psi^{1/4}}\end{gathered} \tag{F-42}$$

[6] $(a+x)^{1/2}=a^{1/2}(1+x/2a)$ is applied

[7] We can expect that $\Psi^{\frac{1}{2}}\left(1+\frac{\Phi}{2\Psi^{3/4}}\right)$ is approximated from $\Psi^{\frac{1}{2}}\left(1+\frac{\Phi}{\Psi^{3/4}}\right)^{1/2}$ through Tayler expansion and it is verified with followed discussion with the simplification of right-hand side term.

doi:10.6342/NTU202600018

With this, it is known that the requirement of $\Psi \gg \Phi\Delta^{1/2}$ is equivalent to requirement of $\Phi\Psi^{-3/4} \ll 1$.

Therefore, one can find out the peak repulsive force with DMT model for contact phase (since the nonconservative term is ignored) as

$$
\begin{aligned}
F_{peak} &= -\frac{HR^*}{6a_0^2} + \frac{4}{3}E^*\sqrt{R^*}\left(a_{p.vD.D} - d_0 + a_0\right)^{\frac{3}{2}} \\
&= -\frac{HR^*}{6a_0^2} + \frac{4}{3}E^*\sqrt{R^*}(\delta)^{\frac{3}{2}} \\
&= -\frac{HR^*}{6a_0^2} + \frac{4}{3}E^*\sqrt{R^*}\left(a_{p.vD.D}\Delta\right)^{\frac{3}{2}} \\
&\approx -\frac{HR^*}{6a_0^2} + \frac{4}{3}E^*\sqrt{R^*}\left[\left(A_{ratio}a_{p.vD}\right)\left(\Psi^{1/2} + \frac{\Phi}{2\Psi^{1/4}}\right)\right]^{\frac{3}{2}} \\
&= -\frac{HR^*}{6a_0^2} + \frac{4}{3}E^*\sqrt{R^*}A_{ratio}^{\frac{3}{2}}A_{0.v}{}^{\frac{3}{2}}\left[\Psi^{1/2} + \frac{\Phi}{2\Psi^{1/4}}\right]^{\frac{3}{2}} \qquad \text{(F-43)} \\
&\approx -\frac{HR^*}{6a_0^2} + \frac{4}{3}E^*\sqrt{R^*}A_{ratio}^{\frac{3}{2}}A_{0.v}{}^{\frac{3}{2}}\left[\Psi^{3/4} + \frac{3}{4}\Phi\right] \\
&= -\frac{HR^*}{6a_0^2} + \frac{4}{3}E^*\sqrt{R^*}A_{ratio}^{\frac{3}{2}}A_{0.v}{}^{\frac{3}{2}}\Psi^{3/4} + \frac{4}{3}E^*\sqrt{R^*}A_{ratio}^{\frac{3}{2}}A_0^{\frac{3}{2}}\frac{3}{4}\Phi \\
&= 2^{\frac{1}{8}}3^{-\frac{1}{4}}\pi^{\frac{3}{4}}E^{*\frac{1}{4}}R^{*\frac{1}{8}}A_{ratio}^{\frac{9}{8}}A_{0.v}^{\frac{9}{8}}k_r^{\frac{3}{4}}Q_{eff}^{-\frac{3}{4}}\chi_{vD}^{\frac{3}{4}} + \left(\frac{HR^*}{4a_0^2}\right) - \frac{HR^*}{6a_0^2}
\end{aligned}
$$

Finally, following with [376] as shown above, approximate the DMT model with Taylor series expansion on indentation around π and make $\bar{\bar{A}}$ integrable analytically, one can get the peak repulsive force formular by approximating $A_{ratio} = \frac{a_{p.vD.D}}{a_{p.vD}} = \frac{a_{p.vD.D}}{A_{0.v}} \approx \frac{d_0}{A_{0.v}}$ as

$$
F_{vD.D.peak.} = 2^{\frac{1}{8}}3^{-\frac{1}{4}}\pi^{\frac{3}{4}}E^{*\frac{1}{4}}R^{*\frac{1}{8}}k_r^{\frac{3}{4}}d_0^{\frac{9}{8}}Q_{eff}^{-\frac{3}{4}}\chi_{vD}^{\frac{3}{4}} + \frac{F_{ad}}{2} \qquad \text{(F-44)}
$$

doi:10.6342/NTU202600018

F.3 Arranging, Extension and Discussion

If ignore the effect of Duffing term and van der Pol term, (F-35) can be reduced and represented as

$$\chi = Q_{eff}\left({\Omega_d}^2 - 1\right) + \sqrt{\frac{1}{A_{ratio}^2}\left[{\Omega_d}^2 + Q_{eff}\left(1 - {\Omega_d}^2\right)^2\right] - {\Omega_d}^2} \tag{F-45}$$

If drive at center frequency $\omega_{D.d_0} = \omega_n\left(1 - \frac{3}{8}\frac{k_3}{k_r}d_0^2\right)$ or ω_n, both (F-35) and (F-45) reduced as

$$\chi_c = \chi_{vD}|_{\omega_d=\omega_{D.d_0}} = \chi|_{\omega_d=\omega_n} = \sqrt{\left(\frac{A_0}{d_0}\right)^2 - 1} \tag{F-46}$$

Taking the derivative with respect to the gap clearance for (F-44), and operating device at center frequency, it can be found that there exists an optimal value of gap distance as

$$d_{0.op} = 3^{-\frac{1}{2}}A_{0.v} \approx 0.5773A_{0.v} \tag{F-47}$$

Substitute (F-47) back into (F-44), the largest contact force for any given driving force at center resonant frequency can be found as

$$F_{vD.D.peak.op} = 2^{\frac{1}{8}}\pi^{\frac{3}{4}}\left(3^{-\frac{7}{6}} - 3^{-\frac{13}{2}}\right)^{\frac{3}{8}}E^{*\frac{1}{4}}R^{*\frac{1}{8}}k_r^{\frac{3}{4}}d_0^{\frac{9}{8}}Q^{-\frac{3}{4}}A_{0.v}^{\frac{9}{8}} + \frac{F_{ad}}{2} \tag{F-48}$$

If ignore the effect of van der Pol term, (F-47) and (F-48) reduced as

$$d_{0.op} = 3^{-\frac{1}{2}}A_0 \approx 0.5773A_0 \tag{F-49}$$

$$F_{D.D.peak.op} = 2^{\frac{1}{8}}\pi^{\frac{3}{4}}\left(3^{-\frac{7}{6}} - 3^{-\frac{13}{2}}\right)^{\frac{3}{8}}E^{*\frac{1}{4}}R^{*\frac{1}{8}}k_r^{\frac{3}{4}}d_0^{\frac{9}{8}}Q^{-\frac{3}{4}}A_0^{\frac{9}{8}} + \frac{F_{ad}}{2} \tag{F-50}$$

doi:10.6342/NTU202600018

Appendix G: The Temperature Coefficient of Frequency and Abnormal Frequency Responses

G.1 TCF and TCQ of the Comb-driven Resonator

As shown on the Figure G-1, the temperature coefficient of frequency (TCF) of a CMOS-MEMS comb driven resonator, similar to that of Figure 4-2 (with 45-μm beam length) but with longer folded beam (with 50-μm beam length), is reported in this appendix. Setting the resonance frequency at 35 °C as reference, the 1st order TCF is about 44.7 ppm/°C and the 2nd order TCF is about 0.135 ppm/°C. In addition, the temperature coefficient of quality factor (TCQ) is also reported in which the quality factors are extracted based on 3-dB formular of (A-34). The quality factor of the device is about 2900 at 35 °C while decay to about 2350 at 110 °C.

G.2 Influence of Parasitic Current on the Tapping-mode Frequency Response

Feedthrough parasitic currents can often distort the frequency response, leading to failure in performance estimation [405, 406]. Some details are provided in Appendix B.6. Additionally, various methods have been suggested to remove the impact of feedthrough on frequency response characterization of linear resonators. These include,

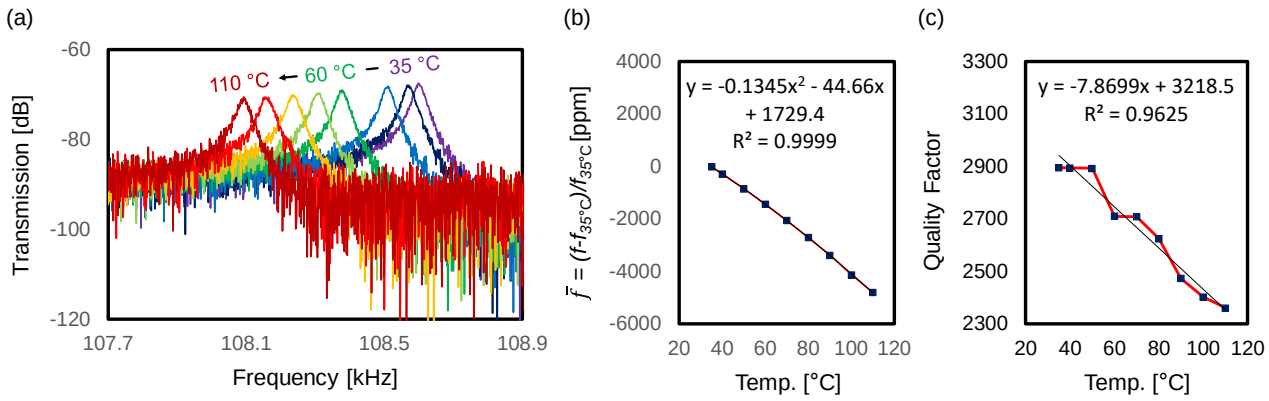


Figure G-1: Experimental characterization of the resonator's thermal properties, showing (a) the frequency response, (b) the Temperature Coefficient of Frequency (TCF), and (c) the Temperature Coefficient of Quality Factor (TCQ).

doi:10.6342/NTU202600018

but are not limited to, the two-port measurement configuration [405, 406], the RF/LO driving scheme [562], pulsed-mode actuation [563], and adding a cancellation path for feedthrough currents [564].

In contract to characterization of linear resonators, [407, 565-567] offer valuable insights into how parasitic feedthrough affects the electrical frequency response of nonlinear MEMS resonators. Among them, [407] presents the measured frequency response under various driving conditions. It illustrates the device's steady-state frequency response using Nyquist plots and highlights the frequency shift with and without the feedthrough effect. The study employed ring-down measurements to distinguish the motional current from the total current output (comprising motional and feedthrough currents, *cf.* (3-15) or (B-170)). It demonstrates that the ratio between parasitic capacitance and motional resistance is a crucial factor in managing the effect on both current ratio and phase offset at the device level. Additionally, [565] demonstrate that parasitic feedthrough drastically alters the frequency response, leading to various hysteretic cycle topologies, including counterclockwise, clockwise and bow-tie cycles. They highlight that the jump directions between stable solution branches in electrical measurements are influenced by the parasitic current and do not align with those in the mechanical domain.

doi:10.6342/NTU202600018

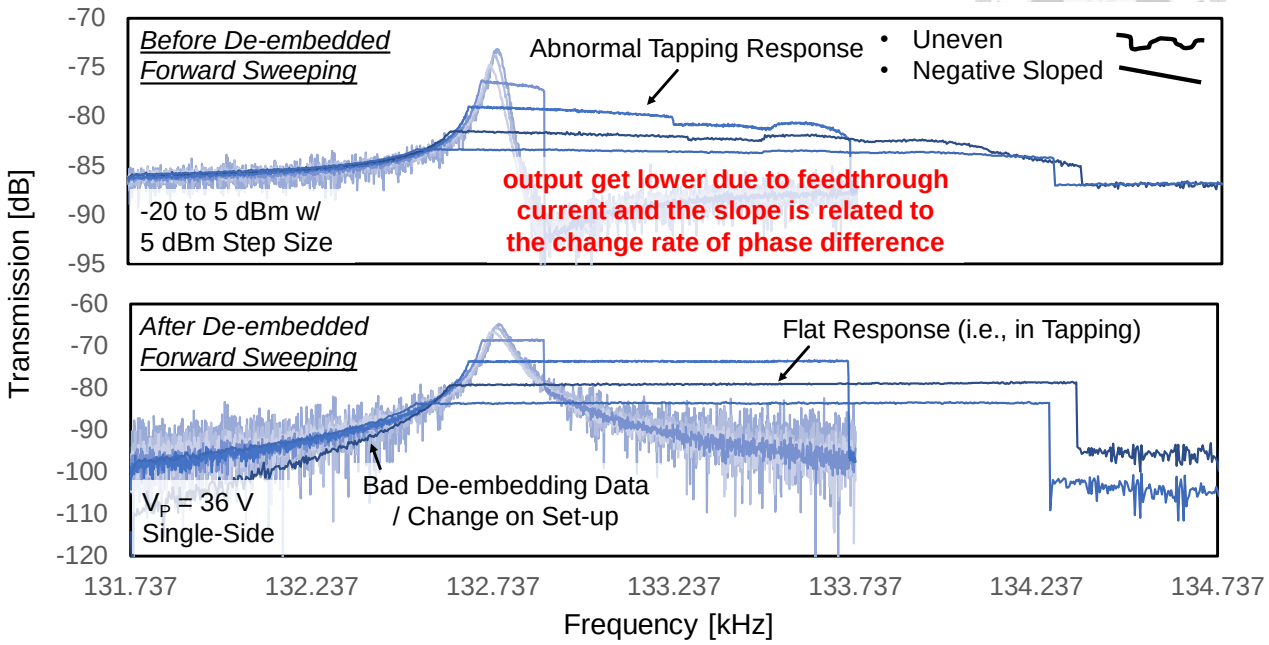


Figure G-2: The measured forward-sweeping frequency response of the resonator, shown (a) before and (b) after the application of a de-embedding procedure to correct for parasitic effects.

Both studies from [407] and [565] thoroughly present the theoretical models and provide a clearer understanding of the phenomenon. However, the impact of feedthrough current on vibro-impact nonlinear resonators remains unclear. In this appendix, the influence of parasitic current on the nonlinear electrical response of capacitively sensed comb-driven vibro-impact resonators is examined preliminary. The frequency response with a negative slope in the tapping region, caused by feedthrough current is observed. In addition, an uneven pattern is also identified in the measured responses. These findings demonstrate that mechanisms such as period-doubling bifurcation may influence vibro-impact resonator responses, and feedthrough current could amplify results in NA based measurement set-up where transitions are absent in de-embedded responses but appear prominently in feedthrough-embedded ones.

Figure G-2 (a) shows the forward-sweeping frequency responses measured by a network analyzer with varying driving voltage. Figure G-3 (a) shows the backward-sweeping frequency responses measured by the network analyzer with two near-

doi:10.6342/NTU202600018

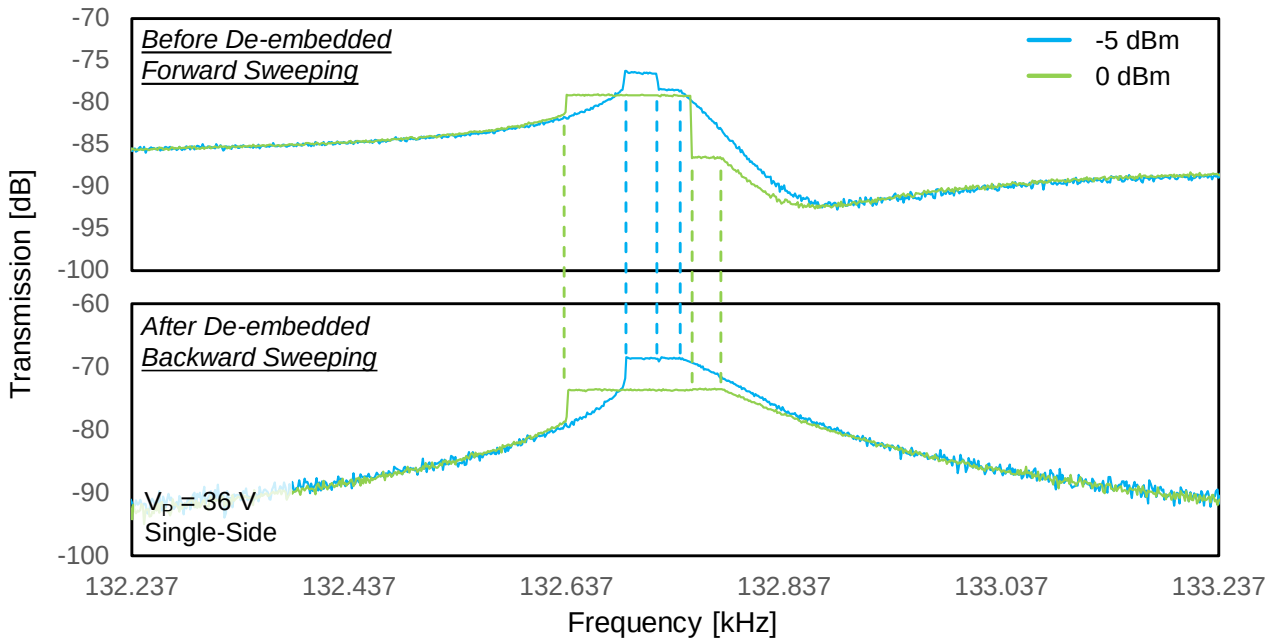


Figure G-3: The measured backward-sweeping frequency response of the resonator, comparing the data (a) without de-embedding and (b) with de-embedding applied.

grazing driving voltage. The responses before and after de-embedding are shown in Figure G-2 (b) and Figure G-3 (b), respectively. According to previous simulation results in linear case, it is expected that the transmission gets lower due to feedthrough current and the slope and the uneven tapping responses are related to the phase difference. On the other hand, as shown in Figure G-2 (a), a sudden change in device motion would create an uneven tapping response. According to Figure D-14 and Figure D-15, this unevenness might be attributed to the bifurcation point and amplified by the resultant interaction between the signal and feedthrough current.

doi:10.6342/NTU202600018

Reference

[1] K. Petersen, "A new age for mems," in *The 13th International Conference on Solid-State Sensors, Actuators and Microsystems, 2005. Digest of Technical Papers. TRANSDUCERS'05.*, 2005, vol. 1: IEEE, pp. 1-4.

[2] H. Fujita, "A decade of mems and its future," in *Proceedings IEEE The Tenth Annual International Workshop on Micro Electro Mechanical Systems. An Investigation of Micro Structures, Sensors, Actuators, Machines and Robots*, 1997: IEEE, pp. 1-7.

[3] R. Bogue, "Mems sensors: Past, present and future," *Sensor Review*, vol. 27, no. 1, pp. 7-13, 2007.

[4] S. Nagod and S. Halse, "Evolution of mems technology," *Evolution*, vol. 4, no. 12, 2017.

[5] R. Wilfinger, P. Bardell, and D. Chhabra, "The resonistor: A frequency selective device utilizing the mechanical resonance of a silicon substrate," *IBM Journal of Research and Development*, vol. 12, no. 1, pp. 113-118, 1968.

[6] K. E. Petersen, "Silicon as a mechanical material," *Proceedings of the IEEE*, vol. 70, no. 5, pp. 420-457, 1982.

[7] J. Stasiak, S. Richards, and S. Angelos, "Hewlett packard's inkjet mems technology: Past, present, and future," in *Micro-and Nanotechnology Sensors, Systems, and Applications*, 2009, vol. 7318: SPIE, pp. 202-206.

[8] K. D. Wise, "Integrated sensors, mems, and microsystems: Reflections on a fantastic voyage," *Sensors and Actuators A: Physical*, vol. 136, no. 1, pp. 39-50, 2007.

[9] S. Tiwari and R. N. Candler, "Using flexural mems to study and exploit nonlinearities: A review," *Journal of Micromechanics and Microengineering*, vol. 29, no. 8, p. 083002, 2019.

[10] M. Intelligence. "Mems market size - industry report on share, growth trends & forecasts analysis (2025 - 2030)." https://www.mordorintelligence.com/industry-reports/mems-market (accessed Apr. 04, 2025).

[11] Y. Group. "2021 was an exceptional year for mems companies. What is next?" https://www.yolegroup.com/press-release/2021-was-an-exceptional-year-for-mems-companies-what-is-next/ (accessed Apr. 4, 2025).

[12] Y. Group. "Mems industry: Looking back at the last 20 years of innovation and growth." https://www.yolegroup.com/strategy-insights/mems-industry-looking-back-at-the-last-20-years-of-innovation-and-growth/ (accessed Apr. 4, 2025).

[13] J. Classen *et al.*, "Evolution of bosch inertial measurement units for consumer electronics," in *2020 IEEE SENSORS*, 2020: IEEE, pp. 1-4.

[14] J. Classen *et al.*, "World's smallest accelerometer," in *2025 IEEE International Symposium on Inertial Sensors and Systems (INERTIAL)*, 2025: IEEE, pp. 1-4.

doi:10.6342/NTU202600018

[15] G. Langfelder, M. Bestetti, and M. Gadola, "Silicon mems inertial sensors evolution over a quarter century," *Journal of Micromechanics and Microengineering*, vol. 31, no. 8, p. 084002, 2021.
[16] T. Peng and Z. You, "Reliability of mems in shock environments: 2000–2020," *Micromachines*, vol. 12, no. 11, p. 1275, 2021.
[17] J. Iannacci, "Reliability of mems: A perspective on failure mechanisms, improvement solutions and best practices at development level," *Displays*, vol. 37, pp. 62-71, 2015.
[18] M. Varghese, "Reduced-order modeling of mems using modal basis functions," Massachusetts Institute of Technology, 2001.
[19] J. Mehner, W. Doetzel, B. Schauwecker, and D. Ostergaard, "Reduced order modeling of fluid structural interactions in mems based on model projection techniques," in *TRANSDUCERS'03. 12th International Conference on Solid-State Sensors, Actuators and Microsystems. Digest of Technical Papers (Cat. No. 03TH8664)*, 2003, vol. 2: IEEE, pp. 1840-1843.
[20] V. Kolchuzhin, J. E. Mehner, T. Gessner, and W. Doetzel, "Parametric finite element analysis for reduced order modeling of mems," in *EuroSime 2006-7th International Conference on Thermal, Mechanical and Multiphysics Simulation and Experiments in Micro-Electronics and Micro-Systems*, 2006: IEEE, pp. 1-6.
[21] V. A. Kolchuzhin, W. Doetzel, and J. E. Mehner, "Efficient generation of mems reduced-order macromodels using differentiation of finite elements," *Sensor Letters*, vol. 6, no. 1, pp. 97-105, 2008.
[22] M. Naumann, D. Lin, J. Mehner, A. McNeil, and T. Miller, "Design evaluation of shock induced failure mechanisms of mems by correlation of numerical and experimental results," in *2011 16th International Solid-State Sensors, Actuators and Microsystems Conference*, 2011: IEEE, pp. 2891-2894.
[23] J. E. Mehner, A. Schaporin, V. Kolchuzhin, W. Doetzel, and T. Gessner, "Parametric model extraction for mems based on variational finite element techniques," in *The 13th International Conference on Solid-State Sensors, Actuators and Microsystems, 2005. Digest of Technical Papers. TRANSDUCERS'05.*, 2005, vol. 1: IEEE, pp. 776-779.
[24] V. Kolchuzhin, W. Doetzel, and J. Mehner, "A derivatives-based method for parameterization of mems reduced order models," in *EuroSimE 2008-International Conference on Thermal, Mechanical and Multi-Physics Simulation and Experiments in Microelectronics and Micro-Systems*, 2008: IEEE, pp. 1-5.
[25] V. Kolchuzhin, J. Mehner, T. Gessner, and W. Doetzel, "Application of higher order derivatives method to parametric simulation of mems," in *2007 International Conference on Thermal, Mechanical and Multi-Physics Simulation Experiments in Microelectronics and Micro-Systems. EuroSime 2007*, 2007: IEEE, pp. 1-6.

doi:10.6342/NTU202600018

[26] A. H. Nayfeh, M. I. Younis, and E. M. Abdel-Rahman, "Reduced-order models for mems applications," *Nonlinear Dynamics,* vol. 41, pp. 211-236, 2005.
[27] A. Opreni and P. Degenfeld-Schonburg, "Model order reduction for nonlinear modal analysis of mems devices: Theory and recent advancements," in *2023 24th International Conference on Thermal, Mechanical and Multi-Physics Simulation and Experiments in Microelectronics and Microsystems (EuroSimE)*, 2023: IEEE, pp. 1-7.
[28] A. Frangi and G. Gobat, "Reduced order modelling of the non-linear stiffness in mems resonators," *International Journal of Non-Linear Mechanics,* vol. 116, pp. 211-218, 2019.
[29] K. Park and M. S. Allen, "Quasi-static modal analysis for reduced order modeling of geometrically nonlinear structures," *Journal of Sound and Vibration,* vol. 502, p. 116076, 2021.
[30] J. J. Hollkamp and R. W. Gordon, "Reduced-order models for nonlinear response prediction: Implicit condensation and expansion," *Journal of Sound and Vibration,* vol. 318, no. 4-5, pp. 1139-1153, 2008.
[31] A. Opreni, A. Vizzaccaro, A. Frangi, and C. Touzé, "Model order reduction based on direct normal form: Application to large finite element mems structures featuring internal resonance," *Nonlinear Dynamics,* vol. 105, no. 2, pp. 1237-1272, 2021.
[32] G. Gobat, V. Zega, P. Fedeli, L. Guerinoni, C. Touzé, and A. Frangi, "Reduced order modelling and experimental validation of a mems gyroscope test-structure exhibiting 1: 2 internal resonance," *Scientific Reports,* vol. 11, no. 1, p. 16390, 2021.
[33] A. Keşkekler, V. Bos, A. M. Aragón, P. G. Steeneken, and F. Alijani, "Multimode nonlinear dynamics of graphene resonators," *Physical Review Applied,* vol. 20, no. 6, p. 064020, 2023.
[34] G. Gobat, V. Zega, P. Fedeli, C. Touzé, and A. Frangi, "Frequency combs in a mems resonator featuring 1: 2 internal resonance: Ab initio reduced order modelling and experimental validation," *Nonlinear dynamics,* vol. 111, no. 4, pp. 2991-3017, 2023.
[35] S. Fresca, G. Gobat, P. Fedeli, A. Frangi, and A. Manzoni, "Deep learning-based reduced order models for the real-time simulation of the nonlinear dynamics of microstructures," *International Journal for Numerical Methods in Engineering,* vol. 123, no. 20, pp. 4749-4777, 2022.
[36] M. O. Akinsolu *et al.*, "Efficient design optimization of high-performance mems based on a surrogate-assisted self-adaptive differential evolution," *IEEE Access,* vol. 8, pp. 80256-80268, 2020.
[37] P. Wang, Q. Lu, and Z. Fan, "Evolutionary design optimization of mems: A review of its history and state-of-the-art," *Cluster Computing,* vol. 22, pp. 9105-9111, 2019.

doi:10.6342/NTU202600018

[38] D. Schiwietz, M. Hörsting, E. M. Weig, M. Wenzel, and P. Degenfeld-Schonburg, "Shape optimization of geometrically nonlinear modal coupling coefficients: An application to mems gyroscopes," *Scientific Reports*, vol. 15, no. 1, p. 10957, 2025.
[39] D. Schiwietz, M. Hörsting, E. M. Weig, P. Degenfeld-Schonburg, and M. Wenzel, "Shape optimization of eigenfrequencies in mems gyroscopes," *arXiv preprint arXiv:2402.05837*, 2024.
[40] A. Keyvani, H. Sadeghian, M. S. Tamer, J. F. L. Goosen, and F. van Keulen, "Minimizing tip-sample forces and enhancing sensitivity in atomic force microscopy with dynamically compliant cantilevers," *Journal of Applied Physics*, vol. 121, no. 24, 2017.
[41] D. J. Wagg, "Vibro-impact dynamics of engineering systems," Ph.D Thesis, Centre for Nonlinear Dynamics & its Applications, University College London, England., 1999.
[42] J. Drelich and K. L. Mittal, *Atomic force microscopy in adhesion studies*, 1st ed. London: CRC Press, 2005.
[43] A. Fidlin, *Nonlinear oscillations in mechanical engineering*, 1st ed. Berlin/Heidelberg: Springer, 2005.
[44] M. Bernardo, C. Budd, A. R. Champneys, and P. Kowalczyk, *Piecewise-smooth dynamical systems: Theory and applications* (Applied mathematical sciences). London: Springer, 2008.
[45] R. A. Ibrahim, *Vibro-impact dynamics: Modeling, mapping and applications* (Lecture notes in applied and computational mechanics). Berlin/Heidelberg: Springer, 2009.
[46] A. C. Luo and Y. Guo, *Vibro-impact dynamics*. John Wiley & Sons, 2012.
[47] V. I. Babitsky, *Theory of vibro-impact systems and applications*, 1st ed. (Foundations of engineering mechanics). Berlin/Heidelberg: Springer, 2013.
[48] R. I. Leine and H. Nijmeijer, *Dynamics and bifurcations of non-smooth mechanical systems*, 1st ed. (Lecture notes in applied and computational mechanics). Berlin/Heidelberg: Springer, 2013.
[49] F. Peterka, "Vibro-impact systems," in *Encyclopedia of vibration*, vol. 55, D. J. Ewins, Rao, Singiresu S., Braun, Simon G. Ed. San Diego, United States: Elsevier, 2001, pp. 1531-1548.
[50] H. Meijer, F. Dercole, and B. E. Oldeman, "Numerical bifurcation analysis," in *Mathematics of complexity and dynamical systems* R. A. Meyers Ed. New York: Springer, 2009, pp. 1172-1194.
[51] B. Krauskopf, H. M. Osinga, and J. Galán-Vioque, *Numerical continuation methods for dynamical systems: Path following and boundary value problems* (Understanding complex systems). Dordrecht: Springer, 2007.
[52] A. H. Nayfeh and B. Balachandran, *Applied nonlinear dynamics: Analytical, computational, and experimental methods*. John Wiley & Sons, 2008.
[53] A. H. Nayfeh and D. T. Mook, *Nonlinear oscillations*. John Wiley & Sons, 2008.

doi:10.6342/NTU202600018

[54] J. Tamayo and R. Garcia, "Deformation, contact time, and phase contrast in tapping mode scanning force microscopy," *Langmuir,* vol. 12, no. 18, pp. 4430-4435, 1996.
[55] A. Kühle, A. H. So/rensen, and J. Bohr, "Role of attractive forces in tapping tip force microscopy," *Journal of Applied Physics,* vol. 81, no. 10, pp. 6562-6569, 1997.
[56] B. Cappella and G. Dietler, "Force-distance curves by atomic force microscopy," *Surface Science Reports,* vol. 34, no. 1-3, pp. 1-104, 1999.
[57] R. Garcia and A. San Paulo, "Attractive and repulsive tip-sample interaction regimes in tapping-mode atomic force microscopy," *Physical Review B,* vol. 60, no. 7, p. 4961, 1999.
[58] S. Lee, S. Howell, A. Raman, and R. Reifenberger, "Nonlinear dynamics of microcantilevers in tapping mode atomic force microscopy: A comparison between theory and experiment," *Physical Review B,* vol. 66, no. 11, p. 115409, 2002.
[59] R. W. Stark, G. Schitter, and A. Stemmer, "Tuning the interaction forces in tapping mode atomic force microscopy," *Physical Review B,* vol. 68, no. 8, p. 085401, 2003.
[60] D. Platz, E. A. Tholén, D. Pesen, and D. B. Haviland, "Intermodulation atomic force microscopy," *Applied Physics Letters,* vol. 92, no. 15, p. 153106, 2008.
[61] R. W. Stark, "Bistability, higher harmonics, and chaos in afm," *Materials Today,* vol. 13, no. 9, pp. 24-32, 2010.
[62] M. Mita, M. Arai, S. Tensaka, D. Kobayashi, and H. Fujita, "A micromachined impact microactuator driven by electrostatic force," *Journal of Microelectromechanical Systems,* vol. 12, no. 1, pp. 37-41, 2003.
[63] X. Zhao, H. Dankowicz, C. K. Reddy, and A. H. Nayfeh, "Modeling and simulation methodology for impact microactuators," *Journal of Micromechanics and Microengineering,* vol. 14, no. 6, p. 775, 2004.
[64] H. Dankowicz and X. Zhao, "Local analysis of co-dimension-one and co-dimension-two grazing bifurcations in impact microactuators," *Physica D: Nonlinear Phenomena,* vol. 202, no. 3-4, pp. 238-257, 2005.
[65] X. Zhao and H. Dankowicz, "Unfolding degenerate grazing dynamics in impact actuators," *Nonlinearity,* vol. 19, no. 2, p. 399, 2005.
[66] W. Kang, P. Thota, B. Wilcox, and H. Dankowicz, "Bifurcation analysis of a microactuator using a new toolbox for continuation of hybrid system trajectories," *Journal of computational and nonlinear dynamics,* vol. 4, no. 1, 2009.
[67] M. Soliman, E. Abdel-Rahman, E. El-Saadany, and R. Mansour, "A wideband vibration-based energy harvester," *Journal of Micromechanics and Microengineering,* vol. 18, no. 11, p. 115021, 2008.

doi:10.6342/NTU202600018

[68] D. Hoffmann, B. Folkmer, and Y. Manoli, "Fabrication, characterization and modelling of electrostatic micro-generators," *Journal of Micromechanics and Microengineering*, vol. 19, no. 9, p. 094001, 2009.
[69] M. S. Soliman, E. M. Abdel-Rahman, E. F. El-Saadany, and R. R. Mansour, "A design procedure for wideband micropower generators," *Journal of Microelectromechanical Systems*, vol. 18, no. 6, pp. 1288-1299, 2009.
[70] Y. Zhang, T. Wang, A. Luo, Y. Hu, X. Li, and F. Wang, "Micro electrostatic energy harvester with both broad bandwidth and high normalized power density," *Applied Energy*, vol. 212, pp. 362-371, 2018.
[71] H. Kulah and K. Najafi, "Energy scavenging from low-frequency vibrations by using frequency up-conversion for wireless sensor applications," *IEEE Sensors Journal*, vol. 8, no. 3, pp. 261-268, 2008.
[72] H. Liu, C. J. Tay, C. Quan, T. Kobayashi, and C. Lee, "Piezoelectric mems energy harvester for low-frequency vibrations with wideband operation range and steadily increased output power," *Journal of Microelectromechanical Systems*, vol. 20, no. 5, pp. 1131-1142, 2011.
[73] H. Liu, C. Lee, T. Kobayashi, C. J. Tay, and C. Quan, "A new s-shaped mems pzt cantilever for energy harvesting from low frequency vibrations below 30 hz," *Microsystem Technologies*, vol. 18, no. 4, pp. 497-506, 2012.
[74] H. Liu, C. Lee, T. Kobayashi, C. J. Tay, and C. Quan, "Piezoelectric mems-based wideband energy harvesting systems using a frequency-up-conversion cantilever stopper," *Sensors and Actuators A: Physical*, vol. 186, pp. 242-248, 2012.
[75] H. Liu, C. Lee, T. Kobayashi, C. J. Tay, and C. Quan, "Investigation of a mems piezoelectric energy harvester system with a frequency-widened-bandwidth mechanism introduced by mechanical stoppers," *Smart Materials and Structures*, vol. 21, no. 3, p. 035005, 2012.
[76] R. Dauksevicius *et al.*, "Nonlinear piezoelectric vibration energy harvester with frequency-tuned impacting resonators for improving broadband performance at low frequencies," *Smart Materials and Structures*, vol. 28, no. 2, p. 025025, 2019.
[77] B. McCarthy, G. G. Adams, N. E. McGruer, and D. Potter, "A dynamic model, including contact bounce, of an electrostatically actuated microswitch," *Journal of Microelectromechanical Systems*, vol. 11, no. 3, pp. 276-283, 2002.
[78] A. Granaldi and P. Decuzzi, "The dynamic response of resistive microswitches: Switching time and bouncing," *Journal of Micromechanics and Microengineering*, vol. 16, no. 7, p. 1108, 2006.
[79] Z. Guo, N. McGruer, and G. Adams, "Modeling, simulation and measurement of the dynamic performance of an ohmic contact, electrostatically actuated rf mems switch," *Journal of Micromechanics and Microengineering*, vol. 17, no. 9, p. 1899, 2007.

doi:10.6342/NTU202600018

[80] Y. Lin, W.-C. Li, Z. Ren, and C. T.-C. Nguyen, "A resonance dynamical approach to faster, more reliable micromechanical switches," in *IEEE International Frequency Control Symposium*, Honolulu, HI, May. 2008, pp. 640-645.
[81] Y. Lin, W.-C. Li, Z. Ren, and C. T.-C. Nguyen, "The micromechanical resonant switch ("resoswitch")," in *Tech. Digest, Solid-State, Actuators, and Microsystems Workshop*, Hilton Head, South Carolina, Jun. 2008, pp. 40-43.
[82] R. Liu, J. N. Nilchi, Y. Lin, T. Naing, and C.-C. Nguyen, "Zero quiescent power vlf mechanical communication receiver," in *18th International Conference on Solid-State Sensors, Actuators and Microsystems (TRANSDUCERS)*, Anchorage, AK, USA, Jun. 2015, pp. 129-132.
[83] R. Liu, J. N. Nilchi, W.-C. Li, and C. T.-C. Nguyen, "Soft-impacting micromechanical resoswitch zero-quiescent power am receiver," in *29th International Conference on Micro Electro Mechanical Systems (MEMS)*, Shanghai, China, Jan. 2016, pp. 51-54.
[84] R. Liu, J. N. Nilchi, and C. T.-C. Nguyen, "Cw-powered squegging micromechanical clock generator," in *IEEE 30th International Conference on Micro Electro Mechanical Systems (MEMS)*, Jan. 2017, pp. 905-908.
[85] J. J. Bernstein *et al.*, "Resonant acoustic mems wake-up switch," *Journal of Microelectromechanical Systems*, vol. 27, no. 4, pp. 625-634, 2018.
[86] E. H. Cook *et al.*, "Low-power resonant acceleration switch for unattended sensor wake-up," *Journal of Microelectromechanical Systems*, vol. 27, no. 6, pp. 1071-1081, 2018.
[87] S.-C. Lu, C.-P. Tsai, and W.-C. Li, "A cmos-mems cc-beam metal resoswitch for zero quiescent power receiver applications," in *IEEE Micro Electro Mechanical Systems (MEMS)*, Jan. 2018, pp. 801-804.
[88] W. Z. Zhu *et al.*, "Design and fabrication of an electrostatic aln rf mems switch for near-zero power rf wake-up receivers," *IEEE Sensors Journal*, vol. 18, no. 24, pp. 9902-9909, 2018.
[89] C.-P. Tsai, Y.-Y. Liao, and W.-C. Li, "A 125-khz cmos-mems resoswitch embedded zero quiescent power ook/fsk receiver," in *IEEE 33rd International Conference on Micro Electro Mechanical Systems (MEMS)*, Jan. 2020, pp. 106-109.
[90] J. F. Rhoads, S. W. Shaw, and K. L. Turner, "Nonlinear dynamics and its applications in micro-and nanoresonators," in *Dynamic Systems and Control Conference*, 2008, vol. 43352, pp. 1509-1538.
[91] R. M. May, "Simple mathematical models with very complicated dynamics," in *The theory of chaotic attractors*, B. R. Hunt, T.-Y. Li, J. A. Kennedy, and H. E. Nusse Eds. New York: Springer, 2004, pp. 85-93.
[92] S. Foale, "Bifurcations in impact oscillators: Theoretical and experimental studies," Ph.D Thesis, Centre for Nonlinear Dynamics & its Applications, University College London, England, 1993.

doi:10.6342/NTU202600018

[93] J. G. de Weger, "The grazing bifurcation and chaos control," Ph.D Thesis, Applied Physics and Science Education, Technische Universiteit Eindhoven, Eindhoven, 2005.
[94] S. W. Shaw and P. Holmes, "A periodically forced piecewise linear oscillator," *Journal of Sound and Vibration,* vol. 90, no. 1, pp. 129-155, 1983.
[95] J. Ing, E. Pavlovskaia, M. Wiercigroch, and S. Banerjee, "Experimental study of impact oscillator with one-sided elastic constraint," *Philosophical Transactions of the Royal Society A: Mathematical, Physical and Engineering Sciences,* vol. 366, no. 1866, pp. 679-705, 2008.
[96] S. Wiggins, *Introduction to applied nonlinear dynamical systems and chaos*. New York: Springer, 2003.
[97] S. H. Strogatz, *Nonlinear dynamics and chaos: With applications to physics, biology, chemistry, and engineering*. CRC press, 2018.
[98] M. Amabili, *Nonlinear mechanics of shells and plates in composite, soft and biological materials*. Cambridge University Press, 2018.
[99] H. Kantz and T. Schreiber, *Nonlinear time series analysis*. Cambridge University Press, 2004.
[100] S. Zaitsev, O. Shtempluck, E. Buks, and O. Gottlieb, "Nonlinear damping in a micromechanical oscillator," *Nonlinear Dynamics,* vol. 67, pp. 859-883, 2012.
[101] M. Imboden and P. Mohanty, "Dissipation in nanoelectromechanical systems," *Physics Reports,* vol. 534, no. 3, pp. 89-146, 2014.
[102] M. Amabili, "Nonlinear damping in large-amplitude vibrations: Modelling and experiments," *Nonlinear Dynamics,* vol. 93, no. 1, pp. 5-18, 2018.
[103] U. Nabholz, W. Heinzelmann, J. E. Mehner, and P. Degenfeld-Schonburg, "Amplitude-and gas pressure-dependent nonlinear damping of high-q oscillatory mems micro mirrors," *Journal of Microelectromechanical Systems,* vol. 27, no. 3, pp. 383-391, 2018.
[104] V. Zega *et al.*, "Numerical modelling of non-linearities in mems resonators," *Journal of Microelectromechanical Systems,* vol. 29, no. 6, pp. 1443-1454, 2020.
[105] H. Farokhi, R. T. Rocha, A. Z. Hajjaj, and M. I. Younis, "Nonlinear damping in micromachined bridge resonators," *Nonlinear Dynamics,* vol. 111, no. 3, pp. 2311-2325, 2023.
[106] D. Meng, K. Huang, and W. Xu, "Impacts of small-scale effect and nonlinear damping on the nonlinear vibrations of electrostatic microresonators," *Micromachines,* vol. 14, no. 1, p. 170, 2023.
[107] C.-P. Tsai and W.-C. Li, "Micromechanical vibro-impact systems: A review," *Journal of Micromechanics and Microengineering*, 2023.
[108] P. Cvitanovic *et al.*, "Chaos: Classical and quantum," *ChaosBook.org (Niels Bohr Institute, Copenhagen),* vol. 69, p. 25, 2005.
[109] M. Kleczka, E. Kreuzer, and W. Schiehlen, "Local and global stability of a piecewise linear oscillator," *Philosophical Transactions of the Royal Society of*

doi:10.6342/NTU202600018

London. Series A: Physical and Engineering Sciences, vol. 338, no. 1651, pp. 533-546, 1992.
[110] S. Yin, G. Wen, J. Ji, and H. Xu, "Novel two-parameter dynamics of impact oscillators near degenerate grazing points," *International Journal of Non-Linear Mechanics,* vol. 120, p. 103403, 2020.
[111] J. Thompson, A. Bokaian, and R. Ghaffari, "Subharmonic resonances and chaotic motions of a bilinear oscillator," *IMA Journal of Applied Mathematics,* vol. 31, no. 3, pp. 207-234, 1983.
[112] Y. Kim and S. Noah, "Stability and bifurcation analysis of oscillators with piecewise-linear characteristics: A general approach," *Journal of Applied Mechanics,* vol. 58, no. 2, pp. 545-553, 1991.
[113] J.-Y. Lee, "Motion behavior of impact oscillator," *Journal of Marine Science and Technology*, vol. 13, no. 2, p. 3, 2005.
[114] U. Andreaus, L. Placidi, and G. Rega, "Numerical simulation of the soft contact dynamics of an impacting bilinear oscillator," *Communications in Nonlinear Science and Numerical Simulation,* vol. 15, no. 9, pp. 2603-2616, 2010.
[115] J. Ing, E. Pavlovskaia, M. Wiercigroch, and S. Banerjee, "Bifurcation analysis of an impact oscillator with a one-sided elastic constraint near grazing," *Physica D: Nonlinear Phenomena,* vol. 239, no. 6, pp. 312-321, 2010.
[116] S. Foale, "Analytical determination of bifurcations in an impact oscillator," *Philosophical Transactions of the Royal Society of London. Series A: Physical and Engineering Sciences,* vol. 347, no. 1683, pp. 353-364, 1994.
[117] M. Liao, J. Ing, J. P. Chávez, and M. Wiercigroch, "Bifurcation techniques for stiffness identification of an impact oscillator," *Communications in Nonlinear Science and Numerical Simulation,* vol. 41, pp. 19-31, 2016.
[118] J. Feng, "Analysis of chaotic saddles in a nonlinear vibro-impact system," *Communications in Nonlinear Science and Numerical Simulation,* vol. 48, pp. 39-50, 2017.
[119] D. Costa *et al.*, "Chaos in impact oscillators not in vain: Dynamics of new mass excited oscillator," *Nonlinear Dynamics,* vol. 102, no. 2, pp. 835-861, 2020.
[120] F. Peterka and J. Vacik, "Transition to chaotic motion in mechanical systems with impacts," *Journal of Sound and Vibration*, vol. 154, no. 1, pp. 95-115, 1992.
[121] F. e. Peterka, "Bifurcations and transition phenomena in an impact oscillator," *Chaos, Solitons & Fractals,* vol. 7, no. 10, pp. 1635-1647, 1996.
[122] F. Peterka, "Global view on dynamics of impact oscillator," *Proc. Engineering Mechanics,* pp. 207-208, 2001.
[123] A. Guerrieri, A. Frangi, and L. Falorni, "An investigation on the effects of contact in mems oscillators," *Journal of Microelectromechanical Systems,* vol. 27, no. 6, pp. 963-972, 2018.
[124] J. de Weger, W. van de Water, and J. Molenaar, "Grazing impact oscillations," *Physical Review E,* vol. 62, no. 2, p. 2030, 2000.

doi:10.6342/NTU202600018

[125] A. Nordmark, "Effects due to low velocity impact in mechanical oscillators," *International Journal of Bifurcation and Chaos*, vol. 2, no. 03, pp. 597-605, 1992.
[126] J. de Weger, D. Binks, J. Molenaar, and W. van de Water, "Generic behavior of grazing impact oscillators," *Physical Review Letters*, vol. 76, no. 21, p. 3951, 1996.
[127] H. Jiang, A. S. Chong, Y. Ueda, and M. Wiercigroch, "Grazing-induced bifurcations in impact oscillators with elastic and rigid constraints," *International Journal of Mechanical Sciences*, vol. 127, pp. 204-214, 2017.
[128] A. Narimani, M. Golnaraghi, and G. N. Jazar, "Frequency response of a piecewise linear vibration isolator," *Journal of Vibration and Control*, vol. 10, no. 12, pp. 1775-1794, 2004.
[129] L. Yu, L. Tang, L. Xiong, and T. Yang, "Capture of high energy orbit of duffing oscillator with time-varying parameters," *Chaos: An Interdisciplinary Journal of Nonlinear Science*, vol. 30, no. 2, p. 023106, 2020.
[130] H.-Y. Chen, M.-H. Li, and S.-S. Li, "A new finding on nonlinear damping and stiffness of flexural mode capacitive mems resonators," in *IEEE 36th International Conference on Micro Electro Mechanical Systems (MEMS)*, Jan. 2023, pp. 526-529.
[131] Y. Jia, S. Du, and A. A. Seshia, "Twenty-eight orders of parametric resonance in a microelectromechanical device for multi-band vibration energy harvesting," *Scientific Reports*, vol. 6, no. 1, p. 30167, 2016.
[132] C. Van der Avoort *et al.*, "Amplitude saturation of mems resonators explained by autoparametric resonance," *Journal of Micromechanics and Microengineering*, vol. 20, no. 10, p. 105012, 2010.
[133] M. Defoort, L. Rufer, L. Fesquet, and S. Basrour, "A dynamical approach to generate chaos in a micromechanical resonator," *Microsystems & Nanoengineering*, vol. 7, no. 1, p. 17, 2021.
[134] X. Shi and Y.-P. Zhao, "Comparison of various adhesion contact theories and the influence of dimensionless load parameter," *Journal of Adhesion Science and Technology*, vol. 18, no. 1, pp. 55-68, 2004.
[135] Y.-P. Zhao, L. Wang, and T. Yu, "Mechanics of adhesion in mems—a review," *Journal of Adhesion Science and Technology*, vol. 17, no. 4, pp. 519-546, 2003.
[136] D. Grierson, E. Flater, and R. Carpick, "Accounting for the jkr–dmt transition in adhesion and friction measurements with atomic force microscopy," *Journal of Adhesion Science and Technology*, vol. 19, no. 3-5, pp. 291-311, 2005.
[137] E. Barthel, "Adhesive elastic contacts: Jkr and more," *Journal of Physics D: Applied Physics*, vol. 41, no. 16, p. 163001, 2008.
[138] V. L. Popov, *Contact mechanics and friction*, 1st ed. Berlin/Heidelberg: Springer, 2010.
[139] J. N. Israelachvili, *Intermolecular and surface forces*. Academic Press, 2011.

doi:10.6342/NTU202600018

[140] F. L. Leite, C. C. Bueno, A. L. Da Róz, E. C. Ziemath, and O. N. Oliveira, "Theoretical models for surface forces and adhesion and their measurement using atomic force microscopy," *International Journal of Molecular Sciences,* vol. 13, no. 10, pp. 12773-12856, 2012.
[141] M. Ciavarella, J. Joe, A. Papangelo, and J. Barber, "The role of adhesion in contact mechanics," *Journal of the Royal Society Interface,* vol. 16, no. 151, p. 20180738, 2019.
[142] L. Wang, "The role of damping in phase imaging in tapping mode atomic force microscopy," *Surface Science,* vol. 429, no. 1-3, pp. 178-185, 1999.
[143] P.-A. Thorén *et al.*, "Modeling and measuring viscoelasticity with dynamic atomic force microscopy," *Physical Review Applied*, vol. 10, no. 2, p. 024017, 2018.
[144] P. Stoyanov and R. R. Chromik, "Scaling effects on materials tribology: From macro to micro scale," *Materials*, vol. 10, no. 5, p. 550, 2017.
[145] N. Burnham, A. Kulik, G. Gremaud, and G. Briggs, "Nanosubharmonics: The dynamics of small nonlinear contacts," *Physical Review Letters,* vol. 74, no. 25, p. 5092, 1995.
[146] Y. Lin, R. Liu, W.-C. Li, and C. T.-C. Nguyen, "Polycide contact interface to suppress squegging in micromechanical resoswitches," in *IEEE 27th International Conference on Micro Electro Mechanical Systems (MEMS)*, San Francisco, CA, USA, Jan. 2014, pp. 1273-1276.
[147] G. E. Box, "Robustness in the strategy of scientific model building," in *Robustness in statistics*: Academic Press, 1979, pp. 201-236.
[148] A. Okolewski and B. Blazejczyk-Okolewska, "Hard vs soft impacts in oscillatory systems' modeling revisited," *Chaos: An Interdisciplinary Journal of Nonlinear Science,* vol. 31, no. 8, p. 083110, 2021.
[149] G. Gilardi and I. Sharf, "Literature survey of contact dynamics modelling," *Mechanism and machine theory*, vol. 37, no. 10, pp. 1213-1239, 2002.
[150] B. Blazejczyk-Okolewska, K. Czolczynski, and T. Kapitaniak, "Hard versus soft impacts in oscillatory systems modeling," *Communications in Nonlinear Science and Numerical Simulation,* vol. 15, no. 5, pp. 1358-1367, 2010.
[151] E. Corral, R. G. Moreno, M. García, and C. Castejón, "Nonlinear phenomena of contact in multibody systems dynamics: A review," *Nonlinear Dynamics,* vol. 104, no. 2, pp. 1269-1295, 2021.
[152] L. Skrinjar, J. Slavič, and M. Boltežar, "A review of continuous contact-force models in multibody dynamics," *International Journal of Mechanical Sciences,* vol. 145, pp. 171-187, 2018.
[153] Y. Zhang and K. Murphy, "Multi-modal analysis on the intermittent contact dynamics of atomic force microscope," *Journal of Sound and Vibration,* vol. 330, no. 23, pp. 5569-5582, 2011.

doi:10.6342/NTU202600018

[154] A. J. Dick *et al.*, "Utilizing nonlinear phenomena to locate grazing in the constrained motion of a cantilever beam," *Nonlinear Dynamics*, vol. 57, no. 3, pp. 335-349, 2009.
[155] F. A. Rahim and M. I. Younis, "Control of bouncing in mems switches using double electrodes," *Mathematical Problems in Engineering*, vol. 2016, 2016.
[156] W. Zhang, W. Zhang, and K. L. Turner, "Nonlinear dynamics of micro impact oscillators in high frequency mems switch application," in *13th International Conference on Solid-State Sensors, Actuators and Microsystems (TRANSDUCERS)*, Seoul, Korea, Jun. 2005, pp. 768-771.
[157] G. K. Rao, P. Mitcheson, and T. Green, "Simulation toolkit for energy scavenging inertial micro power generators," in *PowerMEMS Workshop Proceedings*, 2007, pp. 137-140.
[158] L. G. W. Tvedt, L.-C. J. Blystad, and E. Halvorsen, "Simulation of an electrostatic energy harvester at large amplitude narrow and wide band vibrations," in *Symposium on Design, Test, Integration and Packaging of MEMS/MOEMS*, Apr. 2008, pp. 296-301.
[159] L.-C. J. Blystad, E. Halvorsen, and S. Husa, "Piezoelectric mems energy harvesting systems driven by harmonic and random vibrations," *IEEE Transactions on Ultrasonics, Ferroelectrics, and Frequency Control*, vol. 57, no. 4, pp. 908-919, 2010.
[160] L.-C. J. Blystad and E. Halvorsen, "A piezoelectric energy harvester with a mechanical end stop on one side," *Microsystem Technologies*, vol. 17, no. 4, pp. 505-511, 2011.
[161] C. P. Le and E. Halvorsen, "Microscale energy harvesters with nonlinearities due to internal impacts," *Small-Scale Energy Harvesting*, pp. 265-282, 2012.
[162] C. P. Le and E. Halvorsen, "Mems electrostatic energy harvesters with end-stop effects," *Journal of Micromechanics and Microengineering*, vol. 22, no. 7, p. 074013, 2012.
[163] L. Dhakar, F. Tay, and C. Lee, "Investigation of contact electrification based broadband energy harvesting mechanism using elastic pdms microstructures," *Journal of Micromechanics and Microengineering*, vol. 24, no. 10, p. 104002, 2014.
[164] K. Tao, S. W. Lye, J. Miao, L. Tang, and X. Hu, "Out-of-plane electret-based mems energy harvester with the combined nonlinear effect from electrostatic force and a mechanical elastic stopper," *Journal of Micromechanics and Microengineering*, vol. 25, no. 10, p. 104014, 2015.
[165] M. Mita, M. Ataka, H. Fujita, and H. Toshiyoshi, "An inertia driven micro-actuator for space applications," *Electronics and Communications in Japan*, vol. 97, no. 3, pp. 60-67, 2014.
[166] Z. Yang, H. Cai, G. Ding, H. Wang, and X. Zhao, "Dynamic simulation of a contact-enhanced mems inertial switch in simulink®," *Microsystem Technologies*, vol. 17, no. 8, pp. 1329-1342, 2011.

doi:10.6342/NTU202600018

[167] X. Zhanwen, Z. Ping, N. Weirong, D. Liqun, and C. Yun, "A novel mems omnidirectional inertial switch with flexible electrodes," *Sensors and Actuators A: Physical*, vol. 212, pp. 93-101, 2014.
[168] N. Krakover, R. Maimon, T. Tepper-Faran, N. Yitzhak, and S. Krylov, "Reliability of an 1000 g range vertically integrated silicon on insulator (soi) impact switch," in *IEEE International Symposium on Inertial Sensors and Systems (INERTIAL)*, 2020, pp. 1-3.
[169] J. Bienstman, J. Vandewalle, and R. Puers, "The autonomous impact resonator: A new operating principle for a silicon resonant strain gauge," *Sensors and Actuators A: Physical*, vol. 66, no. 1-3, pp. 40-49, 1998.
[170] X. Zhao, C. K. Reddy, and A. H. Nayfeh, "Bifurcations and chaotic dynamics in an electrostatically actuated impact microactuator: A numerical exploration," in *International Design Engineering Technical Conferences and Computers and Information in Engineering Conference*, 2003, pp. 1789-1794.
[171] X. Zhao, C. Reddy, and A. Nayfeh, "Nonlinear dynamics of an electrically driven impact microactuator," *Nonlinear Dynamics*, vol. 40, no. 3, pp. 227-239, 2005.
[172] P. Thota, X. Zhao, and H. Dankowicz, "Co-dimension-two grazing bifurcations in single-degree-of-freedom impact oscillators," *Journal of Computational and Nonlinear Dynamics*, vol. 1, no. 4, pp. 328-335, 2006.
[173] X. Zhao and H. Dankowicz, "Control of impact microactuators for precise positioning," *Journal of Computational and Nonlinear Dynamics*, pp. 65-70, 2006.
[174] R. V. Field Jr and D. S. Epp, "Development and calibration of a stochastic dynamics model for the design of a mems inertial switch," *Sensors and Actuators A: Physical*, vol. 134, no. 1, pp. 109-118, 2007.
[175] M. Basso, L. Giarre, M. Dahleh, and I. Mezic, "Numerical analysis of complex dynamics in atomic force microscopes," in *IEEE International Conference on Control Applications*, Trieste, Italy, Sep. 1998, pp. 1026-1030.
[176] S. Rützel, S. I. Lee, and A. Raman, "Nonlinear dynamics of atomic–force–microscope probes driven in lennard–jones potentials," *Proceedings of the Royal Society of London. Series A: Mathematical, Physical and Engineering Sciences*, vol. 459, no. 2036, pp. 1925-1948, 2003.
[177] N.-S. Pai, C.-C. Wang, and D. T. Lin, "Bifurcation analysis of a microcantilever in afm system," *Journal of the Franklin Institute*, vol. 347, no. 7, pp. 1353-1367, 2010.
[178] J. M. Balthazar, A. M. Tusset, A. M. Bueno, and B. R. de Pontes Junior, "On an overview of nonlinear and chaotic behavior and their controls of an atomic force microscopy (afm) vibrating problem," *Nonlinearity, bifurcation and chaos: Theory and Applications*, vol. 1, pp. 45-68, 2012.

doi:10.6342/NTU202600018

[179] A. Chandrashekar, P. Belardinelli, U. Staufer, and F. Alijani, "Robustness of attractors in tapping mode atomic force microscopy," *Nonlinear Dynamics,* vol. 97, no. 2, pp. 1137-1158, 2019.
[180] H. N. Arafat, A. H. Nayfeh, and E. M. Abdel-Rahman, "Modal interactions in contact-mode atomic force microscopes," *Nonlinear Dynamics,* vol. 54, pp. 151-166, 2008.
[181] M. Marth, D. Maier, J. Honerkamp, R. Brandsch, and G. Bar, "A unifying view on some experimental effects in tapping-mode atomic force microscopy," *Journal of Applied Physics,* vol. 85, no. 10, pp. 7030-7036, 1999.
[182] R. W. Stark, G. Schitter, M. Stark, R. Guckenberger, and A. Stemmer, "State-space model of freely vibrating and surface-coupled cantilever dynamics in atomic force microscopy," *Physical Review B,* vol. 69, no. 8, p. 085412, 2004.
[183] K. Yagasaki, "Nonlinear dynamics of vibrating microcantilevers in tapping-mode atomic force microscopy," *Physical Review B,* vol. 70, no. 24, p. 245419, 2004.
[184] K. Yagasaki, "Bifurcations and chaos in vibrating microcantilevers of tapping mode atomic force microscopy," *International Journal of Non-linear Mechanics,* vol. 42, no. 4, pp. 658-672, 2007.
[185] A. Bahrami and A. H. Nayfeh, "On the dynamics of tapping mode atomic force microscope probes," *Nonlinear Dynamics,* vol. 70, no. 2, pp. 1605-1617, 2012.
[186] I. Manoubi, F. Najar, S. Choura, and A. Nayfeh, "Nonlinear dynamical analysis of an afm tapping mode microcantilever beam," in *MATEC Web of Conferences*, Jul. 2012, p. 04002.
[187] A. Bahrami and A. H. Nayfeh, "Nonlinear dynamics of tapping mode atomic force microscopy in the bistable phase," *Communications in Nonlinear Science and Numerical Simulation,* vol. 18, no. 3, pp. 799-810, 2013.
[188] R. McCarty and S. N. Mahmoodi, "Dynamic mulitmode analysis of non-linear piezoelectric microcantilever probe in bistable region of tapping mode atomic force microscopy," *International Journal of Non-Linear Mechanics,* vol. 74, pp. 25-37, 2015.
[189] W. Xiang, Y. Tian, and X. Liu, "Dynamic analysis of tapping mode atomic force microscope (afm) for critical dimension measurement," *Precision Engineering,* vol. 64, pp. 269-279, 2020.
[190] U. Andreaus, L. Placidi, and G. Rega, "Microcantilever dynamics in tapping mode atomic force microscopy via higher eigenmodes analysis," *Journal of Applied Physics,* vol. 113, no. 22, p. 224302, 2013.
[191] S.-C. Lu, C.-P. Tsai, Y.-C. Huang, W.-R. Du, and W.-C. Li, "Surface condition influence on the nonlinear response of mems cc-beam resoswitches," *IEEE Electron Device Letters,* vol. 39, no. 10, pp. 1600-1603, 2018.
[192] C.-P. Tsai, H.-W. Wang, and W.-C. Li, "Tapping bandwidth widening of cmos-mems vibro-impacting resonators based on double-sided stopper structures," in

doi:10.6342/NTU202600018

21st International Conference on Solid-State Sensors, Actuators and Microsystems (TRANSDUCERS), Orlando, FL, USA, Jun. 2021, pp. 1387-1391.
[193] Y.-C. Wu, W. Yang, and D. Peroulis, "Significance of adhesion-reduced bouncing in dynamic contacts of ohmic rf mems switches," *Journal of Microelectromechanical Systems*, vol. 24, no. 5, pp. 1487-1494, 2015.
[194] L. Wang, "Analytical descriptions of the tapping-mode atomic force microscopy response," *Applied Physics Letters*, vol. 73, no. 25, pp. 3781-3783, 1998.
[195] A. Sebastian, A. Gannepalli, and M. V. Salapaka, "The amplitude phase dynamics and fixed points in tapping-mode atomic force microscopy," in *Proceedings of the American Control Conference*, 2004, vol. 3, pp. 2499-2504.
[196] A. Keyvani, M. S. Tamer, J.-W. van Wingerden, J. Goosen, and F. van Keulen, "A comprehensive model for transient behavior of tapping mode atomic force microscope," *Nonlinear Dynamics*, vol. 97, no. 2, pp. 1601-1617, 2019.
[197] G. Gee and B. D. Jensen, "A dynamic model of microscale contact breaking in rf mems switches," in *International Joint Tribology Conference*, 2006, vol. 42592, pp. 1475-1479.
[198] C. Do, M. Cychowski, M. Lishchynska, M. Hill, and K. Delaney, "Integrated modeling of nonlinear dynamics and contact mechanics of electrostatically actuated rf-mems switches," in *36th Annual Conference on IEEE Industrial Electronics Society*, Glendale, AZ, USA, Nov. 2010, pp. 2293-2298.
[199] C. Do, M. Hill, M. Lishchynska, M. Cychowski, and K. Delaney, "Modeling, simulation and validation of the dynamic performance of a single-pole single-throw rf-mems contact switch," in *12th International Conference on Thermal, Mechanical & Multi-Physics Simulation and Experiments in Microelectronics and Microsystems*, Linz, Austria, 2011, pp. 1-6.
[200] P. Decuzzi, G. Demelio, G. Pascazio, and V. Zaza, "Bouncing dynamics of resistive microswitches with an adhesive tip," *Journal of Applied Physics*, vol. 100, no. 2, p. 024313, 2006.
[201] R. C. Tung, A. Fruehling, D. Peroulis, and A. Raman, "Multiple timescales and modeling of dynamic bounce phenomena in rf mems switches," *Journal of microelectromechanical systems*, vol. 23, no. 1, pp. 137-146, 2013.
[202] B. Ma, Z. You, and Y. Ruan, "Vacuum bouncing dynamics dominated by van der waals forces in mems relays," in *IEEE 29th International Conference on Micro Electro Mechanical Systems (MEMS)*, Shanghai, China, Jan. 2016, pp. 593-596.
[203] I. Sari, T. Balkan, and H. Külah, "An electromagnetic micro power generator for low-frequency environmental vibrations based on the frequency upconversion technique," *Journal of Microelectromechanical Systems*, vol. 19, no. 1, pp. 14-27, 2009.
[204] T. D. Jacobs, C. Mathew Mate, K. T. Turner, and R. W. Carpick, "Understanding the tip–sample contact: An overview of contact mechanics from the macro-to

doi:10.6342/NTU202600018

the nanoscale," *Scanning Probe Microscopy in Industrial Applications: Nanomechanical characterization*, pp. 15-48, 2013.
[205] D. C. Lin, E. K. Dimitriadis, and F. Horkay, "Robust strategies for automated afm force curve analysis-ii: Adhesion-influenced indentation of soft, elastic materials," *Journal of Biomechanical Engineering*, vol. 129, no. 6, pp. 904-12, Dec Dec. 2007, doi: 10.1115/1.2800826.
[206] D. Kiracofe, J. Melcher, and A. Raman, "Gaining insight into the physics of dynamic atomic force microscopy in complex environments using the veda simulator," *Review of Scientific Instruments*, vol. 83, no. 1, p. 013702, 2012.
[207] E. A. López-Guerra and S. D. Solares, "Modeling viscoelasticity through spring–dashpot models in intermittent-contact atomic force microscopy," *Beilstein journal of nanotechnology*, vol. 5, no. 1, pp. 2149-2163, 2014.
[208] Y. M. Efremov, T. Okajima, and A. Raman, "Measuring viscoelasticity of soft biological samples using atomic force microscopy," *Soft Matter*, vol. 16, no. 1, pp. 64-81, 2020.
[209] J. Zhang, W. Li, L. Zhao, and G. He, "A continuous contact force model for impact analysis in multibody dynamics," *Mechanism and Machine Theory*, vol. 153, p. 103946, 2020.
[210] P. Flores, "Contact mechanics for dynamical systems: A comprehensive review," *Multibody System Dynamics*, pp. 1-51, 2021.
[211] J. Alves, N. Peixinho, M. T. da Silva, P. Flores, and H. M. Lankarani, "A comparative study of the viscoelastic constitutive models for frictionless contact interfaces in solids," *Mechanism and Machine Theory*, vol. 85, pp. 172-188, 2015.
[212] M. R. da Silva, F. Marques, M. T. da Silva, and P. Flores, "A compendium of contact force models inspired by hunt and crossley's cornerstone work," *Mechanism and Machine Theory*, vol. 167, p. 104501, 2022.
[213] K. L. Johnson, "One hundred years of hertz contact," *Proceedings of the Institution of Mechanical Engineers*, vol. 196, no. 1, pp. 363-378, 1982.
[214] H. Hertz, "On the contact of elastic solids," in *Miscellaneous papers*. London: Macmillan & Co. Ltd, 1896, pp. 146-162.
[215] B. Voigtländer, *Atomic force microscopy*. Cham: Springer, 2019.
[216] H. Hertz, "Ueber die berührung fester elastischer körper," *Journal für die reine und angewandte Mathematik*, vol. 92, pp. 156-171, 1882.
[217] K. L. Johnson, K. Kendall, and a. Roberts, "Surface energy and the contact of elastic solids," *Proceedings of the royal society of London. A. mathematical and physical sciences*, vol. 324, no. 1558, pp. 301-313, 1971.
[218] B. V. Derjaguin, V. M. Muller, and Y. P. Toporov, "Effect of contact deformations on the adhesion of particles," *Journal of Colloid and interface science*, vol. 53, no. 2, pp. 314-326, 1975.

doi:10.6342/NTU202600018

[219] R. S. Bradley, "Lxxix. The cohesive force between solid surfaces and the surface energy of solids," *The London, Edinburgh, and Dublin Philosophical Magazine and Journal of Science,* vol. 13, no. 86, pp. 853-862, 1932.
[220] X. Wang, S. Ramírez-Hinestrosa, J. Dobnikar, and D. Frenkel, "The lennard-jones potential: When (not) to use it," *Physical Chemistry Chemical Physics,* vol. 22, no. 19, pp. 10624-10633, 2020.
[221] J. Peña, A. Menéndez, J. Garcia-Ravelo, and J. Morales, "Mie-type potential from a class of multiparameter exponential-type potential: Bound state solutions in d dimensions," in *Journal of Physics: Conference Series*, 2015, vol. 633, no. 1: IOP Publishing, p. 012025.
[222] M. Ashhab, M. Salapaka, M. Dahleh, and I. Mezić, "Melnikov-based dynamical analysis of microcantilevers in scanning probe microscopy," *Nonlinear Dynamics,* vol. 20, pp. 197-220, 1999.
[223] K. Johnson and J. Greenwood, "An adhesion map for the contact of elastic spheres," *Journal of Colloid and Interface Science,* vol. 192, no. 2, pp. 326-333, 1997.
[224] Q. J. Wang and Y.-W. Chung, *Encyclopedia of tribology*. New York: Springer, 2013.
[225] J. Greenwood, "Adhesion of elastic spheres," *Proceedings of the Royal Society of London. Series A: Mathematical, Physical and Engineering Sciences,* vol. 453, no. 1961, pp. 1277-1297, 1997.
[226] D. Maugis, "Adhesion of spheres: The jkr-dmt transition using a dugdale model," *Journal of Colloid and Interface Science,* vol. 150, no. 1, pp. 243-269, 1992.
[227] S. Liao, *Homotopy analysis method in nonlinear differential equations*. Springer, 2012.
[228] J. Fei, B. Lin, S. Yan, and X. Zhang, "Approximate solution of a piecewise linear–nonlinear oscillator using the homotopy analysis method," *Journal of Vibration and Control,* vol. 24, no. 19, pp. 4551-4562, 2018.
[229] A. M. Elshurafa, K. Khirallah, H. H. Tawfik, A. Emira, A. K. A. Aziz, and S. M. Sedky, "Nonlinear dynamics of spring softening and hardening in folded-mems comb drive resonators," *Journal of Microelectromechanical Systems,* vol. 20, no. 4, pp. 943-958, 2011.
[230] H. Nawaz, M. U. Masood, M. M. Saleem, J. Iqbal, and M. Zubair, "Surface roughness effects on electromechanical performance of rf-mems capacitive switches," *Microelectronics Reliability,* vol. 104, p. 113544, 2020.
[231] H. V. Guzman, P. D. Garcia, and R. Garcia, "Dynamic force microscopy simulator (dforce): A tool for planning and understanding tapping and bimodal afm experiments," *Beilstein Journal of Nanotechnology,* vol. 6, no. 1, pp. 369-379, 2015.
[232] W. Menacho, G. M. Ramírez-Ávila, and H. V. Guzman, "Pydampf: A python package for modeling mechanical properties of hygroscopic materials under

doi:10.6342/NTU202600018

interaction with a nanoprobe," in *Proceedings of the 21st Python in Science Conference (SCIPY)*, Austin, Texas, Jul. 2022, pp. 202-209.
[233] H. Dankowicz and F. Schilder, *Recipes for continuation*. SIAM, 2013.
[234] A. Dhooge, W. Govaerts, and Y. A. Kuznetsov, "Matcont: A matlab package for numerical bifurcation analysis of odes," *ACM Transactions on Mathematical Software (TOMS)*, vol. 29, no. 2, pp. 141-164, 2003.
[235] E. J. Doedel *et al.*, "Auto-07p: Continuation and bifurcation software for ordinary differential equations," 2007. [Online]. Available: http://cmvl.cs.concordia.ca/auto/.
[236] M. Krack and J. Gross, *Harmonic balance for nonlinear vibration problems*. Cham: Springer, 2019.
[237] C.-P. Tsai and W.-C. Li, "A micromechanical frequency controlled pulse density modulator," in *IEEE 35th International Conference on Micro Electro Mechanical Systems Conference (MEMS)*, 2022, pp. 204-207.
[238] Q. Zhong, D. Inniss, K. Kjoller, and V. Elings, "Fractured polymer/silica fiber surface studied by tapping mode atomic force microscopy," *Surface Science Letters*, vol. 290, no. 1-2, pp. L688-L692, 1993.
[239] R. Garcia, "Nanomechanical mapping of soft materials with the atomic force microscope: Methods, theory and applications," *Chemical Society Reviews*, vol. 49, no. 16, pp. 5850-5884, 2020.
[240] K. Wang, K. G. Taylor, and L. Ma, "Advancing the application of atomic force microscopy (afm) to the characterization and quantification of geological material properties," *International Journal of Coal Geology*, vol. 247, p. 103852, 2021.
[241] G. Stan and S. W. King, "Atomic force microscopy for nanoscale mechanical property characterization," *Journal of Vacuum Science & Technology B, Nanotechnology and Microelectronics: Materials, Processing, Measurement, and Phenomena*, vol. 38, no. 6, p. 060801, 2020.
[242] P. Gleyzes, P. Kuo, and A. Boccara, "Bistable behavior of a vibrating tip near a solid surface," *Applied Physics Letters*, vol. 58, no. 25, pp. 2989-2991, 1991.
[243] S. Hu and A. Raman, "Chaos in atomic force microscopy," *Physical Review Letters*, vol. 96, no. 3, p. 036107, 2006.
[244] S. Hornstein and O. Gottlieb, "Nonlinear multimode dynamics and internal resonances of the scan process in noncontacting atomic force microscopy," *Journal of Applied Physics*, vol. 112, no. 7, p. 074314, 2012.
[245] M. Mita, K. Takahashi, M. Ataka, H. Fujita, and H. Toshiyoshi, "Highly-mobile 2d micro impact actuator for space applications," in *14th International Solid-State Sensors, Actuators and Microsystems Conference (TRANSDUCERS)*, Jun. 2007, pp. 675-678.
[246] M. F. Daqaq, R. Masana, A. Erturk, and D. Dane Quinn, "On the role of nonlinearities in vibratory energy harvesting: A critical review and discussion," *Applied Mechanics Reviews*, vol. 66, no. 4, 2014.

doi:10.6342/NTU202600018

[247] M. Huang *et al.*, "A low-frequency mems piezoelectric energy harvesting system based on frequency up-conversion mechanism," *Micromachines,* vol. 10, no. 10, p. 639, 2019.
[248] L. Gu, "Low-frequency piezoelectric energy harvesting prototype suitable for the mems implementation," *Microelectronics Journal,* vol. 42, no. 2, pp. 277-282, 2011.
[249] S. Moss, A. Barry, I. Powlesland, S. Galea, and G. Carman, "A broadband vibro-impacting power harvester with symmetrical piezoelectric bimorph-stops," *Smart Materials and Structures,* vol. 20, no. 4, p. 045013, 2011.
[250] M. Borowiec, G. Litak, and S. Lenci, "Noise effected energy harvesting in a beam with stopper," *International Journal of Structural Stability and Dynamics,* vol. 14, no. 08, p. 1440020, 2014.
[251] T. Liu, R. St Pierre, and C. Livermore, "Passively-switched energy harvester for increased operational range," *Smart Materials and Structures,* vol. 23, no. 9, p. 095045, 2014.
[252] J. Yang *et al.*, "Broadband vibrational energy harvesting based on a triboelectric nanogenerator," *Advanced Energy Materials,* vol. 4, no. 6, p. 1301322, 2014.
[253] K. Vijayan, M. Friswell, H. H. Khodaparast, and S. Adhikari, "Non-linear energy harvesting from coupled impacting beams," *International Journal of Mechanical Sciences,* vol. 96, pp. 101-109, 2015.
[254] J. Zhang and L. Qin, "A tunable frequency up-conversion wideband piezoelectric vibration energy harvester for low-frequency variable environment using a novel impact-and rope-driven hybrid mechanism," *Applied Energy,* vol. 240, pp. 26-34, 2019.
[255] B. Guo and J. V. Ringwood, "Non-linear modeling of a vibro-impact wave energy converter," *IEEE Transactions on Sustainable Energy,* vol. 12, no. 1, pp. 492-500, 2020.
[256] Q. Wu, S. Gao, L. Jin, X. Zhang, Z. Yin, and C. Wang, "A tuning fork frequency up-conversion energy harvester," *Sensors,* vol. 21, no. 21, p. 7285, 2021.
[257] W.-C. Li, "Micromechanical vibro-impact resonator-enabled sensing applications," in *21st International Conference on Solid-State Sensors, Actuators and Microsystems (TRANSDUCERS)*, Jun. 2021, pp. 609-613.
[258] C.-P. Tsai and W.-C. Li, "Cmos-mems vibro-impact devices and applications," (in English), *Frontiers in Mechanical Engineering,* Review vol. 8, 2022-June-09 2022, doi: 10.3389/fmech.2022.898328.
[259] Y. Lin, W.-C. Li, Z. Ren, and C. T.-C. Nguyen, "The micromechanical resonant switch ("resoswitch")," *Tech. Digest*, pp. 40-43, 2008.
[260] Y. Lin, R. Liu, W.-C. Li, M. Akgul, and C. T.-C. Nguyen, "A micromechanical resonant charge pump," in *Transducers & Eurosensors XXVII: The 17th International Conference on Solid-State Sensors, Actuators and Microsystems (TRANSDUCERS & EUROSENSORS XXVII)*, 2013, pp. 1727-1730.

doi:10.6342/NTU202600018

[261] T.-J. Liou, C.-P. Tsai, T.-Y. Chen, and W.-C. Li, "Towards a better cmos-mems resoswitch using electroless plating for contact engineering," in *IEEE 36th International Conference on Micro Electro Mechanical Systems (MEMS)*, Munich, Germany, Jan. 2023, pp. 1206-1209.
[262] M. Riverola, G. Vidal-Álvarez, G. Sobreviela, A. Uranga, F. Torres, and N. Barniol, "Dynamic properties of three-terminal tungsten cmos-nem relays under nonlinear tapping mode," *IEEE Sensors Journal*, vol. 16, no. 13, pp. 5283-5291, 2016.
[263] Y. Lin, R. Liu, W.-C. Li, M. Akgul, and C. T.-C. Nguyen, "A micromechanical resonant charge pump," in *17th International Conference on Solid-State Sensors, Actuators and Microsystems (TRANSDUCERS & EUROSENSORS XXVII)*, Barcelona, Spain, Jun. 2013, pp. 1727-1730.
[264] T. Wu, G. Chen, Z. Qian, W. Zhu, M. Rinaldi, and N. McGruer, "A microelectromechanical aln resoswitch for rf receiver application," in *19th International Conference on Solid-State Sensors, Actuators and Microsystems (TRANSDUCERS)*, Kaohsiung, Taiwan, Jun. 2017, pp. 2123-2126.
[265] W.-C. Li, Y. Lin, and C. T.-C. Nguyen, "Metal micromechanical filter-power amplifier utilizing a displacement-amplifying resonant switch," in *17th International Conference on Solid-State Sensors, Actuators and Microsystems (TRANSDUCERS & EUROSENSORS XXVII)*, Barcelona, Spain, Jun. 2013, pp. 2469-2472.
[266] S. Rizehbandi, M. Reshadi, M. Baghelani, and A. Khademzadeh, "Asymmetric rf mems resonant switch for high speed switching applications," *Microsystem Technologies*, vol. 24, no. 12, pp. 4729-4735, 2018.
[267] Y. Lin, T. Riekkinen, W.-C. Li, E. Alon, and C. T.-C. Nguyen, "A metal micromechanical resonant switch for on-chip power applications," in *International Electron Devices Meeting*, Washington, DC, Dec. 2011, pp. 20.6. 1-20.6. 4.
[268] R. Liu, J. N. Nilchi, and C. T.-C. Nguyen, "Rf-powered micromechanical clock generator," in *IEEE International Frequency Control Symposium (IFCS)*, May. 2016, pp. 1-6.
[269] Q. Jin, K. Zheng, and C. T.-C. Nguyen, "Bit rate-adapting resoswitch," in *International Electron Devices Meeting (IEDM)*, San Francisco, CA, USA, Dec. 2022, pp. 16.5. 1-16.5. 4.
[270] K. H. Zheng, Q. Jin, and C. T.-C. Nguyen, "Ferrite-rod antenna driven wireless resoswitch receiver," in *IEEE 36th International Conference on Micro Electro Mechanical Systems (MEMS)*, Munich, Germany, Jan. 2023, pp. 173-176.
[271] R. Wei *et al.*, "A self-sustained frequency comb oscillator via tapping mode comb-drive resonator integrated with a feedback asic," in *IEEE 32nd International Conference on Micro Electro Mechanical Systems (MEMS)*, Seoul, South Korea, Jan. 2019, pp. 165-168.

doi:10.6342/NTU202600018

[272] Y.-H. Huang, H.-S. Zheng, C.-P. Tsai, and W.-C. Li, "Micromechanical rssi based on force interaction derived tapping bandwidth variation in vibro-impact resonators," in *IEEE 36th International Conference on Micro Electro Mechanical Systems (MEMS)*, Munich, Germany, Jan. 2023, pp. 487-490.
[273] C.-P. Tsai and W.-C. Li, "Attractor exchanger for open-loop operation of micromechanical nonlinear resonators using gap-spacing continuation," in *IEEE 36th International Conference on Micro Electro Mechanical Systems (MEMS)*, Munich, Germany, Jan. 2023, pp. 181-184.
[274] L. Ruzziconi, N. Jaber, L. Kosuru, and M. I. Younis, "Activating internal resonance in a microelectromechanical system by inducing impacts," *Nonlinear Dynamics*, vol. 110, no. 2, pp. 1109-1127, 2022.
[275] R. P. LaRose III and K. D. Murphy, "Impact dynamics of mems switches," *Nonlinear Dynamics*, vol. 60, no. 3, pp. 327-339, 2010.
[276] L. T. Govindaraman, A. Arjunan, A. Baroutaji, J. Robinson, and A.-G. Olabi, "Metamaterials for energy harvesting," in *Encyclopedia of smart materials*, A.-G. Olabi Ed. Oxford: Elsevier, 2022, pp. 522-534.
[277] Z. Chen, B. Guo, Y. Yang, and C. Cheng, "Metamaterials-based enhanced energy harvesting: A review," *Physica B: Condensed Matter*, vol. 438, pp. 1-8, 2014.
[278] T. A. Hewage, K. L. Alderson, A. Alderson, and F. Scarpa, "Double-negative mechanical metamaterials displaying simultaneous negative stiffness and negative poisson's ratio properties," *Advanced Materials*, vol. 28, no. 46, pp. 10323-10332, 2016.
[279] Z. Ren, Y. Chang, Y. Ma, K. Shih, B. Dong, and C. Lee, "Leveraging of mems technologies for optical metamaterials applications," *Advanced Optical Materials*, vol. 8, no. 3, p. 1900653, 2020.
[280] S. Koul, C. Mahajan, A. Poddar, and U. Rohde, "A microelectromechanical switch with metamaterial contacts, part i: Concepts and technology," *Microwave Journal*, pp. 82-108, 2020.
[281] S. K. Koul and S. Dey, *Micromachined circuits and devices*. Singapore: Springer, 2022.
[282] S. K. Koul, P. K. Srivastava, A. K. Poddar, and U. L. Rohde, "A microelectromechanical switch with metamaterial contacts, part iii: Reducing stiction," *Microwave Journal*, pp. 52-68, 2020.
[283] S. K. Koul, C. Mahajan, A. K. Poddar, and U. L. Rohde, "A microelectromechanical switch with metamaterial contacts: Concepts and technology part ii," *Structure*, vol. 2, p. 5, 2020.
[284] M. Huff, *Process variations in microsystems manufacturing*. Cham: Springer, 2020.
[285] Olympus replacement afm probes [Online] Available: https://www.nanoandmore.com/Olympus-replacement-AFM-probes

doi:10.6342/NTU202600018

[286] L.-Y. Ma, N. Soin, M. H. M. Daut, and S. F. W. M. Hatta, "Comprehensive study on rf-mems switches used for 5g scenario," *IEEE Access,* vol. 7, pp. 107506-107522, 2019.
[287] H.-C. Liu, Y.-H. Lin, and W. Hsu, "Sidewall roughness control in advanced silicon etch process," *Microsystem Technologies,* vol. 10, no. 1, pp. 29-34, 2003.
[288] R. R. Reddy, Y. Okamoto, and Y. Mita, "An on-chip micromachined test structure to study the tribological behavior of deep-rie mems sidewall surfaces," *IEEE Transactions on Semiconductor Manufacturing,* vol. 33, no. 2, pp. 187-195, 2020.
[289] K. M. Kumar, P. V. Shanmuganathan, and A. Sethuramiah, "Tribology of silicon surfaces: A review," *Materials Today: Proceedings,* vol. 5, no. 11, pp. 24809-24819, 2018.
[290] L. T. Govindaraman, A. Arjunan, A. Baroutaji, J. Robinson, M. Ramadan, and A.-G. Olabi, "Nanomaterials theory and applications," in *Encyclopedia of smart materials*, A.-G. Olabi Ed. Oxford: Elsevier, 2022, pp. 302-314.
[291] Z. Zhang, J. Páez Chávez, J. Sieber, and Y. Liu, "Controlling grazing-induced multistability in a piecewise-smooth impacting system via the time-delayed feedback control," *Nonlinear Dynamics,* vol. 107, no. 2, pp. 1595-1610, 2022.
[292] H. Li, C. Touzé, A. Pelat, F. Gautier, and X. Kong, "A vibro-impact acoustic black hole for passive damping of flexural beam vibrations," *Journal of Sound and Vibration,* vol. 450, pp. 28-46, 2019.
[293] H. Li, M. Sécail-Géraud, A. Pelat, F. Gautier, and C. Touzé, "Experimental evidence of energy transfer and vibration mitigation in a vibro-impact acoustic black hole," *Applied Acoustics,* vol. 182, p. 108168, 2021.
[294] M. Ramírez-Barrios, F. Dohnal, and J. Collado, "Enhanced vibration decay in high-q resonators by confined of parametric excitation," *Archive of Applied Mechanics,* vol. 90, no. 8, pp. 1673-1684, 2020.
[295] B. Jeong *et al.*, "Utilizing intentional internal resonance to achieve multi-harmonic atomic force microscopy," *Nanotechnology,* vol. 27, no. 12, p. 125501, 2016.
[296] F. M. Alsaleem, M. H. Hasan, and M. K. Tesfay, "A mems nonlinear dynamic approach for neural computing," *Journal of Microelectromechanical Systems,* vol. 27, no. 5, pp. 780-789, 2018.
[297] T. Zheng, W. Yang, J. Sun, X. Xiong, Z. Li, and X. Zou, "Parameters optimization method for the time-delayed reservoir computing with a nonlinear duffing mechanical oscillator," *Scientific Reports,* vol. 11, no. 1, p. 997, 2021.
[298] S. Pagliano *et al.*, "Micro 3d printing of a functional mems accelerometer," *Microsystems & Nanoengineering,* vol. 8, no. 1, p. 105, 2022.
[299] S. Stassi, I. Cooperstein, M. Tortello, C. F. Pirri, S. Magdassi, and C. Ricciardi, "Reaching silicon-based nems performances with 3d printed nanomechanical resonators," *Nature Communications,* vol. 12, no. 1, p. 6080, 2021.

doi:10.6342/NTU202600018

[300] R. Liu, J. N. Nilchi, W.-C. Li, and C. T.-C. Nguyen, "Soft-impacting micromechanical resoswitch zero-quiescent power am receiver," in *2016 IEEE 29th International Conference on Micro Electro Mechanical Systems (MEMS)*, 2016: IEEE, pp. 51-54.
[301] C.-P. Tsai, Y.-Y. Liao, and W.-C. Li, "A 125-khz cmos-mems resoswitch embedded zero quiescent power ook/fsk receiver," in *2020 IEEE 33rd International Conference on Micro Electro Mechanical Systems (MEMS)*, 2020: IEEE, pp. 106-109.
[302] W.-C. Li, C.-P. Tsai, and H.-W. Wang, "Device and method for monitoring surface condition of contact surface of detected object," ed: Google Patents, 2023.
[303] S.-C. Lu, W.-R. Du, Y.-C. Huang, C.-P. Tsai, and W.-C. Li, "Mems surface coating condition monitoring via nonlinear tapping of resoswitches," in *2018 IEEE International Frequency Control Symposium (IFCS)*, 2018: IEEE, pp. 1-5.
[304] C.-P. Tsai and W.-C. Li, "A micromechanical frequency controlled pulse density modulator," in *2022 IEEE 35th International Conference on Micro Electro Mechanical Systems Conference (MEMS)*, 2022: IEEE, pp. 204-207.
[305] C.-P. Tsai and W.-C. Li, "Attractor exchanger for open-loop operation of micromechanical nonlinear resonators using gap-spacing continuation," in *2023 IEEE 36th International Conference on Micro Electro Mechanical Systems (MEMS)*, 2023: IEEE, pp. 181-184.
[306] C.-P. Tsai and W.-C. Li, "Vibro-impact perturbation based attractor exchanger for open-loop nonlinear resonators," in *2023 22nd International Conference on Solid-State Sensors, Actuators and Microsystems (Transducers)*, 2023: IEEE, pp. 465-468.
[307] R. Liu, J. N. Nilchi, and C. T.-C. Nguyen, "Rf-powered micromechanical clock generator," in *2016 IEEE International Frequency Control Symposium (IFCS)*, 2016: IEEE, pp. 1-6.
[308] R. Liu, J. N. Nilchi, and C. T.-C. Nguyen, "Cw-powered squegging micromechanical clock generator," in *2017 IEEE 30th International Conference on Micro Electro Mechanical Systems (MEMS)*, 2017: IEEE, pp. 905-908.
[309] H.-S. Zheng, C.-P. Tsai, T.-Y. Chen, and W.-C. Li, "Cmos-mems resonators with sub-100-nm transducer gap using stress engineering," in *2022 IEEE 35th International Conference on Micro Electro Mechanical Systems Conference (MEMS)*, 2022: IEEE, pp. 13-16.
[310] T.-J. Liou, C.-P. Tsai, T.-Y. Chen, and W.-C. Li, "Towards a better cmos-mems resoswitch using electroless plating for contact engineering," in *2023 IEEE 36th International Conference on Micro Electro Mechanical Systems (MEMS)*, 2023: IEEE, pp. 1206-1209.

doi:10.6342/NTU202600018

[311] C.-M. Lee, T.-J. Liou, C.-P. Tsai, T.-Y. Chen, and W.-C. Li, "Toward high-bit-rate cmos-mems resoswitches," in *2024 IEEE 37th International Conference on Micro Electro Mechanical Systems (MEMS)*, 2024: IEEE, pp. 178-181.
[312] K. H. Zheng, Q. Jin, and C. T.-C. Nguyen, "Resoswitch squegging control by compact model-assisted impact electrode design," in *2024 IEEE 37th International Conference on Micro Electro Mechanical Systems (MEMS)*, 2024: IEEE, pp. 1071-1074.
[313] C. J. Gomez and R. Garcia, "Determination and simulation of nanoscale energy dissipation processes in amplitude modulation afm," *Ultramicroscopy*, vol. 110, no. 6, pp. 626-633, 2010.
[314] A. Keyvani, M. S. Tamer, J.-W. van Wingerden, J. Goosen, and F. van Keulen, "A comprehensive model for transient behavior of tapping mode atomic force microscope," *Nonlinear Dynamics*, vol. 97, pp. 1601-1617, 2019.
[315] A. Mikrajuddin, F. G. Shi, H. Kim, and K. Okuyama, "Size-dependent electrical constriction resistance for contacts of arbitrary size: From sharvin to holm limits," *Materials Science in Semiconductor Processing*, vol. 2, no. 4, pp. 321-327, 1999.
[316] C.-P. Tsai and W.-C. Li, "Cmos-mems resoswitches—design, modeling, and characterization," *Journal of Microelectromechanical Systems*, 2025.
[317] D. Kumar, C. M. Walker, and M. P. de Boer, "Low voltage cold and hot switching in nanoswitches cleaned by in situ oxygen plasma can achieve low stable contact resistance," *Journal of Applied Physics*, vol. 135, no. 2, 2024.
[318] C.-C. Nguyen and R. T. Howe, "An integrated cmos micromechanical resonator high-q oscillator," *IEEE Journal of Solid-State Circuits*, vol. 34, no. 4, pp. 440-455, 1999.
[319] W. C.-K. Tang, *Electrostatic comb drive for resonant sensor and actuator applications*. University of California, Berkeley, 1990.
[320] R. Legtenberg, A. Groeneveld, and M. Elwenspoek, "Comb-drive actuators for large displacements," *Journal of Micromechanics and microengineering*, vol. 6, no. 3, p. 320, 1996.
[321] Y. Zhang and M. Kahrizi, "327. Surface micromachined comb drive with superior stability for application as an actuator," *Journal of Vibroengineering*, vol. 10, no. 1, 2008.
[322] S.-W. Chyuan, Y.-S. Liao, and J.-T. Chen, "Computational study of the effect of finger width and aspect ratios for the electrostatic levitating force of mems combdrive," *Journal of Microelectromechanical Systems*, vol. 14, no. 2, pp. 305-312, 2005.
[323] P. G. Del Corro, M. Imboden, D. J. Bishop, and H. Pastoriza, "Comb drive designs with minimized levitation," *Journal of Microelectromechanical Systems*, vol. 25, no. 6, pp. 1025-1032, 2016.

doi:10.6342/NTU202600018

[324] W. C. Tang, M. G. Lim, and R. T. Howe, "Electrostatic comb drive levitation and control method," *Journal of Microelectromechanical systems*, vol. 1, no. 4, pp. 170-178, 1992.
[325] S. Timpe, D. Hook, M. Dugger, and K. Komvopoulos, "Levitation compensation method for dynamic electrostatic comb-drive actuators," *Sensors and Actuators A: Physical*, vol. 143, no. 2, pp. 383-389, 2008.
[326] C.-E. Hsu and W.-C. Li, "Enhancing the release process yield for cmos-mems metal resonators based on diffusion-controlling structures," in *2021 IEEE 34th International Conference on Micro Electro Mechanical Systems (MEMS)*, 2021: IEEE, pp. 937-940.
[327] C.-L. Dai, "A maskless wet etching silicon dioxide post-cmos process and its application," *Microelectronic Engineering*, vol. 83, no. 11-12, pp. 2543-2550, 2006.
[328] H. Xie and G. K. Fedder, "A cmos-mems lateral-axis gyroscope," in *Technical Digest. MEMS 2001. 14th IEEE International Conference on Micro Electro Mechanical Systems (Cat. No. 01CH37090)*, 2001: IEEE, pp. 162-165.
[329] S. V. Iyer, H. Lakdawala, T. Mukherjee, and G. K. Fedder, "Modeling methodology for a cmos-mems electrostatic comb," in *Design, Test, Integration, and Packaging of MEMS/MOEMS 2002*, 2002, vol. 4755: SPIE, pp. 114-125.
[330] H. Xie and G. K. Fedder, "Vertical comb-finger capacitive actuation and sensing for cmos-mems," *Sensors and Actuators A: Physical*, vol. 95, no. 2-3, pp. 212-221, 2002.
[331] C.-L. Cheng, M.-H. Tsai, and W. Fang, "Determining the thermal expansion coefficient of thin films for a cmos mems process using test cantilevers," *Journal of Micromechanics and Microengineering*, vol. 25, no. 2, p. 025014, 2015.
[332] W.-C. Chen, W. Fang, and S.-S. Li, "A generalized cmos-mems platform for micromechanical resonators monolithically integrated with circuits," *Journal of Micromechanics and Microengineering*, vol. 21, no. 6, p. 065012, 2011.
[333] J. L. Lopez *et al.*, "Integration of rf-mems resonators on submicrometric commercial cmos technologies," *Journal of Micromechanics and Microengineering*, vol. 19, no. 1, p. 015002, 2008.
[334] C.-L. Dai, C.-H. Kuo, and M.-C. Chiang, "Microelectromechanical resonator manufactured using cmos-mems technique," *Microelectronics journal*, vol. 38, no. 6-7, pp. 672-677, 2007.
[335] C.-L. Dai, H.-J. Peng, M.-C. Liu, C.-C. Wu, H.-M. Hsu, and L.-J. Yang, "A micromachined microwave switch fabricated by the complementary metal oxide semiconductor post-process of etching silicon dioxide," *Japanese journal of applied physics*, vol. 44, no. 9R, p. 6804, 2005.
[336] J.-R. Liu, S.-C. Lu, C.-P. Tsai, and W.-C. Li, "A cmos-mems clamped–clamped beam displacement amplifier for resonant switch applications," *Journal of Micromechanics and Microengineering*, vol. 28, no. 6, p. 065001, 2018.

doi:10.6342/NTU202600018

[337] M.-H. Li, C.-Y. Chen, C.-S. Li, C.-H. Chin, and S.-S. Li, "Design and characterization of a dual-mode cmos-mems resonator for tcf manipulation," *Journal of Microelectromechanical Systems*, vol. 24, no. 2, pp. 446-457, 2014.
[338] M.-H. Li, C.-Y. Chen, C.-S. Li, C.-H. Chin, and S.-S. Li, "A monolithic cmos-mems oscillator based on an ultra-low-power ovenized micromechanical resonator," *Journal of Microelectromechanical Systems*, vol. 24, no. 2, pp. 360-372, 2014.
[339] C.-C. Tsai, S.-C. Tsai, and Y.-C. Huang, "Investigation of a seesaw structure for elevating the micro-optical device by cmos-mems process," in *MOEMS and Miniaturized Systems VI*, 2007, vol. 6466: SPIE, pp. 203-213.
[340] P. G. Slade, *Electrical contacts: Principles and applications*. CRC press, 2017.
[341] M. Braunovic, N. K. Myshkin, and V. V. Konchits, *Electrical contacts: Fundamentals, applications and technology*. CRC press, 2017.
[342] C.-Y. Chen, M.-H. Li, A. A. Zope, and S.-S. Li, "A cmos-integrated mems platform for frequency stable resonators-part i: Fabrication, implementation, and characterization," *Journal of Microelectromechanical Systems*, vol. 28, no. 5, pp. 744-754, 2019.
[343] C.-Y. Chen, M.-H. Li, C.-S. Li, and S.-S. Li, "A cmos-integrated mems platform for frequency stable resonators—part ii: Design and analysis," *Journal of Microelectromechanical Systems*, vol. 28, no. 5, pp. 755-765, 2019.
[344] C.-Y. Chen, A. A. Zope, M.-H. Li, and S.-S. Li, "A generic tin-c process for cmos feol/beol-embedded vertically-coupled capacitive and piezoresistive resonators," in *2019 20th International Conference on Solid-State Sensors, Actuators and Microsystems & Eurosensors XXXIII (TRANSDUCERS & EUROSENSORS XXXIII)*, 2019: IEEE, pp. 531-534.
[345] M.-H. Li, C.-Y. Chen, and S.-S. Li, "A reliable cmos-mems platform for titanium nitride composite (tin-c) resonant transducers with enhanced electrostatic transduction and frequency stability," in *2015 IEEE International Electron Devices Meeting (IEDM)*, 2015: IEEE, pp. 18.4. 1-18.4. 4.
[346] H. Xiao, *Introduction to semiconductor manufacturing technology* (Vol. Pm220). Prentice Hall, 2012, pp. 451-507.
[347] R. Holm, *Electric contacts: Theory and application*. Springer Science & Business Media, 2013.
[348] Y. Chen, R. Nathanael, J. Jeon, J. Yaung, L. Hutin, and T.-J. K. Liu, "Characterization of contact resistance stability in mem relays with tungsten electrodes," *Journal of Microelectromechanical Systems*, vol. 21, no. 3, pp. 511-513, 2012.
[349] D. A. Czaplewski, C. D. Nordquist, C. W. Dyck, G. A. Patrizi, G. M. Kraus, and W. D. Cowan, "Lifetime limitations of ohmic, contacting rf mems switches with au, pt and ir contact materials due to accumulation of ‘friction polymer’on the contacts," *Journal of Micromechanics and Microengineering*, vol. 22, no. 10, p. 105005, 2012.

doi:10.6342/NTU202600018

[350] C. Do, A. Erbes, J. Yan, and A. A. Seshia, "Design and implementation of a low-power hybrid capacitive mems oscillator," *Microelectronics Journal*, vol. 56, pp. 1-9, 2016.
[351] H. A. Tilmans, "Equivalent circuit representation of electromechanical transducers: I. Lumped-parameter systems," *Journal of Micromechanics and Microengineering*, vol. 6, no. 1, p. 157, 1996.
[352] H. A. Tilmans, "Equivalent circuit representation of electromechanical transducers: Ii. Distributed-parameter systems," *Journal of Micromechanics and Microengineering*, vol. 7, no. 4, p. 285, 1997.
[353] H.-W. Park, Y.-K. Kim, H.-G. Jeong, J. W. Song, and J.-M. Kim, "Feed-through capacitance reduction for a micro-resonator with push–pull configuration based on electrical characteristic analysis of resonator with direct drive," *Sensors and Actuators A: Physical*, vol. 170, no. 1-2, pp. 131-138, 2011.
[354] S. S. Rao and F. F. Yap, *Mechanical vibrations*. Addison-Wesley New York, 1995.
[355] C.-Y. Chen, M.-H. Li, and S.-S. Li, "Cmos-mems resonators and oscillators: A review," *Sensors & Materials*, vol. 30, 2018.
[356] R. Liu, J. N. Nilchi, Y. Lin, T. Naing, and C.-C. Nguyen, "Zero quiescent power vlf mechanical communication receiver," in *2015 Transducers-2015 18th International Conference on Solid-State Sensors, Actuators and Microsystems (TRANSDUCERS)*, 2015: IEEE, pp. 129-132.
[357] R. Liu, "All-mechanical receivers," University of California, Berkeley, 2017.
[358] O. Rezvanian, M. Zikry, C. Brown, and J. Krim, "Surface roughness, asperity contact and gold rf mems switch behavior," *Journal of Micromechanics and Microengineering*, vol. 17, no. 10, p. 2006, 2007.
[359] C. Brown, O. Rezvanian, M. Zikry, and J. Krim, "Temperature dependence of asperity contact and contact resistance in gold rf mems switches," *Journal of micromechanics and microengineering*, vol. 19, no. 2, p. 025006, 2009.
[360] D. B. Heinz, V. A. Hong, C. H. Ahn, E. J. Ng, Y. Yang, and T. W. Kenny, "Experimental investigation into stiction forces and dynamic mechanical anti-stiction solutions in ultra-clean encapsulated mems devices," *Journal of Microelectromechanical Systems*, vol. 25, no. 3, pp. 469-478, 2016.
[361] B. F. Toler, R. A. Coutu, and J. W. McBride, "A review of micro-contact physics for microelectromechanical systems (mems) metal contact switches," *Journal of Micromechanics and Microengineering*, vol. 23, no. 10, p. 103001, 2013.
[362] S. Majumder, N. McGruer, G. G. Adams, P. Zavracky, R. H. Morrison, and J. Krim, "Study of contacts in an electrostatically actuated microswitch," *Sensors and Actuators A: Physical*, vol. 93, no. 1, pp. 19-26, 2001.
[363] J. A. Greenwood and J. P. Williamson, "Contact of nominally flat surfaces," *Proceedings of the royal society of London. Series A. Mathematical and physical sciences*, vol. 295, no. 1442, pp. 300-319, 1966.

doi:10.6342/NTU202600018

[364] J. A. Greenwood and J. Tripp, "The contact of two nominally flat rough surfaces," *Proceedings of the institution of mechanical engineers,* vol. 185, no. 1, pp. 625-633, 1970.
[365] C.-P. Tsai, H.-W. Wang, and W.-C. Li, "Tapping bandwidth widening of cmos-mems vibro-impacting resonators based on double-sided stopper structures," in *2021 21st International Conference on Solid-State Sensors, Actuators and Microsystems (Transducers)*, 2021: IEEE, pp. 1387-1391.
[366] K. L. Johnson and K. L. Johnson, *Contact mechanics*. Cambridge university press, 1987.
[367] S. Eichenlaub, C. Chan, and S. P. Beaudoin, "Hamaker constants in integrated circuit metalization," *Journal of Colloid and Interface Science,* vol. 248, no. 2, pp. 389-397, 2002.
[368] D.-L. Liu, J. Martin, and N. Burnham, "Optimal roughness for minimal adhesion," *Applied Physics Letters,* vol. 91, no. 4, 2007.
[369] J. Chawla, X. Zhang, and D. Gall, "Effective electron mean free path in tin (001)," *Journal of Applied Physics,* vol. 113, no. 6, 2013.
[370] R. Vijgen and J. Dautzenberg, "Mechanical measurement of the residual stress in thin pvd films," *Thin solid films,* vol. 270, no. 1-2, pp. 264-269, 1995.
[371] B. Johansson, J. E. Sundgren, J. Greene, A. Rockett, and S. Barnett, "Growth and properties of single crystal tin films deposited by reactive magnetron sputtering," *Journal of Vacuum Science & Technology A: Vacuum, Surfaces, and Films,* vol. 3, no. 2, pp. 303-307, 1985.
[372] T. Futase, N. Hashikawa, T. Hayashi, H. Tobimatsu, H. Yamamoto, and H. Kozawa, "Low contact-resistance metallization process for a nickel self-aligned contact of beyond 65nm node cmos," in *2007 International Symposium on Semiconductor Manufacturing*, 2007: IEEE, pp. 1-4.
[373] J.-Y. Yun, S.-W. Rhee, S. Park, and J.-G. Lee, "Remote plasma enhanced metalorganic chemical vapor deposition of tin from tetrakis-dimethyl-amido-titanium," *Journal of Vacuum Science & Technology A: Vacuum, Surfaces, and Films,* vol. 18, no. 6, pp. 2822-2826, 2000.
[374] D. Chen, Y. Wang, Y. Guan, X. Chen, X. Liu, and J. Xie, "Methods for nonlinearities reduction in micromechanical beams resonators," *Journal of Microelectromechanical Systems,* vol. 27, no. 5, pp. 764-773, 2018.
[375] M. I. Younis, *Mems linear and nonlinear statics and dynamics*. Springer Science & Business Media, 2011.
[376] S. Hu, "Nonlinear dynamics and force spectroscopy in dynamic atomic force microscopy," Purdue University, 2007.
[377] A. Keyvani, H. Sadeghian, H. Goosen, and F. Van Keulen, "On the origin of amplitude reduction mechanism in tapping mode atomic force microscopy," *Applied Physics Letters,* vol. 112, no. 16, 2018.
[378] R. A. Coutu, P. E. Kladitis, R. Cortez, R. E. Strawser, and R. L. Crane, "Micro-switches with sputtered au, aupd, au-on-aupt, and auptcu alloy electric contacts,"

doi:10.6342/NTU202600018

in *Proceedings of the 50th IEEE Holm Conference on Electrical Contacts and the 22nd International Conference on Electrical Contacts Electrical Contacts, 2004.*, 2004: IEEE, pp. 214-221.
[379] A. Broué *et al.*, "Multi-physical characterization of micro-contact materials for mems switches," in *56th IEEE Holm Conference on Electrical Contacts*, 2010, p. 10 pages.
[380] Y.-H. Song, M.-W. Kim, J. O. Lee, S.-D. Ko, and J.-B. Yoon, "Complementary dual-contact switch using soft and hard contact materials for achieving low contact resistance and high reliability simultaneously," *Journal of microelectromechanical systems,* vol. 22, no. 4, pp. 846-854, 2013.
[381] J. Oberhammer and G. Stemme, "Active opening force and passive contact force electrostatic switches for soft metal contact materials," *Journal of microelectromechanical systems,* vol. 15, no. 5, pp. 1235-1242, 2006.
[382] Q. Ma *et al.*, "Metal contact reliability of rf mems switches," in *Reliability, Packaging, Testing, and Characterization of MEMS/MOEMS VI*, 2007, vol. 6463: SPIE, pp. 42-54.
[383] Y.-C. Lin, S. Yen, T. Mukherjee, and G. K. Fedder, "Lateral flexure contact on cmos mems electrothermal metal-metal contact switch by platinum ald sidewall patterning," in *2021 IEEE 34th International Conference on Micro Electro Mechanical Systems (MEMS)*, 2021: IEEE, pp. 974-977.
[384] W. Lee, K. Harrison, J. Provine, S. Mitra, H.-S. Wong, and R. Howe, "Laterally actuated nanoelectromechanical relays with compliant, low resistance contact," in *2013 IEEE 26th International Conference on Micro Electro Mechanical Systems (MEMS)*, 2013: IEEE, pp. 520-523.
[385] C. Oh and M. P. de Boer, "Optimization and contact reliability of tin-coated microswitches in various gas environments," *Journal of Microelectromechanical Systems,* vol. 28, no. 1, pp. 95-106, 2018.
[386] G. Wexler, "The size effect and the non-local boltzmann transport equation in orifice and disk geometry," *Proceedings of the Physical Society,* vol. 89, no. 4, p. 927, 1966.
[387] H. Kwon *et al.*, "Investigation of the electrical contact behaviors in au-to-au thin-film contacts for rf mems switches," *Journal of Micromechanics and Microengineering,* vol. 18, no. 10, p. 105010, 2008.
[388] G. M. Rebeiz, *Rf mems: Theory, design, and technology*. John Wiley & Sons, 2004.
[389] Y. Lin, R. Liu, W.-C. Li, and C. T.-C. Nguyen, "Polycide contact interface to suppress squegging in micromechanical resoswitches," in *2014 IEEE 27th International Conference on Micro Electro Mechanical Systems (MEMS)*, 2014: IEEE, pp. 1273-1276.
[390] B. D. Jensen, L.-W. Chow, K. Huang, K. Saitou, J. L. Volakis, and K. Kurabayashi, "Effect of nanoscale heating on electrical transport in rf mems

doi:10.6342/NTU202600018

switch contacts," *Journal of microelectromechanical systems,* vol. 14, no. 5, pp. 935-946, 2005.
[391] M. Von Arx, O. Paul, and H. Baltes, "Process-dependent thin-film thermal conductivities for thermal cmos mems," *Journal of Microelectromechanical systems,* vol. 9, no. 1, pp. 136-145, 2000.
[392] A. Broue *et al.*, "Validation of bending tests by nanoindentation for micro-contact analysis of mems switches," *Journal of Micromechanics and Microengineering,* vol. 20, no. 8, p. 085025, 2010.
[393] R. Hennessy, N. McGruer, and G. Adams, "Modeling of a thermal-electrical-mechanical coupled field contact," 2012.
[394] T. V. Laurvick and R. A. Coutu, "Improving gold/gold microcontact performance and reliability under low-frequency ac through circuit loading," *IEEE Transactions on Components, Packaging and Manufacturing Technology,* vol. 7, no. 3, pp. 345-353, 2016.
[395] L. Yu, L. Tang, L. Xiong, and T. Yang, "Capture of high energy orbit of duffing oscillator with time-varying parameters," *Chaos: An Interdisciplinary Journal of Nonlinear Science,* vol. 30, no. 2, 2020.
[396] X. Liu *et al.*, "Dynamics of piezoelectric micro-machined ultrasonic transducers for contact and non-contact resonant sensors," *Journal of Applied Physics,* vol. 126, no. 12, 2019.
[397] H. Zhang, C. Zhao, X. Ning, J. Huang, and J. Zhang, "Harmonic excitation response performance and active regulation of the high-frequency piezoelectric ultrasonic transducer used in the thermosonic bonding for microelectronics," *Sensors and Actuators A: Physical,* vol. 304, p. 111839, 2020.
[398] M. Brennan, I. Kovacic, A. Carrella, and T. Waters, "On the jump-up and jump-down frequencies of the duffing oscillator," *Journal of Sound and Vibration,* vol. 318, no. 4-5, pp. 1250-1261, 2008.
[399] K.-C. Woo, A. A. Rodger, R. D. Neilson, and M. Wiercigroch, "Phase shift adjustment for harmonic balance method applied to vibro-impact systems," *Meccanica,* vol. 41, pp. 269-282, 2006.
[400] K. H. Zheng, Q. Jin, and C. T.-C. Nguyen, "Ferrite-rod antenna driven wireless resoswitch receiver," in *2023 IEEE 36th International Conference on Micro Electro Mechanical Systems (MEMS)*, 2023: IEEE, pp. 173-176.
[401] P. M. Polunin, Y. Yang, M. I. Dykman, T. W. Kenny, and S. W. Shaw, "Characterization of mems resonator nonlinearities using the ringdown response," *Journal of Microelectromechanical Systems,* vol. 25, no. 2, pp. 297-303, 2016.
[402] G. Gonzalez, *Microwave transistor amplifiers: Analysis and design*. Prentice hall New Jersey, 1997.
[403] D. M. Pozar, *Microwave engineering*. John wiley & sons, 2011.

doi:10.6342/NTU202600018

[404] Y. Yi, C. P. Tsai, and W. C. Li, "Sensitivity enhancement for micromechanical vibro-impact resonators using snap-through curved beams," *Micro & Nano Letters*, vol. 18, no. 1, p. e12155, 2023.
[405] J. R. Clark, W.-T. Hsu, and C. T.-C. Nguyen, "Measurement techniques for capacitively-transduced vhf-to-uhf micromechanical resonators," in *Transducers' 01 Eurosensors XV: The 11th International Conference on Solid-State Sensors and Actuators June 10–14, 2001 Munich, Germany*, 2001: Springer, pp. 1090-1093.
[406] J. R. Clark, W.-T. Hsu, and C.-C. Nguyen, "High-q vhf micromechanical contour-mode disk resonators," in *International Electron Devices Meeting 2000. Technical Digest. IEDM (Cat. No. 00CH37138)*, 2000: IEEE, pp. 493-496.
[407] D. Chen *et al.*, "Feedthrough parasitic nonlinear resonance in micromechanical oscillators," *Applied Physics Letters*, vol. 117, no. 13, 2020.
[408] C.-Y. Chen, M.-H. Li, C.-S. Li, and S.-S. Li, "Design and characterization of mechanically coupled cmos-mems filters for channel-select applications," *Sensors and Actuators A: Physical*, vol. 216, pp. 394-404, 2014.
[409] Z. Wu *et al.*, "Piezoelectrically transduced high-q silica micro resonators," in *2013 IEEE 26th International Conference on Micro Electro Mechanical Systems (MEMS)*, 2013: IEEE, pp. 122-125.
[410] J.-R. Liu, C.-P. Tsai, W.-R. Du, T.-Y. Chen, J.-S. Chen, and W.-C. Li, "Vibration mode suppression in micromechanical resonators using embedded anti-resonating structures," *Journal of Microelectromechanical Systems*, vol. 30, no. 1, pp. 53-63, 2021.
[411] L. Chen, Z. Guo, N. Joshi, H. Eid, G. Adams, and N. McGruer, "An improved spm-based contact tester for the study of microcontacts," *Journal of Micromechanics and Microengineering*, vol. 22, no. 4, p. 045017, 2012.
[412] M. Riverola, G. Vidal-Alvarez, G. Sobreviela, A. Uranga, F. Torres, and N. Barniol, "Dynamic properties of three-terminal tungsten cmos-nem relays under nonlinear tapping mode," *IEEE Sensors Journal*, vol. 16, no. 13, pp. 5283-5291, 2016.
[413] F. Souchon, A. Peschot, P. L. Charvet, and C. Poulain, "Impact of creep and softening mechanisms on the contact resistance of rf mems ohmic switches: Study of the current and time effects on au-to-au microcontacts in static contact conditions," in *2010 Proceedings of the 56th IEEE Holm Conference on Electrical Contacts*, 2010: IEEE, pp. 1-7.
[414] G. Schrag, T. Künzig, and G. Wachutka, "Modeling reliablity issues in rf mems switches," in *2013 international conference on simulation of semiconductor processes and devices (SISPAD)*, 2013: IEEE, pp. 432-435.
[415] C. Birleanu and M. Pustan, "Analysis of the adhesion effect in rf-mems switches using atomic force microscope," *Analog Integrated Circuits and Signal Processing*, vol. 82, pp. 571-581, 2015.

doi:10.6342/NTU202600018

[416] E. Pavlovskaia, J. Ing, M. Wiercigroch, and S. Banerjee, "Complex dynamics of bilinear oscillator close to grazing," *International Journal of Bifurcation and Chaos*, vol. 20, no. 11, pp. 3801-3817, 2010.
[417] D. Costa *et al.*, "Chaos in impact oscillators not in vain: Dynamics of new mass excited oscillator," *Nonlinear Dynamics*, vol. 102, pp. 835-861, 2020.
[418] Q. Jin, K. Zheng, and C. T.-C. Nguyen, "Bit rate-adapting resoswitch," in *2022 International Electron Devices Meeting (IEDM)*, 2022: IEEE, pp. 16.5. 1-16.5. 4.
[419] L. Chen *et al.*, "Contact resistance study of noble metals and alloy films using a scanning probe microscope test station," *Journal of applied physics*, vol. 102, no. 7, 2007.
[420] H. Lee, R. A. Coutu, S. Mall, and K. D. Leedy, "Characterization of metal and metal alloy films as contact materials in mems switches," *Journal of Micromechanics and Microengineering*, vol. 16, no. 3, p. 557, 2006.
[421] F. Ke, J. Miao, and J. Oberhammer, "A ruthenium-based multimetal-contact rf mems switch with a corrugated diaphragm," *Journal of microelectromechanical systems*, vol. 17, no. 6, pp. 1447-1459, 2008.
[422] D. A. Czaplewski, C. D. Nordquist, G. A. Patrizi, G. M. Kraus, and W. D. Cowan, "Rf mems switches with ruo2–au contacts cycled to 10 billion cycles," *Journal of microelectromechanical systems*, vol. 22, no. 3, pp. 655-661, 2013.
[423] Kurmendra and R. Kumar, "Materials selection approaches and fabrication methods in rf mems switches," *Journal of Electronic Materials*, vol. 50, no. 6, pp. 3149-3168, 2021.
[424] V. B. Sawant, S. S. Mohite, and L. N. Cheulkar, "Comprehensive contact material selection approach for rf mems switch," *Materials Today: Proceedings*, vol. 5, no. 4, pp. 10704-10711, 2018.
[425] M. Antler and M. Drozdowicz, "Fretting corrosion of gold-plated connector contacts," *Wear*, vol. 74, no. 1, pp. 27-50, 1981.
[426] R. S. Mroczkowski, "Connector design/materials and connector reliability," *AMP Tech. Pap. P*, pp. 351-93, 1993.
[427] M. Antler and M. Drozdowicz, "Wear of gold electrodeposits: Effect of substrate and of nickel underplate," *Bell System Technical Journal*, vol. 58, no. 2, pp. 323-349, 1979.
[428] H. AG and R. Hüske, "Contact plating material options for electronic connectors."
[429] Z. Yang, D. J. Lichtenwalner, A. S. Morris, J. Krim, and A. I. Kingon, "Comparison of au and au–ni alloys as contact materials for mems switches," *Journal of Microelectromechanical Systems*, vol. 18, no. 2, pp. 287-295, 2009.
[430] A. Broué *et al.*, "Comparative study of rf mems micro-contact materials," *International Journal of Microwave and Wireless Technologies*, vol. 4, no. 4, pp. 413-420, 2012.

doi:10.6342/NTU202600018

[431] J. W. Ko *et al.*, "Electroless gold plating on aluminum patterned chips for cmos-based sensor applications," *Journal of The Electrochemical Society*, vol. 157, no. 1, p. D46, 2009.
[432] S. S. Bedair *et al.*, "A cmos mems gold plated electrode array for chemical vapor detection," in *SENSORS, 2006 IEEE*, 2006: IEEE, pp. 1074-1077.
[433] S.-B. Kim, H.-W. Min, Y.-B. Lee, S.-H. Kim, P.-K. Choi, and J.-B. Yoon, "Utilizing mechanical adhesion force as a high contact force in a mems relay," *Sensors and Actuators A: Physical*, vol. 331, p. 112894, 2021.
[434] A. Bahrami and A. H. Nayfeh, "On the dynamics of tapping mode atomic force microscope probes," *Nonlinear Dynamics*, vol. 70, pp. 1605-1617, 2012.
[435] C. Maragliano, A. Glia, M. Stefancich, and M. Chiesa, "Effective afm cantilever tip size: Methods for in-situ determination," *Measurement Science and Technology*, vol. 26, no. 1, p. 015002, 2014.
[436] Y. M. Efremov, W.-H. Wang, S. D. Hardy, R. L. Geahlen, and A. Raman, "Measuring nanoscale viscoelastic parameters of cells directly from afm force-displacement curves," *Scientific reports*, vol. 7, no. 1, p. 1541, 2017.
[437] S. Santos, L. Guang, T. Souier, K. Gadelrab, M. Chiesa, and N. H. Thomson, "A method to provide rapid in situ determination of tip radius in dynamic atomic force microscopy," *Review of Scientific Instruments*, vol. 83, no. 4, 2012.
[438] E. Rull Trinidad, T. Gribnau, P. Belardinelli, U. Staufer, and F. Alijani, "Nonlinear dynamics for estimating the tip radius in atomic force microscopy," *Applied Physics Letters*, vol. 111, no. 12, 2017.
[439] P. M. Theiler, C. Ritz, and A. Stemmer, "Shortcomings of the derjaguin–muller–toporov model in dynamic atomic force microscopy," *Journal of Applied Physics*, vol. 130, no. 24, 2021.
[440] M. E. Galanko, A. Kochhar, G. Piazza, T. Mukherjee, and G. K. Fedder, "Cmos-mems resonant demodulator for near-zero-power rf wake-up receiver," in *2017 19th International Conference on Solid-State Sensors, Actuators and Microsystems (TRANSDUCERS)*, 2017: IEEE, pp. 86-89.
[441] A. Kochhar *et al.*, "Resonant microelectromechanical receiver," *Journal of Microelectromechanical Systems*, vol. 28, no. 3, pp. 327-343, 2019.
[442] Atmel, "Interface ic for 125 khz wake-up function ata5283 preliminary," *ATA5283 datasheet*.
[443] M. Chip, "Three-channel analog front-end device mcp2030," *MCP2030 datasheet*.
[444] Austriamicrosystems, "As3932 3d low frequency wakeup receiver," *AS3292 datasheet*.
[445] Q. Kang, Z. Xie, Y. Liu, and M. Zhou, "125khz wake-up receiver and 433mhz data transmitter for battery-less tpms," in *2017 IEEE 12th International Conference on ASIC (ASICON)*, 2017: IEEE, pp. 1101-1104.
[446] W. Xu, Z. Zou, J. Lei, Q. Tong, and W. Wu, "A 13. 8 μw wake-up receiver with 0.4 mvpp sensitivity for low frequency applications," in *2018 IEEE*

doi:10.6342/NTU202600018

International Conference on Integrated Circuits, Technologies and Applications (ICTA), 2018: IEEE, pp. 18-19.
[447] A. Mazzanti and P. Andreani, "Class-c harmonic cmos vcos, with a general result on phase noise," *IEEE Journal of Solid-State Circuits*, vol. 43, no. 12, pp. 2716-2729, 2008.
[448] J. Niu, Y. Ding, Z. Geng, L. Zhu, and H. Ding, "Patterns of regenerative milling chatter under joint influences of cutting parameters, tool geometries, and runout," *Journal of Manufacturing Science and Engineering*, vol. 140, no. 12, p. 121004, 2018.
[449] J.-Y. Chen, M. P. Flynn, and J. P. Hayes, "A fully integrated auto-calibrated superregenerative receiver," in *2006 IEEE International Solid State Circuits Conference-Digest of Technical Papers*, 2006: IEEE, pp. 1490-1499.
[450] J. P. Davim, *Modern machining technology: A practical guide*. Elsevier, 2011.
[451] A. Hajjaj, N. Jaber, S. Ilyas, F. Alfosail, and M. I. Younis, "Linear and nonlinear dynamics of micro and nano-resonators: Review of recent advances," *International Journal of Non-Linear Mechanics*, vol. 119, p. 103328, 2020.
[452] G. Chakraborty and N. Jani, "Nonlinear dynamics of resonant microelectromechanical system (mems): A review," *Mechanical Sciences*, pp. 57-81, 2021.
[453] G. Abeloos, L. Renson, C. Collette, and G. Kerschen, "Stepped and swept control-based continuation using adaptive filtering," *Nonlinear Dynamics*, vol. 104, no. 4, pp. 3793-3808, 2021.
[454] E. Bureau, F. Schilder, I. Santos, J. J. Thomsen, and J. Starke, "Experimental bifurcation analysis for a driven nonlinear flexible pendulum using control-based continuation."
[455] E. Bureau, F. Schilder, I. F. Santos, J. J. Thomsen, and J. Starke, "Experimental bifurcation analysis of an impact oscillator—tuning a non-invasive control scheme," *Journal of Sound and Vibration*, vol. 332, no. 22, pp. 5883-5897, 2013.
[456] M. Defoort, L. Rufer, L. Fesquet, and S. Basrour, "A dynamical approach to generate chaos in a micromechanical resonator," *Microsystems & nanoengineering*, vol. 7, no. 1, pp. 1-11, 2021.
[457] A. Gusso, R. L. Viana, A. C. Mathias, and I. L. Caldas, "Nonlinear dynamics and chaos in micro/nanoelectromechanical beam resonators actuated by two-sided electrodes," *Chaos, Solitons & Fractals*, vol. 122, pp. 6-16, 2019.
[458] D. Costa, V. Vaziri, E. Pavlovskaia, M. A. Savi, and M. Wiercigroch, "Switching between periodic orbits in impact oscillator by time-delayed feedback methods," *Physica D: Nonlinear Phenomena*, p. 133587, 2022.
[459] H. K. Lee, R. Melamud, S. Chandorkar, J. Salvia, S. Yoneoka, and T. W. Kenny, "Stable operation of mems oscillators far above the critical vibration amplitude in the nonlinear regime," *Journal of microelectromechanical systems*, vol. 20, no. 6, pp. 1228-1230, 2011.

doi:10.6342/NTU202600018

[460] Y. Liu, M. Wiercigroch, J. Ing, and E. Pavlovskaia, "Intermittent control of coexisting attractors," *Philosophical Transactions of the Royal Society A: Mathematical, Physical and Engineering Sciences,* vol. 371, no. 1993, p. 20120428, 2013.
[461] Z. Zhang, J. P. Chávez, J. Sieber, and Y. Liu, "Controlling coexisting attractors of a class of non-autonomous dynamical systems," *Physica D: Nonlinear Phenomena,* vol. 431, p. 133134, 2022.
[462] Y. Liu and J. P. Chavez, "Controlling coexisting attractors of an impacting system via linear augmentation," *Physica D: Nonlinear Phenomena,* vol. 348, pp. 1-11, 2017.
[463] J.-Y. Liu, V. Chalivendra, and W. Huang, "Finite element based contact analysis of radio frequency mems switch membrane surfaces," *Journal of Micromechanics and Microengineering,* vol. 27, no. 10, p. 105012, 2017.
[464] C. Bora *et al.*, "Multiscale roughness and modeling of mems interfaces," *Tribology Letters,* vol. 19, no. 1, pp. 37-48, 2005.
[465] A. Keyvani, H. Sadeghian, H. Goosen, and F. van Keulen, "Transient tip-sample interactions in high-speed afm imaging of 3d nano structures," in *Metrology, Inspection, and Process Control for Microlithography XXIX*, 2015, vol. 9424: SPIE, pp. 858-867.
[466] S. K. Janbahan, "Dynamics and control of atomic force microscopy," 2019.
[467] R. J. Monroe and S. W. Shaw, "Nonlinear transient dynamics of pendulum torsional vibration absorbers—part i: Theory," *Journal of Vibration and Acoustics,* vol. 135, no. 1, p. 011017, 2013.
[468] R. J. Monroe and S. W. Shaw, "On the transient response of forced nonlinear oscillators," *Nonlinear Dynamics,* vol. 67, pp. 2609-2619, 2012.
[469] Q. Jin, K. Zheng, and C. T.-C. Nguyen, "Push-pull resoswitch communication receiver," in *2023 Joint Conference of the European Frequency and Time Forum and IEEE International Frequency Control Symposium (EFTF/IFCS)*, 2023: IEEE, pp. 1-4.
[470] H. Jiang, Y. Liu, L. Zhang, and J. Yu, "Anti-phase synchronization and symmetry-breaking bifurcation of impulsively coupled oscillators," *Communications in Nonlinear Science and Numerical Simulation,* vol. 39, pp. 199-208, 2016.
[471] Y. Fu, H. Ouyang, and R. B. Davis, "Nonlinear dynamics and triboelectric energy harvesting from a three-degree-of-freedom vibro-impact oscillator," *Nonlinear Dynamics,* vol. 92, no. 4, pp. 1985-2004, 2018.
[472] C. Mastrangelo, "Suppression of stiction in mems," *MRS Online Proceedings Library (OPL),* vol. 605, p. 105, 1999.
[473] B. Bhushan, "Adhesion and stiction: Mechanisms, measurement techniques, and methods for reduction," *Journal of Vacuum Science & Technology B: Microelectronics and Nanometer Structures Processing, Measurement, and Phenomena,* vol. 21, no. 6, pp. 2262-2296, 2003.

doi:10.6342/NTU202600018

[474] Z. Yapu, "Stiction and anti-stiction in mems and nems," *Acta Mechanica Sinica,* vol. 19, no. 1, pp. 1-10, 2003.
[475] L. Haobing and F. Chollet, "Layout controlled one-step dry etch and release of mems using deep rie on soi wafer," *Journal of Microelectromechanical Systems,* vol. 15, no. 3, pp. 541-547, 2006.
[476] T. Abe, W. C. Messner, and M. L. Reed, "Effective methods to prevent stiction during post-release-etch processing," in *Proceedings IEEE Micro Electro Mechanical Systems. 1995*, 1995: IEEE, p. 94.
[477] J. W. Rogers and L. M. Phinney, "Process yields for laser repair of aged, stiction-failed, mems devices," *Journal of microelectromechanical systems,* vol. 10, no. 2, pp. 280-285, 2001.
[478] V. Gupta, R. Snow, M. C. Wu, A. Jain, and J.-c. Tsai, "Recovery of stiction-failed mems structures using laser-induced stress waves," *Journal of microelectromechanical systems,* vol. 13, no. 4, pp. 696-700, 2004.
[479] V. A. Hong *et al.*, "Overcoming stiction forces with resonant over-travel stops," in *2016 IEEE 29th International Conference on Micro Electro Mechanical Systems (MEMS)*, 2016: IEEE, pp. 47-50.
[480] H. Zuo and S. He, "Post-fabrication melting procedure with i-shaped beams for stiction-free release of 2-d surface-micromachined micromirrors equipped with repulsive-force actuators," *Journal of Microelectromechanical Systems,* vol. 27, no. 4, pp. 706-718, 2018.
[481] W. J. Bottega, *Engineering vibrations*. Crc Press, 2014.
[482] D. J. Inman, *Engineering vibration*.
[483] W. O. Davis, "Measuring quality factor from a nonlinear frequency response with jump discontinuities," *Journal of microelectromechanical systems,* vol. 20, no. 4, pp. 968-975, 2011.
[484] H.-Y. Chen, M.-H. Li, and S.-S. Li, "A new finding on nonlinear damping and stiffness of flexural mode capacitive mems resonators," in *2023 IEEE 36th International Conference on Micro Electro Mechanical Systems (MEMS)*, 2023: IEEE, pp. 526-529.
[485] M. Imboden, O. Williams, and P. Mohanty, "Nonlinear dissipation in diamond nanoelectromechanical resonators," *Applied Physics Letters,* vol. 102, no. 10, 2013.
[486] L. Catalini, M. Rossi, E. C. Langman, and A. Schliesser, "Modeling and observation of nonlinear damping in dissipation-diluted nanomechanical resonators," *Physical Review Letters,* vol. 126, no. 17, p. 174101, 2021.
[487] L. Catalini, Y. Tsaturyan, and A. Schliesser, "Soft-clamped phononic dimers for mechanical sensing and transduction," *Physical Review Applied,* vol. 14, no. 1, p. 014041, 2020.
[488] T. Kaisar, J. Lee, D. Li, S. W. Shaw, and P. X.-L. Feng, "Nonlinear stiffness and nonlinear damping in atomically thin mos2 nanomechanical resonators," *Nano Letters,* vol. 22, no. 24, pp. 9831-9838, 2022.

doi:10.6342/NTU202600018

[489] S. Kumar *et al.*, "Temperature-dependent nonlinear damping in palladium nanomechanical resonators," *Nano Letters*, vol. 21, no. 7, pp. 2975-2981, 2021.
[490] Z. Wang *et al.*, "Black phosphorus nanoelectromechanical resonators vibrating at very high frequencies," *Nanoscale*, vol. 7, no. 3, pp. 877-884, 2015.
[491] P. Zhang *et al.*, "Probing linear to nonlinear damping in 2d semiconductor nanoelectromechanical resonators toward a unified quality factor model," *Nano Letters*, vol. 23, no. 20, pp. 9375-9382, 2023.
[492] W. C. Messner, "The last jedi: Step response identification of overdamped second order systems," in *2018 Annual American Control Conference (ACC)*, 2018: IEEE, pp. 368-373.
[493] W. C. Messner, "The t26. 4 method for step response identification of overdamped 2 nd order systems," in *2023 American Control Conference (ACC)*, 2023: IEEE, pp. 277-282.
[494] R. Morgan, "Linearization and stability analysis of nonlinear problems," *Rose-Hulman Undergraduate Mathematics Journal*, vol. 16, no. 2, p. 5, 2015.
[495] R. H. Rand, "Lecture notes on nonlinear vibrations," 2012.
[496] R. Sujith and S. A. Pawar, "An introduction to dynamical systems theory," in *Thermoacoustic instability: A complex systems perspective*: Springer, 2021, pp. 31-85.
[497] S. Sastry, *Nonlinear systems: Analysis, stability, and control*. Springer Science & Business Media, 2013.
[498] A. Fuchs, "Dynamical systems in one and two dimensions: A geometrical approach," in *Nonlinear dynamics in human behavior*: Springer, 2011, pp. 1-33.
[499] D. K. Misra, *Radio-frequency and microwave communication circuits: Analysis and design*. John Wiley & Sons, 2012.
[500] K. Tanaka, R. Kihara, A. Sánchez-Amores, J. Montserrat, and J. Esteve, "Parasitic effect on silicon mems resonator model parameters," *Microelectronic engineering*, vol. 84, no. 5-8, pp. 1363-1368, 2007.
[501] H. D. Young, R. A. Freedman, T. Sandin, and A. L. Ford, *University physics*. Addison-Wesley Reading, MA, 1996.
[502] P. W. Anderson, "More is different: Broken symmetry and the nature of the hierarchical structure of science," *Science*, vol. 177, no. 4047, pp. 393-396, 1972.
[503] J. Achenbach, *Wave propagation in elastic solids*. Elsevier, 2012.
[504] K. F. Graff, *Wave motion in elastic solids*. Courier Corporation, 2012.
[505] F. T. Ulaby and U. Ravaioli, *Fundamentals of applied electromagnetics*. Pearson Upper Saddle River, NJ, 2015.
[506] N. S. Podolefsky and N. D. Finkelstein, "Use of analogy in learning physics: The role of representations," *Physical Review Special Topics—Physics Education Research*, vol. 2, no. 2, p. 020101, 2006.
[507] E. K. Miller, "Electromagnetics without equations," *IEEE Potentials*, vol. 20, no. 2, pp. 16-20, 2001.

doi:10.6342/NTU202600018

[508] J. R. Tessman and J. T. Finnell Jr, "Electric field of an accelerating charge," *American Journal of Physics*, vol. 35, no. 6, pp. 523-527, 1967.
[509] E. K. Miller, *Charge acceleration and the spatial distribution of radiation emitted by antennas and scatterers*. Institution of Engineering and Technology, 2022.
[510] D. A. Frickey, "Conversions between s, z, y, h, abcd, and t parameters which are valid for complex source and load impedances," *IEEE Transactions on microwave theory and techniques*, vol. 42, no. 2, pp. 205-211, 1994.
[511] Z. Instruments. "Hf2ta current amplifier data sheet - hf2 user manual." https://docs.zhinst.com/hf2_user_manual/ta_datasheet.html (accessed July 6, 2025).
[512] S. R. Systems. "Low-noise current preamplifier sr570 — dc to 1 mhz current preamplifier." https://www.thinksrs.com/downloads/pdfs/catalog/SR570c.pdf (accessed July 6, 2025).
[513] A. Rumiantsev and N. Ridler, "Vna calibration," *IEEE Microwave magazine*, vol. 9, no. 3, pp. 86-99, 2008.
[514] D. Rytting, "Network analyzer error models and calibration methods," *White Paper, September*, 1998.
[515] S. Ilyas, F. K. Alfosail, and M. I. Younis, "On the response of mems resonators under generic electrostatic loadings: Theoretical analysis," *Nonlinear Dynamics*, vol. 97, no. 2, pp. 967-977, 2019.
[516] C. Acar and A. M. Shkel, "An approach for increasing drive-mode bandwidth of mems vibratory gyroscopes," *Journal of microelectromechanical systems*, vol. 14, no. 3, pp. 520-528, 2005.
[517] G. Pillai and S.-S. Li, "Piezoelectric mems resonators: A review," *IEEE Sensors Journal*, vol. 21, no. 11, pp. 12589-12605, 2020.
[518] R. Lu, M.-H. Li, Y. Yang, T. Manzaneque, and S. Gong, "Accurate extraction of large electromechanical coupling in piezoelectric mems resonators," *Journal of Microelectromechanical Systems*, vol. 28, no. 2, pp. 209-218, 2019.
[519] Y. Wang *et al.*, "Parasitic analysis and π-type butterworth-van dyke model for complementary-metal-oxide-semiconductor lamb wave resonator with accurate two-port y-parameter characterizations," *Review of Scientific Instruments*, vol. 87, no. 4, 2016.
[520] Y. Sabry, M. Medhat, B. Saadany, T. Bourouina, and D. Khalil, "Parameter extraction of mems comb-drive near-resonance equivalent circuit: Physically-based technique for a unique solution," *Journal of Micro/Nanolithography, MEMS, and MOEMS*, vol. 11, no. 2, pp. 021205-021205, 2012.
[521] J. E.-Y. Lee and A. A. Seshia, "Direct parameter extraction in feedthrough-embedded capacitive mems resonators," *Sensors and Actuators A: Physical*, vol. 167, no. 2, pp. 237-244, 2011.
[522] A. T. Lin, J. E. Lee, J. Yan, and A. A. Seshia, "Enhanced transduction methods for electrostatically driven mems resonators," in *TRANSDUCERS 2009-2009*

doi:10.6342/NTU202600018

International Solid-State Sensors, Actuators and Microsystems Conference, 2009: IEEE, pp. 561-564.
[523] K. Wang and C.-C. Nguyen, "High-order medium frequency micromechanical electronic filters," *Journal of Microelectromechanical systems*, vol. 8, no. 4, pp. 534-556, 1999.
[524] Nguyen and Howe, "Quality factor control for micromechanical resonators," in *1992 International Technical Digest on Electron Devices Meeting*, 1992: IEEE, pp. 505-508.
[525] F. D. Bannon, J. R. Clark, and C.-C. Nguyen, "High-q hf microelectromechanical filters," *IEEE Journal of solid-state circuits*, vol. 35, no. 4, pp. 512-526, 2002.
[526] 近野正, 中村尚, 日下部千春, and 富川義朗, "線形機械振動系の電気回路網による類推解析," *日本機械学会誌*, vol. 66, no. 531, pp. 496-508, 1963.
[527] M. Konno and H. Nakamura, "Equivalent electrical network for the transversely vibrating uniform bar," *The Journal of the Acoustical Society of America*, vol. 38, no. 4, pp. 614-622, 1965.
[528] M. Konno, S. Oyama, and Y. Tomikawa, "Equivalent electrical networks for transversely vibrating bars and their applications," *IEEE Transactions on Sonics and Ultrasonics*, vol. 26, no. 3, pp. 191-201, 1979.
[529] S.-S. Li, M. U. Demirci, Y.-W. Lin, Z. Ren, and C.-C. Nguyen, "Bridged micromechanical filters," in *Proceedings of the 2004 IEEE International Frequency Control Symposium and Exposition, 2004.*, 2004: IEEE, pp. 280-286.
[530] L. D. Gabbay, "Computer aided macromodeling for mems," Massachusetts Institute of Technology, 1998.
[531] L. Del Tin, "Reduced-order modelling, circuit-level design and soi fabrication of microelectromechanical resonators," 2007.
[532] N. F. Bonet, D. G. Cava, and M. Vélez, "Quartz crystal microbalance and atomic force microscopy to characterize mimetic systems based on supported lipids bilayer," *Frontiers in Molecular Biosciences*, vol. 9, p. 935376, 2022.
[533] M. Robinson and J. Clegg, "Improved determination of q-factor and resonant frequency by a quadratic curve-fitting method," *IEEE Transactions on Electromagnetic Compatibility*, vol. 47, no. 2, pp. 399-402, 2005.
[534] K. Naeli and O. Brand, "An iterative curve fitting method for accurate calculation of quality factors in resonators," *Review of scientific instruments*, vol. 80, no. 4, 2009.
[535] V. Agmo Hernández, "An overview of surface forces and the dlvo theory," *ChemTexts*, vol. 9, no. 4, p. 10, 2023.
[536] V. I. Babitsky, *Theory of vibro-impact systems and applications*. Springer Science & Business Media, 2013.
[537] S. Merdol and Y. Altintas, "Multi frequency solution of chatter stability for low immersion milling," *J. Manuf. Sci. Eng.*, vol. 126, no. 3, pp. 459-466, 2004.

doi:10.6342/NTU202600018

[538] Y. Altintas and M. Weck, "Chatter stability of metal cutting and grinding," *CIRP annals*, vol. 53, no. 2, pp. 619-642, 2004.
[539] B. Guo and J. V. Ringwood, "Parametric study of a vibro-impact wave energy converter," *IFAC-PapersOnLine*, vol. 53, no. 2, pp. 12283-12288, 2020.
[540] L. Bu, E. Arroyo, and A. A. Seshia, "Frequency combs: A new mechanism for mems vibration energy harvesters," in *2021 21st International Conference on Solid-State Sensors, Actuators and Microsystems (Transducers)*, 2021: IEEE, pp. 136-139.
[541] T. Zhang and A. A. Seshia, "A mems frequency comb energy harvester," *Journal of Microelectromechanical Systems*, vol. 32, no. 6, pp. 516-518, 2023.
[542] H. M. Hussein, S. Kim, M. Rinaldi, A. Alù, and C. Cassella, "Passive frequency comb generation at radiofrequency for ranging applications," *Nature communications*, vol. 15, no. 1, p. 2844, 2024.
[543] A. Donmez, H. Herath, and H. Cho, "Theoretical insights into 1: 2 and 1: 3 internal resonance for frequency stabilization in nonlinear micromechanical resonators," *Nonlinear Dynamics*, pp. 1-20, 2025.
[544] H. Mouharrar *et al.*, "Generation of soliton frequency combs in nems," *Nano Letters*, vol. 24, no. 35, pp. 10834-10841, 2024.
[545] J. Wu, P. Song, S. Zang, Z. Mao, W. Zhang, and L. Shao, "Self-injection locked and phase offset-free micromechanical frequency combs," *Physical Review Letters*, vol. 134, no. 10, p. 107201, 2025.
[546] T. Y. Chen, C. P. Tsai, and W. C. Li, "1: 6 internal resonance in cmos-mems multiple-stepped cc-beam resonators," in *2022 IEEE 35th International Conference on Micro Electro Mechanical Systems Conference (MEMS)*, 2022: IEEE, pp. 196-199.
[547] T.-Y. Chen, C.-P. Tsai, and W.-C. Li, "Constructing micromechanical frequency combs in bifurcating attractor branches for event triggered sensors," in *2023 22nd International Conference on Solid-State Sensors, Actuators and Microsystems (Transducers)*, 2023: IEEE, pp. 461-464.
[548] T.-Y. Chen, C.-P. Tsai, and W.-C. Li, "A cmos-mems ultrasensitive thermometer using internal resonance iuduced frequency combs," in *2023 IEEE 36th International Conference on Micro Electro Mechanical Systems (MEMS)*, 2023: IEEE, pp. 185-188.
[549] T.-Y. Chen and W.-C. Li, "True random number generation in nonlinear internal-resonating mems resonators," *IEEE Electron Device Letters*, vol. 45, no. 1, pp. 116-119, 2023.
[550] T.-Y. Chen and W.-C. Li, "Bifurcation generated true random numbers in nonlinear micromechanical resonators," in *2024 IEEE 37th International Conference on Micro Electro Mechanical Systems (MEMS)*, 2024: IEEE, pp. 533-536.

doi:10.6342/NTU202600018

[551] T.-Y. Chen and W.-C. Li, "A micromechanical frequency comb-based binary phase shift keying demodulator," in *2024 IEEE Ultrasonics, Ferroelectrics, and Frequency Control Joint Symposium (UFFC-JS)*, 2024: IEEE, pp. 1-2.
[552] T.-Y. Chen and W.-C. Li, "Cmos-mems physical unclonable functions based on unbalanced bimodal frequency combs," in *2025 IEEE 38th International Conference on Micro Electro Mechanical Systems (MEMS)*, 2025: IEEE, pp. 137-140.
[553] K. S. Bhosale and S.-S. Li, "Multi-harmonic phononic frequency comb generation in capacitive cmos-mems resonators," *Applied Physics Letters*, vol. 124, no. 16, 2024.
[554] J. Bienstman, R. Puers, and J. Vandewalle, "Periodic and chaotic behaviour of the autonomous impact resonator," in *Proceedings MEMS 98. IEEE. Eleventh Annual International Workshop on Micro Electro Mechanical Systems. An Investigation of Micro Structures, Sensors, Actuators, Machines and Systems (Cat. No. 98CH36176*, 1998: IEEE, pp. 562-567.
[555] L. Ruzziconi, N. Jaber, A. Z. Hajjaj, and M. I. Younis, "Subcombination internal resonance of the additive type in the response dynamics of micromachined resonators crossing the impacting threshold," *Chaos, Solitons & Fractals*, vol. 189, p. 115615, 2024.
[556] X. Wang *et al.*, "Frequency comb in a parametrically modulated micro-resonator," *Acta Mechanica Sinica*, vol. 38, no. 10, p. 521596, 2022.
[557] S. Moss, A. Barry, I. Powlesland, S. Galea, and G. P. Carman, "A low profile vibro-impacting energy harvester with symmetrical stops," *Applied Physics Letters*, vol. 97, no. 23, 2010.
[558] N. D. Mermin, "Could feynman have said this?," *Physics Today*, vol. 57, no. 5, pp. 10-11, 2004.
[559] M. H. Holmes, *Introduction to perturbation methods*. Springer Science & Business Media, 2012.
[560] A. H. Nayfeh, *Perturbation methods*. John Wiley & Sons, 2024.
[561] S. Hu and A. Raman, "Analytical formulas and scaling laws for peak interaction forces in dynamic atomic force microscopy," *Applied Physics Letters*, vol. 91, no. 12, 2007.
[562] A.-C. Wong and C.-C. Nguyen, "Micromechanical mixer-filters (" mixlers")," *Journal of Microelectromechanical Systems*, vol. 13, no. 1, pp. 100-112, 2004.
[563] A. Brenes, J. Juillard, F. V. Dos Santos, and A. Bonnoit, "Characterization of mems resonators via feedthrough de-embedding of harmonic and subharmonic pulsed-mode response," *Sensors and Actuators A: Physical*, vol. 229, pp. 211-217, 2015.
[564] X. Wang, R. Huan, W. Zhu, Z. Shi, X. Wei, and G. Cai, "Amplitude region for triggering frequency locking in internal resonance response of two nonlinearly coupled micro-resonators," *International Journal of Non-Linear Mechanics*, vol. 130, p. 103673, 2021.

doi:10.6342/NTU202600018

[565] G. Vidal-Álvarez, F. Torres, N. Barniol, and O. Gottlieb, "The influence of the parasitic current on the nonlinear electrical response of capacitively sensed cantilever resonators," *Journal of Applied Physics,* vol. 117, no. 15, 2015.
[566] C. Zhao, G. Sobreviela, M. Pandit, S. Du, X. Zou, and A. Seshia, "Experimental observation of noise reduction in weakly coupled nonlinear mems resonators," *Journal of Microelectromechanical Systems,* vol. 26, no. 6, pp. 1196-1203, 2017.
[567] Y. Xu *et al.*, "Frequency stabilization in a pseudo-linear micromechanical parametric oscillator," *International Journal of Mechanical Sciences,* vol. 280, p. 109610, 2024.

doi:10.6342/NTU202600018